

A NUMERICAL INVESTIGATION OF THE COMPRESSIBLE REACTING MIXING LAYER

By
Olivier H. Planché
and William C. Reynolds

Prepared with the support of the
Air Force Office of Scientific Research
under contract 90-0151-C



Report No. TF-56

Thermosciences Division
Department of Mechanical Engineering
Stanford University
Stanford, California 94305

October 1992

A numerical investigation of the compressible reacting mixing layer

by

Olivier H. Planché and William C. Reynolds

Prepared with the support of the
Air Force Office of Scientific Research
under contract 90-0151-C

Report No. TF-56

Thermosciences Division
Department of Mechanical Engineering
Stanford University
Stanford, California 94305

October 1992

©Copyright by O.H. Planche 1992
All Rights Reserved

Acknowledgements

The authors would like to acknowledge the financial support from the Air Force Office of Scientific Research under contract 90-0151-C and the computer facilities provided by Central Computing Facility and National Aerodynamic Simulation at NASA-Ames Research Center. Other important facility support was provided by the NASA/Stanford Center for Turbulence Research. The authors would also like to acknowledge the assistance provided by a CIFRE fellowship from SNECMA that supported O.H.P.

Special thanks are due to Dr. N.N. Mansour and Professor M.G. Mungal for their helpful input throughout this work, and to Professor S. Lele for his comments on the draft of this report. Dr. A.A. Wray and Dr. R.S. Rogallo provided precious help with the implementation of the direct numerical solvers on the iPSC860. We would like to thank our friends and colleagues at Stanford for their help and encouragement. The authors want to thank Mr. T.R. Bewley and Mr. B.E. Mitchell for carefully proof-reading the manuscript.

The authors would also like to thank Dr. D.S. Shin and Professor J.H. Ferziger for many useful discussions and ideas. The permission of Mr. M. Miller, Dr. B. Yip and Professor C.T. Bowman to reprint some of their experimental results is also gratefully acknowledged.

Abstract

An important aspect of supersonic combustion is the proper mixing of fuel and oxidizer. Here, linear stability analysis and direct numerical simulations (DNS) are used to examine the effect of heat release and compressibility on mixing in high-speed mixing layers. The results suggest that mixing of fuel and oxidizer by large-scale engulfment of fluid from both sides of a mixing layer does not occur at high Mach numbers.

Linear stability analysis indicates that the existence of two maxima on the mean density weighted vorticity profile ($\rho d\bar{u}/dy$) leads to the existence of two distinct "outer modes", each associated with one of the free streams. Each mode mixes only fresh gas from this stream with product from the middle of the layer, and its phase velocity is comparable with the mean velocity on its side of the reaction zone. Increasing heat release is shown to reduce the obliquity of the outer modes and to increase the spreading angle of the layer. The usual convective Mach number is inappropriate for the outer modes. Instead, the "flame convective Mach numbers" are introduced and shown to be preferable parameters for correlating compressibility effects on the outer modes. The possibility of controlling the mixing by judicious positioning of the flame sheet is also suggested by the analysis.

DNS of the temporally-developing mixing layer were run both on the Cray Y-MP and on the Intel iPSC860 Hypercube to confirm linear stability results and to study non-linear effects related to growth and pairing. It is shown that the reacting mixing layer behaves as two independent colayers arising from the outer modes, with mixing occurring between fuel and product on one side of the layer and between oxidizer and product on the other side. The reaction zone remains approximately plane, with little creation of new flame surface. The development of each outer mode is shown to be governed by the baroclinic torque. The familiar vortex roll-up and pairing seen in low-speed mixing layer are not observed. Instead, it is shown that the growth of each outer mode modifies of the mean density and baroclinic torque profiles, which in turn causes the decay of this outer mode and the emergence of new outer modes of larger scale.

The transition to turbulence was simulated and shown to preserve the two colayers. Transition arises from the rapid growth of streamwise vortices, and strongly increases the total reaction rate. The resulting turbulent mixing layer appears dominated by large fast and slow independent outer eddies and smaller-scale streamwise vortices. Comparison with ongoing experiments are presented.

Table of Contents

	Page
Acknowledgements	iii
Abstract	v
Table of Contents	vii
List of Tables	xiii
List of Figures	xiv
Nomenclature	xxx
1 Introduction	1
1.1 Motivation	1
1.2 Survey of previous observations in incompressible mixing layers ..	2
1.3 Survey of previous studies of compressible or reacting mixing layers	4
1.3.1 Structure of the compressible mixing layer	4
1.3.2 Compressibility effects on mixing	7
1.4 Objectives and Overview	8
2 Linear stability analysis	11
2.1 Introduction	11
2.1.1 Background and motivation	11
2.1.2 Chapter outline	14
2.2 Formulation	15
2.2.1 Solution for the mean flow	16
2.2.2 Equation of the perturbations	21
2.3 Necessary condition of instability	24
2.3.1 Incompressible case	24
2.3.2 Compressible case	25

2.4	Results	26
2.4.1	Existence of multiple instability modes	26
2.4.2	Spatial analysis of these instability modes	27
2.4.2.1	No heat release	27
2.4.2.2	Moderate heat release	29
2.4.2.3	High heat release	30
2.4.3	Influence of the modification of the mean profile with M_c on the linear stability results	31
2.4.3.1	No heat release $\Theta = 0$	31
2.4.3.2	Moderate heat release $\Theta = 1$	32
2.4.3.3	High heat release $\Theta = 4.85$	32
2.4.4	Flame convective Mach numbers	33
2.4.4.1	Formulation	33
2.4.4.2	Validation of the flame convective Mach numbers	35
2.4.5	Obliquity of the disturbance waves	36
2.4.5.1	No heat release	37
2.4.5.2	Small heat release ($\Theta = 0.5$)	38
2.4.5.3	Moderate heat release ($\Theta = 1$)	39
2.4.5.4	High heat release cases ($\Theta = 2$ and $\Theta = 4.85$)	41
2.4.5.5	Conclusion	42
2.4.6	Effect of the magnitude of the heat release	42
2.4.7	Effect of the position of the flame zone	45
2.5	Comparison with experiments	46
2.5.1	Comparison to Stanford experiments	46
2.5.2	Comparison to Caltech experiments	48
2.6	Eigenfunctions	49
2.7	Absolute versus convective instability	53
2.7.1	Formulation and resolution of the problem in the Fourier space .	53

2.7.2	Transformation of the Fourier solution to the physical space	56
2.7.2.1	Integration over the ω contour	56
2.7.2.2	Integration over the α contour	58
2.7.3	Absolute or convective instability	59
2.8	Chapter summary	61
3	Numerical method for DNS	63
3.1	Equations	63
3.2	Time advancement	66
3.3	Evaluation of the partial derivatives and boundary conditions	68
3.3.1	Partial derivatives in x and z using spectral methods in SC	68
3.3.2	Partial derivatives in x and z using PLC	69
3.3.3	Inflow and outflow boundary conditions in PLC	70
3.4	Evaluation of the partial derivatives and free stream boundary conditions in the cross-stream direction	74
3.5	Initialization of the temporal simulation	76
3.6	Implementation of SC on the Hypercube	78
3.6.1	Motivation	78
3.6.2	Management of data on the Cray Y-MP	79
3.6.3	Management of data on the iPSC860	80
3.6.4	Performances comparison between Y-MP and iPSC860	82
3.6.5	Conclusions	83
4	2-D temporal direct numerical simulation	85
4.1	Survey of previous DNS of reacting mixing layers	87
4.2	Review of the low Mach number, low heat release instability mode	87
4.2.1	Overview of a low Mach number, low heat release mode	87
4.2.2	Interaction between a central mode and its central subharmonics	89
4.2.3	Mean profile and time history of various quantities for a typical central mode	90

4.3	Overview of one slow compressible outer mode	92
4.3.1	Reynolds number effects	92
4.3.2	Two-dimensional structure	94
4.3.3	Surface plot and PDF of the mixture fraction	97
4.3.4	Mean temperature and reaction rate profiles	98
4.3.5	Saturation and decay of the compressible slow outer mode	99
4.3.6	Effect of the evolution of the mean $\bar{\rho} d\bar{u}/dy$ profile on the linear stability of the layer	101
4.3.7	Decay of the initial slow outer mode and growth of a new slow outer mode at $Re = 8000$	103
4.3.8	Recapitulation of section 4.3.	104
4.4	Absence of interaction between the fast and the slow outer modes .	104
4.5	Influence of the Damköhler number on the structure of the layer ..	106
4.6	Overview of the instability modes of the low Mach number reacting mixing layer	108
4.6.1	Simulation initialized with the fast and the slow outer modes ...	109
4.6.2	Simulation initialized with the central mode	109
4.6.3	Conclusion of section 4.6	111
4.7	Interaction of the outer modes with their subharmonics	111
4.7.1	Influence of the subharmonic amplitude	113
4.7.2	Influence of the initial relative phase	114
4.7.3	Simulation initialized with the fast and slow outer modes and their fast and slow subharmonics	116
4.7.4	Conclusion of section 4.7.	118
4.8	Comparison to experiment	119
4.8.1	2-D structure from DNS	119
4.8.2	Time history and statistics	122
4.8.3	Experimental results	123

4.9	Summary of chapter 4	125
5	3-D temporal direct numerical simulation	127
5.1	Survey of previous results concerning the transition in incompressible mixing layers	129
5.2	Pretransition structures at early time	132
5.2.1	Streamwise vorticity before transition	133
5.2.2	Cross-stream vorticity before transition	134
5.2.3	Spanwise vorticity before transition	135
5.2.4	Mixture fraction, pressure and reaction rate contours before transition	137
5.2.5	Statistics before transition	137
5.2.6	Conclusion	139
5.3	Transition to turbulence	140
5.3.1	Streamwise and cross-stream vorticity during transition	141
5.3.2	Spanwise vorticity during transition	142
5.3.3	Statistics during transition	143
5.4	Final time	145
5.4.1	Mixture fraction and reaction rate contours after transition	145
5.4.2	Streamwise and cross-stream vorticity after transition	146
5.4.3	Spanwise vorticity after transition	147
5.4.4	Statistics after transition	148
5.5	Influence of the mixing transition on the temperature and reaction rates	149
5.6	Summary of chapter 5	151
6	Conclusion	155
6.1	Linear stability analysis	156
6.2	2-D temporal DNS	157
6.3	3-D temporal DNS	158

A	Application of the Tau method to the stability analysis	161
A.1	Chebyshev transformation	162
A.2	Resolution of the eigenvalue problem	164
B	2-D spatial simulations	165
C	Flow regime	169
D	Archives	171
D.1	Linear stability analysis code	171
D.2	PLC code	171
D.3	SC code	174
D.4	Plotting program	177
	References	179

List of tables

Table

2.1.	Influence of the fuel equivalence ratio on the flame sheet location and on the flame convective Mach numbers	46
2.2.	New growth rate model for compressible reacting mixing layers	48
2.3.	Influence of M_c , \bar{T}_f and \bar{T}_2 on the absolute growth rate of the layer	60
3.1.	Wavenumbers α , temporal amplification rates ω_i and velocities c_r of the 2-D incompressible eigenmodes used in the simulations	78
3.2.	Wavenumbers α , temporal amplification rates ω_i and velocities c_r of the 2-D compressible eigenmodes used in the simulations	178
3.3.	Hypercube activity costs (seconds) for a 256×1024 2-D simulation vs. number of processors used	82
3.4.	Hypercube activity costs (seconds) for a 256×1024 2-D simulation vs. pencil size used	83
4.1.	Energy flux carried away by the radiating pressure waves in the fast and in the slow free streams	96
4.2.	Experimental conditions for the PLIF images shown on figures 4.59 to 4.61. Stanford experiment	124
B.1.	Parameters used in the 2-D spatial simulations	155

List of figures

Table

2.1	Mean Flow Configuration	189
2.2	Comparison of the mean species profiles (left) and temperature profiles (right) calculated using the self-similar solution to the solution obtained by solving the complete compressible finit-chemistry boundary layer equations	189
2.3	Comparison of the mean density-weighted vorticity profiles calculated using the self-similar solution to the solution obtained by solving the complete compressible finite-chemistry boundary layer equations	190
2.4	Mean temperature (left) and density weighted vorticity ($\bar{\rho} d\bar{u}/dy$) (right) profiles of the compressible mixing layer without heat release	190
2.5	Compressibility effects on the amplification rate and phase speed of the central mode of the compressible mixing layer without heat release. The mean profile is dependent on M_c	191
2.6	Compressibility effects on the spatial amplification rate of the fast outer mode of the compressible mixing layer without heat release ($M_c > 1$)	191
2.7	Compressibility effects on the phase speed of the fast outer mode of the compressible mixing layer without heat release ($M_c > 1$)	192
2.8	Mean temperature (left) and density weighted vorticity ($\bar{\rho} d\bar{u}/dy$) (right) profiles of the compressible mixing layer with heat release ($\Theta = 1$).	192
2.9	Amplification rate and phase speed of the fast outer mode of the compressible mixing layer with heat release ($\Theta = 1$).	193
2.10	Amplification rate and phase speed of the slow outer mode of the compressible mixing layer with heat release ($\Theta = 1$)	193

2.11	Mean temperature (left) and density-weighted vorticity ($\bar{\rho} d\bar{u}/dy$) (right) profiles of the compressible mixing layer with heat release ($\Theta = 4.85$).	194
2.12	Amplification rate and phase speed of the fast outer mode of the compressible mixing layer with heat release ($\Theta = 4.85$)	194
2.13	Amplification rate and phase speed of the slow outer mode of the compressible mixing layer with heat release ($\Theta = 4.85$)	195
2.14	Compressibility effects on the amplification rate and phase speed of the central mode of the compressible mixing layer without heat release.	195
2.15	Compressibility effects on the amplification rate and phase speed of the fast outer mode the compressible mixing layer with heat release ($\Theta = 1$. Mean profile corresponding to $M_c = 0.01$)	196
2.16	Compressibility effects on the amplification rate and phase speed of the slow outer mode the compressible mixing layer with heat release ($\Theta = 1$. Mean profile corresponding to $M_c = 0.01$)	196
2.17	Compressibility effects on the amplification rate and phase speed of the fast outer mode of the mixing layer with high heat release ($\Theta = 4.85$. Mean profile corresponding to $M_c = 0.01$)	197
2.18	Compressibility effects on the amplification rate and phase speed of the slow outer mode of the mixing layer with high heat release ($\Theta = 4.85$. Mean profile corresponding to $M_c = 0.01$)	197
2.19	Compressibility effects on the amplification of various 2-D instability modes for various heat release (H) (mean profile at $M_c = 0.01$).	198
2.20	Validation of the flame convective Mach numbers.	198
2.21	Mach number effects on the obliquity of the central mode of the compressible mixing layer without heat release ($\Theta = 0$): Amplification rates at various obliquities.	199
2.22	Mach number effects on the obliquity of the central mode of the compressible mixing layer without heat release ($\Theta = 0$): Phase speeds at various obliquities.	199
2.23	Mach number effects on the obliquity of the instability modes of	

the compressible mixing layer without heat release ($\Theta = 0$). Left: amplification rate of the fast outer mode. Right: amplification rate of the slow outer mode.	199
2.24 Mach number effects on the obliquity of the instability modes of the compressible mixing layer with low heat release ($\Theta = 0.50$). Left: amplification rate of the fast instability mode. Right: amplification rate of the slow instability mode.	200
2.25 Mach number effects on the obliquity of the instability modes of the compressible mixing layer with low heat release ($\Theta = 0.50$). Left: phase speed of the fast instability mode. Right: phase speed of the slow instability mode.	200
2.26 Mach number effects on the obliquity of the instability modes of the compressible mixing layer with low heat release ($\Theta = 0.50$). Top: wavenumber of the fast instability mode. Bottom: wavenumber of the slow instability mode.	201
2.27 Mach number effects on the obliquity of the instability modes of the compressible mixing layer with moderate heat release ($\Theta = 1$). Left: amplification rate of the fast instability mode. Right: amplification rate of the slow instability mode.	202
2.28 Mach number effects on the obliquity of the instability modes of the compressible mixing layer with moderate heat release ($\Theta = 1$). Left: phase speed of the fast instability mode. Right: phase speed of the slow instability mode.	202
2.29 Mach number effects on the obliquity of the instability modes of the compressible mixing layer with moderate heat release ($\Theta = 1$). Left: wavenumber of the fast instability mode. Right: wavenumber of the slow instability mode.	203
2.30 Comparison of compressibility effects on the amplification rate of the fast (left) and slow (right) outer modes when the profile is changed with M_c or kept equal to the profile at $M_c = 0.01$ ($\Theta = 1$)	203
2.31 Comparison of compressibility effects on the phase speed of the fast (left) and slow (right) outer modes when the profile is changed with M_c or kept equal to the profile at $M_c = 0.01$ ($\Theta = 1$)	204

2.32	Comparison of compressibility effects on the wavenumber of the fast (left) and slow (right) outer modes when the profile is changed with M_c or kept equal to the profile at $M_c = 0.01$ ($\Theta = 1$)	204
2.33	Mach number effects on the obliquity of the instability modes of the compressible mixing layer with high heat release ($\Theta = 2$). Left: amplification rate of the fast instability mode. Right: amplification rate of the slow instability mode.	205
2.34	Mach number effects on the obliquity of the instability modes of the compressible mixing layer with high heat release ($\Theta = 2$). Left: phase speed of the fast instability mode. Right: phase speed of the slow instability mode.	205
2.35	Mach number effects on the obliquity of the instability modes of the compressible mixing layer with high heat release ($\Theta = 2$). Left: wavenumber of the fast instability mode. Right: wavenumber of the slow instability mode.	206
2.36	Mach number effects on the obliquity of the instability modes of the compressible mixing layer with high heat release ($\Theta = 4.85$). Left: amplification rate of the fast instability mode. Right: amplification rate of the slow instability mode.	206
2.37	Mach number effects on the obliquity of the instability modes of the compressible mixing layer with high heat release ($\Theta = 4.85$). Left: phase speed of the fast instability mode. Right: phase speed of the slow instability mode.	1207
2.38	Mach number effects on the obliquity of the instability modes of the compressible mixing layer with high heat release ($\Theta = 4.85$). Left: wavenumber of the fast instability mode. Right: wavenumber of the slow instability mode.	207
2.39	Left: Comparison of heat release effects on the amplification rates of the central and fast outer modes at $M_c = 0.01$. Right: same for the central and slow outer modes	208
2.40	Left: Comparison of heat release effects on the phase speeds of the central and fast outer modes at $M_c = 0.01$. Right: same for the central and slow outer modes	208

2.41	Top: Comparison of heat release effects on the wavenumbers of the central and fast outer modes at $M_c = 0.01$. Bottom: same for the central and slow outer modes	209
2.42	Left: Comparison of heat release effects on the amplification rate of the central and fast outer modes at $M_c = 1.20$. Right: Same for the central and slow outer modes	210
2.43	Left: Comparison of heat release effects on the wavenumber of the central and fast outer modes at $M_c = 1.20$. Right: Same for the central and slow outer modes	210
2.44	Comparison of heat release effects on the wavenumbers of the central and slow outer modes at $M_c = 1.20$. Right: Same for the central and slow outer modes	211
2.45	Top: Influence of the fuel-equivalence ratio on the mean density-weighted vorticity profile ($\bar{\rho}d\bar{u}/dy$). Bottom:Influence of the fuel equivalence ratio on the mean vorticity profile ($d\bar{u}/dy$). ($M_c = 0.01$)	211
2.46	Influence of the fuel-equivalence ratio on the amplification rates of the fast (left) and slow (right) outer modes. ($M_c = 0.01$)	212
2.47	Influence of the fuel equivalence ratio on the phase speeds of the fast (left) and slow (right) outer modes. ($M_c = 0.01$)	212
2.48	Influence of the fuel-equivalence ratio on the amplification rates of the fast (left) and slow (right) outer modes. ($M_c = 1$)	213
2.49	Influence of the fuel-equivalence ratio on the phase speeds of the fast (left) and slow (right) outer modes. ($M_c = 1$)	213
2.50	Comparison to experiment: Mean density-weighted vorticity profiles for various heat releases ($\bar{T}_2 = 0.21$, $M_c = 0.8$, $\bar{u}_2 = 0.11$)	214
2.51	Amplification rate of the slow instability mode versus frequency for the low heat release case. ($\Theta = 0.142$). No fast mode present.	214
2.52	Amplification rates of the fast and slow instability modes versus frequency for the medium heat release case. ($\Theta = 0.356$). Left: fast outer mode; Right: slow outer mode	215
2.53	Phase speeds of the fast and slow instability modes versus frequency for the medium heat release case. ($\Theta = 0.356$)	215

2.54	Amplification rates of the fast and slow instability mode versus frequency for the high heat release case. ($\Theta = 0.571$). Left: fast outer mode; Right: slow outer mode	216
2.55	Phase speeds of the fast and slow instability mode versus frequency for the high heat release case. ($\Theta = 0.571$)	216
2.56	Linear eigenfunction of the most amplified central mode. (No heat release $\Theta = 0$, $M_c = 0.10$). \hat{u} (top left), \hat{v} (top right), \hat{T} (bottom left) and \hat{z} (bottom right) components	217
2.57	Linear eigenfunction of the most amplified central mode. (No heat release $\Theta = 0$, $M_c = 0.875$). \hat{u} (top left), \hat{v} (top right), \hat{T} (bottom left) and \hat{z} (bottom right) components	218
2.58	Compressibility effects on the linear eigenfunction of the most amplified central mode. (No heat release $\Theta = 0$). Amplitude of the \hat{u} (top left), \hat{v} (top right), \hat{T} (bottom left) and \hat{z} (bottom right) components	219
2.59	Linear eigenfunction of the most amplified slow outer mode. (Heat release $\Theta = 4.85$, $M_c = 0.1$). \hat{u} (top left), \hat{v} (top right), \hat{T} (bottom left) and \hat{z} (bottom right) components	220
2.60	Linear eigenfunction of the most amplified slow outer mode. (Heat release $\Theta = 4.85$, $M_c = 0.8$). \hat{u} (top left), \hat{v} (top right), \hat{T} (bottom left) and \hat{z} (bottom right) components	221
2.61	Compressibility effects on the linear eigenfunction of the most amplified slow outer mode. (Heat release $\Theta = 4.85$). Amplitude of the \hat{u} (top left), \hat{v} (top right), \hat{T} (bottom left) and \hat{z} (bottom right) components	222
2.62	Linear eigenfunction of the most amplified central mode. (No heat release $\Theta = 0$, $M_c = 0.8$)	223
2.63	Linear eigenfunction of the most amplified central mode. (No heat release $\Theta = 0$, $M_c = 0.8$). Superimposed on mean flow ($T_f = 3, M_c = 0.8$)	224
2.64	Linear eigenfunction of the most amplified slow outer mode. (Heat release $T_f = 3$, $M_c = 0.8$)	225

2.65	Path of integration in the complex α , β and ω planes. (from Huerre and Montewitz 1985)	226
2.66	Dispersion relation for an absolutely unstable mixing layer. $\bar{u}_2 = 0.01$, $\bar{T}_2 = 1$, $M_c = 0.05$ and $T_f = 6$. left ω_r , right ω_i	227
2.67	Dispersion relation for an convectively unstable mixing layer. $\bar{u}_2 = 0.01$, $\bar{T}_2 = 1$, $M_c = 1.20$ and $T_f = 4$. left ω_r , right ω_i	227
2.68	Dispersion relation for an limit convectively unstable mixing layer. $\bar{u}_2 = 0.01$, $\bar{T}_2 = 0.5$, $M_c = 1.20$ and $T_f = 4$. left ω_r , right ω_i	228
2.69	Influence of the slow-stream temperature on the transition from absolute to convective instability. (Heat release $T_f = 3$, $\bar{u}_2 = 0.01$).	228
2.70	Schematic of the compressible reacting mixing layer.	229
3.1	Amplification rates of the fast (sup) and slow (inf) incompressible outer modes at two different obliquities (2-D and 45 degrees). $T_f = 3$, $M_c = 0.8$, $\bar{u}_2 = 0.5$, $\bar{T}_2 = 1$, $M_{f1} = M_{f2} = 0.02$	230
3.2	Convective speeds of the fast (sup) and slow (inf) incompressible outer modes at two different obliquities (2-D and 45 degrees). $T_f = 3$, $M_c = 0.05$, $\bar{u}_2 = 0.5$, $\bar{T}_2 = 1$, $M_{f1} = M_{f2} = 0.02$	230
3.3	Amplification rates of the fast (sup) and slow (inf) compressible outer modes at two different obliquities (2-D and 45 degrees). $T_f = 3$, $M_c = 0.05$, $\bar{u}_2 = 0.5$, $\bar{T}_2 = 1$, $M_{f1} = M_{f2} = 0.292$	231
3.4	Convective speeds of the fast (sup) and slow (inf) compressible outer modes at two different obliquities (2-D and 45 degrees). $T_f = 3$, $M_c = 0.8$, $\bar{u}_2 = 0.5$, $\bar{T}_2 = 1$, $M_{f1} = M_{f2} = 0.292$	231
3.5	Management of Data on the Hypercube. Each processor is allocated a certain number of $x - z$ or $x - y$ planes.	232
3.6	Transpose of data from a situation where each processor is allocated Nyn $x - z$ planes to a situation where each processor is allocated Nzn $x - y$ planes.	233
3.7	Same in 2-D, showing the two configurations, the first one for the computation of partial x derivatives and the second one for the computation of partial y derivatives.	234

4.1	Developed typical central mode. (Low heat release $\Theta = 0.1$, $M_c = 0.2$, $Da = 5$, $Ze = 0$, $\bar{u}_2 = -1$, $Re = 200$, $t = 21$).	235
4.2	Interaction of a developed typical central mode with its subharmonic at three instants of time. a) $t=31$. b) $t=35$. c) $t=41$. (Low heat release $\Theta = 0.1$, $M_c = 0.2$, $Da = 5$, $Ze = 0$, $\bar{u}_2 = -1$, $Re = 200$).	237
4.3	Mean vorticity profiles (X-averaged) of the central mode of figure 4.1 at 4 instants of time.	240
4.4	Mean profiles of vorticity production (dilatation term + baroclinic term) at 4 instants of time for the central mode of figure 4.1	240
4.5	Mean temperature profiles (X-averaged) of the central mode of figure 4.1 at 4 instants of time.	241
4.6	Mean reaction rate profiles (X-averaged) of the central mode of figure 4.1 at 4 instants of time	241
4.7	Growth of vorticity thickness with time for the central mode of figure 4.1	242
4.8	Time history of the total (left) and maximum (right) reaction rates of the mixing layer of figure 4.1	242
4.9	Time history of the maximum vorticity of a typical slow outer mode for different Reynolds numbers. (Heat release $T_f = 3$, $M_c = 0.8$, $Da = 6$, $Ze = 2$, $\bar{u}_2 = 0.5$).	243
4.10	Time history of the vorticity thickness of the slow outer mode of figure 4.15 at different Reynolds numbers.	243
4.11	Effect of the Reynolds number on the time variation of the logarithm of kinetic energy of the slow outer modes of figure 4.15.	244
4.12	Time history of the maximum pressure gradient of the slow outer mode of figure 4.15 at different Reynolds numbers.	244
4.13	Influence of Reynolds number on the slow outer mode ($T_f = 3$, $M_c = 0.8$, $Da = 6$, $Ze = 2$, $\bar{u}_2 = 0.5$, Time = 64). $Re = 2000$	245
4.14	Influence of Reynolds number on the slow outer mode ($T_f = 3$, $M_c = 0.8$, $Da = 6$, $Ze = 2$, $\bar{u}_2 = 0.5$, Time = 64). $Re = 8000$	245
4.15	Typical slow outer mode ($T_f = 3$, $M_c = 0.8$, $Da = 6$, $Ze = 2$, $\bar{u}_2 = 0.5$,	

<i>Re</i> = 4000, <i>Time</i> = 64)	246
4.16 Pressure contours of the slow outer mode of figure 4.15 $t = 80$	248
4.17 Left: Pressure contours of the slow outer mode of figure 4.15 at time 96. Right: Same at $Re = 8000$	248
4.18 Surface plot of the mixture fraction of the typical central mode of figure 4.1. $t = 21$	249
4.19 Surface plot of the mixture fraction of the typical slow outer mode of figure 4.15. <i>Time</i> = 64	249
4.20 Mixture fraction PDF for the central mode of figure 4.1 (top left) and for the slow outer mode of figure 4.15 at time 64 (top right), 80 (bottom left), 96 (bottom right)	250
4.21 Mean (X-averaged) profiles of temperature (top left), reaction rate (top right), fuel (bottom left) and oxidizer (bottom right) at five instants of time for the slow outer mode of figure 4.15	251
4.22 Mean (X-averaged) profiles of vorticity sources at times $t = 64$ (left) and $t = 80$ (right). Mean profile of vorticity transport at time 64. Mean profile of total vorticity sources (baroclinic + dilatational term) at five instants of time. (slow mode of figure 4.15)	252
4.23 Mean (X-averaged) profile of vorticity at five instants of time (slow outer mode of figure 4.15)	253
4.24 Mean (X-averaged) profile of density-weighted vorticity ($\rho d\bar{u}/dy$) normalized by \bar{u}_1 at five instants of time (slow outer mode of figure 4.15)	
253	
4.25 Decay of the slow outer mode: Contour plots of mixture fraction and vorticity at time 80 (top) and 96 (bottom).	254
4.26 Comparison of the phase speeds and amplification rates of the fast and slow outer modes for the linear stability analysis based on the mean profiles at times $t = 0$ and $t = 64$. Two obliquities considered: 0 degree and 45 degrees. Top: fast mode; bottom: slow mode.	255
4.27 Same as figure 4.26 with the mean profile at $t = 64$ normalized to get $\delta_\omega = 1$	256

4.28	Behavior of the slow outer mode at high Reynolds number ($Re = 8000$) as its kinetic energy oscillates (see fig. 4.12). (time $t = 96$).	257
4.29	Behavior of the slow outer mode at high Reynolds number ($Re = 8000$) as its kinetic energy oscillates (see fig. 4.12). (time $t = 112$).	258
4.30	Behavior of the slow outer mode at high Reynolds number ($Re = 8000$) as its kinetic energy oscillates (see fig. 4.12). (time $t = 128$).	259
4.31	Simulation initialized with the fast and slow outer modes (Heat release $T_f = 3$, $M_c = 0.8$, $Da = 6$, $Ze = 2$, $\bar{u}_2 = 0.5$, $Re = 4000$).	260
4.32	Pressure contours of the fast and slow outer modes of figure 4.31.	262
4.33	Simulation initialized with the fast and the slow outer mode. Same simulation as figure 4.32 at time $t = 80$. Same simulation as figure 4.32 at time $t = 80$	262
4.34	PDF of the mixture fraction for the simulation of figure 4.31 at time $t = 80$).	263
4.35	Surface-plot of the mixture fraction corresponding to figure 4.33.	263
4.36	Influence of the Damköler number on the slow outer mode ($T_f = 3$, $Re = 4000$, $Da = 1$, $M_c = 0.8$, $Ze = 2$) to be compared with the slow outer mode of figure 4.15	264
4.37	Influence of the Damkhöler number, of the interaction between fast and slow outer modes and of the Reynolds number on the (top) total reaction rate and (bottom) maximum reaction rate. Laminar (no outer mode) mixing layer with $Re = 4000$ shown for comparison	265
4.38	Typical slow incompressible outer mode and its subharmonics (Heat release $T_f = 3$, $M_c = 0.05$, $Da = 3$, $Ze = 2$, $\bar{u}_2 = 0.5$, $Re = 1000$, $\phi = 0$, Amplitudes: 0.001 (fundamental) and 0.0005 (subharmonic), $t = 150$)	266
4.39	Transition from the central mode to the two outer modes. ($T_f = 4$, $M_c = 0.2$, $Re = 500$, $Da = 3$, $Ze = 2$, $\bar{u}_2 = -1$, Time $t = 20$)	268
4.40	History of the kinetic energies of the fast outer mode and on its fast subharmonic for the simulation of figure 4.42. ($T_f = 3$, $M_c = 0.8$, $Re = 4000$, $Da = 6$, $Ze = 2$, $\phi = \pi$)	270
4.41	Interaction between a fast outer mode and its fast subharmonic. ($T_f = 3$, $M_c = 0.8$, $Re = 4000$, $Da = 6$, $Ze = 2$, $\phi = \pi$, Amplitudes:	

0.002 (fundamental) and 0.001 (subharmonic)). Time $t = 80$. Time $t = 112$. Time $t = 176$	271
4.42 Pressure contours during the interaction of the fast outer mode and the fast subharmonic of figure 4.41. (Times (a) $t = 80$, (b) $t = 112$, (c) $t = 176$, (d) $t = 224$)	274
4.43 Influence of the initial phase delay on the kinetic energies of the subharmonic (top) and of the fundamental (bottom). ($T_f = 3$, $M_c = 0.8$, $\bar{u}_2 = 0.5$, $Ze = 2$, $Da = 0.85$, Amplitudes: 0.001 for fund. and subh.)	275
4.44 Influence of the initial phase delay on the growth rate of the layer: top: vorticity thickness; bottom: momentum thickness. ($T_f = 3$, $M_c = 0.8$, $\bar{u}_2 = 0.5$, $Ze = 2$, $Da = 0.85$, Amplitudes: 0.001 for fund. and subh.)	276
4.45 Influence of the initial phase delay on the total reaction rate. Gulping. ($T_f = 3$, $M_c = 0.8$, $\bar{u}_2 = 0.5$, $Ze = 2$, $Da = 0.85$, Amplitudes: 0.001 for fund. and subh.)	277
4.46 Interaction between a slow outer mode and its slow subharmonic. Gulping. ($T_f = 3$, $M_c = 0.8$, $\bar{u}_2 = 0.5$, $Ze = 2$, $Da = 0.85$, $\phi = \pi$, Amplitudes: 0.001 for fund. and subh.) Times: $t = 96$, $t = 112$, and $t = 128$	277
4.47 Time variations of the kinetic energy of the fast and slow fundamentals and subharmonics of figure 4.48. ($T_f = 3$, $M_c = 0.8$, $\bar{u}_2 = 0.5$, $Ze = 2$, $Da = 0.85$, $\phi = \pi$, Amplitudes: 0.001 for fund. and 0.0005 subh.)	279
4.48 Mixture fraction contours for a simulation started with a fast and a slow outer mode and their fast and slow subharmonic. ($T_f = 3$, $M_c = 0.8$, $\bar{u}_2 = 0.5$, $Ze = 2$, $Da = 0.85$, $\phi = \pi$, Amplitudes: 0.001 for fund. and 0.0005 subh.) Time: $t = 80$, $t = 112$, $t = 192$, $t = 288$	280
4.49 Variation of various thicknesses (momentum, product, visual, etc) for the simulation presented in figure 4.48.	281
4.50 Left: Maximum temperature and maximum and minimum pressures	

for the simulation presented in figure 4.48. Right: Total and maximum reaction rates for the same simulation.	281
4.51 Simulation of Stanford Experiment: ($\Theta = 0.142$, $M_c = 0.8$, $Re = 1200$, $\bar{u}_2 = 0.11$, $\bar{T}_2 = 0.21$, $Z_e = 0$, $\phi = \pi$, Amplitudes: 0.001 for fund. and 0.0005 subh.) Time $t = 50.3$	282
4.52 Simulation of Stanford experiment: Same as figure 4.51 at time: $t = 82$	284
4.53 Mixture fraction and pressure contours for the same simulation as figure 4.51 at time $t = 102$	285
4.54 Mixture fraction contours for the same simulation as figure 4.51 at times $t = 119$ and $t = 130$	285
4.55 Comparison to experiment at time $t = 140$	286
4.56 Simulation of the Stanford experiment (Same simulation as figure 4.51) at time: $t = 180$	287
4.57 Variation of the logarithm of kinetic energies for the same simulation as figure 4.51. The discontinuity at the left corresponds to pressure waves generated at the initialization	288
4.58 Variation of the total and maximum reaction rates versus time for the same simulation as figure 4.51.	288
4.59 Results from the Stanford experiment: Comparison of OH Emission and OH PLIF.	289
4.60 Results from the Stanford experiment: Image interpretation.	290
4.61 Results from the Stanford experiment: Mixing layer structure at four different unrelated instants, showing the two colayers.	291
5.1 Computational domain showing the flow direction and the position of the reaction zone. The location of the plane-cuts used in this chapter is indicated. The plane Y_2 is located into the slow colayer and the plan Y_1 in the middle of the reaction zone.	292
5.2 Plane cuts of the mixture fraction and spanwise vorticity at $t = 70.9$ in the planes Z_1 (left) and Z_2 (right).	293
5.3 Streamwise vorticity production terms in plane Z_3 ($t = 70.9$).	294

5.4	Plane-cut of the streamwise vorticity and vorticity production terms at $t = 70.9$ in the plane X_1 , through the slow outer mode large-scale structure	295
5.5	Plane-cut of the streamwise vorticity and vorticity production terms at $t = 70.9$ in the plane X_2 , through the slow outer mode braids	296
5.6	Cross-stream vorticity production terms in plane Z_3 (braid region) at $t = 70.9$	297
5.7	Plane-cuts of the cross-stream vorticity and vorticity production terms at $t = 70.9$ in the plane X_1 , through the slow outer mode large-scale structure	298
5.8	Spanwise vorticity in a plane of strong positive straining ($t = 70.9$). .	299
5.9	Plane-cut of the spanwise vorticity and vorticity production terms at $t = 70.9$ in the plane X_1	300
5.10	Plane-cut of the spanwise vorticity and vorticity production terms at $t = 70.9$ in the plane X_2 , through the slow outer mode braids	301
5.11	Top-view of the spanwise vorticity and vorticity production terms at $t = 70.9$ in the plane Y_2 (through the slow outer mode large-scale structure).	302
5.12	Contours of pressure, temperature and reaction rate in the plane Z_1 . 303	
5.13	(Top) Modal energy content at time $t = 70.9$ (E_1). (bottom left) Same taking into account the density variations (E_2). (bottom right) contour plot of the modal energy content shown on top.	304
5.14	(Top) Mean Reynolds stress at various y -location of the layer. (Bottom) Same as top multiplied by density.	305
5.15	(Top) Turbulent transport of species. (Bottom) Mean profiles of \bar{zz} and \overline{Oof} where z,o,f are the passive scalar, fuel mass fraction and oxidizer mass fraction, respectively.	306
5.16	(Top) Production rate, dissipation rate and magnitude of the kinetic energy at $t = 70.9$. (bottom) Components of enstrophy.	307
5.17	Time variation of the kinetic energies of various spectral modes. .	308

5.18	Transition to turbulence mechanism.	309
5.19	View of the layer at $t = 105.5$, in the planes Z_1 (left) and Z_2 (right).	310
5.20	Streamwise vorticity and vorticity production terms in plane Z_2 ($t = 105.6$).	311
5.21	Plane cut of the streamwise vorticity and vorticity production terms at $t = 105.6$ in the plane X_1 , through the fast outer mode large-scale structure and the braids of the slow outre mode.	312
5.22	Cross-stream vorticity and vorticity production terms in plane Z_2 ($t = 105.6$).	313
5.23	Plane-cut of the cross-stream vorticity and vorticity production terms at $t = 105.6$ in the plane X_1 , through the fast outer mode large-scale structure and the braids of the slow outre mode.	314
5.24	Spanwise vorticity and vorticity production terms in plane Z_2 at $t = 105.6$	315
5.25	Plane-cut of the spanwise vorticity and vorticity production terms at $t = 105.6$ in the plane X_1	316
5.26	(Top) Logarithm of the modal kinetic energy content at time $t = 105.6$. (bottom) Contour plot corresponding to the modal energy content shown on top.	317
5.27	(Top) Mean Reynolds stresses profiles. (Bottom) Same as top multiplied by density.	318
5.28	(Top) Turbulent transport of species. (Bottom) Profiles of $\bar{z}\bar{z}$ and $\bar{o}\bar{f}$	319
5.29	(Top) Production, dissipation and magnitude of the kinetic energy at $t = 105.6$. (Bottom) Components of enstrophy	320
5.30	Averaged values of Kolmogorov, Taylor and integral scales in all the $y=\text{constant}$ planes, accounting for the fluctuation of viscosity with temperature (left) or using the cold stream viscosity (right).	321
5.31	Marching PDF across the layer.	321
5.32	Top: View of the mixture fraction contours at $t = 145.3$ in the plane Z_2 (left) and Z_1 (right). Bottom: Temperature and reaction rate	

contours in the plane Z_2 .	322
5.33 End views (flow is coming at you) of the mixture fraction in the plane $x = 01$ (plane X_1) and plane $x = 3.6$ ($t = 145.3$)	323
5.34 Plane-cuts of the mixture fraction and reaction rate in the plane Y_1 (left) and Y_2 (right) ($t = 145.3$)	324
5.35 Streamwise vorticity and vorticity production terms in planes Z_2 (left) and Z_1 (right) ($t = 145.3$)	325
5.36 Plane cuts of the streamwise vorticity and vorticity production terms at $t = 145.3$ in the plane X_2 , through the slow outer mode large-scale structure.	326
5.37 Plane cuts of the cross-stream vorticity and vorticity production terms at $t = 145.3$ in the plane X_2 .	327
5.38 Plane cuts of the spanwise vorticity and vorticity production terms at $t = 145.3$ in the plane X_2	328
5.39 (Top) Modal energy content at time $t = 145.3$. (Bottom) contour plot corresponding to the modal energy content shown on top.	329
5.40 (Top) Mean Reynolds stress at various y -locations of the layer ($t = 145.3$). (Bottom) Components of enstrophy.	330
5.41 (Top) Turbulent transport of species ($t = 145.3$). (Bottom) Variation along y of \overline{zz} and \overline{of}	331
5.42 (Top) Mean temperature profile at three instants of time ($t = 70.9, t = 105.6, t = 145.3$). (Bottom) Mean reaction rate profile at the same times.	332
5.43 History of the maximum temperature in the layer	333
5.44 History of the maximum and total reaction rates	333
B.1 Ignition of a low Mach number, slow chemistry reacting mixing layer	
	334
B.2 Ignition of the same low Mach number mixing layer as in figure B.1, but with faster chemistry	336
B.3 Ignition of a compressible mixing layer with slow chemistry	338

C.1	Regime chart of a mixing layer with equal free-stream temperatures and $\bar{u}_2 = 0.5\bar{u}_1$	340
-----	--	-----

Nomenclature

Roman symbols

A_f	Amplitude of the fundamental eigenmode
A_r	Preexponential constant in the reaction rate
A_s	Amplitude of the subharmonic eigenmode
a_1, a_2	Constants in time advance
a, b, c	Constants in Pade schemes
b_y	Stretching parameter of the cross-stream coordinate
CFL	Courant-Friedrichs-Lowy number
c	Complex phase velocity ($= \omega/\alpha$)
\bar{c}	Sound speed
\bar{c}_1	Sound speed of stream 1
\bar{c}_2	Sound speed of stream 2
c_f	Convective speed of the fast outer mode
\bar{c}_f	Sound speed in the reaction zone
c_p	Specific heat at constant pressure
c_s	Convective speed of the slow outer mode
c_t	Constant used in the determination of the time step
c_v	Specific heat at constant volume
D_c, D_μ	Terms in equation for time step
D_i	Diffusivity of the species i
Da, Da_c, Da_1	Damköhler numbers
E_{away}	Radiating energy leaving the computational domain
E_{k_x, k_z}	Kinetic energy of the mode k_x, k_z
e	Internal energy per unit mass

e_t	Total energy per unit mass
g	Parameter in stability analysis
ΔH_r^*	Enthalpy of reaction per unit mass of fuel
$h_{f_i}^o$	Enthalpy of formation of species i per unit mass and at standart temperature and pressure
h_i	Enthalpy per unit mass of species i
h_t	Total enthalpy per unit mass
k_x	Integer wavenumber in the x direction
k_z	Integer wavenumber in the z direction
Le	Lewis number
Le_i	Lewis number of species i
L_i	Characteristic variable at the boundary
L_x	Computational box length in the x direction
L_y	Computational box length in the y direction
L_z	Computational box length in the z direction
M_1	Mach number of the stream 1
M_2	Mach number of the stream 2
M_c	Convective Mach number ($= \frac{\bar{u}_1 - \bar{u}_2}{\bar{c}_1 + \bar{c}_2}$)
M_{c1}	Convective Mach number relative the stream 1
M_{c2}	Convective Mach number relative the stream 2
M_{f1}	Flame convective Mach number associated with stream 1
M_{f2}	Flame convective Mach number associated with stream 2
N_p	Number of processors used on the Hypercube
N_q	Number of independent variable per gridpoint
N_x	Number of points in the x direction
N_y	Number of points in the y direction
N_z	number of points in the z direction
n	Mass of oxidizer reacting per unit-mass of fuel

Pr	Prandtl number
p	Pressure
p_s	Pressure at the stagnation points
Q_1, Q_2	Storage location in time advance
q_j	Heat flux
Re	Reynolds number
Re_l	Reynolds number relative to the fast stream velocity ($= \rho_1^* u_1^* \delta_\omega^* / \mu_1^*$)
r	Gas constant per unit mass
r, r_1, r_2	Velocity ratios. $r = \bar{u}_1 / \bar{u}_2$, $r_1 = \bar{u}_f / \bar{u}_1$ and $r_2 = \bar{u}_2 / \bar{u}_f$
s, s_1, s_2	Density ratios. $s = \bar{T}_1 / \bar{T}_2$, $s_1 = \bar{T}_f / \bar{T}_1$ and $s_2 = \bar{T}_2 / \bar{T}_f$
\bar{T}	Mean temperature
\bar{T}_1	Temperature of stream 1 (upper)
\bar{T}_2	Temperature of stream 2 (lower)
\bar{T}_f	Flame temperature
T_a	Activation temperature
t	Time
u	Velocity component in the x direction
\bar{u}	Mean velocity
\bar{u}_1	Velocity of stream 1 (upper)
\bar{u}_2	Velocity of stream 2 (lower)
\bar{u}_c	Convective velocity
\bar{u}_f	Mean velocity at the cross-stream location of the flame
v	Velocity component in the y direction
w	Velocity component in the z direction
\dot{w}	Reaction rate
X_1, X_2	$y - z$ Plane-cuts of the 3-D variable fields
x	Streamwise direction
x_i	Cartesian coordinates

Y_1, Y_2	$x - z$ Plane-cuts of the 3-D variable fields
Y_i	Mass fraction of the species i
Y_o	Mass fraction of oxidizer
Y_f	Mass fraction of fuel
y	Cross stream direction
Z, Z_1, Z_2, Z_3	Mean passive scalar
Z_1, Z_2	$x - y$ Plane-cuts of the 3-D variable fields
Ze	Zeldovich number
z	Spanwise direction

Roman symbols

α	Streamwise eigenvalue from linear stability
α_i	Imaginary part of the spatial eigenvalue
α_r	Real part of the spatial eigenvalue
β	Spanwise eigenvalue from linear stability
γ	Ratio of the specific heat
Γ_x	Initial circulation of the streamwise vortices
Γ^a	Nondimensionalized initial circulation of the streamwise vortices
γ_e	Euler constant
γ_s	Mean rate of strain
γ_1	Ratio of the specific heat in the stream 1
γ_2	Ratio of the specific heat in the stream 2
δ_{vis}	Visual mixing layer thickness
δ_m	Momentum thickness
δ_p	Density thickness
δ_T	Temperature thickness
δ_w	Vorticity thickness of the mixing layer
δ_{ij}	Kronecker delta

Δx	Grid spacing in x
Δy	Grid spacing in y
Δz	Grid spacing in z
ϵ	Constant in Dimotakis growth rate model
η	Mapped coordinate in the cross-stream direction
η	Independent variable in the solution for the mean flow
λ	Velocity ratio parameter ($= \Delta \bar{u} / \bar{u}$)
λ_c	Conductivity
λ_i	Characteristic velocity at the boundary
μ	Viscosity
ν	Kinematic viscosity
ϕ_{fo}	Fuel-equivalence ratio
ϕ	A general variable
ϕ_k	Relative phase of the eigenmode k used in forcing
ϕ_F	Phase of the fundamental
ϕ_S	Phase of the subharmonic
ψ	Stream function
ρ	Density
$\bar{\rho}$	Mean density
$\bar{\rho}_2$	Density of stream 1 (upper)
$\bar{\rho}_2$	Density of stream 2 (lower)
τ_{ij}	Shear stress tensor
θ	Angle of the disturbance
Θ	Heat release parameter
χ	Independent variable in shooting method
ξ	Mapped coordinate in the streamwise direction
ω_x	Streamwise vorticity
ω_y	Cross-stream vorticity

ω_z	Spanwise vorticity
ω	Temporal eigenvalue from linear stability
ω_r	Real part of the temporal eigenvalue
ω_i	Imaginary part of the temporal eigenvalue

CHAPTER 1

Introduction

1.1. Motivation

One of the central problems in combustion is to accomplish efficient mixing of fuel and oxidizer in the shortest possible length. This requirement, which is achieved in subsonic flows by using high turbulence intensities, is complicated in supersonic flows by the high velocities and short residence times. In recent years, a renewed interest in supersonic propulsion has lead to considerable experimental and computational work to investigate the effect of compressibility and heat release on mixing.

Of particular concern for supersonic combustion systems is the possible reduction in shear-induced mixing at increasingly high Mach numbers. The stabilizing effect of compressibility on turbulence has been well documented for various type of shear flows. Landau (1944) first showed that the vortex sheet (Kelvin-Helmoltz instability) becomes stable when the relative Mach number between the two streams exceeds a critical value. In more recent experiments, both the growth rate of non-reacting turbulent free shear-layers and their Reynolds Stresses were shown to decrease with increasing Mach number (Chinzei *et al.* 1986, Clemens *et al.* 1990, Papamoschou and Roshko 1986, Papamoschou 1990, Samimy and Elliot 1988, Shau and Dolling 1989, Ikawa and Kubota 1975). While compressible shear flows generally contain density gradients, density effects alone are not responsible for the large decrease in growth rates (Brown and Roshko 1974). There is therefore a large effect associated with the Mach number itself. As compressibility increases, the domain over which a large-scale structure can affect the flow field is reduced. As observed by Morkovin (1987), upstream and cross-flow communications are essential for instabilities in compressible flows.

In order to better understand the physics of mixing, it is often useful to view a complex flow as a collection of mixing layers. Incompressible mixing layers have

therefore been studied extensively. Similarly, the plane compressible mixing layer is a good apriori candidate to study the effect of compressibility on turbulent shear flows. Three main reasons can be advocated: (1) the relative Mach number between the fast and the slow stream is constant, resulting in a constant compressibility effect with downstream distance; (2) a considerable body of information already exists at low Mach numbers for this flow configuration, which constitutes a valuable reference set for comparison; (3) the geometry is simple enough to use direct numerical simulation (DNS) as a means of investigation.

In the present work, we numerically address the issue of the existence and topology of the large-scale structures in the compressible reacting mixing layer. We are interested in the coupling between chemical reaction and fluid dynamics caused by the non-homogeneous density distribution. To date, this issue, which has important implications in terms of entrainment and the subsequent mixing process, remains an open question for compressible flows. Another important aspect of compressible reacting mixing layers arises from the competition between high turbulent mixing rates and finite chemical reaction rates in supersonic shear flows (low Damkhöler number effect). The question of how the flow field affects the chemical reaction is also addressed. The final objective of this work is to help the interpretation of the companion experiment conducted at Stanford, and to clarify these and other recent experimental results (see section 1.2.2).

1.2. Survey of previous observations in incompressible mixing layers

Incompressible mixing layers have been well documented for the last few decades, and a vast quantity of information can be found on the subject. A general consensus exists on a large number of observations, which will be summarized below.

One of the key findings was that incompressible turbulent mixing layers are dominated by large-scale two-dimensional structures, which persist at high Reynolds numbers (Brown and Roshko 1974, Dimotakis and Brown 1976). These coherent structures, which had initially been associated with a transition phenomena, were shown to have long lifetimes and to increase their size with downstream distance. These two-dimensional rollers play a central role in the entrainment and mixing process in incompressible mixing layers (Dimotakis and Brown 1976, Broadwell and Breidenthal

1982).

Pairing was identified as the mechanism for growth in low Reynolds number shear flows (Winant and Browand 1974) and was also observed at higher Reynolds numbers (Dimotakis and Brown 1976). For high Reynolds numbers flow, “tearing”, where one structure is ripped apart by the strain field of two other structures, was shown to be very common (Dimotakis and Brown 1976). The pure reactant entrained by the large-scale structure was shown to persist unmixed for long times inside the rollers, after which mixing occurs rapidly. Vortex amalgamation, either through pairing or tearing, was shown to be associated with the rapid mixing of previously entrained reactants, a result which was later numerically observed by Moser and Rogers (1991).

The existence of streamwise streaks (ribs) in the braid between successive rollers was observed in the initial work of Brown and Roshko (1974). The origin of these streaks is still subject to controversy. A possible explanation (Corcos and Lin 1984a,b, Lasheras *et al.* 1986, 1988) is that residual three-dimensional turbulence subjected to the high strain rate in the stagnation region between large-scale vortices will be stretched, leading to the formation of longitudinal vortices. Detailed investigation of these streaks by Bernal and Roshko (1986) revealed the existence of counter-rotating pairs of streamwise vortices in the braid, the ends of which become wrapped around the neighboring large rollers. These pairs of vortices move fluid up and down across the braids, and form mushroom shaped structures in the scalar field. The appearance of the ribs at $Re = 3,000 - 10,000$ was seen to correspond to the onset of three-dimensionality and to a “mixing transition”, with a sudden increase in the amount of molecularly-mixed fluid (Breidenthal 1981). Ribs contain a high level of vorticity, suggesting they are responsible for energetic mixing when they interact with the spanwise rollers (Jimenez 1985).

Scalar measurements showed that the entrainment is controlled by large-scale vortical structures. Temperature traces exhibit a linear or ramped behavior in the streamwise direction, while being relatively uniform in the cross-stream direction (Friedler 1974). The observation of the role of the large-scale structures on mixing leads to entrainment and mixing models. Dimotakis (1986) proposed a model for entrainment which predicts the asymmetric entrainment of fluid from both sides. Later Broadwell and Breidenthal (1982, see also Broadwell and Mungal 1988) introduced a model of mixing where the flow is divided in three distinct regions: pure reactants, homogeneously mixed fluid whose concentration is set by the entrainment ratio, and strained

laminar diffusion sheets.

1.3. Survey of previous studies of compressible or reacting mixing layers

Whereas for incompressible mixing layers much experimental evidence supports the key results recalled above, in the compressible case the experiments are less numerous, less conclusive, and the interpretation of the results leads to divergent conclusions (*e.g.* regarding mixing efficiency). Most of the available information on the structure of the compressible mixing layer is numerical (Blumen *et al.* 1975, Gropengiesser 1970, Lele 1989, Ragab *et al.* 1989, 1990, Sandham and Reynolds 1990, 1991). The results of Sandham and Reynolds from linear stability analysis and direct numerical simulation indicate an increased obliquity of the large-scale structures with the convective Mach number M_c (see below). The influence of the heat release and the effect of walls were also investigated (Ragab and Shin 1990, Shin and Ferziger 1991b). Key issues such as the existence of large-scale structures and the topology of these structures remain open questions. Recent observations for compressible and reacting mixing layers will now be presented, and some striking observations noted.

1.3.1. Structure of the compressible mixing layer

There is a clear consensus that the growth rate of a mixing layer is reduced by compressibility. This has been observed by various researchers for various types of compressible shear flows (Chinzei *et al.* 1986, Clemens *et al.* 1990a, Papamoschou 1989, Samimy and Elliot 1988, Shau and Dolling 1989). Based on the existence of a saddle point region between two coherent structures, the convective Mach number

$$M_c = \frac{\bar{u}_1 - \bar{u}_2}{\bar{c}_1 + \bar{c}_2} \quad (1.1)$$

(where \bar{u}_1 and \bar{u}_2 are the speed of the fast and slow stream and \bar{c}_1 and \bar{c}_2 the speed of sound into those streams) was introduced (Bogdanoff 1983, Papamoschou 1988). The convective Mach number collapses growth rate data when the growth rate is normalized by the growth rate of the incompressible mixing layer having the same free-stream density ratio and velocity ratio (Bogdanoff 1983, Papamoschou and Roshko 1988).

Mach-wave radiation in one or the other free streams has been observed in various experiments (Oertel H. 1979, Hall *et al.* 1991a, Tam 1971, Lowson and Ollerhead

1968). These travelling waves and their spacing, which is on the order of the local shear layer visual thickness δ_{vis} , suggest that some form of large-scale structure is present.

However, no conclusive observation of the nature and shape of these structures has been made. Papamoschou's results (1989) from tilted side-view Schlieren images suggested that the structure are two-dimensional. His two-spark Schlieren images further show that the structures appear frozen as they are convected downstream, with no evidence of vortex pairing. In contrast, Fourguette *et al.* (1990) show that the structure are highly three-dimensional and suggest the presence of streamwise vortices. The observations of Clemens (1991) also indicate an increase in streamwise organization with compressibility. His end-view Mie-scattering images at $M_c = 0.6$ show highly convoluted regions of mixed fluid that span the entire width of the layer. These convolutions, which suggest the existence of large-scale streamwise vortices, are on the scale of the large lumps of mixed fluid seen in the side-view images. As recalled above, in incompressible mixing layers the streamwise structures are small and only convolute the braids but not the primary rollers. In Clemens' work, only convoluted mixed-fluid structures are seen rather than thin braid regions or large core regions of mixed fluid. Pictures taken by Hall (fig. 5.2, 1991) in the reacting medium-compressibility case do not exhibit any vortex core but instead suggest the presence of two layers inside the layer. One must be cautious, however, since his Schlieren images only give information spatially integrated in the spanwise direction.

The results of McIntyre and Settles (1991) reveal large-scale but poorly-organized structures which become less obvious as M_c increases, evolve rapidly with downstream distance (contrary to Papamoschou's results), and are always inclined toward the fast stream. These structures are referred to as being quasi-coherent in that they have a reasonably well-defined convective velocity but a highly irregular wavelength. Spectrum analysis shows that the velocity fluctuations are broadband with no sharp concentration of energy at any particular frequency, but that the structures clearly grow with downstream distance, leading to the observed decrease in the spectrum peak frequency. Although some regularly-spaced structures can be seen at discrete instants of time on some of their pictures, the lifetimes of these structures do not seem long enough to produce a discrete peak in the power spectrum.

Another striking observation is that the large-scale structures do not travel at the speed implied by the convective Mach number M_c (Papamoschou 1989, Erdos *et*

al. 1992). Papamoschou (1989) found that the structures do not convect at the predicted velocity \bar{u}_c but rather at a speed very close to the speed of one of the two free streams. McIntyre and Settles' (1991) convective velocity measurements for $M_c > 1$ show that the large-scale structures are supersonic with respect to one but not both of the free streams. Their results for $M_c = 1.50$ with $\bar{p}_2/\bar{p}_1 = 4.83$ and $\bar{u}_2/\bar{u}_1 = 0.38$ show that structure develops in the slow stream, while for a jet in ambient air with $M_c = 1.1$ and $\bar{p}_2/\bar{p}_1 = 0.36$ the structure develops in the fast stream. Finally, Hall (1991) observed the existence of radiating pressure waves emanating from the layer, and determined the convective speed of these structures using the Mach angle of those waves. His results for two non-reacting high Mach number cases ($M_c = 0.962$, $M_c = 0.906$) showed that the structures travel subsonically with respect to the slow stream. The convective speed calculated from the Mach angle was very close to that obtained using cross-correlation from pressure signals.

The concept of the usual convective Mach number, which implies the existence of a stagnation point in the braid between large-scale structures, is therefore not supported by high Mach number or reacting experiments. To reconcile the pressure-matching hypothesis at the braid, various researchers have speculated that shock waves exist on one side of the shear layer (Dimotakis 1989, Papamoschou 1989). However, considering the measured convective speed, grossly unequal stagnation pressure losses must occur on the two sides of the layer in order to satisfy the requirement of a stagnation pressure balance at the convective-frame stagnation point. As stated by Hall (1991), it seems therefore rather curious that the fairly strong shock waves required by this process have not been observed in any experiment. Also, given the value of the convective speed \bar{u}_c measured by Hall (1991), one would expect higher recovery temperatures for fluid from the slow stream, than what is observed experimentally either by thermocouples measurements or inferred from Schlieren photographs.

We will show that a different flow model prevails in high speed and reacting mixing layers. Two separated sets of large-scale structures develop, one on each side of the layer, each of which only mixes fresh outer fluid from its side with fluid from the middle of the layer. This “colayer” structure has two sets of stagnation points (in the moving frames), and when the convective Mach number idea is applied to each the relevant Mach numbers are obtained (the “flame convective Mach numbers”). This new picture of the flow structure is the central contribution of the present work (fig. 2.70).

1.3.2. Compressibility effects on mixing

The effect of compressibility and heat release on mixing and chemical reaction is also a subject of controversy. Hall, Dimotakis and Rosemann (1991) use the temperature rise from chemical reaction to measure molecular mixing in compressible reacting shear layers. They conclude that the amount of fluid molecularly mixed inside the layer is reduced by compressibility, accompanied by a reduction of the shear layer spreading rate. They also found more high-speed fluid than low-speed fluid in the reacted mixture. Using particle scattering measurements, Dutton *et al.* (1990) came to the opposite conclusion with regard to the effect of compressibility on molecular mixing. However, they were measuring a passive scalar rather than a reaction product. An interesting experiment has been conducted by Glawe and Samimy (1992), where particles injected through an injection wedge mounted on the subsonic side of the splitter plate were tracked using a Yag laser. The results showed that, at $M_c = 0.51$, particles are present deep into the supersonic fast stream, indicating that these particles were entrained into large-scale structures and subsequently thrown out of the layer due to centrifugal forces. However, the same experiment at $M_c = 0.86$ shows that the particles injected into the low-speed side of the mixing layer remain in the low-speed side, which supports the colayer flow model developed herein.

At low Mach number ($M_c = 0.28$), PLIF images taken at Stanford University by Clemens (1991) exhibit streamwise ramps with steep gradient between pure and mixed fluid, suggesting that the turbulent large-scale structures in the incompressible case are dominated by two-dimensional rollers. However, the compressible PLIF images ($M_c = 0.62$) are typically ramped in the cross-stream direction, suggesting that entrainment may occur through streamwise rather than spanwise motion. Furthermore, some PLIF images suggest that two separate regions of mixed fluid may exist in the compressible case, yielding two parallel streamwise ramps on the PLIF images. At $M_c = 0.62$, the PDF of mixture fraction (obtained from the PLIF images) exhibits a “marching” behavior as in the low M_c case. However, with increasing M_c , the PDF at each location has a higher peak and a smaller width, showing that a smaller range of mixture fractions is present at a given location. The mixture fraction PDF in the center of the layer ($y = 0$) is thinner at $M_c = 0.62$ than at $M_c = 0.28$, and is slightly shifted towards the low-speed stream, indicating that mixing preferentially occurs on the low-speed side. The authors conclude that the mixing layer is better mixed at $M_c = 0.62$ than at $M_c = 0.28$. However, noting the contradictory results of Hall

et al. (1991a), they suggest that compressibility may act to increase the amount of small-scale stirring but decrease the amount of molecular mixing. We will see that the colayer model is able to resolve the disparity.

The “flip” experiment conducted by Hall (1991) shows that, as the fuel equivalence ratio was changed (“flipped”) from $\phi_{f,o} = 1/4$ to $\phi_{f,o} = 4$, the temperature thickness was increased by 30% and the product thickness by 23%. In the case $\phi_{f,o} = 1/4$, the temperature profile is shown to extend further into both free streams. No explanation was given for this observation. The calculation of the entrainment shows that compressibility effects on the reacting mixing layer are rather large, changing the entrained mixture from one rich in high-speed fluid to one with an almost equal composition from each stream. The entrainment ratio calculated from the measured product thickness and temperature thickness in the flip experiment is different from that calculated using Dimotakis’ entrainment model (1986). This model, where fluid from each of the free streams is entrained by large-scale structures, is not appropriate for those compressible flows where the colayer structure will occur.

1.4. Objectives and overview

The objective of this work is to identify the basic flow structure and growth mechanism in compressible reacting mixing layers. This was accomplished using a combination of stability analysis and direct numerical simulations. It led to the formulation of the colayer model outlined above, which is the central contribution of this work. The thesis focuses on the following four questions:

- (1) Are there large-scale structures in compressible reacting mixing layers?
- (2) Are those structure 2-D or 3-D, spanwise oriented or streamwise oriented?
- (3) Is mixing increased or decreased by heat release and compressibility?
- (4) And finally, is there some way to control the flow ?

Chapter 2 presents the linear stability analysis conducted for a plane reacting compressible shear layer in order to study the effects of a diffusion flame on the shear layer’s stability characteristics. The effects of the heat release, compressibility, and fuel equivalence ratio on the disturbance amplification rate are examined. Key information is obtained concerning the initial behavior of the layer and the development of organized structures. The linear stability analysis also provides eigenfunctions to initialize the direct numerical simulations.

In chapter 3, the two codes used in the DNS are presented. One code is two-dimensional and was used to simulate both temporally and spatially-developing mixing layers. The other code can only handle temporally-developing mixing layers, but can be used to simulate two and three-dimensional flow. This latter code was implemented on the Intel Hypercube. The details of the implementation, the performances and the comparison with the Cray Y-MP are also presented in chapter 3.

Chapter 4 gives the results of two-dimensional simulations performed on the Cray Y-MP and on the Hypercube. The interaction of the two colayers is studied as well as the effect of the baroclinic and dilatation terms on pairing. The effect of the fast and slow outer modes on mixing is analyzed, and simulations corresponding to the Stanford experiment are presented.

The key results of the three-dimensional simulation are presented in chapter 5. The simulation was initialized with a small set of 2-D and oblique eigenmodes and sub-harmonics from the linear stability analysis. Small-scale streamwise vortices appear in the simulation, and the transition to turbulence was observed. The total reaction rate is seen to increase during the transition.

Chapter 6 provides a brief summary of the major findings in Chapters 2-5. The reader seeking an overview may skip to this chapter.

There are four appendices. The first provides an alternative method for solving the linear stability eigenvalue problem of chapter 2 that is useful if the full set of eigenvalues is desired. Appendix B presents some limited results for spatially-developing 2-D simulations, which are not yet fully completed. Appendix C presents a method for estimating the flow structure under different free-stream conditions, which may be useful to experimentalists. Appendix D is a directory of the archives of programs and DNS data fields which are maintained at NASA/Ames Research Center by the Center for Turbulence Research.

Notes

CHAPTER 2

Linear Stability Analysis

In this chapter, linear stability analysis is presented for a plane reacting compressible shear layer in order to study the effects of a diffusion flame on the shear layer's stability characteristics. The effects of heat release, compressibility and fuel equivalence ratio on the disturbance amplification rate are examined. The results indicate that the obliquity of the disturbance waves of the compressible reacting shear layer is reduced by increased heat release, while the amplification rate is increased. It is shown that the reacting mixing layer can be viewed as a system of two non-interacting mixing layers: a fast one, travelling at a speed close to that of the fast stream, and a slow one, travelling at a speed close to that of the slow stream. We call these two non-interacting mixing layers, the "colayers". Eigenmodes are associated with either the fast or slow colayer for short wavelengths, while for long wavelengths the eigenmodes are associated with the entire shear layer.

The usual convective Mach number based on the free-stream velocities is not useful for a reacting mixing layer because it assumes that fluid from each of the free-streams comes to rest at the stagnation point between eddies (in a frame moving with the eddies) *isentropically*. The "flame convective Mach number" is introduced and shown to be the preferable parameter for correlating the behavior of compressible reacting shear layers. The possibility of controlling the mixing rate by judicious positioning of the flame sheet is suggested by the results. The existence of an optimum heat release to maximize the instability of the mixing layer is also established.

2.1. Introduction

2.1.1. Background and motivation

Two different philosophies of turbulence can be found in the literature. One sees turbulence as a quasi random process which can only be described statistically. The other considers deterministic structures as the building blocks of many turbulent flows

such as the turbulent mixing layer and the boundary layer. Major initial contributions to this latter school are Crow and Champagne (1971), who saw the turbulent mixing layer as a finely tuned amplifier of vortex structure, and Brown and Roshko (1974), who discovered vortex structure in turbulent mixing layers.

Among this second school, one may distinguish two main approaches to the dynamics of the turbulent mixing layer. The first one treats the mixing layer as a collection of non-linearly interacting vortex structures in physical space. The second approach relies on linear stability analyses to describe the initial development of the layer. In the presence of shear, small perturbations develop and eventually evolve into turbulence. In the incompressible case, transition to turbulence involves three stages: (a) the growth of two-dimensional coherent structures and the development of secondary instabilities, (b) the merging of these structures, and (c) the breakdown into small-scale three-dimensional turbulence. Whereas the two last stages can be studied using direct numerical simulations, linear and secondary stability analysis are useful to understand the initial growth of the large-scale structures, to investigate the development of the ribs, and to predict the mechanism of breakdown towards turbulence. In secondary stability theory, one assumes that the primary instability has developed and then solves a new eigenvalue problem in which the mean flow and eigenfunction are both functions of the streamwise and cross-stream coordinates. This theory has been very successful in predicting the K (Klebanoff) and H (Herbert) transition to turbulence in channel flows (Herbert 1983).

Linear stability analyses also gives valuable information on the overall development of the layer (linear growth rate for example) and on the influence of various parameters on the layer behavior (Mach number, heat release, etc.). Linear stability has been used extensively for non-reacting free shear flows (Lin 1955, Michalke 1965, and Drazin and Howard 1981). The non-reacting mixing layer vorticity distribution possesses a maximum, and the layer is therefore unstable to small perturbations via the Kelvin-Helmoltz instability mechanism. This mechanism is inviscid in essence (viscosity effects are negligible for Reynolds number greater than 30 or 40 based on the velocity difference and the shear layer thickness) and leads to the formation of large-scale structures.

Some previous achievements from linear stability analysis can be summarized as follows:

1. Linear stability analysis of the incompressible mixing layer has indicated that three dimensional instability waves have smaller spatial growth rates than their two-dimensional counterparts, a feature in agreement with the dominantly two dimensional character of the large-scale structure of incompressible mixing layers observed experimentally.
2. Linear stability has been used to predict mixing layer growth rates when one associates the spatial growth rate obtained by linear stability analysis with the thickening of the layer. Sandham (1990, 1991) showed that

$$\frac{d\delta_p}{dx} = -0.60 \alpha_{i,max} \quad (2.1)$$

$$\frac{d\delta_w}{dx} = -0.45 \alpha_{i,max}. \quad (2.2)$$

In particular, the trends in growth rate due to velocity ratio and density ratio were correctly predicted by stability analysis.

3. Associating the spatial growth rate with the mean thickening of the layer, linear stability also predicted the observed strong reduction of the amplification rate of the large-scale structures of the layer at high Mach numbers. Gropengiesser (1970) found the second mode of instability, previously observed by Lessen *et al.* (1965), which keeps the layer unstable in 2-D at high Mach numbers. Linear stability analysis also indicated that the large scale structures become more 3-D at high Mach numbers (Sandham and Reynolds 1990), a result confirmed by direct numerical simulation (Sandham and Reynolds 1991) and experimentally observed by Clemens *et al.* (1990).
4. The linear stability analysis of confined shear layers exhibited the existence of additional modes of instabilities. These “acoustic” modes of instability, first mentioned by Mack (1990) in wall boundary layers, were also found by Greenough *et al.* (1989) and Shin and Ferziger (1991b). For sufficiently close walls, the amplification rates of these confined modes were shown to be significantly higher than the amplification rates of the instability modes of the unconfined layer.
5. Linear stability analysis was also conducted for incompressible reacting plane shear layers (Shin and Ferziger 1991a) and low Mach number free jets (Mahalaningam *et al.* 1989) and indicated a significant stabilization of the flow by heat release.

These results were confirmed experimentally (Hermanson *et al.* 1886) and by direct numerical simulation (McMurtry *et al.* 1989, Mahalingan *et al.* 1989).

6. Jackson and Grosch (1990) studied the linear stability of the reacting compressible shear layer using a hyperbolic tangent velocity profile and an infinite reaction rate. Their results indicated that heat release has complex effects on the shear layer stability. For low Mach number reacting mixing layers, and in contrast to the non-reacting case, they showed the existence of multiple subsonic neutral modes. For the compressible reacting mixing layer, and similarly for the non-reacting case, they found two groups of instability modes, the “fast supersonic mode” and the “slow supersonic mode”.
7. Huerre and Monkewitz (1985) introduced the notion of convective and absolute instabilities for free-shear layers. For convectively unstable flows, spatial stability analysis ($\alpha_i \neq 0$) must be used, while for absolutely unstable flows temporal stability analysis ($\omega_i \neq 0$) must be used. They found that the non-reacting mixing layer with equal free-stream temperatures becomes absolutely unstable only with significant counterflow ($U_2 = -0.136U_1$).

These past achievements suggest that linear stability analysis can be used to predict the growth rate of a mixing layer, and to gain insight into the influence of temperature ratio, velocity ratio, compressibility or heat release on the mixing layer behavior. Linear stability analysis is also useful when eigenfunctions are needed to initialize temporal direct numerical simulations or to provide inlet conditions for spatial simulations.

2.1.2. Chapter outline

In this chapter, we present the linear inviscid stability analysis of the plane reacting compressible mixing layer. The mean flow profiles are calculated using a self-similar solution of the compressible boundary-layer equations in the limit of infinite reaction rate. The fluctuations of the reaction rate are ignored in the disturbance analysis, and in essence the chemical reaction only comes into play through the modification that heat release induces on the mean profile. Viscosity is also neglected in the disturbances equations. The main contributions of the linear stability analysis presented in this chapter are:

1. The existence of two maxima on the mean density-weighted vorticity profile is shown to lead to the existence of two distinct “outer modes”. Each of the outer modes is

associated with one of the free-streams, and its phase velocity is comparable with the speed of this free-stream. It is shown that the compressible reacting mixing layer behaves as two superposed mixing layers, the two colayers. Thus, large-scale entrainment of fluid from both sides into a single eddy is not likely to occur in compressible reacting mixing layers.

2. The possibility of controlling the obliquity of the fast and slow outer modes by changing the flame temperature or modifying the position of the flame is demonstrated. Increasing heat release stabilizes the low Mach number, low heat-release mixing layer, and destabilizes the high Mach number, high heat-release mixing layer. Increasing heat release is also shown to make the two outer modes more 2-D while having no effect on the obliquity of the central mode. At high Mach number, changing the fuel equivalence ratio is shown to have large effects, making the outer mode associated with the lean side of the layer more 2-D and less affected by compressibility than the outer mode associated with the reactant rich side of the layer.
3. The usual convective Mach number is shown to be of limited use for compressible reacting shear layers. Instead, the “flame convective Mach numbers” are introduced and shown to be preferable parameters for correlating the behavior of the reacting shear layer with high heat release. The flame convective Mach numbers consistently explain the effects of (1) the flame temperature, (2) the position of the flame and (3) the free-stream temperature ratio on the obliquity and amplification rate of the outer modes.
4. Absolute instability of the slow outer mode is shown to occur, even in the absence of counterflow. Increasing the fuel equivalence ratio, increasing the temperature of the flame, and lowering the temperature of the slow stream all lead to the transition from convective instability to absolute instability.

2.2. Formulation

In this section, a self-similar formulation of the compressible reacting boundary layer equations is derived for infinite reaction rate and unity Prandtl and Lewis numbers. The self-similar equations are solved using a shooting method based on a fourth order Runge-Kutta integration. The linearized disturbance equations are then solved

using a shooting method based on fifth-order Runge-Kutta integration and Newton-Raphson iteration. A computationally less effective resolution of the linear stability eigenvalue problem, based on Chebyshev polynomials and Q-R algorithm, is also presented in Appendix A

2.2.1 Solution for the mean flow

The mean flow consists of a reacting plane free shear layer between one low-speed air flow and one high-speed mixture of fuel and inert gas (fig. 2.1). The nondimensionalized mean velocity and temperature profiles $\bar{u}(y), \bar{T}(y)$ are calculated using the compressible boundary layer equations. A self-similar solution is derived on the basis of infinite reaction rate, for Prandtl and Lewis numbers equal to unity, and viscosity proportional to temperature \bar{T} . The mass fraction of fuel in the fast stream is assumed to be small, thus the specific heat c_p and the ratio of the specific heats γ are assumed to be functions only of the passive scalar Z and not functions of \bar{T} .

Previous researchers (Monkewitz and Huerre 1982, Shin and Ferziger 1991a) have shown that the accuracy of the mean profile was essential in the analysis of the disturbances. For an incompressible non-reacting shear-layer, only the linear stability calculations based on a Blasius velocity profile were shown to give amplification rates proportional to $\lambda = \Delta\bar{u}/\bar{u}$ as found in experiments (Monkewitz and Huerre 1982). In the reacting case, Shin and Ferziger (1991a) showed that the definition of the mean profile becomes even more important. Whereas incompressible non-reacting shear-layer velocity profiles possess only one maximum of vorticity, in the reacting case the mean flow exhibits two maxima of density-weighted vorticity near the outer edges of the mixing layer, and this will be shown in section 2.3 to lead to the existence of two new instability modes. The use of analytic profiles ($\text{erf}(y)$ or $\tanh(y)$), which coincide with the Blasius profile in the central part of the mixing layer but differ from it in the outer regions, can lead to large errors in the amplification rates of these outer modes. Therefore, we have performed our calculations using a more accurate cubic-spline fit to the laminar profile developed from self-similar theory for each case.

The boundary layer equations for a steady, two-dimensional laminar reacting flow with zero streamwise pressure gradient are (Kuo 1982)

$$\frac{\partial \rho^* u^*}{\partial x^*} + \frac{\partial \rho^* v^*}{\partial y^*} = 0 \quad (2.3)$$

$$\rho^*(u^* \frac{\partial u^*}{\partial x^*} + v^* \frac{\partial u^*}{\partial y^*}) = -\frac{\partial p^*}{\partial x^*} + \frac{\partial}{\partial y^*}(\mu^* \frac{\partial u^*}{\partial y^*}) \quad (2.4)$$

$$\begin{aligned} \rho^*(u^* \frac{\partial h_t^*}{\partial x^*} + v^* \frac{\partial h_t^*}{\partial y^*}) &= \frac{\partial}{\partial y^*} \left(\frac{\mu^*}{Pr} \left[\frac{\partial h_t^*}{\partial y^*} + (Pr - 1) \frac{\partial}{\partial y^*} (u^{*2}/2) \right] \right) \\ &\quad + \frac{\partial}{\partial y^*} \left(\sum_{n=1}^N (Le_i^{-1} - 1) h_i^* \frac{\partial Y_i}{\partial y^*} \right) \end{aligned} \quad (2.5)$$

$$\rho^*(u^* \frac{\partial Y_i}{\partial x^*} + v^* \frac{\partial Y_i}{\partial y^*}) = \frac{\partial}{\partial y^*} \left(\frac{\mu^*}{Pr Le_i} \frac{\partial Y_i}{\partial y^*} \right) + w_i^* \quad (2.6)$$

$$p^* = \rho^* r^* T^*. \quad (2.7)$$

Here x^* and y^* are the streamwise and normal directions respectively, u^* and v^* are the velocity components in those directions, ρ^* is the density, μ^* is the viscosity, Y_i is the mass fraction of the species i (fuel or oxidizer), and r^* the gas constant. The superscript * denotes a dimensional quantity, and the subscripts $_1$ and $_2$ refer to the fast and the slow streams, respectively. The Lewis number and the Prandtl numbers are defined as

$$Le_i = \frac{\lambda_c^*}{\rho^* D_i^* c_p^*}, \quad Pr = \frac{c_p^* \mu^*}{\lambda_c^*} \quad (2.8)$$

where D_i^* is the diffusivity of the species i , c_p^* the specific heat at constant pressure, and λ_c^* the conductivity. The energy equation is written in term of total enthalpy,

$$h_t^* = \sum_{i=1}^N Y_i h_i^* + u^{*2}/2 \quad (2.9)$$

where

$$h_i^* = \int_{T_o^*}^{T^*} C_{p,i}^* dT^* + \Delta h_{f,i}^*. \quad (2.10)$$

The above equations are non-dimensionalized by dividing all of the dimensional quantities by their respective values in the high-speed stream, using the vorticity thickness, δ_ω , as the reference length. Assuming unity Prandtl and Lewis numbers, and neglecting transverse pressure gradients, the boundary layer equations in dimensionless form become

$$\frac{\partial \rho u}{\partial x} + \frac{\partial \rho v}{\partial y} = 0 \quad (2.11)$$

$$\rho u \frac{\partial u}{\partial x} + \rho v \frac{\partial u}{\partial y} = \frac{1}{Re_l} \frac{\partial}{\partial y} (\mu \frac{\partial u}{\partial y}) \quad (2.12)$$

$$\rho u \frac{\partial h_t}{\partial x} + \rho v \frac{\partial h_t}{\partial y} = \frac{1}{Re_l} \frac{\partial}{\partial y} (\mu \frac{\partial h_t}{\partial y}) \quad (2.13)$$

$$\rho u \frac{\partial Y_i}{\partial x} + \rho v \frac{\partial Y_i}{\partial y} = \frac{1}{Re_l} \frac{\partial}{\partial y} (\mu \frac{\partial Y_i}{\partial y}) + w_i \quad (2.14)$$

$$\rho r T = 1 \quad (2.15)$$

$$Y_f(\eta) = \max(Z(\eta), 0) \quad \text{and} \quad Y_o(\eta) = -n \min(Z(\eta), 0). \quad (2.33)$$

The energy equation (2.32) is then solved. The method used is the same as for the species equation. The boundary conditions are

$$h_t(+\infty) = \frac{\gamma_1 r_1}{(\gamma_1 - 1)} \bar{T}_1 + Y_{f1} \Delta h_{ff}^o + \bar{u}_1^2 / 2 \quad (2.34)$$

$$h_t(-\infty) = \frac{\gamma_2 r_2}{(\gamma_2 - 1)} \bar{T}_2 + Y_{o2} \Delta h_{fo}^o + \bar{u}_2^2 / 2. \quad (2.35)$$

Once $F(\eta)$, $h_t(\eta)$ and $Y_f(\eta)$ are known, the temperature and velocity profiles are calculated using

$$u(\eta) = F(\eta) \quad (2.36)$$

$$T(\eta) = (h_t(\eta) - Y_f \Delta h_{ff}^o - Y_o \Delta h_{fo}^o - u^2 / 2) / c_p(Z(\eta)). \quad (2.37)$$

The last step of the procedure is to reverse the Howarth's transform by integrating

$$\frac{dy}{d\eta} = \sqrt{\frac{2x}{Re_l}} T \quad \text{with} \quad y(0) = 0 \quad (2.38)$$

where x is determined by the condition $\delta_\omega = 1$. The v profile can then be determined at the given x location by:

$$v = \frac{-1}{\rho(y)} \sqrt{\frac{2x}{Re_l}} \left[\frac{F - \eta F'}{2x} + F' \frac{\int_0^y (\partial \rho / \partial x) dy}{\int_0^y \rho dy} \right]. \quad (2.39)$$

The x -momentum and energy equations are decoupled, and only the v equation couples the dilatation (due to heat release) with the mean momentum equation.

The self-similar mean \bar{u} and \bar{T} profiles are compared with the profile obtained by solving the compressible boundary layers equations using a Crank-Nicholson method. This comparison is presented on figure 2.2 to 2.3 for a convective Mach number $M_c = 0.8$ with $\Theta = 2$ and $U_2 = 0.5U_1$. Figure 2.2 shows the mean species profile and the mean temperature profile, and figure 2.3 shows the mean density-weighted vorticity profile. The Reynolds number Re_l is equal to 8000 and the numerical solution of the compressible boundary layers was initialized with two step-functions. The agreement between the self-similar solution and the numerical solution is excellent. Note that when the reaction becomes slower (smaller Damkhöler number $Da = A\rho_f Y_{f,\infty} \exp(-\bar{T}_a / \bar{T}_f) \delta_\omega / \bar{u}_1$ where \bar{T}_a is the activation temperature), the mean temperature slightly decreases, which makes the two distinct mean density-weighted

vorticity peaks slightly less pronounced. We will see in section 2.3 that the two peaks of the mean density-weighted vorticity profile determine the instability characteristics of the layer, and that slight modifications of these peaks can have large effects on the amplification rates and phase speeds of the instability modes.

2.2.2. Equation of the perturbations

Whereas viscosity is responsible of the Tollmien-Schlichting instability of the boundary layer over a flat plate, it is only a damping factor in the Kelvin-Helmoltz instability of the mixing layer. At high Reynolds number ($Re > 30$), viscosity is expected to have very little effect on the large-scale motion. This has been verified numerically and experimentally. Calculations taking into account viscosity were performed by Ersch (1957) and showed that as $\mu \rightarrow 0$ the neutral mode approaches inviscid behavior. Lin (1955) considered an analytic velocity profile and demonstrated that all solutions of the Rayleigh equation having a positive amplification rate could be interpreted as the limit of solutions to the Orr-Sommerfeld equation, whereas the solutions with negative amplification rate were meaningless. Based on these arguments, viscosity was neglected in the present analysis.

Previous investigations (Shin and Ferziger 1991a) has shown that the fluctuation of the reaction rate due to the fluctuations of the concentrations has little effect on the linear stability results. Hence, fluctuations of the reaction rate are ignored in the disturbance analysis. In essence, the chemical reaction only comes into play through the mean-profile modifications that heat release induces. We also assume that the flow is quasi-parallel and neglect \bar{v} , the mean velocity in the y direction.

The linear stability analysis is obtained by decomposing all the flow variables into their mean values, and their disturbances, assumed to be small and expressed as three-dimensional waves,

$$u = \bar{u} + \tilde{u}, \quad T = \bar{T} + \tilde{T}, \quad p = 1 + \tilde{p}, \quad v = \bar{v}, \quad w = \tilde{w}, \quad \rho = \bar{\rho} + \tilde{\rho} \quad (2.40)$$

with

$$[\tilde{u}, \tilde{T}, \tilde{p}, \tilde{v}, \tilde{w}, \tilde{\rho}](x, y, z, t) = [\hat{u}, \hat{T}, \hat{p}, \hat{v}, \hat{w}, \hat{\rho}](y) e^{i(\alpha x + \beta z - \omega t)} \quad (2.41)$$

where $\hat{u}, \hat{T}, \hat{p}, \hat{v}, \hat{w}, \hat{\rho}$ are complex eigenfunctions of the variable y , and α, β, ω are the streamwise and spanwise complex wavenumbers and frequency, respectively. For the spatial stability analysis, ω is real so that disturbances grow in space and not in time,

whereas for the temporal stability problem α is real and disturbances grow in time and not in space. Finally, the angle of the disturbance, θ , is defined as

$$\tan \theta = \frac{\beta}{\alpha_r} \quad (\text{real}). \quad (2.42)$$

Note that β has to be real, since we require the disturbances not to amplify for $z \rightarrow \pm\infty$.

The Euler equations for the conservation of mass, momentum, passive scalar Z and total enthalpy are

$$\frac{\partial \rho^*}{\partial t^*} + \frac{\partial \rho^* u_i^*}{\partial x_i^*} = 0 \quad (2.43)$$

$$\rho^* \left(\frac{\partial u_i^*}{\partial t^*} + u_j^* \frac{\partial u_i^*}{\partial x_j^*} \right) = - \frac{\partial p^*}{\partial x_i^*} \quad (2.44)$$

$$\rho^* \left(\frac{\partial Z}{\partial t^*} + u_j^* \frac{\partial Z}{\partial x_j^*} \right) = 0 \quad (2.45)$$

$$\rho^* \left(\frac{\partial h_i^*}{\partial t^*} + u_j^* \frac{\partial h_i^*}{\partial x_j^*} \right) = \frac{\partial p^*}{\partial t^*} \quad (2.46)$$

$$p^* = \rho^* r^* T^*. \quad (2.47)$$

Using the definition of h_i^* , the perfect gas assumption, and the mass-continuity equation, one can rewrite the energy equation as

$$\rho^* c_v^* \left(\frac{\partial T^*}{\partial t^*} + u_j^* \frac{\partial T^*}{\partial x_j^*} \right) = -p^* \frac{\partial u_i^*}{\partial x_i^*} - \rho^* T^* \left(\frac{\partial c_v^*}{\partial t^*} + u_j^* \frac{\partial c_v^*}{\partial x_j^*} \right) \quad (2.48)$$

or

$$\rho^* \left(\frac{\partial T^*}{\partial t^*} + u_j^* \frac{\partial T^*}{\partial x_j^*} \right) = -p^* \frac{(\gamma - 1)}{r^*} \frac{\partial u_i^*}{\partial x_i^*}. \quad (2.49)$$

This second equation is based on the assumption that c_p^* is only a function of Z , and on the use of the passive scalar equation. After nondimensionalization, one gets the following system of partial differential equations:

$$\frac{\partial \rho}{\partial t} + \frac{\partial \rho u_i}{\partial x_i} = 0 \quad (2.50)$$

$$\rho \left(\frac{\partial u_i}{\partial t} + u_j \frac{\partial u_i}{\partial x_j} \right) = -\frac{1}{\gamma_1 M_1^2} \frac{\partial p}{\partial x_i} \quad (2.51)$$

$$\rho \left(\frac{\partial Z}{\partial t} + u_j \frac{\partial Z}{\partial x_j} \right) = 0 \quad (2.52)$$

$$\rho \left(\frac{\partial T}{\partial t} + u_j \frac{\partial T}{\partial x_j} \right) = -p(\gamma - 1)/r \frac{\partial u_i}{\partial x_i} \quad (2.53)$$

$$p = \rho r T. \quad (2.54)$$

We substitute equations (2.40) and (2.41) into equations (2.50) to (2.54) and get the following linearized equations for continuity, the three components of momentum, passive scalar, energy and the perfect gas law:

$$\hat{\rho}i(\alpha\bar{u} - \omega) + \hat{v}\bar{p}' + \bar{p}[i(\alpha\hat{u} + \beta\hat{w}) + \hat{v}'] = 0 \quad (2.55)$$

$$\bar{p}[i(\alpha\bar{u} - \omega)\hat{u} + \hat{v}\bar{u}'] = \frac{-i\alpha\hat{p}}{\gamma_1 M_1^2} \quad (2.56)$$

$$\bar{p}i(\alpha\bar{u} - \omega)\hat{v} = \frac{-1}{\gamma_1 M_1^2}\hat{p}' \quad (2.57)$$

$$\bar{p}i(\alpha\bar{u} - \omega)\hat{w} = \frac{-i\beta\hat{p}}{\gamma_1 M_1^2} \quad (2.58)$$

$$\bar{p}[i(\alpha\bar{u} - \omega)\hat{Z} + \hat{v}\bar{Z}'] = 0 \quad (2.59)$$

$$[i(\alpha\bar{u} - \omega)\hat{T} + \hat{v}\bar{T}'] = -(\gamma - 1)[i(\alpha\hat{u} + \beta\hat{w}) + \hat{v}']/r \quad (2.60)$$

$$\hat{p} = \bar{p}\bar{r}\hat{T} + \hat{p}\bar{r}\bar{T} + \bar{p}\hat{r}\bar{T} \quad (2.61)$$

where i represents the operator d/dy . \hat{T} , $\hat{\rho}$, \hat{u} and \hat{w} can be eliminated successively. First, equation (2.55) is multiplied by \bar{T} and added to equation (2.60). Using the relation $\bar{p}'\bar{r}\bar{T} + \bar{p}\bar{r}'\bar{T} + \bar{p}\bar{r}\bar{T}' = 0$ we obtain

$$i(\alpha\bar{u} - \omega)[\hat{p}\bar{r} - \bar{p}\hat{r}] - \hat{v}\bar{p}\bar{T}\bar{r}\bar{r}' = -i[(\alpha\hat{u} + \beta\hat{w}) + \hat{v}']\gamma\bar{r} \quad (2.62)$$

or

$$i(\alpha\bar{u} - \omega)\hat{p} = -i[(\alpha\hat{u} + \beta\hat{w}) + \hat{v}']\gamma \quad (2.63)$$

if we use the linearized passive scalar equation and assume that r depends only on Z . Then, \hat{u} and \hat{w} can be eliminated using equations (2.56) and (2.58). We get a set of two coupled differential equations in \hat{v} and \hat{p}

$$(\alpha\bar{u} - \omega)\hat{v}' - \alpha\hat{v}\bar{u}' = \frac{-i\alpha^2 g\hat{p}}{\gamma_1 M_1^2} \quad (2.64)$$

$$\bar{p}i(\alpha\bar{u} - \omega)\hat{v} = \frac{-1}{\gamma_1 M_1^2}\hat{p}' \quad (2.65)$$

with g defined as

$$g = \frac{\alpha^2 + \beta^2}{\alpha^2\bar{p}} - \frac{\gamma_1}{\gamma}M_1^2\frac{(\alpha\bar{u} - \omega)^2}{\alpha^2}. \quad (2.66)$$

Following the method of Gropengiesser (1970), this set of two coupled differential equations can be reduced to a single first order equation,

$$\chi' = \frac{\alpha^2(\bar{u} - c)}{\bar{T}} - \frac{\chi(\chi g + \bar{u}')}{\bar{u} - c} \quad (2.67)$$

with the new variable χ , the complex velocity c , and the boundary conditions being

$$\chi = \frac{i\alpha \hat{p}}{\gamma M_1^2 \hat{v}} \quad (2.68)$$

$$c = \frac{\omega}{\alpha}, \quad (2.69)$$

$$\text{and } \chi(y = \pm\infty) = \frac{\alpha(\bar{u} - c)}{\sqrt{g\bar{T}}}. \quad (2.70)$$

Note that equation (2.67) has been obtained without assuming that the fast and slow streams have the same specific heat ratio (γ) or the same molar mass. It is, however, very similar to the equation derived by Sandham (1989) under these two hypotheses. If r is assumed to be only a function of Z , it can be eliminated from the perturbation equations. The solution to the above equation described by Sandham (1989) is obtained as follows:

- First, for spatial (or temporal) analysis, at a given ω (or α) a guess is made on the complex eigenvalue α (or ω).
- The differential equation is then integrated from the two free-streams to the center-line using a fifth-order Runge-Kutta scheme. The two values $\chi(0^+)$ and $\chi(0^-)$ obtained are compared.
- A new value of α (ω) is obtained using a Newton-Raphson iteration.

2.3. Necessary condition of instability

In this section, the necessary condition for temporal instability, $(\bar{\rho}\bar{u}')' = 0$ is derived for the incompressible case. This condition is a global and not a local condition. It is therefore not sufficient to predict the number of instability modes. In particular, we will show below that two instability modes can be present even when $(\bar{\rho}\bar{u}')' = 0$ only once in the flowfield. In the compressible case, no criteria can be demonstrated. It is however suggested that the criteria derived in the incompressible case can be extended to the compressible case.

2.3.1. Incompressible case

In the incompressible case, equation (2.67) can be rewritten as

$$(\bar{\rho}\hat{v}')' = [\frac{\alpha^2}{\bar{T}} + \frac{1}{(\bar{u} - c)}(\bar{\rho}\bar{u}')']\hat{v}. \quad (2.71)$$

We multiply equation 2.71 by \hat{v}^* , the complex conjugate of \hat{v} , and integrate from $-\infty$ to $+\infty$. Then, using the boundary condition that $\hat{v} \rightarrow 0$ when $y \rightarrow \pm\infty$, we obtain

$$\int_{-\infty}^{\infty} \bar{\rho} |\hat{v}'|^2 + \frac{\alpha^2}{T} |\hat{v}|^2 dy = \int_{-\infty}^{\infty} \frac{1}{(\bar{u} - c)} (\bar{\rho} \bar{u}')' |\hat{v}|^2 dy. \quad (2.72)$$

For a temporal stability analysis, α is real and the imaginary part of the previous equation gives

$$c_i \int_{-\infty}^{\infty} \frac{1}{|\bar{u} - c|^2} (\bar{\rho} \bar{u}')' |\hat{v}|^2 dy = 0. \quad (2.73)$$

It follows that a necessary condition of temporal instability ($c_i \neq 0$) is that

$$(\bar{\rho} \bar{u}')' = 0 \quad (2.74)$$

and changes sign at one or more points in the flowfield, which amounts to the existence of an extremum of the density-weighted vorticity.

One can derive (following the method of Fjørtoft 1955) a stronger necessary condition for instability, namely

$$(\bar{\rho} \bar{u}')' (\bar{u} - \bar{u}_s) < 0 \quad (2.75)$$

somewhere in the flowfield, where $\bar{u}_s = \bar{u}(y_s)$ and where y_s is a point where $(\bar{\rho} \bar{u}')' = 0$.

A proof comes from the real part of equation (2.72),

$$-\int_{-\infty}^{\infty} \bar{\rho} |\hat{v}'|^2 + \frac{\alpha^2}{T} |\hat{v}|^2 dy = \int_{-\infty}^{\infty} \frac{1}{|\bar{u} - c|^2} (\bar{\rho} \bar{u}')' (\bar{u} - c_r) |\hat{v}|^2 dy. \quad (2.76)$$

Adding

$$(c_r - \bar{u}_s) \int_{-\infty}^{\infty} \frac{1}{|\bar{u} - c|^2} (\bar{\rho} \bar{u}')' |\hat{v}|^2 dy = 0 \quad (2.77)$$

to the right-hand side of equation (2.76) we get

$$\int_{-\infty}^{\infty} \frac{1}{|\bar{u} - c|^2} (\bar{\rho} \bar{u}')' (\bar{u} - c_r) |\hat{v}|^2 dy = - \int_{-\infty}^{\infty} \bar{\rho} |\hat{v}'|^2 + \frac{\alpha^2}{T} |\hat{v}|^2 dy < 0 \quad (2.78)$$

which establishes equation (2.75).

2.3.2 Compressible case

In the compressible case, one can classify the inviscid disturbances as subsonic, sonic, or supersonic at one point according to whether the phase velocity of the disturbance (relative to an observer moving with the flow) is less than, equal to, or greater than the local speed of sound (Shivamoggi 1977). Using equation (2.66), these conditions

are as follows:

$$\text{subsonic: } \frac{1}{\cos^2 \theta \bar{\rho}} > \frac{\gamma_1}{\gamma} M_1^2 (\bar{u} - c_r)^2$$

$$\text{sonic: } \frac{1}{\cos^2 \theta \bar{\rho}} = \frac{\gamma_1}{\gamma} M_1^2 (\bar{u} - c_r)^2$$

$$\text{supersonic: } \frac{1}{\cos^2 \theta \bar{\rho}} < \frac{\gamma_1}{\gamma} M_1^2 (\bar{u} - c_r)^2$$

For these three cases, the disturbance equation is elliptic, parabolic or hyperbolic, respectively. This criterion is local, and a disturbance travelling at velocity c_r is always subsonic with respect to the region of the mixing layer where \bar{u} is close to c_r . In this region, the disturbance equation is elliptic. In essence, compressibility effects come into play by determining the extent of this elliptic region. For incompressible flow, the entire flow domain is elliptic, whereas for compressible flow only a small part of the mixing layer is elliptic with respect to the disturbance. Free-shear layers act as resonators, and only the elliptic region of the layer can interact with the disturbance. For confined shear layers, the disturbance can generate a radiating pressure wave, which crosses the supersonic region, reflects on the wall, comes back and interacts with the mixing layer.

The Kelvin-Helmoltz instability, which arises from the existence of a distinct extremum in the density-weighted vorticity distribution, is a local phenomena. The phase velocity c_r of the Kelvin-Helmoltz instability modes is close to the mean velocity at this peak. Since, as recalled above, disturbances travelling at velocity c_r are subsonic with respect to the region of the mixing layer where \bar{u} is close to c_r , the instability modes are subsonic with respect to the mean flow at the location of the density-weighted vorticity peak. We therefore believe that instability criteria demonstrated in the incompressible case ($(\bar{\rho} \bar{u}')' = 0$) should remain valid in the compressible case, at least for high frequency (small wavelength) disturbances (*e.g.* the neutral mode), and this is consistent with all of our numerical results.

2.4. Results

2.4.1. Existence of multiple instability modes

The mean density-weighted vorticity profile $\bar{\rho} d\bar{u}/dy$ of the reacting or strongly compressible mixing layer exhibits two peaks. (Figures 2.2 and 2.3 show mean temperature and density-weighted vorticity profiles for a case with $\bar{u}_2/\bar{u}_1 = 0.5$, $\bar{T}_1 = \bar{T}_2$, $M_c = 0.2$ and $\Theta = 2$). The existence of these two peaks leads to the existence of two

instability modes and suggests that the compressible or reacting mixing layer will behave like two independent parallel shear layers, which we call “colayers”. The phase velocities of these modes are comparable with the mean velocities at the peaks, and the greatest disturbance amplitudes occur near the peaks. The “fast outer mode” is associated with the peak in the fast stream, and the “slow outer mode” is associated with the peak in the slow stream.

Two lengthscales appear important in the problem: (a) the thickness of the layer, and (b) the wavelength of the disturbance being considered. For wavelengths that are short compared to the layer thickness (or high wavenumbers), the two density-weighted vorticity peaks can be viewed as two independent amplifiers, and distinct fast and slow outer modes exist. However, for long wavelengths (short wavenumbers), low Mach numbers and small heat releases, the presence of both peaks affects the eigenmode associated with each peak. In this case, one of the modes behaves like the usual “central” instability mode of the shear layer, with a phase speed approximately equal to the average speed of the free-streams (Brown and Roshko 1974) and its largest disturbance amplitudes in the center of the layer. The other mode is “neutral” (not amplified). Since, the “central” and “neutral” modes only exist when the two peaks cannot be considered independent, they will therefore be referred to as the “coupled” modes.

2.4.2. Spatial analysis of these instability modes

In this section of the work, we study in more detail the characteristics of these outer modes. Three values of the heat release are considered, $\Theta = 0$ (non-reacting shear layer), $\Theta = 1$ (low heat release) and $\Theta = 4.85$ (very high heat release). For each value, the influence of compressibility on the amplification rate and phase speed of the instability mode is examined. We restrict here to a single free-stream velocity ratio ($\bar{u}_2/\bar{u}_1 = 0.5$) and to a unity free-stream temperature ratio ($\bar{T}_2 = \bar{T}_1$). The mass fraction of oxidizer in the slow stream is $Y_{o,\infty} = 0.20$ while the mass fraction of fuel in the fast stream is $Y_{f,\infty} = 0.14$, which moves the flame towards the high-speed side. The self-similar profile derived in section 2.1 is used. The main purpose of this section is to illustrate the change from central mode to outer modes with increasing Mach numbers. It will also help clarify some notions introduced further.

2.4.2.1. No heat release

Figure 2.4 shows the mean temperature and density-weighted vorticity profiles for various M_c . The stagnation temperature increase like $(\gamma - 1)M_c^2/2$, and in the highest

Mach number case ($M_c = 3.0$) the stagnation temperature is high enough for the two density-weighted vorticity peaks to appear.

Figure 2.5 shows the growth rate and the phase velocity of the 2-D instability modes of this no-heat release mixing-layer below $M_c = 1$. Here, only one instability curve exists at each Mach number, and this amplification curve has only one maximum, which corresponds to the central mode. The “neutral” mode has a zero amplification rate and is not shown. The growth rate and the frequency of the central mode are strongly reduced with increased M_c , and the phase velocity of this mode is equal to the average speed of the free-streams (usual convective speed). On the $M_c = 1$ amplification and phase-speed curves, a transition can be observed in the high frequency region, where the neutral point is moved to higher frequencies and the phase speed is shifted toward the fast stream velocity. This transition, which corresponds to the appearance of the outer modes, is more obvious at higher Mach numbers.

Figure 2.6 shows the growth rate of the 2-D instability modes of this no-heat release mixing-layer above $M_c = 1$. The phase speed is shown on figure 2.7. Note that, above $M_c = 1$, two instability modes exist, a fast instability mode and a slow instability mode. At low frequencies, each density-weighted vorticity peak affects the eigenmode associated with the other peak and the instability modes are coupled (central and neutral modes). As the frequency is increased, the two density-weighted vorticity peaks act like two independent amplifiers, and the fast and slow outer modes exist. Therefore, at a given Mach number, the phase speed of each outer mode moves towards the speed of the associated free-stream when the frequency is increased. Three maxima exist on the amplification curves, two on the fast amplification curves and one on the slow amplification curve. Each of them is associated with one instability mode. The maximum at the left of the fast amplification curve corresponds to the central mode which was dominant at low Mach number. The maxima on the right of the fast curve and on the slow amplification curve correspond to the outer modes.

Note that the central mode is present until $M_c = 1.2$ but that the fast outer mode becomes more rapidly amplified than the central mode around $M_c = 1.1$. Since the central mode is present at the left of the fast amplification curve, the neutral mode has to be present at the left of the slow amplification curve. Indeed, the growth rate of the slow instability mode is zero in this region.

The outer modes are analogous to the “radiating vorticity mode” described by Mack (1989). These modes are supersonic with respect to one of the free-streams (fig. 2.7)

and radiate pressure waves into that stream. Compressibility effects measured with M_c are weak on the amplification rates of those modes. The amplification rate of the central mode is reduced by nearly a factor of 4 between $M_c = 1.12$ and $M_c = 1.25$, but the amplification rates of the fast and slow outer mode drops by only 15%. The amplification rate of the fast and slow outer modes are approximately equal, but the frequency of the fast outer mode is approximately twice that of the slow outer mode. The phase speed of the outer mode is a function of the frequency in contrast to what is observed for the central mode. Therefore, a fundamental and its subharmonic will have different phase speeds. This will have important consequences for the transfer of energy from one mode to its subharmonic (see chapter 4).

As M_c is increased, the influence of each peak on the eigenmode associated with the other peak is reduced, and so the fast and slow outer modes become uncoupled. The convective speed of each outer mode moves towards the speed of the associated free-stream, and the low frequency region where the central mode exists disappears. Indeed, above $M_c = 1.2$ the distinct peak corresponding to the central mode disappears as well as the zero amplification domain at the left of the slow amplification curve. No instability mode has a convective speed close to the average speed of the free-streams. The frequencies of the outer modes are smaller than the frequencies of the central mode, thereby suggesting that the large-scale structures will be smaller in compressible reacting mixing layers (outer modes) than in their incompressible counterparts (central mode).

2.4.2.2. Moderate heat release

Figure 2.8 shows the mean temperature and mean density-weighted vorticity profile of a reacting mixing layer with low heat release ($\Theta = 1$) at various M_c . Here, the two density-weighted vorticity peaks are present at all Mach numbers. As previously shown, with increasing M_c the stagnation temperature increases, the minimum of the density-weighted vorticity between the two peaks becomes more pronounced, and the two peaks become narrower. The maximum temperature is located in the fast stream (at approximately $\bar{u}_f = 0.8$) as expected since the flow is slightly fuel lean.

Figures 2.9 and 2.10 show the growth rates and the phase speeds of the slow and fast 2-D instability modes. Here, in contrast to the no heat release case, the distinct maximum corresponding to the central mode is absent even at low Mach numbers and low frequencies. For this moderate heat release case, the two density-weighted vorticity peaks are distinct, but at low M_c and low frequencies the presence of both

mean density-weighted vorticity peaks still affects the eigenmode associated with each peak. As a consequence, the phase velocity of the slow instability mode (fig. 2.10) is intermediate between the average speed of the two streams ($\bar{u}_c = 0.75$) and the velocity at the slow mean density-weighted vorticity peak ($\bar{u} \approx 0.65$). At $M_c = 0.75$, the presence of a small bump at the left of the slow instability curve reveals the underlying existence of the central mode in the low frequency region. Also below $M_c = 0.75$, the amplification rate is zero at the left of the fast instability curve, indicating the presence of the neutral mode.

With increasing Mach number, the influence of each peak on the eigenmode associated with the other peak decreases. The frequencies of the fast (and slow) instability modes increase, and their phase velocities move toward the fast (or slow) free-stream speeds. The low-frequency domain, where the neutral mode is present, disappears, and as in the non-reacting case at large M_c no instability mode has a convective speed close to the average speed of the free-streams. Instead, at all frequencies the speed of the fast (or slow) mode is within 10% of the speed of the fast (or slow) stream.

At high M_c , the amplification rates of the slow and fast outer mode are comparable, and the frequency of the fast outer mode is more than twice that of the slow outer mode. Note that the amplification rates of the fast and slow outer mode increase with M_c above $M_c = 2.25$. This striking result, which is contrary to what is observed for the central mode of the non-reacting mixing layer, is due to the modification of the mean profile with M_c . A detailed investigation of the consequences of the modification of the density-weighted vorticity profile with M_c on the linear stability results is given in section (2.4.3.).

2.4.2.3. High heat release

Figure 2.11 shows the mean temperature and density-weighted vorticity profiles of the mixing layer in the high heat release case ($\Theta = 4.85$). Due to the large heat release, the influence of M_c on the mean density-weighted vorticity profile is smaller. At all Mach numbers, the two density-weighted vorticity peaks are distinct and widely separated. This suggests that the influence of each peak on the eigenmodes associated with the other peak will be smaller than in the moderate heat release case.

Figures 2.12 and 2.13 show the growth rate and the phase speed of the fast and slow outer modes. At all frequencies and all Mach numbers, the coupled modes are absent and only the outer modes are observed. Here, the phase velocity of the slow or fast instability mode is never equal to the convective speed ($\bar{u}_c = 0.75$), except for $\omega = 0$

where the amplification rate is 0. Only the zero-wavenumber eigenmode of each peak is affected by the presence of the other peak. In the high-frequency region the phase speed of the outer mode is independent of M_c .

At $M_c = 0.01$, the slow outer mode has a frequency approximately half that of the fast outer mode, but its growth rate is twice that of the fast outer mode. The amplification rate of the outer mode is reduced as M_c is increased, but significantly less than the reduction observed for the central mode of the non-reacting mixing layer. For example, between $M_c = 0.01$ and $M_c = 1.5$ the amplification rate of the slow outer mode is only reduced about 30% while the amplification rate of the central mode of the non-reacting mixing layer is reduced by more than 90%. Note also that the effects of compressibility, measured in term of M_c , are not the same for the two outer modes. Between $M_c = 0$ and $M_c = 1.5$, the growth rate of the slow outer mode is reduced by nearly 30% (fig. 2.13) whereas the growth rate of the fast outer mode is only reduced by approximately 15% (fig. 2.12). This observation will be clarified by the introduction of the flame convective Mach number in section 2.4.4.

Finally, by comparison with the low heat release case (fig. 2.9 and 2.10), heat release increases the frequency of the outer modes, and shifts their phase speeds toward the speeds of their associated free-streams. This effect is due to the modification of the mean profile. As heat release is increased, the density-weighted vorticity peaks move toward the free-streams and become sharper (fig. 2.8 and 2.11), yielding the observed increase in frequencies and modifying the phase speeds.

2.4.3. Influence of the modification of the mean profile with M_c on the linear stability results

As seen in the previous section, as M_c is increased, the mean temperature profile is changed, which yields a modification of the mean density-weighted vorticity distribution. In the moderate heat release case ($\Theta = 1$) for example, at $M_c = 3.5$ the increase in temperature at the stagnation point is equal to $(\gamma - 1)M_c^2 / 2 = 2.45$, more than twice the temperature rise due to combustion. In order to separate compressibility effects due to density change from those due to Mach number itself, we performed a new stability analysis in which M_c was varied but the mean profile was kept constant and equal to the mean profile at $M_c = 0.01$. The cases in section 2.3.3 were again considered.

2.4.3.1. No heat release $\Theta = 0$

Figure 2.14 shows the growth rate and the phase velocity of the 2-D instability modes

of the no-heat release mixing-layer below $M_c = 1$ for the fixed mean profile. By comparison with figure 2.5, it appears that the modification of the mean profile with M_c has weak effects on the growth rate and phase speed of the central mode. It leads to a small decrease of the amplification rate and frequency of the central mode (roughly 15% at $M_c = 0.87$) and slightly enhances the transition to the outer modes at $M_c = 1$. Therefore, density effects alone are not responsible for the large decrease in growth rate seen in section 2.4.2.1, so there must be a strong effect associated with the Mach number itself.

2.4.3.2. Moderate heat release $\Theta = 1$

Figures 2.15 and 2.16 show the amplification rate and phase speed of the slow and fast outer modes for the fixed mean profile. Comparison with figure 2.9 and 2.10 shows that, unlike what is observed for the central mode, density effects associated with M_c are important for the outer modes. In particular, the increase in frequency and amplification rate seen with increasing M_c (section 2.4.2.2) appear to be due to density effects and not Mach number. We note that, when the mean profile is fixed, the usual compressibility trends (reduction of the spreading rate and smaller frequencies) are observed.

In the low-frequency region where the central mode is present, the density effects are weak and Mach number effects dominate. The amplification curves and phase speed in this region are unchanged between figure 2.9 and 2.15 or 2.10 and 2.16. The decoupling of the two modes and the disappearance of the low-frequency region with M_c are observed. In the high-frequency region, on the contrary, the modification of the mean profile due to compressibility appears to have a very large effect on the outer modes and counteracts the effects of the Mach number itself on those modes. Density effects associated with compressibility yield narrower mean density-weighted vorticity peaks and hence increase the frequency and amplification rate of the outer modes. Meanwhile, as M_c is increased, these peaks are closer to the fast and slow free streams, causing the phase velocities to move towards the fast and slow free stream speeds.

2.4.3.3. High heat release $\theta = 4.85$

Here, compressibility effects on the mean temperature profile $((\gamma - 1)M_c^2 / 2)$ are comparatively lower than in the zero or low heat release cases. For that reason, in this case, the results of the linear stability obtained when the constant mean profile at $M_c = 0.01$ is used (fig. 2.17 and 2.18) are closer to the linear stability results obtained

when the effect of M_c on the mean density profile are taken into account (variable mean profile in fig. 2.12 and 2.13). When the mean profile is kept constant, only the pure compressibility effects are observed: (1) Decoupling of the outer modes and (2) strong reduction of the amplification rates and frequencies of the fast and slow outer modes with M_c . However, this reduction is of the order of 60% between $M_c = 0.01$ and $M_c = 3.5$ to be compared to 90% between $M_c = 0.01$ and $M_c = 0.87$ for the central mode in the non-reacting case. The introduction of the flame convective Mach number M_f will clarify this observation.

2.4.4. Flame convective Mach numbers

We show in this section that the usual convective Mach number M_c is inappropriate for the outer modes in a strongly compressible or reacting mixing layer, and introduce a new convective Mach number, “the flame convective Mach number”, that is appropriate.

2.4.4.1. Formulation

Papamoschou and Roshko (1986) proposed to characterize the compressibility of the flow in a frame of reference in which the structure is stationary by defining the convective Mach numbers as follows:

$$\begin{aligned} M_{c1} &= \frac{\bar{u}_1 - \bar{u}_c}{\bar{c}_1} \\ M_{c2} &= \frac{\bar{u}_c - \bar{u}_2}{\bar{c}_2} \end{aligned} \quad (2.79)$$

where \bar{u}_c is the convective speed of the structure. The assumption that fluid from each of the free streams comes to rest *isentropically* at the stagnation point in a frame moving with the large-scale transverse structure. The isentropic assumption is invalid if the fluid particle passes through a shock wave or flame front. For streams with equal specific-heat ratios ($\gamma_1 = \gamma_2$), the isentropic assumption yields $M_{c1} = M_{c2}$ and the usual convective Mach number was defined as $M_c = M_{c1} = M_{c2}$. Noting that $P_1 = P_2$, the convective speed of the structure becomes

$$\bar{u}_c = \frac{\bar{u}_1 \sqrt{\rho_1} + \bar{u}_2 \sqrt{\rho_2}}{\sqrt{\rho_1} + \sqrt{\rho_2}}, \quad (2.80)$$

showing that, for uniform density, the structures travel at the average speed of the free-streams. However, experiments by Papamoschou (1989) showed that as the convective Mach number exceeds 1 the disturbance phase velocity departs from the mean velocity and approaches either \bar{u}_1 or \bar{u}_2 . Hence the convective Mach number will not correlate experimental observation above $M_c = 1$.

From our linear stability analysis, several results contradict the ideas behind the usual convective Mach number M_c :

1. The phase velocities of the outer modes depart from the average mean flow velocity as in experiments of Papamoschou.
2. The reduction of the amplification rate with M_c is stronger for the central mode than for the outer modes, especially at high heat release.
3. The effects of compressibility measured by M_c are different on the fast and slow outer modes whether the mean profile is changed or not. This result is particularly obvious in the high heat release case.

Therefore, we have introduced a new convective Mach number, “the flame convective Mach number”, M_f . The fast outer mode experiences a shear between the fast free-stream (\bar{u}_1, \bar{T}_1) and the flame sheet (\bar{u}_f, \bar{T}_f). If we assume that all the chemical reaction occurs at the flame sheet, the assumption of isentropy between the free-stream and the flame sheet can be made. Then, following the arguments of Papamoschou and Roshko (1988), one can show that the convective Mach number between the fast stream and the flame is

$$M_{f1} = \frac{\bar{u}_1 - \bar{u}_f}{\bar{c}_1 + \bar{c}_f} \quad (2.81)$$

which we call the “fast flame convective Mach number”. Similarly, the “slow flame convective Mach number” is

$$M_{f2} = \frac{\bar{u}_f - \bar{u}_2}{\bar{c}_f + \bar{c}_2}. \quad (2.82)$$

The slow and fast flame convective Mach numbers are related to the conventional Mach number M_c by

$$M_{f1} = \frac{\bar{u}_1 - \bar{u}_f}{\bar{u}_1 - \bar{u}_2} \left(\frac{\sqrt{\gamma_1 r_1 \bar{T}_1} + \sqrt{\gamma_2 r_2 \bar{T}_2}}{\sqrt{\gamma_1 r_1 \bar{T}_1} + \sqrt{\gamma_f r_f \bar{T}_f}} \right) M_c \quad (2.83)$$

$$M_{f2} = \frac{\bar{u}_f - \bar{u}_2}{\bar{u}_1 - \bar{u}_2} \left(\frac{\sqrt{\gamma_1 r_1 \bar{T}_1} + \sqrt{\gamma_2 r_2 \bar{T}_2}}{\sqrt{\gamma_f r_f \bar{T}_f} + \sqrt{\gamma_2 r_2 \bar{T}_2}} \right) M_c \quad (2.84)$$

where r is the gas constant per unit mass. Written in this form, one sees that the two flame convective Mach numbers are not equal, and that they both depend on the flame sheet position (through \bar{u}_f), on the flame sheet temperature \bar{T}_f , and on the free-stream temperature ratio. This suggests that compressibility effects (obliquity, reduction of the spreading angle...) can be significantly different for the two outer modes.

Changing the position of the flame sheet (for example by modifying the mass fraction of fuel in the fast stream for a constant mass fraction of oxidant in the slow stream) will modify the respective values of the two flame convective Mach numbers. When the flame sheet position (\bar{u}_f) is moved towards one of the free streams, the flame convective Mach number associated with this free-stream decreases, and the flame convective Mach number associated with the other free stream increases. At high Mach number, the outer mode corresponding to the “rich” side of the mixing layer will tend to be more two-dimensional and to have a larger amplification rate than the outer mode corresponding to the lean side of the mixing layer. This suggests possible ways to control the mixing in supersonic combustors.

An increase of heat release leads to a reduction of both flame convective Mach numbers, which suggest that increasing \bar{T}_f should yield an increase in the growth rate of the layer. Indeed, Hall (1991) indicates that the shear layer thickness derived from a fitted temperature profile is seen to increases with increasing heat release (by 10% at $M_c = 0.5$ when the heat release Θ is changed approximately from 0.3 to 1.2), which reverses the thinning effect seen in incompressible shear layers (Hermanson and Dimotakis 1989). Hall suggests that a coupling between compressibility effects and heat release distribution may explain the observed behavior. We believe that the flame convective Mach numbers embodies this coupling and may explain the 10% increase observed by Hall (see section 2.5.2).

2.4.4.2. Validation of the flame convective Mach numbers

Figure 2.19 show the normalized amplification rate of the most amplified 2-D central or outer modes for various heat release rate versus M_c for a fixed mean profile. The reduction of the amplification rate with increasing M_c is very strong for the central mode of the non-reacting case. As the flame temperature increases, this reduction of the spreading angle with M_c become milder. We also note that compressibility effects measured with M_c are different for the fast and slow outer modes, the fast outer mode being less stabilized than the slow outer mode, as expected for a fuel-lean case. The slope change on the amplification curve of the slow instability mode at $\Theta = 1$ ($H = 1$ on fig. 2.19) corresponds to a transition where at low Mach numbers the central mode is more amplified than the slow outer mode, while at high Mach numbers the opposite is true. In the low Mach number region where the central mode dominates, we note that the reduction of amplification rate of the slow instability mode with M_c matches the no-heat release amplification curve of the central mode.

Figure 2.20 shows the same information than figures 2.19, however here we plot the variation of the central mode versus M_c but the variation of the outer modes versus M_f . The comparison shows that the flame convective Mach numbers are preferred parameters to correlate compressibility effects for three reasons. (1) The curves are less scattered than when M_c is used for the outer modes, and all of the amplification rates are within 20% of the correlation. (2) The flame convective Mach number becomes a better parameter as the heat release increases, making the two mean density-weighted vorticity peaks more distinct. For example, the agreement between the central mode curve versus M_c and the outer modes curves at $\Theta = 5$ versus M_f is excellent. (3) The effect of the position of the flame (*i.e.* \bar{u}_f) on the compressibility effect is correctly predicted. Whereas the fast and slow instability mode amplification curves are distinct when M_c is used, these curves coincide with each other when M_f is used.

In the small heat release case ($\Theta = 1$) of figure 2.19, the amplification rate of the slow mode shows a slope change with increasing M_c , indicating a change from central mode to outer mode. Here, M_c ($\neq M_f$) should be used before the change and M_f ($\neq M_c$) should be used after the change. The flame convective Mach number is the preferred parameter to describe compressibility effects on the outer modes, especially in the high heat release cases, whereas at low heat release and low Mach numbers the usual convective Mach number M_c should be used. For intermediate heat release, using both M_c and M_f would give a range of prediction within which one would expect to find the experimental data.

2.4.5. Obliquity of the disturbance waves

In this section the amplification rate and phase speed of the most amplified central fast and slow outer modes are presented for various obliquities, heat release rates and Mach numbers. It is shown that, in the absence of heat release and at low M_c , the central 2-D mode dominates, while at high M_c the most amplified modes are either oblique central modes (Sandham and Reynolds 1990) for moderate Mach numbers ($M_c < 2$) or 2-D and oblique outer modes for large M_c . With increasing heat release, the influence of each density-weighted vorticity peak ($\bar{\rho} d\bar{u}/dy$) on the eigenmode associated with the other peak is reduced. The fast and slow outer modes become more amplified than the central mode and the flame convective Mach numbers become the proper correlating parameters. Hence, at a given heat release, increasing M_c increases M_f and the obliquity of the outer modes. On the contrary, at a given M_c

increasing the heat release reduces M_f and the obliquity of the outer modes. Due to density effects, the amplification rate and the two-dimensionality of the outer modes increase with increasing M_c at low or moderate heat release.

2.4.5.1. No heat release

Figures 2.22 and 2.23 show the amplification rates and phase speed of the most rapidly amplified central, fast and slow disturbance modes for different obliquities in the absence of heat release.

At low Mach numbers, the central mode is the only instability mode. Several observations can be made: (1) The growth rate of the 2-D central mode is strongly reduced with M_c as in experiments. (2) The amplification rates of eigenmodes having various obliquities can be very similar (*e.g.* angle 0° to 45° at $M_c = 0.6$). (3) The phase speed of the central mode is the same at all M_c and all obliquities (fig. 2.22). (4) The obliquity of the central mode increases with increasing M_c and oblique central modes dominate 2-D central modes for $M_c > 0.6$.

This fourth point, found by Sandham and Reynolds (1990, 1991) in their linear stability analysis and direct numerical simulations results, has experimental support from Clemens and Mungal (1992). It can also be obtained mathematically following the method of Squire (1933). Equation (2.67) can be rewritten as:

$$\frac{d\chi^t}{dy^t} = \frac{\alpha^2(\bar{u} - c)}{\bar{T}} - \frac{\chi^t(\chi^t g^t + d\bar{u}/dy^t)}{\bar{u} - c} \quad (2.85)$$

where

$$M_c^t = M_c \cos \theta \quad y^t = \frac{y}{\cos \theta} \quad (2.86)$$

$$\chi^t = \frac{\chi}{\cos \theta} \quad g^t = g \cos^2 \theta \quad (2.87)$$

Written in this form, one sees that any three-dimensional disturbance equation with parameters $(M_c, \bar{T}(M_c), \theta, \delta)$ can be reduced to a two dimensional disturbance equation with parameters $(M_c^t, \bar{T}(M_c), 0, \delta^t)$, provided that the mean profiles are fixed. Hence, the behavior of a three-dimensional disturbance $(M_c, \bar{T}(M_c), \theta, \delta)$ can be derived from the two dimensional case with parameters $(M_c^t, \bar{T}(M_c), 0, \delta^t)$ but not from the two dimensional case with parameters $(M_c^t, \bar{T}(M_c^t), 0, \delta^t)$. As the modification of the mean profile with M_c has weak effects on the instability of the central mode (section 2.3.4), the Sandham and Reynolds correlations is foreseeable. The three-dimensional disturbances they obtained at high Mach numbers are identical to the two-dimensional disturbances of similar mixing layers at lower Mach numbers.

Above $M_c = 0.9$, the slow outer modes appear first as M_c is increased, followed by the fast outer modes (fig. 2.23). After an initial steep rise corresponding to the uncoupling of the outer modes, the amplification rate of the slow outer mode decreases up to $M_c = 2$, before increasing due to the modification of the mean profile with M_c . Above an angle of 60° , Mach number effects are weaker than density effects, and the amplification rate of the slow outer mode steadily increases with M_c . The amplification rates of the fast and slow outer modes are comparable at all obliquities. Due to the uncoupling of the outer modes and to the modification of the mean profile with M_c , the phase speed of each outer mode moves towards the velocity of the associated free stream as M_c increases.

We have shown that the proper parameter to correlate the behavior of the outer modes is M_f . Since $M_f < M_c$ for any layer, compressibility effects are weaker on the outer modes than on the central mode. In particular, the reduction of the amplification rate with increasing M_c is small and the outer modes are more two-dimensional. In the high convective Mach number regions ($M_c \approx 3$), the 2-D slow outer modes become more rapidly amplified than the 3-D central modes, suggesting that even in the absence of heat release outer modes should dominate the flow at high Mach numbers. Thus, the flame convective Mach numbers are the describing parameters for high-speed mixing layer, even in the absence of a flame.

2.4.5.2. Small heat release case ($\Theta = 0.5$)

The small heat release case is the most complicated case for two reasons. (1) First, the two mean density-weighted vorticity peaks are not widely separated, and at low M_c the presence of each peak affects the eigenmode associated with the other peak. (2) Second, the modification of the mean profile with M_c is large compared to that produced by heat release, and distinguishing between density effects and Mach number effects is harder than in higher heat release cases. Figures 2.24 to 2.26 show the amplification rates, convective speeds and wavenumbers of the fast and slow instability modes in this low heat release case. Note that the fast and the slow outer modes are present at all M_c .

At low M_c , the amplification rate of the fast instability mode is very low (0.03 at $M_c = 0$ and $\theta = 0^\circ$), while the slow instability mode behaves like the central mode of the non-reacting case. The phase velocity of the slow mode is equal to the average speed of the free streams and its amplification rate is close to the amplification rate of the central mode of the non-reacting compressible mixing layer (fig. 2.25). Oblique

slow instability modes become dominant around $M_c = 0.6$ as in the no-heat-release case. The amplification rates and the frequencies of the fast and slow instability mode are significantly reduced as M_c is increased, suggesting that M_c is the correct parameter to describe compressibility effects in this region.

As M_c is increased, the influence of each mean density-weighted vorticity peak on the instability mode associated with the other peak is reduced, and above a certain M_c ($M_c \approx 1$ for the 2-D mode) the convective speeds of the fast and the slow outer modes progressively move towards the speeds of their associated free streams. This compressibility effect obviously depends on the obliquity of the instability mode, and at a given M_c the convective speed is closer to the average of the two free-stream speeds when the obliquity is increased. The amplification rates of the outer modes first decrease with M_f and the fast oblique outer modes become dominant around $M_c = 1.3$ corresponding to $M_f = 0.5$. As M_c is increased further, the modification of the mean profile leads to a reduction of compressibility effects, yielding an increase of the amplification rate and reduced obliquities. In particular, at $M_c = 3$ the 2-D slow outer mode becomes more rapidly amplified than the 3-D outer mode.

The behavior of the wavenumber of the slow instability mode is shown on figure 2.26. For low M_c we observe a decrease of the wavenumber with M_c due to compressibility. At some M_c ($M_c \approx 0.7$ for 2-D mode) the outer modes decouple and the wavenumber of the most amplified slow instability mode jumps to a higher value. Compressibility effects are still present, but should now be measured by M_f . The reduction of the wavenumber with M_c is milder than before the jump. At higher M_c , the modification of the mean temperature profile yields higher wavenumbers.

2.4.5.3. Moderate heat release case ($\Theta = 1$)

Figures 2.27 to 2.29 show the amplification rates, phase speeds and wavenumbers of the fast and slow instability modes at $\Theta = 1$. Note that the amplification curves are smoother than in the low heat release case, showing that increasing M_c has less complex effects as heat release is increased. For example, the amplification curve of the 2-D fast instability mode exhibits a bump at $M_c = 1$ that is much smaller at $\Theta = 1$ than at $\Theta = 0.5$.

Here, the two mean density-weighted vorticity peaks are more pronounced than at $\Theta = 0.5$ and the effect of each peak on the eigenmode associated with the other peak is smaller, even at low M_c . The low-frequency domain where the central mode dominates is reduced, and the most amplified slow and fast instability modes become

independent of the central mode. The amplification rate of the fast instability mode is higher than at $\Theta = 0.5$, while that of the slow instability mode (which at low M_c and Θ was dominated by the influence of the central mode) is smaller. As a result, the ratio of the slow to fast amplification rate at $M_c \approx 0$ becomes closer to 0.5, the value observed at high heat release (see below). Also, even at $M_c = 0$ the phase velocities of the most amplified fast and slow instability modes are never equal to the average speed of the two streams (contrary to what is observed at $\Theta = 0$ or $\Theta = 0.5$ for the central mode).

As M_c is increased, the outer modes progressively decouple and the phase speeds of the most amplified fast and slow instability modes move towards the speeds of the associated free-streams (fig. 2.28). Here as Θ increases, the transition from a central mode (where the phase speed is equal to the average speed of the free-streams) to the outer modes (where the phase speed is close to the speed of one of the free-streams) is more progressive and starts earlier than at lower Θ . At $\Theta = 0$ or $\Theta = 0.5$ (fig. 2.23 and 2.25), the phase speed changes rapidly and at high M_c ($M_c \approx 1$ for $\Theta = 0$ and $M_c \approx 0.7$ for $\Theta = 0.5$) whereas at $\Theta = 1$ the instability modes are already partially uncoupled at $M_c = 0$ and the variation of their phase speed with M_c is smoother. Finally, as heat release increases, it plays a larger part than compressibility in the uncoupling of the outer modes, and, as expected, the effect of obliquity on the phase speed of the outer mode decreases as Θ increases.

As in the low heat release case, two different regions of M_c must be distinguished. At low Mach number, the slow instability mode is intermediate between the central mode and the slow outer mode. M_c is the proper correlating parameter for this mode. The reduction of its amplification rate with M_c (fig. 2.27 right) is comparable to the variation of the amplification rate of the central mode of the non-reacting mixing layer with M_c (fig. 2.22), and its obliquity increases with M_c . As M_c increases, the outer modes progressively decouple and the proper correlating parameter becomes M_f . Since M_f is smaller than M_c , compressibility effects are reduced. Around $M_c = 1$ the slow 2-D mode become more rapidly amplified than the slow 3-D modes. The transition to M_f also leads to a small bump on the amplification curve of the fast instability mode (fig. 2.27 left). As M_c (and thus M_f) is further increased, the obliquity increases again and the slow instability modes become three-dimensional again at $M_c = 1.2$ (fig. 2.27 left). Finally, at high M_f the modification of the mean profile leads to a reduction of compressibility effects, and at small obliquities the amplification

curves of the fast and the slow instability modes exhibit a minimum around $M_c = 2$. Above $M_c = 2$, the modification of the mean profile yields an increase of the amplification rate of the mixing layer, obliquity is reduced, and the 2-D instability modes become more rapidly amplified than the 3-D instability modes.

In order to estimate the part played by density on obliquity as M_c is increased, the same analysis has been conducted for the 2-D and 45° oblique instability modes, where the mean profile has been kept fixed as the mean profile at $M_c = 0.01$. The comparison of the amplification rates, frequencies and phase speeds of the most amplified slow and fast outer modes when the mean profile is kept constant or changed with M_c is shown on figures 2.30 to 2.32. As seen in section 2.3.4, density effect are large on the outer modes and are already present at $M_c = 0.5$. First, the reduction of compressibility observed at large M_c when the mean profile is varying is not seen when the mean profile is kept constant. The amplification rate, wavenumbers and two-dimensionality of the instability modes decreases with increasing M_c . Second, when the mean profile is kept constant, the flame convective Mach numbers M_f are higher (T_f is smaller) and compressibility effects are stronger. At a given M_c , the amplification rate of the instability modes is smaller (fig. 2.30), their obliquity higher (the 45° fast instability modes become more amplified than the 2-D fast instability modes at lower M_c when the profile is kept constant) (fig. 2.30), and their phase speeds are closer to the associated free-stream velocities (fig. 2.31). Note however, that the instability modes have the same qualitative behavior whether the mean profile is kept fixed or not. In particular, the fact that the slow outer mode is successively 2-D then 3-D then 2-D then 3-D as M_c increases, and the existence of the small bump on the fast mode amplification curve at $M_c = 1$, appears independent of density effects.

2.4.5.4. High heat release cases ($\Theta = 2$ and 4.85)

At high heat release, the influence of each peak on the eigenmode associated with the other peak is reduced, and the influence of compressibility on the mean temperature becomes negligible compared to the influence of heat release. As a result, the effects of compressibility become less complex. Figures 2.33 to 2.35 show the amplification rates, frequencies and phase speeds of the slow and fast outer modes of the $\Theta = 2$ case, and figures 2.36 to 2.38 show the corresponding information for the case $\Theta = 4.85$.

Here even at low M_c , the outer modes are decoupled and the best parameter to describe compressibility effects is the flame convective Mach number. Since the flame

convective Mach number is significantly lower than M_c , compressibility effects (obliquity, strong reduction of the amplification rate, etc.) are weaker. The 2-D modes remain dominant to much higher M_c with heat release, and the reduction of the spreading angle with M_c is not as strong as it is for the non-reacting mixing layer (fig. 2.33 and 2.36). Compressibility effects are not symmetric on the outer modes. In the $\Theta = 4.85$ case, the 0° and 30° instability curves of the slow outer mode cross at $M_c = 3$ (fig. 2.36), where the 2-D fast outer mode is still more amplified than the 30° fast outer mode (fig. 2.36) as expected for a fuel-lean calculation where the flame speed is located in the fast stream at $\bar{u}_f = 0.8$.

At high heat release, compressibility has no effect on the uncoupling of the outer modes which occurs at $M_c = 0$. As expected, as Θ is increased the phase velocities of the fast and slow outer modes become independent of the obliquity, and in the highest heat release case all of the phase speed curves lie on top of each other (fig. 2.37). By comparison with the low and moderate heat release cases, as Θ is increased the phase speeds of the fast and slow outer modes shift towards the associated free stream velocities, while, at a given Θ , increasing M_c leads to the same behavior due to the modification of the mean profile.

2.4.5.5. Conclusion

To summarize, when we use M_f or M_c as appropriate, we retrieve in the compressible reacting case the same behavior as in the non-reacting case. At a given heat release, the obliquity is increased with the convective Mach number (M_c for central modes or M_f for outer modes). The results of Sandham and Reynolds (1990) showing that the angle of the most amplified disturbance was given by $M_c \cos \theta \approx 0.6$ is only valid for low and moderate Mach numbers and in the absence of heat release. In the reacting/compressible case, the obliquity of the outer modes is governed by M_f and the Sandham and Reynolds formula can be extended by replacing M_c by M_f . At high heat release ($\Theta = 5$), the 2-D disturbance modes remain more rapidly amplified until $M_c = 3.5$. Finally, for the small and moderate heat release cases, the density effects associated with M_c lead to a reduction of compressibility effects. At high M_c , higher amplification rates (and hence spreading angles) and reduced obliquity are observed as M_c is increased.

2.4.6. Effect of the magnitude of the heat release

In this section, the effect of increasing heat release on the eigenmodes at various obliquities (0° , 30° and 45° degrees) are analyzed for two values of the convective Mach

numbers ($M_c = 0.01$ and $M_c = 1.2$). Previous investigation of this issue at low speed indicated a stabilization of the flow by heat release. Mahalingham *et al.* (1989), using linear stability analysis and direct numerical simulations of the coflowing reacting jet, predicted an increased stability with heat release. The same effect was observed by Shin and Ferziger (1991a) for the low Mach number mixing layer. Jackson and Grosch (1990) found that, while a very small heat release could stabilize the flow, this trend was reversed when the heat release was increased sufficiently. Our results indicate that heat release has stabilizing effect on the central mode and destabilizing effect on the outer modes. With a low Mach number and a low heat release, the mixing layer (which is then dominated by the central mode) is stabilized by increased heat release. On the contrary, with a high Mach number or a high heat release, the mixing layer is dominated by the outer modes, and heat release has two distinct effects. (1) It modifies the density-weighted vorticity mean profile, yielding more widely separated peaks and reducing the effect of each peak on the instability mode associated with the other peak. (2) It also increases the temperature in the central part of the layer, increasing the speed of sound and resulting in lower flame convective Mach numbers. Both effects yield higher amplification rates of the outer modes, and hence the layer is destabilized by heat release.

At low Mach number ($M_c = 0.01$), increasing heat release modifies the mean profile of the density weighted vorticity but has no effect on compressibility. Figures 2.39 to 2.41 show the modification of the amplification rates, phase speeds, and wavenumbers of the most amplified incompressible central modes and outer modes when heat release is increased. At zero heat release, the central mode is the only amplified instability mode, and one only has to consider the influence of the heat release on the central mode. Increasing the heat release modifies the mean density-weighted vorticity profile and slightly stabilizes the central mode. The obliquity or the phase speed of the most amplified central mode (fig. 2.40) are not modified by the heat release, but its wavenumber is also slightly reduced. As the heat release is increased above 0.2, the outer modes appear (fig. 2.39). As the heat release is increased, the two peaks of maximum density-weighted vorticity become more pronounced, the mutual influence of the peaks on each other decreases, and the central mode stabilizes further. The amplification rates of the outer modes are increased, and their phase speeds are shifted towards their free stream velocities (fig. 2.40). We also note that as the width of the peaks become smaller, the wavenumber of the most amplified mode becomes smaller

and smaller, suggesting that the size of the large-scale structure decreases. Above $\Theta = 1$, the outer modes become more amplified than the central mode (fig. 2.39). Also above $\Theta = 2$, the amplification rate of the outer mode becomes independent of Θ .

At $M_c = 1.2$ case (fig. 2.42 to 2.44), increasing heat release modifies the mean density-weighted vorticity (as seen previously) but also lowers the flame convective Mach numbers, thereby reducing compressibility. At zero heat release, the central mode is strongly damped by compressibility effects and the 45° central mode is more amplified than the 2-D central mode (fig. 2.42). Also (as seen in section 2.4.2) since $M_c > 1$ the outer modes are present even in the absence of heat release, but at low heat release the linear stability results suggest that the central oblique modes dominate the outer modes. At low heat release, the 45° outer modes are slightly more amplified than the 2-D outer modes. As the heat release is increased, the central mode is stabilized but remains three dimensional. The reduction of its amplification rate with Θ is smaller than at $M_c = 0.01$. Its wavenumber is also reduced but its phase speed is unchanged. The outer modes become dominant at $\Theta = 0.25$, much earlier than in the incompressible case. As in the low compressibility case, as the heat release increases the peaks move towards the free streams and become narrower: The phase speeds of the outer modes move towards their free stream speeds, while their wavenumbers increase. The proper correlating parameter becomes M_f . At low heat release, M_f is large (at $\Theta = 0.5$, $M_f = 0.54$) and the outer modes are three-dimensional (fig. 2.42). As the heat release is increased, M_f drops, yielding smaller compressibility effects (at $T_f = 4$, $M_f = 0.4$ and at $T_f = 10$, $M_f = 0.28$). In particular, the 2-D outer modes become more rapidly amplified than the 3-D outer modes around $\Theta = 1$ ($M_f = 0.5$). Also, compared to the low compressibility case ($M_c = 0.01$), the amplification rates of the outer modes at $M_c = 1.2$ is strongly reduced at low heat release but almost unchanged at high heat release.

In conclusion, at low Mach number and low heat release the mixing layer (dominated by the central mode) is stabilized by heat release, while at high Mach number or heat release the mixing layer (dominated by the outer modes) is destabilized by heat release. Heat release has two destabilizing effects. (1) It shifts the two mean density-weighted vorticity peaks outwards and reduces their thicknesses, and (2) it reduces compressibility effects (when T_f is increased, both M_{f1} and M_{f2} decrease). This second point suggests that heat release effect will become more obvious as M_c

increases, yielding an increase in the (inferred) spreading angle of the compressible reacting mixing-layer (as experimentally observed by Hall) and reducing the obliquity of the large-scale structures.

2.4.7. Effect of the position of the flame zone

In this last section, a “flip” experiment has been conducted where for a given heat release $\Theta = 3$ and for two values of M_c ($M_c = 0.01$ and $M_c = 1$) the fuel-equivalence ratio was changed from 0.25 (fuel lean) to 0.5, 1, 2, and 4 (fuel rich). Note that we arbitrarily called fuel the reactant in the fast stream but that the results are identical if we termed oxidizer the reactant in the fast stream. Like the magnitude of the heat release, the position of the flame has two distinct effects: (1) It modifies the mean density-weighted vorticity distribution (fig. 2.45), changing both the magnitude and width of the two peaks (fig. 2.87 and 2.88), and (2) it modifies \bar{u}_f , which increases one flame convective Mach number and reduces the other.

At fixed low M_c ($M_c = 0.01$) only the first effect is seen. Figures 2.46 to 2.47 show the amplification rate and phase speed of the slow and fast instability mode as the fuel equivalence ratio is changed. As the flame is moved from the fast side of the layer to the slow side (by increasing the fuel equivalence ratio), the fast density-weighted vorticity peak magnitude and width are increased and the slow density-weighted vorticity peak magnitude and width are decreased. The amplification rate of the fast mode is increased at low frequencies and decreased at high frequencies, and its phase speed is moved towards the average speed of the free streams. The amplification rate of the slow mode is reduced at low frequencies and increased at high frequencies and its phase speed is moved towards the slow free-stream velocity. Note the distinct bump on the stoichiometric slow amplification curve, indicating the presence of the central mode and the fact that all the fuel rich curves coincide in this region. As the flame is moved towards the slow stream, the fast outer mode tends to become a central mode while the slow outer mode tends to disappear.

At high M_c , the modification of the flame convective Mach numbers with \bar{u}_f becomes important. In addition to modifying the density-weighted vorticity distribution, varying the position of the flame decreases towards one free stream decreases the flame convective Mach number associated with that stream as shown below:

Figures 2.48 and 2.49 show the corresponding information to figures 2.46 and 2.47 at $M_c = 1$. In the fuel lean case ($Y_f/Y_o = 0.25$), $M_{f1} = 0.146$ and $M_{f2} = 0.586$. Compared to

$M_c = 0.01$, the amplification curve of the fast outer mode is unchanged (0.038), whereas the slow outer mode maximum growth rate is reduced from 0.09 to 0.06 (30%). The opposite is true for the fuel rich case, where $M_{f1} = 0.584$ and $M_{f2} = 0.148$: The slow amplification curve is unchanged (0.0286) whereas the maximum amplification rate of the fuel lean mixing layer is reduced from 0.13 to 0.08 (30%).

The modification of the mean density-weighted vorticity and the modification of the flame convective Mach numbers have therefore opposite effects: As the flame is moved towards the slow stream, (1) the density-weighted vorticity effect yields a reduction of the growth rate of the slow outer mode whereas (2) the flame Mach number effect yields an increase of the growth rate of this mode. Although we considered only 2-D modes, the variation of the flame convective Mach numbers M_f with the position of the flame has also important consequences on the obliquity of the fast and slow outer modes. The disturbances on one side of the layer become oblique for $M_f > 0.6$. This suggests possible ways to control the compressible reacting mixing layer.

Table 2.1. Influence of the fuel equivalence ratio on the flame sheet location and on the flame convective Mach numbers

Yf/Yox	\bar{u}_f	fast M_f	slow M_f
0.25	0.9000	0.1464	0.5856
0.50	0.8321	0.2458	0.4862
1.00	0.7498	0.3663	0.3657
2.00	0.6601	0.4976	0.2344
4.00	0.6008	0.5844	0.1476

2.5. Comparison with experiments

2.5.1. Comparison to Stanford experiments

In this section, we give the results of the linear stability analysis of the reacting mixing layer corresponding to the experiment of Miller *et al.* (1992). The main difference with the results of the previous sections is the very different fast and slow stream temperatures. The conditions are $\bar{u}_1^* = 1050\text{m/s}$, $\bar{T}_1^* = 1400\text{K}$ for the fast stream and $\bar{u}_2^* = 115\text{m/s}$, $\bar{T}_2^* = 300\text{K}$ for the slow stream giving $M_1 = 1.35$, $M_2 = 0.3$, and $M_c = 0.8$.

The mean density-weighted vorticity profile ($\bar{\rho} d\bar{u}/dy$) is shown on figure 2.50 for three different values of the heat release ($\Theta = 0.142, 0.356, 0.571$). The mixing layer is slightly

fuel rich, which brings the flame position towards the slow speed side. The large density difference between the two stream has two effects. First, it leads to clearly unequal fast and slow density-weighted vorticity peaks. Second, for small heat release the flame temperature is too low for the fast peak to appear.

Figure 2.51 shows the amplification rate and phase speed of the slow instability mode in the low heat release case. Here, the heat release is not sufficient for the two density-weighted vorticity peaks to appear, and the fast outer mode does not exist. Only one instability mode exists, which travels on the slow-speed side of the layer. The mean flow does have distinct density-weighted vorticity peaks, and the usual convective Mach number is the preferred parameter to describe compressibility effect in this case. We note that at $M_c = 0.8$ the 0° , 30° and 45° modes all have the same amplification rate. At low frequencies, the instability mode resembles a central mode and the 45° mode is more amplified than the 2-D mode, whereas at high frequencies the instability mode resembles an outer mode and the 2-D mode is more amplified.

When the heat release is increased to $\Theta = 0.356$, the two density-weighted vorticity peaks become distinct, and two instability modes are present. Their amplification rates and phase speeds are shown on figure 2.52 and 2.53. Due to the strong asymmetry between the two free-stream densities, the fast outer mode is still an order of magnitude less amplified than the slow outer mode (fig. 2.52). The flame convective Mach number progressively becomes the significant parameter for correlating compressibility effects, and we observe that the 2-D slow outer modes become more amplified than the 3-D slow outer modes, particularly at high frequencies (where the two instability modes are more uncoupled). We note that the convective speed of the fast instability mode is very close to the average speed of the fast free stream. Also, when compared to the lowest heat release case (fig. 2.51), the convective speed of the slow outer mode is shifted towards the speed of the slow stream (fig. 2.53).

In the highest heat release case $\Theta = 0.571$, the obliquities of the fast and slow outer mode are reduced further as the density-weighted vorticity peaks become more distinct and as the fast and slow flame convective Mach numbers become the preferred parameters (fig. 2.54). The low frequency region where the convective speed of the instability modes is close to the average speed of the two streams is reduced. As the outer modes become uncoupled, the frequencies of the fast and slow instability modes shift to higher values and their phase velocities shift towards the mean velocity in their associated free stream (fig. 2.53). However, the fast amplification rate is still

one order of magnitude higher than the slow amplification rate.

2.5.2. Comparison to Caltech experiments

In this section, an expression is proposed for the growth rate of a two-dimensional reacting mixing layer. The results obtained are compared with the results given by Hall (1991). Dimotakis (1986) proposed to evaluate the growth of the two-dimensional shear layer by

$$\frac{\delta}{x} = \epsilon \left(\frac{1-r}{1+\sqrt{sr}} \right) \left[1 + \sqrt{s} - \frac{1-\sqrt{s}}{1+2.9(1+r)/(1-r)} \right] \quad (2.88)$$

where $r = \bar{u}_2/\bar{u}_1$ is the free-stream speed ratio, $s = \bar{\rho}_2/\bar{\rho}_1$ the free-stream density ratio and ϵ a constant equal to 0.085 if δ is the vorticity thickness δ_ω . We apply the same formula to each of the two colayers, multiplying the incompressible growth rate given by (2.88) by a damping term Υ assumed to depend only on the flame convective Mach number. This gives

$$\begin{aligned} \frac{\delta_1}{x} &= \epsilon \left(\frac{1-r_1}{1+\sqrt{s_1}r_1} \right) \left[1 + \sqrt{s_1} - \frac{1-\sqrt{s_1}}{1+2.9(1+r_1)/(1-r_1)} \right] \Upsilon(M_{f1}) \\ \frac{\delta_2}{x} &= \epsilon \left(\frac{1-r_2}{1+\sqrt{s_2}r_2} \right) \left[1 + \sqrt{s_2} - \frac{1-\sqrt{s_2}}{1+2.9(1+r_2)/(1-r_2)} \right] \Upsilon(M_{f2}) \end{aligned} \quad (2.89)$$

where $r_1 = \bar{u}_f/\bar{u}_1$, $s_1 = \bar{\rho}_f/\bar{\rho}_1$, $r_2 = \bar{u}_2/\bar{u}_f$, $s_2 = \bar{\rho}_2/\bar{\rho}_f$. Υ is the reduction of the spreading angle due to compressibility assumed to be proportionnal to the reduction amplification of the amplification rate of the outer modes with M_f . The results are presented below for the case 3a, 3b, 3c, 3d and 3e of Hall (1991).

Table 2.2. New growth rate model for compressible reacting mixing layers

r_1	s_1	r_2	s_2	M_{f1}	M_{f2}	$100\frac{\delta_1}{x}$	$100\frac{\delta_2}{x}$	$100\frac{\delta}{x}$
0.65	0.836	0.362	1.010	0.233	0.254	3.20	7.13	10.33
0.65	0.742	0.362	1.138	0.218	0.239	3.19	7.49	10.68
0.65	0.674	0.362	1.253	0.206	0.227	3.18	7.80	10.98
0.45	0.720	0.522	1.173	0.336	0.121	4.82	5.38	10.19
0.85	0.710	0.276	1.188	0.091	0.346	1.33	8.18	9.51

Hall (1991, table 5.1) reports large variation of the growth rate (measured in term of the temperature thickness) with the position or temperature of the flame. For example, for a given fuel-equivalence ratio (position of the flame), the growth rate is seen to increase with heat release. Equation (2.88) which is independent of the flame temperature or position is inappropriate to predict the growth rate of compressible reacting mixing layer. Taking into account compressibility by multiplying

the incompressible growth rate by $\Upsilon(M_c)$, the growth rate of the layer computed using 2.88 with $s = 1$, $r = 0.235$ and $M_c = 0.5$ is $\delta/x = 7.6810^{-2}$ independent of the position or temperature of the flame. On the contrary, (2.89) depends on the flame temperature and position. We note that the growth rate (measured with δ_ω) is increased by 3.3% when the heat release is increased from $\Theta = 0.3$ to $\Theta = 0.6$, and by 2.8% when the heat release is increased from $\Theta = 0.6$ to $\Theta = 1.2$. Hall's experiment indicates respective increases of 6.5% and 2.7%. The agreement (2.7% versus 2.8%) is excellent at high heat release. At lower heat release, however, although the correct trend is predicted (increase of the spreading angle with T_f) the agreement is not as good. Two reasons can be proposed: (1) the chemistry is slow in the low heat release case and ratio of the temperature thickness to the visual thickness may be reduced. (2) The heat release may be too low for the two peaks of density-weighted vorticity to appear and be distinct.

Hall (1991, table 5.1) also notes a large effect in the flip experiment in which the temperature thickness was increased by 30% when the fuel-equivalence ratio was changed from 1 to 0.25. We believe that this large effect arises from the modification of the layer structure when the relative growth rates of the two colayers are changed. The previous table gives the growth rates δ_1/x and δ_2/x of the two colayers computed with equations 2.89. We note that in all the cases but the fourth one, the fast speed side of the layer is developing slower than the slow speed side, but that in the fourth case the two colayers have similar growth rates. This may yield the large effect seen by Hall. If only one mode is present, the mean temperature profile shifts towards this side (see Hall 1991 fig. 5.4), whereas with the two colayers developing at the same pace (as in this fourth case) the mean temperature and product profiles are broader and have longer tails in both colayers and therefore increased widths. Although this information was not given by Hall, we believe that the flip experiment may not have such a large effect on other thicknesses (momentum or visual thicknesses for example).

2.6 Eigenfunctions

In this section, the most unstable eigenfunctions of the two-dimensional temporal instability are presented to illustrate the effect of compressibility and heat release on the eigenfunctions. The eigenfunctions are normalized so that the maximum value of \hat{u} is unity and the phase of \hat{v} is zero at the centerline ($y = 0$). Eigenfunctions contains

key informations relative to the shape of the large-scale structure and the entrainment and subsequent mixing process.

Figure 2.56 shows the $(\hat{u}, \hat{v}, \hat{T}, \hat{Z})$ eigenfunction of an incompressible non-reacting mixing layer at $M_c = 0.1$. For this central mode, the eigenfunction is symmetric, indicating that the transfer of momentum or species from both sides of the layer is the same. The width of the \hat{Z} eigenfunction is slightly smaller than the width of the velocity or temperature eigenfunctions, and has a faster exponential decrease in the free streams. The magnitude of \hat{v} is about half that of \hat{u} . Note that \hat{z} and \hat{v} have opposite phase and that \hat{T} lags \hat{v} by $\pi/2$. \hat{u} lags \hat{v} by π in the central part of the layer, by approximately $\pi/2$ in the slow stream and by $-\pi/2$ in the fast stream.

Figure 2.57 shows the same information as figure 2.58 for a central mode at $M_c = 0.875$. As M_c is increased, the magnitude of the pressure, density and temperature fluctuations increase strongly (the stagnation temperature and stagnation pressure of fluid from each of the free streams in a frame moving with the large-scale structure vary like M_c^2). The shape of the \hat{v} and \hat{z} eigenfunctions is unchanged, but their amplitudes are reduced, suggesting a more elongated structure and a less efficient convection of species from the two sides of the layer. Also, the exponential decay in the free streams is more gradual than in the low compressibility case. The phase of the \hat{T} and \hat{Z} eigenfunctions is not modified by the increased compressibility, but we note that the phase of \hat{u} outside the layer ($|y| > 0.5$) is slightly increased. Figure 2.58 shows the magnitude of the \hat{u} , \hat{v} , \hat{T} and \hat{Z} eigenfunctions of the most amplified central mode as M_c varies from 0.1 to 0.875. We retrieve the reduced efficiency of entrainment on the \hat{Z} eigenfunctions whose amplitude decrease with M_c . The \hat{v} eigenfunction is reduced by approximately 66%. The \hat{v} is minimum at the centerline but maximum at the edge of the layer (at $y = \pm 0.5$). The exponential decrease in the free stream of the \hat{u} , \hat{v} and \hat{T} eigenfunctions become more gradual as M_c is increased.

Figure 2.59 shows the \hat{u} , \hat{v} , \hat{T} and \hat{Z} eigenfunctions of the most amplified slow outer mode of an incompressible reacting mixing layer with large heat release. The largest disturbance amplitude of all the quantities occurs on the low-speed side, which suggest that direct entrainment of fuel and oxidizer does not occur. Instead, oxidizer is mixed with product from the central part of the layer. The magnitude of the \hat{T} eigenfunction is large due to the strong temperature gradient existing in the reaction zone. The \hat{Z} eigenfunction amplitude is higher than for a central mode, indicating that efficient mixing occurs, but its width is reduced compared to the central mode. The low-speed

sides of the \hat{u} and \hat{v} eigenfunctions appear very similar to the low-speed side of the \hat{u} and \hat{v} eigenfunction of the central mode. The jump in the \hat{T} eigenfunction at the position of the flame zone correspond to the flame sheet discontinuity. The rightmost peak on the \hat{u} eigenfunctions corresponds to fluid from the fast stream accelerating to move around the slow outer-mode structure.

Figure 2.60 shows the same information quantities as figure 2.59 for $M_c = 0.8$. As M_c is increased, the low-speed side of all the eigenfunctions is unchanged, indicating the absence of compressibility effects in this case with high heat release ($M_c = 0.8$ but $M_f = 0.23$). The high-speed side of the \hat{u} and \hat{v} eigenfunctions now exhibit slowly decaying oscillatory behavior arising from a radiating pressure wavesine and cosine functions corresponding to a radiating pressure wave. As expected, the existence of waves radiating *away* from the layer has no effect on the slow-speed side (in the absence of walls). The \hat{Z} and \hat{T} eigenfunctions are unchanged, suggesting no effect of M_c on entrainment. The acceleration of fluid around the slow-stream structure explains the peaks of the \hat{u} eigenfunction in the high-speed region and leads to the existence of the radiating waves.

Figure 2.61 shows the magnitude of the \hat{u} , \hat{v} , \hat{T} and \hat{Z} eigenfunctions of the most amplified slow outer mode as M_c varies from 0.1 to 1.2. It shows that the radiating pressure waves occurs when the Mach number between the fast and the slow stream becomes greater than approximately 1 (or $M_c > 0.5$ approximately). It also indicates a small decrease of the amplitude of \hat{v} with M_c .

Additional information can be found by generating contour plots of the temporal eigenfunctions, and in particular by examining the terms in the compressible vorticity equation,

$$\frac{D\omega_z}{Dt} = -\omega_z \left(\frac{\partial u}{\partial x} + \frac{\partial v}{\partial y} \right) - \frac{1}{\rho^2} \left(\frac{\partial p}{\partial x} \frac{\partial \rho}{\partial y} - \frac{\partial p}{\partial y} \frac{\partial \rho}{\partial x} \right). \quad (2.90)$$

Here, the first term on the right is the dilatational term and the second is the baroclinic term. The vorticity ω_z is negative, and so a positive dilatation or baroclinic term corresponds to a destruction of vorticity.

The contour plot of any quantity can be generated as

$$q = \bar{q} + A \operatorname{real}(\hat{q} e^{i\alpha x}). \quad (2.91)$$

In drawing these plots we have used an amplitude A equal to 0.05. The vorticity, baroclinic term, dilatation term, and vorticity production are shown on figures 2.62

to 2.64 for three different cases. The first case show the central mode of a non-reacting mixing layer at $M_c = 0.8$. The second case shows the same eigenfunction superimposed on the mean flow corresponding to a compressible reacting mixing layer with $M_c = 0.8$ and $\Theta = 2$. This case show the effect of the mean temperature profile on production of vorticity by the dilatation and baroclinic terms. The third case shows the eigenfunction structure of the slow outer mode of the compressible reacting mixing layer with $M_c = 0.8$ and $\Theta = 2$.

Figure 2.62 refers to the first case. As observed by Sandham (1989), in the compressible case, even at $M_c = 0.8$, the plot of ω_z and ω_z/ρ are little different from the vorticity structure found by Michalke (1965) in the incompressible case. Non-linear effects will cause the two “elementary vortices” in the eigenfunction to rotate around each other and merge to form the fundamental vortex in the mixing layer. In the compressible non-reacting case, both the dilatational and baroclinic term are positive in precisely those regions where the elementary vortices develop, and those terms act to reduce vorticity in the region where vortex roll-up occurs. Since the magnitudes of both the dilatational and baroclinic terms increase as the Mach number increases, the growth rate of the two-dimensional instability becomes less as M_c is increased. Note here that the main contribution to this reduction comes from the dilatation term.

When the mean profile of case 1 is replaced by the mean profile of the reacting mixing layer with heat release (case 2), the baroclinic term and dilatation terms keep the same structure (figure 2.63). The vorticity structure is now slightly easier to identify due to a flatter mean vorticity profile. However, compared with figure 2.62, the baroclinic term is increased by more than one order of magnitude due to the large density gradient in the reaction zone. As in case 1, the baroclinic and dilatation terms are large precisely in those regions where vortex roll-up would occur, but now due to the large magnitude of these terms the vortex roll-up is prevented. This explains why the central mode is not seen in the reacting or compressible case.

The eigenfunction structure of the slow outer mode with $M_c = 0.8$ and $\Theta = 2$ is shown on figure 2.64. Note that the gradients are very large and that the baroclinic term dominates the dilatational term. A large negative baroclinic torque region exists which suggests that high (negative) vorticity will build up in this region. In contrast, the existence of a large positive baroclinic torque region located below the large negative baroclinic torque region, and the shape of the high vorticity region, suggest that roll-up will not occur in compressible reacting mixing layers.

2.7 Absolute versus convective instability

We have presented in section 2.2 the linear stability theory. This classic approach analyses the eigenmodes of a flow system and determines if this flow is stable or unstable to particular disturbance modes. However, it is currently known that it is more relevant to model transition to turbulence by studying the evolution of wave packets generated by isolated pulse disturbances (Criminale & Kovasznay 1962, Gaster 1968a,b, Gaster & Davey 1968, Gaster & Grant 1975). The reason is that the natural transition to turbulence usually involves wave modes with a broad range of frequencies and wavelengths. The wave packet generated by idealized pulse excitations can model those generated in natural situations by disturbances such as free-stream turbulence. Also, studying the impulse response of the flow to a Dirac delta function in space and time does provide a useful methodology to decide whether temporal or spatial linear stability analysis are relevant. A flow is “absolutely unstable” (and temporal stability analysis must be used) if the response of the flow at any point is unbounded at large time. A flow is “convectively unstable” (and spatial stability analysis must be used) if the response of the flow at any point is bounded at large time. For a convectively unstable mixing layer, disturbances generated at the splitter plate are convected away as they amplify, whereas for an absolutely unstable mixing layer a transient disturbance generated at any location can propagate upstream and dramatically alter the nature of the whole flowfield. Here, we investigate the convective versus absolute instability issue for the reacting compressible mixing layer. We keep a three dimensional approach, since it is known that for compressible mixing layers the dominant instability modes can be highly three dimensional.

2.7.1 Formulation and resolution of the problem in the Fourier space

We substitute u' , v' , w' , ρ' , T' and p' into equations (2.50) to (2.54) to get

$$\frac{\partial \rho'}{\partial t} + \bar{u} \frac{\partial \rho'}{\partial x} + v' \frac{d\bar{\rho}}{dy} = -\bar{\rho} \left[\frac{\partial u'}{\partial x} + \frac{\partial v'}{\partial y} + \frac{\partial w'}{\partial z} \right] \quad (2.92)$$

$$\bar{\rho} \left[\frac{\partial u'}{\partial t} + \bar{u} \frac{\partial u'}{\partial x} + v' \frac{d\bar{u}}{dy} \right] = \frac{1}{\gamma_1 M_1^2} \frac{\partial p'}{\partial x} \quad (2.93)$$

$$\bar{\rho} \left[\frac{\partial v'}{\partial t} + \bar{u} \frac{\partial v'}{\partial x} \right] = \frac{1}{\gamma_1 M_1^2} \frac{\partial p'}{\partial x} \quad (2.94)$$

$$\bar{\rho} \left[\frac{\partial w'}{\partial t} + \bar{u} \frac{\partial w'}{\partial x} \right] = \frac{1}{\gamma_1 M_1^2} \frac{\partial p'}{\partial x} \quad (2.95)$$

$$\frac{\partial Z'}{\partial t} + \bar{u} \frac{\partial Z'}{\partial x} + v' \frac{d\bar{Z}}{dy} = 0 \quad (2.96)$$

$$\frac{\partial T'}{\partial t} + \bar{u} \frac{\partial T'}{\partial x} + v' \frac{d\bar{T}}{dy} = -\frac{\gamma-1}{r} \left[\frac{\partial u'}{\partial x} + \frac{\partial v'}{\partial y} + \frac{\partial w'}{\partial z} \right] \quad (2.97)$$

$$p' = \bar{\rho} \bar{r} T' + \rho' \bar{r} \bar{T} + \bar{\rho} \bar{T} r'. \quad (2.98)$$

As done in section 2.1 we multiply the first equation by $\bar{r} \bar{T}$ and add it to the last.

Using the perfect gas law and assuming that r is only a function of Z , we obtain

$$\frac{\partial p'}{\partial t} + \bar{u} \frac{\partial p'}{\partial x} = -\gamma \left[\frac{\partial u'}{\partial x} + \frac{\partial v'}{\partial y} + \frac{\partial w'}{\partial z} \right]. \quad (2.99)$$

We now differentiate the previous equation with respect to t and x . Adding the equation differentiated with respect to t and \bar{u} times the equation differentiated with respect to x , we get a system of two coupled differential equations in v', p' ,

$$\left(\frac{\partial}{\partial t} + \bar{u} \frac{\partial}{\partial x} \right)^2 p' = \frac{\gamma}{\gamma_1 M_1^2 \bar{\rho}} \left[\frac{\partial^2 p'}{\partial x^2} + \frac{\partial^2 p'}{\partial z^2} \right] + \gamma \frac{d\bar{u}}{dy} \frac{\partial v'}{\partial x} - \gamma \left(\frac{\partial}{\partial t} + \bar{u} \frac{\partial}{\partial x} \right) \frac{\partial v'}{\partial y} \quad (2.100)$$

$$\bar{\rho} \left[\frac{\partial v'}{\partial t} + \bar{u} \frac{\partial v'}{\partial x} \right] = \frac{1}{\gamma_1 M_1^2} \frac{\partial p'}{\partial y}. \quad (2.101)$$

Equation (2.100) can be rewritten as

$$\frac{\gamma}{\gamma_1 M_1^2} \left[\frac{1}{\bar{\rho}} \left(\frac{\partial^2}{\partial x^2} + \frac{\partial^2}{\partial z^2} \right) - \frac{\gamma_1 M_1^2}{\gamma} \left(\frac{\partial}{\partial t} + \bar{u} \frac{\partial}{\partial x} \right)^2 \right] p' = -\gamma \frac{d\bar{u}}{dy} \frac{\partial v'}{\partial x} + \gamma \left(\frac{\partial}{\partial t} + \bar{u} \frac{\partial}{\partial x} \right) \frac{\partial v'}{\partial y}. \quad (2.102)$$

In order to eliminate p' from equations (2.101) and (2.102), we apply to the first the operators $\frac{\partial}{\partial y}$ and $\frac{1}{\bar{\rho}} \left(\frac{\partial^2}{\partial x^2} + \frac{\partial^2}{\partial z^2} \right) - \frac{\gamma_1 M_1^2}{\gamma} \left(\frac{\partial}{\partial t} + \bar{u} \frac{\partial}{\partial x} \right)^2$. After simplification, one finds

$$\begin{aligned} & \left[\frac{1}{\bar{\rho}} \left(\frac{\partial^2}{\partial x^2} + \frac{\partial^2}{\partial z^2} \right) - \frac{\gamma_1 M_1^2}{\gamma} \left(\frac{\partial}{\partial t} + \bar{u} \frac{\partial}{\partial x} \right)^2 \right]^2 \rho \left[\frac{\partial v'}{\partial t} + \bar{u} \frac{\partial v'}{\partial x} \right] = \\ & \left[\frac{1}{\bar{\rho}} \left(\frac{\partial^2}{\partial x^2} + \frac{\partial^2}{\partial z^2} \right) - \frac{\gamma_1 M_1^2}{\gamma} \left(\frac{\partial}{\partial t} + \bar{u} \frac{\partial}{\partial x} \right)^2 \right] \frac{\partial}{\partial y} \left(\frac{d\bar{u}}{dy} \frac{\partial v'}{\partial x} - \left(\frac{\partial}{\partial t} + \bar{u} \frac{\partial}{\partial x} \right) \frac{\partial v'}{\partial y} \right) - \\ & \frac{\partial}{\partial t} \left[\frac{1}{\bar{\rho}} \left(\frac{\partial^2}{\partial x^2} + \frac{\partial^2}{\partial z^2} \right) - \frac{\gamma_1 M_1^2}{\gamma} \left(\frac{\partial}{\partial t} + \bar{u} \frac{\partial}{\partial x} \right)^2 \right] \left[\frac{d\bar{u}}{dy} \frac{\partial v'}{\partial x} - \left(\frac{\partial}{\partial t} + \bar{u} \frac{\partial}{\partial x} \right) \frac{\partial v'}{\partial y} \right]. \end{aligned} \quad (2.103)$$

To describe the response of a compressible reacting mixing layer to an impulse $\delta(x - x_0) \delta(y - y_0) \delta(z - z_0) \delta(t - t_0)$, we follow the method presented by Huerre and Monkewitz (1985). First since we assume that the mean flow is parallel and constant, we can assume without loss of generality that the point source is located at $(0, y_0, 0, 0)$. The problem amounts to finding the Green's function h solution to the Rayleigh equation written in term of ϕ such that $v = \partial\phi/\partial x$ (equation 2.103 differentiated with respect to x),

$$\begin{aligned} & \frac{\partial}{\partial x} \left\{ \left[\frac{1}{\bar{\rho}} \left(\frac{\partial^2}{\partial x^2} + \frac{\partial^2}{\partial z^2} \right) - \frac{\gamma_1 M_1^2}{\gamma} \left(\frac{\partial}{\partial t} + \bar{u} \frac{\partial}{\partial x} \right)^2 \right]^2 \rho \left[\frac{\partial h}{\partial t} + \bar{u} \frac{\partial h}{\partial x} \right] - \right. \\ & \left. \left[\frac{1}{\bar{\rho}} \left(\frac{\partial^2}{\partial x^2} + \frac{\partial^2}{\partial z^2} \right) - \frac{\gamma_1 M_1^2}{\gamma} \left(\frac{\partial}{\partial t} + \bar{u} \frac{\partial}{\partial x} \right)^2 \right] \frac{\partial}{\partial y} \left(\frac{d\bar{u}}{dy} \frac{\partial h}{\partial x} - \left(\frac{\partial}{\partial t} + \bar{u} \frac{\partial}{\partial x} \right) \frac{\partial h}{\partial y} \right) + \right. \\ & \left. \frac{\partial}{\partial t} \left[\frac{1}{\bar{\rho}} \left(\frac{\partial^2}{\partial x^2} + \frac{\partial^2}{\partial z^2} \right) - \frac{\gamma_1 M_1^2}{\gamma} \left(\frac{\partial}{\partial t} + \bar{u} \frac{\partial}{\partial x} \right)^2 \right] \left[\frac{d\bar{u}}{dy} \frac{\partial h}{\partial x} - \left(\frac{\partial}{\partial t} + \bar{u} \frac{\partial}{\partial x} \right) \frac{\partial h}{\partial y} \right] \right\} = \\ & \left[\frac{1}{\bar{\rho}} \left(\frac{\partial^2}{\partial x^2} + \frac{\partial^2}{\partial z^2} \right) - \frac{\gamma_1 M_1^2}{\gamma} \left(\frac{\partial}{\partial t} + \bar{u} \frac{\partial}{\partial x} \right)^2 \right]^2 \delta(x) \delta(y - y_0) \delta(z) \delta(t) \end{aligned} \quad (2.104)$$

with the boundary conditions and initial conditions:

$$|h(x, y, z, t, y_0)| \rightarrow 0 \quad |y| \rightarrow \pm\infty \quad (2.105)$$

$$|h(x, y, z, t, y_0)| = 0 \quad t < 0. \quad (2.106)$$

We introduce at this point the complex function $H(x, y, z, t, y_0)$ and its Fourier transform \hat{H} , defined as

$$\begin{aligned} H(x, y, z, t, y_0) &= h(x, y, z, t, y_0) - \int_{\zeta=-\infty}^{+\infty} \int_{\xi=-\infty}^{+\infty} \frac{h(x-\xi, y, z-\zeta, t, y_0)}{\pi^2 \xi \zeta} d\xi d\zeta \\ &+ i \int_{\xi=-\infty}^{+\infty} \frac{h(x-\xi, y, z, t, y_0)}{\pi \xi} d\xi + i \int_{\zeta=-\infty}^{+\infty} \frac{h(x-\zeta, y, z, t, y_0)}{\pi \zeta} d\zeta \end{aligned} \quad (2.107)$$

$$H(x, y, z, t, y_0) = \frac{1}{2\pi} \int_{F_\alpha} \int_{F_\beta} \hat{H}(\alpha, y, \beta, t, y_0) e^{i\alpha x + i\beta z} d\alpha d\beta \quad (2.108)$$

$$\hat{H}(\alpha, y, \beta, t, y_0) = \frac{1}{2\pi} \int_L \hat{H}(\alpha, y, \beta, \omega, y_0) e^{-i\omega t} d\omega \quad (2.109)$$

where F_α, F_β and L are integration contours in the complex plane to be specified.

After substitution in equation 2.104 we get

$$[\frac{\partial}{\partial y} (\frac{1}{g} \frac{\partial}{\partial y}) - \bar{\rho} \alpha^2 - (\bar{u} - c)^{-1} \frac{\partial}{\partial y} (\frac{1}{g} \frac{\partial \bar{u}}{\partial y})] \hat{H}(\alpha, y, \beta, \omega, y_0) = -\frac{4H(\alpha)H(\beta)\delta(y-y_0)}{i\alpha(\bar{u}-c)}, \quad (2.110)$$

where H is the Heaviside step function, c the complex phase velocity is defined as $c = \omega/\alpha$ and g is defined as (2.66). The boundary conditions become

$$[\frac{\partial}{\partial y} - \alpha(\bar{\rho} g)^{0.5}] \hat{H}(\alpha, y, \beta, \omega, y_0) = 0 \quad y \rightarrow +\infty \quad (2.111)$$

$$[\frac{\partial}{\partial y} + \alpha(\bar{\rho} g)^{0.5}] \hat{H}(\alpha, y, \beta, \omega, y_0) = 0 \quad y \rightarrow -\infty. \quad (2.112)$$

On either side of the singularity, $\hat{H}(\alpha, y, \beta, \omega, y_0)$ is solution of the homogeneous Rayleigh equation. We call Φ^+ and Φ^- the solutions of the Rayleigh equation from y_0 to $+\infty$ and from $-\infty$ to y_0 , respectively. At the singularity (y_0) the boundary conditions are

$$\Phi^+(\alpha, \beta, \omega, y_0) = \Phi^-(\alpha, \beta, \omega, y_0) \quad (2.113)$$

$$\frac{\partial \Phi^+}{\partial y}(\alpha, \beta, \omega, y_0) = \frac{\partial \Phi^-}{\partial y}(\alpha, \beta, \omega, y_0) + \frac{4H(\alpha)H(\beta)(\bar{T}_0' - M_1^2(\bar{u}_0 - c)^2)}{i\alpha(\bar{u}_0 - c)}. \quad (2.114)$$

The solution of equation (2.110) is

$$\begin{aligned}\hat{H}(\alpha, y, \beta, \omega, y_0) &= -\frac{4H(\alpha)H(\beta)(\bar{T}_0' - M_1^2(\bar{u}_0 - c)^2)}{i\alpha(\bar{u}_0 - c)D(\alpha, \beta, \omega, y_0)} \hat{G} \\ \hat{G} &= \Phi^+(\alpha, \beta, \omega, y)\Phi^-(\alpha, \beta, \omega, y_0) \quad y > y_0 \\ \hat{G} &= \Phi^-(\alpha, \beta, \omega, y)\Phi^+(\alpha, \beta, \omega, y_0) \quad y < y_0\end{aligned}\tag{2.115}$$

where $\bar{T}_0' = \bar{T}(y_0)(\alpha^2 + \beta^2)/\alpha^2$ and $\bar{u}_0 = \bar{u}(y_0)$. $D(\alpha, \beta, \omega, y_0) = 0$ is the dispersion relation of the Rayleigh equation and determines, for a given α and β , the complex frequency ω of the linear instability modes of the shear layer.

2.7.2 Transformation of the Fourier solution to the physical space

Once the problem has been solved in the Fourier space, the resolution of the problem in the physical space requires integration of \hat{H} along L for given α and β fixed on F_α, F_β to obtain H . Then H has to be integrated over F_α, F_β . Those two integration are performed at fixed y and y_0 . We limit ourselves here to the asymptotic solution for large times. As will be shown thereafter, the restriction of the problem to large time will enable us to use the steepest descent method to obtain H . We will also show that the main contribution to the contour integration in ω plane come from discrete eigenmodes given by $D(\alpha, \beta, \omega, y_0) = 0$.

2.7.2.1. Integration over the ω contour The contour L is chosen to be a straight line from $-\infty$ to $+\infty$ position above all complex singularities in the ω plane. This amounts to assigning an imaginary part to the frequency parameter ω such that this imaginary part is larger than the fastest growth rate of the disturbances. This ensures the convergence of the Fourier transform. These singularities are given given by $D(\alpha, \beta, \omega, y_0) = 0$, $(\bar{T}_0' - M_1^2(\bar{u}_0 - c)^2) = 0$ and $(\bar{u}_0 - c) = 0$.

For $t < 0$ the integration contour must be closed by a semi-circle in the upper half of the ω plane to allow the integral to converge. Since there are no singularities above the integration path, the solution for $t < 0$ is identically 0 which is consistent with the principle of causality. For $t > 0$ the integration contour is closed at infinity by a semi-circle in the lower half plane. The contributions to the integral come from all the singularities (from the dispersion relation) and branch cuts. The singularities are poles and give the discrete instability modes while the branch cut correspond to the continuous spectra.

The branch cuts are singularities of the functions Φ^+ and Φ^- and are associated to

the points y_c where

$$\omega = \alpha \bar{u}(y_c) \quad (2.116)$$

$$\omega = \alpha \bar{u}(y_c) \pm \sqrt{\frac{(\alpha^2 + \beta^2)\bar{T}'(y_c)}{M_1^2}}. \quad (2.117)$$

In the vicinity of those points, the Rayleigh equation respectively has the form

$$yh'' + a(y)yh' + b(y)h = 0 \quad (2.118)$$

$$yh'' + a(y)h' + b(y)h = 0 \quad (2.119)$$

where $a(y)$ and $b(y)$ have power series expansion which are convergent for $|y| < \infty$. This can easily be shown by doing a Taylor series expansion. For example, at the point y_c where $\bar{u}(y_c) = \omega/\alpha$ a Taylor expansion gives $\bar{u}(y) - \omega/\alpha = \bar{u}(y_c)'(y - y_c) + \bar{u}(y_c)''(y - y_c)^2/2$ and unless $\bar{u}'(y_c) = 0$, the Frobenius method can be applied. Using the Frobenius method, it is possible to show that the solutions of the Rayleigh equation are of the form

$$\phi_1(y) = \sigma_1(y) \quad \text{and} \quad \phi_2(y) = \sigma_2(y) + c(\log |y - y_c|)\phi_1(y) \quad (2.120)$$

where σ_1 and σ_2 have power series expansion convergent for $|y| < \infty$. The functions Φ^+ and Φ^- have logarithmic singularities at the points given by (2.116) and (2.117). Now, for given y, y_0, β and α we want to evaluate the contribution of this logarithmic branch points to the contour integral. The three branch points are chosen to lie below L as sketched on figure 2.65 and the continuous contribution of the logarithmic branches to the solution is

$$\hat{H}_c(\alpha, \beta, y, t, y_0) = \frac{1}{2\pi} \int_{\Gamma_1, \Gamma_2, \Gamma_3} \hat{H}(\alpha, \beta, y, \omega, y_0) e^{-i\omega t} d\omega. \quad (2.121)$$

To evaluate the contribution of those terms at large t , we apply the method of steepest descent. As shown in Bender and Orzag (1978, p 282), the behavior of the integral

$$I(t) = \int_0^1 \ln \omega e^{i\omega t} d\omega \quad (2.122)$$

as $t \rightarrow \infty$ is

$$I(t) \approx -i \frac{\ln t}{t} - \frac{i\gamma_e + \pi/2}{t} + ie^{it} \sum_{n=1}^{\infty} \frac{(-i)^n (n-1)!}{x^{n+1}}, \quad (2.123)$$

where γ_e is the Euler constant 0.5772. If the same method is applied to the integrand $\omega^n (\ln \omega) e^{i\omega t}$, one finds an asymptotic contribution at large t of the order of $(\ln t)/t^{n+1}$. Therefore the contribution of the three logarithmic branches to the contour integral

in the ω plane decays faster than $(\ln t)/t^{n+1}$ as t goes to ∞ (where n is determined by the first non-zero term of the taylor expansion of σ_1 in equation 2.120).

An other contribution to the contour integral in the ω plane come from the zeros of $D(\alpha, \beta, \omega, y_0)$. If for given α and β , $D(\alpha, \beta, \omega, y_0) = 0$ then the functions Φ^+ and Φ^- are equal. We denote by Φ_n the eigenfunction associated to $(\alpha, \beta, \omega(\alpha, \beta), y_0)$. Using the Cauchy integration formula, one finds

$$\begin{aligned} \hat{H}_{discrete}(\alpha, \beta, y, t, y_0) = \\ \Sigma_n 4H(\alpha)H(\beta) \frac{(\bar{T}_0' - M_1^2(\bar{u}_0 - c)^2)\Phi_n(\alpha, \beta, \omega, y)\Phi_n(\alpha, \beta, \omega, y_0)}{(\bar{u}_0 \alpha - \omega_n(\alpha, \beta))\partial D(\alpha, \beta, \omega, y_0)/\partial \omega} e^{-i\omega_n(\alpha, \beta)t}. \end{aligned} \quad (2.124)$$

2.7.2.2. Integration over the α contour Since we showed that the long term behavior of the continuous spectrum was shown to vary like $(\ln t)/t^{n+1}$ for large t , the discrete part of the solution, which grows exponentially, will be dominant at large t , and the response of the reacting shear layer in physical space will be given by

$$\begin{aligned} H(x, y, z, t, y_0) = \frac{1}{\pi^2} \Sigma_n \int_{F_\alpha, F_\beta} H(\alpha)H(\beta) \\ \frac{(\bar{T}_0' - M_1^2(\bar{u}_0 - c)^2)\Phi_n(\alpha, \beta, \omega, y)\Phi_n(\alpha, \beta, \omega, y_0)}{(\bar{u}_0 \alpha - \omega_n(\alpha, \beta))\partial D(\alpha, \beta, \omega, y_0)/\partial \omega} e^{i(\alpha x + \beta z - \omega_n(\alpha, \beta)t)} d\alpha d\beta \end{aligned} \quad (2.125)$$

where $F_\alpha, (F_\beta)$ are chosen to be the real axis closed at infinity by a quarter circle in the upper half α (β) plane as shown in figure 2.65.

We now follow the method of Gaster (1968a). The contributions to the double integral in the wave number space come from the singularities of the integrand and from the exponential term. We restrict ourselves to the behavior at large t but keep in the analysis the ratios x/t and z/t constant. The waves are followed by an observer moving at the constant velocity $(x/t, z/t)$ on a ray issued from the origin. At large times, the dominant contribution arises from the exponential and can be evaluated using the steepest descent (constant phase) method. The original integration paths along the real axis are deformed onto the steepest descent path into the α and β planes. The largest value of the integrand arises near the local maxima of

$$\psi = (\alpha x/t + \beta z/t - \omega_n(\alpha, \beta)). \quad (2.126)$$

These local maxima may occur at the endpoint of constant phase ψ contour or at an interior point of a constant phase ψ contour (referred to as a saddle point). The contribution to the integral coming from the inferior endpoint $\alpha = 0$ or $\beta = 0$ can be

shown to vary like $1/t$ for large t as x/t and z/t are kept constant. This contribution can be neglected in the asymptotic analysis. The other contribution comes from the saddle point defined by

$$\frac{\partial w_n(\alpha, \beta)}{\partial \alpha} = \frac{x}{t} \quad \text{and} \quad \frac{\partial w_n(\alpha, \beta)}{\partial \beta} = \frac{z}{t}. \quad (2.127)$$

Its contribution can be evaluated as:

$$H(x, y, z, t, y_0) = -\sum_n \frac{(\bar{T}_0' - M_1^2(\bar{u}_0 - c)^2)\Phi_n(\alpha, \beta, \omega, y)\Phi_n(\alpha, \beta, \omega, y_0)}{2\pi(\bar{u}_0\alpha - \omega_n(\alpha, \beta))\frac{\partial D}{\partial \omega}(\alpha, \beta, \omega, y_0)t[J(\alpha, \beta)]^{0.5}} e^{i(\alpha x + \beta z - \omega_n(\alpha, \beta)t)} \quad (2.128)$$

with

$$J(\alpha, \beta) = \frac{\partial^2 \omega_n}{\partial \alpha^2} \frac{\partial^2 \omega_n}{\partial \beta^2} - \left(\frac{\partial^2 \omega_n}{\partial \alpha \partial \beta}\right)^2. \quad (2.129)$$

Equation (2.128) describes the wave packet generated by the pulse as the sum of three-dimensional waves having group velocity $\partial w_n(\alpha, \beta)/\partial \alpha, \partial w_n(\alpha, \beta)/\partial \beta$. The observer traveling at the speed $x/t, z/t$ (equal to the group velocity of the wave) sees the wave growing or decaying according to the sign of the real part of:

$$\psi(\alpha, \beta) = i[\alpha \frac{\partial w_n(\alpha, \beta)}{\partial \alpha} + \beta \frac{\partial w_n(\alpha, \beta)}{\partial \beta} - w_n(\alpha, \beta)]. \quad (2.130)$$

As shown in the following section, (2.130) can be used to determine if the flow is absolutely or convectively unstable.

2.7.3 Absolute or convective instability

We are interested in the growth rate of the wave having a zero group velocity. If the real part of ψ is positive, the stationary wave grows exponentially with time, the mixing layer is absolutely unstable, and temporal linear stability analysis must be used. For the zero-group velocity wave, the condition of absolute instability (2.130) becomes:

$$\text{Im} [\omega_n(\alpha, \beta)] > 0 \quad (2.131)$$

with α and β defined by

$$\frac{\partial w_n(\alpha, \beta)}{\partial \alpha} = 0 \quad \text{and} \quad \frac{\partial w_n(\alpha, \beta)}{\partial \beta} = 0 \quad (2.132)$$

The dispersion relation has been numerically calculated for various parameters (free stream temperature ratio, M_c , free stream velocity ratio and flame temperature) to investigate the effect of this parameters on the transition from convective to absolute

instability. From section 2.3 we know that multiple instability modes are present and susceptible to becoming absolutely unstable. However, investigation of the central mode by various researcher showed that, in the absence of heat release, this mode only becomes absolutely unstable for non-zero counterflows ($\bar{u}_2 < -0.136\bar{u}_1$). Increasing heat release would modify the -0.136 value, but we believe that in the absence of counterflows the outer mode would appear before the central mode become absolutely unstable. Therefore, we restrict the analysis to the outer modes. We also restrict ourselves to the slow outer mode but extrapolation will be made to the fast outer mode in the conclusion. The results are shown in table 2.3.

**Table 2.3. Influence of M_c , T_f and T_2 on
the absolute growth rate of the layer**

M_1	\bar{u}_2	\bar{T}_2	M_c	\bar{T}_f	θ	ω_r	ω_i	α_r	α_i
0.2	.01	1.00	0.10	6.0	0	.152	.0263	.56	-0.93
0.2	.05	1.00	0.10	6.0	0	.168	-.0101	.27	-0.96
0.2	.01	1.00	0.10	4.0	0	.196	.0091	.61	-0.94
0.6	.01	1.00	0.30	4.0	0	.196	.0058	.64	-0.96
1.2	.01	1.00	0.59	4.0	0	.198	-.0061	.72	-1.07
2.4	.01	1.00	1.19	4.0	0	.186	-.0344	.79	-1.43
2.4	.01	0.90	1.22	4.0	0	.185	-.0285	.83	-1.49
2.4	.01	0.70	1.29	4.0	0	.182	-.0158	.90	-1.64
2.4	.01	0.50	1.39	4.0	0	.174	-.0016	.95	-1.83
2.4	.01	0.15	1.71	4.0	0	.121	.0209	.72	-2.14
2.4	.01	0.15	0.93	4.0	0	.101	.0336	.46	-1.49
2.4	.02	0.15	0.93	4.0	0	.104	.0196	.24	-1.36
2.4	.02	0.15	0.93	4.0	45	.066	.0149	.11	-0.88

Figures 2.66 to 2.68 show the dispersion relation in three different cases; an absolutely unstable case, a convectively unstable case and a mildly convectively unstable case. In all cases the dispersion relation appears as a system of two orthogonal sets of hyperbolic functions. The center of the hyperbolic system corresponds to the zero group-velocity point. As can be seen in all the cases we studied, the zero group-velocity point has a positive phase velocity. Also, in all cases, α_i is negative, indicating an eigenmode exponentially growing with downstream distance. A few points should be made:

1. The absolute instability is encountered for negative or very small positive velocity of the slow stream. Typically \bar{u}_2 is a few percents of \bar{u}_1 .

2. Increasing the heat release or diminishing the temperature of the slow stream has the same effect; both changes promote absolute instability (fig. 2.69).
3. The absolute instability of the slow stream is possible even if $M_c > 1$. It only depends on the slow stream parameters \bar{u}_f , \bar{u}_2 , \bar{T}_f and \bar{T}_2 .

For non-reacting mixing layers, an absolute instability can develop if the configuration is able to propagate information upstream. All modification of the flowfield that reduces the group velocity, enables the development of absolute instability. As shown by Trouve (1989), increasing the temperature of the fast stream, which reduces the speed of the eigenfunctions, will favour absolute instability. For the slow colayer between the flame (\bar{u}_f, \bar{T}_f) and the slow stream (\bar{u}_2, \bar{T}_2) the same is true. Slowing down the eigenfunction convective speed by lowering \bar{u}_f (adding fuel to the fast stream) or \bar{u}_2 or by increasing the ratio \bar{T}_f / \bar{T}_2 will help the development of absolute instability.

For the fast stream the opposite is true. The development of absolute instability is enhanced by increasing the ratio \bar{T}_1 / \bar{T}_f , that is cooling the flame and heating the fast stream. It is also enhanced if the flame sheet is moved toward the slow stream. (for example by increasing the fuel equivalence ratio). Since $\bar{T}_1 / \bar{T}_f < \bar{T}_1 / \bar{T}_2$ and $\bar{u}_f > \bar{u}_2$, the fast outer mode will always be less absolutely unstable than the central mode.

2.8. Chapter summary

In this chapter, we have presented linear inviscid stability analysis of the plane reacting compressible mixing layer. The mean flow profiles were calculated using the compressible boundary-layer equations, and the limit of infinite reaction rate was taken. Linear stability analysis was shown to be a very useful tool for investigating the structure of the supersonic reacting mixing layer. In particular:

1. The existence of two maxima on the mean density-weighted vorticity profile was shown to lead to two distinct “outer modes”. At low Mach numbers, low heat releases, and low frequencies, one of these instability mode behaves like the usual central mode and the other one is neutral. Each of the outer modes is associated with one of the free streams, and its phase velocity is close to the speed of this free stream.
2. The usual convective Mach number was shown to be of limited use for compressible

reacting shear layers. The “flame convective Mach numbers” were introduced and shown to be preferable parameters for correlating the behavior of the reacting shear layer with high heat release (or the non-reacting mixing layer at very high M_c). As a consequence, the obliquity of the flow and the strong reduction of the amplification rate at high Mach numbers (M_c) are less pronounced with increased heat release.

3. The large-scale entrainment of fluid from both sides is not likely to occur in compressible reacting mixing layers. Instead, the existence of the outer modes suggests that a two-step mixing could prevail; 1) Fluid from the fast free stream is mixed with product by the fast outer mode, and fluid from the slow free stream is mixed with product by the slow outer mode. 2) The hot mixtures of fuel and product on one side and oxidizer and product on the other side diffuse to the reaction zone. The compressible reacting mixing layer should behave as two colayers (fig. 2.70).
4. The existence of absolute instability was shown to occur for the slow outer mode even in the absence of counterflow. In particular it was shown that increasing the fuel equivalence ratio, increasing the temperature of the flame, and lowering the temperature of the slow stream all lead to a change from convective to absolute instability.
5. The possibility of controlling the obliquity of the fast and slow outer mode by changing the flame temperature or modifying the position of the flame was demonstrated. In particular, it was shown that increasing heat release has a stabilizing effect on the low Mach number, low heat-release mixing layer, for which the central mode is dominant. Increasing heat release has a destabilizing effect on the high Mach number, high heat-release mixing layer, for which the outer modes are dominant. At high Mach number, it was shown that pushing the flame toward one of the outer modes destabilizes this mode and makes it more two-dimensional. Also, increasing the heat release was shown to make the two outer modes more 2-D, while having no effect on the obliquity of the central mode.

CHAPTER 3

Method for Direct Numerical Simulation

Two-dimensional and three-dimensional direct numerical simulations are performed using an extension of the code of Poinsot and Lele (1989) (Poinsot-Lele's code, PLC) for diffusion flames, and an extension of Sandham's code (SC) to allow for reacting flows. The 2-D temporal and spatial simulations using the PLC were run on the Cray Y-MP, while both 2-D and 3-D temporal simulations using the SC were run on the hypercube and on the Cray Y-MP. The 2 codes are written in Vectoral (Wray 1988) and have been implemented at NASA-Ames.

3.1. Equations

The conservation equations for mass, momentum, energy and species are written in term of $(\rho^*, \rho^* u_i^*, \rho^* e_t^*, \rho^* Y_i)$, where ρ^* is the density, u_i^* the three velocity components, e_t^* is the total energy per unit mass defined by

$$e_t^* = e^* + u_i^* u_i^*/2 \quad (3.1)$$

where e^* is the internal energy per unit mass, and Y_o and Y_f are the oxidizer and fuel mass fractions. Using an Eulerian formulation and the Cartesian tensor notation, these equations are

$$\frac{\partial \rho^*}{\partial t^*} + \frac{\partial \rho^* u_i^*}{\partial x_i^*} = 0 \quad (3.2)$$

$$\frac{\partial \rho^* u_i^*}{\partial t^*} + \frac{\partial (\rho^* u_i^* u_j^* + p^* \delta_{ij})}{\partial x_j^*} = \frac{\partial \tau_{ij}^*}{\partial x_j^*} \quad (3.3)$$

$$\frac{\partial \rho^* e_t^*}{\partial t^*} + \frac{\partial [u_i^* (\rho^* e_t^* + p^*)]}{\partial x_i^*} = -\frac{\partial q_i^*}{\partial x_i^*} + \frac{\partial u_j^* \tau_{ij}^*}{\partial x_i^*} + \Delta H_r^* \dot{w}^* \quad (3.4)$$

$$\frac{\partial \rho^* Y_f}{\partial t^*} + \frac{\partial \rho^* u_i^* Y_f}{\partial x_i^*} = \frac{\partial}{\partial x_i^*} (\rho^* D^* \frac{\partial Y_f}{\partial x_i^*}) - \dot{w}^* \quad (3.5)$$

$$\frac{\partial \rho^* Y_o}{\partial t^*} + \frac{\partial \rho^* u_i^* Y_o}{\partial x_i^*} = \frac{\partial}{\partial x_i^*} (\rho^* D^* \frac{\partial Y_o}{\partial x_i^*}) - n \dot{w}^* \quad (3.6)$$

where the superscript * denotes a dimensional quantity. x_i^* , $i = 1, 2$ and 3 are the streamwise, normal, and spanwise direction respectively. The heat flux is q_j^* , τ_{ij}^* is the viscous stress tensor.

The chemical scheme is single step and irreversible: $F + nO \rightarrow (n+1)P$, where n is the mass of oxygen per mass of fuel. The reaction rate (fuel consumption rate) is

$$w^* = A_r^* \rho^{*2} Y_f Y_o e^{-Ta^*/T^*}. \quad (3.7)$$

$Z\epsilon = Ta^*/T_1^*$ is the Zeldovitch number and ΔH_r^* is the enthalpy of reaction per unit mass of fuel. Denoting the heat release by Θ^* ,

$$\Delta H_r^* = \left(\frac{1}{Y_f(+\infty)} + \frac{n}{Y_o(-\infty)} \right) \frac{r^* \gamma \Theta^*}{(\gamma - 1)}. \quad (3.8)$$

We assume a perfect Newtonian gas and Fourier heat conduction, which gives three additional constitutive equations

$$p^* = \rho^* r^* T^* \quad (3.9)$$

$$q_i^* = -\lambda_c^* \frac{\partial T^*}{\partial x_i^*} \quad (3.10)$$

$$\tau_{ij}^* = \mu^* \left(\frac{\partial u_i^*}{\partial x_j^*} + \frac{\partial u_j^*}{\partial x_i^*} - 2/3 \frac{\partial u_k^*}{\partial x_k^*} \delta_{ij} \right) \quad (3.11)$$

where μ^* the viscosity and r^* the gas constant, D_i^* the diffusivity of the i^{th} species, c_p^* the specific heat at constant pressure, and λ_c^* the conductivity. In what follows, the subscripts 1 and 2 refer to the fast and the slow streams, respectively. The Lewis number and the Prandtl number are defined as

$$Le_i = \frac{\lambda^*}{\rho^* D_i^* c_p^*}, \quad Pr = \frac{c_p^* \mu^*}{\lambda^*}. \quad (3.12)$$

In the present application, $Sc = Pr = Le = 1$, $\mu = \mu_{ref}(T/T_{ref})^{0.76}$. Other important parameters in the simulation are the Reynolds numbers and Damkhöler numbers, defined as

$$Re_1 = \frac{\rho_1^* u_1^* \delta_\omega^*}{\mu_1^*} \quad Da_1 = \frac{A_r^* \rho_1^* e^{-Ta^*/T_1^*} \delta_\omega^*}{u_1^*} \quad (3.13)$$

$$Re_c = \frac{\rho_1^* c_1^* \delta_\omega^*}{\mu_1^*} \quad Da_c = \frac{A_r^* \rho_1^* e^{-Ta^*/T_1^*} \delta_\omega^*}{c_1^*} \quad (3.13)$$

where δ_ω^* is the vorticity thickness. We also define the Reynolds number and the Damkhöler number as

$$Re = \frac{\rho_1^* (u_1^* - u_2^*) \delta_\omega^*}{\mu_1^*} \quad Da = \frac{A_r^* \rho_f^* Y_{f,\infty} e^{-Ta^*/T_f^*} \delta_\omega^*}{(u_1^* - u_2^*)}. \quad (3.14)$$

The nondimensionalization of the above equations is different in PLC and SC. In PLC $(\rho^*, T^*, \mu^*, u_i^*)$ are divided by $(\rho_1^*, (\gamma - 1)T_1^*, \mu_1^*, c_1^*)$ where ρ_1^* , μ_1^* and c_1^* are the density, viscosity and sound speed in the fast stream. The vorticity thickness δ_ω^* is chosen as the reference length. The PLC normalization gives

$$\begin{aligned} u_i &= \frac{u_i^*}{c_1^*} & \mu &= \frac{\mu^*}{\mu_1^*} \\ T &= \frac{T^*}{(\gamma - 1)T_1^*} & e &= \frac{e^*}{c_1^{*2}} \\ \rho &= \frac{\rho^*}{\rho_1^*} & p &= \frac{p^*}{\rho_1^* c_1^{*2}} \\ t &= \frac{t^* c_1^*}{\delta_\omega^*} & x_i &= \frac{x_i^*}{\delta_\omega^*}. \end{aligned} \quad (3.15a)$$

After substitution, the non dimensional conservation PLC equations become

$$\frac{\partial \rho}{\partial t} = -\frac{\partial \rho u_i}{\partial x_i} \quad (3.16a)$$

$$\frac{\partial \rho u_i}{\partial t} = -\frac{\partial(\rho u_i u_j + p \delta_{ij})}{\partial x_j} + \frac{\partial \tau_{ij}}{\partial x_j} \quad (3.17a)$$

$$\frac{\partial \rho e_t}{\partial t} = -\frac{\partial[u_i(\rho e_t + p)]}{\partial x_i} - \frac{\partial q_i}{\partial x_i} + \frac{\partial(u_j \tau_{ij})}{\partial x_i} + \beta \dot{w} \quad (3.18a)$$

$$\frac{\partial \rho Y_f}{\partial t} = -\frac{\partial(\rho u_i Y_f)}{\partial x_i} + \frac{\partial}{\partial x_i}(\rho D \frac{\partial Y_f}{\partial x_i}) - \dot{w} \quad (3.19a)$$

$$\frac{\partial \rho Y_o}{\partial t} = -\frac{\partial(\rho u_i Y_o)}{\partial x_i} + \frac{\partial}{\partial x_i}(\rho D \frac{\partial Y_o}{\partial x_i}) - n \dot{w} \quad (3.20a)$$

with

$$q_i = -\frac{\mu}{Pr Re_c} \frac{\partial T}{\partial x_i} \quad (3.21a)$$

$$\tau_{ij} = \frac{\mu}{Re_c} \left(\frac{\partial u_i}{\partial x_j} + \frac{\partial u_j}{\partial x_i} - 2/3 \frac{\partial u_k}{\partial x_k} \delta_{ij} \right) \quad (3.22a)$$

$$\dot{w} = Da_c \rho^2 Y_f Y_o e^{-Z e(1/T - 1/T_f)} \quad (3.23a)$$

$$\beta = \left[\frac{1}{Y_f(+\infty)} + \frac{n}{Y_o(-\infty)} \right] \Theta. \quad (3.24a)$$

The nondimensionalization of equations (3.2) to (3.6) in SC is made by dividing $(\rho^*, T^*, \mu^*, u_i^*)$ by their respective value in the high speed stream $(\rho_1^*, T_1^*, \mu_1^*, u_{i1}^*)$ and the vorticity thickness δ_ω^* is chosen as the reference length. The SC normalization gives

$$u_i = \frac{u_i^*}{u_{i1}^*} \quad \mu = \frac{\mu^*}{\mu_1^*}$$

$$\begin{aligned}
T &= \frac{T^*}{T_1^*} & e &= \frac{e^*}{u_1^{*2}} \\
\rho &= \frac{\rho^*}{\rho_1^*} & p &= \frac{p^*}{\rho_1^* u_1^{*2}} \\
t &= \frac{t^* u_1^*}{\delta_\omega} & x_i &= \frac{x_i^*}{\delta_\omega}.
\end{aligned} \tag{3.15b}$$

After substitution, the non-dimensional SC conservation equations become

$$\frac{\partial \rho}{\partial t} = -\frac{\partial \rho u_i}{\partial x_i} \tag{3.16b}$$

$$\frac{\partial \rho u_i}{\partial t} = -\frac{\partial(\rho u_i u_j + p \delta_{ij})}{\partial x_j} + \frac{\partial \tau_{ij}}{\partial x_j} \tag{3.17b}$$

$$\frac{\partial \rho e_t}{\partial t} = -\frac{\partial[u_i(\rho e_t + p)]}{\partial x_i} - \frac{\partial q_i}{\partial x_i} + \frac{\partial(u_j \tau_{ij})}{\partial x_i} + \beta \dot{w} \tag{3.18b}$$

$$\frac{\partial \rho Y_f}{\partial t} = -\frac{\partial(\rho u_i Y_f)}{\partial x_i} + \frac{\partial}{\partial x_i}(\rho D \frac{\partial Y_f}{\partial x_i}) - \dot{w} \tag{3.19b}$$

$$\frac{\partial \rho Y_o}{\partial t} = -\frac{\partial(\rho u_i Y_o)}{\partial x_i} + \frac{\partial}{\partial x_i}(\rho D \frac{\partial Y_o}{\partial x_i}) - n \dot{w} \tag{3.20b}$$

with

$$q_i = -\frac{\mu}{(\gamma - 1) M_1^2 Pr Re_1} \frac{\partial T}{\partial x_i} \tag{3.21b}$$

$$\tau_{ij} = \frac{\mu}{Re_1} \left(\frac{\partial u_i}{\partial x_j} + \frac{\partial u_j}{\partial x_i} - 2/3 \frac{\partial u_k}{\partial x_k} \delta_{ij} \right) \tag{3.22b}$$

$$\dot{w} = Da_1 \rho^2 Y_f Y_o e^{-Z_e(1/T-1/T_f)} \tag{3.23b}$$

$$\beta = \left[\frac{1}{Y_f(+\infty)} + \frac{n}{Y_o(-\infty)} \right] \frac{\Theta}{M_1^2 (\gamma - 1)}. \tag{3.24b}$$

All the quantities (velocity, vorticity, baroclinic term, vorticity production, etc) presented in chapters 4 and 5 used the PLC nondimensionalization. The only exception (unless otherwise mentioned) is the time t since we believe the convective time is more meaningful than the time based on c . The time based on c is simply equal to the time based on u_1 multiplied by M_1 .

3.2. Time advancement

The time advancement is the same in PLC and SC. It is based on the third-order compact-storage Runge-Kutta method of the family derived by Wray (1986). It is fully explicit, requires three substeps per time step and two memory locations per dependent variable. For the reacting mixing layer the number of variables per grid

point is seven (ρ , ρu , ρv , ρw , ρe_t , ρY_f , ρY_o) in 3-D. At each subset, the two memory locations are updated simultaneously using

$$Q_1^{new} = a_1 \Delta t Q_1^{old} + Q_2^{old} \quad \text{and} \quad Q_2^{new} = a_2 \Delta t Q_1^{old} + Q_2^{old} \quad (3.25)$$

with $(a_1, a_2) = (2/3, 1/4), (5/12, 3/20), (3/5, 3/5)$ for the first, second and third time substeps respectively. Note that Q_1 is used at each substep to store the right hand side of equations (3.16) to (3.20), while Q_2 is only updated at the end of the substep. At the beginning of each full time step the value in Q_2 is set equal to the value in Q_1 .

As described by Sandham (1989), the maximum time step is determined by stability considerations on a model convection-diffusion equation where spatial derivatives are calculated using spectral method in all directions. For simplification, constant fluid properties are assumed in the stability analysis. The model equation

$$\frac{\partial \phi}{\partial t} + u \frac{\partial \phi}{\partial x} + v \frac{\partial \phi}{\partial y} + w \frac{\partial \phi}{\partial z} = a \frac{\partial^2 \phi}{\partial x_i^2} \quad (3.26)$$

is Fourier transformed and rearranged to give

$$\frac{\partial \tilde{\phi}}{\partial t} = -[i2\pi(\frac{k_x u}{L_x} + \frac{k_y v}{L_y} + \frac{k_z w}{L_z}) + a4\pi^2(\frac{k_x^2}{L_x^2} + \frac{k_y^2}{L_y^2} + \frac{k_z^2}{L_z^2})]\tilde{\phi}. \quad (3.27)$$

Once the equations for momentum, species and energy have been written under this canonical form, and using the stability diagram of the third-order Runge-Kutta method, it is possible to find the maximum possible time step. This leads to

$$\Delta t_s = \frac{CFL}{D_c + D_\mu} \quad (3.28)$$

where CFL is the Courant-Friedrichs-Levy number and D_c and D_μ are defined as

$$D_c = \pi c (\frac{1}{\Delta x} + \frac{1}{\Delta y} + \frac{1}{\Delta z}) + \pi (\frac{|u|}{\Delta x} + \frac{|v|}{\Delta y} + \frac{|w|}{\Delta z}) \quad (3.29)$$

$$D_\mu = \frac{\pi^2 \mu / \rho}{Re \min(Pr, Sc_i, 1)} (\frac{1}{\Delta x^2} + \frac{1}{\Delta y^2} + \frac{1}{\Delta z^2}) \quad (3.30)$$

This criteria is computed at every grid point, and the time step is chosen as the minimum of all the computed values. The value of the CFL number is taken equal to 2. Another time-step limitation arises from the reaction term. In both PLC and SC the chemical terms are treated explicitly and the maximum chemical time step is arbitrarily defined as

$$\Delta t_c = \frac{c_i e_t}{\beta \dot{w}} \quad (3.31)$$

where c_t is a constant chosen equal to 0.001, meaning that the maximum relative variation of the total energy due to chemical reaction is less than 0.001 in one time step. For the range of Damkhöler numbers considered, this criteria was usually less stringent than the limitation based on the CFL number.

3.3. Evaluation of the partial derivatives and boundary conditions in the streamwise and spanwise directions

The main difference between the SC and PLC code is in the methods they use to compute spatial derivative in x . SC, which is specific to the computation of compressible shear layers, assumes that the flow is periodic in x and uses spectral derivatives in those directions. PLC, which is more general and can be used to calculate confined flow with inflow and outflow, uses the same high order Pade scheme as in the cross-stream direction and non-reflecting boundary condition (at inflow and outflow) of the type derived by Poinsot and Lele (1989).

For temporal direct numerical simulation (SC), the flow is assumed to be periodic in x and z directions, which allows the use of spectral methods and eliminates the need for boundary conditions in those directions. Spectral methods are highly accurate so a large range of length scales can be captured with a minimum number of grid points. For compressible flows, the use of spectral methods may cause problems if shocks appear, since it is well known that spectral methods lose their exponential convergence when steep gradients are present. In particular, Gibbs phenomena appear and the exponential rate of convergence is lost. For spatial simulations (PLC), the flow is not assumed to be periodic in x . Alternative differentiation schemes must be used, and additional boundary conditions must be provided at inflow and outflow. The PLC is based on the high order Pade finite difference schemes developed by Lele (1990). They have accuracy similar to that of spectral methods, and constitute an alternative to spectral methods, especially for problems with non-periodic boundary conditions. These Pade methods, which artificially damp a narrow band of high wavenumbers, may have less difficulty in capturing shocks than spectral methods.

3.3.1. Evaluation of the partial derivatives in x and z using spectral methods in SC

A quantity to be differentiated is Fourier transformed using a real fast Fourier transform, then multiplied by ik , and then inverse Fourier transformed. As shown in

Sandham (1989), the “oddball” wavenumber should be zeroed out at each substep of every time step to eliminate the round-off error which accumulates at this wavenumber as one goes back and forth between Fourier space and physical space and as data are packed and unpacked when stored to or read from the solid state disk (SSD). This process (Blaisdell *et al.* 1991) amounts to replacing the flowfield by a filtered flowfield, defined as

$$\begin{aligned}\phi_{i,k}^f = & \phi_{i,k} - \frac{(-1)^k}{N_z} \sum_{k'}^{N_z} (-1)^{k'} \phi_{i,k'} \\ & - \frac{(-1)^i}{N_x} \sum_{i'}^{N_x} (-1)^{i'} \phi_{i',k} \\ & + \frac{(-1)^{i+k}}{N_x N_z} \sum_{k'}^{N_z} \sum_{k'}^{N_x} (-1)^{i'+k'} \phi_{i',k'}.\end{aligned}\quad (3.31)$$

This replacement vectorizes efficiently and is substantially cheaper than performing a three-dimensional Fourier transform of the data, setting the appropriate Fourier coefficients to zero and inverting the transform.

3.3.2. Evaluation of partial derivatives in x and z using PLC

The PLC is designed to perform both spatial and temporal 2-D simulations. The non-periodicity of the boundary conditions in the spatial case prevents the use of spectral methods, and so the high order Pade schemes with spectral-like resolution are used. These schemes can be written as

$$\beta\phi'_{i-2} + \alpha\phi'_{i-1} + \phi'_i\alpha\phi'_{i+1} + \beta\phi'_{i+2} = c\frac{\phi_{i+3} - \phi_{i-3}}{6h} + b\frac{\phi_{i+2} - \phi_{i-2}}{4h} + a\frac{\phi_{i+1} - \phi_{i-1}}{2h}. \quad (3.33)$$

In the particular case where β and c are zero, a one-parameter (α) fourth-order scheme is obtained with

$$a = \frac{2}{3}(\alpha + 2) \quad b = \frac{1}{3}(4\alpha - 1). \quad (3.34)$$

It may be noted that $\alpha = 0$ corresponds to the fourth-order central difference scheme and that $\alpha = 1/4$ corresponds to the classical Pade scheme. For $\alpha = 1/3$, the scheme becomes accurate to sixth-order, and this is the value which was used in all of the present work. The Pade approximation for the second derivative is handled in a similar way, where one uses

$$\begin{aligned}\beta\phi''_{i-2} + \alpha\phi''_{i-1} + \phi''_i\alpha\phi''_{i+1} + \beta\phi''_{i+2} = & \\ c\frac{\phi_{i+3} - 2\phi_i + \phi_{i-3}}{9h^2} + b\frac{\phi_{i+2} - 2\phi_i + \phi_{i-2}}{4h^2} + a\frac{\phi_{i+1} - 2\phi_i + \phi_{i-1}}{h^2}.\end{aligned}\quad (3.35)$$

In the particular case where β and c are zero, a one-parameter (α) fourth-order scheme is obtained, where

$$a = \frac{4}{3}(1 - \alpha) \quad b = \frac{1}{3}(10\alpha - 1) \quad (3.36)$$

It may be noted that $\alpha = 0$ corresponds to the fourth-order central difference scheme and that $\alpha = 1/10$ corresponds to the classical Pade scheme. For $\alpha = 2/11$ the scheme becomes sixth-order, and this is the value which was used in all of the present work.

The evaluation of the diffusion term requires the evaluation of successive derivatives due to temperature dependent transfer coefficients, *e.g.*

$$\frac{\partial}{\partial y} \left(\mu \frac{\partial u}{\partial y} \right). \quad (3.37)$$

In a spectral method one would compute this quantity by forward transformation, multiplication and inverse transformation. The Pade scheme attenuates a narrow band of high wavenumber modes, which leads to a much worse representation of the high wavenumber component of the solution when the second differentiation is applied. To resolve this problem, diffusion terms like this are expanded as

$$\frac{\partial \mu}{\partial y} \frac{\partial u}{\partial y} + \mu \frac{\partial^2 u}{\partial y^2} \quad (3.38)$$

and the Pade scheme is used to calculate the derivatives. Note that this formulation for the diffusion terms is non-conservative.

3.3.3. Inflow and outflow boundary condition in PLC

The boundary conditions used are similar to the boundary conditions for spatial simulation developed by Poinsot and Lele (1989). For spatial simulation of free shear layer, the outflow boundary condition must simulate an infinite domain although the computational domain is finite. The basic idea (Thompson 1987) is to consider the characteristic form of the equations at the boundary. Outgoing characteristics, which use information from the computational domain can be computed without problems, whereas for incoming characteristic two situation may occur: (1) Some information is known about the outside domain from which the characteristic variables can be determined (given boundary condition); (2) no information is available and we try to express the outgoing characteristic variables in term of the known ingoing characteristic variables. The equation (3.16) to (3.20) can be rewritten as:

$$\frac{\partial \rho}{\partial t} = -d_1 - \frac{\partial \rho v}{\partial y} \quad (3.39)$$

$$\frac{\partial \rho u}{\partial t} = -ud_1 - \rho d_3 - \frac{\partial \rho uv}{\partial y} + \frac{\partial \tau_{1j}}{\partial x} \quad (3.40)$$

$$\frac{\partial \rho v}{\partial t} = -vd_1 - \rho d_4 - \frac{\partial(\rho v^2 + p)}{\partial y} + \frac{\partial \tau_{2j}}{\partial y} \quad (3.41)$$

$$\begin{aligned} \frac{\partial \rho e_t}{\partial t} &= -\frac{1}{2}d_1(u_1^2) - \frac{d_2}{\gamma - 1} - \rho ud_3 - \rho vd_4 \\ &\quad - \frac{\partial[v(\rho e_t + p)]}{\partial y} - \frac{\partial q_i}{\partial x_i} + \frac{\partial u_j \tau_{ij}}{\partial x_i} + \beta \dot{w} \end{aligned} \quad (3.42)$$

$$\frac{\partial \rho Y_f}{\partial t} = -Y_f d_1 - \rho d_5 - \frac{\partial \rho v Y_f}{\partial y} + \frac{\partial}{\partial x_i}(\rho D \frac{\partial Y_f}{\partial x_i}) - \dot{w} \quad (3.43)$$

$$\frac{\partial \rho Y_o}{\partial t} = -Y_o d_1 - \rho d_6 - \frac{\partial \rho v Y_o}{\partial y} + \frac{\partial}{\partial x_i}(\rho D \frac{\partial Y_o}{\partial x_i}) - n \dot{w} \quad (3.44)$$

in which all the terms can be calculated using information from inside the computational domain except d_1 to d_6 , which involves derivative normal to the boundary. The viscous terms also involve derivatives normal to the boundary, but the characteristics associated with diffusion are lines parallel to the boundary, which suggests that it is possible to use one-sided derivatives to calculate diffusion term. d_1 to d_6 can be rewritten as

$$d_1 = \frac{\partial \rho u}{\partial x} = (L_2 + 0.5L_4 + 0.5L_1)/c^2 \quad (3.45)$$

$$d_2 = \rho c^2 \frac{\partial u}{\partial x} + u \frac{\partial p}{\partial x} = 0.5(L_4 + L_1) \quad (3.46)$$

$$d_3 = u \frac{\partial u}{\partial x} + \frac{\partial p}{\partial x}/\rho = 0.5(L_4 - L_1)/(\rho c) \quad (3.47)$$

$$d_4 = u \frac{\partial v}{\partial x} = L_3 \quad (3.48)$$

$$d_5 = u \frac{\partial Y_f}{\partial x} = L_5 \quad (3.49)$$

$$d_6 = u \frac{\partial Y_o}{\partial x} = L_6 \quad (3.50)$$

where L_1 to L_6 are the characteristic variables defined by

$$L_1 = \lambda_1 \left(\frac{\partial p}{\partial x} - \rho c \frac{\partial u}{\partial x} \right) \quad (3.51)$$

$$L_2 = \lambda_2 \left(c^2 \frac{\partial \rho}{\partial x} - \frac{\partial \rho}{\partial x} \right) \quad (3.52)$$

$$L_3 = \lambda_3 \frac{\partial v}{\partial x} \quad (3.53)$$

$$L_4 = \lambda_4 \left(\frac{\partial p}{\partial x} + \rho c \frac{\partial u}{\partial x} \right) \quad (3.54)$$

$$L_5 = \lambda_5 \frac{\partial Y_f}{\partial x} \quad (3.55)$$

$$L_6 = \lambda_6 \frac{\partial Y_o}{\partial x} \quad (3.56)$$

and the λ_i are the associated characteristic velocities

$$\lambda_1 = u - c \quad \lambda_2 = u \quad \lambda_3 = u$$

$$\lambda_4 = u + c \quad \lambda_5 = u \quad \lambda_6 = u . \quad (3.57)$$

To each of the characteristics is associated a characteristic equation

$$\frac{\partial A_i}{\partial t} + L_i = 0 \quad (3.58)$$

where the wave amplitudes A_i are given by

$$\begin{aligned} A_1 &= p - \rho c u & A_2 &= c^2 \rho - p & A_3 &= v \\ A_4 &= p + \rho c u & A_5 &= Y_f & A_6 &= Y_o . \end{aligned} \quad (3.59)$$

We will now outline the application of this technique to three different types of boundary conditions

Outlet: At all the points of the outlet, the convective speed u is compared to the local speed of sound c . If $u > c$, all the characteristic velocities are positive and all the terms $\frac{\partial A_i}{\partial x}$ can be calculated using information from inside the computational flow domain. If $u < c$, $\lambda_1 < 0$ and A_1 is set equal to 0. In this case, we also add to the right hand side of equation (3.42) a term which tends to bring the pressure p towards the pressure at infinity, $p_\infty = 1/\gamma$. For each point of the outlet boundary

$$(\frac{\partial \rho e_t}{\partial t})_{new} = (\frac{\partial \rho e_t}{\partial t})_{old} - \frac{p - p_\infty}{\gamma - 1} (1 - M_l^2) \frac{c \zeta}{\delta_i} \quad (3.60)$$

where ζ is a constant arbitrarily chosen equal to 0.1, M_l the local Mach number is equal to $M_l = u/c$, and δ_i is the inlet vorticity thickness of the mixing layer. Note that this pressure correction is the one proposed by Rudy and Strikwerda (1981).

Subsonic inlet: For a subsonic inlet, all the characteristic velocities are positive but λ_1 , thus the amplitude $\frac{\partial A_i}{\partial x}$ (except $\frac{\partial A_1}{\partial x}$) cannot be calculated using information from inside the computational domain. Instead, all the L_i , ($i = 2, 6$) are determined using equations (3.45) to (3.50). Five unknowns require five equations. In all the simulations, we chose to keep v, Y_f and Y_o constant at the boundary, which leads to

$$L_3 = 0 \quad (3.61)$$

$$L_5 = 0 \quad (3.62)$$

$$L_6 = 0. \quad (3.63)$$

Two additional equations are obtained by setting $\partial u / \partial x = 0$ and by algebraic identity between the L_i ,

$$L_4 = L_1 \quad (3.64)$$

$$L_2 = (\gamma - 1)L_1 \quad (3.65)$$

where L_1 is determined using information from inside the computational domain. The forcing of the inlet is done at the beginning of each substep as Q_1 and Q_2 are updated (see section 3.2). The value of $(\rho u, \rho v, \rho e_t, \rho Y_f, \rho Y_o)$ at each point of the inlet boundary are imposed equal to

$$(\rho u)^i = M_1 \rho^c (\bar{u} + \sum_{k=1}^n m C_k \Re(\hat{u}_k \exp^{i(\omega_k t + \phi_k)})) \quad (3.66)$$

$$(\rho v)^i = M_1 \rho^c (\sum_{k=1}^n m C_k \Re(\hat{v}_k \exp^{i(\omega_k t + \phi_k)})) \quad (3.67)$$

$$(\rho e_t)^i = \frac{\rho^c}{\gamma(\gamma - 1)} (\bar{T} + \sum_{k=1}^n m C_k \Re(\hat{T}_k \exp^{i(\omega_k t + \phi_k)})) + \frac{0.5}{\rho_c} ((\rho u)^{i2} + (\rho v)^{i2}) \quad (3.68)$$

$$(\rho Y_f)^i = \rho^c \max(0, \bar{Z} + \sum_{k=1}^n m C_k \Re(\hat{Z}_k \exp^{i(\omega_k t + \phi_k)})) \quad (3.69)$$

$$(\rho Y_o)^i = -\rho^c \min(0, \bar{Z} + \sum_{k=1}^n m C_k \Re(\hat{Z}_k \exp^{i(\omega_k t + \phi_k)})) \quad (3.70)$$

where nm is the number of modes used for forcing, C_k is the amplitude of mode k , and ω_k and ϕ_k are its frequency and phase. Both Q_1 and Q_2 are forced at the inlet. t in the formula is the local time, equal to the time of Q_1 and Q_2 at the beginning of each substep. Note that, for a subsonic inlet, the density is not imposed and the current value of ρ in Q_1 (Q_2) as Q_1 (Q_2) is forced.

Supersonic inlet: For a supersonic inlet, all the characteristic velocities are positive, thus all the L_i are set equal to zero meaning that we keep u, v, e_t, ρ, Y_f and Y_o constant at the boundary,

$$L_1 = 0 \quad (3.71)$$

$$L_2 = 0 \quad (3.72)$$

$$L_3 = 0 \quad (3.73)$$

$$L_4 = 0 \quad (3.74)$$

$$L_5 = 0 \quad (3.75)$$

$$L_6 = 0. \quad (3.76)$$

The forcing of the inlet is done at the beginning of each substep as in the subsonic case, but now the density is also forced. We get

$$\rho^i = (1/\bar{T} + \sum_{k=1}^n m C_k \Re(\hat{\rho}_k \exp^{i(\omega_k t + \phi_k)})) \quad (3.77)$$

$$(\rho u)^i = M_1 \rho^i (\bar{u} + \sum_{k=1}^n m C_k \Re(\hat{u}_k \exp^{i(\omega_k t + \phi_k)})) \quad (3.78)$$

$$(\rho v)^i = M_1 \rho^i (\sum_{k=1}^n m C_k \Re(\hat{v}_k \exp^{i(\omega_k t + \phi_k)})) \quad (3.79)$$

$$(\rho e_t)^i = \frac{\rho^i}{\gamma(\gamma-1)} (\bar{T} + \sum_{k=1}^n m C_k \Re(\hat{T}_k \exp^{i(\omega_k t + \phi_k)})) + \frac{0.5}{\rho_i} ((\rho u)^{i2} + (\rho v)^{i2}) \quad (3.80)$$

$$(\rho Y_f)^i = \rho^i \max(0, \bar{Z} + \sum_{k=1}^n m C_k \Re(\hat{Z}_k \exp^{i(\omega_k t + \phi_k)})) \quad (3.81)$$

$$(\rho Y_o)^i = -\rho^i \min(0, \bar{Z} + \sum_{k=1}^n m C_k \Re(\hat{Z}_k \exp^{i(\omega_k t + \phi_k)})). \quad (3.82)$$

3.4. Evaluation of the partial derivatives and free stream boundary conditions in the cross stream direction

In the cross-stream direction, the flow is non-periodic, which prevents the use of spectral methods based on FFT. The sixth-order Pade scheme presented in section 3.3.2 is used both in SC and PLC to calculate partial derivatives in y . To keep the vast majority of points in the vortical region of the layer, the grid is stretched in y . The mapping function is a sinh function, which concentrates points around $y = 0$. We get

$$y = \frac{L_y}{2} \frac{\sinh(b_y \eta)}{\sinh b_y} \quad (3.83)$$

$$y' = \frac{L_y}{2} \frac{b_y \cosh(b_y \eta)}{\sinh b_y} \quad (3.84)$$

$$y'' = \frac{L_y}{2} \frac{b_y^2 \sinh(b_y \eta)}{\sinh b_y} \quad (3.85)$$

where the mapped coordinate is η and b_y is the stretching parameter in the y direction, typically equal to 1 or 2. The partial derivative in y is related to the partial derivative in η calculated using the Pade scheme by

$$\frac{\partial \phi}{\partial y} = \frac{1}{y'} \frac{\partial \phi}{\partial \eta} \quad (3.86)$$

$$\frac{\partial^2 \phi}{\partial y^2} = \frac{1}{y''} \frac{\partial^2 \phi}{\partial \eta^2}. \quad (3.87)$$

The non-reflecting boundary condition are identical to the non-reflecting boundary conditions presented in section 3.3.3. Equations (3.39) to (3.59) can be rewritten to

evaluate the characteristic in the y direction by switching x and y and switching u and v . In particular, d_1 to d_6 and L_1 to L_6 become

$$d_1 = \frac{\partial \rho v}{\partial y} = (L_2 + 0.5L_4 + 0.5L_1)/c^2 \quad (3.88)$$

$$d_2 = \rho c^2 \frac{\partial v}{\partial y} + v \frac{\partial p}{\partial y} = 0.5(L_4 + L_1) \quad (3.89)$$

$$d_3 = v \frac{\partial v}{\partial y} + \frac{\partial p}{\partial y}/\rho = 0.5(L_4 - L_1)/(\rho c) \quad (3.90)$$

$$d_4 = v \frac{\partial u}{\partial y} = L_3 \quad (3.91)$$

$$d_5 = v \frac{\partial Y_f}{\partial y} = L_5 \quad (3.92)$$

$$d_6 = v \frac{\partial Y_o}{\partial y} = L_6 \quad (3.93)$$

with

$$L_1 = \lambda_1 \left(\frac{\partial p}{\partial y} - \rho c \frac{\partial v}{\partial y} \right) \quad (3.94)$$

$$L_2 = \lambda_2 \left(c^2 \frac{\partial \rho}{\partial y} - \frac{\partial \rho}{\partial y} \right) \quad (3.95)$$

$$L_3 = \lambda_3 \frac{\partial u}{\partial y} \quad (3.96)$$

$$L_4 = \lambda_4 \left(\frac{\partial p}{\partial y} + \rho c \frac{\partial v}{\partial y} \right) \quad (3.97)$$

$$L_5 = \lambda_5 \frac{\partial Y_f}{\partial y} \quad (3.98)$$

$$L_6 = \lambda_6 \frac{\partial Y_o}{\partial y}. \quad (3.99)$$

The λ_i are the associated characteristic velocities

$$\begin{aligned} \lambda_1 &= v - c & \lambda_2 &= v & \lambda_3 &= v \\ \lambda_4 &= v + c & \lambda_5 &= v & \lambda_6 &= v. \end{aligned} \quad (3.100)$$

No wall: In the absence of wall, the absence of forcing makes the calculation of the non-reflecting boundary condition easier than in the streamwise direction (section 3.3.3). The outgoing characteristic, which use information within the computational domain, are calculated with no problem. The incoming characteristic are handled by setting the time derivative of their amplitudes equal to zero.

With walls: In the presence of a wall, $\partial \rho c v / \partial y = 0$. The only non-zero characteristics are L_1 and L_4 . For the bottom wall, L_1 is calculated using information from within the computational domain and L_4 is set equal to L_1 , which ensures $\partial \rho c v / \partial y = 0$. For

a top wall, the opposite is true: L_4 is calculated using information from within the computational domain and L_1 is set equal to L_4 .

3.5. Initialization of the temporal simulation

The initialization of the entire flowfield is done at the beginning of the simulation by defining all the flow variables $(\rho, \rho u, \rho v, \rho w, \rho e_t, \rho Y_f, \rho Y_o)$ as

$$\rho = \left(1/\bar{T} + \sum_{k=1}^n mC_k \Re(\hat{\rho}_k \exp^{i(\alpha_k x + \beta_k z + \phi_k)}) \right) \quad (3.101)$$

$$\rho u = M_1 \rho \left(\bar{u} + \sum_{k=1}^n mC_k \Re(\hat{u}_k \exp^{i(\alpha_k x + \beta_k z + \phi_k)}) \right) \quad (3.102)$$

$$\rho v = M_1 \rho \left(\sum_{k=1}^n mC_k \Re(\hat{v}_k \exp^{i(\alpha_k x + \beta_k z + \phi_k)}) \right) \quad (3.103)$$

$$\rho w = M_1 \rho \left(\sum_{k=1}^n mC_k \Re(\hat{w}_k \exp^{i(\alpha_k x + \beta_k z + \phi_k)}) \right) \quad (3.104)$$

$$\begin{aligned} \rho e_t = & \frac{\rho}{\gamma(\gamma-1)} \left(\bar{T} + \sum_{k=1}^n mC_k \Re(\hat{T}_k \exp^{i(\alpha_k x + \beta_k z + \phi_k)}) \right) \\ & + 0.5(\rho u^2 + \rho v^2 + \rho w^2) \end{aligned} \quad (3.105)$$

$$\rho Y_f = \rho \max \left(0, \bar{Z} + \sum_{k=1}^n mC_k \Re(\hat{Z}_k \exp^{i(\alpha_k x + \beta_k z + \phi_k)}) \right) \quad (3.106)$$

$$\rho Y_o = -\rho \min \left(0, \bar{Z} + \sum_{k=1}^n mC_k \Re(\hat{Z}_k \exp^{i(\alpha_k x + \beta_k z + \phi_k)}) \right). \quad (3.107)$$

Here \bar{u} , \bar{T} and \bar{Z} are the mean flow variables calculated in chapter 2 using self-similar solution, and \hat{u} to \hat{z} are the complex eigenfunctions calculated in chapter 2. C_k , α_k , β_k and ϕ_k are respectively the amplitude, complex wavenumber in x and z , and phase of the k^{th} eigenmode.

Figures 3.1 and 3.2 show the growth rates and the phase velocities of the fast and slow instability modes of the non-reacting incompressible mixing-layer with $M_c = 0.05$. 2-D modes and 45° modes are presented. As seen in chapter 2, for large wavenumbers the two outer modes are decoupled and the convective speeds of each instability mode is close to the speed of its associated free stream. At small wavenumbers however, the convective speed of each mode is close to the average speed of the free-streams. The slow outer mode becomes the central mode and its amplification curve exhibits a local maximum corresponding to this instability mode. Note finally that the 2-D

modes are more amplified than the 45° mode at all wavenumbers, suggesting that the incompressible reacting mixing layer will be dominated by two layers of two-dimensional large-scale vortices (the colayers).

Note on figure 3.1 that the maxima for the fast and the slow outer modes do not correspond to the same wavenumbers. For temporal simulation, the size of the computational domain determines the maximum wavelength of the eigenmodes. The wavelength used in the temporal simulation must therefore be chosen arbitrarily between the two wavelengths corresponding to the two peaks. Note also that, since the two eigenmodes have unequal phase velocities, the computational domain cannot follow both structures in time.

The fundamentals and subharmonics used to initialize the simulations have the wavenumbers α , temporal amplification rates ω_i and velocities c_r as shown in Table 3.1.

Figures 3.3 and 3.4 show the same information for the compressible mixing layer. Here, compressibility effects reduce communication between the two sides of the layer, and the low wavenumber domain where the two regions of the layer interact is reduced. The local maximum at the left of the slow amplification curve (which corresponds to the central mode) is almost absent. The fast outer mode has a fast subharmonic and the slow outer mode a slow subharmonic. Some compressibility effects can be seen: (a) The amplification rate of the 3-D outer modes relative to the amplification rate of the 2-D outer modes is higher than in the incompressible case and (b) the oblique central mode is more amplified than the 2-D central mode. However, these effects are still too small for the oblique outer modes to become dominant. M_{f1} and M_{f2} are here equal to 0.3, less than the value of 0.6 which was shown by Sandham and Reynolds (1990,1991) to correspond to the onset of three-dimensionality and the oblique outer modes remain less amplified than the 2D outer modes, whereas $M_c = 0.8$ is higher than 0.6 and the oblique central mode is more amplified than the 2-D central mode.

The fundamentals and subharmonics used in the simulations have wavenumbers α , temporal amplification rates ω_i and velocities c_r as shown in Table 3.2.

Note that the difference between the phase speeds of the fast and slow subharmonic is higher in the compressible case than in the incompressible case: the fast and the slow compressible outer modes have fast and slow subharmonics, whereas the fast and the

slow incompressible outer modes have a more central subharmonic. This difference may slightly affect the transfer of energy from the fundamental to the subharmonic, as will be shown in chapter 4.

Table 3.1. wavenumbers α , temporal amplification rates ω_i and velocities c_r of the 2-D incompressible eigenmodes used in the simulations

incompressible M.L.	α	ω_i	c_r
slow fundamental	0.970	6.39×10^{-2}	0.628
slow subharmonic	0.485	4.47×10^{-2}	0.685
fast fundamental	0.970	5.42×10^{-2}	0.878
fast subharmonic	0.485	3.42×10^{-2}	0.822

Table 3.2. wavenumbers α , temporal amplification rates ω_i and velocities c_r of the 2-D compressible eigenmodes used in the simulations

compressible M.L.	α	ω_i	c_r
slow fundamental	1.750	5.91×10^{-2}	0.592
slow subharmonic	0.875	3.81×10^{-2}	0.620
fast fundamental	1.750	4.78×10^{-2}	0.914
fast subharmonic	0.875	4.50×10^{-2}	0.885

3.6. Implementation of SC on the Hypercube

The simulations were performed on the iPSC860 using a modification of SC. Some modifications were required. However, since the special language Vectoral was installed on the iPSC860 by Allan Wray (1991, private communication), and since SC already featured a management of data using the SSD (solid-state device) the implementation was straightforward and represent a very small fraction of the overall code (less than 10%), mostly the input-output and the management of data (replacing the SSD by node-to-node communication).

3.6.1. Motivation

The simple geometry of the flow under investigation also simplify the implementation on the hypercube. It also leads to a high level of parallelism synonymous with high performance, since the number of points and the number of partial derivatives or

operation to be performed are the same for all processors. The only non-parallel tasks are the input-output and the transposition which involves transfer of information from processor to processor. Communication overhead constitutes less than 15% of the CPU time depending on the size of the problem. An initialization program was also implemented on the hypercube.

The hypercube has 128 processors, each of them having 2Mw of core memory. All the data must be resident in memory, which strongly limits the size of the simulations. Two 2-D simulations were run at $Re = 5,000$ using 256×1024 points. Typical 2-D runs on the Hypercube require 16 or 32 processors. Between one and eight instability modes were included in the 2-D initial field. The 3-D simulation was performed using up to $64 \times 300 \times 128$ points. Eight instability modes were included in the 3-D initial field. We started with a $64 \times 256 \times 64$ grid and 32 processors. After some time, large scale structures generated small scale structures and we had to increase the number of gridpoints to $64 \times 320 \times 128$ and the number of processors to 64. Starting with 32 processors, each processor contains two $x - y$ planes (or 8 $x - z$ planes) stored in its resident memory.

3.6.2. Management of data on the Cray Y-MP

The memory requirement of a 3-D simulation exceed the Cray Y-MP core memory and only portions of the variables field ($Q_1[Nx, Ny, Nz, Nq], Q_2[Nx, Ny, Nz, Nq]$) can therefore be loaded in memory at any instant of time. To overcome this limitation, the SSD is used where data are stored on an auxiliary memory as pencils of size (Nx, Ny_p, Nz_p, Nq) . $Npy \times Npx$ pencils are used where $Npy = Ny/Ny_p$ and $Npz = Nz/Nz_p$

At each time substep, the right hand sides of equations (3.16) to (3.20) must be evaluated, which involves computing x, y, z partial derivatives. Each substep is divided into three passes:

1. By loading the appropriate pencils, the first Ny_p $x - z$ planes are loaded in central memory. All the partial derivatives in x and z appearing in the right hand sides of equations (3.16) to (3.20) and an estimate of the time-step are calculated for these planes. The computed partial derivatives are stored on the SSD using pencils, and the same operation is repeated for the following $x - z$ planes.
2. By loading the appropriate pencils, the first Nz_p $x - y$ planes are loaded in central memory, as well as the partial derivatives in x and z calculated in these planes. All

the partial derivatives in x, y and z appearing in the right hand sides of equations (3.16) to (3.20) and the non-reflecting boundary conditions are calculated for these planes. The computed partial derivatives are stored on the SSD, and the same operation is repeated for the following $x - y$ planes.

3. By loading the appropriate pencils, the first Ny_p $x - z$ planes are loaded in central memory as well as the partial derivatives in x and z calculated in these planes. The right hands side of equations (3.16) to (3.20) and various statistics are calculated in these planes. The new values of Q_1 and Q_2 are computed using equation (3.25) and stored on the SSD.

3.6.3. Management of data on the iPSC860

The implementation is very similar and is as follows. The hypercube is based on a single instruction multiple data (SIMD) architecture, meaning that each of the 128 processor has its own memory and that any instruction in the code applies to all of the 128 processors. The input-output is slow on the Hypercube, and all the data must be resident in memory to achieve high performance. The maximum number of processors is 128 and the core-memory of each processor is 2 Mw (single precision) which limits the total available memory to 256 Mw. The computational domain is decomposed in an array of size $Pen[Np, Np]$ of pencils, where Np is the number of processors. Each pencil has a size $[Nx \times Nz \times Ny/Np \times Nz]$ where $Nyn = Ny/Np$ and $Nzn = Nz/Np$. For a $64 \times 256 \times 64$ calculations with 32 processors and 7 variables per grid point, each pencil has a dimension of $64 \times 7 \times 8 \times 2$.

1. At the beginning of each time substep, the node i contains all the pencils $Pen[i, j], (j = 1, 32)$, which correspond to 8 $x - z$ planes of size 64×64 . Similarly, each processor contains Ny_p $x - z$ planes as described in figure 3.5. Using a FFT in x and z , we compute all the x and z partial derivatives we need in those 8 planes. These derivatives are stored in a work array using the same system of pencils. Note that all this first step is 100% parallel since all the processors contains the same number of planes and do not exchange data with other processors.
2. The second step is to calculate all the partial derivatives in x and y needed to calculate the right hand sides of equations (3.16) to (3.20). To do so, each processor must contain a certain number of $x - y$ planes. The method is as follows (Wray private communication): We synchronize and transpose pencils between processors. The j pencil of the processor i is sent to processor j , and the i pencil of processor j

is sent to processor i , for all pairs (i, j) of processors. Each pencil is then transposed into itself. At the end of this transposition, the node i contains all the pencils $\text{Pen}[j, i], (j = 1, 32)$ which correspond to $2 x - y$ planes of size 256×64 . Both the work array and the data array are transposed this way. This portion of the code was the only one that needed to be changed when the code was transported from the Cray Y-MP to the iPSC860, and its efficiency is critical in the overall performance of the code. All the instructions involving the SSD are replaced by instructions to transfer information from processor to processor. (Wray 1992 personal communication; see fig. 3.6). All the x, y, xy, xx, yy derivatives are computed using the sixth-order Pade scheme and the data array. All the yz partial derivatives are computed using the sixth-order Pade scheme for differentiation, and the work array, which already contains the z partial derivatives. We also calculate the boundary conditions on y for these two $x - y$ planes. Except for the transposition, this step is 100% parallel.

3. We again transpose the data to go back to the initial configuration, where one processor contains $8 x - z$ planes. We use the x, y and z partial derivatives to march in time. The right hand sides of equations (3.16) to (3.20) and various statistics are calculated in these planes. The new value of Q_1 and Q_2 are computed using equation (3.25).

These steps 1 to 3 have to be repeated three times per total time step, when the RK3 method is used. Finally, some extra tasks are performed which involve communication between processors:

1. Initialization of the runs: All the run parameters are read on node 0 and shared to the other nodes. The restart file is read $x - y$ plane by $x - y$ plane, each node successively receiving 2 planes. The data are transposed once (as in step 3 above) to prepare the data for step 1.
2. Computation of certain flow statistics “on the fly” (maximum reaction rate, total reaction rate, maximum pressure, etc). These statistics are computed at the end of each time step, $x - z$ plane by $x - z$ plane.
3. Synchronization and determination of time step. Synchronization is only done before each transposition, which is twice per time substep. The maximum time step for numerical stability is determined in step 2 during the first time substep of each time step. The maximum time step authorized is determined in each $x - y$ planes and the minimum of all of them, define the new time step.

2-D implementation The same implementation is used as in 3-D. Instead of considering pencils, we only consider tiles of size $N_{xn} \times Nq \times N_{yn}$. The schematic is shown in figure 3.7 for a 256×1024 calculation using 16 processors.

3.6.4. Performances compararison between Y-MP and iPSC860

Table 3.3 shows the performance of the hypercube for a 2-D calculation with 256×1024 points using 8, 16, 32 and 64 nodes. Displayed there are the time required to perform various tasks: the partial derivative in x of an $N_x \times N_y$ variable field (t_{DX}); the partial derivative in y of an $N_x \times N_y$ variable field (t_{DY}); read data from disk (t_{read}); save data on disk (t_{save}); transpose the variable field (t_{trQ}) and the work array (t_{trW}) back and forth; calculate the time step (t_{t-step}). The total time per time step is (t_{step}) and t_{stat1} and t_{stat2} are the time required to compute the statistics on the flight.

Table 3.3. Hypercube activity costs (seconds) for a 256×1024 2-D simulation vs. number of processors used

table 3.3	8 nodes	16 nodes	32 nodes	64 nodes
t_{read}	21.375	23.255	22.155	32.969
t_{save}	25.039	36.584	63.247	121.74
t_{DX}	0.0878	0.0443	0.0229	0.0115
t_{DY}	0.6596	0.3411	0.1650	0.0825
t_{tstep}	0.2962	0.1445	0.0711	0.0357
t_{trQ}	2.7450	1.4697	0.9510	0.8172
t_{trW}	6.2625	3.3846	2.1045	1.4151
t_{trt}	9.0075	4.8543	3.0555	2.2323
t_{stat1}	0.2653	0.2380	0.0704	0.0515
t_{stat2}	0.3121	0.2088	0.1473	0.1844
t_{step}	92.154	46.137	23.043	12.645

The results indicate the extent of parallelism. The CPU time per time step (t_{step}) is almost inversely proportional to the number of processors used. The transfer of information per processor, though not inversely proportional to the number of processors, is decreased by a factor of 4 when the number of processors is increased by a factor of 8. This time represents between 10 and 20% of the total CPU time per timestep and varies slightly from run to run, which might be caused by the total load on the machine. The time spent to read and save the data increases with the number of processors. All the input-output are done on node 0, and increasing the number of nodes increases the communication overload.

As a comparison the same results are shown for a Cray Y-MP 1024×256 2-D simulation using the same code. We show the result for different sizes of pencils (32×8 , 64×16 , 128×32 and 512×64) which corresponds to the 32, 16, 8 and 4 nodes on the hypercube. Here, the total time per time step strongly depends on the size of the pencils, and large pencils enabling longer vectors help increase the overall efficiency. The speed of the Cray is equivalent to the speed achieved on the hypercube using a 32 or 64 nodes. The time spent in input-output is strongly reduced on the Cray and the SSD represents roughly 5 to 10 % of the total CPU time. The complete table of the activity cost for a $64 \times 256 \times 64$ calculations on the Cray Y-MP and on the hypercube is not presented here. Note however that the costs per time step are 95s/timestep for the Cray Y-MP using one processor and 40s/timestep on the Hypercube using 64 processors. This represents a speed-up of about 5 between the full iPSC860 (128 processors) and a Cray Y-MP mono-processor. The program runs on the Y-MP at 120 Mflops, which leads to a predicted speed on the full iPSC860 of 600 Mflops.

Table 3.4. Cray activity costs (seconds) for a 256×1024 2-D simulation vs. pencil size used

table 3.4	32×8	64×16	128×32	256×64
t read	0.7094	0.5999	0.5721	0.5664
t save	0.5372	0.4905	0.4823	0.4810
t DX	0.0657	0.0510	0.0494	0.0479
t DY	0.1578	0.1194	0.1036	0.0946
t timestep	0.5628	0.3210	0.2015	0.1404
t SSD	14.057	7.0350	3.7350	2.1030
t stat1	0.4218	0.2360	0.1577	*****
t stat2	1.2045	0.8332	0.6749	*****
t step	30.210	20.338	16.431	14.393

3.6.5. Conclusions

Going from the sequential code to the parallel code involved modifying about 10% of the code. Only the input and output of restart files and the SSD calls needed to be modified. The simple geometry used in DNS (channel flows, isotropic turbulence in a box, reversed step, etc) and the use of an explicit time advancement method (here RK3) enable one to fully use the capacity of parallel processing. In particular, the possibility of having an efficient transfer of data from processor to processor, and the reduction of the synchronization to only twice per time substep, makes the iPSC860

a very suitable machine for DNS.

However, the main limitation arises from the limited memory size of the iPSC860, which limits computation to roughly $256 \times 256 \times 256$ gridpoints on the whole machine. This limitation could be removed either by increasing the number of processors or by increasing the memory per processor.

CHAPTER 4

2-D Temporal Direct Numerical Simulation

In this chapter, 2-D temporal simulations of compressible and incompressible reacting mixing layers are presented. Although the Reynolds number is low, we believe that the general flow structures found are characteristic of what would be found for the large scale structures of high Reynolds number turbulent reacting compressible mixing layers. The purpose of these simulations was to study the development of two-dimensional reacting mixing layers and in particular to investigate several aspects of the evolution of the layer, including: (1) the non-linear effects associated with the growth of a single outer mode, (2) the possibility of interaction between the fast and the slow outer modes and its consequences on the mixing process, (3) the interaction of a mode with its subharmonic and (4) the overall growth mechanism of the layer.

The results confirm the linear stability analysis and the existence of the outer modes for compressible and incompressible shear layers. It is found that (1) with heat release and at large Mach numbers, the fast and the slow outer modes develop without interacting, forming two independent colayers. Thus, (2) the mixing of fuel and oxidizer by large-scale engulfment of fluid from both sides is not likely to occur. Instead, fluid from each of the free streams is first entrained, and then mixed with product before diffusing to the reaction zone. (3) The flame zone is shown to remain between the fast and the slow outer eddies and to occupy only a small extend of the layer. Little or no flame surface appears to be created by the large-scale instability modes. (4) Even when strong subharmonics are present, no pairing was observed in either colayer, which has large effects on the growth mechanism.

4.1. Survey of previous DNS of reacting mixing layers

One of the central issues in combustion is to realize efficient molecular mixing of fuel and oxidizer. A fundamental understanding of the coupling between heat release and fluid dynamics in simple flows is a necessary step towards improving the overall

combustion efficiency of more complex flows. Direct numerical simulations have been used to gain insight into the dynamics of mixing and heat release in subsonic and supersonic mixing layers.

Key previous work on the influence of compressibility and heat release on mixing layers will now be discussed. Direct numerical simulations of Givi *et al.* (1986) for 2-D spatially-developing constant-density reacting shear layers focused on how the flowfield affects the chemical reaction. Their results indicated that, for sufficiently slow chemistry, quenching occurs between large-scale vortices in what would be called the “braids” in a 3-D flow. McMurtry *et al.* (1989) carried out low Mach number simulations including chemical heat release to study the coupling between chemical reaction and fluid dynamics caused by non-homogeneous density distribution. Their results indicated that the amount of mass entrained into the layer and the quantity of product formed decrease with increased heat release. This result was in agreement with the experimental findings of Hermanson and Dimotakis (1989). Heat release was also shown by McMurtry *et al.* (1989) to decrease the vorticity at the center of the vortex structure, resulting in a more diffuse vorticity field. Menon and Fernando (1990) studied numerically the effects of compressibility on the large-scale structure of reacting mixing layers. They confirmed that, at low convective Mach numbers, heat release reduces the growth rate and the amount of product formed, but they demonstrated that, at high Mach numbers, heat release increases the growth rate of the layer. Their simulations also showed the absence of vortex roll-up and pairing for reacting compressible mixing layers. Finally, Sandham and Reynolds (1991) used 3-D temporal simulations, to show that the large-scale structures of the compressible mixing layer become oblique above a convective Mach number of 0.6.

For most of this chapter, we restrict ourselves to a given heat release and position of the reaction zone. 2-D direct numerical simulations are presented for a compressible reacting mixing layer with $M_1 = 3.2$ and $M_2 = 1.6$, a free-stream temperature ratio equal to 1, and a flame temperature equal to 3. This yields values of the flame convective Mach numbers $M_{f1} = M_{f2} = 0.29$. Thus, even at $M_c = 0.8$ for this case, compressibility effects on the reacting mixing layer are weak and linear stability analysis suggests that the large-scale structures are two-dimensional. This justifies the use of 2-D simulations. Simulations are also presented for a reacting mixing layer having the same heat release, free-stream temperature ratio and flame temperature as the previous one, but with $M_c = 0.05$. These simulations show the persistence of the outer

modes to very low M_c , but suggest that the existence of a central subharmonic may destroy the colayers as pairing occurs.

In the last part of this chapter, 2-D simulation of the Stanford experiment, which is characterized by strongly unequal free-stream temperature and low heat release, are presented. These simulations confirm the linear stability analysis and indicate that the flame temperature ratio and the position of the flame have strong effects on the mixing layer structure. For this strongly unequal temperature case ($\bar{T}_1 \gg \bar{T}_2$), we observe that two zones of mixing exist but that the chemical reaction only occurs in the fast-speed side of the layer. This result appears to be in agreement with the experimental findings of Miller *et al.* (1992, 1993).

4.2. Review of the low Mach number, low heat release instability mode

In order to provide a useful reference for comparison a direct numerical simulation initialized with a central mode at low Mach number and low heat release has been performed. Contours plots of several pertinent quantities are shown, as well as their evolution during the merging of fundamental vortices. The results presented in this section review the main characteristics of the central modes, which will not be seen for the outer modes:

- (1) a highly convoluted flame surface with large strain rate, yielding possible extinction;
- (2) large-scale structure entraining and wrapping fluid from both sides;
- (3) mean temperature and reaction profiles having a width comparable to the vorticity thickness of the layer;
- (4) mean vorticity profile having only one maximum. An explanation for the appearance of the outer modes at high heat releases or high Mach numbers is also proposed, based on the vorticity dynamics (baroclinic torque and dilatation).

4.2.1. Overview of a low Mach number, low heat release mode

For later comparison, figure 4.1 shows the typical large-scale structure of an incompressible mixing layer ($M_c = 0.2$) with very low heat release ($\Theta = 0.1$) at low Reynolds number ($Re = 200$). The contours of (a) mixture fraction, (b) vorticity, (c) baroclinic term, (d) dilatational term, (e) vorticity production, (f) density, (g) pressure and (h) reaction rate are shown. In this and all other contours and maps in this thesis,

solid lines represent positive values and dotted lines negative values. The large-scale rollers, similar to the large-scale rollers seen in experiments, entrain and wrap fluid from both sides, increasing the interface between the fuel and oxidizer. Thus, the total flame surface is increased, which augments the total reaction rate. The flame is subject to an intense straining in the region between large-scale vortices in what is called the “braids” in a 3-D flow. We call this the “web” in a 2-D flow. For this low Zeldovich (Ze) case, this straining increases the local reaction rate, and indeed the reaction rate is maximum in the webs (fig. 4.1). For higher Zeldovich cases, this large straining may lead to local extinction as seen in the simulations of Givi *et al.* (1986). The temperature is maximum in the large-scale rollers where hot reacted fluid accumulates, as seen in experiments (Mungal and Dimotakis 1984). The pressure field (fig. 4.1) shows reduced pressure in the vortex core (as expected from the Euler n-equation) and maximum pressure at the isentropic stagnation point in the webs. For $M_c = 0.2$, the pressure at the stagnation point is 2.8% higher than the pressure in the free streams, which agrees well with the familiar formula

$$p_s/p_\infty = \left(1 + \frac{\gamma - 1}{2} M_c^2\right)^{\gamma/(\gamma-1)}. \quad (4.1)$$

The vorticity is maximum in the large-scale structures at the centerline. We have plotted the baroclinic and dilatational terms for this case with very low (but non-zero) heat release, to see the linear effect associated with the existence of a flame. The vorticity production, defined as the sum of the baroclinic and dilatational terms, is also shown (fig. 4.1). A negative contour (dotted) indicates production of negative ω_z and enhances the development of the large-scale structure. As seen on figure 4.1, the baroclinic term is roughly one order of magnitude larger than the dilatational term and plays therefore a major part in the creation or destruction of vorticity. It exhibits a quadrupole structure, as reacting fluid is wrapped into a centrifugal pressure gradient. The dilatational term reaches its extrema inside the large scale structure. It is non-zero in the webs where the large heat release compensates for the low vorticity.

The baroclinic and dilatation terms have also been plotted by Sandham (1989) for a compressible mixing layer without heat release. In the present case, the density gradients associated with compressibility are much smaller than density gradients due to reaction, and despite a higher Mach number, the dilatational term dominates the baroclinic term. However, the baroclinic and dilatational terms surprisingly exhibit

similar contours in the low heat release incompressible case and in the no heat release compressible case. This suggests that the physical mechanism proposed by Sandham (1989 p. 61) to explain the elongation of the large-scale structure at high M_c can be extended to the reacting compressible case: the vorticity production in the upper left-hand side of a structure is positive and fluid approaching the structure from this side experiences a destruction of vorticity ω_z both by baroclinic and dilatation effects. A similar process affects fluid approaching from the lower right hand side. The overall effect is to decrease the vorticity in the second and fourth quadrants, and to increase vorticity in the first and third quadrants. At high heat releases or high M_c , the magnitudes of the baroclinic and dilatation terms strongly increase and this mechanism is enhanced. The large-scale structure can eventually break apart, leading to two vortex structures, one in the fast stream and the other in the slow stream.

4.2.2. Interaction between a central mode and its central subharmonic

In the incompressible no-heat release case, the transfer of energy from the fundamental to the subharmonic can occur through pairing or tearing. Pairing is forced by imposing a phase difference between the fundamental and its subharmonics ($\phi_F = \pi/2$ and $\phi_S = 0$ in equation 4.6), whereas tearing (where one vortex is trapped in the strain field of its subharmonic and pulled apart) occurs for a different phase relationship ($\phi_F = 3\pi/2$ and $\phi_S = 0$ in equation 4.6). Figure 4.2 shows at three instants of time the (a) mixture fraction, (b) vorticity, (c) vorticity production and (d) reaction rate during the transfer of energy from the fundamental to the subharmonic when the initial phase difference is 180° , intermediate between pairing and tearing. Note that the two fundamental structures are initially strained before rotating around each other and forming a single large-scale vortex.

Sandham (1989) analyzed the effect of Mach number on pairing and showed that both linear (growth of the subharmonic) and non-linear phases of pairing were damped by compressibility. Several reasons were proposed for the reduction in growth rate in the non-linear region: (1) More elongated structures may be less inclined to pair; (2) Due to the finite sound velocity, the delay in the Biot-Savart induction process may make the pairing less efficient; (3) Baroclinic and dilatational terms increase with compressibility and may be slowing the rotation of the two fundamental structures around each other. Lele (private communication 1988) has also shown in the non-reacting case that tearing may be more common at higher Mach numbers. Both these

first and third explanations can be extended to the low heat release incompressible case of figure 4.2. In our simulation, both the dilatation and baroclinic terms are initially positive (destruction of ω_z) in the region between the two merging vortices (fig. 4.2 a), and the merging of these vortex is first preceded (fig. 4.2 b) by a reduction of the baroclinic and dilatational terms in this region.

For central modes, the subharmonic and the fundamental have the same convective speed and the phase difference between them is constant in time. Note that the positions of the fundamental and of the subharmonic (large-scale structure at the right of the computational domain) are fixed in time as seen on figures 4.2 (a) to 4.2 (c). A phase lock is possible and the transfer of energy from the fundamental to the subharmonic which is long (Between fig. 4.2 (a) and fig. 4.2 (c), $\Delta t = 10$ based on \bar{u}_1) can be achieved. If the convective speeds of the fundamental and its subharmonic were different, their relative phase would vary in time and a distinct pairing or tearing mechanism would not be observed. As shown in section 4.7, the outer modes and their subharmonics have unequal convective speeds, which prevents a phase lock from occurring. This is one of several possible explanations for the absence of pairing in reacting mixing layers (section 4.7).

4.2.3. Mean profile and time history of various quantities for a typical central mode

Figures 4.3 and 4.4. show at various instants of time the mean (averaged over x) profiles of vorticity and vorticity production. Initially and during the linear growth of the central mode, the mean vorticity profile only has one maximum. As the two fundamental large-scale structures start to rotate around each other, the thickness of the vorticity profile suddenly increases, reach a maximum when the one lies above the other (Sandham 1989) before slightly decreasing when the structure on top begins to move downwards. We also observe that two symmetric peaks of vorticity are present when one the two fundamental structures lies above the other (fig. 4.3). At $t = 41$, the mean vorticity production is negative at the centerline ($y = 0$) and negative ω_z is created in the middle of the layer as the two structures start merging. Simultaneously, positive vorticity production at the location of the two symmetric vorticity peaks yields a reduction of these peaks. At later times, the two peaks have disappeared and a mean vorticity profile similar to the initial mean vorticity profile is obtained.

The mean temperature profile of a central mode is symmetric and its width is comparable with the width of the layer (fig. 4.5). Initially, the average temperature is

around 1.04, intermediate between 1.1, the temperature in the cores, and 1.0 the temperature of the free streams. During the merging of the two vortices, the web regions disappear and only hot wrapped fluid remains present in the center part of the layer (fig. 4.2a). Although the maximum temperature is unchanged, the average temperature increases at the centerline ($y = 0$).

The mean reaction rate profile is also symmetric (fig. 4.6) and extends across the total width of the layer, indicating that for central modes, mean chemical reaction is occurring at every cross-stream location of the layer. It will be shown below (section 4.3) that this is not the case for the outer modes. Note that the merging of the fundamental structures (between $t = 35$ and $t = 41$) is accompanied by a reduction of the reaction rate. We believe that this reduction arises from the disruption of the webs when the two large-scale structures start merging: with the disappearance of the web region between large-scale structures (fig. 4.2b), the straining and wrapping of pure fluid from both sides become less efficient which yields a decrease of the local reaction rate and a diminution of the total flame surface. As a result, the total reaction rate is sharply reduced.

Figure 4.7 shows the variation of the vorticity thickness versus time for the simulation of figure 4.1 (dotted line). The vorticity thickness history is similar to the curve obtain by Sandham and Reynolds (1991) and it exhibits the distinct bump around $t = 20$, when the fundamental grows and saturates, and the kink around $t = 35$, when the two structures lie one on top of the other. The solid line shows the same quantity for a laminar mixing layer having the same Reynolds number and, by comparison with the dotted line, shows the major role of the central modes in the transfer of species and momentum for incompressible mixing layers.

Finally, figure 4.8 shows the variation of the total and maximum reaction rates versus time for the simulation of figure 4.2 (dotted) and for a laminar mixing layer having the same Reynolds number (solid). In the absence of instability modes, the total reaction rate decays approximately like \sqrt{t} as can be estimated for the Burke-Schuman flow assuming infinite reaction rate (Kuo 1982). With the existence of the central instability mode, the total reaction rate strongly increases both by an increase of the flame surface and by an increase of the reaction rate by unit flame surface area (straining effect). The pairing process, which disrupts the intense straining and the creation of an interface between fuel and oxidizer, leads to a strong decrease in total and maximum reaction rates. However, as the fundamental develops, the total and

maximum reaction rates again increase.

4.3. Overview of one slow compressible outer mode

This simulation is intended to study the non-linear growth rate of a single outer mode and to evaluate the influence of the Reynolds number on a slow outer mode. The simulations show that the slow outer mode develops on its respective side of the reaction zone without spreading across the whole layer. The Reynolds number required for a slow outer mode to develop is large ($Re > 500$). We found that the behavior of the slow outer mode becomes qualitatively independent of Re for $Re > 4000$. A similar simulation for a fast outer mode yielded the same conclusion. The simulation at $Re = 4000$ used 201×801 points.

4.3.1. Reynolds number effects

Five simulations have been run corresponding to five different values of the Reynolds number ($Re = 500, 1000, 2000, 4000, 8000$). Figures 4.9 and 4.10 show the time history of the vorticity and vorticity thickness for these five Re number cases. The vorticity thickness for the three lowest Re is almost unaffected by the presence of the slow outer mode and grows like \sqrt{t} as it would in laminar flow. In the two high Re cases, however the vorticity thickness levels out or decreases due to the existence of the slow outer mode. In the highest Re case, the vorticity exhibit a damped oscillation in time as the outer mode completes two cycles of growth, saturation and decay. The short lifetime of the outer modes may explain why the compressible reacting mixing layer spreads more slowly than their incompressible counterparts. Namely, the absence of roll-up, the decay of the outer modes (accompanied by the transfer of their kinetic energy back to the mean flow) suggests that these outer modes will less efficiently transport momentum (and thus enhance the growth rate) than the central modes of the incompressible mixing layers.

Figure 4.11 show the time variation of logarithm of (twice) the kinetic energy $E_{1,0}$ of the fundamental, where

$$2E_{k,0} = \int_{-Ly}^{+Ly} \bar{\rho}(\hat{u}_k^2 + \hat{v}_k^2) dy. \quad (4.2)$$

Initially, the growth rate of the two highest Re cases are similar and match the growth rate expected from linear stability analysis. As viscosity is increased, the amplification rate of the slow outer mode is reduced, and for $Re < 500$ the growth rate of the slow

outer mode becomes negative. A similar observation has been made for the central mode of the compressible non-reacting mixing layer (Sandham 1989). However, the minimum Reynolds number above which the outer modes develop is higher in the reacting case than in the non-reacting case. This difference may arise (1) from the large temperature variations with heat release, yielding higher average viscosity, or (2) from the size of the outer modes, which have shorter wavelengths than the central mode and only develop on one side of the layer. At high Re , the energy of the slow outer mode increases, saturates and decays. As shown in section 4.2.3, this decay may arise from the modification of the mean profile when the slow outer mode convects hot fluid from the reaction zone to the slow colayer. In the highest Re number case, the modification of the mean profile also leads to the slow outer mode decay, but in this case, the growth of a new and distinct slow outer mode (see section 4.3.5) leads to the observed damped oscillation in time.

Figure 4.12 shows the time variation of the maximum pressure gradient versus time. The initial pressure gradient is caused by the pressure waves generated at the ignition, when an infinite reaction rate self similar solution is used to initialize a fast or moderate Damkhöler number simulation. At time $t = 25.6$ ($t_c = 8$) these pressure waves leave the domain and this initial pressure gradient disappears. As the large-scale structure of the slow outer mode develops, the maximum pressure in the web region and the minimum pressure in the core of the slow outer mode respectively increases and decreases, yielding growing pressure gradients. Indeed, in the two highest Re cases, the pressure gradient exhibits a local maximum at the time of the slow outer mode saturation. At latter times, a second large maximum is observed. This second maximum corresponds to the transient steepening of the pressure waves in the fast stream. These transient high pressure gradients leave the domain at $t \approx 140$ and the maximum pressure gradient decays until new maxima appear due to the development of a new slow outer mode in the two highest Re cases. Note that, although the maximum pressure gradients have different amplitudes in the two largest Re cases, their time history is qualitatively similar, which supports the use of $Re = 4000$ in the following simulations.

The mixture fraction and reaction rate contours for the $Re = 2000$ and $Re = 8000$ cases are presented on figures 4.13 and 4.14 at time $t = 64$. The thickness of the layer is larger at low Reynolds number since the layer spreads faster. Also, as the Reynolds

number is increased, the gradients of the mixture fraction in the web between large-scale structures get higher and the number of points necessary to resolve the flow increase. Nevertheless, the appearance of the layer remains unchanged from $Re = 2000$ to $Re = 8000$. In both cases, only the slow part of the layer is affected by the slow outer mode. In both cases, the reaction zone remains flat and the reaction rate is maximum at the top of the large-scale structure. Also, the large-scale structure is located at the same x position, implying that the convective speed of the slow outer mode is not affected by viscosity. Qualitatively, the results are the same at these two Reynolds numbers.

Based on this observation and unless otherwise specified (*e.g.* section 4.3.7), the Reynolds number defined with the mean velocity difference, the vorticity thickness and the free stream viscosity will henceforth be kept at $Re = 4000$. As we have shown the results should be characteristic of higher Re cases.

4.3.2. Two-dimensional structure

Figure 4.15 shows the contour plots of (a) mixture fraction, (b) vorticity ω_z , (c) vorticity multiplied by density ($\rho\omega_z$), (d) reaction rate, (e) baroclinic term, (f) dilatational term, (g) vorticity production, and (h) reaction rate for a typical developed slow outer mode of the reacting compressible shear layer with equal free stream temperatures, $M_c = 0.8$ and $T_f = 3$. Only the vortical region of the computational domain is shown here ($y \in [-2, 2]$) but the computational domain extends further ($y \in [-8, 8]$). The Damköhler number is equal to 6 and the Zeldovich number is 2. Here, fuel is almost undisturbed and must diffuse into the reaction zone, while oxidizer and hot product are mixed by the slow mode large-scale structure. No direct engulfment of fluid from both sides is observed. The chemical reaction occurs at the interface of the fuel and the hot mixture of product and oxidizer, and no additional flame surface is created. The reaction rate is maximum at the location of the large-scale structure where the straining is maximum. However, the variation of the reaction rate along the flame surface is less than 30%, and the persistence of a hot temperature region in the middle of the layer makes quenching unlikely to occur even for this large M_c and for higher Ze numbers.

The maximum vorticity region appears as a thin elongated region located in the slow speed region close to the centerline and does not cross this centerline (fig. 4.15 b). This strongly elongated shape, to be compared to the tubular shape of the high vorticity region for the central mode (fig. 4.1), suggests that the roll-up and the

engulfment of fluid will not be as efficient for the outer mode as for the central mode. The high vorticity region is located precisely where the magnitude of the vorticity production (baroclinic + dilatation) is high. The baroclinic and dilatation terms are large, representing 10% of the vorticity values, which suggests that these terms, and not the convective terms, control the vorticity dynamics. The baroclinic term is negative at the left of the large-scale structure where it contributes to the creation of vorticity. It is positive at the bottom right of the structure and thus prevents the high-vorticity region from spreading to the right. The dilatation term is lower than the baroclinic term by a factor of 3 to 4 and the vorticity production contours are similar to the baroclinic term contours. The dilatation term attains its extremum values along the webs.

Note that the vorticity production is non zero in the high speed side of the layer. In particular, it is positive at the top of the slow outer mode, which prevents the high vorticity region of the slow mode from spreading into that side: the slow outer mode keeps developing into the slow stream. The existence of regions in the high speed side where the vorticity production is negative does not contribute further to the creation of large-scale structure into that stream. Due to the unequal velocities between the two sides of the layer, each fluid element in the fast stream is alternatively subject to positive and negative vorticity production. As a result no net creation or destruction of ω_z is observed into the high speed side of the layer.

Figure 4.16 show the pressure contour in the full computational domain for the slow outer mode of figure 4.15. The slow outer mode generates radiating pressure waves in the fast stream, when the fast stream flow accelerates as it travels around the large-scale structure of the slow outer mode. A rarefaction wave is issued from the leading edge of the structure and a compression wave is issued from the trailing edge of the structure. Simulations initialized with only the fast outer modes show the same system of Mach waves developing into the slow stream. Note that the pressure fluctuations are small. The magnitude of those wave slowly decays in the fast stream with no evidence of shocks present during this phase of linear growth. The maximum and minimum pressure in the flows are $p_{max} = 0.736$ and $p_{min} = 0.695$ to be compared with the values reported by Sandham (1989 p60) for a typical central mode at $M_c = 0.8$, a pressure reduction in the core of 37.5% and a rise at the saddle point of 48.7% , yielding $p_{max} = 1.062$ and $p_{min} = 0.446$. As shown in section 4.7.3, the use of the flame convective Mach numbers (equation 4.11) would produce values consistent with the

simulation (section 4.7.3). The angle of those waves,

$$\sin \theta \approx \frac{1}{M_1 - M_2} \quad (4.3)$$

and the absence of such pressure waves in the slow stream, confirms that the slow outer mode approximately travels at the slow stream velocity. No radiating pressure waves are seen in the slow-speed stream, where the pressure contours are very similar to the pressure contours of the central mode of figure 4.1. In this stream, the pressure fluctuations further decay exponentially fast, as indicated by stability analysis. Some experimental evidence of these radiating pressure waves exist for compressible reacting mixing layer (Erdos *et al.* 1992, McIntyre and Settles 1991) and Hall (1991) used these radiating Mach waves to determine the convective speed of the large-scale structures, either by looking at their angle or by measuring cross-correlation of guidewall pressure. As seen at the end of this chapter, these radiating pressure waves are absent for incompressible reacting mixing layers.

In the absence of walls, these Mach waves leave the computational domain without reflection and therefore do not interact with the mixing layer. They carry away energy from the layer, E_{away} which can be estimated as the work of the force per unit area exerted by the fluid into the computational domain on the fluid outside the computational domain,

$$E_{away} \text{ (per unit time)} = \int_0^{L_x} (p - p_{avg})(v - v_{avg}) dx \quad (4.4)$$

where p_{avg} and v_{avg} are the average pressure and cross-stream velocity at the top and bottom walls. For the developed outer mode of figure 4.15 we found at times $t_c = 15, 20, 25, 30$ and 40 ($t = 48, 64, 80, 96, 128$). The values are given in table 4.1.

Table 4.1. Energy flux carried away by the radiating pressure waves in the fast and in the slow free streams

t_c	t	$E_{1,0}$	E_{away} bot.	E_{away} top
15	48	2.42410^{-4}	1.49610^{-11}	1.43610^{-6}
20	64	4.90110^{-4}	1.48610^{-11}	6.48210^{-6}
25	80	4.16810^{-4}	2.37610^{-11}	2.41410^{-5}
30	96	1.96710^{-4}	6.17710^{-11}	4.74110^{-5}
40	128	4.32610^{-5}	1.61610^{-10}	2.22910^{-5}

The total energy (integrated over time) carried away from the layer by the pressure wave is negligible in the low stream but large in the fast stream and comparable with

the kinetic energy of the developed slow outer mode. E_{away} is maximum during the decay of the slow outer mode as radiating pressure waves steepen (fig. 4.17). With walls, these waves can reflect and interact with the layer (Ragab and Sheen 1990), which suggests possible ways to increase the instability. Using DNS, Tam and Lele (1990) investigated, in the non-reacting case, the possibility of driving these normal acoustic waves mode into resonant instability by using a wavy outer wall. Their simulations didn't show any tendency for the mixing layer to roll-up and the mixing characteristics remain unchanged, contrary to the linear stability predictions of Tam and Hu (1989).

4.3.3. Surface plot and PDF of the mixture fraction

As shown by figure 4.15 a, the slow outer mode does not entrain fuel from the fast stream and only mixes product and oxidizer. Figure 4.18 shows the surface plot of the mixture fraction for the central mode of figure 4.1 and figure 4.19 shows the same information for the slow outer mode of figure 4.15. On the figure, X designs the streamwise direction and Y the cross-stream directions. The surface plot of the mixture fraction conveys the same information as the contour plot but makes the comparison with the PLIF images of Clemens (1991) easier.

For the central mode of the incompressible case (fig. 4.18), large-scale structures separated by steep concentration gradients corresponding to the webs are seen on the surface plot of the mixture fraction from DNS. It should be noted that the images shown by Clemens (1991) were smoothed in order to increase the signal-to-noise ratio. The PLIF images were averaged on pixels of about 1.5 mm, or about 13 times smaller than the width of the layer. This may make the large-scale structure appears more uniformly mixed than in reality. On the other hand, our simulation does not contain small-scale turbulence and the mixture-fraction gradients in the core may be overpredicted. Nevertheless, the PLIF images obtained by Clemens (1991) at $M_c = 0.28$ are similar to figure 4.18. They also exhibit Brown-Roshko structures separated by the web regions, which are regions of steep gradients containing very little mixed fluid. For the compressible slow outer mode (fig. 4.19), the surface plot obtained from the DNS exhibits only one ramp and one zone of mixing in the slow stream, with no structure wrapping the entrained fluid.

The PDF of the mixture fraction for the central mode of figure 4.1 and the slow outer mode of figure 4.15 are shown on figure 4.20. These PDF were calculated on the full computational domain, but the bins corresponding to pure fluid and pure

oxidizer were truncated. For the incompressible central mode of figure 4.1, the PDF is symmetric, broad and centered at $Z = 0.5$ (fig. 4.20). The PDF of the mixture fraction at the centerline shown by Clemens (1991, fig. 5.16) at low $M_c = 0.28$ is also broad, quasi-symmetric and centered at $Z = 0.5$. For the slow compressible outer mode of figure 4.15, the PDF of the mixture fraction is shown at three instants of time on figure 4.20. In this case, the slow outer mode mixes fluids having a smaller range of mixture fraction and the PDF is thinner, non symmetric and peaks at $Z \approx 0.2$.

4.3.4. Mean temperature and reaction rate profiles

Quantities averaged along the x direction at a given time are analogous to long time exposure pictures from experiment at a given downstream position. Useful information on the variations along y of the mean profile of species, temperature and reaction rate at different instants of the simulation are presented in this section. For comparison, the same quantities have been shown on figures 4.3 to 4.7 during the merging of two typical central modes.

As seen previously (fig. 4.3), the mean temperature profile for the central mode simulation has a width comparable to the width of the layer, a maximum half way between the cold stream temperature and the adiabatic flame temperature and a shape significantly varying with time. The mean temperature profile for the typical compressible slow outer mode of figure 4.15 is clearly different (fig. 4.21 a). It is almost invariant in time and keeps a triangular shape, with the exception of a small step developing in the slow stream due to the action of the slow outer mode. At the centerline, the average temperature is very close to the adiabatic flame temperature, indicating the absence of large temperature fluctuations and making quenching unlikely to occur.

Like the temperature profile, the reaction rate profile for the slow outer mode (fig. 4.21 b) is also almost invariant in time, and for this case with unity free stream temperature ratio, it remains centered at $y = 0$. The mean reaction rate profile only extends in a small portion of the layer ($y \in [-0.2, 0.2]$), contrary to what was observed in the central mode DNS, where chemical reaction was shown to occur at any cross-stream location (fig. 4.6). The fuel mean profile for the compressible slow outer mode (fig. 4.21 c) is undisturbed by the slow outer mode, which only mixes product and oxidizer, yielding the development of a small step on the oxidizer mean profile.

As the outer mode develop, it only entrains fluid from one side of the layer and increases the transport of species, momentum and temperature from this side. Note

that this large-scale transport is weak: in figure 4.21, we only observe a slight shift of the mean reaction rate profile towards the low speed side and the development of a small step on the temperature and species mean profiles. For simulations initialized with the fast outer mode, this step would develop on the fast-speed side. We believe (as seen in section 2.5.2), that the asymmetry of the mean temperature profile and the modification of its thickness, which has experimentally been observed for compressible reacting mixing layers (Hall 1991, fig. 5.4), arises from the preferential development of one or the other outer mode. For example, as the fuel equivalent ratio ($\phi_{f,o}$) is increased (decreased), the flame zone is shifted towards the slow (fast) free-stream and at low M_c the fast (slow) outer mode becomes more amplified (section 2.3.7). Thus, decreasing $\phi_{f,o}$ leads to the development of a step (longer tail) in the fast stream, a result experimentally observed by Hall (1991, fig. 5.4).

4.3.5 Saturation and decay of the compressible slow outer mode

At $Re > 2000$, the slow outer modes complete the same cycle of growth which match the linear stability analysis, saturation and decay. The saturation occurs while the vorticity thickness is only equal to $\delta_\omega = 1.3$ (at $Re = 4000$). During the decay, the radiating pressure waves steepen. In this section, the mean profile of vorticity, density-weighted vorticity, vorticity production terms and vorticity transport terms are presented at various instants of time. The modification of these profiles as the slow outer mode convects hot fluid from the reaction zone to the slow colayer is shown to strongly modify the linear stability of the layer and to destroy this slow outer mode. An explanation for the steepening of the radiating pressure waves is also proposed and the issues of the decay of the outer modes on the transfer of energy from these modes to their subharmonic (pairing) are discussed.

Figure 4.22 shows the respective part of the dilatation and baroclinic terms in the production of vorticity at time $t = 64$ and $t = 80$. At $t = 64$, the dilatation term is positive on both sides of the flame zone and zero or slightly negative at $y = 0$ where the density is constant or slightly increasing. The baroclinic term is on the average zero on the high speed side of the layer where regions of positive and negative baroclinic torque compensate each other. The dilatation term is positive on this side of the layer and the vorticity diffused in this region tends to be destroyed. The dilatation term is negative at the slow edge of the layer, where hot rotational fluid entrained by the slow outer mode is mixed with product and cooled. A large negative baroclinic peak exists at the location of the slow outer mode (large negative ω_z) and enhances

the development of this mode, while a large positive baroclinic peak exist below the slow outer mode and prevents this mode from spreading into the slow stream. The transport of vorticity at $Re = 4000$ is governed by convection in the slow stream (at $t = 64$, vorticity is convected from the high vorticity peak towards the slow stream) and by diffusion in the fast stream.

The mean vorticity production profile is dramatically changed when the slow outer mode starts decaying ($t = 80$). This modification does not arise from the dilatation term, which is almost unchanged, but from the large changes in the mean baroclinic profile as the the slow outer mode convects hot fluid from the reaction zone into the slow stream. The large positive and negative peaks seen in the baroclinic profile of $t = 64$ are both shifted towards the fast stream and the amplitude of the negative peak decreases. A new negative baroclinic peak appears at the edge of the slow stream. The vorticity production becomes positive at the location of the slow outer mode (large negative ω_z), vorticity is destroyed in this region and the high vorticity region is shifted towards the fast stream.

The last plot of figure 4.22 shows the mean vorticity production profile at five instants of time. At the latest time ($t = 96$), the negative vorticity production peak, located slightly below $y = 0$ and which was large at $t = 64$, has disappeared. The negative peak, which appeared at the slow edge of the layer at $t = 80$, has shifted towards the centerline while its amplitude has increased. This new negative production peak (located at $y = -0.7$) yields the development of a new slow outer mode. This new slow outer mode will develop, transport hot fluid from the reaction zone to the slow stream, saturate and decay as the previous one. As a result, the kinetic energy at high Re numbers oscillates as seen on figure 4.12.

The time variation of the mean vorticity is shown in figure 4.23, whereas the mean density-weighted vorticity which was shown to be the important profile to study linear stability analysis is shown on figure 4.24. The variation of the mean vorticity profile results from the balance of the production and convection terms shown in figure 4.22. At $t = 64$, the development of the slow outer mode leads to the existence of a narrow bump in the slow-speed side of the vorticity profile. When the negative baroclinic peak shifts towards the centerline, the slow outer mode follows and this narrow bump moves towards $y = 0$. At $t = 96$, at the slow-speed edge of the layer (at $y = -0.7$, the location of the new negative baroclinic peak appears) the mean vorticity profile levels off, announcing the development of the new slow outer mode.

The mean density-weighted vorticity (fig. 4.24) initially has two peaks which leads to the existence of the two outer modes. As the mixing layer develops, its thickness increases and the amplitudes of these two peaks are reduced due to viscosity. In the slow stream, the slow outer mode convects hot and fast fluid from the reaction zone into the slow stream and thereby modifies the mean density-weighted vorticity distribution. In particular, the slow density-weighted vorticity peak is shifted towards the centerline until $t = 80$. At $t = 96$, the slow peak moves to $y = -0.7$ (in the region where the mean vorticity profile levels off).

Figure 4.25 shows the evolution of the mixture fraction and vorticity contours of the slow outer mode of figure 4.15 at two instants of the decay ($t = 80$ and $t = 96$). The structure becomes elongated, indicating the loss of coherence between the top and the bottom part of the structure which are travelling at different speeds. The entrainment of product and oxidizer are disrupted and the kinetic energy of the slow outer mode is transferred back to mean flow. The highest vorticity value in the flow is strongly reduced and the high vorticity region splits in two, a top part reminiscent of the high vorticity region observed on figure 4.15 which moves towards the centerline and a second part below it travelling slower and located at $y = -0.7$, the new location of the mean density-weighted vorticity peak in the slow stream.

4.3.6 Effects of the evolution of the mean $\bar{\rho} d\bar{u}/dy$ profile on the linear stability of the layer

The mean density weighted vorticity was used to determine the instability characteristics of the compressible mixing layer at $t = 0$ and to calculate the eigenfunctions used to initialize the simulations. As seen in the previous section, the mean profile of density weighted vorticity ($\bar{\rho} d\bar{u}/dy$) is strongly modified when the slow outer mode transports hot and fast fluid from the reaction zone to the low-speed side of the layer. In particular, the slow peak of $\bar{\rho} d\bar{u}/dy$ is reduced and moved towards the centerline when the density distribution becomes more uniform on the low-speed side of the layer. To investigate the resulting modification of the instability, we carried a new linear stability calculation based on the mean $\bar{\rho} d\bar{u}/dy$ profile at time $t = 64$ (figure 4.24). The results show that the evolution of the mean $\bar{\rho} d\bar{u}/dy$ profile with time strongly affects the shear layer stability characteristics and its downstream development.

The amplification rates and phase speeds of the 2-D and 45 degree instability modes obtained at $t = 64$ are compared to the amplification rates and phase speeds of the

instability modes obtained at $t = 0$ (figure 4.26). Figure 4.27 shows the same information when the mean $\bar{\rho} d\bar{u}/dy$ profile at time $t = 64$ is normalized to get $\delta_\omega = 1$. Several effects can be noticed: (1) First, the amplification rates of the fast and slow instability modes are strongly reduced at $t = 64$, even when the normalized mean $\bar{\rho} d\bar{u}/dy$ profile is used. (2) Their frequencies are shifted to lower values and the size of the most amplified instability modes increases. In particular, at $\omega = 1.75$ (the frequency of the most amplified slow outer mode at $t = 0$) the amplification rates of the slow outer modes are now negative and no slow instability mode can develop in the computational domain of length $L_x = 3.59$. (3) The convective speeds of the slow outer modes are shifted towards the average speed of the free streams, while (4) the convective speeds of the fast outer modes are slightly increased. (5) The amplification rates of the slow outer modes at 0° and 45° become equal and the obliquities of the instability modes is increased, especially at low frequencies. (6) A distinct bump corresponding to the underlying presence of the central mode is noticeable at the left of the fast and slow amplification curves.

All these effects indicate a stabilization of a slow outer mode and a destabilization of the central mode. They are consistent with the analysis we develop in chapter 2: As the slow $\bar{\rho} d\bar{u}/dy$ peak becomes less pronounced and moves toward the centerline, the slow outer mode associated with this peak is stabilized and its phase speed tends to the average speed of the two streams. Meanwhile, the amplification rate of the central mode increases and M_c becomes the proper correlating parameter. As M_c is larger than M_f , compressibility effects get stronger and the obliquity of the instability modes is increased.

The large variation of the compressible mixing layer instability characteristics as the eigenmodes develop indicates that (1) diverse instability modes having various obliquities, frequencies and phase speeds can be successively amplified. It also suggest that, (2) at a given instant of time, some of these instability modes may be growing while others are saturating or decaying. In contrast, the development of the non-reacting incompressible mixing layers is much simpler. All the instability modes have the same convective speed, equal to the average speed of the free-streams, and only one vorticity peak is present. Non-linear effects do not affect the location of this peak but do affect its width. As the central mode saturates, the amplification rate of its subharmonic gets larger and pairing is enhanced.

4.3.7 Decay of the initial slow outer mode and growth of the new slow outer mode at $Re = 8000$

In this section, it is shown that the decay of a slow outer mode is quickly followed by the development of a new slow outer mode. We have seen in section 4.3.4 that the decay of the initial slow outer mode is accompanied by the appearance of a new negative peak of vorticity production, which yields the development of a new slow outer mode and explains the kinetic energy oscillations seen on figure 4.12. Here, the 2-D structure of the layer during the decay of the initial slow outer mode and the development of the new outer mode is presented. It is shown that two separate regions of vorticity, travelling at different speeds and separated by a region of high positive baroclinic torque, exist inside the slow colayer as the new slow outer mode develops. Figures 4.28, 4.29 and 4.30 shows the contours of (a) mixture fraction, (b) vorticity, (c) baroclinic term and (d) vorticity production at three instants of time ($t = 96$, $t = 112$ and $t = 128$). The figures show the evolution of the appearance of the layer during the decay of the slow outer mode ($Re = 8000$). Similar information has been shown on figure 4.25 for the same slow outer mode but at earlier times and at $Re = 4000$.

At $t = 96$ (fig 4.28), the two regions of high vorticity are present and lie one on top of the other. The top one corresponds to the decaying slow outer mode which has shifted towards the centerline, while the second one arises from the development of the new slow outer mode. This second region of high ω_z travels slower than the first one (at $t = 80$, fig. 4.25, this second region of high ω_z was located at the right of the first one) and the mixture fraction contours become elongated along x . The contours of the vorticity production, which is the sum of the dilatational term and baroclinic term, are similar to the contours of the baroclinic torque. The vorticity production is positive between the two region of high ω_z and prevents the merging of these two regions. The dilatational terms appears negligible, except in thin elongated layers of hot product and cold oxidizer previously entrained by the developed slow outer mode. In these regions, where the gradients of the mixture fraction are large, the hot rotational products are cooled, which yields negative dilatational term, while the cold oxidizer is heated which yields a positive dilatational term. At $t = 112$ (fig 4.29), only the bottom region of high ω_z remains present in the flow, located closer to the centerline than at $t = 96$. The initial slow outer mode has relaminarized, but the new slow outer mode starts entraining hot fluid from the reaction zone to the slow

stream again. At the latest time, $t = 128$ (fig 4.30), the contours of mixture fraction and vorticity become very similar to the contours of the slow outer mode, which developed from the linear eigenfunction (fig. 4.15).

4.3.8. Recapitulation of section 4.3

Several observations can be made at this point. (1) First, the existence of outer modes with finite amplitude is confirmed. Their 2-D structure is largely different from that of the central mode, which has important consequences on entrainment, mixing and chemical reaction. (2) These outer modes are fairly robust, since the outer modes which develop after the relaminarization of the layer appear very similar to the outer modes which develop from linear eigenfunctions. (3) Each outer mode grows and decays rapidly; its lifetime is short. This result is in agreement with the observations of McIntyre and Settles (1991), who noted the apparent burst of regularly spaced structures and the existence of large-scale poorly organized turbulent structures that evolved rapidly with downstream distance in their compressible mixing layer experiment. This third point also suggests that a large distribution of modes may be present in the layer at a given instant of time.

4.4. Absence of interaction between the fast and the slow outer modes

In this section, it is shown that the two outer modes simultaneously develop on their respective sides of the mixing layer without interacting. The pace at which the fast and the slow outer modes develop is different. The appearance of the layer is shown to vary quickly (estimated $30\mu s$ in Clemens 1991 experiment), which may make the structures hard to distinguish in experiments. The reaction rate is also shown to vary in time when the relative positions of the fast and the slow outer modes vary.

A 2-D simulation of the compressible reacting mixing layers has been performed to study the interaction between the fast and the slow outer modes. This simulation is similar to that of figure 4.15 ($Re = 4000$ and 201×801 points are used), but was initialized with both the fast and the slow outer modes. The outer modes used in the initialization have the same amplitude, $A = 0.001$.

Figure 4.31 shows the contours of (a) mixture fraction, (b) vorticity, (etc.) at $t = 64$ for a simulation initialized with the fast and the slow outer modes. By comparison with fig. 4.15, where only the slow outer mode was used in the initialization, we note

that the fast outer mode has no effect on the contours of mixture fraction or vorticity in the slow colayer. The high vorticity region in each colayer remains located in the high vorticity production region as seen on figure 4.15 for a single outer mode. This suggests a two-step mixing process where fluid from each of the free-streams is first mixed with product and then diffuses to the reaction zone. The fast outer mode remains associated with the fast free-stream and only mixes fuel and product, while the slow outer mode remains associated with the slow free-stream and only mixes oxidizer and product.

Figure 4.31 also indicates that the slow outer mode develops faster than the fast outer mode. This results is consistent with the linear stability results presented in Chapter 2. We have seen in chapter 2 that the amplification rates of the slow and fast outer modes were dependent on the position of the flame, on the free-stream temperature ratio and on the flame temperature. In figure 4.31, with the parameters used in this simulation, the amplification rate of the slow outer mode is higher than the amplification rate of the fast outer mode, and the slow mode is almost at its saturation point whereas the fast outer mode is still growing.

The reaction zone remains flat (fig 4.31), close to the stoichiometric line for this high Damkhöler simulation, and little creation of new flame surface is observed. However, the fast and the slow outer modes increase the local reaction rate by straining the reaction zone. The slow (fast) outer mode convects a hot mixture of oxidizer (fuel) and product into the reaction zone, which in turn augments the total reaction rate. The hot temperature region located between the two colayers (which inhibits quenching) is not distorted by the presence of the second outer mode. Each outer mode is shown to generate radiating pressure waves in the opposite stream (fig 4.32), as seen for a single outer mode.

Figure 4.33 shows the same simulation as the one shown on figure 4.31 at $t = 80$. It first indicates that (1) the decay of one (slow) outer mode is independent of the existence of a (fast) outer mode in the opposite colayer. At $t = 80$ the slow outer mode starts decaying and subsequently becomes elongated (along x) while the fast outer mode saturates. The decay of one outer mode is not affected by the presence of the other outer mode, and the mixture fraction contours in figure 4.33 and 4.25 are identical in the slow colayer.

Comparison between figures 4.33 and 4.31 also shows the rapid variation of the appearance of the layer. The fast and the slow outer modes travel at different speed

and their relative position changes in time. Figure 4.33 shows the mixture fraction contours at time $t = 80$, to be compared with the same information at $t = 64$ (fig 4.31). In $\Delta t = 16$, the slow and the fast outer modes approximately travelled distances of $d = 0.592\Delta t = 9.472$ and $d = 0.914\Delta t = 14.62$, respectively, yielding the locations seen on figure 4.33. Clearly, the appearance of the layer changes rapidly, which we believe can make the large-scale structures harder to identify in experiments. As the relative position of the outer modes changes, so does the intensity of the straining that they exert on the reaction zone. At $t = 80$, the two outer modes lie one on top of the other and the straining is maximal, yielding a maximum reaction rate (fig 4.33 right) almost twice that at $t = 64$ (fig 4.31 right).

Figures 4.34 and 4.35 show the PDF and the surface plot of the mixture fraction for the simulation shown on figure 4.33 (at $t = 80$). The existence of two bumps on the PDF of the mixture fraction Z (Fig 4.34) indicates the two-step mixing process. One bump is located at $Z \approx 0.75$, corresponding to almost equally mixed fuel ($Z = 1$) and product ($Z = 0.5$) and the other bump is located at $Z \approx 0.25$ corresponding to almost equally mixed oxidizer and product. In contrary to the central mode of the incompressible reacting mixing layer of figure 4.20, here almost no equally mixed fuel and oxidizer are observed. The surface plot of the mixture fraction exhibits two ramps (Fig. 4.35) similar to the PLIF images obtained by Clemens (1991) in the non-reacting but compressible case at $M_c = 0.62$. As stated by Clemens, these PLIF images appear to be composed of two separate regions of mixed fluids, seen as two parallel streamwise ramps, separated from each other by relatively steep gradients. Those ramps (fig 4.35) are the direct consequence of the existence of the outer modes, with the Clemens results therefore suggesting that outer modes might be present at moderate convective Mach numbers, even in the non-reacting case.

4.5. Influence of Damkhöler number on the structure of the layer

In this section, the effect of the fast and slow outer modes as well as the influence of Damkhöler number on the structure of the layer are examined. The fast and the slow colayers are seen to exist even at low Damkhöler numbers ($Da < 1$). It is shown that, unlike the central mode, the fast and slow outer modes do not effectively transport species to the reaction zone and have therefore a weak effect on the total reaction

rate in the layer.

Figure 4.36 shows the contours of (a) mixture fraction, (b) density weighted vorticity and (c) reaction rate for the same slow outer mode than on figure 4.15, but for $Da = 1$. The similarity of the contours between figures 4.15 and 4.38 suggest that the existence of the two colayers can persist at very small Damkhöler number, if the flame temperature remains sufficiently high for the two mean $\bar{\rho} d\bar{u}/dy$ peaks to appear. The large-scale structure is located at the same position on figures 4.15 and 4.38, indicating that the slow outer mode travels at the same velocities in the two Da cases. For $Da = 1$, the reaction rate is maximum at the top of the slow outer mode as for $Da = 6$. The flame zone remains plane with the exception of a slight bump on the slow-speed side of the layer, where reacting fluid is entrained by the slow outer mode. The maximum reaction rate is twice smaller at $Da = 1$ than at $Da = 6$, and the reaction zone thickness almost doubles, a result in agreement with the analysis of Gibson and Libby (1972) showing that the reaction zone thickness varies like $Da^{-1/3}$ (factor of 1.8 between $Da = 6$ and $Da = 1$).

Figure 4.37 shows the total and maximum reaction rates for several simulations with different Damkhöler numbers, different instability modes (no mode, slow outer mode or slow and fast outer mode) and different Reynolds numbers ($Re = 4000, 8000$). The effects of the number of modes used in the simulations, of the Damkhöler number and of the Reynolds number are examined. All the curves have $Re = 4000$ except the chain-dashed one for $Re = 8000$. We refer to the mixing layer initialized without instability modes as the laminar mixing layer, since it only develops by laminar diffusion. We note that:

- In the absence of instability modes (laminar case, solid lines), the total and maximum reaction rates increase rapidly during the ignition before decaying slowly as the thickness of the layer increases.
- The slow outer mode (dotted lines) causes only a small increase in the total and maximum reaction rates. As noted in section 4.4, the slow outer mode increases the reaction rate, not by creation of flame surface, but by straining as the outer mode transports more reactant into the reaction zone. The reaction rate is maximum at the time of saturation of the outer mode and decreases towards the reaction rate of the laminar mixing layer (solid line) when the slow outer mode decays away.
- At low Damkhöler number ($Da = 1$), a similar behavior is observed with a longer

ignition time and a slightly lower total reaction rate.

- At high Re number ($Re = 8000$) (chain-dashed line), a similar behavior is also observed. We note a second maximum of the total and maximum reaction rates at latter time as a new slow outer mode develops.
- The total and maximum reaction rates present an oscillatory behavior when the fast and the slow outer modes are used to initialize the simulation. These periodic oscillations arise from the unequal convective speed of the two outer modes. As seen in section 4.4, the relative position of these two modes constantly changes and the straining of the reaction zone is maximum when the two outer modes lie one above the other. The amplitude of these oscillations is large (the maximum reaction rate doubles when the outer modes lie one above the other) and their period is given by

$$T = L_x / (\bar{c}_f - \bar{c}_s) = 11.15 \quad (4.5)$$

where c_f and c_s are the convective speeds of the fast and slow outer modes and L_x is their wavelength.

Note that the effects of the outer modes on the total reaction rate of the compressible mixing layer (fig 4.37) are much smaller than the effects of the central mode on the total reaction rate of the incompressible reacting mixing layer (fig. 4.9). Whereas at $Re = 200$ the total reaction rate of the incompressible mixing layer was shown to increase by five due to the presence of the central mode (fig. 4.9), at $Re = 4000$, the total reaction rate is only 20 – 25% higher than the laminar reaction rate when only the slow outer mode is present and only 35% higher when both the slow and the fast outer modes are present.

4.6. Overview of the instability modes of the low Mach number reacting mixing layer

In this section the results of two simulations of a low Mach number ($M_c = 0.05$) reacting mixing layer are presented. The first simulation, which was initialized with small amplitude ($A = 0.001$) fast and slow outer modes of the incompressible reacting mixing layer ($T_f = 3$, $Re = 500$ and $M_c = 0.05$), confirms the results from linear stability analysis. It exhibits developed large-scale structures very similar to the large-scale structures seen in compressible reacting mixing layer. The second simulation shows the transition from the central mode to the outer modes in incompressible reacting

mixing layers. It was initialized by superposing on the parallel mean flow of a mixing layer with $T_f = 3$, $Re = 500$ and $M_c = 0.05$, the central mode of the same non-reacting mixing layer at $M_c = 0.05$. The results are shown at an intermediate time when the developing central mode breaks apart into a fast and a slow outer mode. Interestingly enough, the instability modes which are observed in the 2-D spatially developing simulation of igniting incompressible mixing layers (Appendix B) are very similar to the large-scale structures observed in this second direct numerical simulation.

4.6.1 Simulation initialized with the fast and the slow outer modes

Figure 4.38 shows the contour plots of (a) mixture fraction, (b) vorticity ω_z , (c) vorticity multiplied by density ($\rho\omega_z$), (d) reaction rate, (e) baroclinic term, (f) dilatational term, (g) vorticity production, and (h) reaction rate for the incompressible reacting mixing layer with equal free-stream temperatures, $M_c = 0.05$ and $T_f = 3$. Only the vortical region of the computational domain is shown here ($y \in [-5, 5]$) but the computational domain extends further ($y \in [-10, 10]$). The Damköhler number is equal to 6, the Zeldovich number is $Ze = 2$ and the Reynolds number is $Re = 500$.

In this simulation, the slow outer mode has a larger amplification rate than the fast outer mode, and the slow outer mode saturates while the fast outer mode is still growing. As in the compressible case, no direct mixing of fuel and oxidizer is observed. The slow outer mode only entrains oxidizer and product while the fast outer mode only entrains fuel and products. The interface of fuel and oxidizer remains nearly plane with little creation of new flame surface. The reaction rate is maximum on top of the large-scale structure, and the existence of a high temperature region located between the two colayers makes quenching unlikely to occur. As for compressible outer modes, the high vorticity region associated with the slow incompressible outer mode is a thin elongated region located on the low speed side of the layer and close to the centerline. The same behavior is found for the fast outer mode. Here at $M_c = 0.05$ the baroclinic torque is approximately 2 times higher than the dilatational term and tends to dominate the vorticity production. The regions of high vorticity are located in the regions of high baroclinic torque, as in the compressible case.

4.6.2 Simulation initialized with the central mode

Figure 4.39 shows the contour plots of (a) mixture fraction, (b) vorticity ω_z , (c) vorticity multiplied by density ($\rho\omega_z$), (d) reaction rate, (e) baroclinic term, (f) dilatational term, (g) vorticity production and (h) reaction rate during the transition from the

developing central mode to the outer modes. Here, the heat release is $\Theta = 3$ which yields $T_f = 4$ but we initialize the simulation with $T_f = 3$. Only the vortical region of the computational domain is shown here ($y \in [-5, 5]$) but the computational domain extends further ($y \in [-10, 10]$). Here, $Da = 6$, $Ze = 2$, and $Re = 500$.

At the beginning of the simulation, the central mode grows and the contours of the mixture fraction shows the development of large-scale, quasi-symmetric structures which travel at the average speed of the free-streams. Figure 4.39 shows the modification of these large-scale structures as they begin to break apart into a fast and a slow eddy. The top part of the structure starts travelling faster than its bottom part and the structure becomes strongly elongated along x and inclined towards the fast stream. The regions of large mixture fraction gradients, which exist between the large-scale structures, are the remnants of the webs of the developing central mode. The flame straining is still large in these regions, and for this low Ze case the chemical reaction is maximum there. Since the transition from the developing central mode to the outer modes occurs before the roll-up of the central mode, we do not see the large-scale engulfment and wrapping of fluid from both sides. The upper right-hand side of the structure appears to entrain only fuel and product, while the lower left hand side of the structure appears to entrain only oxidizer and product. As the top and bottom parts of the structure move apart, the interface of fuel and oxidizer becomes flat, uniform and aligned with the mean flow, as seen for the developed slow outer mode of figure 4.15. Similarly, the temperature, which was initially maximum inside the large-scale structures of the developing central mode, becomes maximum at the centerline.

The physical explanation for the transition from the central mode to the outer mode has been proposed in section 4.2.1. We have shown, for the incompressible low-heat release mixing layer, how the sign of the baroclinic and dilatation terms (positive in the second and fourth quadrant and negative in the first and third quadrant) yielded elongated large-scale structures which could break apart to give slow and fast outer eddies at sufficiently high M_c or heat releases. Here the heat release is large ($T_f = 4$) and two regions of high vorticity appear in each large-scale structure (one in the fast stream and the other one in the slow stream). These regions of high ω_z are strongly elongated in the x direction and are located close to the centerline as for the outer mode of the compressible reacting mixing layer (fig 4.15). We note that these two regions of high vorticity are initially located close to the webs, where the large

pressure and density gradients yield the largest values of the baroclinic torque. The baroclinic contours exhibit a quadrupole structure and, for this low Mach number case, the baroclinic and dilatational terms have comparable magnitudes. At later time, all traces of the central mode have disappeared and the observed developed instability modes are very similar to the outer modes seen in section 4.6.1.

4.6.3 Conclusion of section 4.6

The two simulations presented above indicate that, with sufficient heat release and even at low M_c , the central mode can break apart into fast and slow incompressible outer modes. The non-linear rupture of the central mode, caused by the positive baroclinic torque in the web region, yields the appearance of large-scale structures elongated along x and inclined towards the fast stream. The reaction zone initially located in the web region rotates and becomes aligned with the mean flow when the outer modes develop. Identical results are obtained in the 2-D spatial simulations of the igniting mixing layer presented in appendix 2. The simulations also suggest that, with the exception of the absence of radiating pressure waves, the incompressible outer modes are very similar to the compressible outer modes. In particular, other simulations not shown here reveal that the low Mach number outer modes saturate and decay like their compressible counterparts.

4.7. Interaction of the outer modes with their subharmonics

In this section, we examine the interaction of one outer mode with its subharmonic for reacting compressible mixing layers. For low heat release incompressible mixing layers, the usual mechanism of interaction can be pairing or tearing, where the energy is transferred from the fundamental to the subharmonic as seen in section 4.1. Pairing or tearing is a relatively long process ($\Delta t = 10$ for the slow outer mode of figure 4.1), but for incompressible non-reacting mixing layers, the convective speed of the fundamental and the subharmonic are the same and the phase lag between these two modes remains constant. For compressible reacting mixing layers however, pairing does not occur. Here, the fundamental and its subharmonic have unequal phase velocities and their relative phase is constantly changing in time which inhibits pairing.

We believe, however, that other mechanisms presented in this section play a larger part in the suppression of pairing in a compressible reaction mixing layer:

- The first and main mechanism is the large baroclinic torque in the regions between

the two fundamentals, where pairing tries to occur (see figure 4.38). The rotation of two adjacent structures in a colayer around one another is prevented by the baroclinic torque.

- Other factors are the absence of roll-up and the elongated shape of the outer modes (which also arise from the baroclinic torque) since elongated structures may be less inclined to pair.
- A third factor is the short lifetime of the outer modes. In incompressible mixing layers, a central fundamental grows, saturates and rolls-up (keeping its kinetic energy constant) until the subharmonic is large enough for pairing to occur. In contrast, for the compressible reacting mixing layer, the outer modes and their outer subharmonic usually grow, saturate and decay almost independently from one another (section 4.7.1). Therefore, unless the amplitude of subharmonic is large (having an amplitude larger than the fundamental) the fundamental decays before the subharmonic is large enough to cause pairing.

The fundamental (F) and the subharmonic (S) wavelengths are included in the initialization with amplitudes A_F and A_S and phases ϕ_F and ϕ_S . A second index is used to differentiate the fast F and the slow S instability modes. We use:

$$u = \bar{u} + \text{real}[A_{F,S}(y)e^{i(\alpha_{F,S}x+\phi_{F,S})} + A_{S,S}(y)e^{i(\alpha_{S,S}x+\phi_{S,S})}]. \quad (4.6)$$

Here, the phase of the fundamental is always set equal to zero and different values of the other parameters are chosen in an attempt to force the transfer of energy from the fundamental to the subharmonic. In the first section (4.7.1), it is shown that because the outer modes quickly grow, saturate and decay (as seen in section 4.3.3), no transfer of energy can occur from the fundamental to the subharmonic if A_F is not of the same order as A_S . The 2-D contours of the compressible reacting mixing layer are seen to be laminar if the fundamental decayed before the development of the subharmonic. In the second section (4.7.2), for a large amplitude of the fundamental, different phase lags are tried to obtain the best transfer of energy from the fundamental to the subharmonic. The results do not show any pairing where two structures start rotating around each other, but certain phase lags are seen to increase the growth rate of both the subharmonic and the fundamental. In this case, contour plots show that the growing subharmonic “swallows” the decaying fundamentals on the same side of the layer. This mechanism, which we denote by “gulping”, does not destroy

the two colayers. The fast outer modes remain associated with the fast colayer and the slow outer modes remain associated with the slow colayer.

4.7.1 Influence of the subharmonic amplitude

Figure 4.40 shows the kinetic energy of the fundamental and the kinetic energy of the subharmonic for two different simulations initialized with two different amplitudes of the subharmonic, $A_{Sf} = 0.0004$ in the first case and $A_{Sf} = 0.001$ in the second. The amplitude of the fundamental and the phase of the subharmonics are the same in both simulations, $\phi_{Sf} = 180$ and $A_{Ff} = 0.002$. Figure 4.40 shows that, in both cases, the fundamental decays before the subharmonic is strong enough for pairing to occur. Its kinetic energy is transferred back to the mean flow and the kinetic energies of all the Fourier modes having higher wavenumbers are temporarily increased. As seen in section 4.3.6, the decay of the fundamental is accompanied by a modification of the mean $\bar{p} d\bar{u}/dy$ profile, which yields a reduction of the fast and slow outer modes amplification curves. Indeed, the growth rates of the subharmonics are strongly reduced when the fundamental saturates. At $t \approx 120$ the kinetic energy of the instability modes is minimum (fig 4.40 top). After the decay of the fundamental, the fast subharmonic outer mode resumes its linear growth rate, develops and then, at its turn, saturates and decays (fig. 4.41).

Figure 4.41 shows the contours of mixture fraction, vorticity, baroclinic and vorticity production for the simulation with $\phi_{Sf} = 180$, $A_{Sf} = 0.001$ and $A_{Ff} = 0.002$ at three instants of time, $t = 80$ (fully developed outer modes), $t = 112$ (after the decay of the fast fundamentals) and $t = 176$ (during the development of the fast subharmonics). The simulation indicate that the appearance of the layer changes rapidly and that after the decay of the fundamentals (but before the development of the subharmonics) the mixing layer looks laminar with no evidence of large-scale structures present (fig. 4.41).

- At time $t = 80$, the vorticity production increases and eventually becomes positive at the left of the high ω_z regions. The fast fundamental starts decaying. The contours of the baroclinic torque and the contours of the vorticity production are similar, implying that the dilatation term is negligible.
- At time $t = 112$, the fast fundamental has relaminarized. Despite the large amplitude of the subharmonics used in the initialization ($A_{Ss} = 0.5$, $A_{Fs} = 0.002$) the fundamentals decay before the development of the subharmonic. Note that in this case the

top edge of the layer is flat and we believe that no large-scale structures would be seen in experiments at this stage. The mixture fraction and vorticity contours reveals the presence of the developing subharmonic. We note that, as for the slow outer mode of figure 4.25, the decay of the fast outer mode does not significantly affect the slow colayer, which remains laminar. After the decay of the fundamental, the vorticity production contours exhibit strongly elongated stripes of alternatively positive and negative vorticity production. As already seen in section 4.3.7, these stripes arise from the existence of large positive and negative dilatational regions where hot product and cold fuel previously entrained by the fast outer mode are respectively cooled and heated.

- Although the simulation was initialized with only fast outer modes, the decay of the fast fundamental is accompanied by a small transfer of vorticity in the slow stream which, due to the inflexional instability of the slow colayer, yields the development of a slow subharmonic. Note that this small transfer of vorticity does not destroy the two colayers. At $t = 176$, the presence of the developing fast subharmonic is seen on the mixture fraction and vorticity contours, while the less developed slow subharmonic is only seen in the vorticity contours. The dilatation term remains negligible in the vorticity production.

The pressure contours shown in figure 4.46 convey the same information. At $t = 112$, the fundamental relaminarizes and the radiating pressure waves in the slow stream steepen as seen for the slow outer mode of figure 4.15. At $t = 224$, the wavelength of the pressure waves in the slow stream has doubled. Radiating pressure waves appear in the fast stream as the slow subharmonics develop.

4.7.2 Influence of the initial relative phase

As seen in the previous section, the fundamental can decay before the subharmonic is large enough to interact with it. This suggests that, unless the initial amplitude of the subharmonic is already comparable to the amplitude of the fundamental, no transfer of energy will occur between an outer mode and its subharmonic. Another difficulty is the non-constant phasing between one outer mode and its subharmonic, which has a different phase velocity. Furthermore, we have seen that the phase speeds of the instability modes varies in time. As shown in section 4.3.6., the development of one outer mode modifies the mean $\bar{\rho} d\bar{u}/dy$ profile, which in turns modifies the linear stability of the layer and the convective speeds of the outer modes. Thus, the relative phase of the fundamental and subharmonic is difficult to predict. Here, we have used

equal amplitude of the fundamental and the subharmonic $A_F = A_S = 0.001$ and have tried different initial phase delays to force the interaction. The results show some influence of the initial phase on the history of kinetic energies of both the fundamental and the subharmonic. 2-D contours do not show pairing (where two structure start rotating around each other is not observed) but indicate that, for certain initial phasing, the growing subharmonics can swallow the decaying fundamental in the same colayer, hence the term “ gulping ”.

Figures 4.44 shows the variation of the kinetic energy of a slow compressible fundamental and of its slow outer subharmonics for various initial phase differences ($\phi_i = \phi_{S_i} - \phi_F = 0^\circ, 90^\circ, 180^\circ, 270^\circ$). After an initial linear phase (up to $t = 80$), where the behavior of the subharmonic and the fundamental is independent of ϕ_i , non-linear effects appear and two different situations are observed:

1. In the first situation (for $\phi_i \neq 0$) the fundamental saturates around $t = 100$ and its kinetic energy only slowly decays thereafter. In this case, the subharmonic pursues its linear growth rate after the saturation of the fundamental until $t = 120$ and keeps growing slowly afterwards.
2. On the contrary, in the second situation (for $\phi_i = 0$) the fundamental starts decaying at $t = 80$ and completely relaminarizes at $t = 140$. In this case the subharmonics also saturates at $t = 80$, decays and only resumes its growth after the kinetic energy of the fundamental has been transferred back to the mean flow.

The effect of the initial phasing is large. At $t = 140$, the kinetic energies of the fundamentals and the subharmonic for $\phi_i = 0$ are more than two order of magnitude higher than the kinetic energies of the fundamentals and the subharmonic for $\phi_i \neq 0$. Interestingly, in the $\phi_i \neq 0$ case, the decay of the fundamental and its subharmonic is followed by a new cycle of growth, saturation and decay. We note that at $t = 250$ the kinetic energies of the fundamentals and the subharmonics are both independent of ϕ_i (fig 4.43).

An explanation for the large ϕ_i effect will now be proposed. We have seen in section 4.3.2 that the vorticity dynamics of the outer modes was dominated by the baroclinic torque. We have also seen in section 4.3.6 how the decay of one developed outer mode was associated with a modification of the mean $\bar{\rho} d\bar{u}/dy$ profile and with the appearance of a positive baroclinic torque in the large ω_z region of this fundamental. In that sense, the large effect of the initial phasing and the cyclic growth, saturation and decay of

the fundamental (similar but stronger than what we observed in section 2.3.5) suggest that the initial phase has strong effects on the baroclinic torque. In particular, we believe that the reduced growth of the fundamental and the subharmonic in the $\phi_i = 0$ case corresponds to a situation of “mutual destruction” where the positive baroclinic torque of the decaying fundamental is located where the subharmonic tries to develop.

Figure 4.44 indicates the influence of ϕ_i on the mixing layer growth. The time history of the momentum and vorticity thickness is shown for the four simulations presented above. Although the overall effect is small, the momentum thickness and vorticity thickness appear to grow faster ($\approx 20\%$ after $t = 80$) for $\phi_i \neq 0$ than for $\phi_i = 0$. This effect would become more obvious if the subharmonic of the subharmonic was also included in the simulation. Note that the phase of the sub-subharmonic would however have to be chosen so that the positive baroclinic torque region of both the fundamental, its subharmonic and the subharmonic of the subharmonic do not overlap. ϕ_i also influences the total reaction rate in the layer which is maximum for $\phi_i = 180$.

If $\phi_i = 180$, the contour plots of the mixture fraction (fig. 4.46) reveals that the growing subharmonic swallows the decaying fundamental in the same colayer (“ gulping ”). We have plotted (fig 4.46) the mixture fraction contours at three instants of the interaction between the fundamental and the subharmonic for the 180° case, where the transfer of energy from the fundamental to the subharmonic is optimal. Pairing, where the subharmonic grows and two of the fundamental structures begin to rotate around each other, is not observed. Instead, the slow fundamental at saturation appears to be swallowed by the growing fundamental (fig. 4.46). This gulping does not destroy the two colayers. Note also, that during the “ gulping ”, the maximum vorticity becomes positive (at $t = 112$, $\omega_{max} = 0.134$). As will be seen in our simulation of the Stanford experiment (section 4.8), this positive vorticity occurs as a counter-rotating vortex is generated below the large-scale structure during the gulping.

4.7.3 Simulation initialized with the fast and slow outer modes and their fast and slow subharmonics

This last 2-D simulation with unity free stream temperature ratio was performed as a model of the compressible reacting mixing layer. The fast and the slow outer modes as well as their subharmonic were present in the initialization. We used $\phi_{Ss} = \phi_{Fs} = 180^\circ$, $A_{Ss} = A_{Sf} = 0.0005$ and $A_{Fs} = A_{Ff} = 0.001$. In this case, we will show that the slow colayer exhibits gulping, while in the fast colayer the fast fundamental and the fast subharmonics have a destructive interaction. Figure 4.47 shows the kinetic energies

of the fundamentals and of the subharmonics versus time. The small oscillations on these curves are caused by the varying relative positions of the fast and slow outer modes as they slide one over the other. Similar oscillations were observed on figure 4.37. We note that the fundamentals develop, saturate and decay at $t \approx 80$. As seen in section 4.7.1 the kinetic energy of the instability modes is minimum at $t = 100$ after the decay of the fundamentals but before the development of the subharmonics. The fast and the slow subharmonics then develop, saturate and decay independently from one another. The slow subharmonic, which has a larger growth rate saturates and decays first at $t = 170$, whereas the fast subharmonic saturates and decays at $t = 300$.

Figure 4.48 shows the contour plots of mixture fraction at four different instants of time. Here, only the vortical region of the computational domain is shown ($y \in [-3, 3]$) but the computational domain extends further ($y \in [-6, 6]$). Here $Da = 6$, $Ze = 2$, and $Re = 4000$. At $t = 80$, four different structures are present in the layer and the fast and slow fundamentals saturate. At $t = 112$, " gulping" is seen in the slow colayer. In the fast colayer the fast fundamental and subharmonics destroy each other. Consequently, at $t = 192$, the development of the slow colayer is more advanced than that of the fast colayer, and the slow subharmonic saturates whereas the fast subharmonic is just starting to develop. In the last picture, at $t = 288$, the thickness of the layer is approximately twice the initial thickness and the layer exhibits the developed fast and slow subharmonics.

Figure 4.49 shows several thicknesses of the layer for the simulation of figure 4.48 initialized with the fast and the slow outer modes and their subharmonic. The vorticity thickness δ_ω , momentum thickness δ_m , temperature thickness δ_T and visual thickness δ_v plotted on figure 4.49 are defined as

$$\delta_\omega = (\bar{u}_1 - \bar{u}_2) / (d\bar{u}/dy)_{max} \quad (4.7)$$

$$\delta_m = \int (\bar{u}_1 - \bar{u})(\bar{u} - \bar{u}_2) dy \quad (4.8)$$

$$\delta_T = \int (T - T_1) dy \quad (4.9)$$

$$\delta_v = (y_a - y_b) \quad (4.10)$$

with $\bar{u}(y_a) = 0.9\bar{u}_1 + 0.1\bar{u}_2$ and $\bar{u}(y_b) = 0.9\bar{u}_2 + 0.1\bar{u}_1$. We also plotted for comparison the vorticity thickness of a laminar (initialized without outer mode) mixing layer having same Re , M_c , Ze , Da , etc. Since the Prandtl number is equal to unity, the temperature thickness and the product thickness are equivalent and constitute (at high Damköhler number) a measure of the extent of molecular mixing. Figure 4.49

shows the effect of the outer modes on the growth rate of the layer measured by these four thicknesses. For comparison the growth rate of the laminar layer having the same Mach number and same Reynolds number is also shown. The results indicate that the growth rate of the layer is almost unaffected by the presence of the 2-D outer modes (less than 10% at time $t = 450$).

Figure 4.50 shows the maximum and minimum pressure (normalized by the free-stream pressure) and the maximum temperature (normalized by the adiabatic flame temperature) in the flow. The small oscillations on these curves are caused by the varying relative positions of the fast and slow outer modes as they slide one over the other. The temperature is maximum at the initialization (where infinite reaction rate and adiabatic flame temperature are assumed). The maximum and minimum pressures increase when the fast and the slow outer mode develop but remain approximately constant after. We note that the increased pressure gradient as the outer modes decay (see figure 4.12) arise from a steepening of the pressure wave at constant p_{max} and p_{min} . $p_{max} \approx 1.06$ and $p_{min} \approx 0.94$ which (for $M_f = 0.29$) agrees well with the familiar stagnation pressure relation,

$$p_s/p_\infty = (1 + \frac{\gamma - 1}{2} M_f^2)^{\gamma/(\gamma-1)}. \quad (4.11)$$

Figure 4.50 shows the maximum and total reaction rates and also exhibits the oscillations due to the changing relative position of the fast and the slow outer modes. Note that, when the fast and the slow subharmonics become the dominant modes, the period of the oscillation doubles.

4.7.4 Conclusion of section 4.7

For incompressible non-reacting mixing layers, the pairing process is a selective mechanism in which a subharmonic of the fundamental is amplified preferentially. Only one large-scale structure naturally dominates the incompressible mixing layer at any downstream distance (time in the simulation). In contrast, the absence of a similar selection mechanism in the compressible reacting case suggests that (1) a larger distribution of instability modes can be present at a given time in the layer, all having different growth rates, with some growing, some saturating and some decaying; (2) the growth mechanism is not through pairing. It may result from the *net* growth rates of all the instability modes present in the layer at a given instant of time.

4.8. Comparison to experiment

In this section, the 2-D simulation of the compressible reacting mixing layer corresponding to the experiment of Miller *et al.* (1992, 1993, thereafter referred to as the Stanford experiment) is presented. The parameters of this simulation are ($\Theta = 0.142$, $M_c = 0.8$, $Re = 1200$, $U_2 = 0.11$, $T_2 = 0.21$) and Ze is set equal to zero. The experiment has the same values of heat release and free-stream temperature ratio but is at a much higher Reynolds number. We note here that simulation with higher Ze would tends to move the flame towards the hot fast stream. The purpose of this simulation was to compare the DNS and linear stability analysis results with some experimental results shown at the end of this section. This simulation can also be viewed as an extreme case with large free-stream temperature ratio and very low heat release. Linear stability analysis suggests that only one of the two outer modes appears in this case (chapter 2).

The 2-D simulation of the Stanford experiment presented in this section indicates the persistence of the two colayers to very low heat release and large free-stream temperature ratio. The chemical reaction is shown to only occurs in the fast colayer, but tongues of hot reacting fluid from the fast stream are seen to penetrate deeply into the slow stream. The PLIF images presented in section 4.8.3. agree suprisingly well with the numerical results and support the existence of the two colayers with chemical reaction only occurring at the inner edge of the fast colayer.

4.8.1 2-D structure from DNS

Figure 4.51 shows the developed slow outer mode corresponding to the lowest heat release case ($\Theta = 0.142$) analysed in section 2.4. In chapter 2 we showed that, for this low heat release and high free-stream temperature ratio ($\bar{T}_1 \gg \bar{T}_2$) case, only one density-weighted vorticity peak is present, which leads to the existence of a unique instability mode. This slow instability mode develops in the slow stream and only mixes fluid from that stream with product. The 2-D structure of the slow outer mode which develops in this case (fig. 4.51) is very similar to the slow outer mode obtained for unity free-stream temperature ratio (fig. 4.15). For example, the high vorticity region shows the same thin elongated shape in the slow stream as the slow outer mode of fig. 4.15. The region of high ω_z is located in the region of high vorticity production and the baroclinic contours are very similar to the vorticity contours. The similitude between the slow colayer of figure 4.15 and the slow colayer figure 4.51 arises from

the independence of the two colayers. Here, the slow colayer between a reaction zone at $\bar{T}_f = 0.8$ and the cold stream at $\bar{T}_2 = 0.21$ is independent of the fast stream temperature (and of the free-stream temperature ratio).

As in the simulation for unity free stream temperature ratio, the reaction rate remains plane with the maximum reaction rate occurring on top of the large-scale structures (fig. 4.51). At this early time, the flame is still located in the middle of the layer, but as already mentioned at higher Ze this flame would be shifted into the fast stream. The density is large into the slow stream and the density weighted vorticity is significantly larger in the slow stream than in the fast stream. Although $M_c = 0.8$, the Mach number of the slow outer mode with respect to the fast stream (and based on the Mach number in this stream) is less than 1 and the system of radiating pressure waves seen on figure 4.16 is not seen here. We nevertheless can notice the slight inclination of the pressure contours.

Figure 4.52 shows the appearance of the mixing layer during the interaction between the slow outer mode and its slow subharmonic ($t = 82$). The small-scale wiggles on the baroclinic and vorticity production contours are a plotting artifact. At $t = 82$, the gulping (presented in section 4.7.2) is observed. The developing subharmonic is seen to swallow the decaying fundamental. At this instant of time, three regions of large vorticity exist in the flow (fig 4.52 b): a top one extending across the whole computational domain which corresponds to the subharmonics and two smaller ones below it, one in the middle of the domain corresponding and the other one inside the large-scale structure at the left of the computational domain.

Compared to the simulation presented on figure 4.46, we note a large increase of the magnitude of the baroclinic term. The existence of a strong positive baroclinic torque below the large-scale structure of the subharmonics creates intense positive ω_z vorticity. This creation of positive vorticity was also present in figure 4.46 but was not as strong. We believe that in the present case higher compressibility effects may explain the increased magnitude of the baroclinic torque and the creation of the positive counter rotating vortices. As seen in section 2.4, at this low heat release the slow outer mode is close to the central mode and the proper correlating parameter is intermediate between M_f and M_c (suggesting obliquity).

Figure 4.53 shows the mixture fraction and pressure contours for the same simulation at $t = 102$ and figure 4.54 shows the mixture fraction contours at two subsequent times, $t = 119$ and $t = 120$. These figures reveal two interesting features.

- First, the existence of shocks in the fast stream is observed. These transient shocks appear during the gulping and arise from the steepening of the weakly inclined pressure waves observed at $t = 50.3$. The mechanism is similar to the one observed during the decay of the slow outer mode (fig 4.12). The transient shocks leave the domain at the top boundary after $t = 102$.
- Second, fluid from the fast stream is entrained inside the slow stream and yields the creation of a tongue of burning fuel. The gulping creates a positive baroclinic torque which produces a counter-rotating vortex at the bottom left of the subharmonic large-scale structure. This counter-rotating vortex interacts with the large-scale structure and entrains fluid from the fast stream into the slow stream. A tongue of burning fuel is created into the slow-stream. At time $t = 130$, this tongue of burning fuel breaks apart and a pocket of fuel is seen in the slow colayer.

At $t = 119$ (fig 4.54), the large-scale structure of the slow instability subharmonic is intermediate between that of an outer mode and that of a central mode: (1) it spans the whole thickness of the layer; (2) it travels at the average speed of the free-stream (it is located at the left of the picture at $t = 130$); (3) it exhibits roll-up; and (4) it partially entrains fluids from both streams as would a central mode. We believe that the modification of the mean $\bar{p} d\bar{u}/dy$ profile may explain this behavior. As seen in section 4.3.6, the modification of the mean profile was shown to stabilize the slow outer mode and to destabilize the central mode, resulting in more oblique instability modes having a longer wavelength and a convective speed closer to the average of the two free-stream speeds. For this low heat release case, the instability mode used in the initialization is intermediate between a central mode and a typical outer mode. The modification of the mean profile in this case yields the development of an instability mode which travels at the average speed of the free-streams. However, we note that the two colayers are to a large extend preserved and that the high-speed side of the layer remains almost undisturbed in comparison with the low-speed side. At later times (fig 4.55 and 4.56), the transient large-scale structure of figure 4.54 left is not present and no large-scale structures are seen in the middle of the layer.

At $t = 130$ (fig 4.54) or $t = 140$ (fig. 4.55), the slow speed side of the layer appears much more disturbed than in the simulation of the compressible reacting mixing layer with equal free-stream temperature and large heat release (fig 4.46). Here, the gulping process between the slow outer mode and its subharmonic (travelling at the average speed of the freestream) has created multiple small-scale structure

in the slow speed side of the layer. Several explanations can be proposed for the absence of such small-scale structures in compressible reacting mixing layer with large heat release: (1) The first and most likely one is that with large heat release, only instability modes close to the outer mode and distinct from the central mode can develop, even after the modification of the mean profile. On the contrary, if the heat release is low, a subharmonic, similar to a central mode, travelling faster than the fundamental can develop. In this case, the interaction between the fundamental and the subharmonic creates small-scale structures. (2) The flame convective Mach numbers are the proper correlating parameter with high heat release. These flame convective Mach numbers are lower ($M_{f1} = M_{f2} = 0.3$) than the usual convective Mach number $M_c = 0.8$, the proper correlating parameter in low heat release compressible reacting mixing layers (chapter 2, especially section 2.4). The pressure gradients seen in the flow are proportional to M_f^2 if outer modes are present and to M_c^2 if central modes are present. Increased compressibility yields higher baroclinic torque, the mechanism for the generation of small scale structures. (3) Viscosity may also play a part in the observed difference between the high heat-release and the low heat-release cases.

At the latter time, the shear layer has a fast stream almost undisturbed and a very convoluted slow colayer with multiple small-scale structures present (fig 4.56). Even for this low Damkhöler number the reaction rate is high, suggesting an efficient turbulent transport of oxidizer in the slow stream by the small scale structures. At $t = 180$, the pressure field exhibits steep gradients in the fast and the slow stream and is clearly less organized than for the slow outer mode having equal free-stream densities (fig 4.16).

4.8.2 Time history and statistics

Figure 4.57 shows the variation of the kinetic energy of various Fourier modes. The top line represents the mean profile. Initially, only the fundamental and the subharmonic have non-zero kinetic energy. The fundamental grows and saturates at $t = 80$ and the subharmonic becomes then the dominant instability mode. Similarly, if the computational domain was larger one could expect the second subharmonic to become dominant around $t = 130$. The pressure waves generated at the ignition leave the domain at $t_c = 6$ ($t = 9$) on the fast speed side of the layer and at $t_c = 14$ ($t = 20$) on the slow speed side of the layer, yielding the two discontinuities seen on the kinetic energy of the Fourier modes with large wavenumber. At the end of the simulation

the turbulent kinetic energy appears distributed among several Fourier modes, indicating the existence of small scale-structures and in agreement with the 2-D contours of figure 4.56. Then the flow possesses a broad band spectrum. We note here the importance of the interaction between modes and subharmonics for the establishment of an enstrophy cascade.

Figure 4.58 shows the total and maximum reaction rates in the flow. Here, the instability modes strongly increase the total reaction and maximum reaction rates, especially around $t = 100$ during the gulping. The reaction rate is maximum at $t = 130$, when the entrainment of fuel into the slow stream increases the flame surface and strains the flame. This confirms that the instability modes which develop in compressible reacting mixing layers with low heat release are intermediate between the slow outer mode of fig. 4.15 (with very little new flame surface created and no large effect on the reaction rate) and the central mode of figure 4.1 (with a strong increase of the total reaction rate due to both an increase in flame surface and an increase of the reaction rate per unit flame surface area (straining effect)). The short-time fluctuations at later times arise from the small-scale structures (figure 4.56) which wrinkle the reaction zone and increase turbulent convection of oxidizer to the reaction zone. The existence of a subharmonic at the later time would keep the total reaction rate high.

4.8.3 Experimental results

The PLIF images presented in this section have been obtained by Miller *et al.* (1992, 1993) at Stanford. The visualization technique for simultaneous imaging of OH radicals and unburnt fuel within a turbulent diffusion flame was developed by Yip *et al.* (1992). The LIF fluorescence from OH radicals indicates the location of the reaction zone while the LIF from acetone molecules seeded into the cold low-speed stream indicates the location of unburnt fuel gases. With this technique, a visualization of an instantaneous slice of the flow is obtained. The technique was used by Miller for the experimental conditions given in table 4.2.

The results we presented in section 4.8.1 are now compared to figures 4.59 to 4.61, where three PLIF images are presented. The first figure (fig. 4.59) gives the location of the reaction zone and compares the location of the average OH emission with the instantaneous PLIF images of OH. The first frame of the first picture shows the time averaged OH emission from the full test section, where the splitter tip is at the left hand edge of the image. The emission indicates that the average flame standoff is

approximately 5 cm. The two bottom images contrast the averaged OH emission and the instantaneous PLIF images, for the section indicated on the top image. Note that the image is located 22 cm downstream of the splitter tip. The relatively flat OH zone is consistent with the colayer model of fig. 2.70.

Table 4.2. Experimental conditions for the PLIF images shown on figures 4.59 to 4.61. Stanford experiment

	Stream 1	stream 2
Total Temperature [K]	1600	270
Mach Number	1.4	0.3
Static temperature [K]	1250	265
Velocity [m/s]	970	110
Molar Composition	$X_{O_2} = 0.23$ $X_{H_2O} = 0.25$ $X_{N_2} = 0.52$	$X_{H_2} = 0.1$ $X_{N_2} = 0.9$
Mass Flowrate [Kg/s]	0.60	0.45

The two upper frames of the second image (fig. 4.60) show the instantaneous acetone (left) and OH (right) PLIF images. The acetone marks the location of the cool unburned fuel and two shades can be seen in the layer, the lighter shade corresponding to the lower free-stream. The boundary between the light and dark areas coincide with the lower edge of the mixing layer. The OH image (right) marks the location of chemical reaction and hot combustion products. The upper edge of the layer coincides with the upper edge of the OH signal. The superimposed images (below) show clearly that the area of OH and acetone do not overlap or intertwine, supporting the idea of the two colayers, a hot colayer where combustion occurs and a cool colayer containing only unburnt fuel. On the top left frame, the dark circular zone at the right of the image suggests the existence of a large slow outer mode in this region.

The last image (fig 4.61) represents four independent pictures of the instantaneous OH and acetone PLIF images taken at different instants of time. In those four images the same evidence of the two colayers is seen with the combustion only occurring in the upper portion of the mixing layer. The remainder of the mixing layer contains only unburnt fluid. We note the existence of pockets of OH burning deep into the slow stream. The bottom edge of the layer shows some evidence of large-scale structures, with smaller scales imbedded (particularly evident on the right bottom frame). Also, the appearance of the layer is seen to vary greatly over time.

4.9. Summary of chapter 4

In this chapter 2-D temporal direct numerical simulations of compressible and incompressible reacting mixing layers were shown. The linear stability analysis results were confirmed. In particular, the following results were presented:

1. The existence of the fast and slow outer modes yields **the existence of two colayers** inside the layer both at low and high convective Mach numbers. These colayers, since observed in experiment, create a two-step mixing process where fluid from each free-stream is first mixed with product and then diffuses to the reaction zone. No direct mixing of fuel and oxidizer is observed and little new flame surface is formed. The outer modes of the compressible reacting mixing layer have less influence on the total reaction rate in the layer than the central mode of the incompressible reacting mixing layer. The persistence of a hot temperature region in the middle of the layer and the low straining exerted by the outer modes on the flame make quenching less likely to occur in compressible than in incompressible reacting mixing layers (at same Da and Ze).
2. The existence of large density and pressure gradients in compressible reacting mixing layer generates **large baroclinic torques** which dominate the vorticity dynamics of the compressible reacting mixing layers. We showed that, (1) for small heat release, the baroclinic torque forces the large-scale structure of the central mode to become more elongated in the x direction and inclined towards the fast stream. At higher heat release, the baroclinic torque was identified as the main cause behind the disappearance of the central mode and the appearance of the outer modes. Second (2), the 2-D vorticity contours of the outer modes are similar to the baroclinic contours. The baroclinic torque was shown to dominate the vorticity dynamics of the outer modes, to prevent their roll-up and to prevent transfer of vorticity from one colayer to the other. (3) Finally, the positive baroclinic torque located between the two fundamental outer modes was proposed as an explanation for the absence of pairing in compressible reacting mixing layers.
3. It was also shown that the outer modes have **short lifetime**: Each outer mode having wavelength L_x develops, saturates and decays in approximately 10 to 20 L_x . The mechanism behind this decay was identified: The outer mode convects hot fluid from the centerline to its associated freestream and thereby modifies the mean density profile, the mean baroclinic profile and the mean density weighted

vorticity profile. This affects the linear stability characteristics of the layer and modifies the position of the high baroclinic torque region, which in turn results in the relaminarization of the mixing layer. It was also shown that an outer mode can relaminarize and then develop again in the same colayer, which suggests that multiple modes having various obliquities, various amplification rates and various wavelengths may develop simultaneously in the layer and that some of these modes can be growing while the others are saturating or decaying.

4. The fast and the slow outer modes develop on their respective sides of the layer without interacting. The straining of the flame zone and the local reaction rate were shown to be maximum when the two outer modes lie one on top of the other. The 2-D simulations also indicate that **the appearance of the layer varies quickly** ($\delta t \approx 30\mu s$ for the Stanford experiment) due to the changing position of the two outer modes with respect to each other. As a consequence, the large-scale structures may be harder to identify in experiments.
5. Pairing, where two fundamental structures start to rotate around each other was not observed. Instead another mechanism of interaction (**gulping**) was suggested by the simulation and shown to preserve the two colayers. Four principal explanations were proposed for the **absence of pairing**: (1) The short lifetime of the outer modes since the outer mode may decay before the subharmonic is large enough to interact, (2) the unequal and varying phase speeds of one mode and of its subharmonics which may prevent phase lock from occurring, (3) the shape of the large-scale structures (since elongated ω_z region may be less inclined to rotate around each other), (4) the baroclinic torque which destroys vorticity in the region between the two fundamental outer modes, where the subharmonic tries to roll-up.

CHAPTER 5

3-D Temporal Direct Numerical Simulation

At this stage of the discussion, the results of the linear stability analysis conducted in Chapter 2 have been confirmed in Chapter 4 and the mechanism of interaction between outer modes and their subharmonics has been discussed. In this chapter, a 3-D temporal direct numerical simulation is used to investigate the topology of the large-scale structures, which is important in terms of its effects on the entrainment of fuel and oxidizer and the subsequent mixing process. Experiments of Clemens (1991) for non-reacting compressible mixing layers suggest an increased three-dimensionality and the existence of large-scale streamwise structures at high M_c . The first objective of this chapter is therefore to address the following question: *Does heat release causes the large structures of the reacting shear layer to remain two-dimensional at high Mach numbers as predicted by linear stability analysis?* The simulation suggests that, after an initial linear growth period during which they are two-dimensional, the large-scale structures tend to become more three-dimensional at the end of their lifetime.

Our second objective is to address the question: *What is the mechanism of the transition to small-scale turbulence and is there an associated increased mixing of the reacting species (mixing transition)?* In incompressible, non-reacting mixing layers, the onset of three-dimensionality and the associated mixing transition are known to occur at $Re > 3000$ and to have large effects on molecular mixing with the effects on other properties of the flow (momentum transport or layer growth) being less pronounced. In this chapter, the 3-D dynamics of vorticity in each colayer and the interaction between the ribs and the 2-D rollers are investigated. It is found that, if the flow is sufficiently three-dimensional, the braids can collapse into discrete round vortices which interact with the large-scale spanwise rollers (translative instability). The simulation indicates the existence of turbulent spots, which spread into the layer. It is shown that the flow first becomes turbulent in each colayer, and that the turbulence then invades the central part of the layer. Despite the absence of roll-up and pairing, the beginning of the mixing transition is shown to occur and to increase the total and maximum reaction rates.

In the present 3-D simulation, eight instability modes were included in the initial field: one fast and one slow outer mode, their subharmonics, one fast and one slow 45° mode and their 45° subharmonics. The amplitudes of the 2-D and 45° fundamentals were 0.002 and the amplitudes of their subharmonics 0.001. The initial phases of the 2-D and 45° fundamentals were chosen equal to 0 and the phases of the 2-D and 45° subharmonics were chosen equal to π . The topology of the flow is sensitive to initial phasing between the 2-D and 45° waves (ϕ_{2D-45}), and one may expect that the non-linear growth rate of the 2-D and oblique modes can be significantly affected by their relative position. For instance, the Chen *et al.* (1989) simulations of the wake indicate that if $\phi_{2D-45} = 0$ the streamwise vorticity is convected in the core, creating wavy rollers, whereas if $\phi_{2D-45} = \pi/2$ (the streamwise vorticity is initially in phase with the pressure maximum) the vortex stretching mechanism causes streamwise vorticity to interact with the large-scale rollers to form closed vortex loops. We did not investigate the effect of the initial phasing on the mechanism of the transition to turbulence, and our simulation (initialized with $\phi_{2D-45} = 0$) exhibits wavy rollers as in the simulation of Chen *et al.* (1989) for $\phi_{2D-45} = 0$.

Our simulation of the compressible reacting mixing layer was partly run on the Cray YMP and partly on the Hypercube. The turbulence spectrum was monitored during the run and the initial $32 \times 192 \times 32$ points used in the simulation were increased to $64 \times 320 \times 128$ points as smaller scales were generated.

In the discussion below, the appearance of the layer is shown at three different instants of the simulation: $t = 70.9$, $t = 105.6$, and $t = 145.3$. The first time ($t = 70.9$) (see figures 5.2 to 5.16) corresponds to the end of the linear range where the fast and slow fundamentals are fully developed but before their decay. The results are very similar to those presented in the previous chapters. In particular, the two colayers remain independent and the large-scale structures appear two-dimensional. The second time ($t = 105.6$) (see figures 5.19 to 5.31) corresponds to the saturation of the outer modes and the onset of turbulence. The large-scale rollers have become slightly oblique and small-scale structures are observed. The third time ($t = 145.3$) (see figures 5.32 to 5.41) shows the existence of thin elongated streamwise vortices inside the layer, superimposed on large-scale outer modes. The maximum and the total reaction rates are strongly increased, but the creation of new flame surface remains small.

Planar cuts in the planes indicated on figure 5.1 are used to investigate the structure of the layer. Planes Y_1 and Y_2 give top views of the layer in two $x-z$ planes. The first

one is located close at the centerline in the hot, reacting portion of the layer and gives useful information about the uniformity of the reaction zone as the layer develops. The second is located in the middle of the slow colayer to show the obliquity of the large-scale structure of the slow outer mode. The planes X_1 and X_2 are two end views of the layer, one located into the braids and the other cutting the large-scale structure of the slow outer mode. Finally, Z_1 , Z_2 and Z_3 are three side views of the layer, one located on the side of the computational domain, the second in the middle of the computation domain and the third one through the braids of the slow outer mode fundamental.

Before discussing in more detail the topology of the large-scale structures and the mixing transition mechanism in compressible reacting mixing layers (sections 5.2 to 5.6), we present for comparison purposes (section 5.1) a brief review of the known results for incompressible non-reacting mixing layers.

5.1. Survey of previous results concerning the transition in incompressible mixing layers

The secondary stability theory of Pierrehumbert and Widnall (1982) constitutes a major contribution to the analysis of the transition to turbulence. In essence, the theory assumes that the mean flow has evolved due to the development of the primary instability and sets up a new eigenvalue problem in which the eigenfunction is dependent upon both the streamwise and normal coordinates. Their base flow consists of a hyperbolic tangent profile with superposed Stuart (1967) vortices. In addition to the subharmonic instability (responsible for pairing), two other instability modes were found: the translative mode (spanwise antisymmetric) and the bulging mode (spanwise symmetric). They both have the same x wavelength (equal to the spacing of the Stuart vortices), but only the translative mode shows appreciable instability. As the translative instability develops, a loop of the Stuart vortex tube is lifted up in the free streams and stretched up. As a result, a wavy pattern is observed on the large-scale spanwise vortices. The tilting of the spanwise vortices yields the formation of pairs of counter-rotating streamwise vortices with regions of upwelling in between. The analysis of Pierrehumbert and Widnall also indicates the possibility of helical pairing as may have been observed in the experiments of Chandrsuda *et al.* (1978).

Corcos and Lin (1984a) investigated the dynamics of streamwise vorticity in the incompressible mixing layer. They showed that (1) streamwise vorticity (ω_x) stops being sustained by the mean flow wherever in the layer the spanwise vorticity (ω_z) disappears. The resulting streamwise vorticity present in the braids after the spanwise vorticity has migrated to the cores is strained without any change in circulation. (2) If the streamwise circulation is small, they showed that streamwise vorticity is found in a continuous layer which has a simple structure between the large spanwise rollers (ω_x lies along the layer and the circulation associated with it does not continue to increase with time) and which is folded within the primary spanwise vortices. (3) Corcos and Lin (1984b) indicated that strained vortex sheets are fundamentally unstable and yield a redistribution of vorticity towards the region of maximum strength by self-induction. Applying this result to the mixing layer, they proposed that, even at low Reynolds numbers, streamwise vortices whose size is the Taylor microscale are far more typical than vortex sheets. If γ_s is the mean rate of strain in the braid region and ν the kinematic viscosity, the collapsed vortices in planar strain were shown to reach, in a time of order γ_s^{-1} , a well-defined structure, that of an axially symmetric Burgers vortex. The strain tends to generate a vorticity layer with thickness $(\nu/\gamma_s)^{1/2}$ but wherever the strength of such layer is substantially larger than $2(\nu\gamma_s)^{1/2}$, the vorticity is caused by self induction to be concentrated into well segregated round vortices whose radius is asymptotically $(\nu/\gamma_s)^{1/2}$. Vorticity is intensified by a factor proportional to $\nu^{-1/2}$. (4) Corcos and Lin also showed that the effect of the streamwise vorticity on the diffusion of a scalar is slight until the layer has collapsed. Elongated vortices whose circulation is insufficient to cause collapse are also incapable of wrapping material surfaces around their center. They only merely distort the interface (of fuel and oxidizer) into an approximately sinusoidal shape with a small increase in diffusion rate. On the other hand, the analysis indicates that if the streamwise vortex sheet concentrates into Burgers' vortices, a material surface which initially coincides with the streamwise vortex sheet is wrapped by the round vortices and the diffusion of the scalar occurs far more rapidly.

Buell and Mansour (1989) investigated the spanwise vorticity topology. Their results revealed the existence of cup-shaped regions of strong spanwise vorticity inside the large-scale rollers. They showed that the vortex lines inside the large-scale vortices become wavy and inclined to the flow direction. The combined effect of the rib vortices and core streamwise vorticity was shown to create alternating (in z) regions

of strong extensional and compressive spanwise strain in the roller between the rib vortices. This strain stretches and compresses the spanwise vorticity in the roller, creating cup-shaped regions of strong ω_z , alternating with regions of nearly zero ω_z . The increased waviness of the large-scale rollers was seen in turn to enhance the streamwise vorticity, and the mechanism is therefore self-sustained.

All simulations presented in Moser and Rogers (1991) are for an initial Reynolds number based on the vorticity thickness and the velocity difference of 500, with no background small-scale velocity fluctuations included in the initialization. The first result of Rogers and Moser is that, as the mixing layer rolls up, the streamwise vorticity sheet present in the braid region is stretched and eventually collapses into thin, nearly elongated vortices if the circulation of the initial three-dimensional streamwise vorticity is strong enough. The criterion of the collapse of streamwise vortices is

$$L = \Gamma^a A^{2p} > 13.1 \quad (5.1)$$

with $\Gamma^a = \Gamma_x / (\gamma_s \lambda_z^2)$, $p = 0.68$ and $A^2 = \gamma_s \lambda_z^2 / \nu$, where λ_z is the spanwise wavelength and Γ_x the initial circulation. The second result from the Roger and Moser simulation is that the transition to turbulence requires two essential ingredients: (1) a sufficiently high Reynolds number or a sufficiently strong set of streamwise rib vortices and (2) a pairing (a result consistent with the observations of Huang and Ho 1990). Pairing was shown to have two effects: first, the ribs between the pairing rollers are engulfed into the large paired roller and second, the cups of strong ω_z are brought together so that they interact directly. At the end of the first or second pairing, the spanwise vorticity presents many small-scale regions of both signs suggesting the onset of turbulence. Rogers and Moser noted that the small-scale structures in the cores appear first in the rib planes of the spanwise rollers.

We will show in this chapter that the transition to turbulence in compressible reacting mixing layers has some similarities with the transition to turbulence in incompressible mixing layers. In particular, we will show that the initial circulation of the streamwise vortices is sufficient (the amplitudes of the oblique modes included in the initialization is large) for the braids to collapse in round Burgers vortices. Adapting the expression for the strain rate proposed by Corcos and Lin ($\gamma_s \approx (3\Delta U)/(2\lambda_x)$) to each of the colayers, we get

$$\begin{aligned} \gamma_{s1} &\approx (3/2) (\bar{u}_1 - \bar{u}_f) / \lambda_x = 0.334 \\ \gamma_{s2} &\approx (3/2) (\bar{u}_f - \bar{u}_2) / \lambda_x = 0.334 \end{aligned} \quad (5.2)$$

where $\lambda_z = \lambda_x = 3.59$, $\nu = 4 \times 10^{-4}$ and $\Gamma_x \approx 0.15$, which yields: $\Gamma^a = 0.034$, $A^2 = 1.07 \times 10^4$ and $L = 19.01$, higher than the 13.1 criteria suggested by (5.1). The initial circulation of the streamwise vorticity and the Reynolds number used in this simulation therefore appear sufficient for the streamwise vortices to collapse, as seen in the end views of the layer at ($t = 145.3$) (see section 5.5.3). As in the case of incompressible mixing layers, the central role of the translatable instability in the transition to turbulence will also be demonstrated.

The simulation also reveals several marked differences between the transition to turbulence in compressible and incompressible mixing layers. Some of these differences, which arise from differences in the dynamics of the spanwise vorticity, are as follows:

- The dynamics of the spanwise vorticity is governed by the vorticity production terms (baroclinic torque), and vortex roll-up does not occur. Some spanwise vorticity (ω_z) remains present in the braids, where it interacts with ω_x . On the contrary, for incompressible mixing layers the spanwise vorticity migrates to the cores and then, the ω_x present in the braids can only be strained without any change in circulation.
- The large baroclinic torques present in the flow affect both the spanwise and the streamwise vorticity. For example, due to the baroclinic torque in the x direction, the braids are wrapped around the outer mode large-scale structures.
- In the compressible reacting mixing layer, the transition to turbulence occurs in the absence of pairing. The existence of the two colayers causes the mixing transition to occur in each colayer independently. Finally, the simulation indicates that gulping may enhance the creation of small-scale structures.

5.2. Pretransition structures at early time

At the end of the linear growth ($t \approx 70$) the two colayers are present and no interaction is observed between the fast and the slow outer modes. The large-scale structures are two-dimensional and the results are similar to those presented in the fourth chapter.

Figure 5.2 shows the vorticity and mixture fraction contours in the plane Z_1 ($z = 3.6$) and Z_2 ($z = 0$) at $t = 70.9$. The flow is from left to right. Here at $t = 70.9$, the fast and slow outer fundamentals are completely developed. The contours plots indicate the presence of the two colayers separated by a hot flame region where reaction occurs. Eddies in the two colayers travel at two very different speeds, and hence the

appearance of the layer changes rapidly. The contours are very similar in the planes Z_1 and Z_2 , indicating that the large-scale structures are two-dimensional at this time. Although the amplitudes of the 2-D and 45° modes are equal at $t = 0$, we note that the 2-D modes have grown significantly faster than the 3-D modes (as predicted by linear stability analysis) and dominate the flow.

In 3-D, the vorticity equation (2.81) becomes (neglecting diffusion)

$$\begin{aligned}\frac{D\omega_x}{Dt} &= -\omega_x \left(\frac{\partial u}{\partial x} + \frac{\partial v}{\partial y} + \frac{\partial w}{\partial z} \right) - \frac{1}{\rho^2} \left(\frac{\partial p}{\partial y} \frac{\partial \rho}{\partial z} - \frac{\partial p}{\partial z} \frac{\partial \rho}{\partial y} \right) + (\omega_x \frac{\partial u}{\partial x} + \omega_y \frac{\partial u}{\partial y} + \omega_z \frac{\partial u}{\partial z}) \\ \frac{D\omega_y}{Dt} &= -\omega_y \left(\frac{\partial u}{\partial x} + \frac{\partial v}{\partial y} + \frac{\partial w}{\partial z} \right) - \frac{1}{\rho^2} \left(\frac{\partial p}{\partial z} \frac{\partial \rho}{\partial x} - \frac{\partial p}{\partial x} \frac{\partial \rho}{\partial z} \right) + (\omega_x \frac{\partial v}{\partial x} + \omega_y \frac{\partial v}{\partial y} + \omega_z \frac{\partial v}{\partial z}) \\ \frac{D\omega_z}{Dt} &= -\omega_z \left(\frac{\partial u}{\partial x} + \frac{\partial v}{\partial y} + \frac{\partial w}{\partial z} \right) - \frac{1}{\rho^2} \left(\frac{\partial p}{\partial x} \frac{\partial \rho}{\partial y} - \frac{\partial p}{\partial y} \frac{\partial \rho}{\partial x} \right) + (\omega_x \frac{\partial w}{\partial x} + \omega_y \frac{\partial w}{\partial y} + \omega_z \frac{\partial w}{\partial z})\end{aligned}\quad (5.3)$$

where the first term on the right is the dilatational term, the second is the baroclinic term and the third is the straining term. Figures 5.2 to 5.11 shows the 2-D contours of these terms for the x -vorticity, y -vorticity and z -vorticity in several planes.

5.2.1. Streamwise vorticity before transition

For compressible reacting mixing layers, the existence of two colayers yields the existence of two system of braids (fig. 5.3a), one in each colayer. As seen in 2-D (section 4.4), the slow outer mode develops faster than the fast outer mode and the braids are stronger in the slow stream than in the fast stream. In the braids, the straining term is the dominant production term of ω_x and we note that the magnitude of ω_x is large (approximately half the magnitude of the ω_z fluctuations of figure 5.8). The contours of ω_x coincide with the contours of ω_x production, indicating that initially, due to the high shear rate in the braid region, ω_x is governed by the production terms and not by the convection terms. The baroclinic torque destroys ω_x at the centerline (top left of the slow outer mode large-scale structure) but enhances ω_x in the braid region and at the top right of the slow outer mode large scale structure. As a result, the streamwise vorticity is wrapped around the top of the slow outer mode (and the bottom of the fast outer mode), a result not seen for incompressible central modes.

Figure 5.4 shows the streamwise components of vorticity and vorticity production in the plane $X_1(x = 0)$ through the slow outer mode large-scale structure. The mean flow is into the page. The x vorticity contours clearly show the two colayers and, in each colayer, the braids connecting to the top and the bottom of the large-scale structures. The braids appear as four juxtaposed counter-rotating flat vortices. The sign of the streamwise vorticity is the same in the braids connecting to the top or the

bottom of a large-scale structure but is opposite inside the large-scale structure. The streamwise vorticity in the large-scale structures is apparently secondary vorticity driven by the strong streamwise vorticity in the braids through viscous coupling, and thus the vorticity has opposite sign in the braids and in the large-scale structures. For example, at the left of figure 5.4 (a) and in the slow colayer, the x vorticity is negative inside the large-scale structure and is positive on top and below it, in the braids. The straining term is larger than the baroclinic terms and, even in the cores of the large-scale structures, dominates the production of ω_x .

Figure 5.5 shows the contours of cross-stream and streamwise vorticity and vorticity production in the plane X_2 ($x = 1.79$) through the slow outer mode braids and the fast outer mode large-scale structure. Here (fig. 5.5), the contours of ω_x are much simpler than in the core (fig. 5.4). The braids in the slow colayer appear as the juxtaposition of four counter-rotating and flat vortices. The straining term (which dominates the production of ω_x), the streamwise vorticity and the streamwise vorticity production are higher in the braids than in the cores. The baroclinic torque on the contrary is smaller in the braids (where the density gradient and pressure gradient are aligned) than in the core.

5.2.2. Cross-stream vorticity before transition

The y vorticity and vorticity production contours in the plane Z_3 (fig. 5.6) also exhibit the two system of braids. At $t = 70.9$, the streamwise and cross-stream vorticity behave similarly. We note that the y vorticity and the x vorticity have the same sign in the braids, and the magnitude of ω_y is about half that of ω_x . The y baroclinic term is small, since the mean density gradients are zero in the x and z directions. We do not observe (as in the streamwise direction) creation of ω_y at the top (bottom) of the slow (fast) outer modes. As a consequence, the contours of ω_y do not overlap with the contours of ω_y production in the plane $X_1(x = 0)$ through the slow outer mode large-scale structure (fig. 5.7).

The y straining term, which is more than one order of magnitude larger than the baroclinic term, dominates the y vorticity production in the braids (fig. 5.6). Like the streamwise vorticity, the cross-stream vorticity in the large-scale structures is driven by the strong cross-stream vorticity in the braids through viscous coupling. As seen in figure 5.6, the vorticity has opposite sign in the braids and in the large-scale structures.

We note that: (1) the cross-stream vorticity is larger in the braids than in the core, (2) the baroclinic term is small and the straining term dominates the cross-stream vorticity production, (3) the straining terms tends to enhance vorticity in the braids whereas the baroclinic term tends to destroy vorticity in the braids.

5.2.3. Spanwise vorticity before transition

In this section, the dynamics of the spanwise vorticity before the transition is investigated. At $t = 70.9$, the spanwise vorticity remains strongly 2-D. However, it is shown that since the outer modes do not roll-up, a large fraction of ω_z remains present in the braids where it interacts with ω_x , yielding increased large-scale rollers and enhanced ω_x in the braids.

Figure 5.8 shows the spanwise vorticity and spanwise vorticity production in the plane $Z_1(z = 3.59)$, located between two counter-rotating streamwise vortices, which exert a compressive spanwise strain rate on the spanwise vorticity. As in the 2-D simulations, the regions of high ω_z appear thin, elongated and are located close to the centerline. They do not cross the centerline. We saw in section 4.3.2 how this strongly elongated shape (to be compared to the tubular shape of the high vorticity region for the central mode) was suggesting a less efficient engulfment of fluid by the outer modes.

In 2-D, the high vorticity region was shown to be located in the large baroclinic torque region, suggesting that the baroclinic torque, and not the convective terms, was controlling the vorticity dynamics. In the current 3-D simulation, at $t = 70.9$, the straining term becomes important. Although, the baroclinic term is still larger than the straining term, the latter starts to modify the contours of spanwise vorticity production. We note that the straining term has opposite signs on top and bottom of the large-scale structures. The straining effect is largest in the region where the braids connect to the large-scale structures. Note that the spanwise vorticity remains large in the braids and that the straining term is non-zero there. This constitutes an essential difference from the dynamics of spanwise vorticity in incompressible mixing layers, where ω_z migrates to the core and therefore does not interact with ω_x in the braids.

Figure 5.9 shows the contours of the spanwise vorticity and spanwise vorticity production terms in the plane X_1 , through the slow outer mode large-scale structure. At $t = 70.9$, the contours of ω_z and of the baroclinic torque exhibit parallel lines due to the quasi two-dimensionality of the large-scale rollers. As in the 2-D simulations,

the baroclinic term is negative inside the large-scale structure where ω_z is created. Note that the baroclinic term and the straining term have comparable magnitudes inside the core but that the straining term is strongly non-uniform in the spanwise direction. The combined effect of the ribs vortices and core spanwise vorticity is to create alternating (in z) regions of strong extensional and compressive spanwise strain in the roller between the rib vortices. At $z = 0$ or $z = 3.59$, the straining term is negative and ω_z is enhanced while at $z = 1.79$ or $z = 5.38$ the straining term is positive and ω_z is destroyed. The existence of alternating region of strong extensional and compressive spanwise strain is not typical of the outer mode and has been observed for the central mode of the incompressible mixing layer by Rogers and Moser (1989) and Buell and Mansour (1989) (section 5.1). It is associated with the translative instability discovered by Pierrehumbert and Widnall (1982). The strong variation of the straining term in the spanwise direction yields the wavy pattern of the spanwise vorticity production seen on figure 5.9 and forecasts an increase in the obliquity of the spanwise rollers at later times.

Figure 5.10 shows the contours of the spanwise vorticity and vorticity production terms in the X_2 plane, through the braids of the slow outer mode. The contours appear as parallel lines, which confirms the strong two-dimensionality of the vorticity and baroclinic terms. As in 2-D, the baroclinic torque in the z direction tends to destroy the spanwise vorticity in the braids. Interestingly, although the straining term is smaller in the braids than in the core, it is non-zero, as previously mentioned, due to the interaction between streamwise and spanwise vorticity. The straining term exhibits the same wavy pattern as in the large-scale structure. We note that in compressible reacting mixing layers (due to the absence of roll-up and contrary to what is observed for incompressible mixing layers) a large fraction of the initial spanwise vorticity remains present in the braids even after the full development of the outer modes. The remaining spanwise vorticity has two effects: (1) first the streamwise and spanwise vorticity in the braids can continue to be fed by the mean flow even after the complete development of the large-scale structures, and (2) the mutual interaction of streamwise and spanwise vorticity in the braids enhances the waviness of the large-scale outer modes and the circulation of the streamwise vortices. The staining term exhibits the same wavy pattern as in the core and tends to counteract the effects of the baroclinic torque. The spanwise vorticity production contours appear two-dimensional in the slow stream.

The contours of ω_z and the ω_z production terms in the plane Y_2 (top view) are shown in figure 5.11. The flow is from left to right. The baroclinic contours are at this early time still strongly two dimensional and strongly negative in the region of high ω_z . The straining term on the other hand exhibits alternating positive and negative contours at the left of the large-scale structure where the braids connect to the central mode. The baroclinic torque is the dominant term at this time and its magnitude is about twice that of the straining term but the alternating positive and negative strain regions yield an s-shaped vorticity production and in turn an s-shaped ω_z . ω_z is maximum at $z = 1.79$ and $z = 5.38$, in the regions of high extensional strain rate. Interestingly, we note that the stronger spanwise vorticity in these regions generates higher strain rates in the x direction, which in turn increases ω_x and ω_z . The magnitude of spanwise baroclinic torque is also increased in the region of high ω_z , which in turn further increases ω_z . The interaction of the spanwise and streamwise vorticity appears to be fundamentally unstable, thereby providing the mechanism for the transition to small-scale turbulence.

5.2.4. Mixture fraction, pressure and reaction rate contours before transition

The pressure contours shown for the full computational domain (fig. 5.12) exhibit a system of radiating Mach waves as seen in the 2-D simulations. We also note the persistence of an undisturbed hot zone between the fast and slow outer modes. This high temperature layer is located in the middle of the layer and is unaffected by the presence of the instability modes; no additional flame surface is created and quenching does not occur. The maximum non-dimensional temperature is $T = 2.92$ (close to the adiabatic flame temperature) and the reaction zone remains flat with very little creation of new flame surface (fig. 5.12). The magnitude of the maximum reaction rate and the thickness of the reaction zone are comparable to their counterparts in figure 4.31 at $t = 64$.

5.2.5. Statistics before transition

The modal energy content at this time of the simulation is shown on figure 5.13. The energy at each wavenumber is defined as

$$E_1(k_x, k_z) = \frac{1}{2} \int_{-Ly}^{+Ly} [|\hat{u}|^2(k_x, y, k_z) + |\hat{v}|^2(k_x, y, k_z) + |\hat{w}|^2(k_x, y, k_z)] dy \quad (5.4)$$

$$E_2(k_x, k_z) = \frac{1}{2} \int_{-Ly}^{+Ly} \bar{\rho} [|\hat{u}|^2(k_x, y, k_z) + |\hat{v}|^2(k_x, y, k_z) + |\hat{w}|^2(k_x, y, k_z)] dy \quad (5.5)$$

where $\hat{u}, \hat{v}, \hat{w}$ are the Fourier transforms in x and z of u, v, w . The top plot (fig. 5.13 (a)) shows a surface plot of the logarithm of E_1 and the second plot (fig. 5.13 (b)) shows the same information when the density is taken into effect (E_2). The two surface plots look similar and at later time only E_1 will be shown. The third plot (fig. 5.13 (c)) shows the contours of iso-kinetic energy (E_1) for all the wavenumbers used in the simulation. At this early time, $64 \times 256 \times 64$ points are used in the calculation but we note that the kinetic energy is concentrated in a few wavenumbers ($k_x < 8$, $k_z < 8$) justifying the number of points used. The iso-kinetic energy lines are circular indicating that the transfer of kinetic energy towards the small-scale is equally efficient in the spanwise and streamwise directions.

The mean Reynolds stress profiles (averaged in each $x - z$ plane) are shown on figure 5.14. At $t = 70.9$, all the Reynolds stresses (except \overline{uu}) are close to zero at the centerline, especially when the Reynolds stresses are multiplied by $\bar{\rho}$ which is minimum at the centerline. The magnitude of the large peak of \overline{uu} at the centerline varies with the relative position of the outer modes. It is minimum when the fast and the slow eddies lie one on top of the other and maximum when the fast and slow eddies are separated by half a wavelength (180° out of phase). The maxima of \overline{vv} and \overline{ww} (located at $y \approx \pm 0.5$) mark the location of the fast and slow eddies and of the associated braid regions in each colayer. We note the existence of two peaks of $-\overline{uv}$, approximately located at $y = \pm 0.3$ at the mean density weighted vorticity peak and in the region of large ω_z . Each of these maximum is associated with the transfer of kinetic energy from the mean flow to one of the outer modes.

Figure 5.15 (top) shows the turbulent transport terms of fuel and oxidizer, which also varies with the relative position of the outer modes. We note that \overline{vo} and \overline{vf} are both zero at the centerline. They do not overlap and therefore do not contribute significantly to the transport of reactants inside the reaction zone. At this early time, \overline{vo} and \overline{vf} are small due to the weakness of the streamwise vortices. The second plot (fig. 5.15 bottom) shows the second order correlation of fuel and oxidizer (\overline{of}) and the passive scalar root-mean square (\overline{zz}). In the present simulation, the chemistry is fast and \overline{of} is small (compared to \overline{zz}). \overline{zz} has two maxima, one in each colayer, and is minimum at the centerline since each outer mode mixes only product with fluid from its associated free stream with no direct mixing of fuel and oxidizer. The reaction zone is at this early time a laminar strained flame with no flame wrinkling and no turbulent transport of fuel and oxidizer inside the reaction zone.

We define the rates of production and dissipation of turbulent kinetic energy as

$$P = -\bar{\rho} \bar{u}\bar{v} d\bar{u}/dy \quad (5.6)$$

$$D = -\bar{\rho} \mu (\bar{\omega}_x \bar{\omega}_x + \bar{\omega}_y \bar{\omega}_y + \bar{\omega}_z \bar{\omega}_z)/Re. \quad (5.7)$$

Figure 5.16 (top) shows the rate of production, magnitude and rate of dissipation of kinetic energy inside the layer at $t=70.9$. The production is maximum at the two peaks of density-weighted vorticity where $\bar{u}\bar{v}$ is large, and is nearly zero at the centerline. The production is also larger in the slow stream than in the fast stream. At this early time (with only large-scale structures present) and at this high Reynolds number, the dissipation is very small. The turbulent kinetic energy (the trace of the Reynolds stress tensor) is larger in the slow colayer than in the fast colayer since the slow outer mode develops faster.

The three components of enstrophy are shown on figure 5.16 (bottom). We note that at this early time the z-component of enstrophy is one order of magnitude larger than the two other components of enstrophy. The enstrophy is minimum in the middle of the layer and maximum inside the two colayers.

5.2.6. Conclusion

At this early time, the dynamics of the streamwise and spanwise vorticity in the colayers is different from what is observed for the central mode of the incompressible non-reacting mixing layer. We note four main differences likely to have important effects in the transition to turbulence. (1) Roll-up does not occur in the compressible reacting mixing layer. The spanwise vorticity dynamics is governed by the production terms (baroclinic torque) and not by the convection terms. As a result, roll-up is not seen and only a fraction of the spanwise vorticity is convected to the vortex cores. (2) The large fraction of the initial spanwise vorticity remaining in the braids (even when the outer modes are fully developed) interacts with ω_x , and the streamwise vorticity continues to be fed by the mean flow. We recall that Corcos and Lin (1984a) showed the opposite for the central mode, where the migration of spanwise vorticity in the cores results in the streamwise vorticity only increasing as a result of the strain of the base flow but without change in circulation. (3) The spanwise vorticity remaining in the braids is strained and enhanced by the energetic streamwise vorticity between large-scale structures. (4) The large baroclinic torques generated by compressibility and heat release are seen to affect the dynamics of both the streamwise and spanwise vorticity.

5.3. Transition to turbulence

The four differences noted above yield a transition mechanism different in the compressible case from that in the incompressible case. We will see in this section that the transition to turbulence occurs in each colayer independently, and that the small-scale structures do not initially invade the central part of the layer. The transition is seen to occur without pairing (although the interaction of the outer modes with their subharmonics (gulping) is seen to enhance the production of small-scale structures), and to increase the total and maximum reaction rates. This transition is preceded by the rapid growth of streamwise vortices (spectral modes $(0, 2)$ and $(0, 1)$) generated by the interaction of growing 2-D modes $((2, 0)$ or $(1, 0)$) and growing 45° modes $((2, 2)$ or $(1, 1)$) (Craik type resonances 1971). Here we used the notation (k_x, k_z) to designate the spectral modes. Figure 5.17 shows the variation of the logarithm of kinetic energy of various instability modes versus time. Among all the eigenmodes (modes $(1, 0), (1, 1), (2, 0), (2, 2)$) used in the simulation, the fastest growing ones are initially the 2-D modes, and (as seen in the previous section) at $t = 70.9$, the flow appears dominated by four strong spanwise vortices, two on each side of the layer. Two non-interacting colayers, travelling at different velocities and separated by the hot flame region, are present.

The oblique eigenmodes $((1, 1)$ and $(2, 2)$ modes), though less amplified than the 2-D modes, are also amplified and might eventually catch up with 2-D modes when the latter saturate or decay as seen in figure 5.17. The transition to turbulence is caused by the interaction of the growing streamwise vortices (braids) with the large-scale spanwise structures as in incompressible mixing layers (Rogers and Moser, 1989). The mechanism is sketched in figure 5.18. The end view of the layer (fig. 5.18 top) shows the two colayers separated by the hot reaction zone. The transition to turbulence occurs in each of the two colayers and does not destroy the colayers. A pair of counter-rotating vortices exerts a large straining on the spanwise vortex (enhancing ω_z) and moves a large segment of the spanwise vortex upward into a region of higher mean velocity. This central segment travels faster than the remaining spanwise vortex, and the spanwise vortex becomes wavy in the $x - z$ plane and $x - y$ plane (fig. 5.18). Intense x and y vorticity are generated in the region connecting the two parts of the initial spanwise vortex, which in turn increases the waviness of the spanwise vortex. The configuration of the braids and the 2-D rollers is thereby intrinsically unstable.

Figure 5.19 shows the contours of the mixture fraction and of the reaction rate in two planes at $t = 105.6$. At this time, the slow subharmonic is developing and starts to dominate the slow colayer. In the slow colayer, gulping starts to occur. Due to the non-constant straining in the z direction, the large-scale structures start losing their two-dimensionality in the two colayers. The two colayers remain present and the reaction zone remains flat with little creation of new flame surface. As at the earlier time, the reaction rate is maximum where the two braid regions are closest together.

5.3.1. Streamwise and cross-stream vorticity during transition

In this section, the collapse of the braids into a set of discrete streamwise vortices is presented. The driving role of the straining term in the collapse is confirmed. It is shown that the baroclinic torque tends to prevent the collapse, and the existence of discrete turbulent spots which spread into the layer is revealed.

The streamwise vorticity and streamwise vorticity production terms in the plane Z_2 ($z = 0$) are shown on figure 5.20. The presence of the two braids system is confirmed and the contour plots indicate the strong development of ω_x , which is now approximately four times stronger than at $t = 70.9$ (fig. 5.3). The straining term has increased in the same proportion, but the baroclinic term has increased even faster and has become comparable to the straining term. The streamwise vorticity is large in the high straining region and its contours are similar to the streamwise vorticity-production contours. As at the earlier time, the baroclinic torque generates ω_x at the bottom (or top) of the slow (or fast) outer modes but destroys ω_x at the centerline.

The end view of the ω_x contours in the plane X_1 ($x = 0$) through the fast-mode large-scale structure is shown in figure 5.21. The simulation reveals the beginning of the collapse of the flat streamwise vortices into round Burgers vortices under the action of the strain field. We note that the straining-term contours are more cylindrical than the streamwise vorticity contours, whereas the baroclinic torque contours are still very flat, elongated and parallel to the hot reaction zone. The collapse of the braid regions into well-defined streamwise vortices appears favored by the straining term (positive effect) but prevented by the baroclinic term (negative effect). We note that, with the collapse of the braids, the simple structure observed at $t = 70.9$ (flat juxtaposed and counter-rotating braids connecting to the top and the bottom of the large-scale spanwise rollers) disappears.

The cross-stream vorticity (in the plane Z_2 ($z = 0$), fig. 5.22) has developed proportionally to the streamwise vorticity and has grown fourfold when compared with figure 5.6. The straining term remains the dominant ω_y production term. We note the small size and irregular shape of the y -baroclinic torque especially, in the region where the gulping is occurring ($x \approx 3$ in the slow colayer).

The cross-stream vorticity in the plane X_1 ($x = 0$) (fig. 5.23) indicates the existence of two regions of higher activity at $z \approx 4$ and $z \approx 7.2$. In those two regions, several counter-rotating quasi-circular streamwise vortices are observed. These small-scale structures do not completely overlap with the vorticity productions contours, thereby indicating that the convection terms are becoming more important in the dynamics of the cross-stream vorticity.

5.3.2. Spanwise vorticity during transition

Figure 5.24 shows the dynamics of spanwise vorticity in the plane Z_2 ($z = 0$). We note that, due to the development of energetic streamwise vortices, the magnitude of the straining term is now larger than the magnitude of the baroclinic term. The baroclinic term is large below the large-scale gulping fundamental as observed in the 2-D simulation presented in chapter 4 (section 4.7 and 4.8). The straining is also large in the region of the gulping where the spanwise fundamentals strongly interact with the gulping subharmonics. Gulping is therefore seen to enhance the creation of small-scale structures (although no roll-up is seen), and therefore in the transition to turbulence of compressible reacting mixing layers gulping may play a similar role to pairing in incompressible mixing layers. In the plane Z_2 , the straining term and the baroclinic torque have opposite sign. However, one should note that the sign of the baroclinic torque and the sign of the straining term are independent.

The spanwise vorticity contours in the plane X_1 through the slow outer mode large-scale structure (fig. 5.25) confirm the loss of the two-dimensionality. We note (fig. 5.25 a) that the spanwise vortex has split in several segments having distinct y positions. The straining term (yielding three-dimensional large-scale structures) now dominates the baroclinic term (yielding two-dimensional large-scale structures). The straining term is large and negative in the regions where the spanwise vorticity is large and located close to the centerline. The baroclinic remains strongly 2-D, except in the region of intense activity around $z = 4$ where multiple small-scale structures of cross-stream vorticity are observed. In this region, juxtaposed contours of positive and negative region of z-straining are observed.

5.3.3. Statistics during transition

The modal energy content at this time indicates a much wider spectrum (fig. 5.26). Here at $t = 105.6$, turbulent kinetic energy is present (larger than 10^{-10} for all $k_x < 16$ and $-32 < k_z < 32$). The energy cascade appears faster in the spanwise than in the streamwise direction, an observation which will become more obvious at later time. This observation is consistent with the previous end and side views of the layer indicating the development of small-scale streamwise vortices. As the high spanwise wavenumbers gain energy, the number of points in the z -direction was increased from 64 to 128 at $t \approx 110$.

At $t = 105.6$, the amplitude of the Reynolds stress (fig. 5.27) has approximately doubled when compared with $t = 70.9$ (fig. 5.14). The shape of the profiles has also significantly changed. Note the large change of $\bar{u}u$ profile, which now has two peaks, one in each colayer, and a local minimum at the centerline. We believe that the variation of the relative positions of the fast and slow outer mode at least partially accounts for the modification of the $\bar{u}u$ profile. At this time, $\bar{u}u$ remains the dominant term, but the other normal stresses have clearly developed and $\bar{v}v$ and $\bar{w}w$ are now 30% of $\bar{u}u$. This observation, and the comparable magnitudes of $\bar{v}v$ and $\bar{w}w$, suggest some redistribution of turbulent kinetic energy from the large-scale spanwise structures to the streamwise vortices. All the Reynolds stresses remain minimum in the central part of the layer, but the minimum is less pronounced than at earlier times. We also note the emergence of $\bar{u}w$ and $\bar{v}w$ when the streamwise vortices develop.

Figure 5.28 shows the turbulent transport of fuel and oxidizer at $t = 105.6$ and should be compared with figure 5.15, showing the same information at $t = 70.9$. We note that the turbulent transport of fuel and oxidizer to the centerline ($\bar{v}o$ and $\bar{v}f$) remain small and do not overlap at the centerline. The second plot of the figure 5.28 shows the second order correlation of fuel and oxidizer ($\bar{o}f$) and the mixture fraction root mean square. Note that $\bar{o}f$ is still very small, but has increased as compared with earlier time, which suggests an increase mixing of fuel and oxidizer and a lower turbulent Damkhöler number. The development of small-scale structures in each colayer is responsible for increased turbulent convection of fuel and oxidizer to the flame and for wrinkling the reaction zone in the spanwise direction. We still observe two zones of mixing, one in each colayer, but these zones are wider and the local minimum at the centerline is less pronounced than at earlier time. Mixing still occurs primarily between fuel and product on one side of the layer and between oxidizer and product

on the other side.

The magnitude of turbulent kinetic energy, shown on figure 5.29, has increased four-fold since $t = 70.9$. We note that the turbulent kinetic energy profile is large and similar to the turbulent kinetic energy production profile at previous times. Here, the turbulent production profile becomes more uniform and the turbulent kinetic energy peaks shift towards the centerline. At this time, the dissipation is still very small. We also note the development of the x and y enstrophy components as turbulence develops. $\overline{\omega_x \omega_z}$ and $\overline{\omega_y \omega_z}$ are now comparable. Also, $\overline{\omega_x \omega_x}$ and $\overline{\omega_y \omega_y}$ are large into the two peaks while $\overline{\omega_z \omega_z}$ which initially had two peaks become more uniform. We also note that the slow speed side of the layer develops faster than the fast speed side giving a skewed profile.

We have plotted the integral scale, the Kolmogorov scale and the Taylor microscale at this time of the simulation. These three quantities, defined respectively as

$$L_{int}(y) = \frac{(u^2 + v^2 + w^2)^{3/2}}{\nu(\overline{\omega_x \omega_x} + \overline{\omega_y \omega_y} + \overline{\omega_z \omega_z})} \quad (5.8)$$

$$\lambda(y) = \left(\frac{u^2 + v^2 + w^2}{\overline{\omega_x \omega_x} + \overline{\omega_y \omega_y} + \overline{\omega_z \omega_z}} \right)^{1/2} \quad (5.9)$$

$$\eta = \left(\frac{\nu^2}{\overline{\omega_x \omega_x} + \overline{\omega_y \omega_y} + \overline{\omega_z \omega_z}} \right)^{1/4}, \quad (5.10)$$

are plotted on figure 5.30. The right plot shows these quantities when the viscosity of the free stream is used, while the plot on the left shows the same information when an average viscosity (calculated using the mean temperature in each $x-z$ plane) is used at each location. Taking into account the mean temperature variation across the layer yields an increase of the Kolmogorov scale and a reduction of the integral scale. We didn't plot the variation of the turbulence length scales in the free streams where these quantities become large. The integral scale is of the order of the large-scale structure wavelength ($L_x = 7.20$), and the integral scale is approximately 0.5. We note that the Kolmogorov scale calculated using (5.10) is comparable to the smallest scale resolvable on our mesh.

Figure 5.31 shows the marching PDF of the mixture fraction. Seven slices were considered, and for each of them the PDF of the mixture fraction was computed. We note a narrow PDF at each location and the absence of oxidizer (or fuel) in the fast (or slow) stream. Furthermore, the mixing of fuel and oxidizer is poor and limited to the central part of the layer (only at the centerline does the PDF extend both in the fuel and the oxidizer). The PDF in the middle of the layer ($y = 0$) has a longer

tail in the oxidizer than in the fuel and peaks at $Z = 0.4$. This indicates that the entrainment of oxidizer by the slow outer mode is more efficient than the entrainment of fuel by the fast outer mode. It is consistent with the slow outer mode having a larger amplification rate than its fast counterpart. The PDF of mixture fraction in the compressible non-reacting mixing layer ($M_c = 0.6$) obtained by Clemens (1991) using PLIF images also indicates (1) a thin and higher PDF at each location and (2) a PDF at the centerline which is skewed towards $Z = 0$ and which peaks at $Z = 0.4$, thereby indicating a greater entrainment of fluid from the slow stream than from the fast stream.

5.4 Final time

At this later time, the compressible reacting mixing layer exists as two colayers surrounding a flat reaction zone, with large-scale three-dimensional outer modes present in each colayer with superimposed small-scale streamwise vortices. In the middle of the layer, the temperature remains large, but regions of large scalar dissipation are observed. These regions are separated by streaks of relatively unmixed fluid from both the high speed side and the slow speed side. The reaction rate is maximum in the region of large passive scalar gradients and is small in the streaks.

5.4.1. Mixture fraction and reaction rate contours after transition

The contours of mixture fraction, temperature and reaction rate after transition are presented in this section. The main effect of the transition is the increased wrinkling of the reaction zone by energetic small-scale streamwise vortices. We also observe the existence of streaks of unmixed fluid from either side of the layer, separated by regions of large mixture fraction gradients where the reaction rate is maximum.

The side views of the layer in the planes Z_1 ($z = 0$) and Z_2 ($z = 3.59$) show that the large-scale outer modes have lost their two-dimensionality due to the strongly non-uniform straining in the spanwise direction (fig. 5.32). For example, the large-scale structure of the fast outer mode is located at the left of the domain in Z_1 and at the right of the domain in Z_2 . Note that gulping is occurring in the slow stream, where the large-scale subharmonic is swallowing the decaying fundamental. The mixture fraction contours of figure 5.32 appear very similar to those of figure 4.48 and 4.49. The temperature contours show the large temperature region in the middle of the layer and the persistence of the two colayers. Note also that the maximum temperature has

decreased with the increase of turbulent diffusion to the centerline (lower turbulent Damköhler number). The reaction zone remains plane, with little creation of new flame surface, and the maximum reaction rate is increased compared to earlier times. The end views of the mixture fraction and reaction rate are shown on figure 5.33 in the plane $x = 0$ and $x = 3.6$ (through the slow outer mode large-scale structure). Here the flow is out of the page. The existence of strong streamwise vortices yields a more convoluted interface of fuel and oxidizer and larger reactions rates. Some creation of new flame surface is observed and the reaction exhibit large fluctuation in the spanwise direction, between regions of high and low scalar dissipation. We note that the fast and slow edge of the mixing layer are also disturbed by the small-scale streamwise vorticity. Clemens (1991) end-views Mie-scattering images for the compressible mixing layer ($M_c = 0.6$) indicate an increase in streamwise organization with compressibility and show highly convoluted regions of mixed fluid on the scale of the large lumps of mixed fluid seen in the side views images. The small-scale streamwise vortices present on figure 5.40 may be responsible for these convolutions, with the large-scale structures remaining primarily spanwise oriented.

The bottom view of the mixture fraction and reaction rate contours inside the layer are shown on figure 5.34 in two planes, the plane Y_2 ($y = -0.4$ through the slow outer mode large-scale structure and the plane Y_1 ($y = 0^-$) located at the centerline. The flow is moving from left to right. The mixture fraction contours at the centerline layer reveal the existence of region of large scalar dissipation (parallel to the mean flow) separated by streaks of relatively unmixed fluid from each of the free streams. The existence of this large mixture fraction gradient yields an increase of the chemical reaction and at $t = 145.3$, the maximum reaction rate is approximately twice higher than at earlier time. In the plane cut through the large-scale structure, the region of high scalar dissipation are either spanwise oriented (cut through the braids of the outer modes) or streamwise oriented and caused by smaller scale streamwise vortices. We note that, despite the increased turbulent mixing, the chemical reaction remains restricted to the central part of the layer.

5.4.2. Streamwise and cross-stream vorticity after transition

The streamwise vorticity and streamwise vorticity production in the plane Z_1 and Z_2 are shown in figure 5.35. The contours plots on the x-y plane show little evidence of circular contours, except in the core of the spanwise large-scale rollers. This confirms the dominantly streamwise orientation of the small-scale structures. The smaller

and more circular contours of the streamwise vorticity and vorticity production in the core at the time of the gulping suggest that the gulping process may play a similar part in the transition to turbulence for compressible mixing layer as pairing for incompressible mixing layers. By wrapping streamwise vortices, gulping enhances the mutual straining of ω_x and ω_z . However, we note that the absence of roll-up in the compressible case may delay the transition.

The streamwise vorticity in the plane through the slow outer mode large-scale structure ($x = 3.2$) is shown on figure 5.36. We note the presence of multiple small-scale counter-rotating structures. The contours are more circular than at earlier time, and the typical radius of the small-scale structures is approximately 0.3. The convolution of the fast and slow edges of the layer is caused with pairs of counter-rotating streamwise vortices. The contours of the straining and baroclinic term exhibit small-scale structures and the baroclinic has lost its predominantly streamwise orientation. The straining term is still larger than the baroclinic term, but the region of large baroclinic torque or straining appears more and more discrete.

The same observations applies to the cross-stream vorticity as seen in figure 5.37. Compared to earlier times, the streamwise and cross-stream vorticity contours ceased to be correlated, and regions of high positive streamwise vorticity are now associated both with high positive and negative cross-stream vorticity.

5.4.3. Spanwise vorticity after transition

After transition, the large-scale structures have lost their two-dimensionality. The contours suggest that the loss of two-dimensionality is due to the straining term and that the baroclinic torque instead tends to conserve the two-dimensionality of the large-scale structures. In that sense, the linear stability analysis predicts the correct trend, and heat release (which increases the baroclinic torque but does not affect the straining term) causes the large structures of the reacting shear layer to remain two-dimensional at high Mach numbers. However, the large amplitude of the straining term observed after transition suggest that the heat release required for the large-scale rollers to remain two-dimensional may be higher than the linear stability prediction.

The spanwise vorticity and vorticity production contours are shown on figure 5.38, in the plane X_2 through the gulping slow outer mode eddy. We note that the baroclinic torque contours tends to have larger scales and to be more parallel to the centerline than the straining term contours, where circular small-scale structures are more

typical. This suggests that the baroclinic term will enhance two-dimensional and spanwise oriented large-scale structures. In that sense, the obliquity of the large-scale structures seems to result from the balance of the baroclinic term, which enhances two-dimensionality (contours parallel to the centerline), and the straining term, which tends to destroy two-dimensionality. As suggested by the linear stability analysis, an increase of heat release which proportionaly increases the baroclinic term will tend to make the large-scale structures more two-dimensional. At $t = 145.3$, the straining term is approximately 6 times larger than the baroclinic term.

5.4.4. Statistics after transition

We present in this section some statistics at $t = 145.3$, when the growing fast and slow subharmonics become the dominant modes. The statistics presented here are not self-similar. The statistics obtained after the complete development of the outer subharmonics and in the presence of the subharmonics of the outer subharmonics would be different. Finally, these statistics (especially the Reynolds stress components (\bar{uu} and \bar{vw}) and turbulent transport terms (\bar{vf} and \bar{vo}) depend on the relative phase of the fast and slow outer modes. Accumulating reliable statistics would require to average on a large enough sample of the largest structures for simulations initialized with various phases and amplitudes of the instability modes, and this is beyond the reach of the present computations. The statistics presented here (and obtained by averaging over the computational domain) can however give some useful information regarding the dynamics and the kinetic energy of the small-scale structures.

The modal energy content at this time (shown on figure 5.39) confirms the earlier observation that turbulent kinetic energy cascade is faster in the spanwise Fourier modes than in the streamwise Fourier modes. The iso-kinetic energy are elliptic in the wavenumber space which is consistent with the plane cuts showing the development of small-scale streamwise vortices. At $t = 145.3$, turbulent kinetic energy is present (larger than 10^{-10}) for all $k_x < 24$ and $-64 < k_z < 64$.

At this time (fig. 5.40), the amplitudes of the Reynolds stresses (and the magnitude of the turbulent kinetic energy) are approximately one order of magnitude larger than at the previous time ($t = 105.6$). The shape of the profiles has also significantly changed due to the varying positions of the fast and slow outer modes. $(\bar{uu})^{0.5}/(\bar{u}_1 - \bar{u}_2) \approx 0.1$ at this time and \bar{uu} is the larger of the normal stresses. \bar{ww} has increased faster than the other normal stresses and is now 30% of \bar{uu} , confirming the redistribution of the turbulent kinetic energy from the large-scale structures to the streamwise vortices.

We note that \overline{ww} , which is likely to be less affected by the relative positions of the two outer modes, has two peaks, one in each colayer, as at earlier time. \overline{uw} and \overline{vw} remain small as expected from symmetry.

The enstrophy components $\overline{\omega_x \omega_x}$, $\overline{\omega_y \omega_y}$ and $\overline{\omega_z \omega_z}$ shown on figure 5.40 have all comparable magnitudes. At this time, the dissipation is still very small. We also note the development of the x and y enstrophy components as turbulence develop. As shown on figure 5.32, the development of the slow outer mode is more advanced than the development of the fast outer mode, and the three enstrophy components are larger in the slow colayer than in the fast colayer. Compared to the previous time, $\overline{\omega_x \omega_x}$, $\overline{\omega_y \omega_y}$ and $\overline{\omega_z \omega_z}$ are almost an order of magnitude larger in the slow stream. The gulping process occurring in the fast stream yields this strong increase of the enstrophy components as kinetic energy from the large-scale structures is transferred to the small-scale structures. In the fast colayer where no gulping has occurred, a local maximum can be observed around $y = 0.6$ on the $\overline{\omega_x \omega_x}$ and $\overline{\omega_z \omega_z}$ curve. We note the limited increase of $\overline{\omega_x \omega_x}$ compared to earlier time but a larger increase of $\overline{\omega_z \omega_z}$ when the fast outer mode develop. The enstrophy-containing eddies are the small-scale eddies, and the cascade to small-scale turbulence makes the enstrophy components independent of the large-scale structures. The relative position of the large-scale structure is therefore not likely to affect the x -averaged profiles of the enstrophy components.

Figure 5.41 shows the turbulent transport of fuel and oxidizer at $t = 145.3$ and should be compared to figure 5.15, showing the same information at $t = 70.9$. We note that the turbulent transports of fuel and oxidizer to the centerline (\overline{wo} and \overline{vf}) have significantly increased and now overlap at the centerline. \overline{wo} and \overline{vf} exhibits symmetric profiles in the fast and in the slow stream. The large maxima of \overline{wo} and \overline{vf} depends from the relative position of the fast and slow outer modes. The second plot of the figure 5.41 shows the second order correlation of fuel and oxidizer and the mixture fraction r.m.s. \overline{of} is still small but has increased compared to earlier time, as the chemistry gets slower. The development of small-scale structures in each colayers are responsible for an increase turbulent convection of fuel and oxidizer to the flame and for the wrinkling of the reaction zone in the spanwise direction.

5.5. Influence of the mixing transition on the temperature and reaction rates

In this last section, the influence of the mixing transition on the reaction rate and maximum temperature inside the layer is studied. It is shown that the mixing transition, which decreases the convection time and the turbulent Damkhöler number, yields increased reaction rate and reduces the flame temperature.

Figure 5.42 (top) shows the mean temperature profiles inside the layer at three instants of the simulations ($t = 70.9$, $t = 105.6$ and $t = 145.3$). At the two earlier times, the two temperature profiles are similar and present the triangular shape seen in the 2-D simulations of chapter 4 (fig. 4.21). The mean temperature profiles have the same maximum, located in the middle of the layer and close to the adiabatic flame temperature. The slow outer mode developing faster than the fast outer mode which results in a slightly non-symmetric profile. On the contrary, at $t = 145.3$, the mixing transition yields a new temperature profile with a maximum different from the adiabatic flame temperature. The drop of the flame temperature indicates that the increased diffusion due to the presence of the small-scale structure lower the turbulent Damkhöler number. The chemistry cannot keep up with diffusion and the temperature is reduced.

Figure 5.42 (bottom) shows the mean (x-averaged and noted “av” on fig. 5.42) reaction rate and the reaction rate root mean square (root mean square noted “rm” on fig. 5.42) at the $t = 70.9$, $t = 105.6$ and $t = 145.3$. Initially ($t = 70.9$) and as in the 2-D simulation, the width of the reaction rate is small compared to the width of the layer. The variation of the reaction rate along x depends on the relative position of the outer modes but remains small (10-15% at $t = 70.9$). At $t = 105.6$, the mean reaction rate increases as the relative position of the fast and slow outer modes with respect to each other varies. The variation of the reaction rate along x are large as seen in 2-D (section 4.37). We note however, that the width of the reaction rate profile is unchanged. At the later time, the mixing transition has occurred and the appearance of the reaction rate profile is strongly modified. We note a much larger width, and the reaction rate fluctuations become larger than the mean. After the mixing transition, the reaction zone becomes wrinkled under the action of energetic streamwise vortices (fig. 5.33), and the reaction rate becomes maximum in the region of large mixture fraction gradients.

The time variation of the maximum temperature (fig. 5.43), the maximum and total reaction rates, also indicates the mixing transition. We note that the temperature is almost constant until $t = 110$ but sharply drops after, when the chemical time becomes

small compared to the turbulent convection time. The maximum and total reaction rates increase due to the mixing transition, and at $t = 145$ (fig. 5.43), the maximum reaction rate is approximately 4 times higher than its 2-D counterpart at the same time (fig. 4.50).

5.6. Summary of Chapter 5

In this chapter, the results from the 3-D temporal direct numerical simulation of a compressible reacting mixing layer have been presented. The topology of the large-scale structures (2-D or 3-D, outer modes preserved or not, etc) has been addressed. The mechanism of the transition to turbulence in compressible reacting mixing layers and the influence of the small-scale turbulence on the two colayers have been studied. The dynamics of vorticity for the outer mode has been compared to the dynamics of vorticity for the central mode and the following results were shown:

1. The initial development of the layer confirms the 2-D results of chapter 4. The 2-D modes are the dominant instability modes and develop faster than the 45° modes. The two colayers are independent, the reaction zone remains flat with little creation of new flame surface. The outer modes do not roll-up and are governed by the baroclinic torque. The interaction of 2-D and 45° modes generates streamwise vortices. **Two systems of braids are present, one in each colayer.**
2. The strained braid regions are fundamentally unstable and at sufficient Reynolds number yield a redistribution of vorticity towards the region of maximum strength. For the Reynolds number used in the simulation they collapse into Burgers vortices. The discrete **streamwise vortices** exert alternative compressive and extensional strain rate on the large-scale rollers (**translative instability**). As the translative instability develops, a loop of the large-scale rollers is lifted up in the free streams and stretched up, creating wavy large-scale spanwise vortices.
3. The dynamics of the streamwise and spanwise vorticity in the colayers is different from what is observed for the central mode of the incompressible non-reacting mixing layer. (1) Due to the absence of roll-up, only a fraction of the spanwise vorticity is convected to the cores. (2) A large fraction of the initial spanwise vorticity remain present in the braids and enhances the streamwise vorticity. (3) Simultaneously, the spanwise vorticity remaining in the braids is strained and enhanced by the streamwise vorticity between large-scale structures. (4) Finally, the large

baroclinic torques generated by compressibility and heat release were seen to affect both the dynamics of the streamwise and spanwise vorticity.

4. The simulation indicates the emergence of streamwise vortices and the existence of turbulent spot which spreads into the layer. The interaction of the spanwise large-scale structures of the outer modes with the streamwise vortices (translative instability) plays a major part in the transition. The transition occur in the **absence of pairing** in contrast to the simulation of Moser and Rogers (1991) for incompressible mixing layers. In compressible reacting mixing layers, spanwise and streamwise vorticity are seen to coexist in the braids, which may explain why the transition can occur without pairing. Gulping is seen to enhance the creation of small-scale structures.
5. The mixing transition occurs on both sides of the layer and preserves the two colayers. The rapid growth rate of the streamwise vortices lead to increased mixing between the fast and the slow sides of the layer and to enhanced reaction rate. **The reaction rate is increased.** The turbulent convection of fuel and oxidizer to the reaction zone is increased (smaller convection time) whereas the chemical time is unchanged. The turbulent Damköhler number goes down and slow chemistry effects appear (*e.g.* the maximum temperature goes down).
6. The compressible reacting mixing layer appear dominated by **preferentially spanwise oriented large-scale structures with superimposed small-scale energetic streamwise vortices**. The large scale rollers are initially 2-D but become increasingly 3-D due to the spanwise variation of the straining term. The obliquity of the large-scale structures seems to result from the competition between the baroclinic term (which increases two-dimensionality) and the straining term (which increases three-dimensionality). Heat release which increases the baroclinic term is therefore likely to yield more two-dimensional structure, a result consistent with the linear stability results of section 2.4.6.
7. The dynamics of the 3-D small-scale vortices strongly depends on the strain field generated by the 2-D rollers which suggest that the growth rate of the large-scale rollers (the amplification rate calculated linear stability analysis) control the spreading angle of the layer. The mechanism of growth is two-dimensional and little affected by the presence of the three-dimensional motion. This suggests that (despite the saturation and decay of the outer modes) the flame convective Mach numbers introduced in chapter 2 to correlate compressibility effects on the outer modes will

also be the appropriate correlating parameters.

8. The existence of large baroclinic torque breaking off the central mode and the little mixing of fuel and oxidizer obtained with outer mode suggest that spanwise forcing might be of limited use to enhance mixing in compressible reacting mixing layer. The results presented in this chapter suggest the **use of streamwise vortices to enhance mixing and combustion** in compressible mixing layers. Future work should examine the optimum location and size of these vortices. Two possibilities seem of particular interest, (1) first, two sets of counter-rotating vortices located in each colayer to enhance the transition to turbulence in these colayers, and second (2) a single set of large counter-rotating vortices located at the centerline to wrap fuel and oxidizer and thereby increase their interface. The Side Wall Shock Vortex Generator (SWSVG discussed by Clemens 1991) is a possible method to generate this single set of large-scale streamwise vortices. Oblique shocks generated by ramps located on the fast-stream wall may also be used to generate this single set of streamwise vortices by creating baroclinic torques.

Notes

CHAPTER 6

Conclusion

This work has been concerned with a numerical study of the compressible mixing layer. It is part of a joint experimental and numerical effort undertaken at Stanford University to investigate mixing and combustion in high-speed mixing layers. The purpose of this work was to determine the basic flow structure in these flows, to examine the effects of heat release and compressibility on mixing, and to guide the design and interpretation of the companion experiments. The following specific questions were addressed:

- Are there large-scale structures present in compressible reacting mixing layers? If so, what is the nature of these structures? What are the effects of these structures on the entrainment and the subsequent mixing process? How are these structures affected by compressibility or heat release?
- What is the growth mechanism of the compressible reacting mixing layer and why is it less than for the incompressible case?
- How does the transition to small-scale three-dimensional turbulence occur? What is the structure of the small-scale turbulence and how does it impact the reaction rate?
- Does the scalar PDF change in compressible reacting mixing layers? Does chemical reaction behave differently in compressible reacting mixing layers? Where is the reaction zone located and does quenching exist?

These issues were addressed using linear stability analysis and direct numerical simulations of compressible reacting mixing layers. The mean profile used in the linear stability analysis was calculated using a self-similar formulation of the compressible reacting boundary layer equations derived on the basis of infinite reaction rate and unity Prandtl and Lewis numbers. The linearized disturbance equations were solved using a shooting method based on fifth-order Runge-Kutta and Newton-Raphson

method. The DNS were run both on the Cray Y-MP and on the iPSC860 Hypercube. Two different codes were used: (1) an adaptation of the Poinsot Lele code (PLC) to diffusion flames, and (2) an extension of the Sandham code (SC) to reacting flows. These two codes are explicit (third-order Runge-Kutta) and the partial derivatives are calculated using mixed spectral and high-order Pade methods (in SC) and high order Pade schemes in (PLC). Non-reflecting boundary conditions are used in the cross-stream direction. The main results of this work are summarized below, and some open questions for future research are posed.

6.1. Linear stability analysis

- In mixing layers with variable density, instability modes are associated with peaks in the mean density-weighted vorticity (section 2.3). In reacting mixing layers, the temperature is high around the flame sheet in the middle of the layer, yielding two mean density-weighted vorticity peaks and hence two instability modes, **the fast and the slow outer modes**. The motion produced by each mode is concentrated on its side of the flame sheet, giving rise to the “colayer” structure. Similar effects are observed in non-reacting mixing layers at sufficiently high Mach numbers (section 2.4.2).
- Because of the colayers structure, the usual convective Mach number is an inappropriate parameter for compressible reacting mixing layers. However, the same argument may be applied to each of the colayers to develop the **flame convective Mach numbers**, which we have shown to be the important parameters for this flow (section 2.4.4).
- The two flame convective Mach numbers are not equal, and they both depend on the flame sheet position (through \bar{u}_f), on the flame sheet temperature \bar{T}_f , and on the free-stream temperature ratio. This suggests that compressibility effects (obliquity, reduction of the spreading angle, etc) can be significantly different for the two outer modes (section 2.4.2.3).
- The **obliquity** of the outer modes is controlled by the flame convective Mach numbers (section 2.4.5). The criteria for the obliquity angle found by Sandham and Reynolds (1990) for non reacting compressible mixing layers, $M_c \cos \theta = 0.6$, can be extended for the outer modes by replacing M_c by the appropriate flame convective Mach number. At high Mach number, the outer modes are increasingly oblique but

increasing the heat release reduces the obliquity, and at $M_f < 0.6$, the modes are two-dimensional (section 2.4.6).

- The mean temperature and velocity profiles are extremely important in determining the nature and behavior of these instability modes. This fact offers some opportunity for control of the structures in the mixing layer (sections 2.4.6 and 2.4.7).
- Whereas the incompressible non-reacting mixing layer is only convectively unstable without counterflow, with sufficient heat release the flow can become **absolutely unstable** without counterflow (section 2.4.7). This may yield new opportunities for enhancing the mixing.

6.2. 2-D temporal DNS

- Linear stability analysis is confirmed. The existence of the fast and slow outer modes leads to the existence of **two colayers** inside the layer (section 4.2). The eddies in the two colayers move at very different speeds and therefore do not interact. The **appearance of the layer changes rapidly** as the fast and the slow outer eddies slide past each other (section 4.4).
- Each outer mode only mixes fluid from its associated free stream with product from the middle of the layer. The slow outer mode only mixes oxidizer and product, and the fast outer mode only mixes fuel and product (section 4.3). No direct mixing of fluid from both sides is observed, and hence the Broadwell-Breidenthal model used for incompressible flow is of limited use for compressible reacting mixing layers. Little creation of new flame surface is observed, and the chemical reaction only occurs in a very flat flame in the central part of the layer. The creation of a high temperature zone located between the two colayers and the small strain-rate created by the outer modes make quenching unlikely (fig. 4.31).
- The mixture fraction PDF derived from the simulation exhibits **two bumps** corresponding to the two zones of mixing (fig. 4.4). The strain rate and the reaction rate have large periodic oscillations, and the reaction rate is highest when the fast and slow outer eddies lie one above the other (fig. 4.31 and fig. 4.33).
- The outer modes have a **short lifetime** because the distortion of the mean profiles that they produce restabilize these modes (sections 4.3.5 to 4.3.7). Subsequently, new outer modes appear at a different scale and then decay for the same reason.

Thus, the layer grows in thickness without the pairing observed in low-speed mixing layers.

- The large density and pressure gradients present in compressible reacting mixing layers generate large **baroclinic torques**. The baroclinic torque dominates the convection of spanwise vorticity, contributes to the appearance of the outer modes, and suppresses the roll-up process that would lead to vortex pairing (section 4.3.2).
- **No pairing of vortical structures** occurs in either colayer (section 4.7). The absence of roll-up, the short lifetime of the outer modes, a mismatch between the phase speeds of a fundamental and its subharmonics, and the large baroclinic torques all contribute to the absence of pairing.
- **Gulping**, where the growing fundamental swallows the decaying subharmonics, may be the preferred mode of interaction, and contributes to the growth of the layer (section 4.7). It does not destroy the colayers.
- In the compressible case, each outer mode associated with one free stream generates **radiating pressure waves** in the other stream (fig. 4.32). For unconfined shear layers, these pressure waves carry a significant amount of energy away from the layer, and may help identify the large-scale structures, their wavelengths, and convective speeds. The decay of the slow mode was shown to lead to transient shocklets in the fast stream (by steepening of the radiating pressure waves) (fig. 4.16 and fig. 4.17). For confined shear layers the radiating pressure waves can reflect from the wall and interact with the layer.

6.3. 3-D temporal DNS

- The 3-D simulation initially follows the behavior of the 2-D simulations, but soon develops two sets of streamwise vortices (braids), one in each colayer (section 5.2.1).
- As the braids are strained, the streamwise vortices exert alternative compressive and extensional strain rate on the large-scale rollers and create **wavy large-scale spanwise vortices**. The interaction of the spanwise large-scale structures of the outer modes with the streamwise vortices plays a major part in the transition to turbulence (section 5.2.4).
- The dynamics of the streamwise and spanwise vorticity in the colayers is different from what is observed for the single set of eddies in the incompressible non-reacting

mixing layer. Due to the absence of roll-up, only a fraction of the spanwise vorticity is convected to the spanwise cores. The spanwise vorticity remaining in the braids and the streamwise vorticity mutually strain and enhance each other. The large baroclinic torques generated by compressibility and heat release affect the dynamics very strongly (section 5.2).

- The small-scale transition occurs in the **absence of pairing** (section 5.3), in contrast to the behavior for incompressible mixing layers. In compressible reacting mixing layers, spanwise and streamwise vorticity are seen to coexist in the braids, which may explain why the transition can occur without pairing. Gulping may enhance the creation of small-scale structures (fig. 4.55). The small-scale transition occurs in each of the colayers, which continue to behave independently.
- The small-scale transition **increases mixing** between the fast and the slow sides of the layer and enhances the reaction rate. The turbulent convection of fuel and oxidizer to the reaction zone is increased and the chemical time is unchanged. Hence, the maximum temperature drops after mixing transition (fig. 5.43).
- After mixing transition, the compressible reacting mixing layer appears dominated by **preferentially spanwise large-scale structures with superimposed small-scale energetic streamwise vortices** (section 5.5, fig. 5.32 and 5.33). The large scale rollers are initially 2-D but become increasingly 3-D at the end of their lifetimes. This structure results from a competition between the baroclinic torque (which promotes two-dimensionality) and the straining term (which increases three-dimensionality).
- The most promising way to enhance mixing and combustion in compressible mixing layers appears to be the **use of streamwise vortices**. Future work should examine the optimum location and size of these vortices.

Notes

APPENDIX A

Application of the Tau method to the stability analysis

In section 1.2, the linear stability problem was solved using a shooting method based on variable step fifth-order Runge-Kutta scheme and a root finder based on Newton-Raphson. The main disadvantage of this method is the necessity of providing an initial guess for the complex eigenvalue, and the influence of this initial guess on the convergence. If more than one instability mode are present, the Newton method or any rootfinder might fail to converge to some of the eigenvalues.

An alternative is to use a direct method. In the Chebyshev tau method, the mean and the disturbance flow variables are expressed as linear combinations of Chebyshev polynomials. The linear stability problem becomes a linear eigenvalue problem which is solved using the QR algorithm. The main advantage of the direct method is that it solves for all the eigenvalues of the stability problem simultaneously.

We start from the system of two coupled ordinary differential equations, (2.64) and (2.65) obtained in chapter 2

$$(\alpha \bar{u} - \omega) \hat{v}' - \alpha \hat{v} \bar{u}' = \frac{-i\alpha^2 g \hat{p}}{\gamma_1 M_1^2} \quad (a.1)$$

$$\bar{p} i(\alpha \bar{u} - \omega) \hat{v} = \frac{-1}{\gamma_1 M_1^2} \hat{p}' \quad (a.2)$$

For simplicity, we assume here that γ is constant and that r is a function of Z . \hat{p} can be eliminated leading to a second order differential equation in \hat{v} :

$$(\bar{u} - c)[(\frac{1}{g} \hat{v}')' - \rho \alpha^2 \hat{v}] = \hat{v}[(\frac{1}{g} \bar{u}')'] \quad (a.3)$$

with the boundary conditions: $\hat{v} = 0$ at $(\pm\infty)$ and g defined as $g = (\alpha^2 + \beta^2)/(\alpha^2 \bar{p}) - M_1^2(\bar{u} - c)^2$

By substituting g , with ' and " denoting the first and second derivatives with respect to y , equation a.3 can be rewritten as

$$\begin{aligned} \bar{\rho} \alpha^2 (\bar{u} - c) \hat{v} \left[\frac{\alpha^2 + \beta^2}{\alpha^2 \bar{\rho}} - M_1^2 (\bar{u} - c)^2 \right]^2 = \\ (\hat{v} \bar{u}'' - (\bar{u} - c) \hat{v}'') \left[\frac{\alpha^2 + \beta^2}{\alpha^2 \bar{\rho}} - M_1^2 (\bar{u} - c)^2 \right] - \\ (\hat{v} \bar{u}' - (\bar{u} - c) \hat{v}') \left[\frac{\alpha^2 + \beta^2}{\alpha^2 \bar{\rho}^2} \bar{\rho}' - 2M_1^2 (\bar{u} - c) \bar{u}' \right]. \end{aligned} \quad (a.4)$$

For temporal stability analysis, α is real and c is sought. Equation a.4 is developed, giving

$$(\bar{u} - c)^5 A_1 + (\bar{u} - c)^3 A_2 + (\bar{u} - c)^2 A_3 + (\bar{u} - c) A_4 + A_5 = 0, \quad (a.5)$$

or

$$\begin{aligned} c^5 (A_1) + c^4 (-5\bar{u} A_1) + c^3 (10\bar{u}^2 A_1 + A_2) + c^2 (-10\bar{u}^3 A_1 - 3\bar{u} A_2 - A_3) \\ + c (5\bar{u} u^4 A_1 + 3\bar{u}^2 A_2 + 2\bar{u} A_3 + A_4) + (-\bar{u}^5 A_1 - \bar{u}^3 A_2 - \bar{u}^2 A_3 - \bar{u} A_4 - A_5) = 0. \end{aligned} \quad (a.6)$$

with

$$\begin{aligned} A_1 &= M_1^4 [\rho \alpha^2 \hat{v}] \\ A_2 &= M_1^2 [-2(\alpha^2 + \beta^2) \hat{v} + \ddot{\hat{v}}] \\ A_3 &= M_1^2 (\bar{u} - c)^2 [-\hat{v} \ddot{\bar{u}} - 2\dot{\hat{v}} \dot{\bar{u}}] \\ A_4 &= [(\alpha^2 + \beta^2) \hat{v} \bar{\rho} - \frac{(\alpha^2 + \beta^2)}{\alpha^2} \bar{\rho} \ddot{\hat{v}} + 2M_1^2 \bar{\rho}^2 \dot{\bar{u}}^2 \hat{v} - \frac{(\alpha^2 + \beta^2)}{\alpha^2} \dot{\bar{\rho}} \dot{\hat{v}}] / \bar{\rho}^2 \\ A_5 &= \frac{(\alpha^2 + \beta^2)}{\alpha^2 \bar{\rho}^2} [\hat{v} \ddot{\bar{u}} \bar{\rho} + \dot{\bar{\rho}} \dot{\hat{v}} \dot{\bar{u}}] = 0. \end{aligned} \quad (a.7)$$

This equation is linear in \hat{v} . In the incompressible case $M_1 = 0$, most of the terms drop out, and the equation becomes

$$(\bar{u} - c) [\alpha^2 \hat{v} \bar{\rho} - \bar{\rho} \ddot{\hat{v}} - \dot{\bar{\rho}} \dot{\hat{v}}] + [\hat{v} \ddot{\bar{u}} \bar{\rho} + \dot{\bar{\rho}} \dot{\hat{v}} \dot{\bar{u}}] = 0. \quad (a.8)$$

A.1 Chebyshev transformation

The Chebyshev tau method is as follows. First, $y \in [-\infty, \infty]$ is mapped to $\eta \in [-1, 1]$ using

$$\begin{aligned} y &= \tanh(\eta) \\ dy &= (1 - \eta^2) d\eta \end{aligned} \quad (a.9)$$

which is particularly appropriate since the mean velocity profile can be approximated by a hyperbolic tangent profile.

Then all the flow variables are expanded in Chebyshev polynomials:

$$\begin{aligned}\hat{v} &= \sum_0^N a_i T_i(\eta) \\ \bar{u} &= \sum_0^N b_i T_i(\eta) \\ \bar{p} &= \sum_0^N c_i T_i(\eta).\end{aligned}\quad (a.10)$$

The expression of the derivative of any flow variable (for example \hat{v}) in terms of Chebyshev polynomials is

$$\begin{aligned}\hat{v}' &= (1 - \eta^2) \sum \tilde{a}_i T_i(\eta) \\ &= 1/2 (T_0(\eta) - T_2(\eta)) \sum \tilde{a}_i T_i(\eta)\end{aligned}\quad (a.11)$$

with

$$\tilde{a}_n = \frac{2}{C_n} \sum_{\substack{p=n+1, N \\ p+n \equiv 1[2]}} p a_p$$

and with $C_n = 1$ if $n \neq 0$ or $n \neq N$, and $C_n = 2$ if $n = 0$ or $n = N$.

The multiplication rule for Chebyshev polynomials is

$$2T_n(\eta)T_m(\eta) = T_{n+m}(\eta) + T_{|n-m|}(\eta) \quad (n + m < N). \quad (a.12)$$

We substitute \hat{v} , \bar{u} and \bar{p} into the Rayleigh equation. Using the rules derivatives and multiplication, we get

$$(c^5 B_5 + c^4 B_4 + c^3 B_3 + c^2 B_2 + c B_1 + B_0)[a_i] = 0. \quad (a.13)$$

where B_0, B_1, B_2, B_3, B_4 , and B_5 are $N + 1$ by $N + 1$ matrices functions of b_i and c_i . The above system of equations contains as many equations as unknowns. In order to enforce the boundary conditions one has to drop the two last equations ($N - 1, N$) and replace them by the 2 boundary conditions that $\sum a_i (+1)^i = 0$ ($\hat{v}(+1) = 0$) and $\sum a_i (-1)^i = 0$ ($\hat{v}(-1) = 0$). An eigenvalue problem is obtained where the eigenvalue does not appear linearly. This eigenvalue problem is solved following the method

proposed by Bridges and Morris (1984). We introduce the two new matrices C_1 and C_2 defined as:

$$C_1 = \begin{pmatrix} -B_4 & -B_3 & -B_2 & -B_1 & -B_0 \\ I & 0 & 0 & 0 & 0 \\ 0 & I & 0 & 0 & 0 \\ 0 & 0 & I & 0 & 0 \\ 0 & 0 & 0 & I & 0 \end{pmatrix} \quad C_2 = \begin{pmatrix} B_5 & 0 & 0 & 0 & 0 \\ 0 & I & 0 & 0 & 0 \\ 0 & 0 & I & 0 & 0 \\ 0 & 0 & 0 & I & 0 \\ 0 & 0 & 0 & 0 & I \end{pmatrix} \quad (a.14)$$

which gives the equivalent eigenvalue problem

$$(C_1 - cC_2)\hat{V} = 0 \quad \text{with} \quad \hat{V} = (c^4\hat{v}^\perp, c^3\hat{v}^\perp, c^2\hat{v}^\perp, c\hat{v}^\perp, \hat{v}^\perp)^\top \quad (a.15)$$

A.2. Resolution of the eigenvalue problem

If C_2 is invertible, the eigenvalue problem (a.15) can be rewritten as

$$(C_2^{-1}C_1 - cI)\hat{v} = 0 \quad (a.16)$$

and the Q-R algorithm can be used.

Otherwise, we transform the linear system of equations to reduce the problem to the above form. The method is in four steps (described in Gary and Helgason 1970):

- We diagonalise C_2 . If the rank of C_2 is k , then its first k coefficients on the diagonal are non zero, and all its other terms are zero. We reorganize the diagonal elements such that $|C_{2i,i}| \geq |C_{2i+1,i+1}|$.
- We lower-triangularize the $k+1, N$ lines and columns of the matrix C_1 . This does not affect the matrix C_2 which only has 0 in its $k+1, N$ lines and columns.
- Define C'_1 and C'_2 which are the matrices obtained by dropping the last $N-k$ lines and columns of matrices C_1 and C_2 .
- Repeat the process until the order and the rank of C'_2 are equal.

The eigenvalues of $(C_1 - cC_2)$ and $(C'_1 - cC'_2)$ are equal. Since C'_2 is invertible we can solve the eigenvalue problem by using the Q-R algorithm.

The main advantage of the tau Chebyshev method presented above is to give all the eigenvalues in a single calculation and without requiring an initial guess. However, the accuracy of the method strongly depends on the number of Chebyshev polynomials used. The results we obtained with the spectral method usually require a larger computational time and are less accurate than the results obtained with the shooting method.

APPENDIX B

2-D Spatial simulations

Several 2-D spatial direct numerical simulations of igniting mixing layers have been performed for the parameters given in table B.1. In all the simulations, the temperature of the fast and slow streams are equal ($\bar{T}_1 = \bar{T}_2$) and the velocity of the slow stream is half that of the fast stream ($\bar{u}_2 = 0.5\bar{u}_1$). The purpose of these simulations was to study the transition from the central modes to the outer modes as ignition increases the heat release.

The mean temperature and velocity profiles used at the inlet are that of a non-reacting mixing layer with uniform density and no premixing of fuel and oxidizer. With an uniform mean profile and for the low M_c considered, the only unstable modes are the central mode. The inlet was only forced with a central mode and its subharmonic and no outer modes were forced.

The central modes develop with downstream distance and eventually pair. The computational box used in this simulation is of the order of ten wavelengths, which imposed a low Reynolds number due to the memory limitation. However, despite lack of sufficient mesh resolution, the low Re , and the short L_x and L_y , the preliminary results presented below exhibit some interesting features.

Table B.1. Parameters used in the 2-D spatial simulations

RUN	N_y	N_x	L_y	L_x	Da	Z_e	Θ	M_c	Re
<i>MS013HR</i>	101	801	10	80	1.75	4	2	0.1	1000
<i>MS014HR</i>	201	801	20	80	1.75	4	2	0.1	1000
<i>MS015HR</i>	201	801	20	80	0	4	2	0.1	1000
<i>MS016HR</i>	201	801	20	120	1.83	4	3	0.1	500
<i>MS017HR</i>	201	801	20	120	1.22	4	3	0.15	1000
<i>MS018HR</i>	201	801	20	120	0.66	0	3	0.15	1000
<i>MS019HR</i>	201	801	20	120	0.03	0	3	0.15	1000
<i>MS021HR</i>	221	901	20	140	0.04	0	3	0.6	1200
<i>MS022HR</i>	221	901	20	140	0.04	0	4	0.6	1200

Figure B.1 shows the (a) mixture fraction, (b) density, (c) pressure and (d) reaction rate for the run MS019HR with slow chemistry. We retrieve in this case, the familiar large-scale structures separated by thin webs as observed in incompressible mixing layers. Pairing occurs at the left of the computational domain and we note the large-scale engulfment of fluid from both sides. The reaction rate develops and, for this zero Zeldovich case, no quenching is observed. The reaction rate is maximum in the webs. The pressure variations grows exponentially at the left of the computational domain, as the central modes develop, after which the maximum and minimum pressure remain approximately constant. As suggest by formula (4.1), this implies that the compressibility effects remains constant with downstream distance. The density is uniform at the inlet, and for this slow chemistry simulation, the flame temperature remains small. The adiabatic flame temperature is 4 but the maximum temperature observed in the domain in approximately 2.

Figure B.2 shows the (a) mixture fraction, (b) density, (c) pressure and (d) reaction rate for the run MS018HR which has a much faster chemistry. All the parameters are the same as in the previous case and the same amplitude of the eigenmodes was used in the forcing. Here, the heat release begins earlier than in the previous case, and the maximum temperature, $T_{max} = 3.2$, is closer to the adiabatic flame temperature $T_{adia} = 4$. Interestingly, the shape of the large-scale structures become elongated along x as the heat release increases. We recall that a similar mechanism was discussed in section 4.6.2. The reaction rate which initially was maximum in the webs, becomes aligned with the mean flow and is maximum close to the centerline. Finally, as the flame temperature increases and as the large-scale structures become inclined, a reduction of pressure fluctuations (and thus of compressibility) is noted at the right of the computational domain. Whether this observation is associated with the transition from a central mode to the outer mode (and with the transition from M_c to M_f) is an interesting question which may require further investigation.

Figure B.3 shows the (a) mixture fraction, (b) density, (c) pressure and (d) reaction rate for the run MS022HR with a higher convective Mach number $M_c = 0.6$. Here, the chemistry is slow as in run MS019HR and the adiabatic flame temperature is 4 but the maximum temperature observed in the domain in approximately 2.5. However, due to higher M_c , a behavior similar to MS018HR is observed. The shape of the large-scale structures become elongated along x as the heat release increases and the reaction rate which initially maximum in the webs, becomes aligned with the mean

flow. Also as in MS018HR, when the flame temperature increases and when the large-scale structures become inclined, a reduction of pressure fluctuations (and thus of compressibility) is noted at the right of the computational domain.

Although we did not investigate the ignition mechanism fully, the results presented above suggest a transition from the central mode to the outer modes. Further investigation with higher Re and higher Da is however required.

APPENDIX C

Flow regime

In this appendix, a regime chart (fig. C.1) is proposed, showing the most likely types of large-scale structures at a given convective Mach number M_c and heat release Θ . Four type of structures can be present in the flow: 2-D central mode, 2-D outer modes, 3-D central mode and 3-D outer modes.

- Frontier between 2-D and 3-D central modes: The frontier between 2-D and 3-D central modes, proposed by Sandham and Reynolds (1989) and since confirmed by the experiments of Clemens and Mungal (1990), is $M_c = 0.6$, which appears as a vertical line in the domain.
- Frontier between 2-D and 3-D outer modes: Similarly, each outer mode is seen to become oblique above $M_f = 0.6$. M_{f1} and M_{f2} are related to M_c by (2.83) and (2.84). For unity free-stream temperature ratio and if the flame is located in the middle of the layer, we get

$$M_{f1} = M_{f2} = \frac{M_c}{1 + \sqrt{T_f}} \quad (a.17)$$

and $M_f = 0.6$ becomes

$$M_c = 0.6(1 + \sqrt{T_f}) \quad (a.18)$$

which appears as a parabola (plain line) on the regime chart. If the fast stream is more reactant-rich than the slow stream, the location of the reaction zone is shifted towards the slow stream and the two flame convective Mach numbers become unequal. For example, if $\bar{u}_f = 0.25\bar{u}_1 + 0.75\bar{u}_2$ we get

$$\begin{aligned} M_{f1} &= \frac{1.5M_c}{1 + \sqrt{T_f}} \\ M_{f2} &= \frac{0.5M_c}{1 + \sqrt{T_f}} \end{aligned} \quad (a.19)$$

and $M_f = 0.6$ becomes

$$M_c = 0.4(1 + \sqrt{T_f})$$

$$M_c = 1.2(1 + \sqrt{\bar{T}_f}) \quad (a.20)$$

for the fast and the slow outer modes, respectively. These curves appear as two distinct parabolas (dotted lines) on the regime chart. The influence of the non-unity free-stream temperature ratio can also be computed using (2.83) and (2.84).

- Frontier between central and outer modes: As seen in chapters 2 (section 2.6) and 4 (sections 4.1, 4.3.2, 4.6.2) the baroclinic term is responsible for the appearance of the outer modes and the disappearance of the central mode. The frontier between central and outer modes is obtained by evaluating the dependency of the convection of ω_z and the dependency of the baroclinic torque on M_c and Θ , we find that

$$u \frac{\partial \omega_z}{\partial x} \sim M_c^2 \quad (a.21)$$

$$-\frac{1}{\rho^2} \left(\frac{\partial p}{\partial x} \frac{\partial \rho}{\partial y} - \frac{\partial p}{\partial y} \frac{\partial \rho}{\partial x} \right) \sim M_c^2 (M_c^2 + \Theta). \quad (a.22)$$

The line of constant ratio of the convective terms to the baroclinic destruction of vorticity to spanwise vorticity in the (Θ, M_c) plane is therefore given by

$$(M_c^2 + \Theta) \approx c_1, \quad (a.23)$$

where c_1 is a constant, arbitrarily chosen equal to 1 (since as seen in section 2.4.2.1, linear stability shows that the fast and slow supersonic instability modes appear at $M_c = 1$ in the absence of heat release). We note several interesting features:

- a. At low heat release ($\Theta = 0$), the formula predicts that the outer modes will become dominant when compressibility increases (above $M_c = c_1^{1/2}$).
- b. At low Mach number, formula a.23) indicates that the heat release required for the outer modes to appear is approximately 1 and decays like the square of M_c .
- c. The central mode appear limited to a very restricted range of M_c and Θ

Figure C.1 shows the flow regime depending on Θ and M_c . The black and dashed circles corresponds to the Stanford non-reacting and reacting experiments, respectively. We note that the central modes are restricted to a very restricted portion of the (M_c, Θ) plane. The frontier between the 2-D and 3-D outer modes appears to be strongly dependent on the free-stream temperature ratio and on the fuel-equivalence ratio. The heat release considered in Stanford experiment is barely sufficient for the 2-D outer modes to appear and the apperance of the outer modes should become more obvious at higher Θ .

APPENDIX D

Archives

All the files have been transported to Columbia. In this section, the location of all the source codes, script files, input files and results files is given, with a brief description of some of them.

D.1. Linear stability analysis code

The linear stability analysis codes are located in the subdirectory LINEAR(in what follows the names of the subdirectories are indicated by capital letters). Three types of codes are saved, (1) the codes used to calculate the linear stability characteristics (lscsthesis.f, lscsthesis2.f, lscsthesis3.f, ltcs3.f, lscls3.f, lpcls3.f), (2) the codes used to calculate the eigenfunctions (lse13.f, lte13.f, treimyp.f), (3) the codes used to initialize the direct numerical simulations with eigenfunctions from linear stability analysis (conteigen2.f, conteigen6.f, etc). The script files are located in LINEAR/SCRIPT.

D.2. PLC code

The source codes, script files, input files and results files of the simulations performed with the PLC code are located in SIMUL. The PLC source codes are located in SIMUL/TDIF. The script files are located in SIMUL/VECT/JOBS. The following is a brief description of the programs:

- ntmixtel.vec 1-D temporal code with non-reflecting boundary conditions in y .
The script file to run the code is rntdt1.
- ntmixtem.vec 2-D temporal code. It uses periodic boundary conditions in the x direction and non-reflecting boundary condition in the y direction.
The script file to run this code is rntdiftp.job.
- ntmixspa.vec 2-D spatial code with forcing at the inlet and non-reflecting boundary

conditions at the outlet and in the y direction. The script file to run this code is rntdifsp.job.

ntmixsta.vec

2-D spatial code with forcing at the inlet and non-reflecting boundary conditions at the outlet and in the y direction. It differs from ntmixspa.vec by the accumulation of 2-D fields of statistics over time (field of the average temperature, Reynolds stresses, etc). The script file to run this code is rntdifst.job.

The post-processing codes are located in SIMUL/VECT. A brief commentary at the beginning of each program describes the tasks performed in the code. The codes are called by the script files saved in SIMUL/VECT/JOBS.

shrinksx.vec

code to divide by 2 the number of points in the x direction of a spatial simulation. The length L_x is unchanged while the grid size Δ_x is divided by 2. The script file to run this code is shrinksx.job

shrinkx.vec

code to divide by 2 the number of points in the x direction of a temporal simulation. The length L_x is unchanged while the grid size Δ_x is divided by 2. The script file to run this code is shrinkx.job

shrinky.vec

code to divide by 2 the number of points in the y direction of a temporal simulation. The length L_y is divided by two while only the central part of the layer is conserved. Δ_y is unchanged. The script file to run this code is shrinksx.job

calmean.vec

code to compute the mean (x averaged) profiles of \bar{u} , \bar{v} , \bar{T} , \bar{p} , \bar{uu} , \bar{vv} .

mea2.vec

code to compute the mean (x averaged) profiles of \bar{u} , \bar{Z} , \bar{T} in the format of the input files used in the linear stability analysis. Was used to investigate the effect of the mean profile evolution on the instability characteristics of the layer (section 4.3.6).

mean.vec

Same code as mea2.vec but the format of the output file is slightly different.

postm2.vec

code to compute the mean profiles of Q_1 to Q_7 , pressure, temperature, vorticity, species, velocities, baroclinic torque, dilatation term, density weighted vorticity, etc. The script file to run this code is postm2.job

<u>postm21D.vec</u>	same code as postm2.vec for a 1-D calculation. The script file to run this code is postm21D
<u>postm3.vec</u>	code to compute the mean profiles of the Reynolds stresses, turbulent convection of fuel and oxidizer, enstrophy, production rate and dissipation rate of kinetic energies, etc. The script file to run this code is postm3.job
<u>postml.vec</u>	code to extract the 2-D fields of a temporal simulation to be plotted by rplot: Velocities, temperature, pressure, vorticity, baroclinic, dilatation, species, reaction rate, etc. The script file to run this code is postml.job
<u>rpostsp.vec</u>	code to extract 2-D fields of a spatial simulation to be plotted by rplot Velocities, temperature, pressure, vorticity, baroclinic, dilatation, species, reaction rates, etc. The script file to run this code is rpostsp.job
<u>postwk.vec</u>	code to change the format of a restart temporal file to the format of plot3d on workstation. The script file to run this code is postwk.job.

The result files of the temporal and spatial simulations are saved as restart files in SIMUL/RUN-TEMP and SIMUL/RUN-SPAT, respectively. These files contain the parameters used in the simulation (N_x , N_y , etc.) and the scalar fields (ρ , ρu , ρv , ρw , ρe_t , ρY_f , ρY_o). At the beginning (or restart) of a simulation, the fluid-mechanics parameters (Mach number, heat release, Damköhler number, etc) are read from parameter file: a dat.dat file (in SIMUL/DAT.DAT on columbia) for a temporal simulation or a spa.dat file (in SIMUL/SPA.DAT on columbia) for a spatial simulation. This parameter files also contain some numerical parameters (time period to save file, type of Pade scheme used, CFL number, etc).

The fluid-mechanics parameters used in a simulation are saved in each restart file. For spatial simulations, the forcing eigenfunctions are also included in the restart file. When a run is resubmitted, the fluid mechanics parameters saved in the restart file are checked to be equal to the fluid mechanics parameters in the parameter file. The mean profiles used in the simulation were calculated using the code (lvblas) saved in SIMUL/INIDIF.PRO5 (self-similar solution).

The code located in SIMUL/INIDIF.PRO4 solves the complete compressible reacting boundary layer equations. The initialization files called by lvblas are saved in SIMUL/INIDIF.FILE.

D.3. SC code

The SC sources running on the Cray Y-MP (cmix3d.vec and cmix2d.vec for 3-D and 2-D simulations, respectively) are located in SANDHAM/PROG. The initialization programs are cmix2din.vec, cmix3din.vec and cmix3dtu.vec for simulations initialized with 2-D eigenmodes, 3-D eigenmodes and 3-D eigenmodes with superimposed turbulence spectrum, respectively. The vectoral codes call several Fortran subroutines located in the file dhf.f, dhfin.f, dhfturbul.f, etc. Post-processing codes are also located in SANDHAM/PROG. The script files used to compile or run SC are located in SANDHAM/JOBS. The run script start by r and the compiling scripts start by c. The post-processing codes are:

- energy.vec code to compute the kinetic energy of all the Fourier modes in the restart file
- plot3d.vec codes to change the format of the restart file generated by cmix3d to the format of plot3d on the silicon graphics. Return the grid-file and the scalar-file ($\rho, \rho u, \rho v, \rho w, \rho e_t$)
- plot4d.vec codes to change the format of the restart file generated by cmix3d to the format of plot3d on the silicon graphics. Return the grid-file and the scalar-file ($\rho, \rho Y_f, \rho Y_o, \rho(Y_f - Y_o), \dot{w}$)

The SC running on the Ipsc860 (cmix3d.vec and cmix2d.vec for 3-D and 2-D simulations, respectively) are located in I860/PROG. In the same directory, several other codes are stored. These codes are described below:

- refinep.vec code to modify the restart file of a 3-D run to change the number of processors used from N_p to $2N_p$.
- cref2dp.vec code to modify the restart file of a 2-D run to change the number of processors used from N_p to $2N_p$.
- cexpan3dp.vec code to modify the restart file of a 3-D run to change the number of

	processors used from $2N_p$ to N_p .
<u>cexpan2dp.vec</u>	code to modify the restart file of a 2-D run to change the number of processors used from $2N_p$ to N_p .
<u>refinep.vec</u>	code to modify the restart file of a 3-D run to change the number of processors used from N_p to $2N_p$.
<u>refinep.vec</u>	code to modify the restart file of a 3-D run to change the number of processors used from N_p to $2N_p$.
<u>refinex.vec</u>	code to modify the restart file of a 3-D run to change the number of points in the x direction form N_x to $2N_x$.
<u>refiney.vec</u>	code to modify the restart file of a 3-D run to change the number of points in the x direction form N_{y1} to N_{y2} .
<u>refinez.vec</u>	code to modify the restart file of a 3-D run to change the number of points in the x direction form N_z to $2N_z$.
<u>cmix2din.vec</u>	code to initialize a 2-D run with eigenfunctions from linear stability analysis
<u>cmix3din.vec</u>	code to initialize a 3-D run with eigenfunctions from linear stability analysis.
<u>cmix3dtu.vec</u>	code to initialize a 3-D run with eigenfunctions from linear stability analysis and superimposed turbulence spectrum.
<u>cmix3dvo.vec</u>	code to initialize a 3-D run with eigenfunctions from linear stability analysis and superimposed counter-rotating streamwise vortices.
<u>postwk2d.vec</u>	code to change the format of a 2-D restart file to the format of plot3d on the silicon graphics.
<u>postwk3d.vec</u>	code to change the format of a 3-D restart file to the format of plot3d on the silicon graphics.
<u>spectr.vec</u>	code to calculate the modal kinetic energies in a 3-D restart file
<u>stat3d.vec</u>	code to calculate several statistics from a 3-D restart file

Some post-processing of the I860 simulations have been performed on the Cray Y-MP. The method is as follows: First, use the ieeeC code developped by A.A. Wray (script ieeeCjob.job is SIMUL/VECT/JOBS) to convert to the Cray Y-MP format. Then

the following post-processing codes (located in I860/POSTPROC) can be used. The associated script files are located in I860/POSTPROC/JOBs:

- post2d.vec code to compute 2-D fields of pressure, density, baroclinic torque, vorticity, etc to be plotted using plotm2d.f in DEPOUIL/PROG. The script file to run this code is post2d.job
- post2dm.vec code to compute the mean (x averaged) profiles of vorticity, baroclinic torque, scalar dissipation, etc. The script file to run this code is post2dm.job.
- post3dx.vec code to extract 2-D ($x = ct$ plane-cuts) fields of pressure, density, baroclinic torque, vorticity from a 3-D restart file. The plane-cuts are plotted using plotm3d.f in DEPOUIL/PROG. The script file to run this code is post3dx.job.
- post3dy.vec code to extract 2-D ($y = ct$ plane-cuts) fields of pressure, density, baroclinic torque, vorticity from a 3-D restart file. The plane-cuts are plotted using plotm3d.f in DEPOUIL/PROG. The script file to run this code is post3dy.job.
- post3dz.vec code to extract 2-D ($z = ct$ plane-cuts) fields of pressure, density, baroclinic torque, vorticity from a 3-D restart file. The plane-cuts are plotted using plotm3d.f in DEPOUIL/PROG. The script file to run this code is post3dz.job.
- post3de.vec code to compute the modal kinetic energy content for a 3-D restart file. The script file to run this code is post3de.job.
- post3dl.vec code to compute the Taylor length scale, the integral length scale and the Kolmogorov length for a 3-D restart file. The script file to run this code is post3dl.job.
- post3dm.vec code to compute the mean ($x - z$ averaged) profiles of vorticity, baroclinic torque, scalar dissipation, etc for a 3-D restart file. The script file to run this code is post3dm.job
- post3ds.vec code to compute the mixture fraction PDF in a given number of slices ($y \in [y_1, y_2]$) for a 3-D restart file. Called by post3ds.job. The marching PDF obtained is plotted using cloud3Dpdfz.f (see section D.4).

D.4. Plotting programs

The plotting programs are located in DEPOUIL/PROG. They are:

- cloud3Dpdfz.f code to print the marching PDF of the mixture fraction obtained by executing post3ds.vec (see section D.3.) on a 3-D restart file from the Ipsc860 simulation. The script file to run the code is rnuage3d.job
- cloudpdfz.f code to compute and print the PDF of the mixture fraction from a restart file from PLC post-processed with postml.vec. The script file to run the code is rnuage.job.
- colle.f code to attach history files from different simulation together. The script file to run the code is rcolle.job
- colles.f code to attach history files from different simulation together. The script file to run the code is rcolles.job
- depouil.f code to plot the history file of a 2-D temporal simulation on the screen (use DISSPLA library).
- depouils.f code to plot the history file of a 2-D spatial simulation on the screen (use DISSPLA library).
- depouil1.f code to plot the history file of a 1-D temporal simulation on the screen (use DISSPLA library).
- prepare.f code to modify the history file of a 2-D temporal simulation run and create files which can be plotted with myplot.f
- prepares.f code to modify the history files of a 2-D spatial simulation run and create files which can be plotted with myplot.f
- prepare1D.f code to modify the history files of a 1-D temporal simulation run and create files which can be plotted with myplot.f

Notes

References

- BENDER, C.M. & ORSZAG, S.A. 1978 Advanced Mathematical Methods for Scientists and Engineers. McGraw-Hill.
- BERNAL, L.P. & ROSHKO, A. 1986 Streamwise Vortex Structure in Plane Mixing Layers. *J. Fluid Mech.* Vol 170, 499-525.
- BLAISDELL, G.A., MANSOUR, N.N. & REYNOLDS, W.C. 1991 Numerical Simulation of Compressible Homogeneous Turbulence. *Report TF 50*, Stanford University.
- BLUMEN, W., DRAZIN, P.G. & BILLINGS, D.F. 1975 Shear Layer Instability of an Inviscid Compressible Fluid. Part 2. *J. Fluid Mech.* Vol 71, 305-316.
- BOGDANOFF, D.W. 1983 Compressibility Effects in Turbulent Shear-Layers. *AIAA J.* Vol 21, 926-927.
- BREIDENTHAL, R. 1981 Structure in Turbulent Mixing Layers and Wakes Using a Chemical Reaction. *J. Fluid Mech.* Vol 109, 1-24.
- BRIDGES, T.J. & MORRIS P.J. 1984 Differential Eigenvalue Problems in Which the Parameter Appears Nonlinearly. *J. Comput. Phys.* Vol 55, 437-460.
- BROADWELL, J.E. & BREIDENTHAL, R.E. 1982 A simple model of Mixing and Chemical Reaction in a Turbulent Shear Layer. *J. Fluid Mech.* Vol 125, 397-410.
- BROADWELL, J.E & MUNGAL, M.G. 1988 Molecular Mixing and Chemical Reactions in Turbulent Shear Layers. *Twenty-Second International Symposium on Combustion*, University of Washington, Seattle, Washington.
- BROWN, G.L. & ROSHKO, A. 1974 On Density Effects and Large-Scale Structures in Turbulent Mixing Layers. *J. Fluid Mech.* Vol 64, 775-816.
- BUELL, J.C. & MANSOUR, N.N. 1989 Assymmetric effects in three dimensional spatially developing mixing layers. *Seventh Symposium on Turbulent Shear Flows 9-2*, Stanford, California.
- CHANDRSUDA, C., MEHTA, R.D., WEIR, A.D. & BRADSHAW, P. 1978 Effect of free-stream turbulence on large structures in turbulent mixing layers. *J. Fluid Mech.* Vol 85, 693.

- CHEN, J.H. 1991 The Effect of Compressibility on Conserved Scalar Entrainment in a Plane Free Shear Layer. *Eight Symposium on Turbulent Shear Flows 23-2*, Munich, Germany.
- CHEN, J.H., MANSOUR, N.N. & CANTWELL, B.J. 1989 Direct Numerical Simulation of Transition in a Compressible Wake. *Seventh Symposium on Turbulent Shear Flows 9-4*, Stanford, California.
- CHINZEI, N., MASUYA, G., KOMURO, T., MURAKAMI, A. & KUDOU, K. 1986 Spreading of two-stream Supersonic Turbulent Mixing Layers. *Phys. Fluids* Vol **29**, 1345-1347.
- CLEMENS, N.T. 1991 An Experimental Investigation of Scalar Mixing in Supersonic Turbulent Shear Layers. *PhD Thesis*, Stanford University.
- CLEMENS, N.T. & MUNGAL, M.G. 1992 Two and Three-dimensional Effects in Supersonic Mixing Layers. *AIAA J.* Vol **30**, 973-981.
- CLEMENS, N.T. MUNGAL, M.G. BERGER, T.E. & VANDSBURGER, U. 1990 Vizualization of the Structure of the Turbulent Mixing Layer Under Compressible Conditions. *AIAA paper 90-0500*.
- CORCOS, G.M. & LIN, S.J. 1984 The Mixing Layer: Deterministic Models of a Turbulent Flow. Part 2. The Origin of the Three-Dimensional Motion. *J. Fluid Mech.* Vol **139**, 67-95.
- CORCOS, G.M. & LIN, S.J. 1984 The Mixing Layer: Deterministic Models of a Turbulent Flow. Part 3. The effect of plane strain on the dynamics of streamwise vortices. *J. Fluid Mech.* Vol **141**, 139.
- CRAIK, A.D.D. 1971 Non linear resonant instability in Boundary Layers. *J. Fluid Mech.* Vol **50**, 393-413.
- CRAIK, A.D.D. 1982 The growth of laminar disturbances in unstable flows. *Journal of applied mechanics* Vol **49**, 284-290.
- CRIMINALE, W.O. & KOVASZNAY, L.S.G. 1962 The growth of localized disturbances in a laminar boundary layer. *J. Fluid Mech.* Vol **14**, 59-80.
- CROW, S.C. & CHAMPAGNE, F.H. 1971 Orderly Structure in Jet Turbulence. *J. Fluid Mech.* Vol **48**, 547-591.

- DAILY, J.W. & LUNDQUIST, W.J. 1984 Three Dimensional Structure in a Turbulent Combusting Mixing Layer. *Twentieth Symp. on Combustion*, University of Michigan, Ann Arbor, Michigan.
- DIMOTAKIS, P.E. 1986 Two-Dimensional Shear-Layer Entrainment. *AIAA J.* Vol **24**, 1791- 1796.
- DIMOTAKIS, P.E. 1989 Turbulent Free Shear Layer Mixing. AIAA paper 89-0262.
- DIMOTAKIS, P.E. & BROWN, G.L. 1976 The Mixing Layer at High Reynolds Number: Large-Structure Dynamics and Entrainment. *J. Fluid Mech.* Vol **78**, 535-560.
- DRAZIN, P.G. & HOWARD, L.N. 1981 Hydrodynamic Stability of Parallel Flow of Inviscid Fluid. *Adv. Appl. Mech.* Vol **9**, 1.
- DUTTON, J.C., BURR, R.F., GOEBEL, S.G. & MESSERSMITH, N.L. 1990 Compressibility and Mixing in Turbulent Free Shear Layers. *Proc. 12 symp. on Turbulence*, Rolla, MO.
- ERDOS, J., TAMAGNO, J., BAKOS, R. & TRUCCO, R. 1992 Experiments on Shear Layer Mixing at Hypervelocity Conditions. AIAA paper 92-0628.
- ERSCH, R.E. 1957 The Instability of a Shear Layer between two Parallel Streams. *J. Fluid Mech.* Vol **3**, 289-303.
- FEJER, J.A. & MILES, J.W. 1963 On the Stability of a Plane Vortex Sheet with Respect to Three Dimensional Disturbances. *J. Fluid Mech.* Vol **15**, 335-336.
- FIEDLER, H.E. 1974 Transport of Heat Across a Plane Turbulent Mixing Layer. *Adv in Geophys* Vol **18**, 93-109.
- FJORTOFT, R. 1955 Application of integral theorems in Deriving Criteria of Stability for Laminar Flow and for the Baroclinic Circular Vortex. *Geofys. Publ., Oslo* Vol **17**, 1-52.
- FOURGUETTE, D.C., MUNGAL, M.G. & DIBBLE, R.W. 1990 Time evolution of the Shear Layer of a Supersonic Axisymmetric Jet at Matched Conditions. AIAA paper 90-0508.
- GARY J.& HELGASON R. 1970 A matrix method for Ordinary Differential Eigenvalue Problems. *J. Comput. Phys.* Vol **5**, 169-187.
- GASTER, M. 1965 On the generation of spatially growing waves in a boundary layer. *J. Fluid Mech.* Vol **22**, 433-441.

- GASTER, M. 1968 Growths of disturbances in both space and time. *Phys. Fluids* Vol 11, 723-727.
- GASTER, M. 1968 The development of three dimensional waves packet in a boundary layer. *J. Fluid Mech.* Vol 32, 173-184.
- GASTER, M. & DAVEY A. 1968 The development of three dimensional waves packet in unbounded parallel flows. *J. Fluid Mech.* Vol 32, 801-808.
- GASTER, M. & GRANT, I. 1975 An experimental investigation of the formation and development of a wave packet in a laminar boundary layer. *Proc. R Soc. Lond* Vol A347, 253-269.
- GIBSON, C.H. & LIBBY P.A. 1972 On turbulent Flows with Fast Chemical Reaction. Part II. The Distribution of Reactant and Product Near a Reacting Surface. *Combustion Science and Technology* Vol 6, 29-35.
- GIVI, P., JOU, W.H. & METCALFE, R.W. 1986 Flame Extinction in Temporally Developing Mixing Layer. *Twenty First Symposium on Combustion*, Munich, Germany.
- GLAWE, D.D. & SAMIMY, M. 1992 Dispersion of Solid Particles in Compressible Mixing Layers. AIAA paper 92-0176.
- GREENOUGH, J., RILEY, J., SOESTRINO, M. & EBERHARDT, D. 1989 The Effect of Walls on a Compressible Mixing Layer. AIAA paper 89-0372.
- GROPENGIESSER, H. 1970 Study on the Stability of Boundary Layers and Compressible Fluids. *NASA TT* , F-12786.
- HALL, J.L. 1991 An Experimental Investigation of Structure, Mixing and Combustion in Compressible Shear Layers. *PhD Thesis*, G.A.L.C.I.T., Caltech.
- HALL, J.L., DIMOTAKIS, P.E. & ROSEMANN, H. 1991 Experiment in Non Reacting Compressible Shear Layers. AIAA paper 91-0629.
- HALL, J.L., DIMOTAKIS, P.E. & ROSEMANN, H. 1991 Some Measurement of Molecular Mixing in Compressible Turbulent Shear Layers. AIAA paper 91-1719.
- HERBERT, T. 1983 Secondary instability of plane channel flows to subharmonic three dimensional disturbances. *Phys. Fluids* Vol 26, 871-874.
- HERMANSON, J.C., MUNGAL M.G. & DIMOTAKIS, P.E. 1986 Heat Release Effects on Shear-Layer Growth and Entrainment. *AIAA J.* Vol 25, 578-583.

- HERMANSON, J.C. & DIMOTAKIS, P.E. 1989 Effects of Heat Release in a Turbulent Reacting Shear-Layer. *J. Fluid Mech.* Vol 199, 333-375.
- HO, C.M. & HUERRE, P. 1984 Perturbed Free Shear Layers. *Ann. Rev. Fluid Mech* Vol 16, 365.
- HUANG, L.S. & HO, C.M. 1990 Small-scale transition in a plane mixing layer. *J. Fluid Mech.* Vol 210, 475.
- HUERRE, P. & MONKEWITZ, P.A. 1985 Absolute and Convective Instabilities in Free Shear Layers. *J. Fluid Mech.* Vol 159, 151.
- IKAWA, H. & KUBOTA, T. 1975 Investigation of Supersonic Turbulent Mixing Layers with Zero Pressure Gradient. *AIAA J.* Vol 13, 566-572.
- JACKSON, T.L. & GROSCH, C.E. 1990 Inviscid Spatial Stability of a Compressible Mixing Layer. Part 2. The Flame Sheet Model. *J. Fluid Mech.* Vol 217, 391-420.
- JIANG, F. 1991 Asymptotic evaluation of three dimensional wave packet in parallel flows. *J. Fluid Mech.* Vol 226, 573-590.
- JIMENEZ, J., COGOLLOS, M. & BERNAL, L.P. 1985 A perspective View on Plane Mixing Layer. *J. Fluid Mech.* Vol 152, 125-143.
- KUO, K.K. 1982 Principles of combustion. Wiley Interscience.
- LANDAU, L. 1944 Stability of Tangential Discontinuities in Compressible Fluid. *Akad. Nauk. SSSR* Vol 44, 139-141.
- LASHERAS, J.C., CHO, J.S. & MAXWORTHY, T. 1986 On the origin and Evolution of Streamwise Vortical Structures in a Plane Free Shear Layer. *J. Fluid Mech.* Vol 172, 231-258.
- LASHERAS, J.C. & CHOI, H. 1988 Three-Dimensional Instability of a Plane Free Shear Layer: An Experimental Study of the Formation and Evolution of Streamwise Vortices. *J. Fluid Mech.* Vol 189, 53-86.
- LELE, S. 1989 Direct Numerical Simulation of Compressible Free Shear Flows. AIAA paper 89-0374.
- LELE, S. 1990 Compact finite difference schemes with spectral-like resolution. *CTR manuscript 107*, center for turbulence Research, Stanford/NASA Ames.
- LESSEN, M., FOX, J.A. & ZIEN, H.M. 1965 On the inviscid stability of the laminar mixing of two parallel streams of a compressible fluid. *J. Fluid Mech.* Vol 23, 355-367.

- LIN, C.C. 1955 The theory of hydrodynamic stability. .Cambridge University Press
- LOWSON, M.V. & OLLERHEAD, J.B. 1968 Vizualization of Noise from Cold Supersonic Jets. *Jounal of the Acoustical Society of America* Vol 44, 624-630.
- MACK, L.M. 1990 On the inviscid Acoustic-Mode Instabilities of Supersonic Shear Flows. Part 1: Two-Dimensional Waves. *Theoretical and Computational Fluid Dynamics*, Springer-Verlag.
- MCINTYRE, S.S. & SETTLES, G.S. 1991 Optical Experiments on Axisymmetric Compressible Turbulent Mixing Layers. AIAA paper 91-0623.
- McMURTRY, P.A., RILEY, J.J. & METCALFE, R.W. 1989 Effect of Heat Release on the Large-Scale Structure in Turbulent Mixing Layers. *J. Fluid Mech.* Vol 199, 297-332.
- MAHALANINGAM, S., CANTWELL, B.J. & FERZIGER, J.H. 1989 Non-Premixed Combustion: Full Numerical Simulation of a Coflowing Axisymmetric Jet, Inviscid and Viscous Stability Analysis. *Report TF-43*, Stanford University, California.
- MENON, S. & FERNANDO, E. 1990 A numerical Study of Mixing and Chemical Heat Release in Supersonic Mixing Layers. AIAA paper 90-0152.
- MICHALKE, A. 1965 On the Inviscid Instability of the Hyperbolic-Tangent Velocity Profile. *J. Fluid Mech.* Vol 19, 543.
- MILLER, M.F., ISLAND, T.C., YIP, B., BOWMAN, C.T., MUNGAL, M.G. & HANSON, R.K. 1992 An Experimental Study of the Structure of a Compressible, Reacting Mixing Layer. Poster 256. *Presented at the Twenty-fourth Symposium on Combustion*, Sydney, Australia.
- MILLER, M.F., ISLAND, T.C., YIP, B., BOWMAN, C.T., MUNGAL, M.G. & HANSON, R.K. 1993 An Experimental Study of the Structure of a Compressible, Reacting Mixing Layer. AIAA paper 93-0354.
- MONKEWITZ, P.A. & HUERRE, P. 1982 Influence of the Velocity Ratio on the Spatial Instability of Mixing Layers. *Phys. Fluids* Vol 25, 1137-1143.
- MORKOVIN, M.V. 1987 Transition at hypersonic speeds. *NASA-CR-178315*, ICASE Interim Report 1.
- MOSER, R.D. & ROGERS, M.M. 1991 Mixing Transition and the Cascade to Small Scales in a Plane Mixing Layer. *Phys. Fluids* Vol A3, 1128-1134.

- MUNGAL, M.G. & DIMOTAKIS, P.E. 1984 Mixing and combustion with low heat release. *J. Fluid Mech.* Vol 148, 349-382.
- OERTEL, H. 1979 Mach Wave Radiation of Hot Supersonic Jets Investigated by Means of the Shock Tube and New Optical Techniques. *Proceedings of the twelfth International Symposium on Shock Tubes and Waves*, Jerusalem.
- PAPAMOSCHOU, D. 1989 Structure of the Compressible Turbulent Shear Layer. AIAA paper 89-0126.
- PAPAMOSCHOU, D. 1990 Communication Paths in Compressible Shear Layers. AIAA paper 90-0155.
- PAPAMOSCHOU, D. & ROSHKO, A. 1986 Observation of Supersonic Free Shear Layers. AIAA paper 86-0162.
- PAPAMOSCHOU, D. & ROSHKO, A. 1988 The Compressible Turbulent Shear Layer: An Experimental Study. *J. Fluid Mech.* Vol 197, 453-477.
- PIERREHUMBERT, R.T. & WIDNALL, S.E. 1982 The two- and three-dimensional instabilities of a spatially periodic shear layer. *J. Fluid Mech.* Vol 114, 59-82.
- PLANCHE, O.H. & REYNOLDS, W.C. 1991 Compressibility Effect on the Supersonic Reacting Mixing Layer. AIAA paper 91-0739.
- PLANCHE, O.H. & REYNOLDS, W.C. 1991 Direct simulation of a supersonic Reacting Mixing-Layer. *Eighth Symposium on Turbulent Shear Flows 21-1*, Munich, Germany.
- PLANCHE, O.H. & REYNOLDS, W.C. 1992 Heat Release Effect on mixing in supersonic reacting free shear-layers. AIAA paper 92-0092.
- PLANCHE, O.H. & REYNOLDS, W.C. 1992 A Direct Numerical Simulation of the Compressible Reacting Mixing Layer. *Parallel CFD 92*, New Brunswick, New Jersey.
- POINSOT, T.J. & LELE, S.K. 1989 Boundary Conditions for Direct Simulations of Compressible Viscous Reacting Flows. *CTR manuscript 102*, Center for Turbulence Research, Stanford/NASA Ames.
- RAGAB, S.A. & SHEEN, S. 1990 Numerical Simulation of a Compressible Mixing Layer. AIAA paper 90-1669.
- RAGAB, S.A. & WU, J.L. 1989 Linear Instabilities in Two-Dimensional Compressible Mixing Layers. *Phys. Fluids* Vol A, 1, 957-966.

- ROGERS, R.D. & MOSER, M.M. 1989 The development of three-dimensional temporally-evolving mixing layers. *Seventh Symposium on Turbulent Shear Flows* 9-3, Stanford, California.
- ROSHKO, A. 1976 Structure of Turbulent Shear Flow: A New Look. *AIAA J.* Vol 14, 1349.
- RUDY D.H. & STRIKWERDA, J.C. 1980 A Nonreflecting Outflow Boundary Condition for Subsonic Navier-Stokes Calculation. *J. Comput. Phys.* Vol 36, 55-70.
- SAMIMY, M. & ELLIOT, G.S. 1988 Effects of Compressibility on the Structure of Free Shear Layers. AIAA paper 88-3054.
- SANDHAM, N.D. 1989 A Numerical Investigation of the Compressible Mixing Layer. *PhD Thesis*, Stanford University. Also available as SANDHAM, N.D. & REYNOLDS W.C. report No TF-45, Mechanical Engineering Department.
- SANDHAM, N.D. & REYNOLDS, W.C 1990 The Compressible Mixing Layer: Linear theory and Direct Simulation. *AIAA J.* Vol 28, 618-624.
- SANDHAM, N.D. & REYNOLDS, W.C 1991 Three-dimensional simulation of the compressible mixing layer. *J. Fluid Mech.* Vol 224, 133-158.
- SHAU, Y.R. & DOLLING, D.S. 1989 Experimental Study of Spreading Rate Enhancement of High Mach Number Turbulent Shear Layers. AIAA paper 89-2458.
- SHIN, D.S. & FERZIGER, J.H. 1991 Linear Stability of the Reacting Mixing Layer. *AIAA J.* Vol 29, 1634-1642.
- SHIN, D.S. & FERZIGER, J.H. 1991 Effects of Walls on the Supersonic Reacting Mixing Layer. *Annual Research Brief*, Center for Turbulence Research, Stanford/NASA Ames.
- SHIVAMOGGI, B.K 1977 Inviscid Theory of Stability of Parallel Compressible Flows. *Journal of Mecanique* Vol 16, 227.
- SQUIRE, H.B. 1933 On the stability for Three-Dimensional Disturbances of Viscous Fluid Flow Between Parallel Walls. *Proc. Royal Soc of London* Vol 142, 621-628.
- STUART, J.T. 1967 On finite amplitude oscillations in laminar mixing layer. *J. Fluid Mech.* Vol 29, 417.
- TAM, C.K. 1971 Directional Acoustic Radiation from a Supersonic Jet. *J. Fluid Mech.* Vol 46, 757-768.

- TAM, C.K. & HU, F.Q. 1989 The Instability and Acoustic Modes of Supersonic Mixing Layers inside a Rectangular Channel. *J. Fluid Mech.* Vol 203, 51-76.
- TAM, C.K. & LELE, S.K. 1990 Resonant instability of supersonic shear layers. *Proceedings of the 1990 Summer Program*, Center for Turbulence Research, Stanford/NASA Ames.
- THOMPSON, K.W. 1987 Time dependent Boundary Conditions for Hyperbolic Systems. *J. Comput. Phys.* Vol 68, 1-24.
- TROUVE, A. 1989 Instabilités hydrodynamiques et instabilités de combustion et flammes turbulentes prémelangées. *Thèse E.C.P.*, Labo EM2C, Ecole Centrale de Paris, France.
- TROUVE, A. & CANDEL, S.M. 1988 Linear Stability of The Inlet Jet in a Ramjet Dump Combustor. AIAA paper 88-0149.
- WINANT, C.D. & BROWAND, F.K. 1974 Vortex Pairing: The Mechanism of Turbulent Mixing-Layer Growth at Moderate Reynolds Number. *J. Fluid Mech.* Vol 63, 237-255.
- WRAY, A.A. 1986 Very low storage time-advancement schemes. *Internal Report*, NASA-Ames Research Center, Moffett Field, California.
- WRAY, A.A. 1988 Vectoral Manual. *Internal Report*, NASA-Ames Research Center, Moffett Field, California.
- YIP, B., LOZANO, A., & HANSON, R.K. 1992 Simultaneous OH, air and Fuel imaging in turbulent diffusion flames. To be published in Experiments in Fluids.

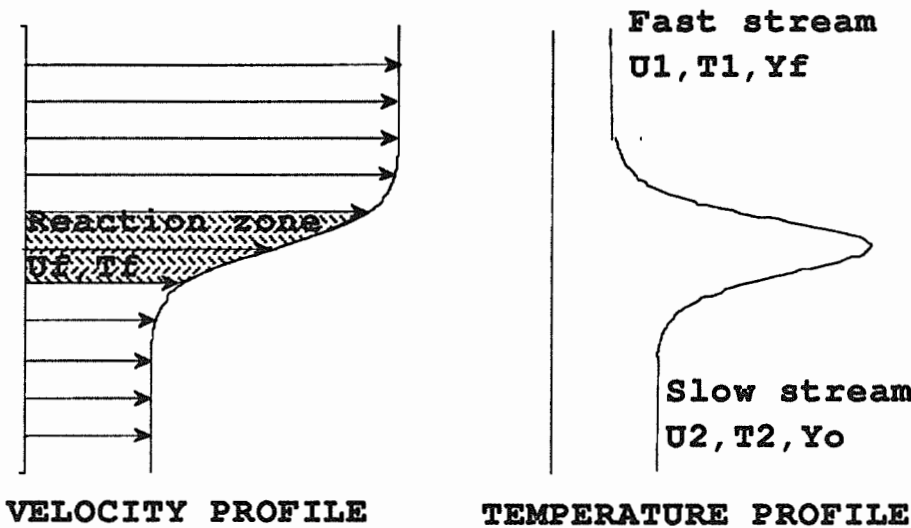


Figure 2.1: Mean Flow Configuration

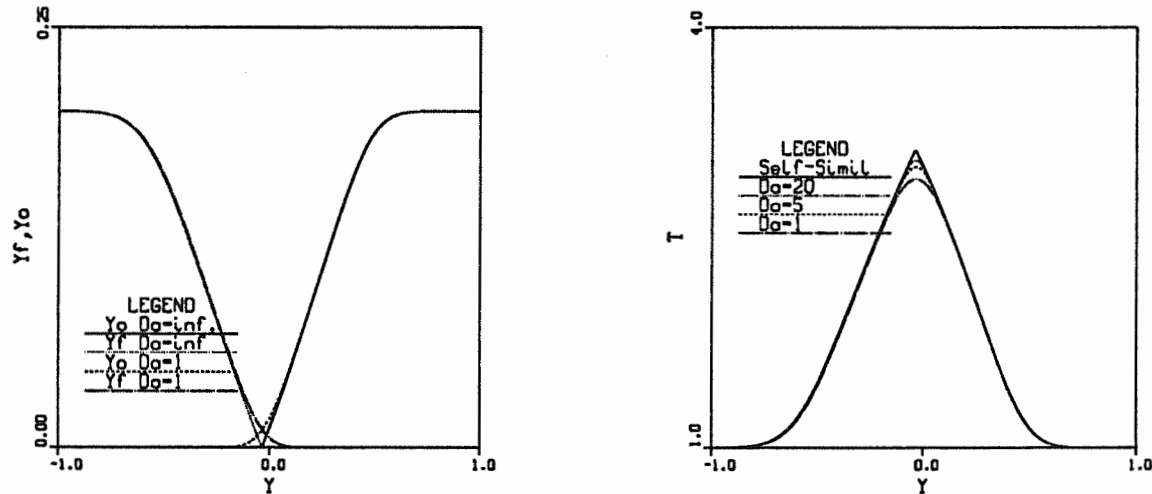


Figure 2.2: Comparison of the mean species profiles (left) and temperature profiles (right) calculated using the self-similar solution to the solution obtained by solving the complete compressible finite-chemistry boundary layer equations

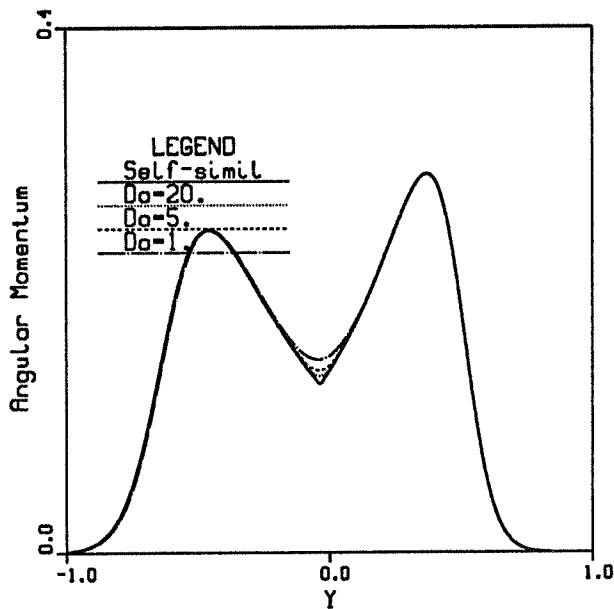


Figure 2.3: Comparison of the mean density-weighted vorticity profiles calculated using the self-similar solution to the solution obtained by solving the complete compressible final-chemistry boundary layer equations

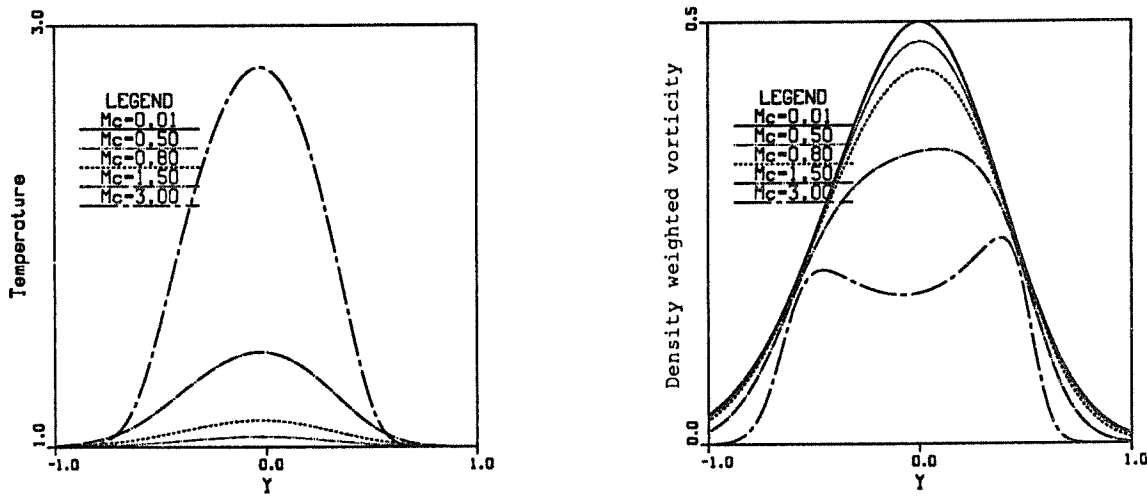


Figure 2.4: Mean temperature (left) and density-weighted vorticity ($\bar{\rho}d\bar{u}/dy$) (right) profiles of the compressible mixing layer without heat release. Note the existence of two peaks at high Mach numbers

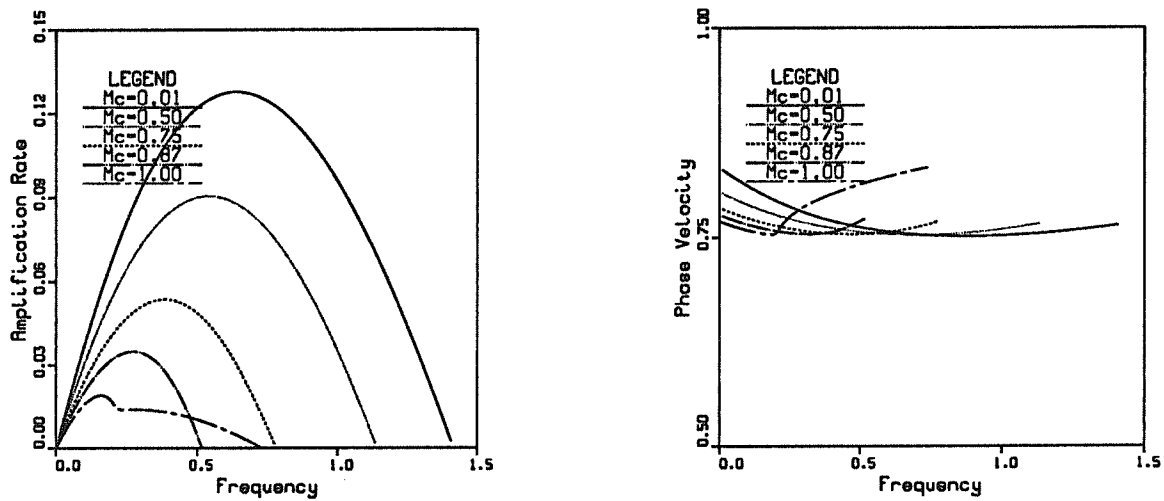


Figure 2.5: Compressibility effects on the amplification rate and phase speed of the central mode of the compressible mixing layer without heat release. The mean profile is dependent on M_c .

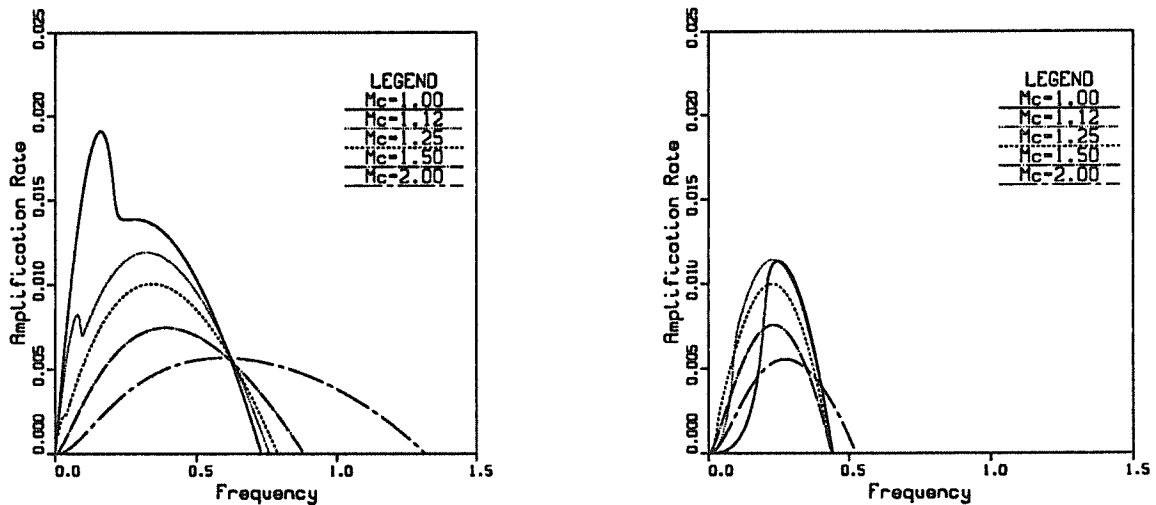


Figure 2.6: Compressibility effects on the spatial amplification rates of the outer modes of the compressible mixing layer without heat release ($M_c > 1.00$) Left: fast instability mode. Right: slow instability mode.

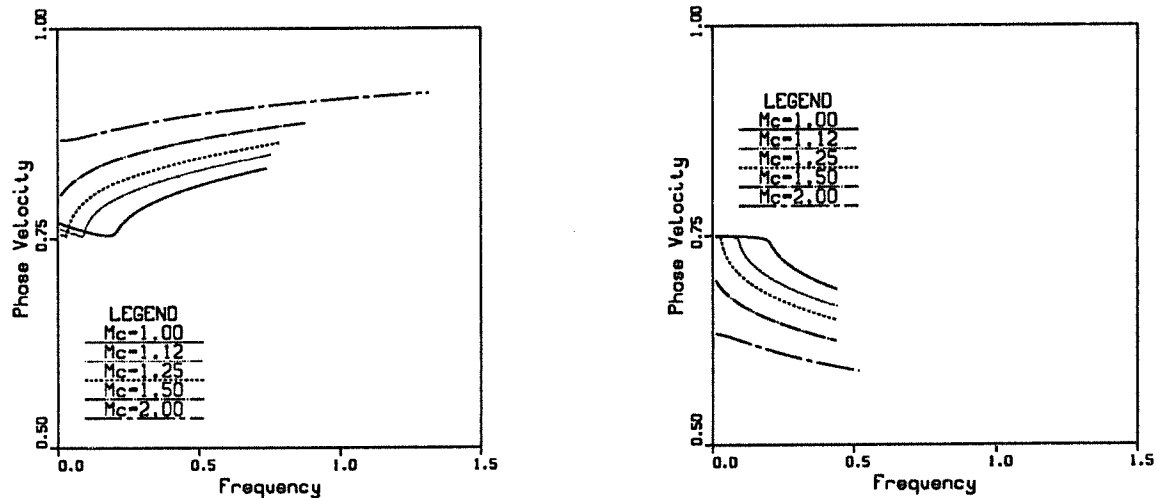


Figure 2.7: Compressibility effects on the phase speeds of the outer modes of the compressible mixing layer without heat release ($Mc > 1.00$) Left: fast instability mode. Right: slow instability mode.

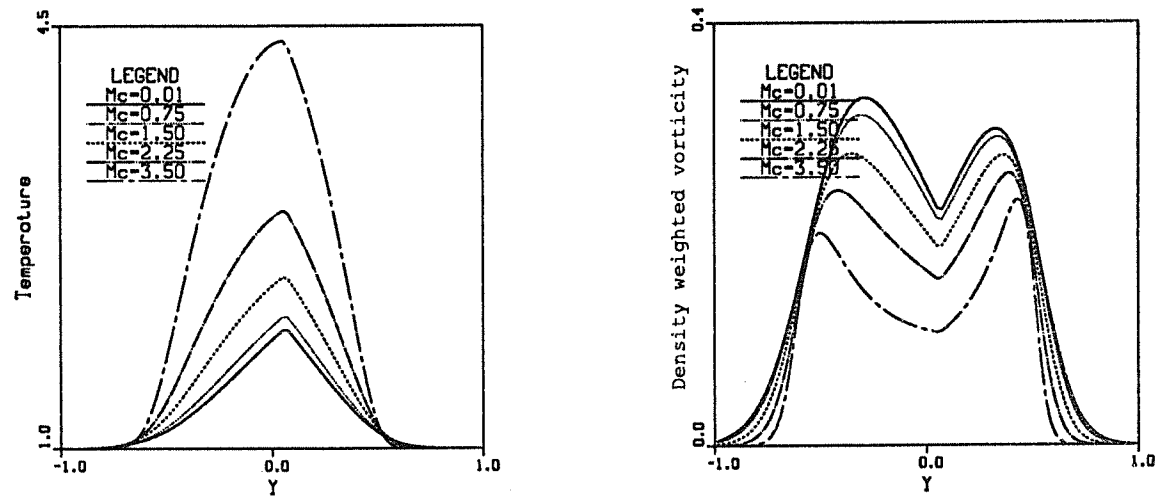


Figure 2.8: Mean temperature (left) and density-weighted vorticity ($\bar{\rho}d\bar{u}/dy$) (right) profiles of the compressible mixing layer with heat release ($\Theta = 1.00$). Note the existence of two peaks at all Mach numbers

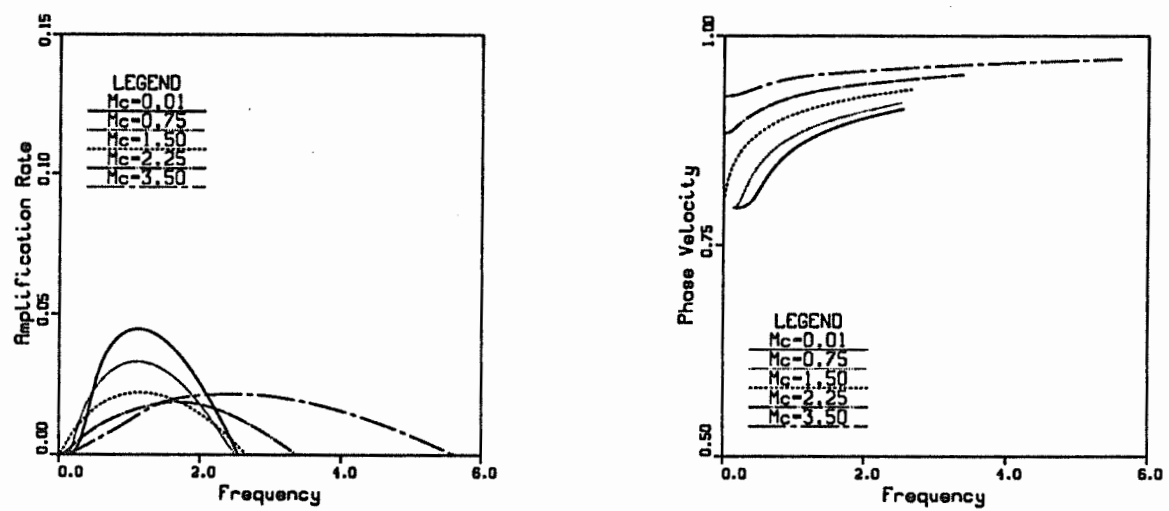


Figure 2.9: Amplification rate and phase speed of the fast outer mode of the compressible mixing layer with heat release ($\Theta = 1.00$).

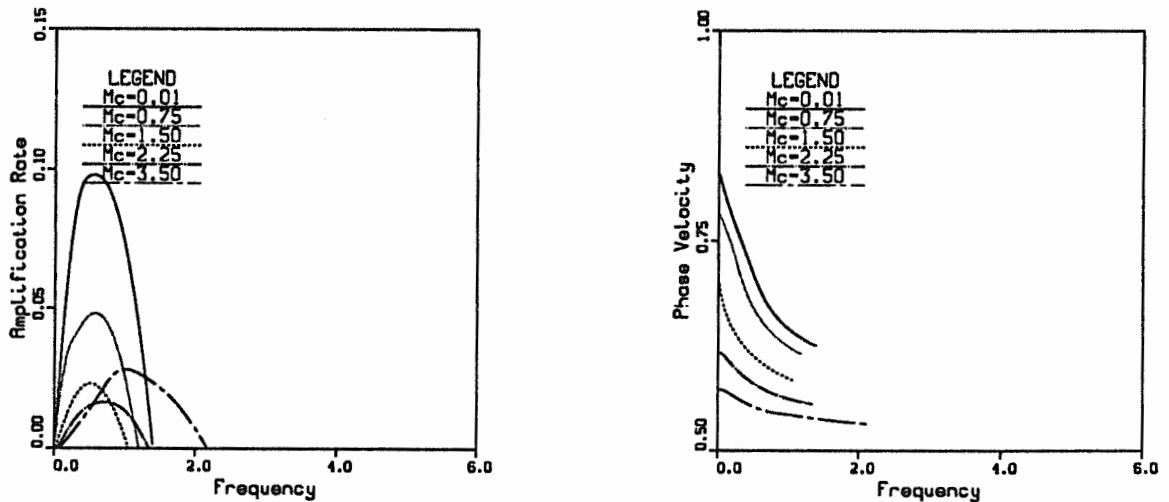


Figure 2.10: Amplification rate and phase speed of the slow outer mode of the compressible mixing layer with heat release ($\Theta = 1.00$)

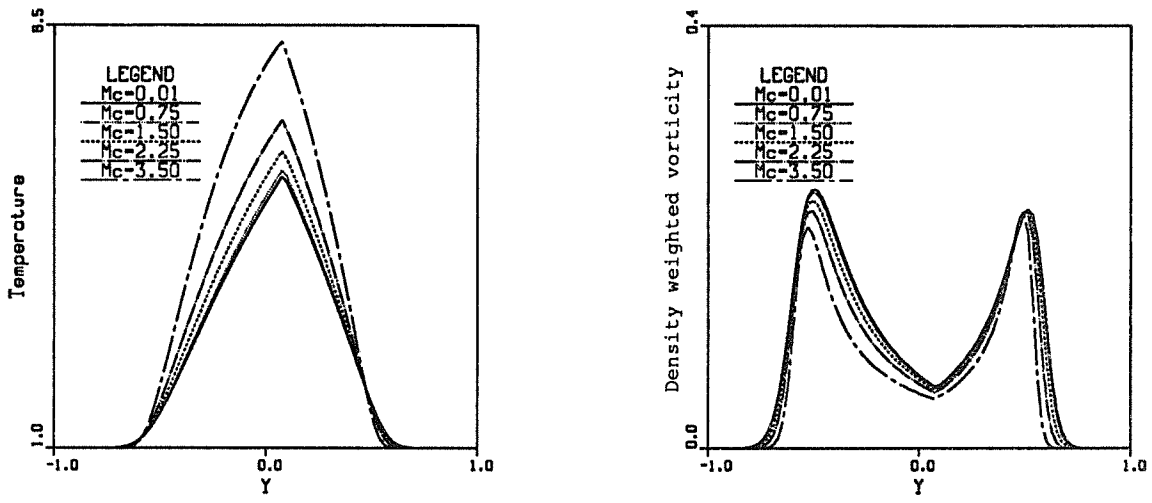


Figure 2.11: Mean temperature (left) and density-weighted vorticity ($\bar{\rho}d\bar{u}/dy$) (right) profiles of the compressible mixing layer with heat release ($\Theta = 4.85$). Note the existence of two peaks at all Mach numbers

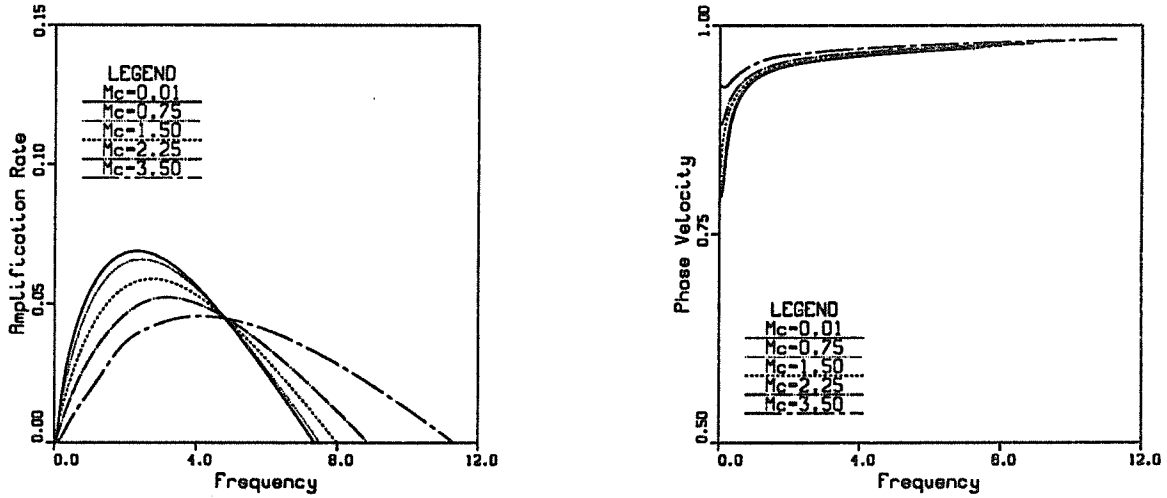


Figure 2.12: Amplification rate and phase speed of the fast outer mode of the compressible mixing layer with heat release ($\Theta = 4.85$)

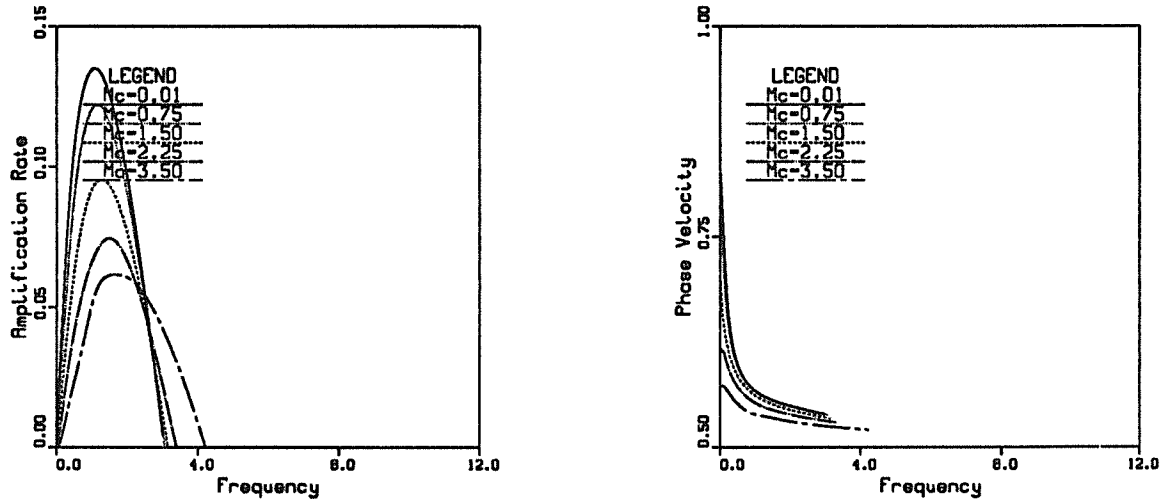


Figure 2.13: Amplification rate and phase speed of the slow outer mode of the compressible mixing layer with heat release ($\Theta = 4.85$)

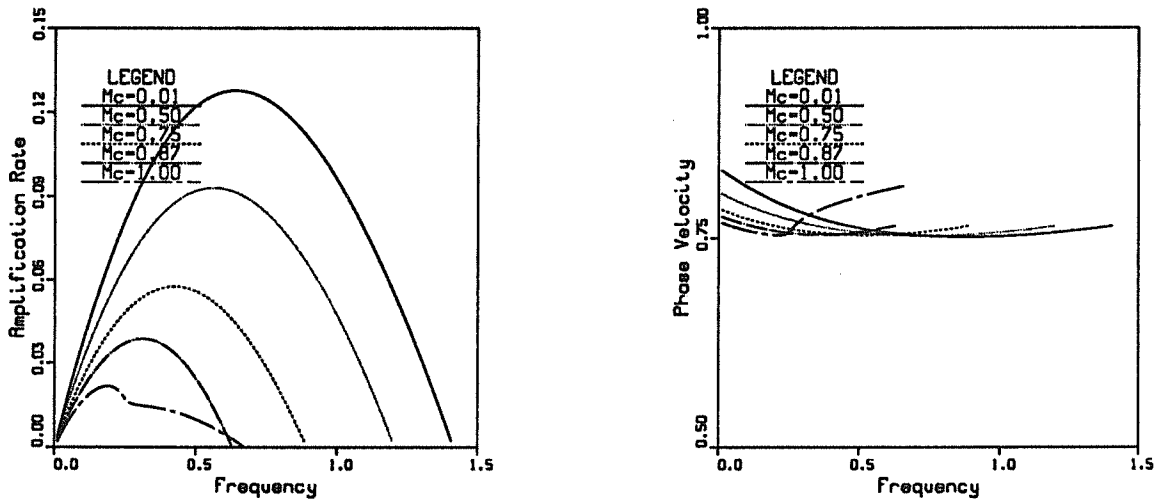


Figure 2.14: Compressibility effects on the amplification rate and phase speed of the central mode of the compressible mixing layer without heat release. (Mean profile corresponding to $M_c = 0.01$).

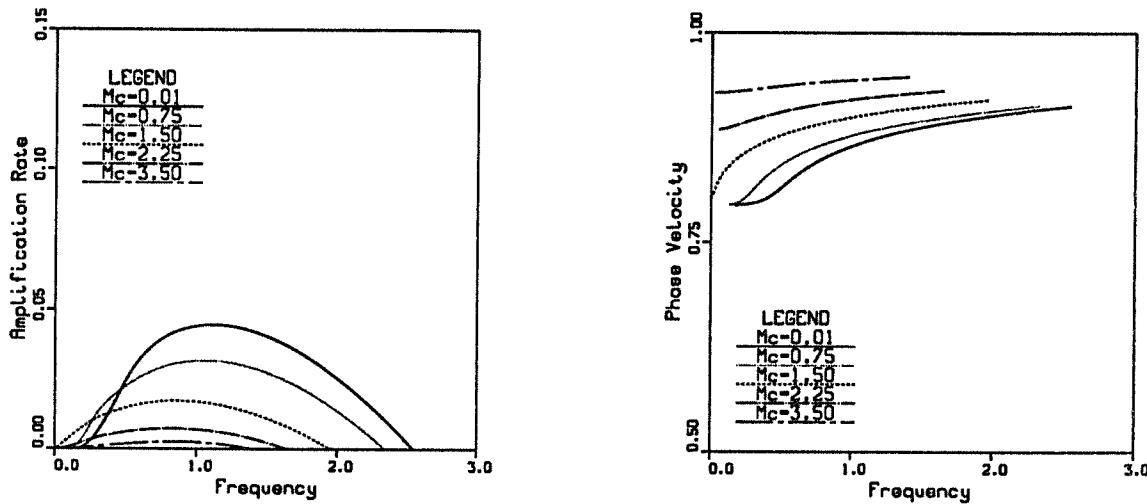


Figure 2.15: Compressibility effects on the amplification rate and phase speed of the fast outer mode the compressible mixing layer with heat release ($\Theta = 1.00$. Mean profile corresponding to $M_c = 0.01$)

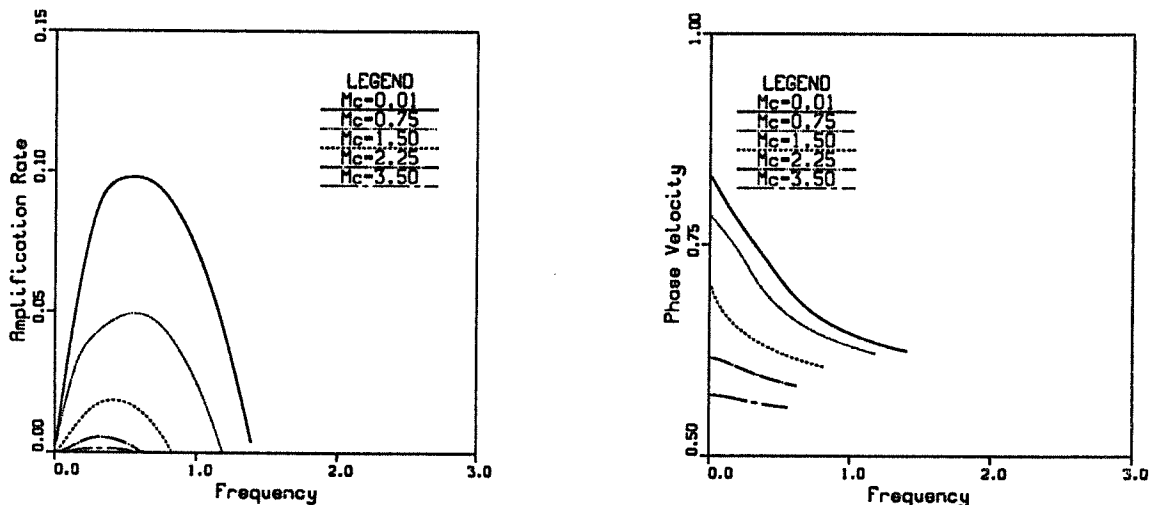
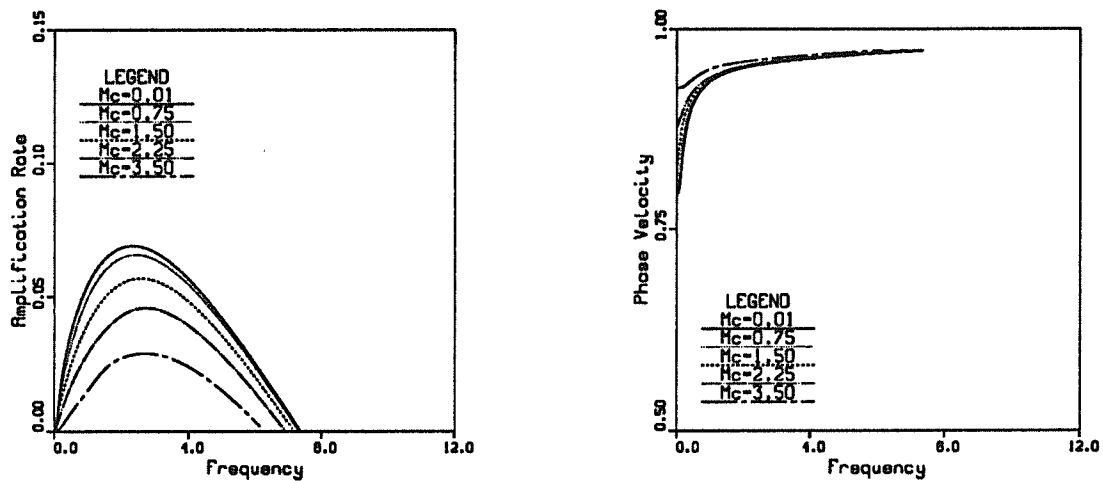


Figure 2.16: Compressibility effects on the amplification rate and phase speed of the slow outer mode the compressible mixing layer with heat release ($\Theta = 1.00$. Mean profile corresponding to $M_c = 0.01$)



Figures 2.17: Compressibility effects on the amplification rate and phase speed of the fast outer mode of the mixing layer with high heat release ($\Theta = 4.85$. Mean profile corresponding to $M_c = 0.01$)

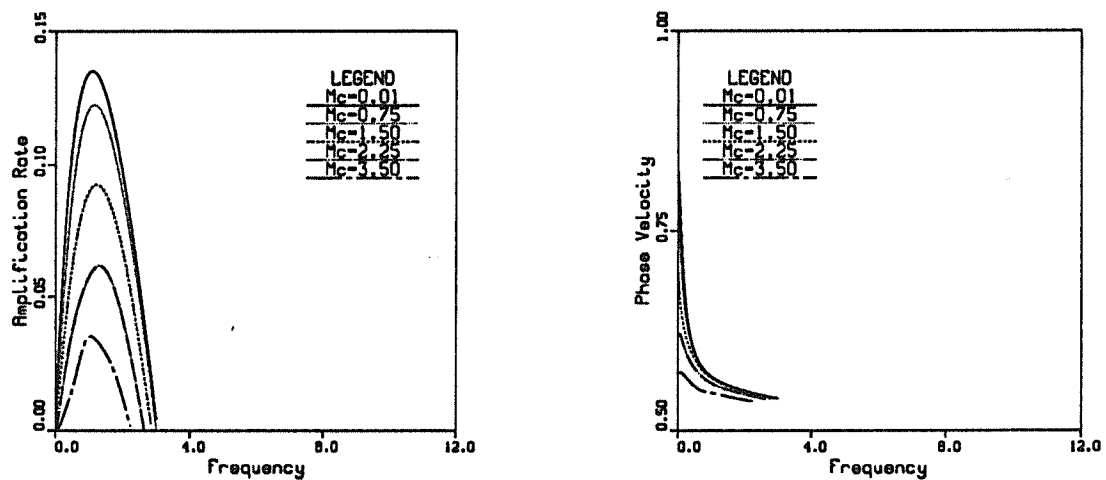


Figure 2.18: Compressibility effects on the amplification rate and phase speed of the slow outer mode of the mixing layer with high heat release ($\Theta = 4.85$. Mean profile corresponding to $M_c = 0.01$)

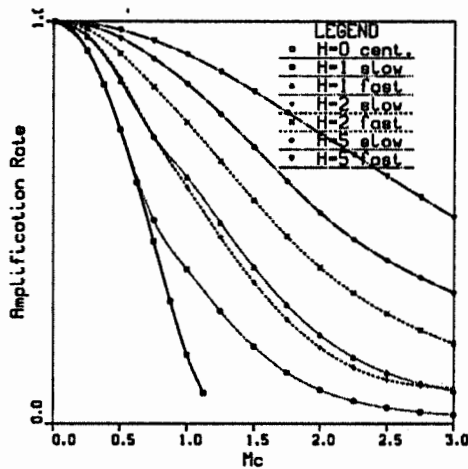


Figure 2.19: Compressibility effects on the amplification of various 2-D instability modes for various heat release (H) (mean profile at $M_c = 0.01$).

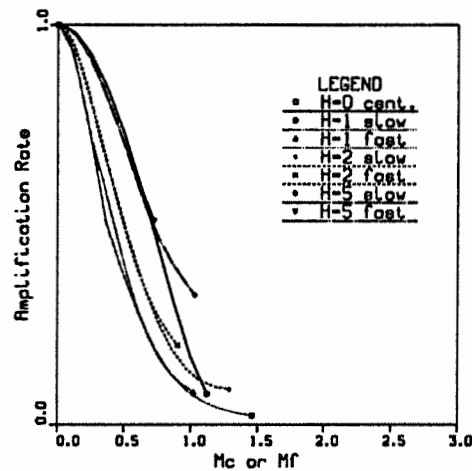


Figure 2.20: Validation of the flame convective Mach numbers. Compressibility effects on the amplification of various 2-D instability modes for various heat release. Here M_c is used for the central mode and M_f for the outer modes. (mean profile at $M_c = 0.01$). Note that the collapse gets better as heat release is increased and that at a given heat release the amplification rates of the fast and the slow outer modes overlap.

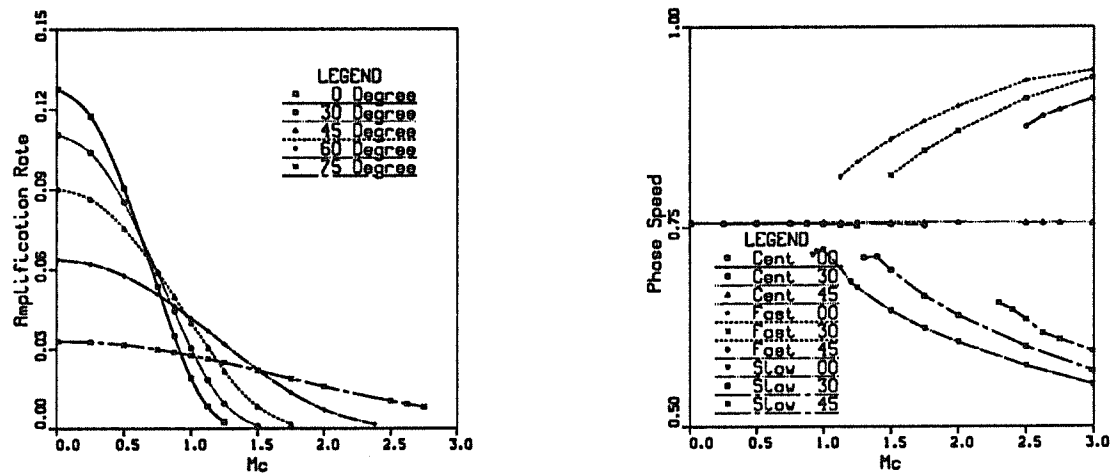


Figure 2.21 (left): Mach number effects on the obliquity of the central mode of the compressible mixing layer without heat release ($\Theta = 0$). Amplification rates at various obliquities.

Figure 2.22 (right): Mach number effects on the obliquity of the central mode of the compressible mixing layer without heat release ($\Theta = 0$). Phase speeds at various obliquities.

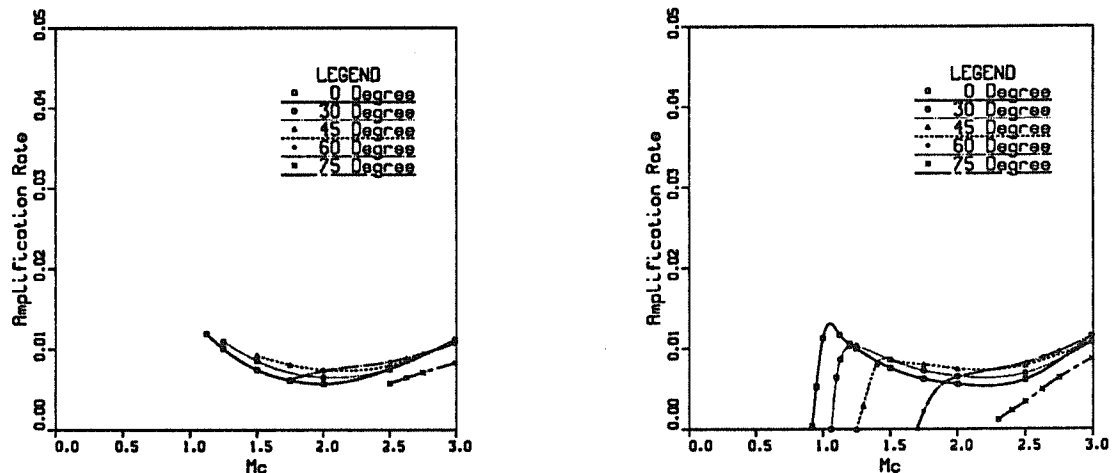


Figure 2.23: Mach number effects on the obliquity of the instability modes of the compressible mixing layer without heat release ($\Theta = 0$). Left: amplification rate of the fast mode. Right: amplification rate of the slow mode.

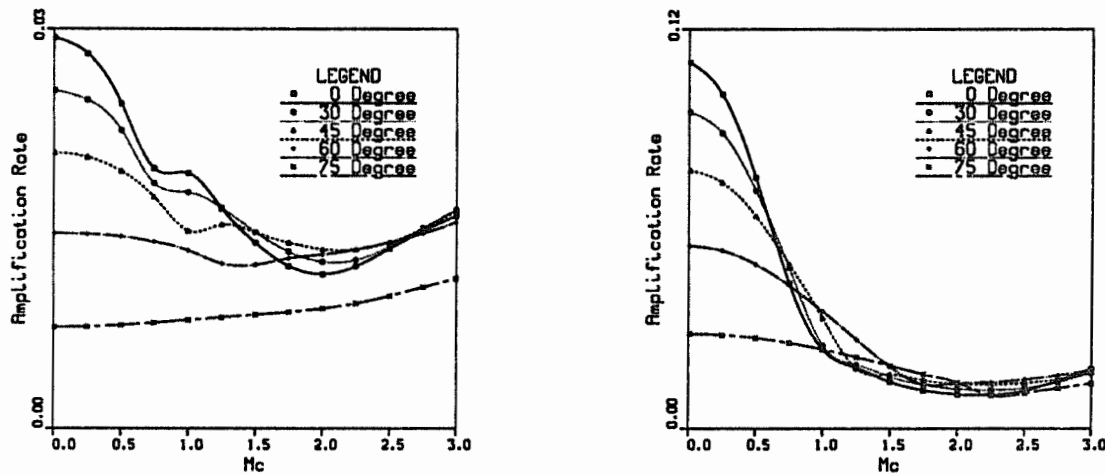


Figure 2.24: Mach number effects on the obliquity of the instability modes of the compressible mixing layer with low heat release ($\Theta = 0.50$). Left: amplification rate of the fast instability mode. Right: amplification rate of the slow instability mode.

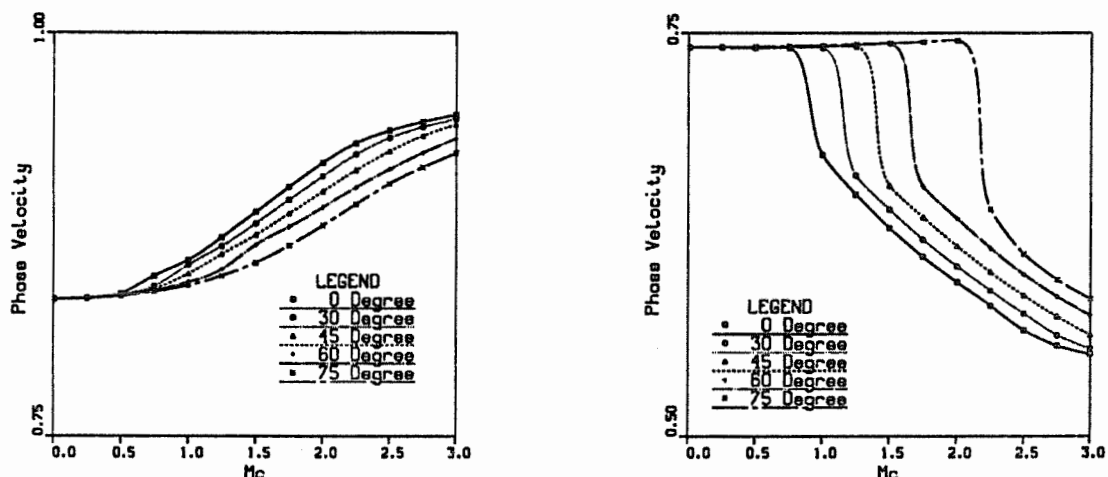


Figure 2.25: Mach number effects on the obliquity of the instability modes of the compressible mixing layer with low heat release ($\Theta = 0.50$). Left: phase speed of the fast instability mode. Right: phase speed of the slow instability mode.

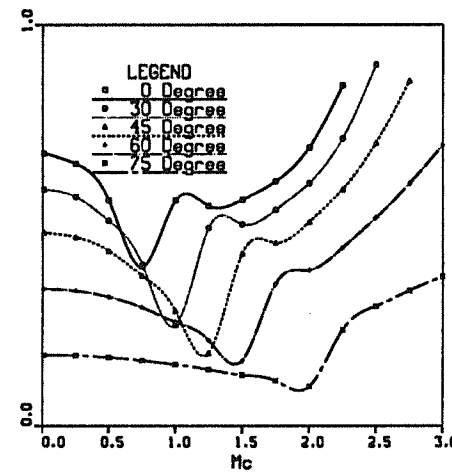
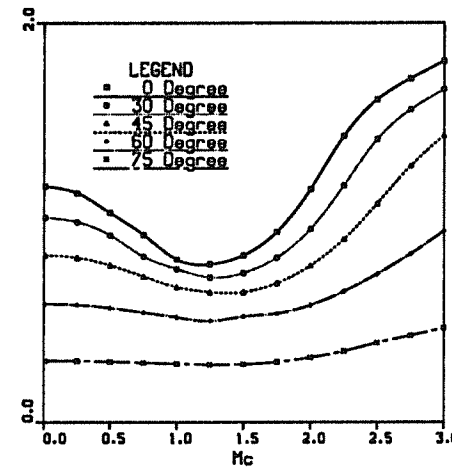


Figure 2.26: Mach number effects on the obliquity of the instability modes of the compressible mixing layer with low heat release ($\Theta = 0.50$). Top: wavenumber of the fast instability mode. Bottom: wavenumber of the slow instability mode.

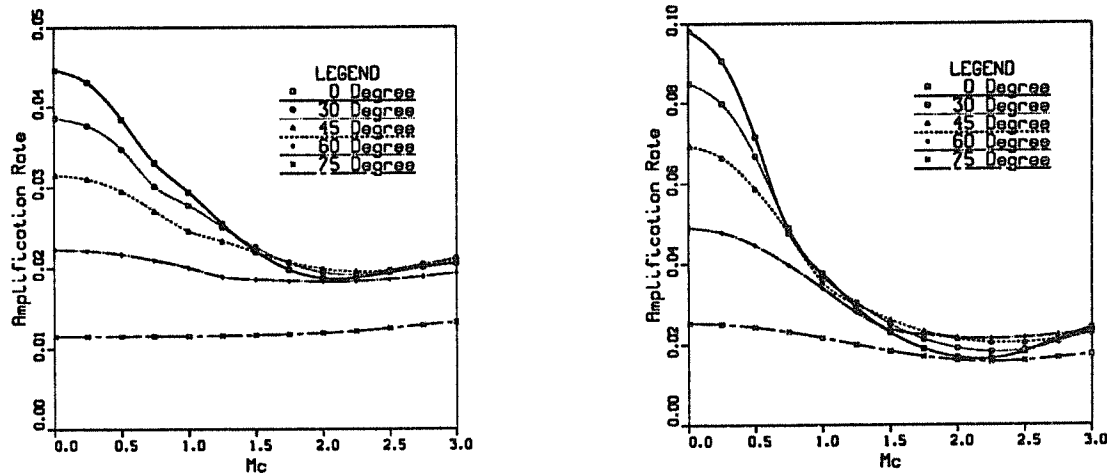


Figure 2.27: Mach number effects on the obliquity of the instability modes of the compressible mixing layer with moderate heat release ($\Theta = 1.00$). Left: amplification rate of the fast instability mode. Right: amplification rate of the slow instability mode.

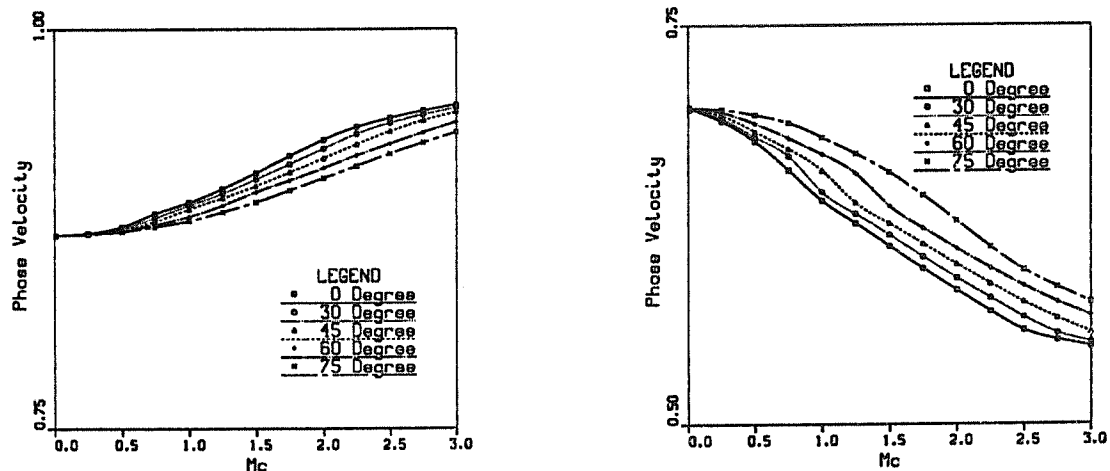


Figure 2.28: Mach number effects on the obliquity of the instability modes of the compressible mixing layer with moderate heat release ($\Theta = 1.00$). Left: phase speed of the fast instability mode. Right: phase speed of the slow instability mode.

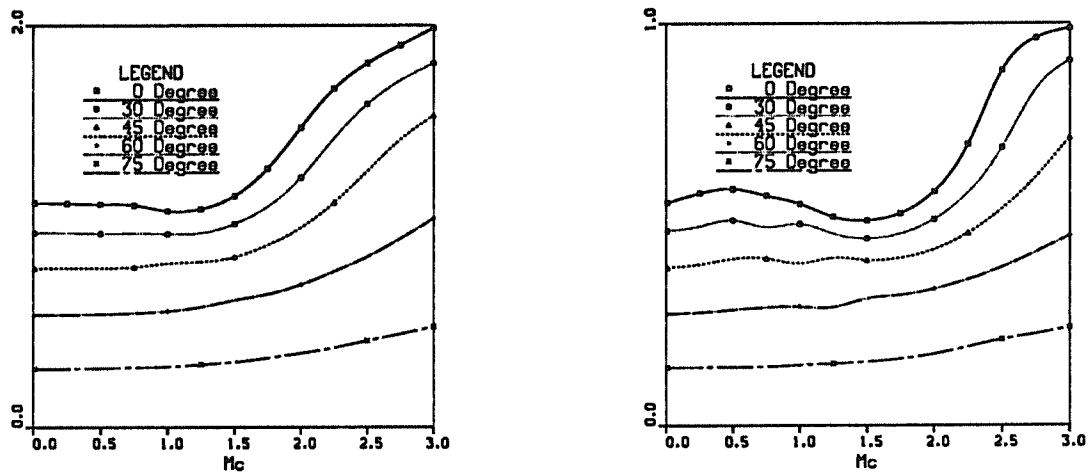


Figure 2.29: Mach number effects on the obliquity of the instability modes of the compressible mixing layer with moderate heat release ($\Theta = 1.00$). Left: wavenumber of the fast instability mode. Right: wavenumber of the slow instability mode.

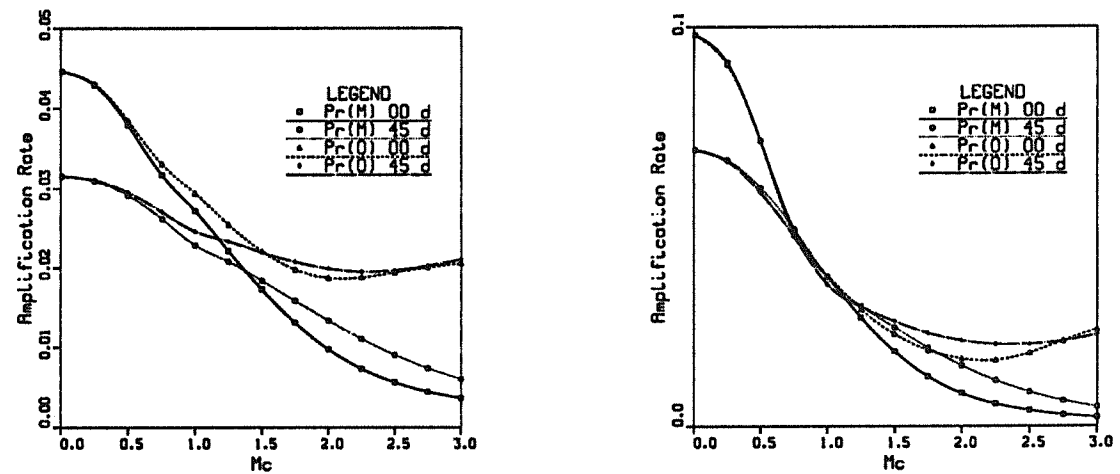


Figure 2.30: Comparison of compressibility effects on the amplification rates of the fast (left) and slow (right) outer modes when the profile is changed with M_c or kept equal to the profile at $M_c = 0.01$ ($\Theta = 1.00$)

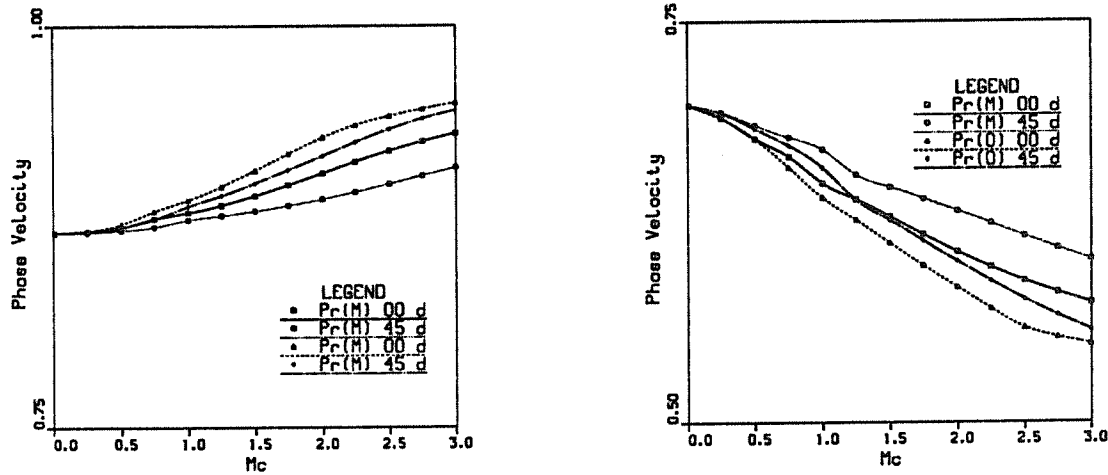


Figure 2.31: Comparison of compressibility effects on the phase speeds of the fast (left) and slow (right) outer modes when the profile is changed with M_c or kept equal to the profile at $M_c = 0.01$ ($\Theta = 1.00$)

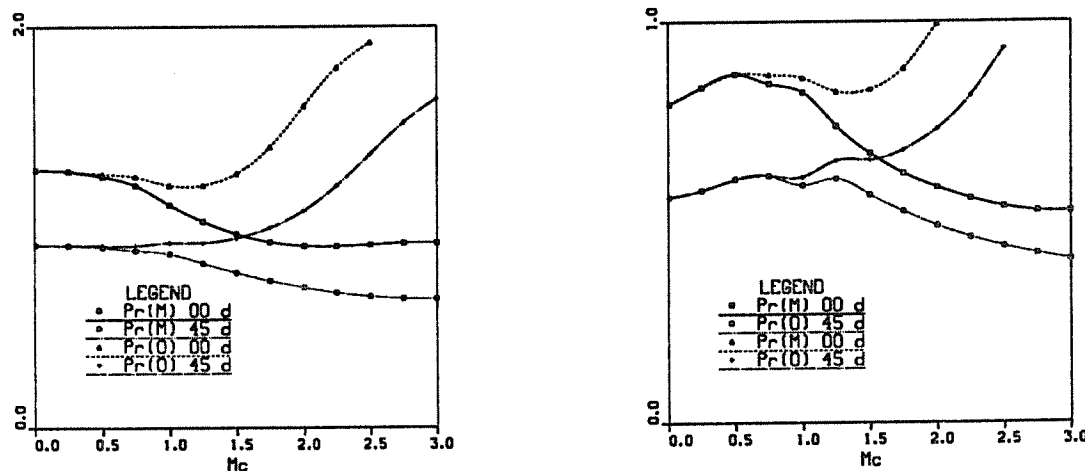


Figure 2.32: Comparison of compressibility effects on the wavenumbers of the fast (left) and slow (right) outer modes when the profile is changed with M_c or kept equal to the profile at $M_c = 0.01$ ($\Theta = 1.00$)

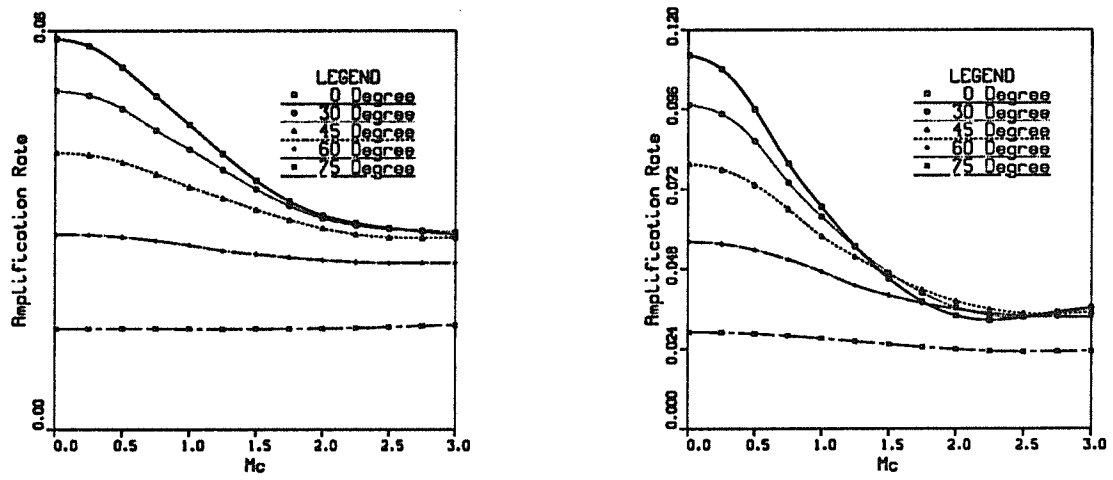


Figure 2.33: Mach number effects on the obliquity of the instability modes of the compressible mixing layer with high heat release ($\Theta = 2.00$). Left: amplification rate of the fast instability mode. Right: amplification rate of the slow instability mode.

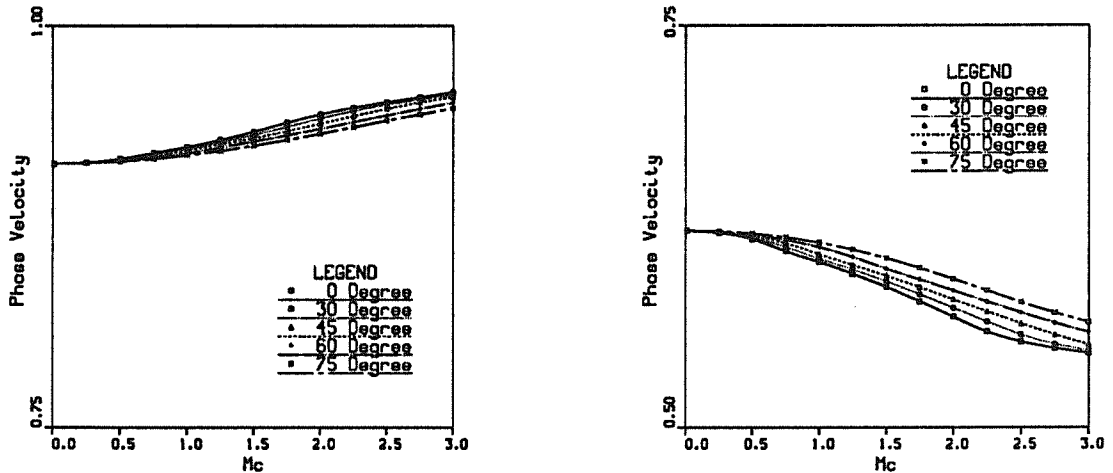


Figure 2.34: Mach number effects on the obliquity of the instability modes of the compressible mixing layer with high heat release ($\Theta = 2.00$). Left: phase speed of the fast instability mode. Right: phase speed of the slow instability mode.

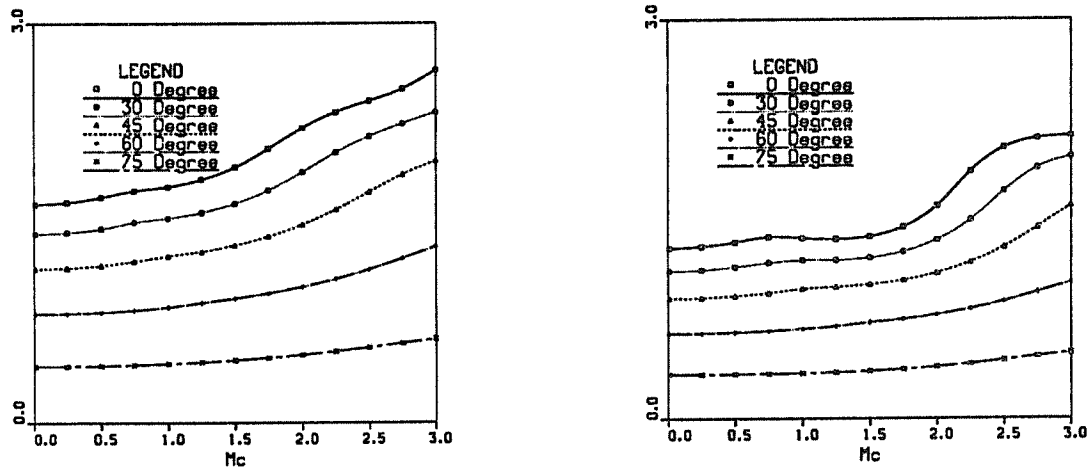


Figure 2.35: Mach number effects on the obliquity of the instability modes of the compressible mixing layer with high heat release ($\Theta = 2.00$). Top: wavenumber of the fast instability mode. Bottom: wavenumber of the slow instability mode.

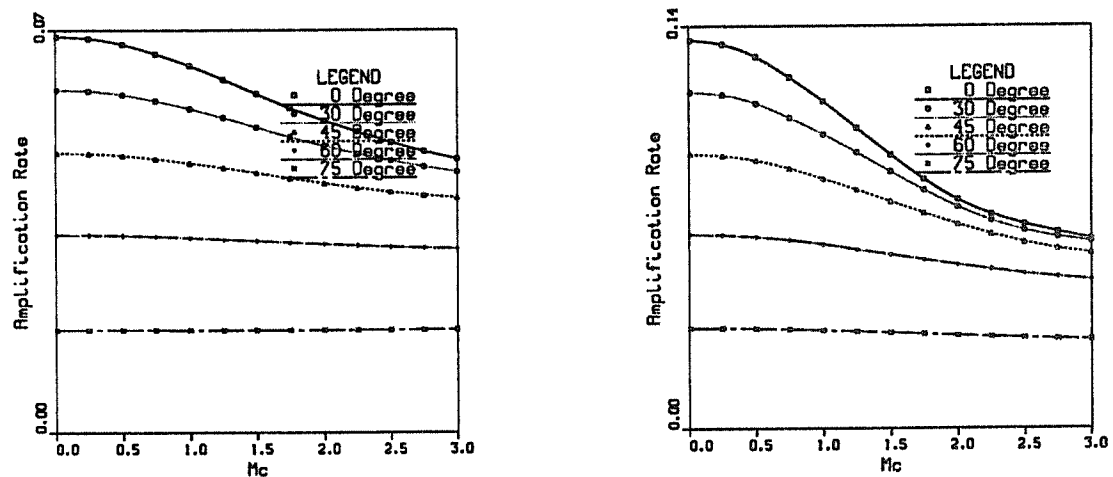


Figure 2.36: Mach number effects on the obliquity of the instability modes of the compressible mixing layer with high heat release ($\Theta = 4.85$). Left: amplification rate of the fast instability mode. Right: amplification rate of the slow instability mode.

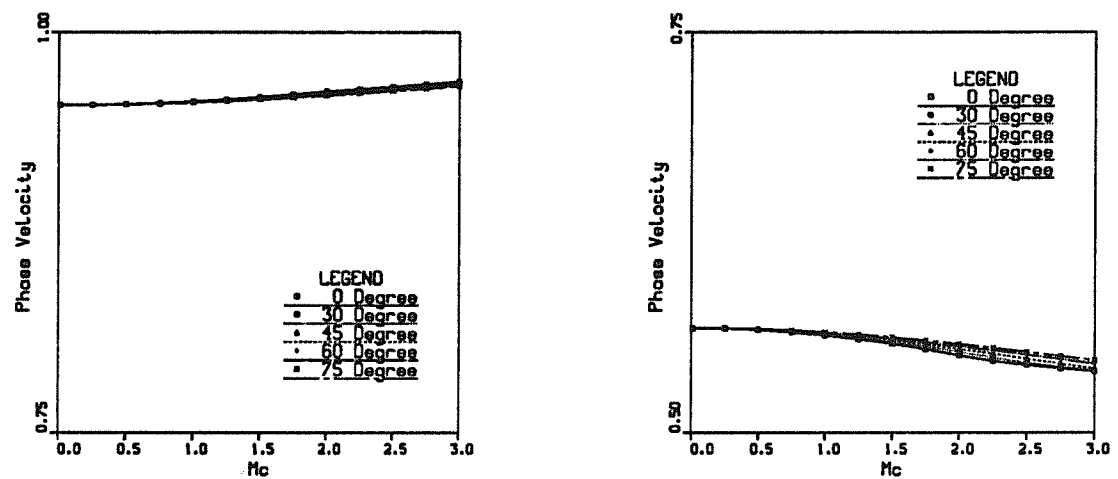


Figure 2.37: Mach number effects on the obliquity of the instability modes of the compressible mixing layer with high heat release ($\Theta = 4.85$). Left: phase speed of the fast instability mode. Right: phase speed of the slow instability mode.

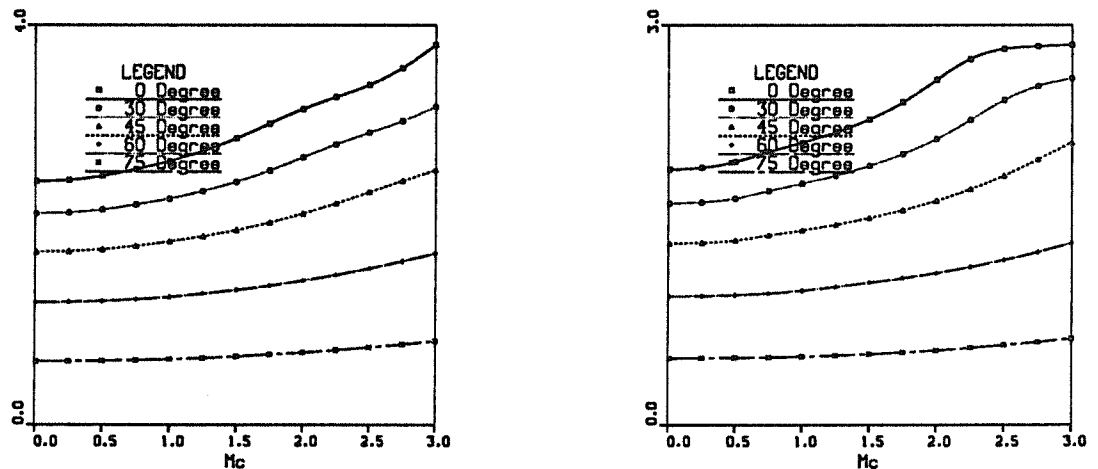


Figure 2.38: Mach number effects on the obliquity of the instability modes of the compressible mixing layer with high heat release ($\Theta = 4.85$). Left: wavenumber of the fast instability mode. Right: wavenumber of the slow instability mode.

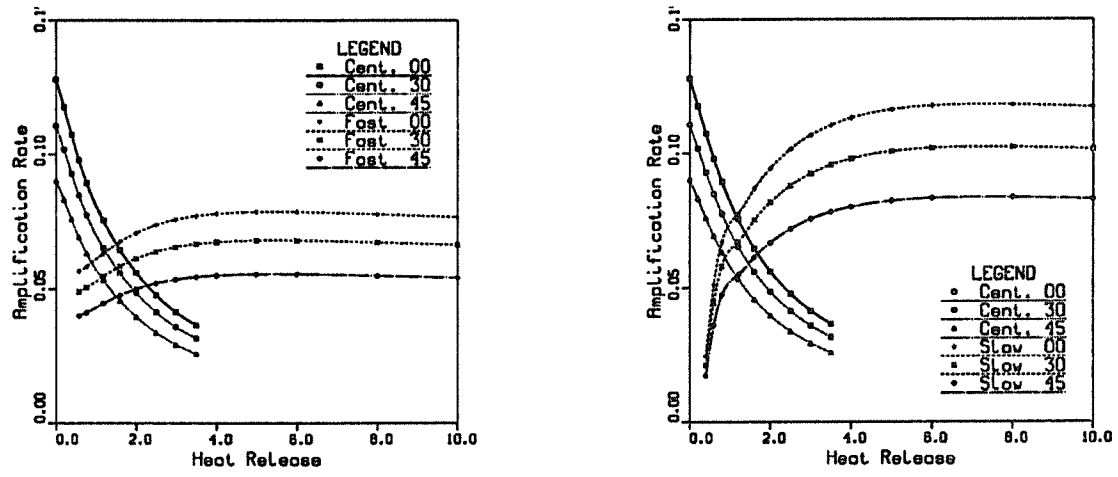


Figure 2.39: Left: Comparison of heat release effects on the amplification rates of the central and fast outer modes at $M_c = 0.01$. Right: same for the central and slow outer modes.

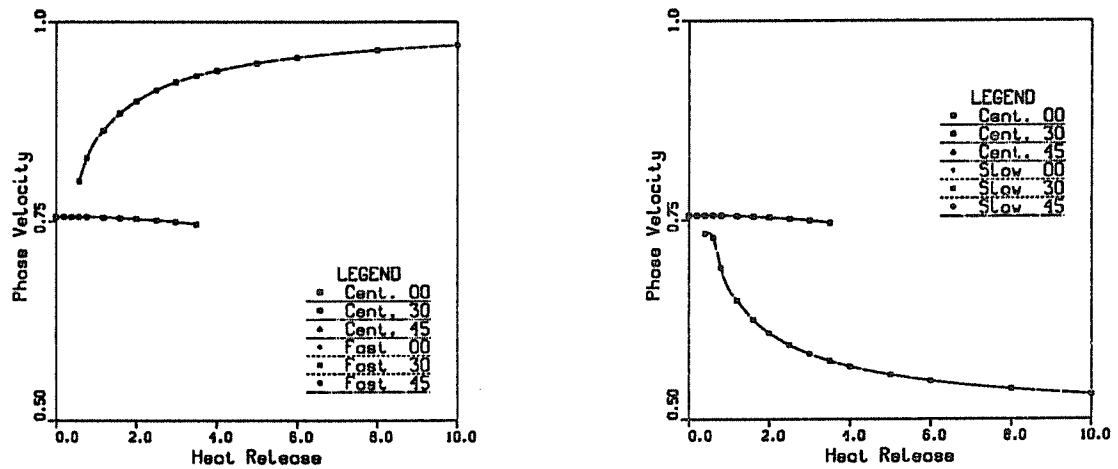


Figure 2.40: Left: Comparison of heat release effects on the phase speeds of the central and fast outer modes at $M_c = 0.01$. Right: same for the central and slow outer modes.

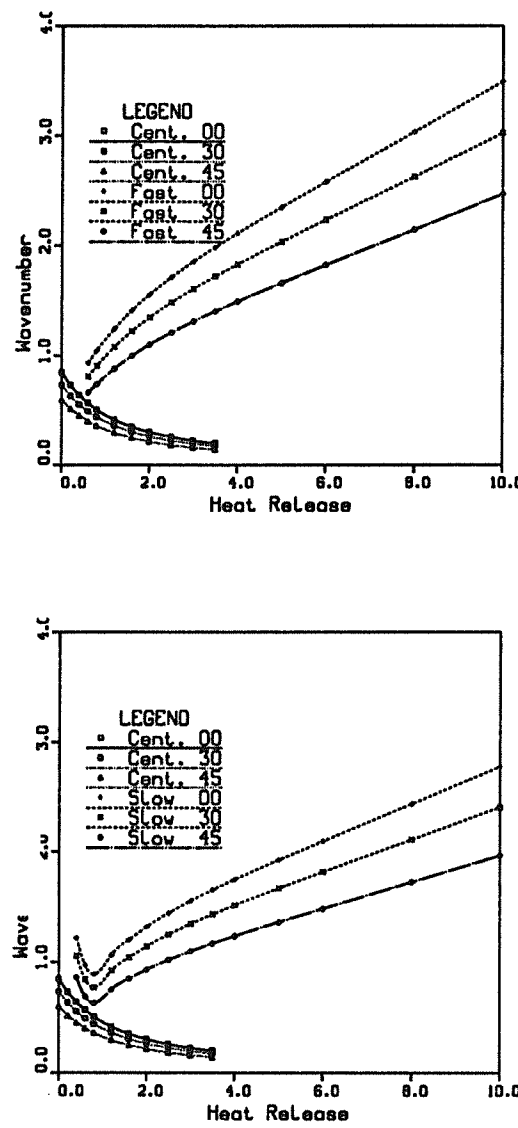


Figure 2.41: Top: Comparison of heat release effects on the wavenumbers of the central and fast outer modes at $M_c = 0.01$. Bottom: same for the central and slow outer modes.

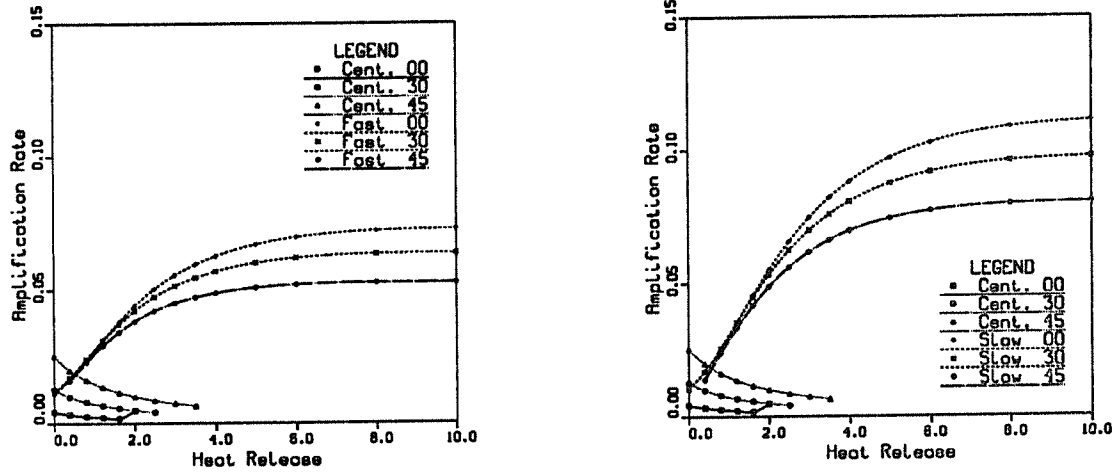


Figure 2.42: Left: Comparison of heat release effects on the amplification rate of the central and fast outer modes at $M_c = 1.20$. Right: Same for the central and slow outer modes.

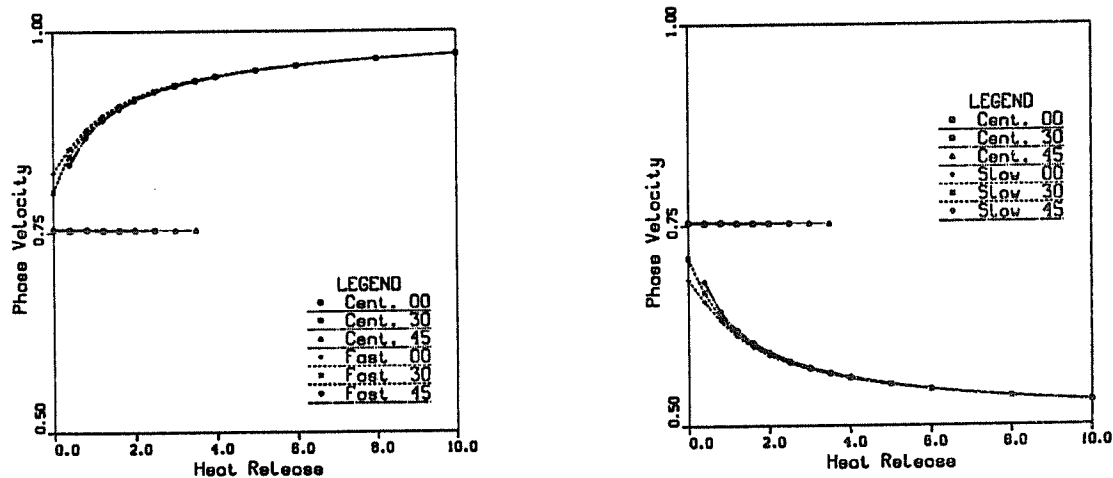


Figure 2.43: Left: Comparison of heat release effects on the wavenumber of the central and fast outer modes at $M_c = 1.20$. Right: Same for the central and slow outer modes.

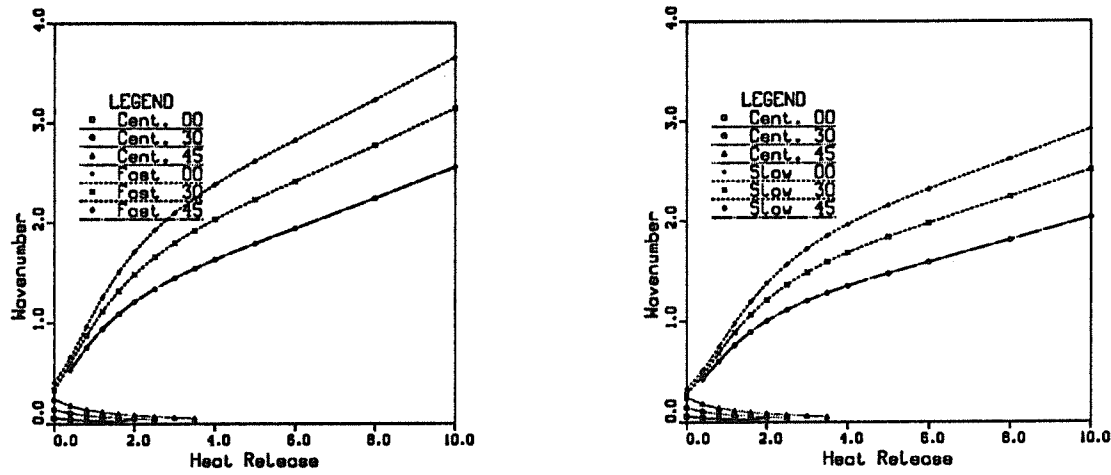


Figure 2.44: Comparison of heat release effects on the wavenumbers of the central and slow outer modes at $M_c = 1.20$. Right: Same for the central and slow outer modes.

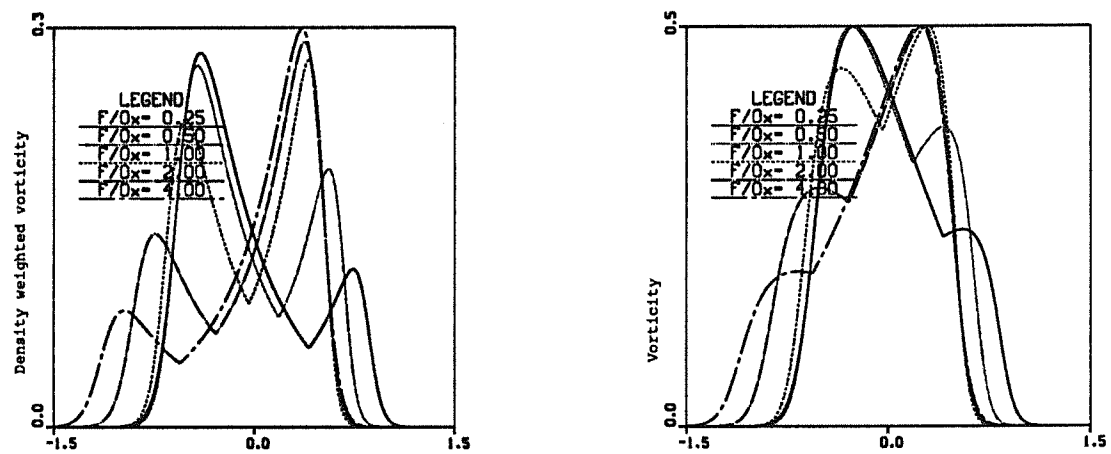


Figure 2.45: Left: Influence of the fuel-equivalence ratio on the mean density-weighted vorticity profile ($\bar{\rho}d\bar{u}/dy$). Right: Influence of the fuel-equivalence ratio on the mean vorticity profile ($d\bar{u}/dy$). ($M_c = 0.01$).

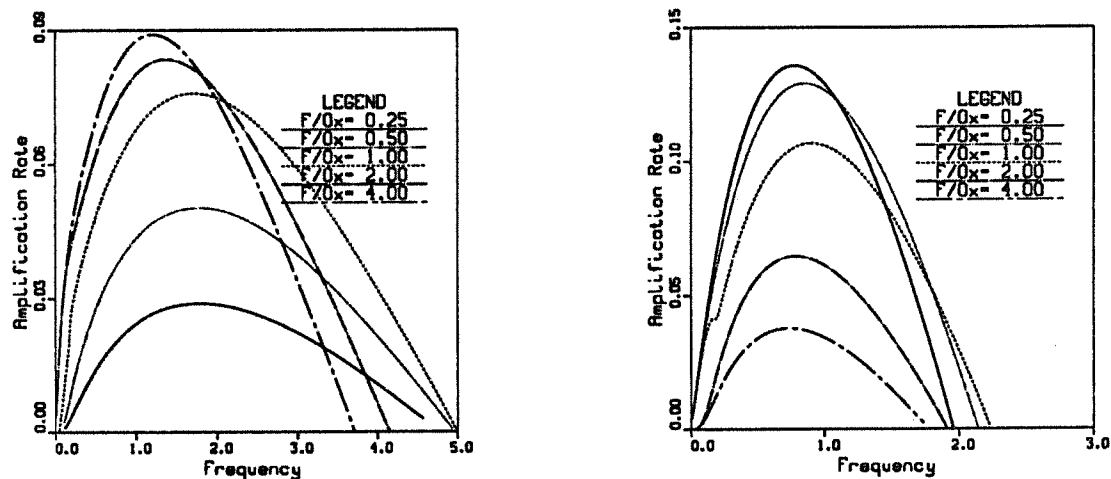


Figure 2.46: Influence of the fuel-equivalence ratio on the amplification rates of the fast (left) and slow (right) outer modes. ($M_c = 0.01$).

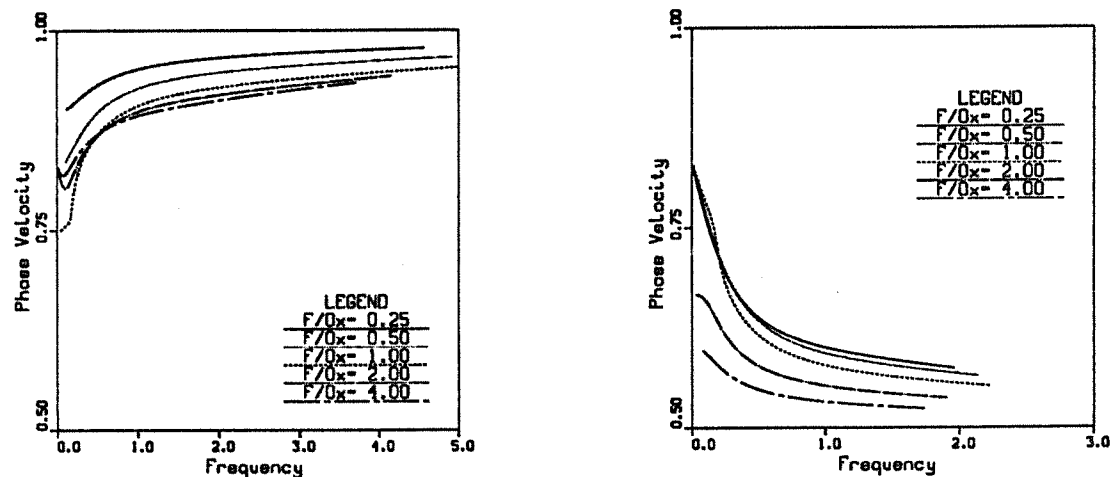


Figure 2.47: Influence of the fuel-equivalence ratio on the phase speeds of the fast (left) and slow (right) outer modes. ($M_c = 0.01$).

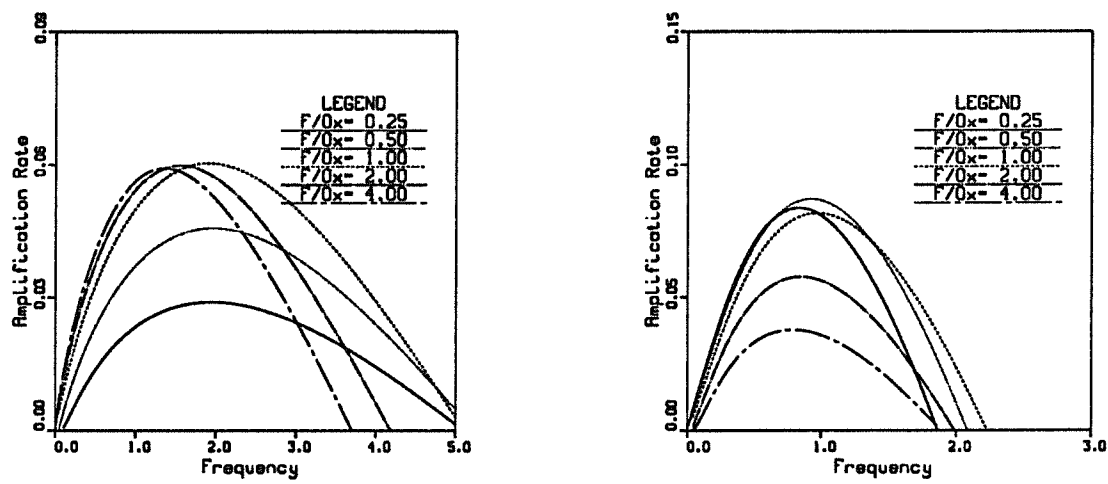


Figure 2.48: Influence of the fuel-equivalence ratio on the amplification rates of the fast (left) and slow (right) outer modes. ($M_c = 1$).

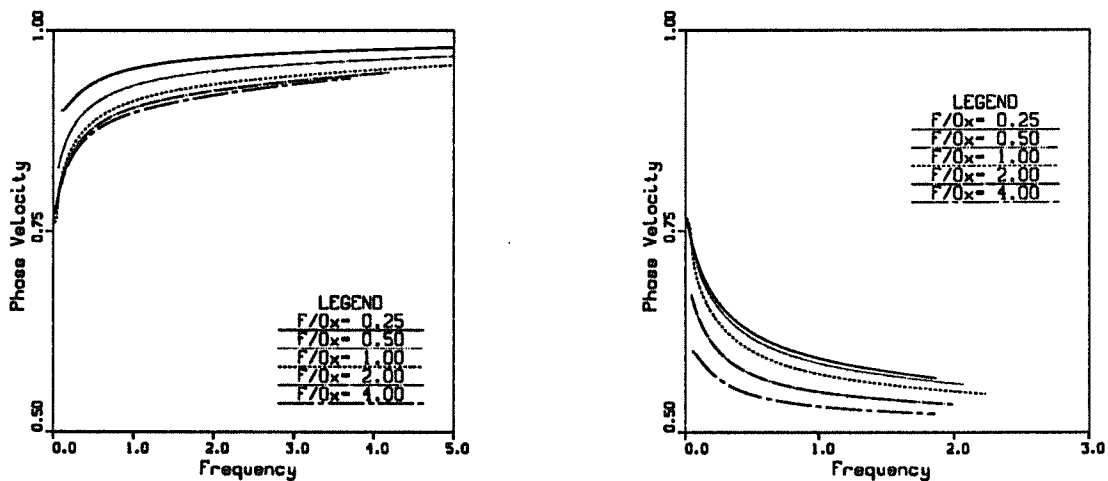


Figure 2.49: Influence of the fuel-equivalence ratio on the phase speeds of the fast (left) and slow (right) outer modes. ($M_c = 1$).

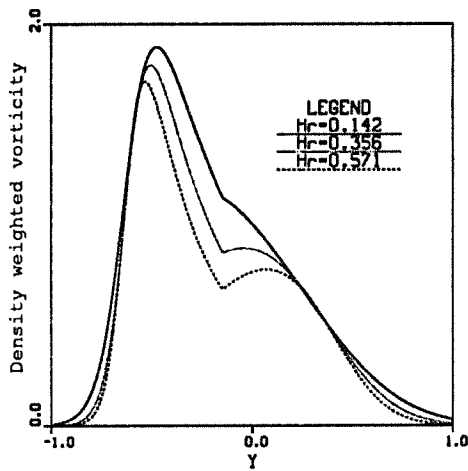


Figure 2.50: Comparison to experiment: Mean density-weighted vorticity profiles for various heat releases ($\bar{T}_2 = 0.21$, $M_c = 0.8$, $\bar{u}_2 = 0.11$)

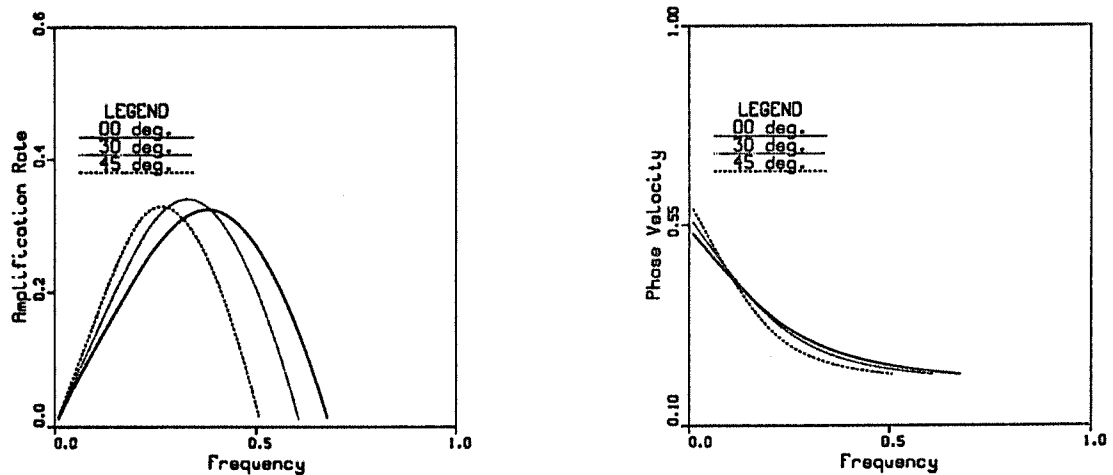


Figure 2.51: Amplification rate of the slow instability mode versus frequency for the low heat release case. ($\Theta = 0.142$). No fast mode present.

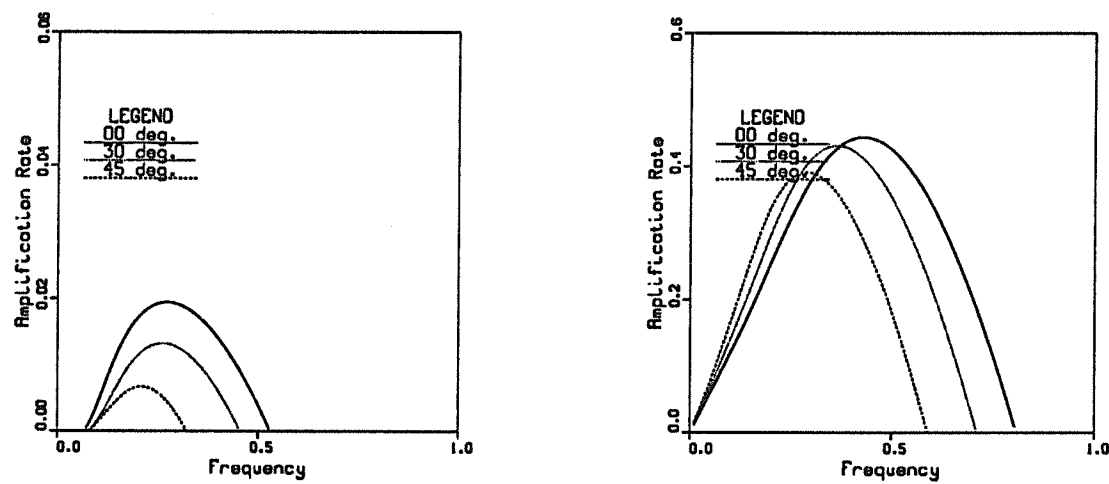


Figure 2.52: Amplification rates of the fast and slow instability modes versus frequency for the medium heat release case. ($\Theta = 0.356$). Left: fast outer mode; Right: slow outer mode.

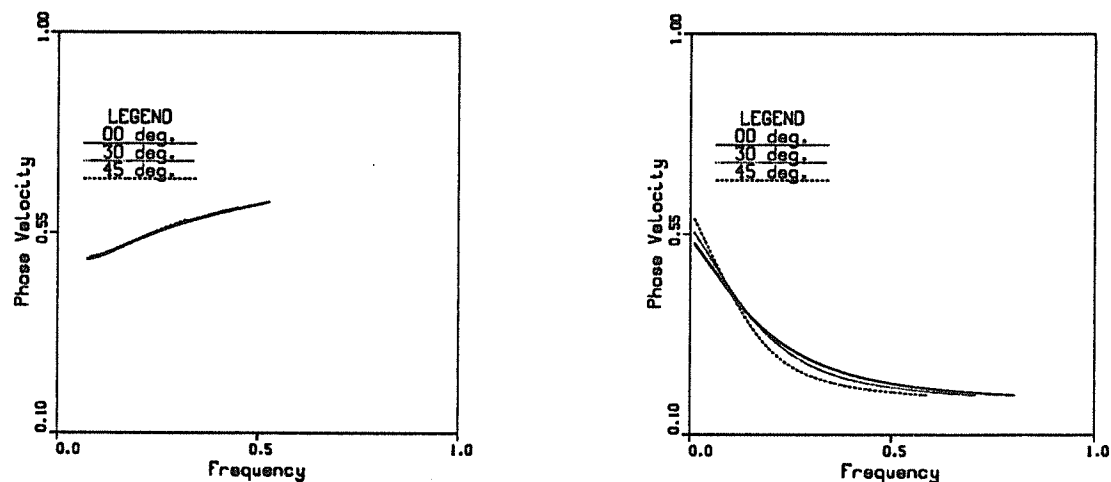


Figure 2.53: Phase speeds of the fast and slow instability modes versus frequency for the medium heat release case. ($\Theta = 0.356$).

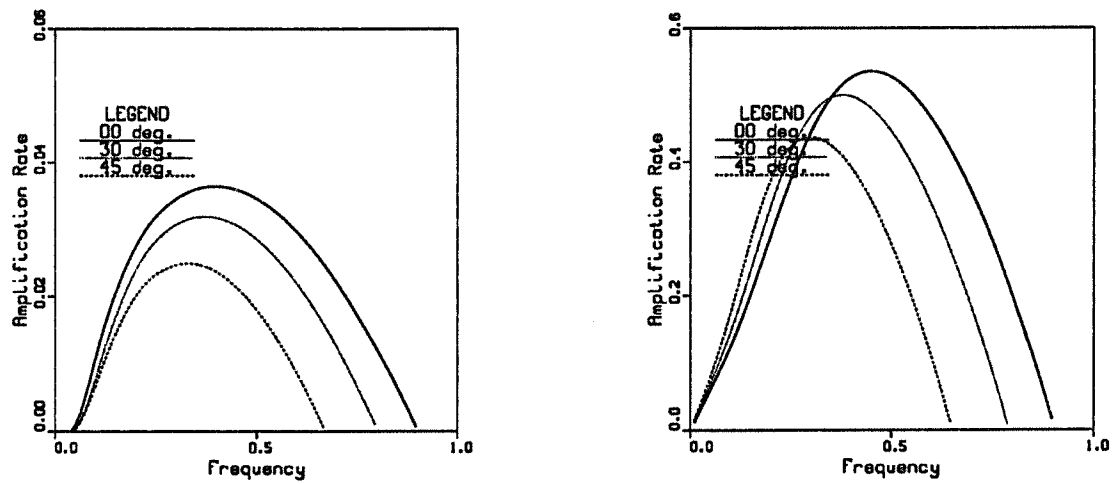


Figure 2.54: Amplification rates of the fast and slow instability mode versus frequency for the high heat release case. ($\Theta = 0.571$). Left: fast outer mode; Right: slow outer mode.

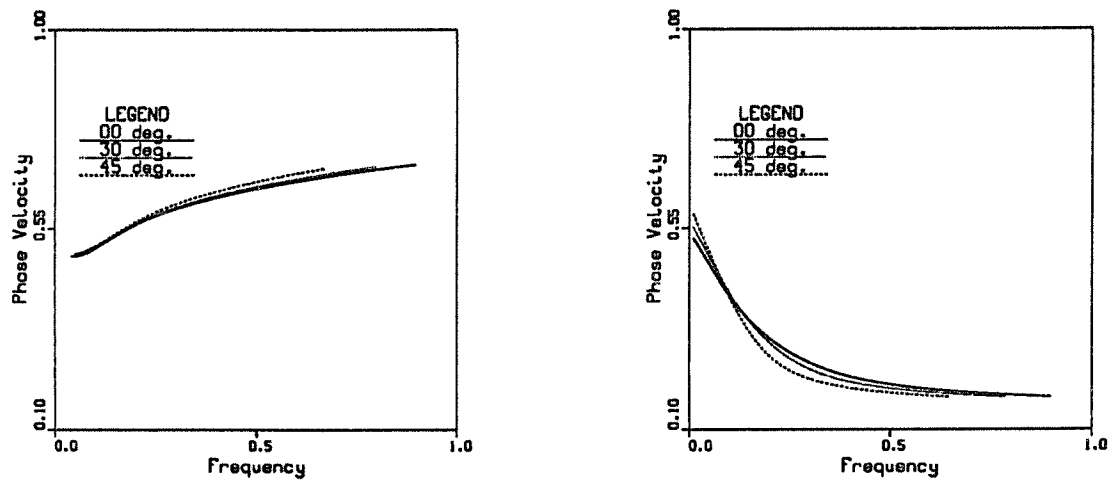


Figure 2.55: Phase speeds of the fast and slow instability mode versus frequency for the high heat release case. ($\Theta = 0.571$).

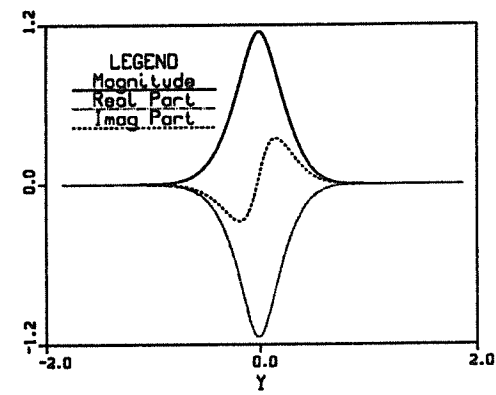
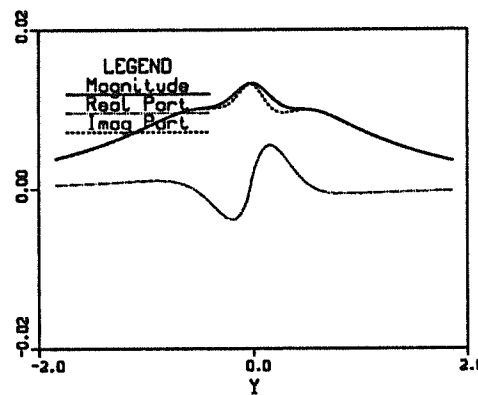
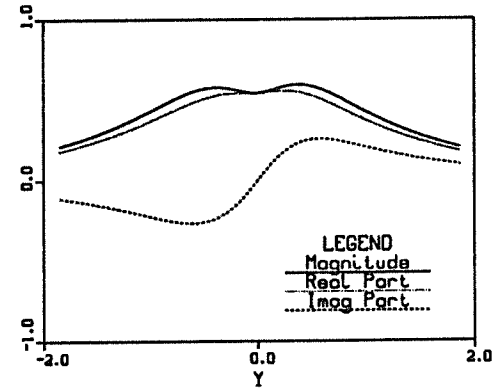
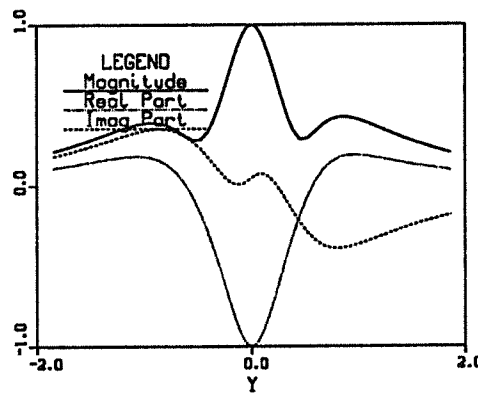


Figure 2.56: Linear eigenfunction of the most amplified central mode. (No heat release $\Theta = 0.$, $M_c = 0.10$). \hat{u} (top left), \hat{v} (top right), \hat{T} (bottom left) and \hat{z} (bottom right) components.

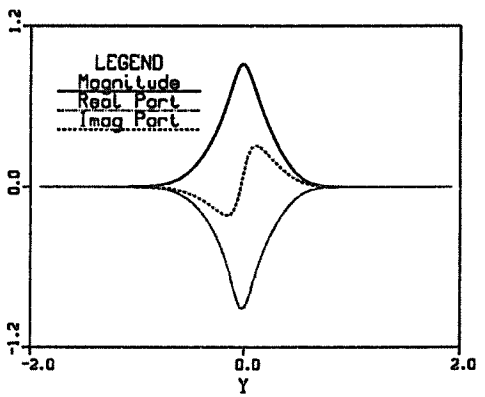
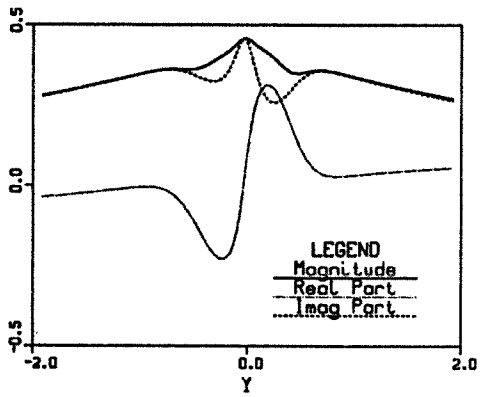
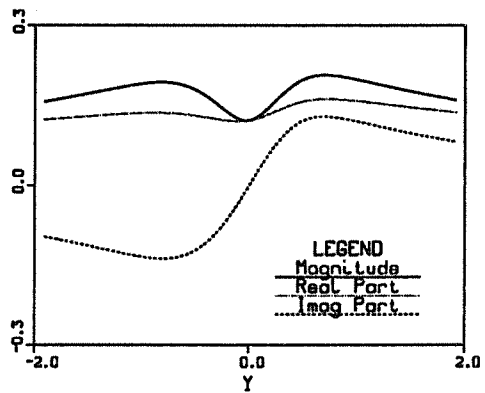
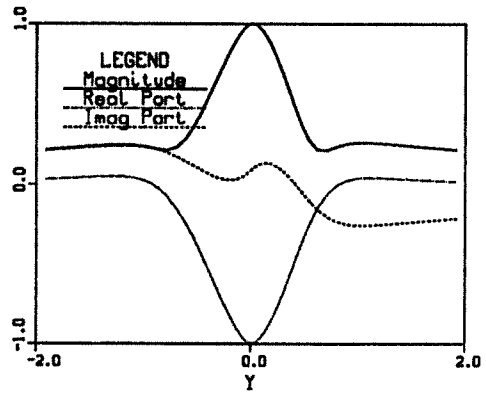


Figure 2.57: Linear eigenfunction of the most amplified central mode. (No heat release $\Theta = 0.$, $M_c = 0.875$). \hat{u} (top left), \hat{v} (top right), \hat{T} (bottom left) and \hat{z} (bottom right) components.

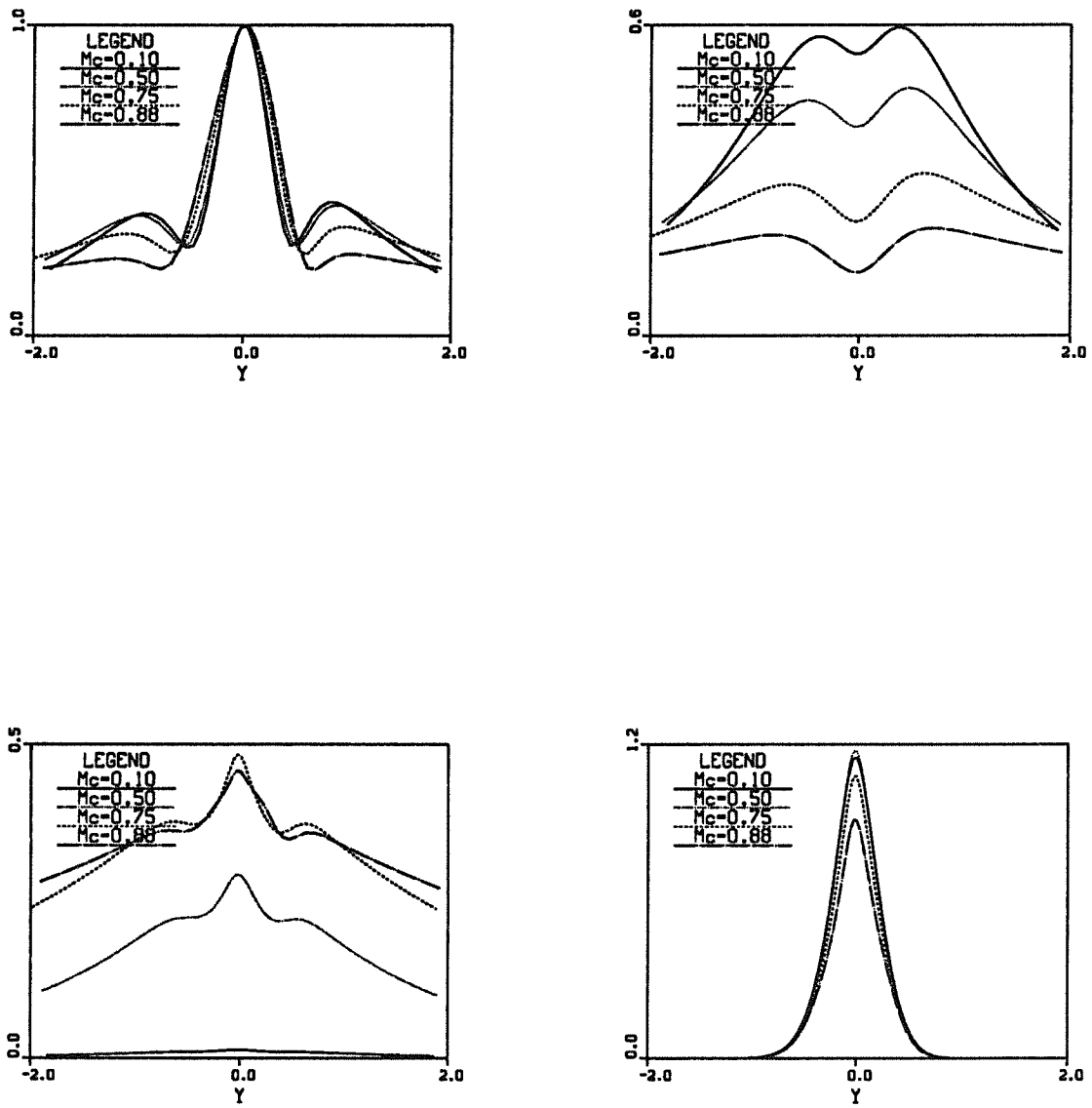


Figure 2.58: Compressibility effects on the linear eigenfunction of the most amplified central mode. (No heat release $\Theta = 0$). Amplitude of the \hat{u} (top left), \hat{v} (top right), \hat{T} (bottom left) and \hat{z} (bottom right) components.

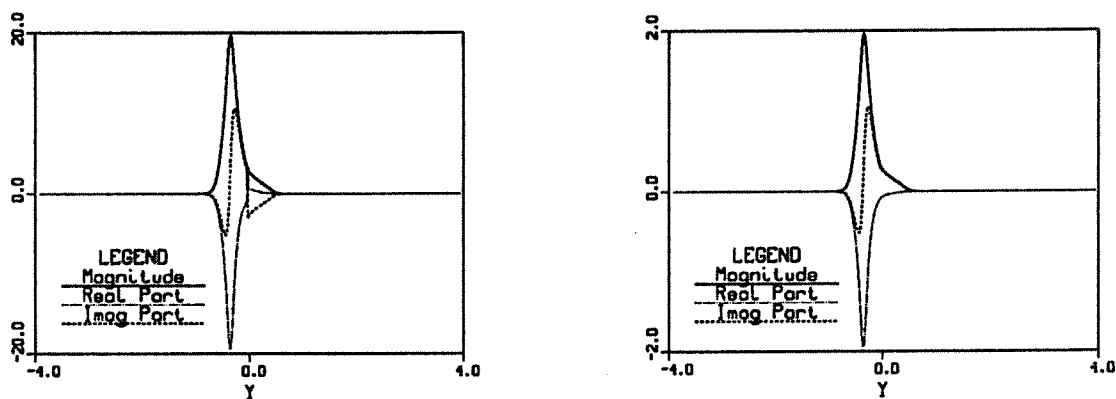
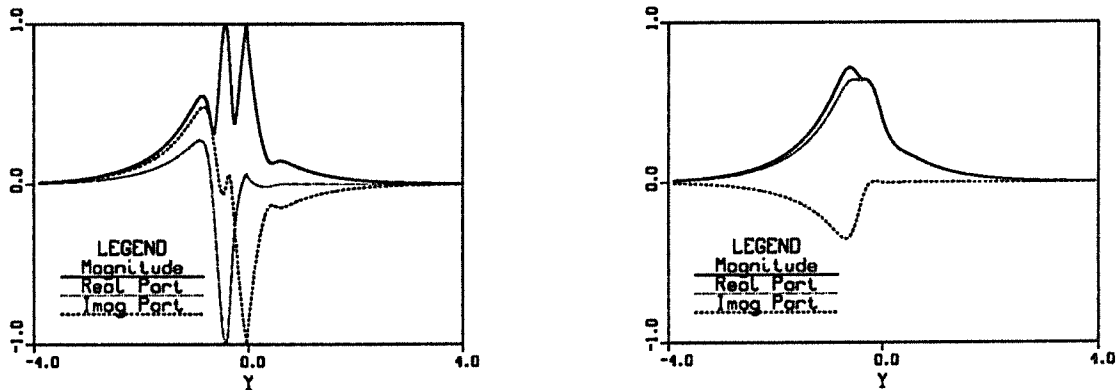


Figure 2.59: Linear eigenfunction of the most amplified slow outer mode. (Heat release $\Theta = 4.85$, $M_c = 0.1$). \hat{u} (top left), \hat{v} (top right), \hat{T} (bottom left) and \hat{z} (bottom right) components.

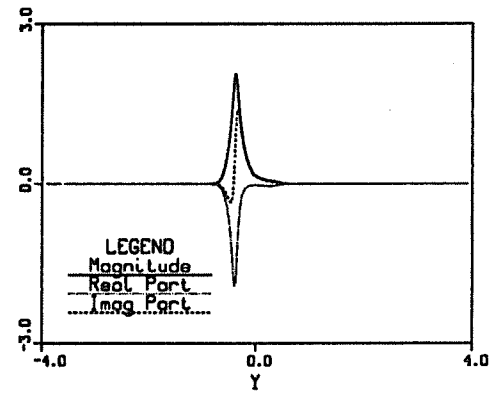
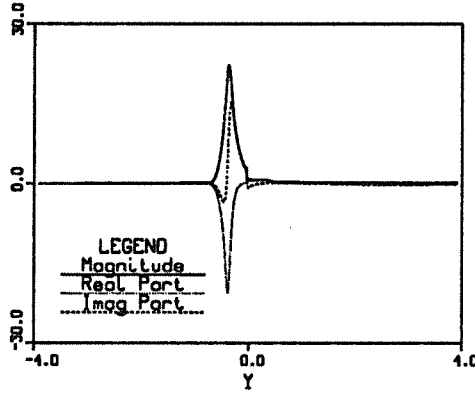
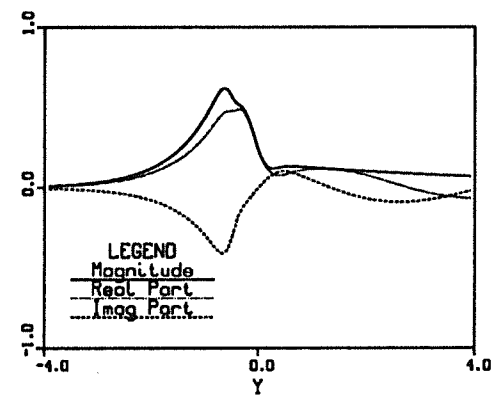
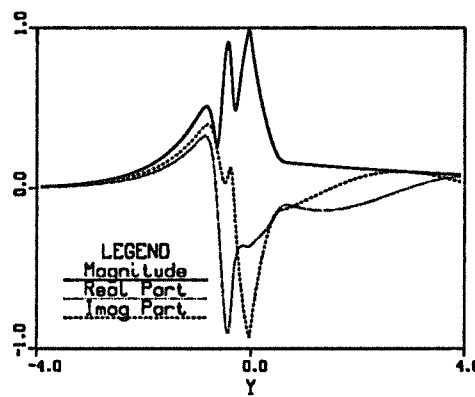


Figure 2.60: Linear eigenfunction of the most amplified slow outer mode. (Heat release $\Theta = 4.85$, $M_c = 0.8$). \hat{u} (top left), \hat{v} (top right), \hat{T} (bottom left) and \hat{z} (bottom right) components.

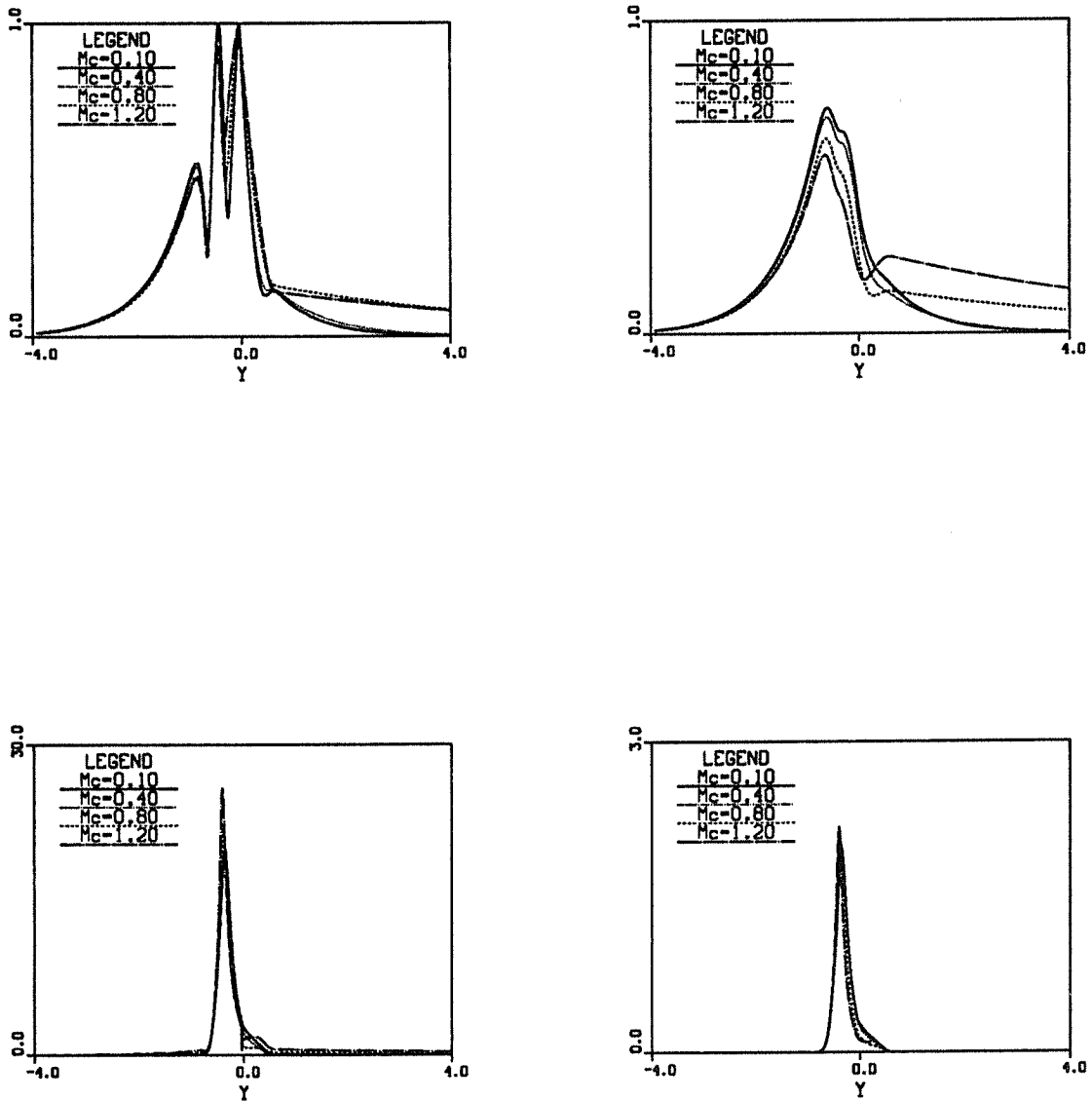


Figure 2.61: Compressibility effects on the linear eigenfunction of the most amplified slow outer mode. (Heat release $\Theta = 4.85$). Amplitude of the \hat{u} (top left), \hat{v} (top right), \hat{T} (bottom left) and \hat{z} (bottom right) components.

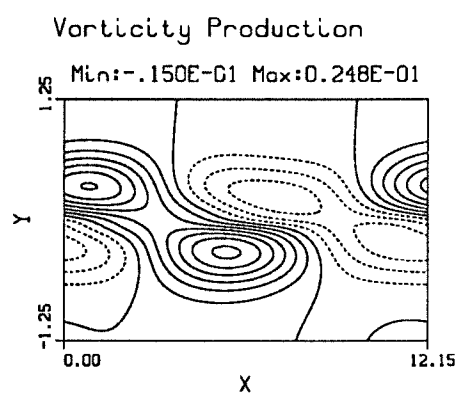
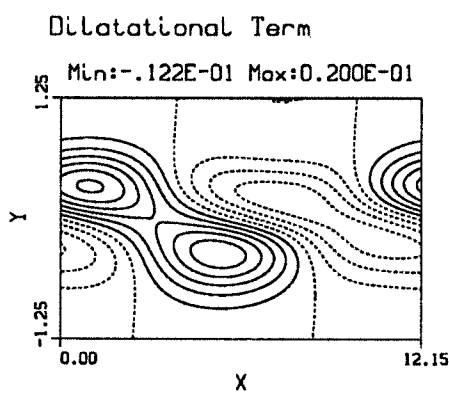
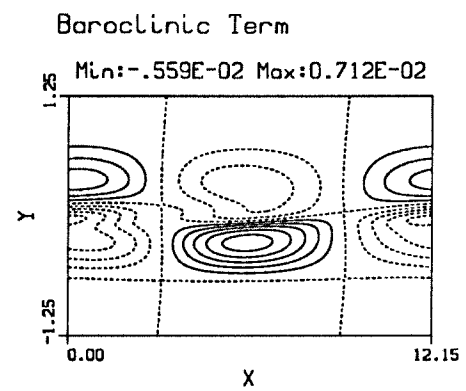
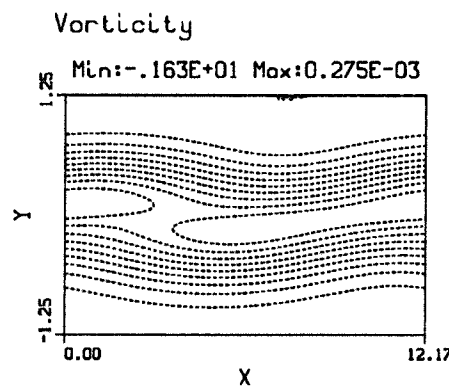


Figure 2.62: Linear eigenfunction of the most amplified central mode. (No heat release $\Theta = 0.$, $M_c = 0.8$).

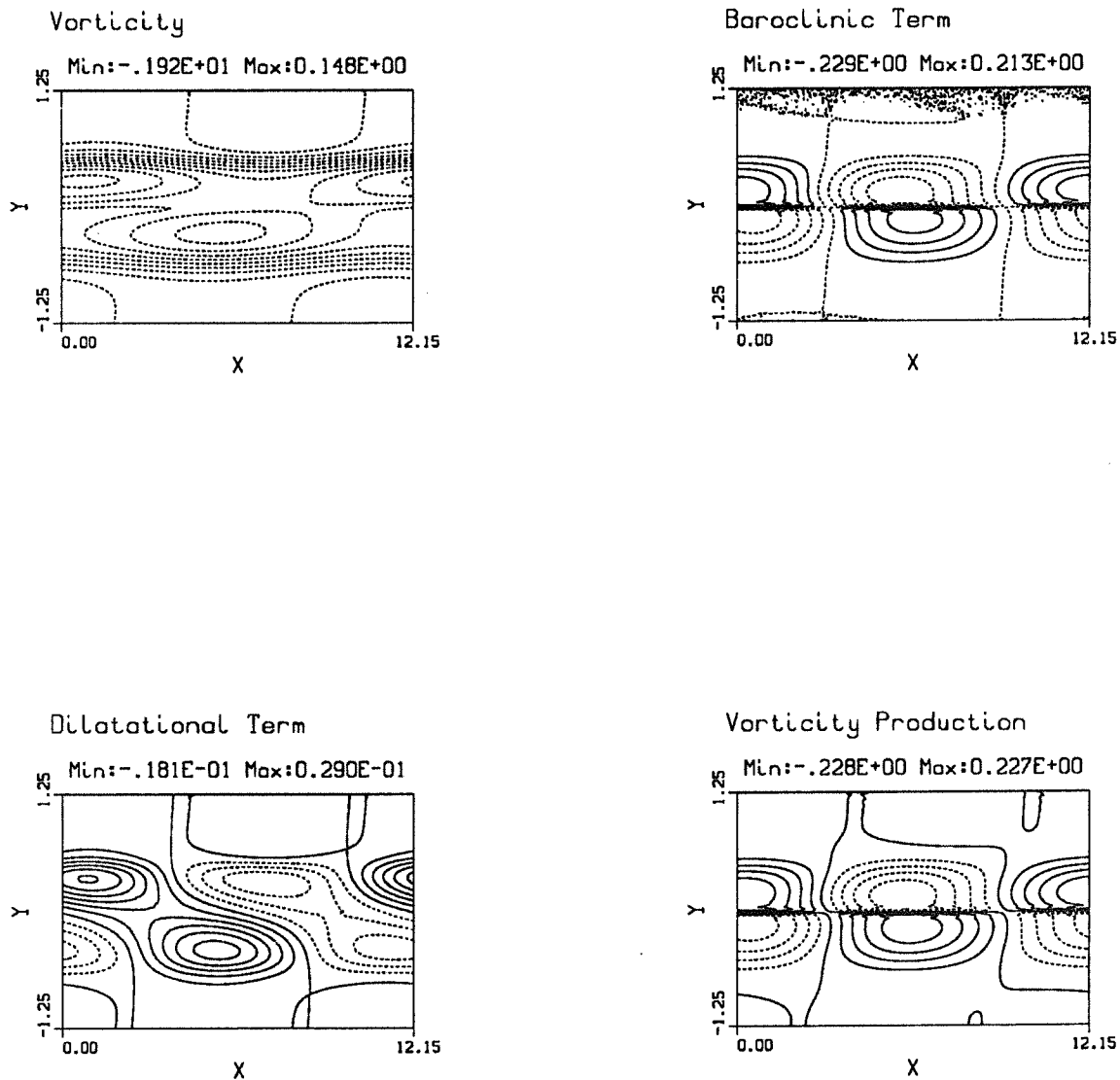


Figure 2.63: Linear eigenfunction of the most amplified central mode. (No heat release $\Theta = 0.$, $M_c = 0.8$). superimposed on mean flow ($T_f = 3., M_c = 0.8$)

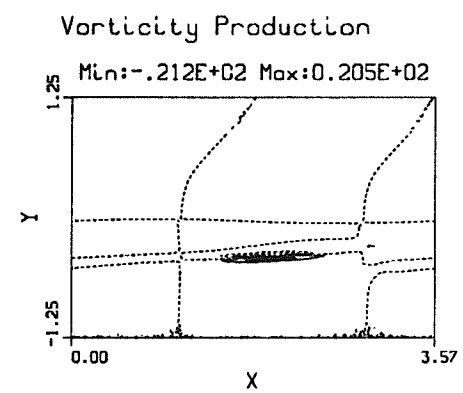
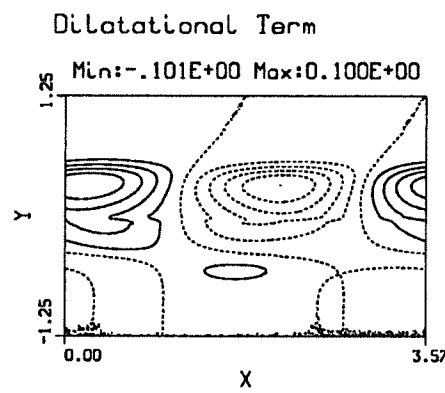
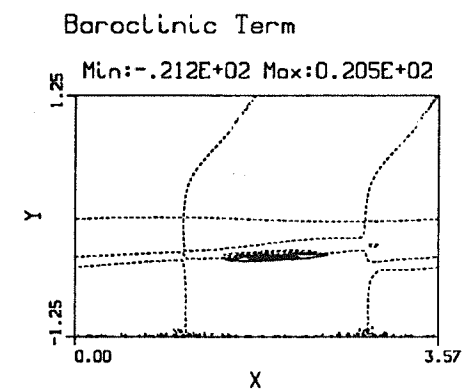
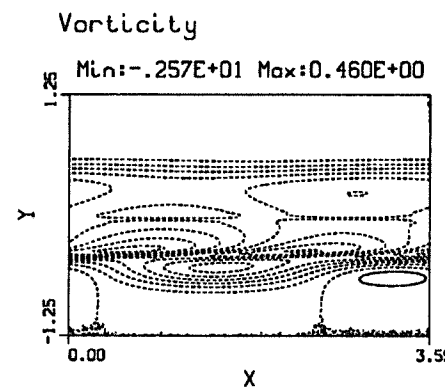
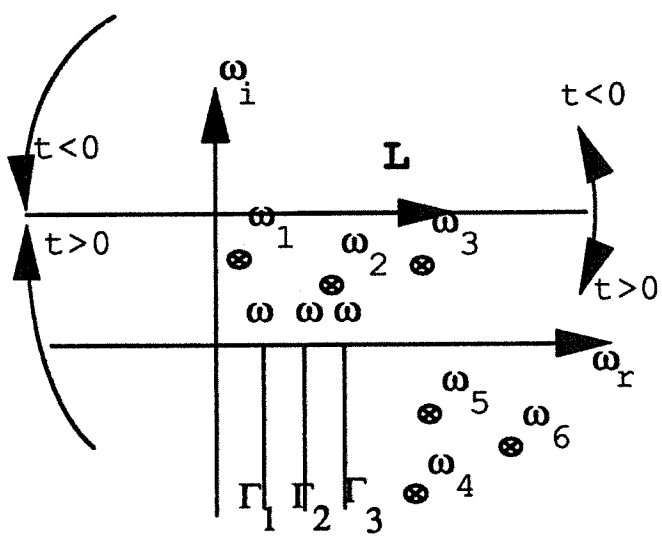
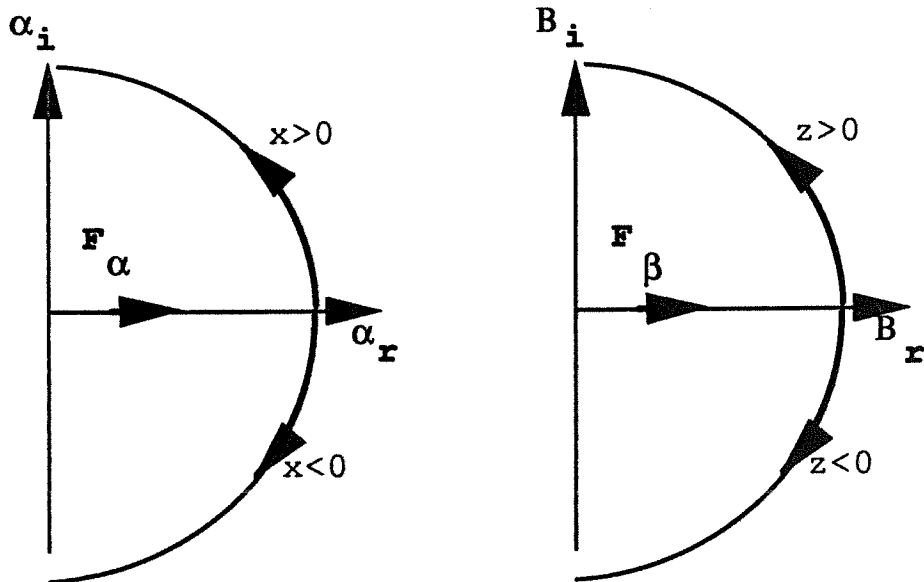


Figure 2.64: Linear eigenfunction of the most amplified slow outer mode. (Heat release $T_J = 3.$, $M_c = 0.8$).



Integration in the complex ω plane



Integration in the complex α, B planes

Figure 2.65: Path of integration in the complex α , β and ω planes. (from Huerre and Monkewitz 1985)

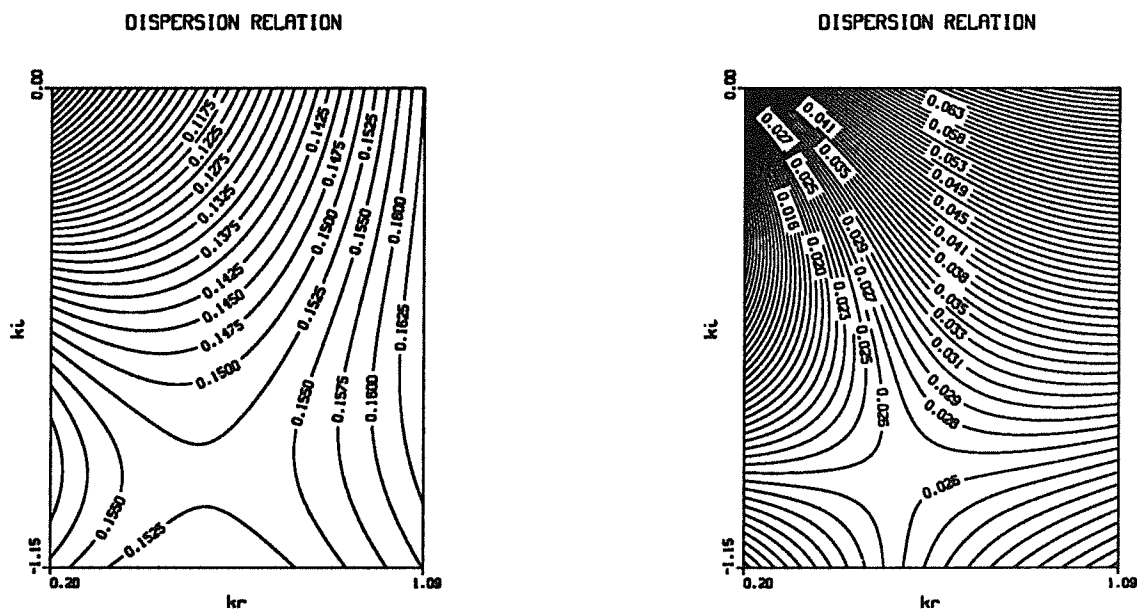


Figure 2.66: Dispersion relation for an absolutely unstable mixing layer. $U_2 = 0.01$, $T_2 = 1.0$, $M_c = 0.05$ and $T_f = 6$. left ω_r , right ω_i

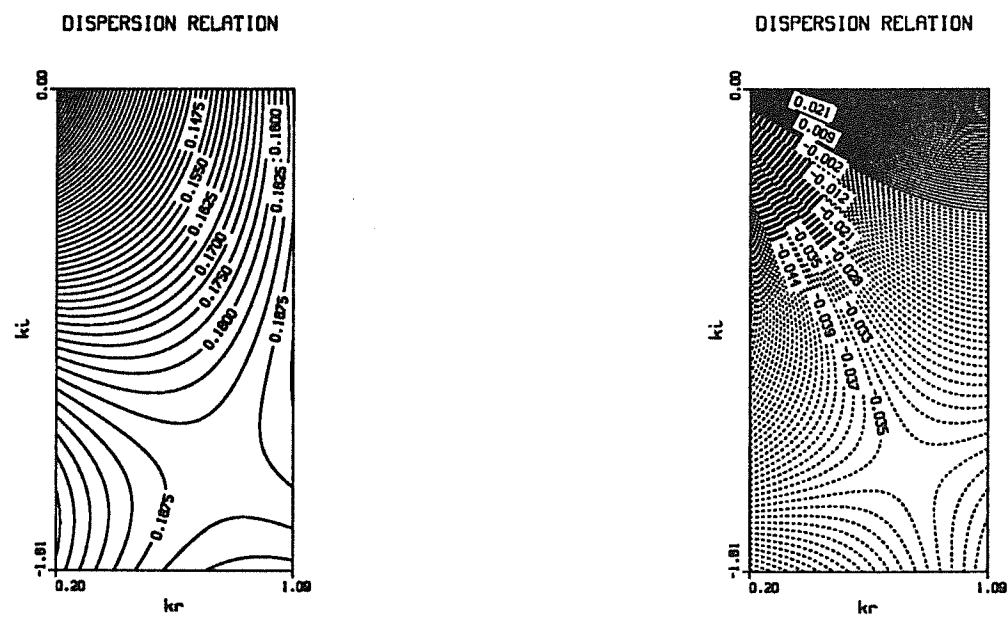


Figure 2.67: Dispersion relation for a convectively unstable mixing layer. $U_2 = 0.01$, $T_2 = 1.0$, $M_c = 1.20$ and $T_f = 4$. left ω_r , right ω_i

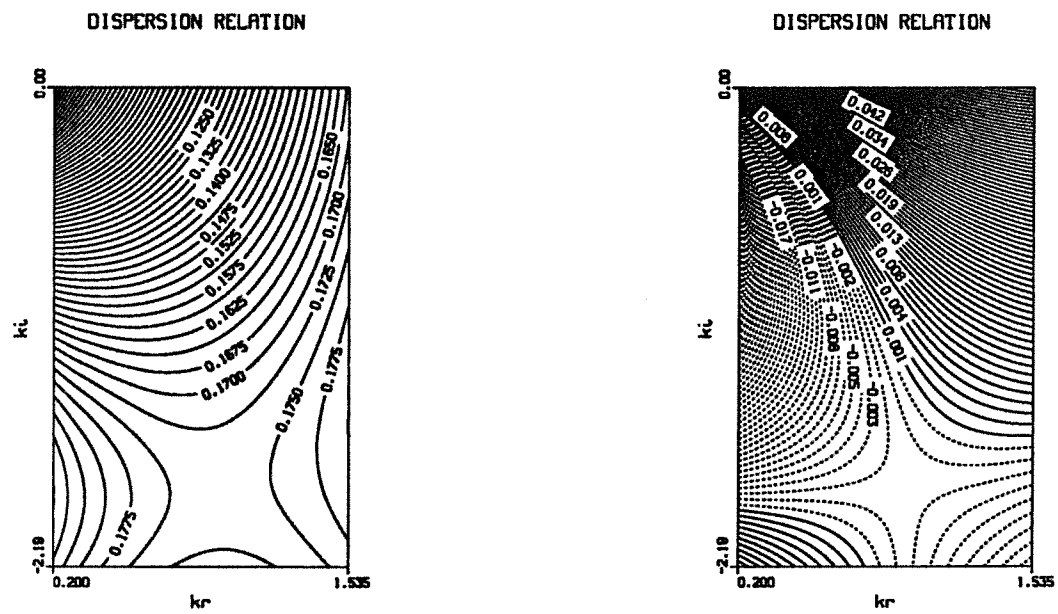


Figure 2.68: Dispersion relation for an limit convectively unstable mixing layer. $U_2 = 0.01$, $T_2 = 0.5$, $M_c = 1.20$ and $T_f = 4$. left ω_r , right ω_i

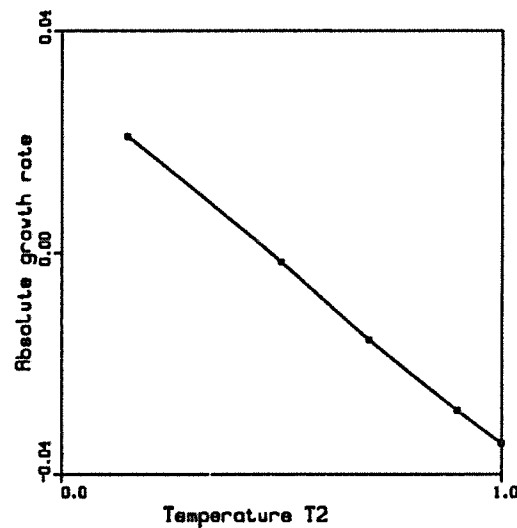


Figure 2.69: Influence of the slow-stream temperature on the transition from absolute to convective instability. (Heat release $T_f = 4.0$, $U_2 = 0.01$, $M_1 = 2.4$).

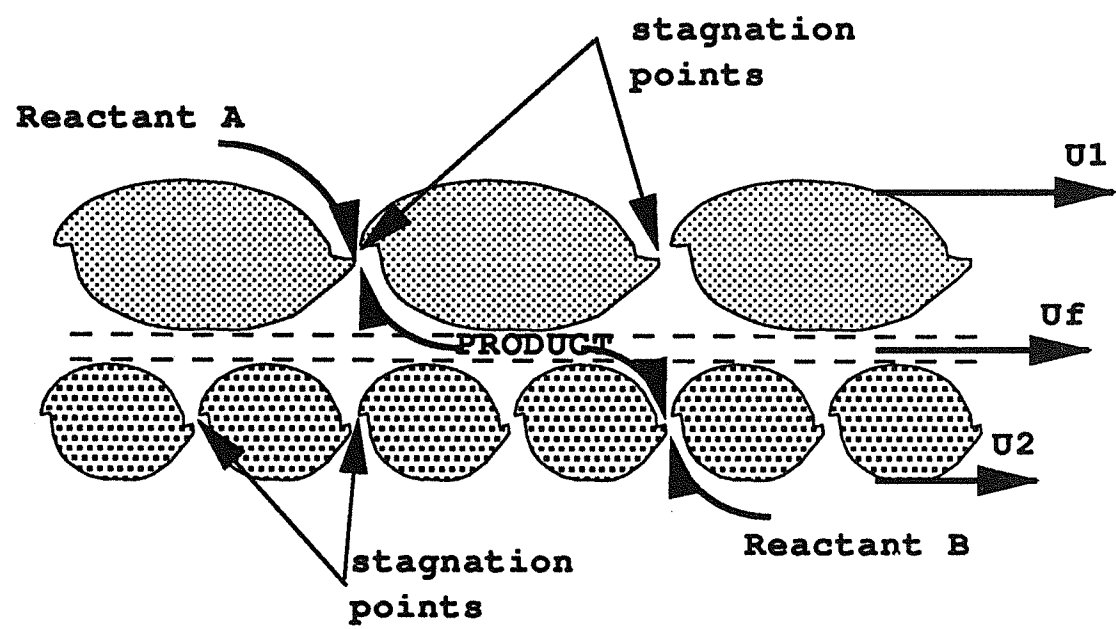


Figure 2.70: Schematic of the compressible reacting mixing layer.

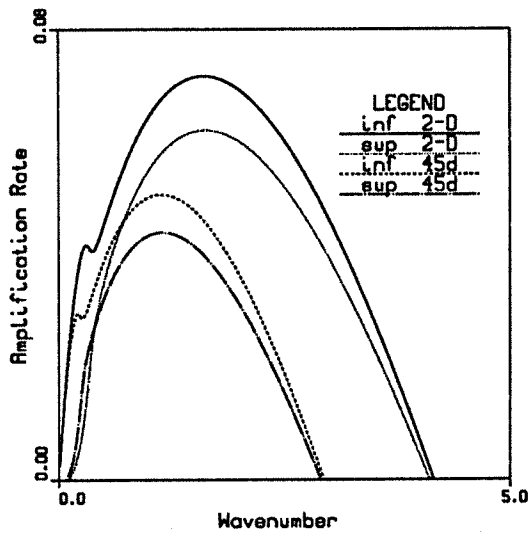


Figure 3.1: Amplification rates of the fast (sup) and slow (inf) incompressible outer modes at two different obliquities (2-D and 45 degrees). $\bar{T}_f = 3.0$, $M_c = 0.05$, $\bar{u}_2 = 0.5$, $\bar{T}_2 = 1$, $M_{f1} = M_{f2} = 0.02$. Note that the fast and slow amplification curves do not peak at the same wavenumber.

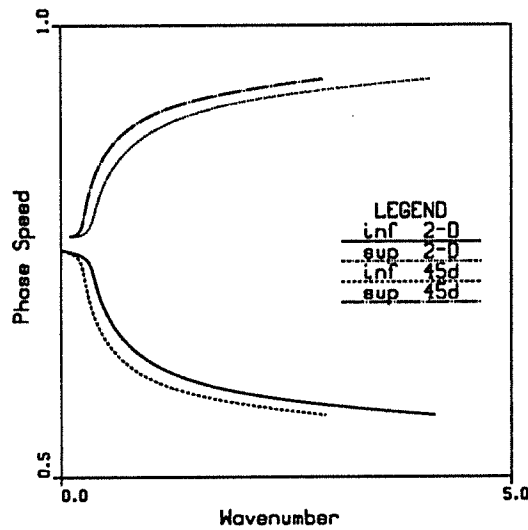


Figure 3.2: Convective speeds of the fast (sup) and slow (inf) incompressible outer modes at two different obliquities (2-D and 45 degrees). $\bar{T}_f = 3.0$, $M_c = 0.05$, $\bar{u}_2 = 0.5$, $\bar{T}_2 = 1$, $M_{f1} = M_{f2} = 0.02$.

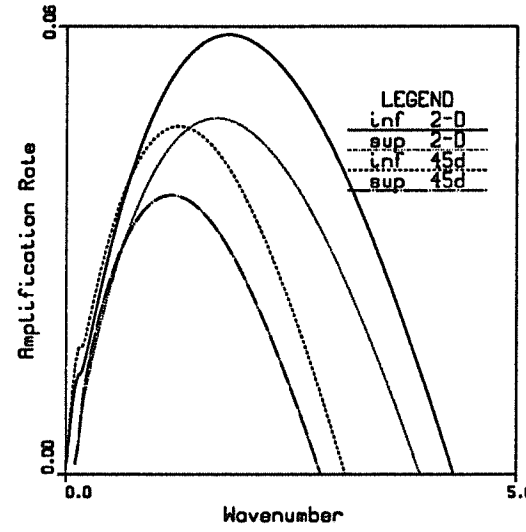


Figure 3.3: Amplification rates of the fast (sup) and slow (inf) compressible outer modes at two different obliquities (2-D and 45 degrees). $\bar{T}_f = 3.0$, $M_c = 0.8$, $\bar{u}_2 = 0.5$, $\bar{T}_2 = 1$, $M_{f1} = M_{f2} = 0.292$. Note that the fast and slow amplification curves do not peak at the same wavenumber. The amplification rates are weakly reduced at $M_c = 0.8$ since $M_f = 0.3$ only.

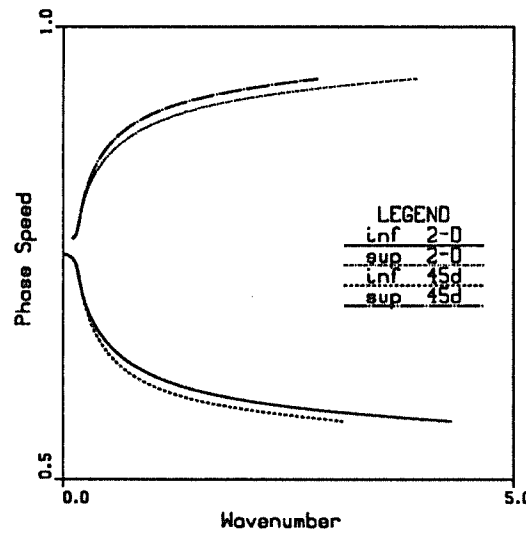
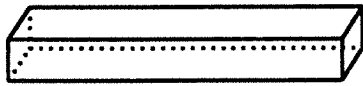


Figure 3.4: Convective speeds of the fast (sup) and slow (inf) compressible outer modes at two different obliquities (2-D and 45 degrees). $\bar{T}_f = 3.0$, $M_c = 0.8$, $\bar{u}_2 = 0.5$, $\bar{T}_2 = 1$, $M_{f1} = M_{f2} = 0.292$.



Pencil of size $N_x.N_y.N_{yn}.N_{zn}$
 $= 64.7.8.2$

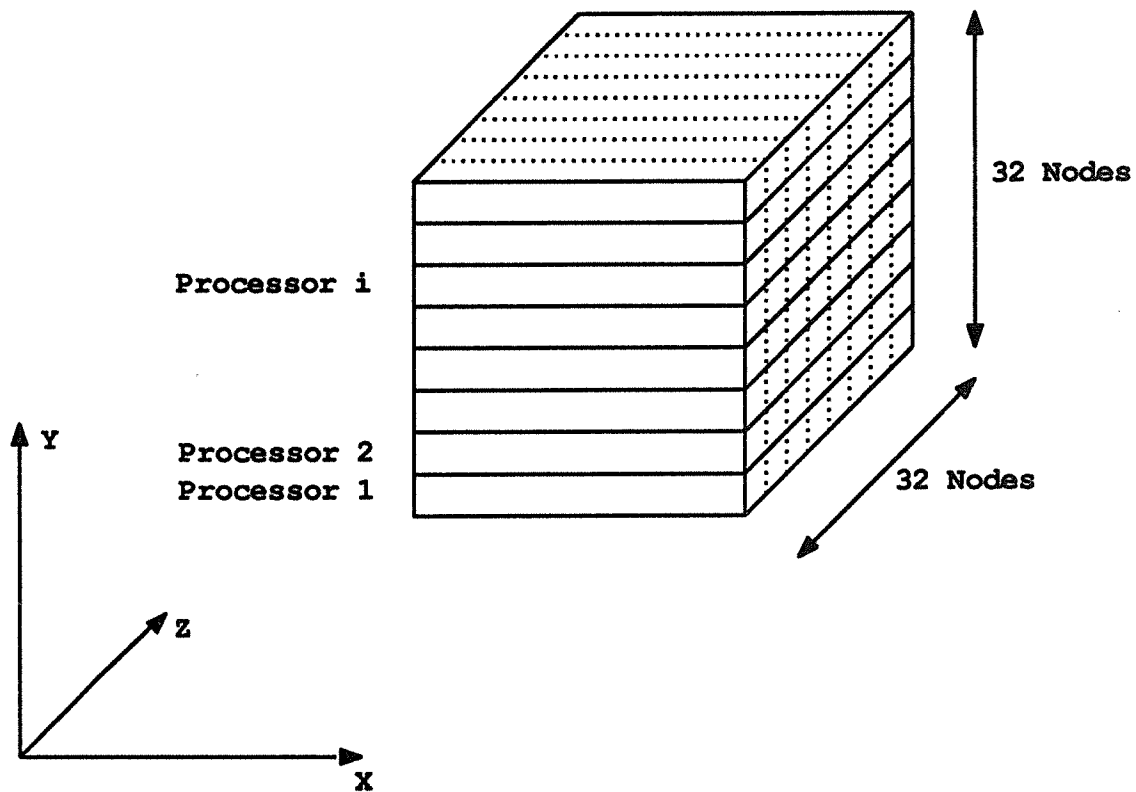


Figure 3.5: Management of data on the Hypercube. Each processor is allocated a certain number of $x - z$ or $x - y$ planes.

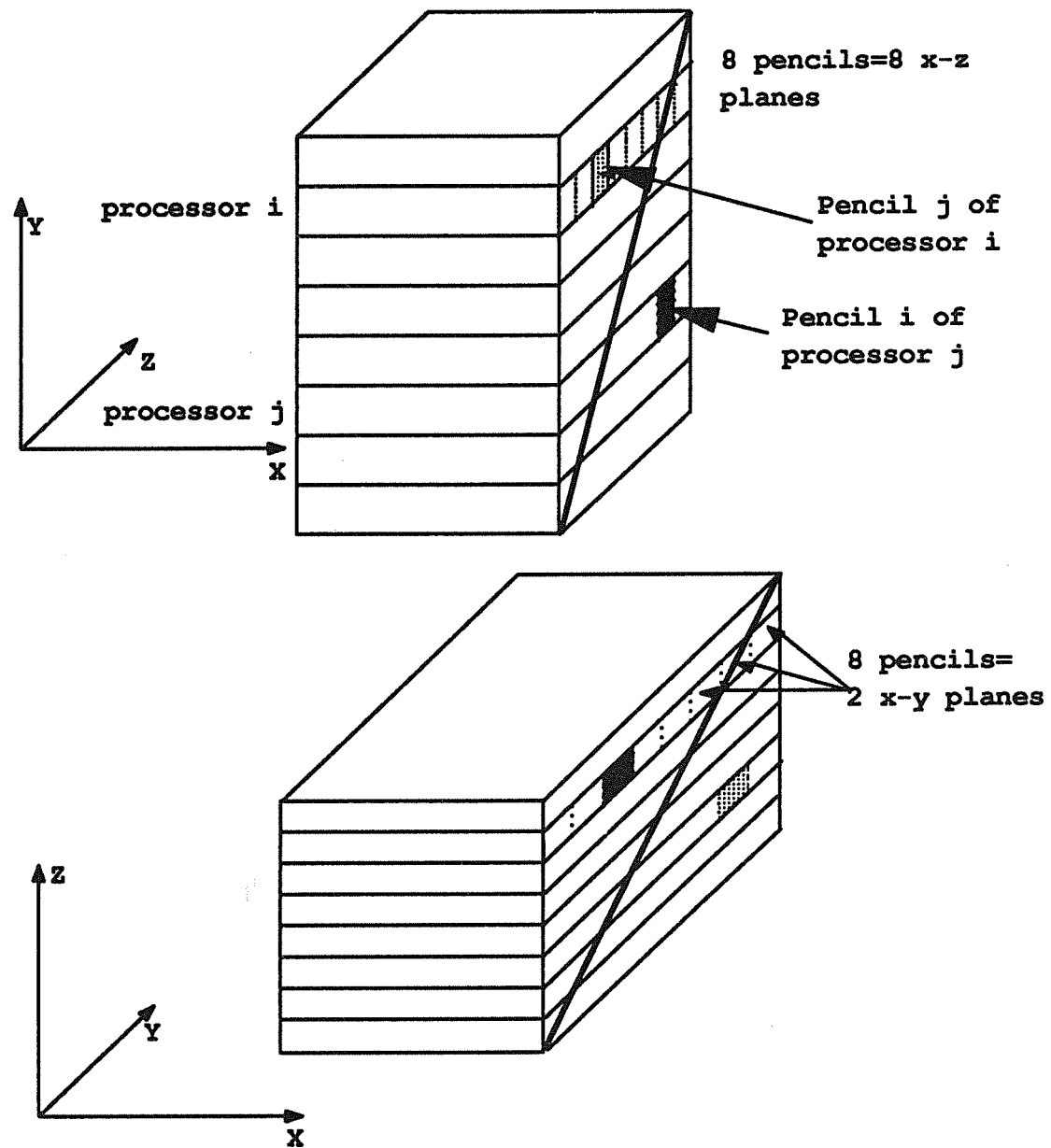


Figure 3.6: Transpose of data from a situation where each processor is allocated N_{yn} $x - z$ planes to a situation where each processor is allocated N_{zn} $x - y$ planes. The transposition is done twice per time substep.

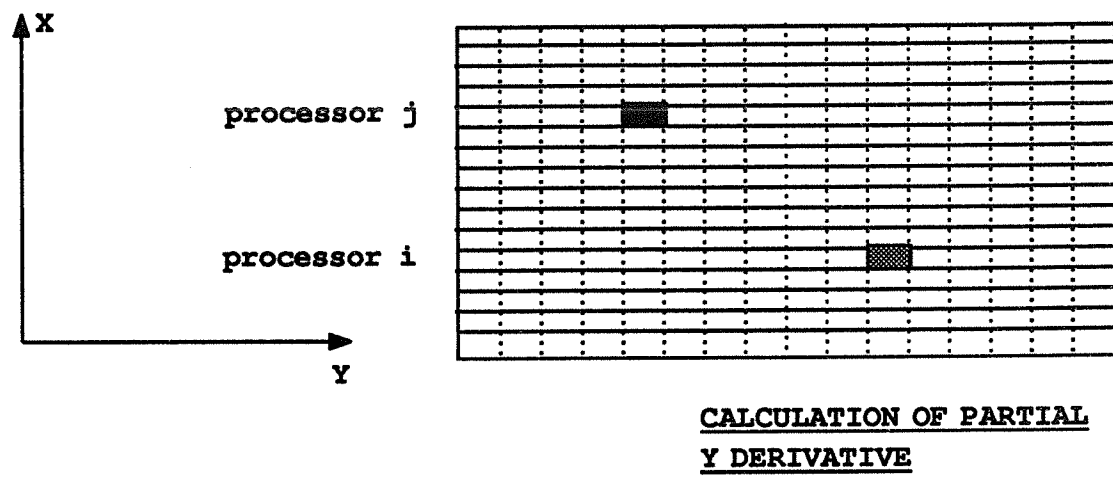
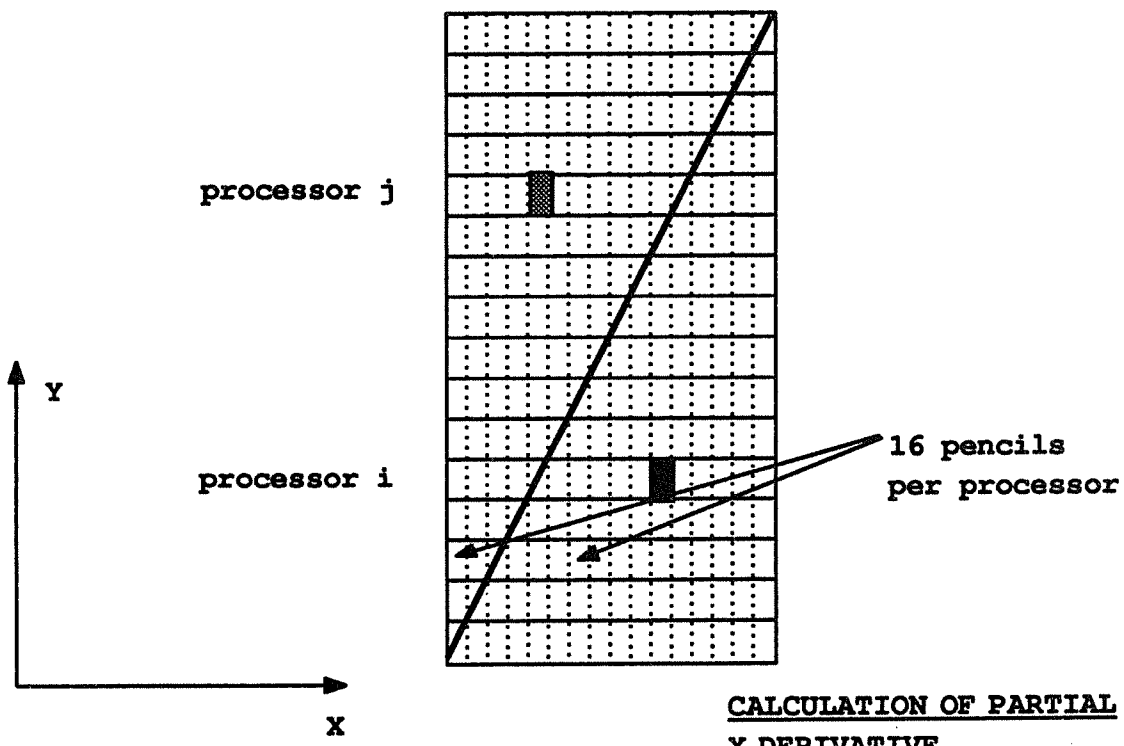


Figure 3.7: Same in 2-D, showing the two configurations, the first one for the computation of partial x derivatives and the second one for the computation of partial y derivatives.

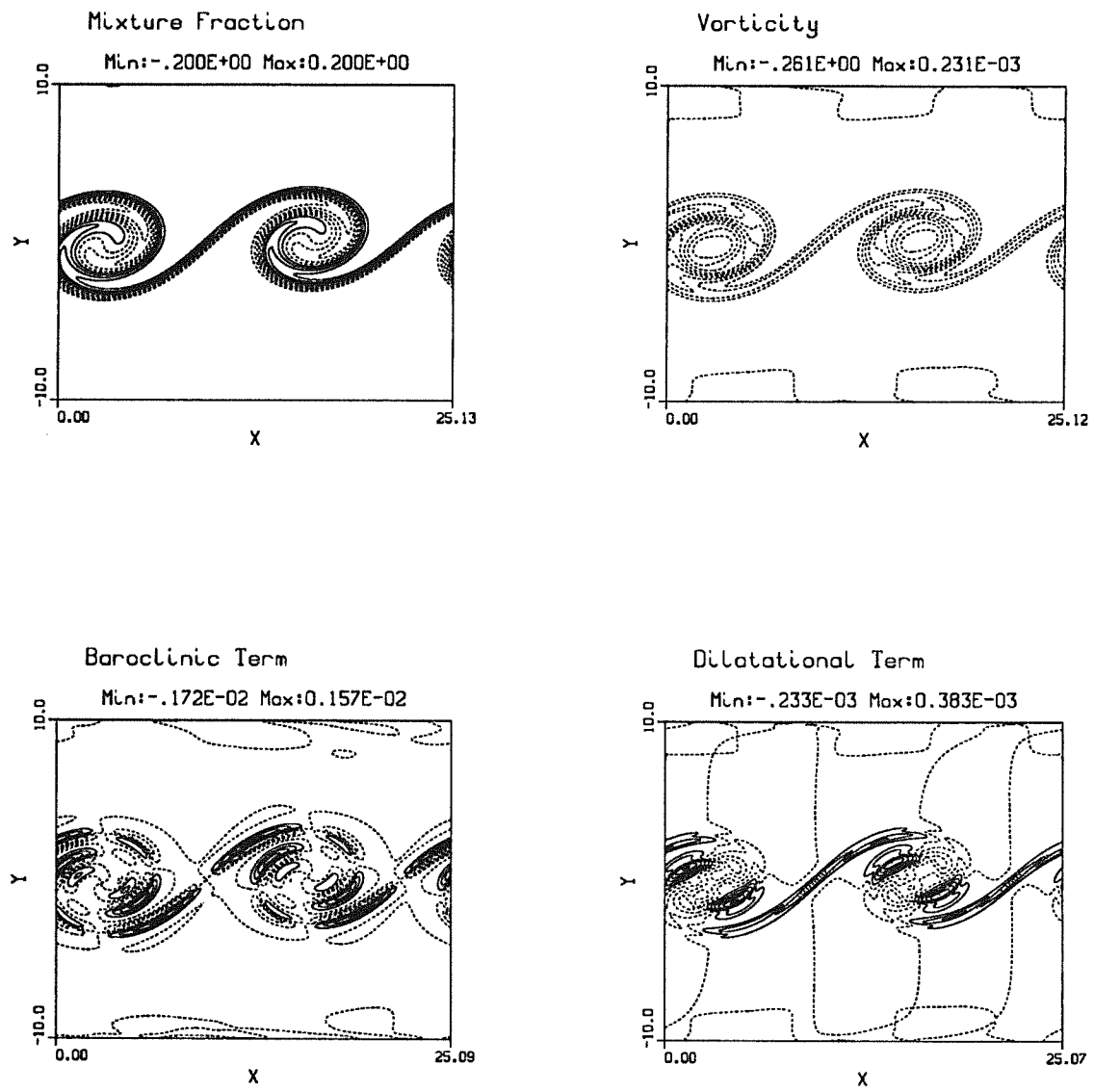


Figure 4.1: Developed typical central mode. (Low heat release $\Theta = 0.1$, $M_c = 0.2$, $Da = 5$, $Ze = 0.$, $U_2 = -1.$, $Re = 200$, $t = 21$). (a) Mixture fraction; (b) vorticity; (c) baroclinic term; (d) dilatation term.

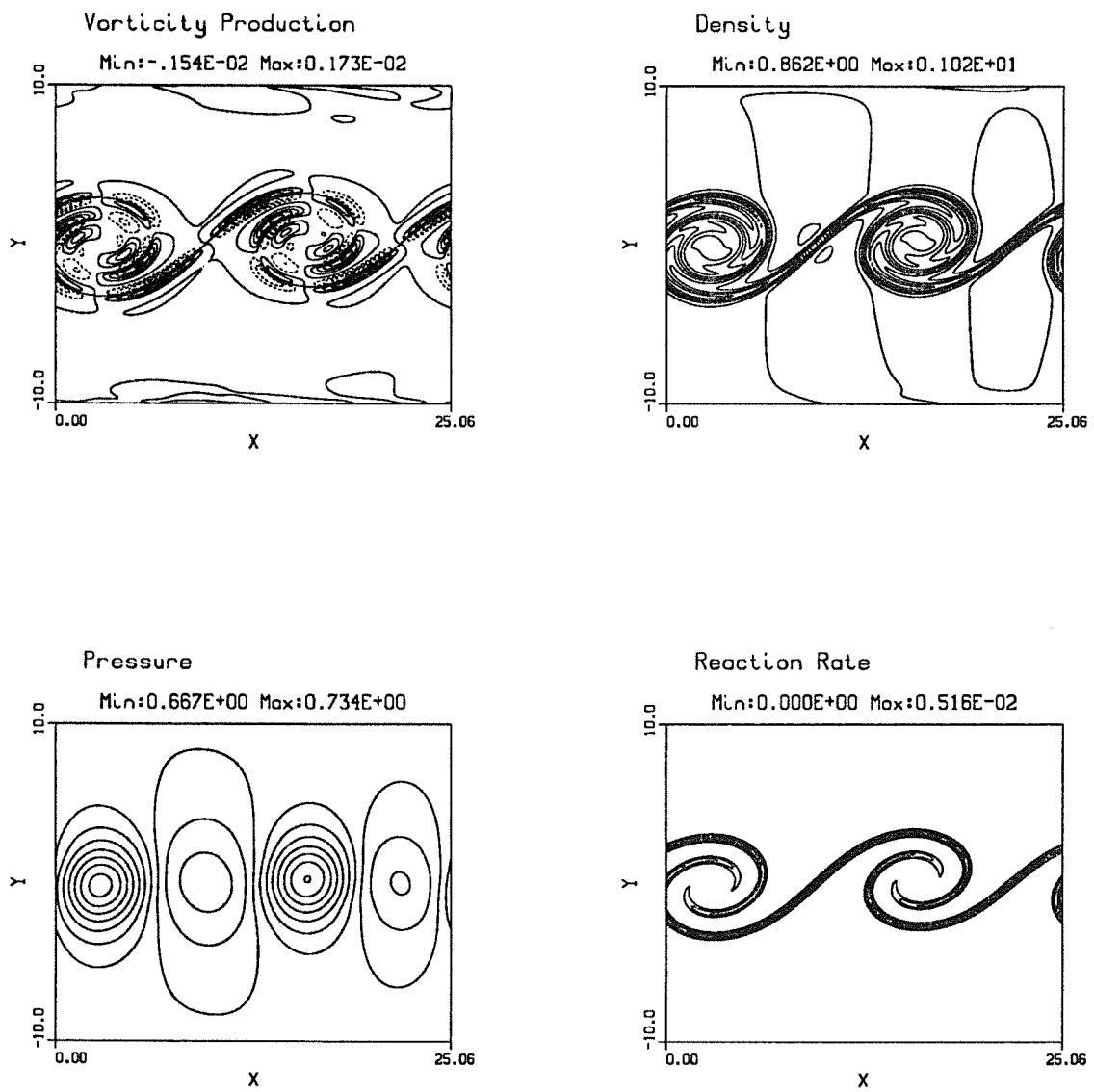


Figure 4.1: Developed typical central mode. Continued. (Low heat release $\Theta = 0.1$, $M_c = 0.2$, $Da = 5$, $Ze = 0.$, $U_2 = -1.$, $Re = 200$, $t = 21$). (e) Vorticity production; (f) density; (g) pressure; (h) reaction rate.

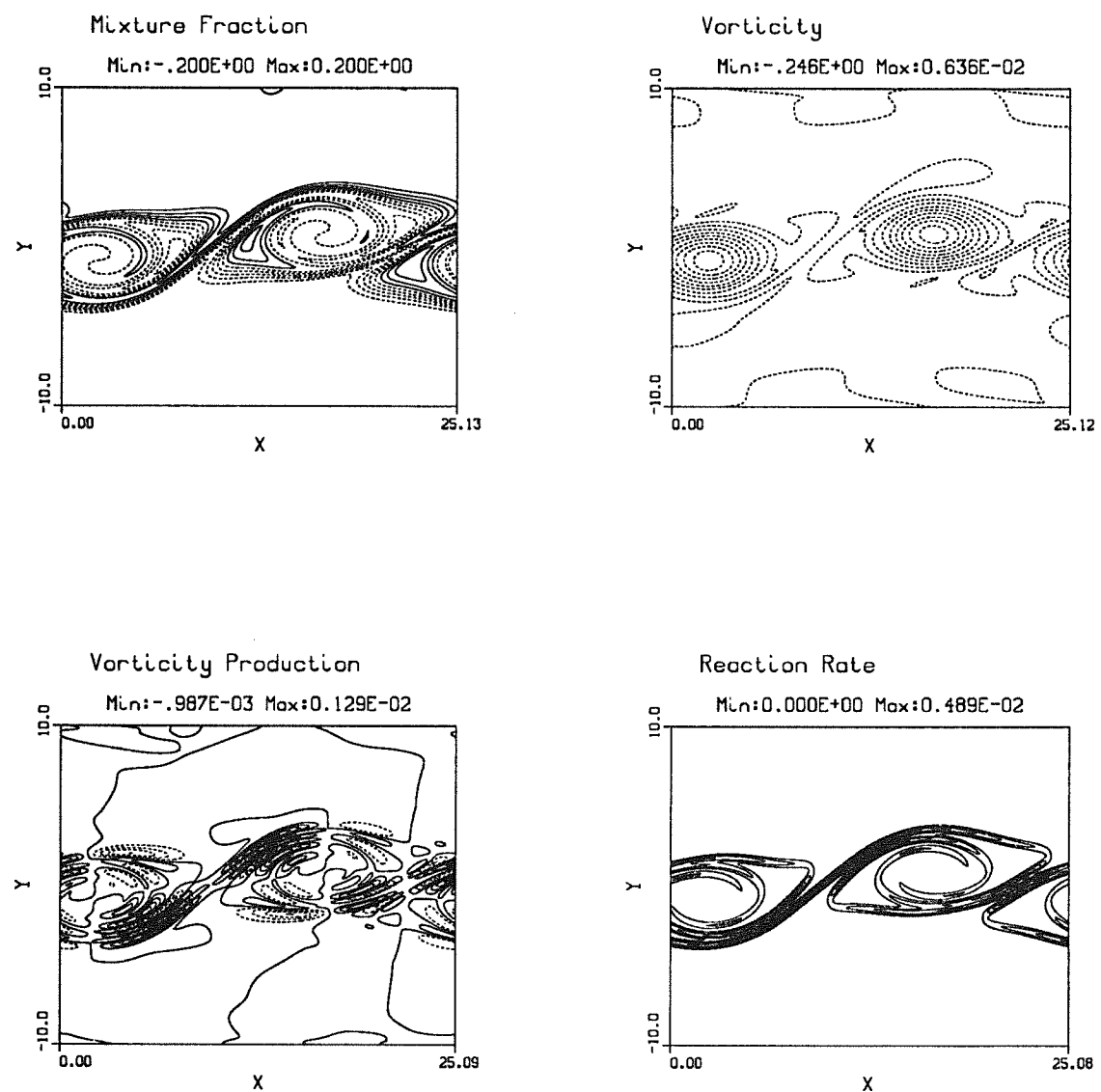


Figure 4.2: Interaction of a developed typical central mode with its subharmonic at three instants of time. a) $t=31$. (Low heat release $\Theta = 0.1$, $M_c = 0.2$, $Da = 5$, $Ze = 0$, $U_2 = -1$, $Re = 200$). (a) Mixture fraction; (b) vorticity; (c) vorticity production; (d) reaction rate.

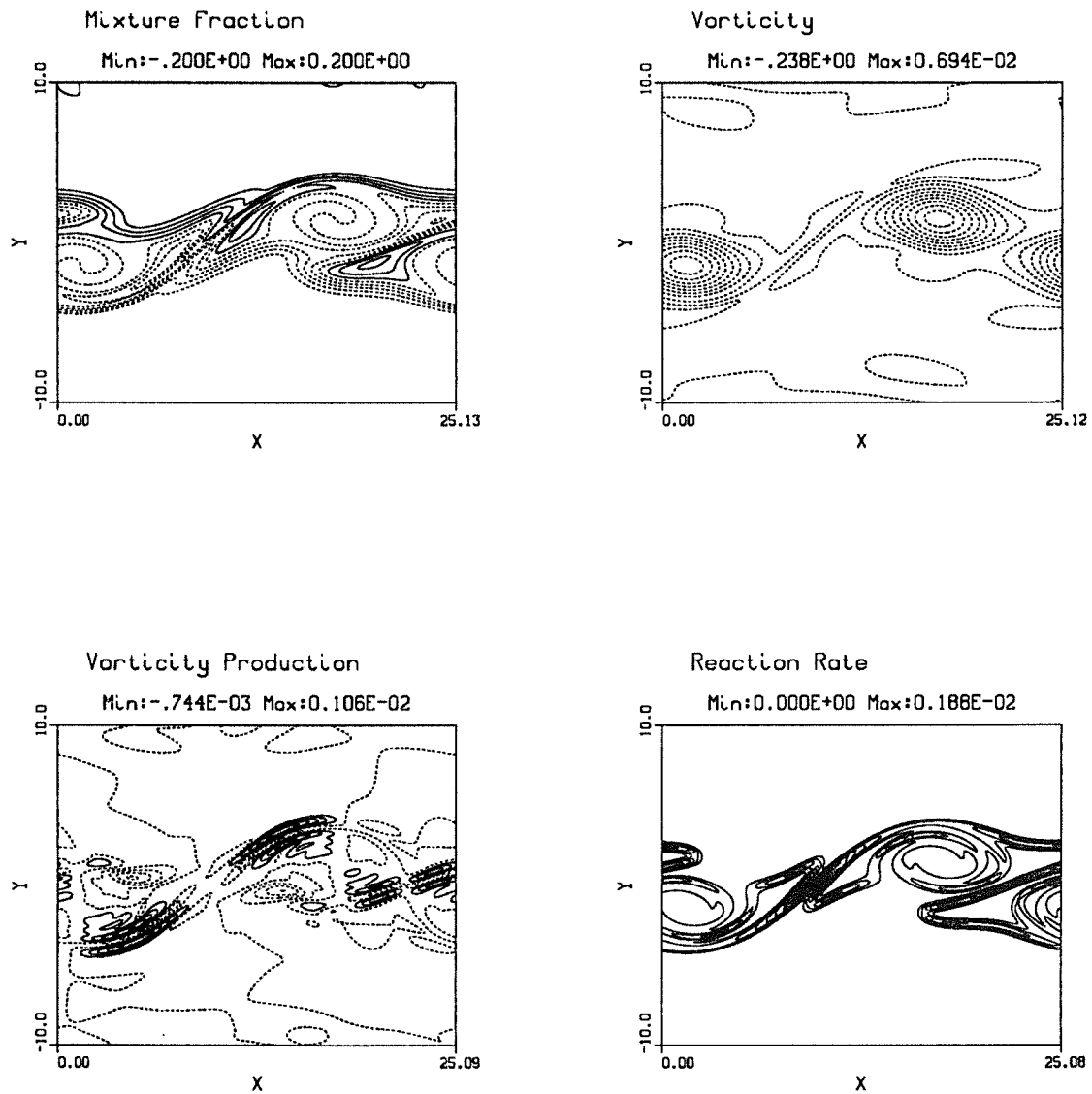


Figure 4.2: Interaction of a developed typical central mode with its subharmonic at three instants of time. b) $t=35$. (Low heat release $\Theta = 0.1$, $M_c = 0.2$, $Da = 5$, $Ze = 0.$, $U_2 = -1.$, $Re = 200$). (a) Mixture fraction; (b) vorticity; (c) vorticity production; (d) reaction rate.

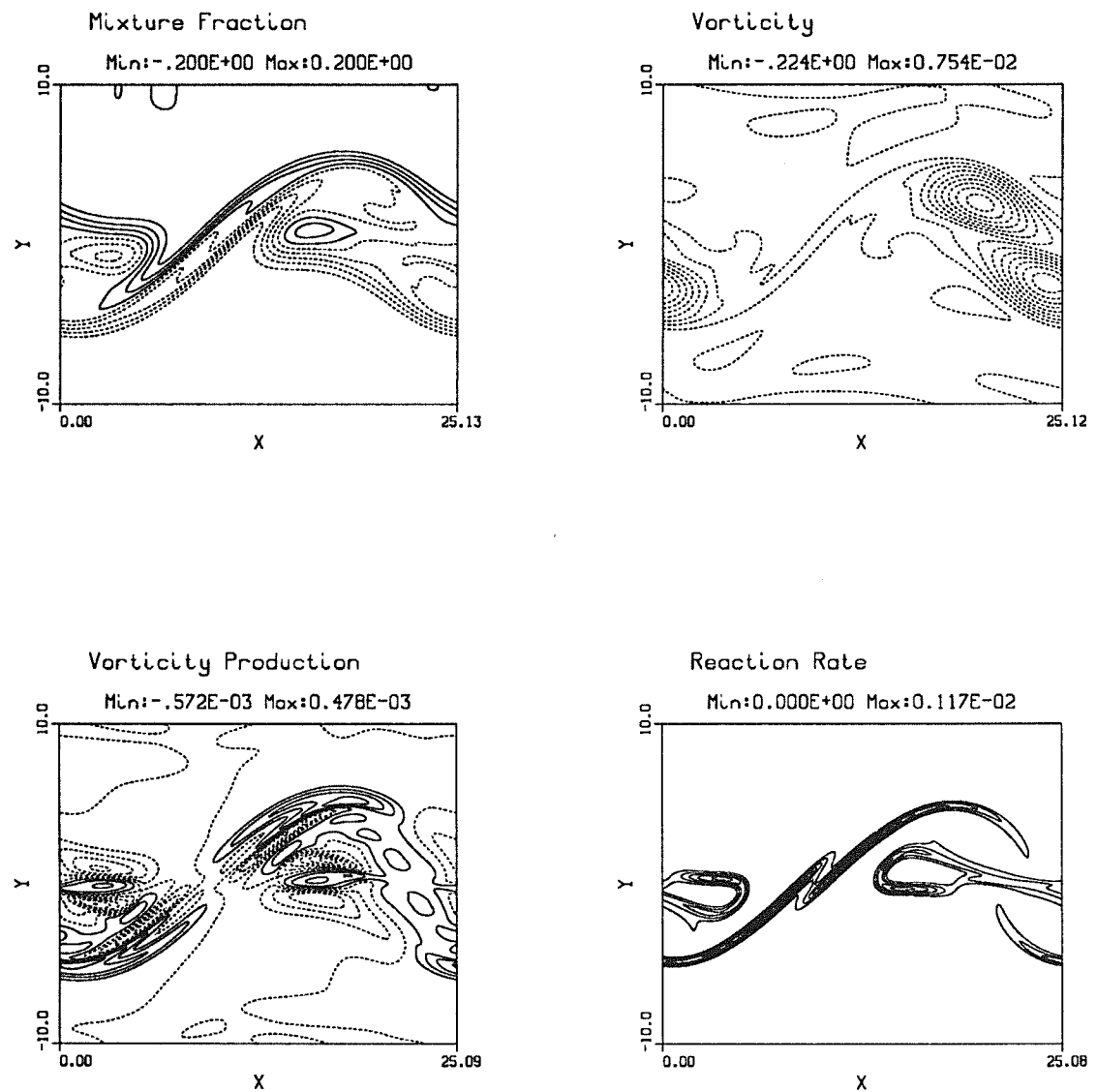


Figure 4.2: Interaction of a developed typical central mode with its subharmonic at three instants of time. c) $t=41$. (Low heat release $\Theta = 0.1$, $M_c = 0.2$, $Da = 5$, $Ze = 0.$, $U_2 = -1.$, $Re = 200$). (a) Mixture fraction; (b) vorticity; (c) vorticity production; (d) reaction rate.

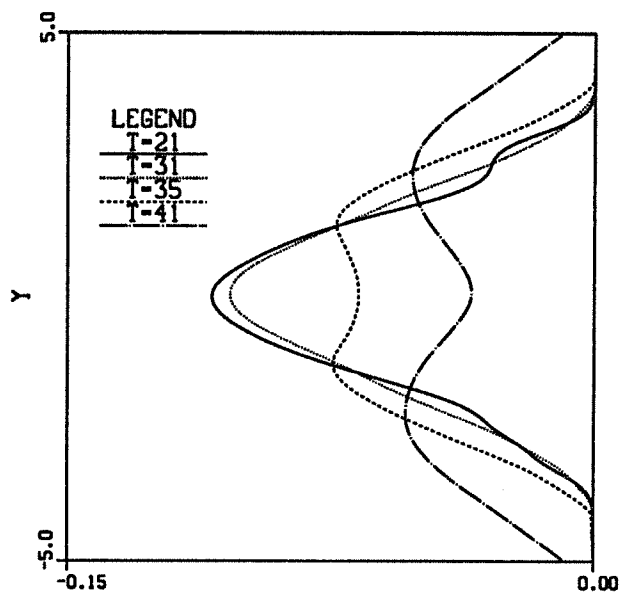


Figure 4.3: Mean vorticity profiles (X-averaged) of the central mode of figure 4.1 at 4 instants of time.

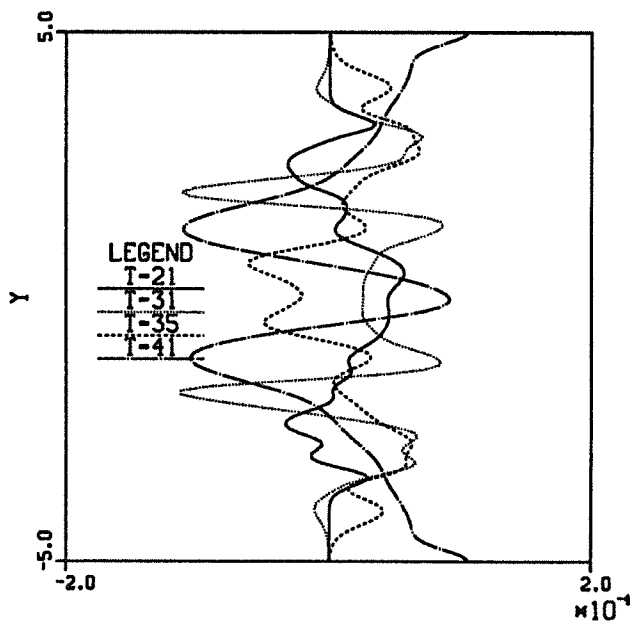


Figure 4.4: Mean profiles of vorticity production (dilatation term + baroclinic term) at 4 instants of time for the central mode of figure 4.1.

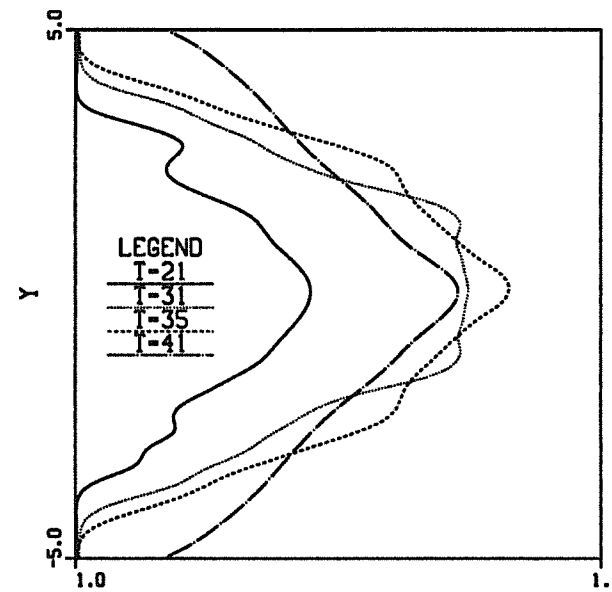


Figure 4.5: Mean temperature profiles (X-averaged) of the central mode of figure 4.1 at 4 instants of time.

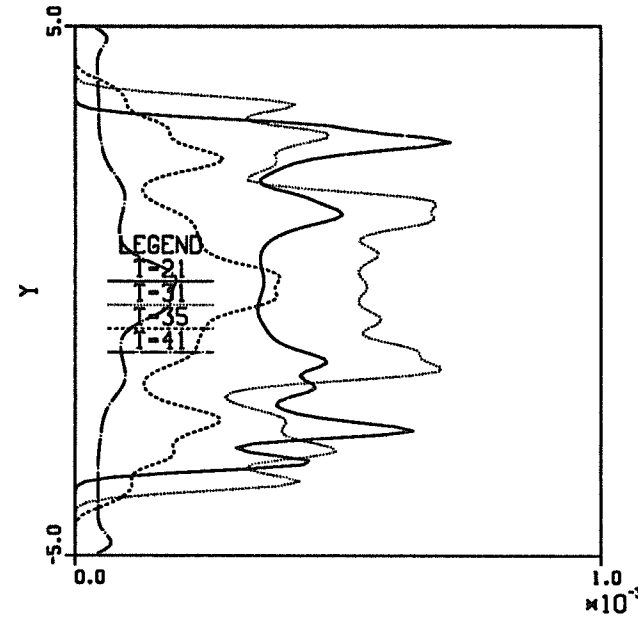


Figure 4.6: Mean reaction rate profiles (X-averaged) of the central mode of figure 4.1 at 4 instants of time. Note that the width of the mean reaction rate profile is comparable with the layer thickness.

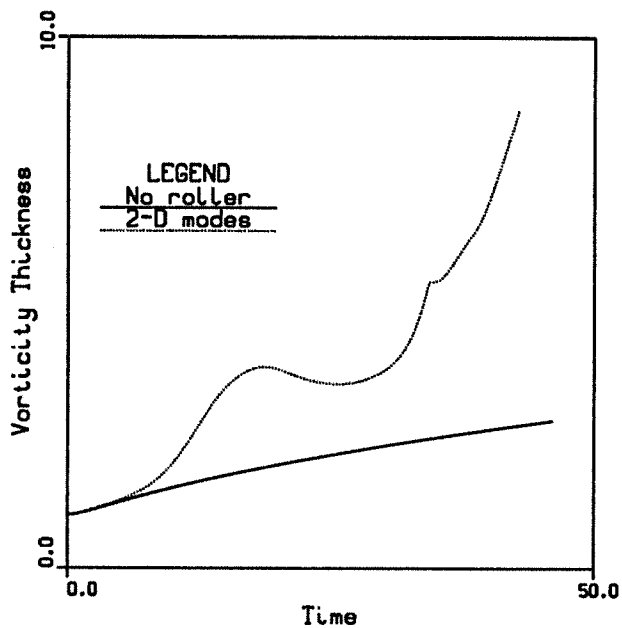


Figure 4.7: Growth of vorticity thickness with time for the central mode of figure 4.1. For comparison the laminar growth rate of the reacting mixing layer with same heat release and Mach number is shown (solid line).

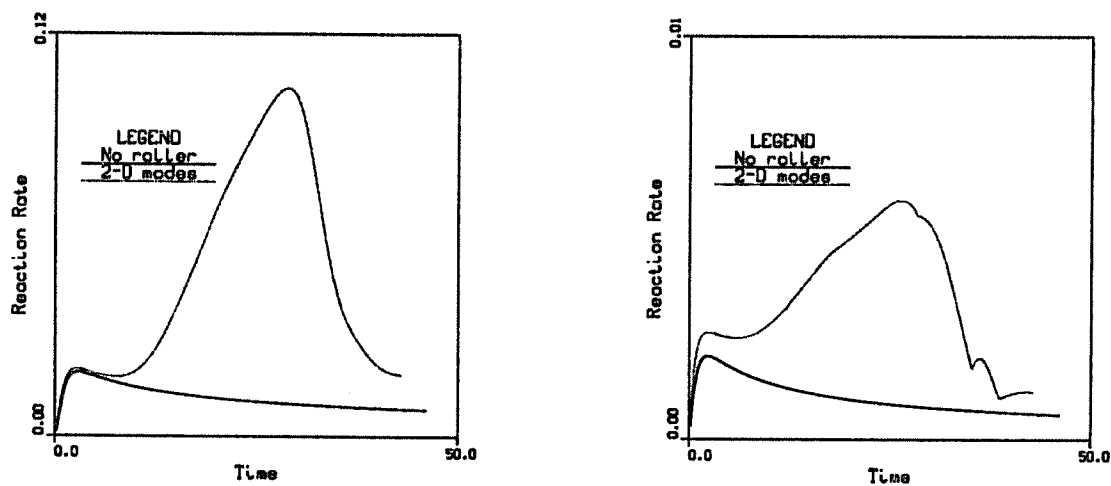


Figure 4.8: Time history of the total (left) and maximum (right) reaction rates of the mixing layer of figure 4.1. For comparison, the maximum and total reaction rate of the laminar mixing layer with same heat release and Mach number are also shown (solid lines).

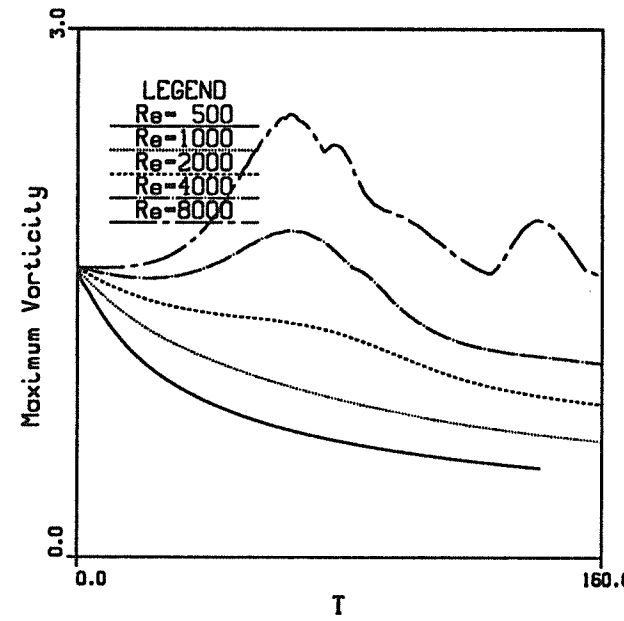


Figure 4.9: Time history of the maximum vorticity of a typical slow outer mode for different Reynolds numbers. (Heat release $T_f = 3.0$, $M_c = 0.8$, $Da = 6$, $Ze = 2.$, $U_2 = 0.5$).

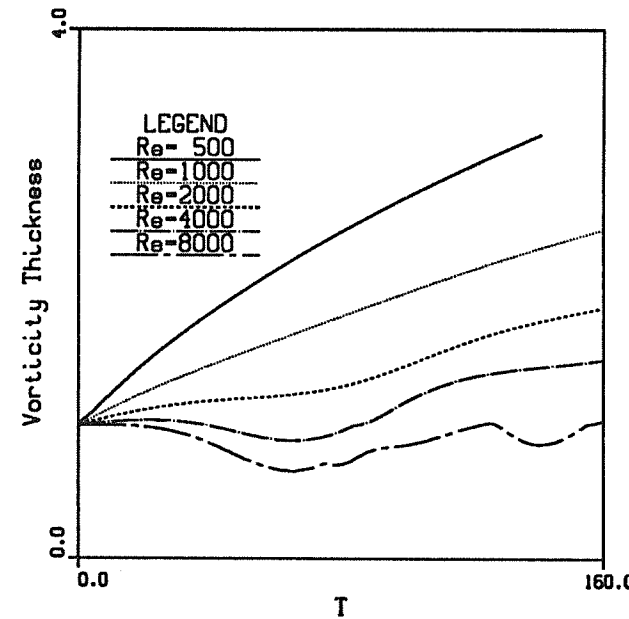


Figure 4.10: Time history of the vorticity thickness of the slow outer mode of figure 4.15 at different Reynolds numbers. Note the weak effect of the slow outer mode on the layer growth.

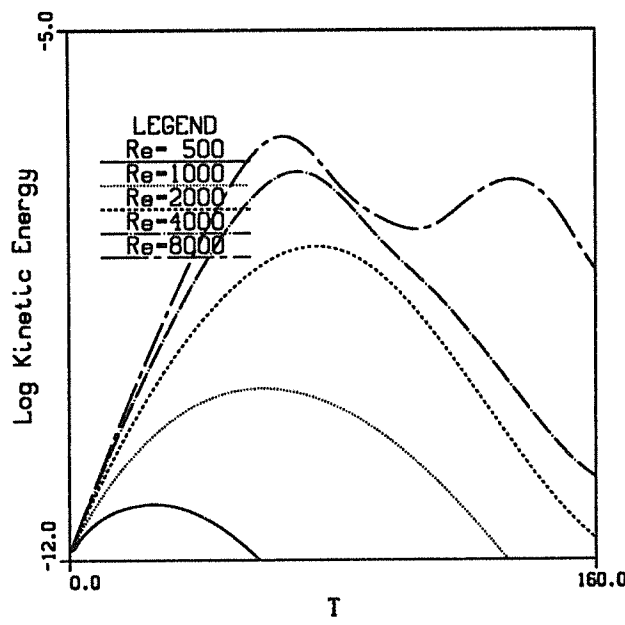


Figure 4.11: Effect of the Reynolds number on the time variation of the logarithm of the kinetic energy of the slow outer modes of figure 4.15. Note the initial linear growth, saturation and decay at all Re.

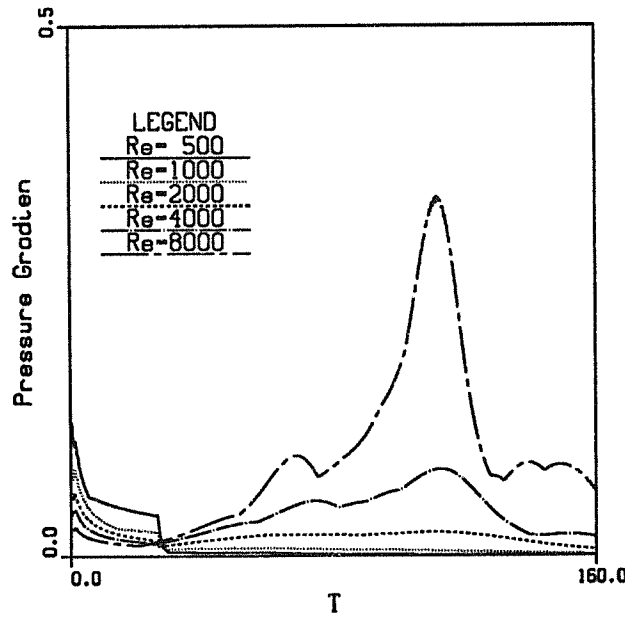


Figure 4.12: Time history of the maximum pressure gradient of the slow outer mode of figure 4.15 at different Reynolds numbers. Note the similarity of the two highest Reynolds curves and the strong peaks during the decay of the outer modes.

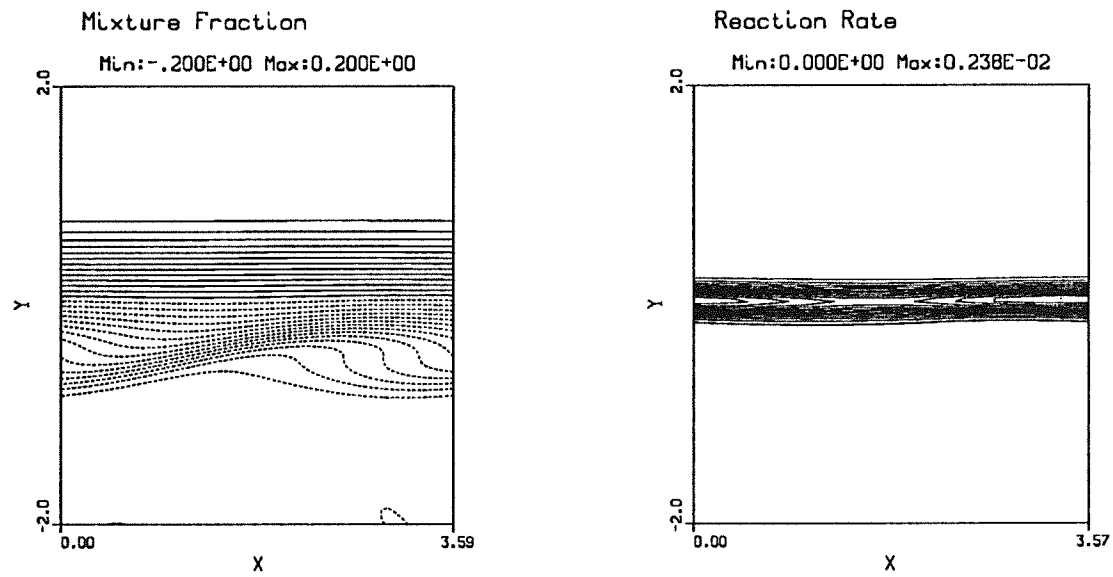


Figure 4.13: Influence of the Reynolds number on the slow outer mode ($T_f = 3.0$, $M_c = 0.8$, $Da = 6$, $Ze = 2.$, $U_2 = 0.5$, Time = 64.). $Re = 2000$

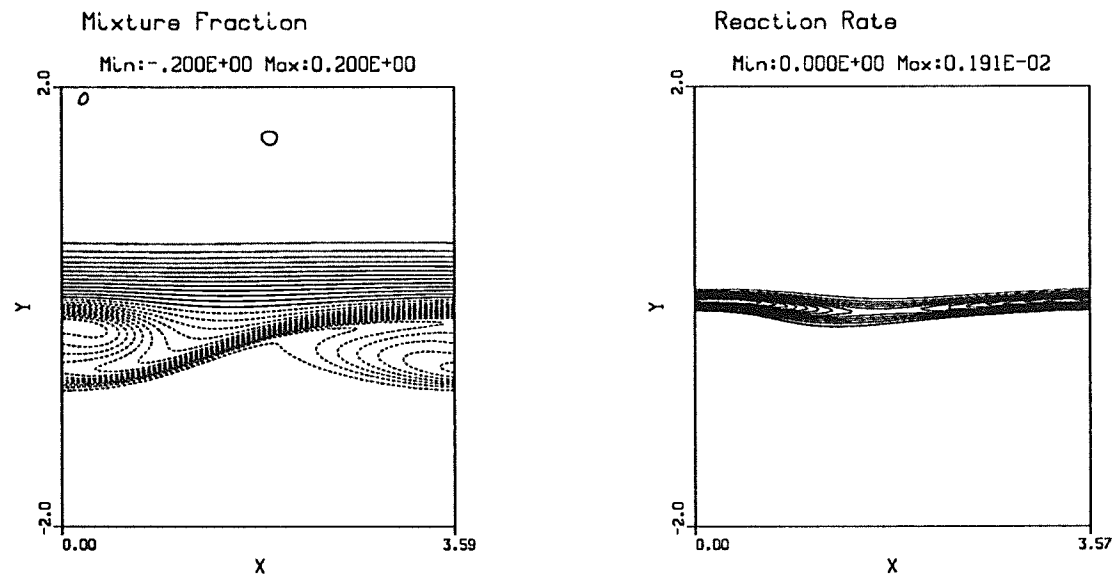


Figure 4.14: Influence of the Reynolds number on the slow outer mode ($T_f = 3.0$, $M_c = 0.8$, $Da = 6$, $Ze = 2.$, $U_2 = 0.5$, Time = 64.). $Re = 8000$

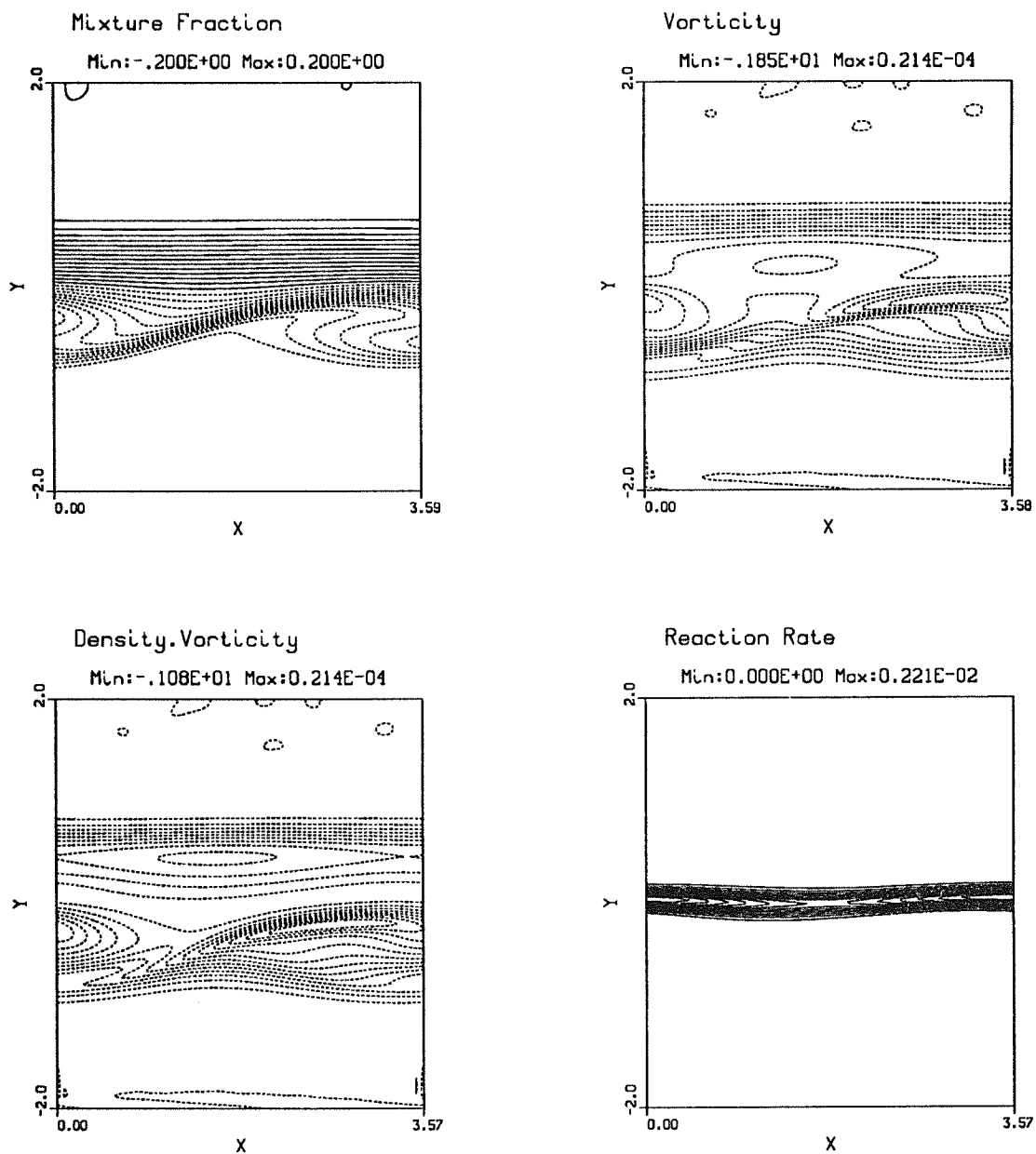


Figure 4.15: Typical slow outer mode ($T_f = 3.0$, $M_c = 0.8$, $Da = 6$, $Ze = 2.$, $U_2 = 0.5$, $Re = 4000$, $Time = 64.$). (a) Mixture fraction; (b) vorticity; (c) density-weighted vorticity; (d) reaction rate.

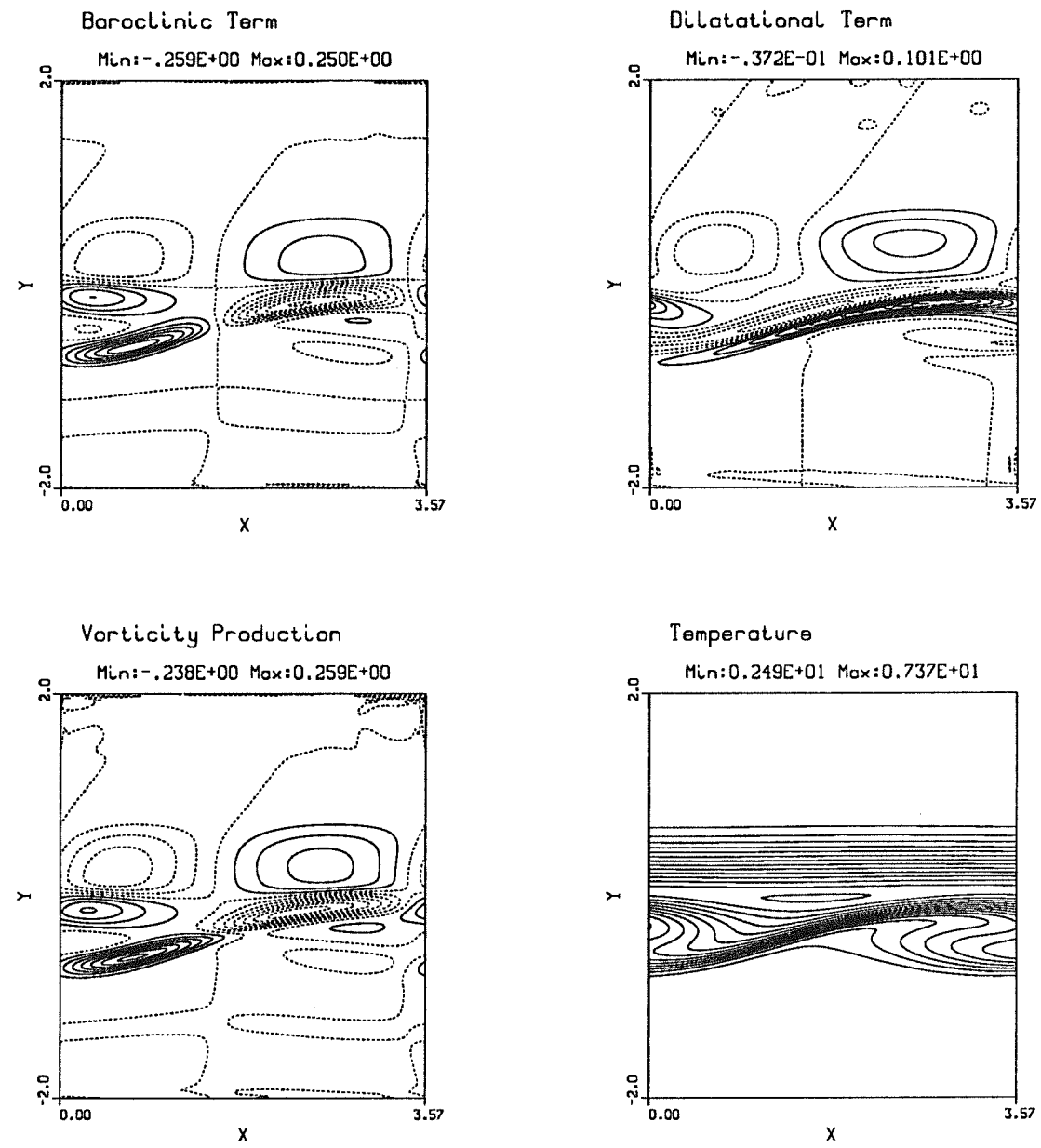


Figure 4.15: Typical slow outer mode ($T_f = 3.0$, $M_c = 0.8$, $Da = 6$, $Ze = 2.$, $U_2 = 0.5$, $Re = 4000$, $Time = 64.$). (e) Baroclinic term; (f) dilatational term; (g) vorticity production; (h) temperature.

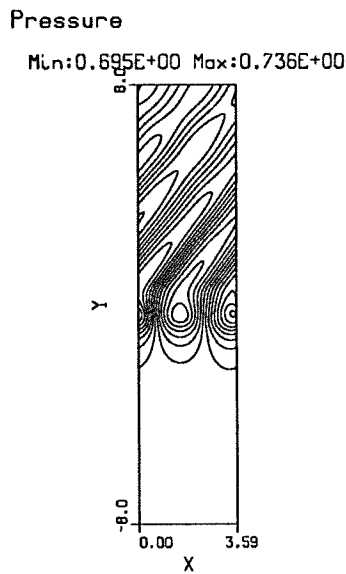


Figure 4.16: Pressure contours of the slow outer mode of figure 4.15 ($t = 80$)

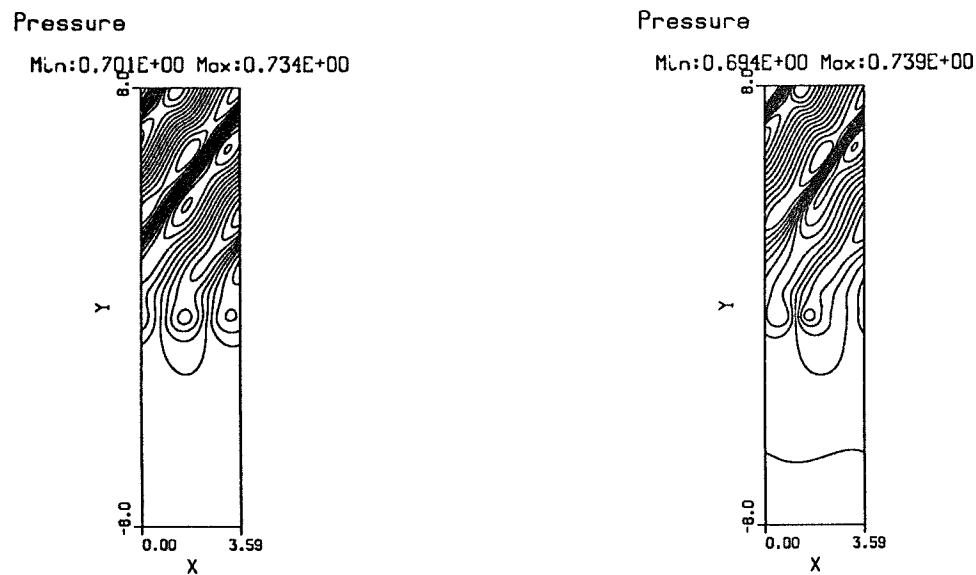


Figure 4.17: Left: Pressure contours of the slow outer mode of figure 4.15 at time 96.
Right: Same at $Re = 8000$.

Mixture Fraction

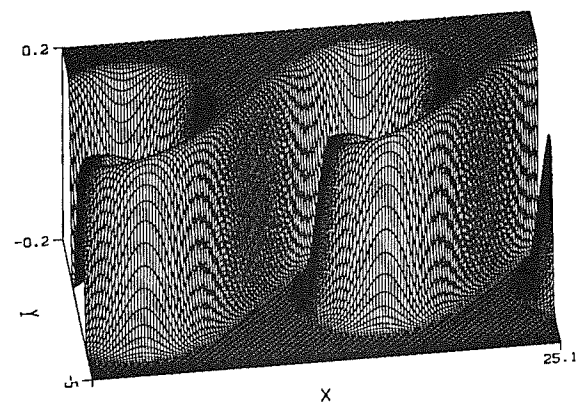


Figure 4.18: Surface plot of the mixture fraction of the typical central mode of figure 4.1. $t = 21$.

Mixture Fraction

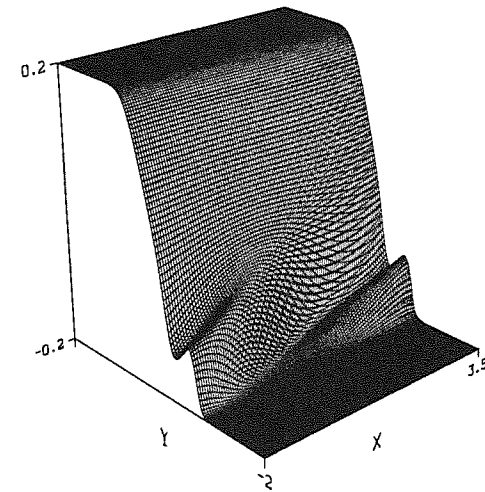
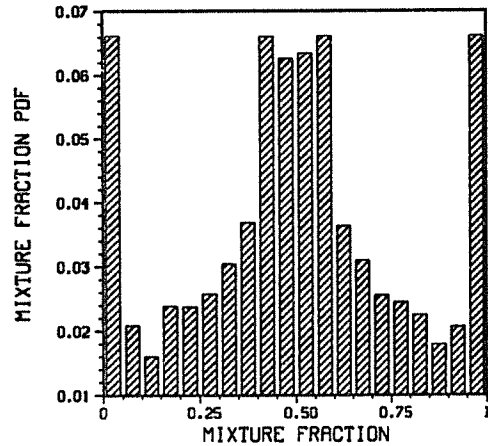
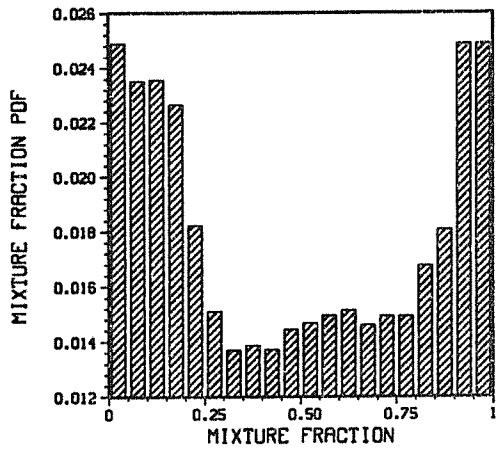


Figure 4.19: Surface plot of the mixture fraction of the typical slow outer mode of figure 4.15. *Time* = 64. Note the existence of a single ramp on the slow-stream side.

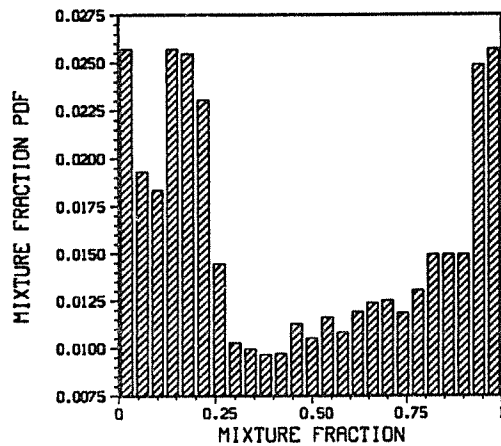
INCOMPRESSIBLE M.L. LOW H.R.



COMPRESSIBLE REACTING M.L.



COMPRESSIBLE REACTING M.L.



COMPRESSIBLE REACTING M.L.

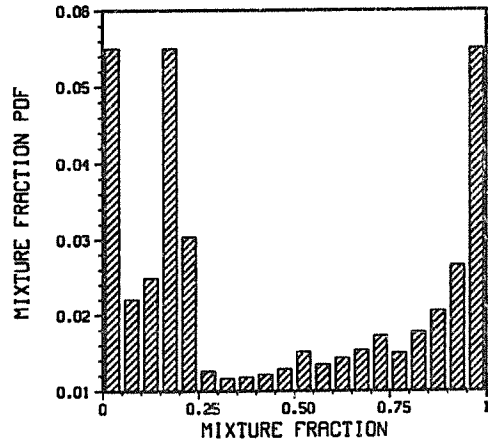


Figure 4.20: Mixture fraction PDF for the central mode of figure 4.1 (top left) and for the slow outer mode of figure 4.15 at times 64 (top right), 80 (bottom left), 96 (bottom right). Note the location of the bump at $Z = 0.2$ for the compressible slow outer mode.

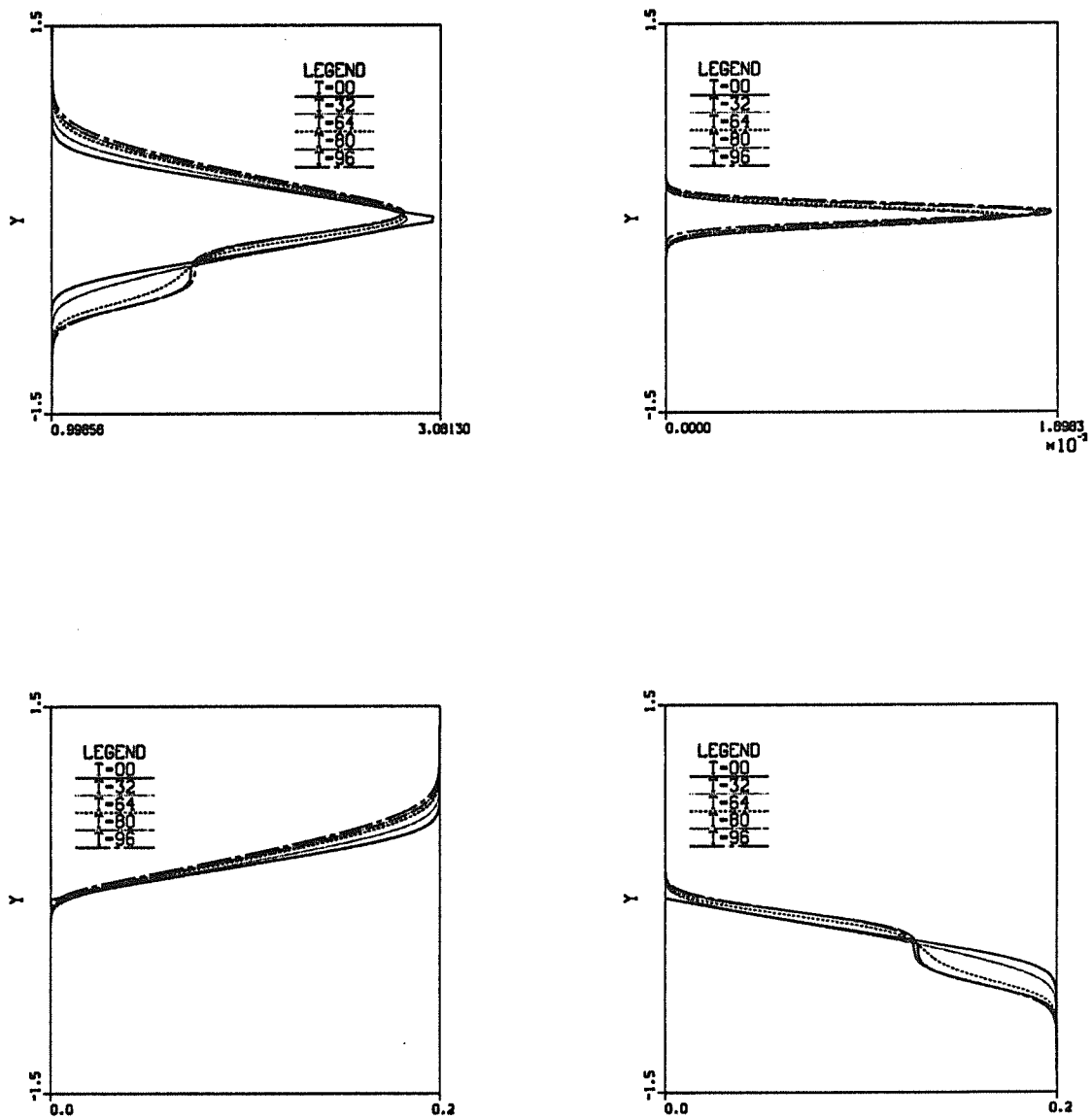


Figure 4.21: Mean (X-averaged) profiles of temperature (top left), reaction rate (top right), fuel (bottom left) and oxidizer (bottom right) at five instants of time for the slow outer mode of figure 4.15. Note the width of the reaction rate profile and the bump on the slow-stream side of the temperature and oxidizer profiles.

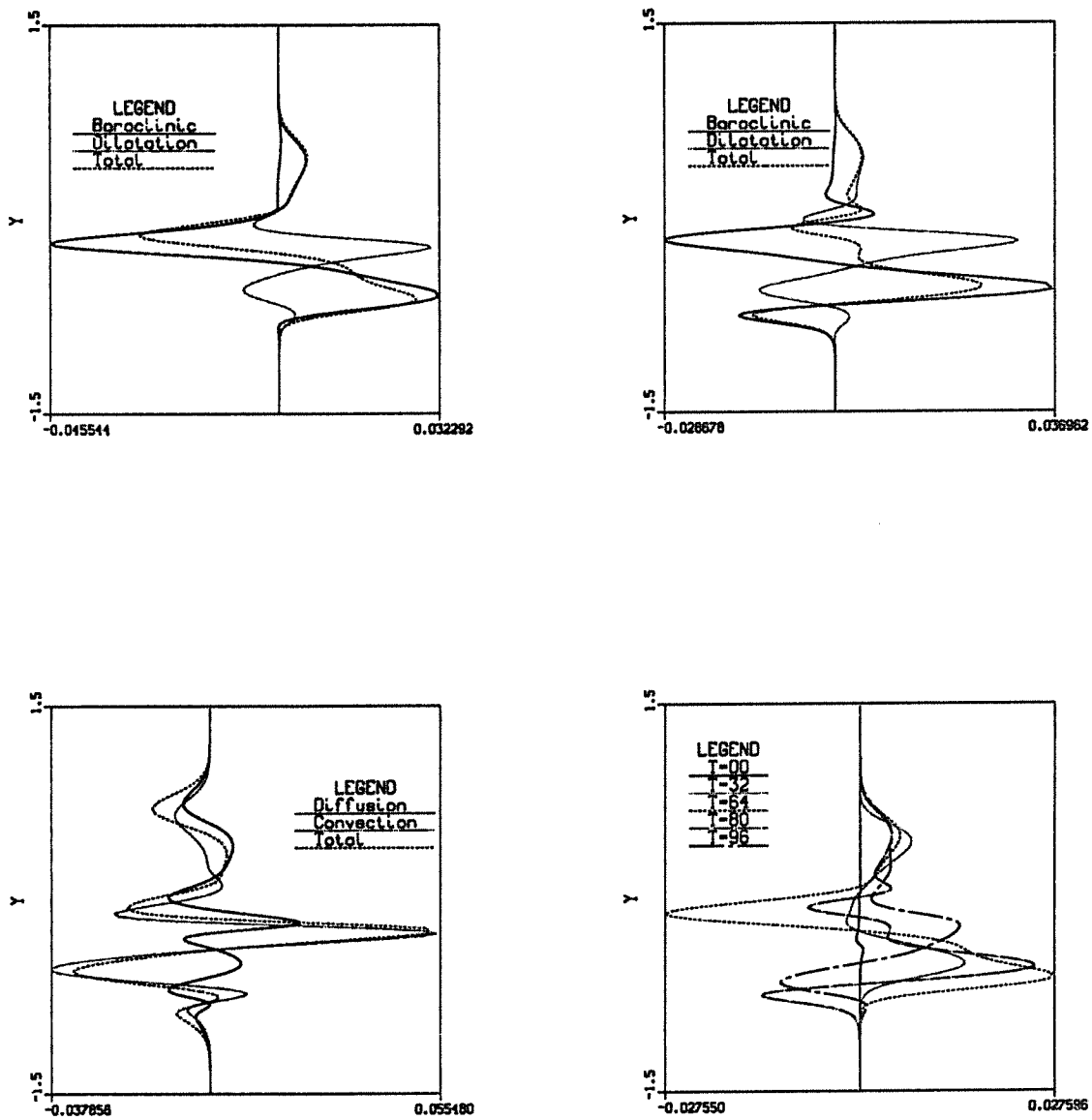


Figure 4.22: Top: Mean (X-averaged) profiles of vorticity sources at times $t = 64$ (left) and $t = 80$ (right). Bottom left: Mean profile of vorticity transport at time $t = 64$. Bottom right: Mean profile of total vorticity sources (baroclinic + dilatational term) at five instants of time. (slow mode of figure 4.15)

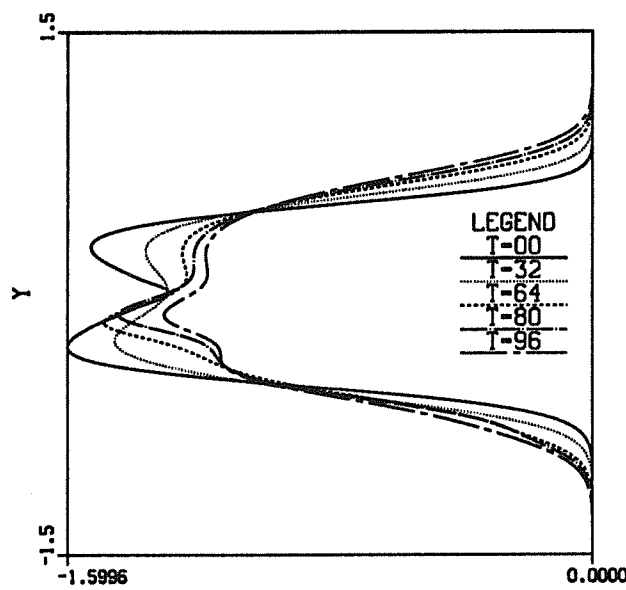


Figure 4.23: Mean (X-averaged) profile of vorticity at five instants of time (slow outer mode of figure 4.15)

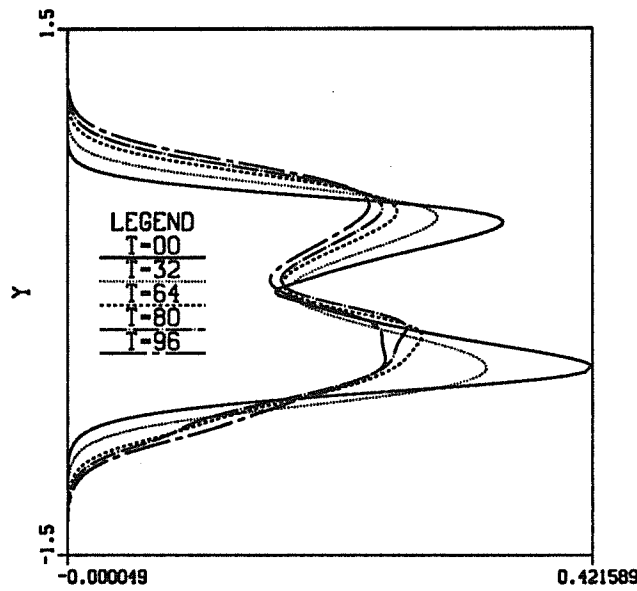


Figure 4.24: Mean (X-averaged) profile of density-weighted vorticity ($\rho d\bar{u}/dy$) normalized by \bar{u}_1 at five instants of time (slow outer mode of figure 4.15)

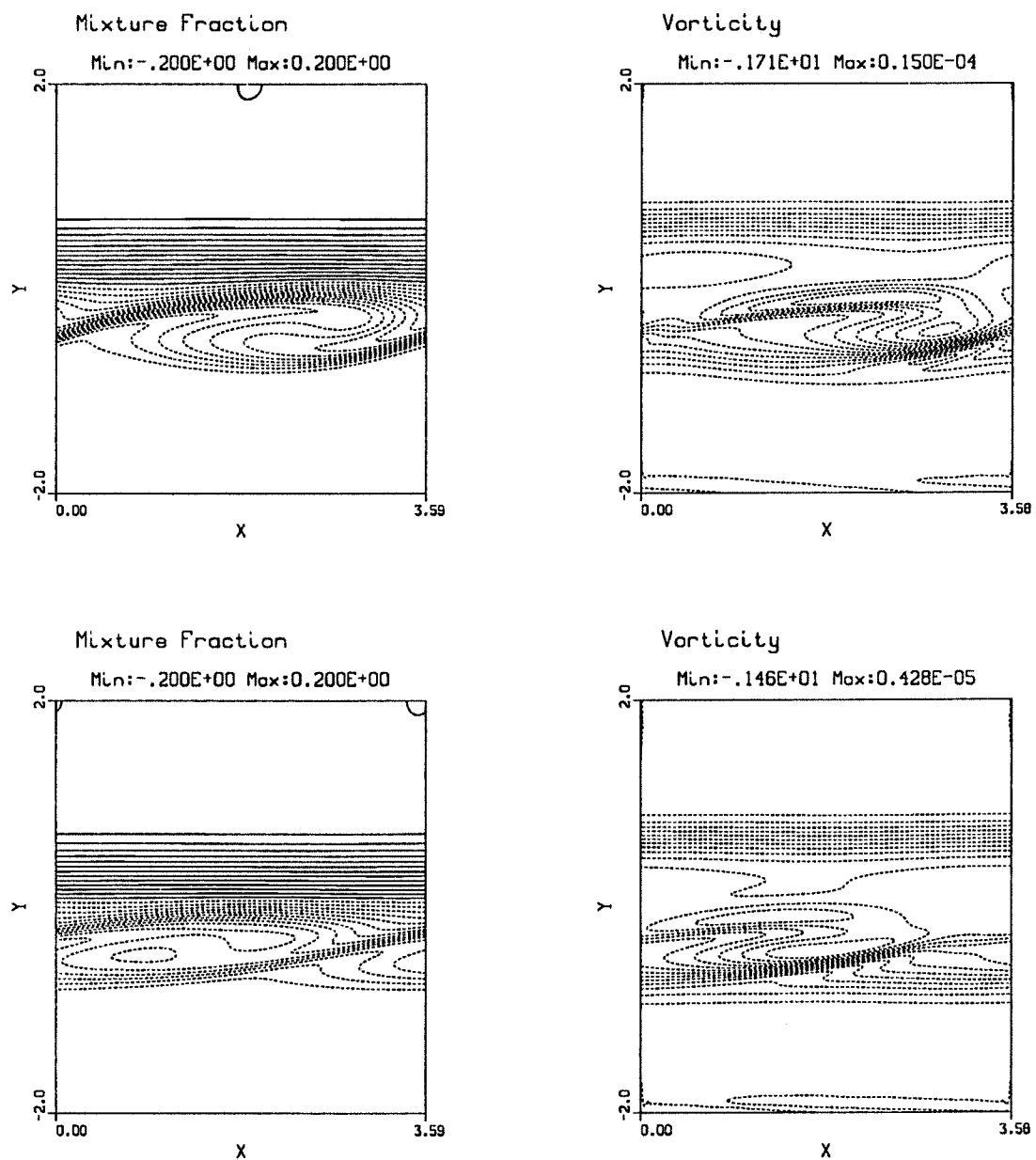


Figure 4.25: Decay of the slow outer mode: Contour plots of mixture fraction and vorticity at time 80 (top) and 96 (bottom). Note the elongation of the structure in the x -direction.

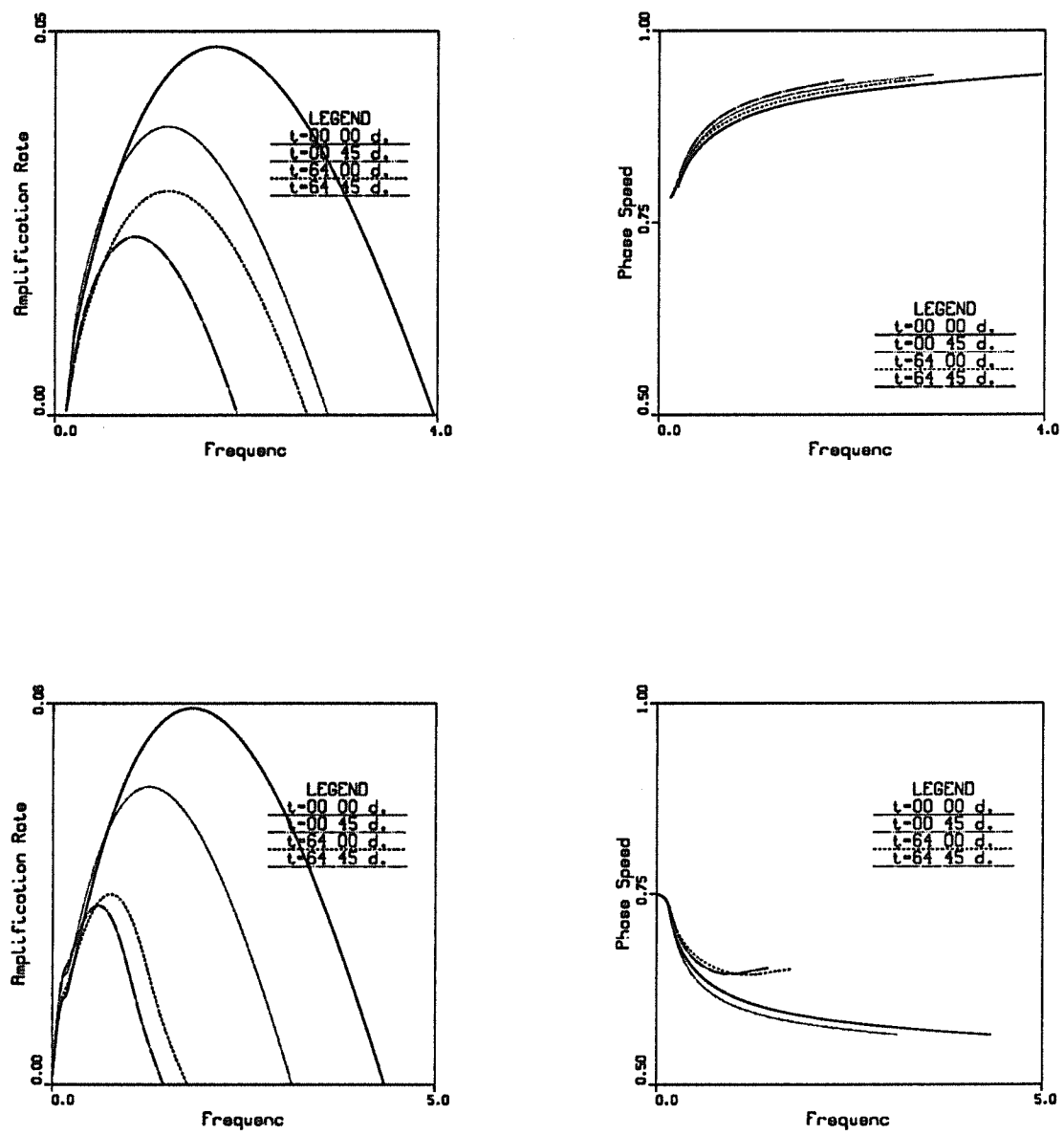


Figure 4.26: Comparison of the phase speeds and amplification rates of the fast and slow outer modes for the linear stability analysis based on the mean profiles at times $t = 0$ and $t = 64$. Two obliquities considered: 2-D and 45 degrees. Top: fast mode; bottom: slow mode.

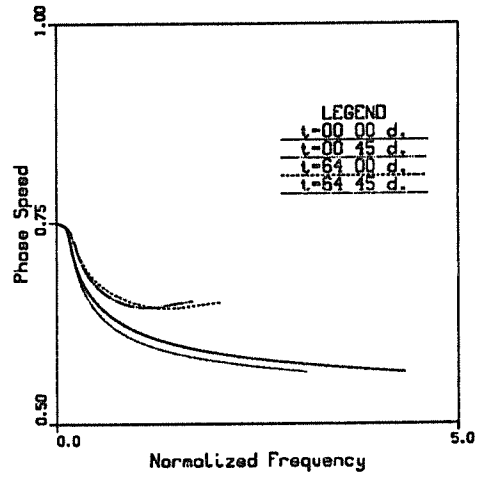
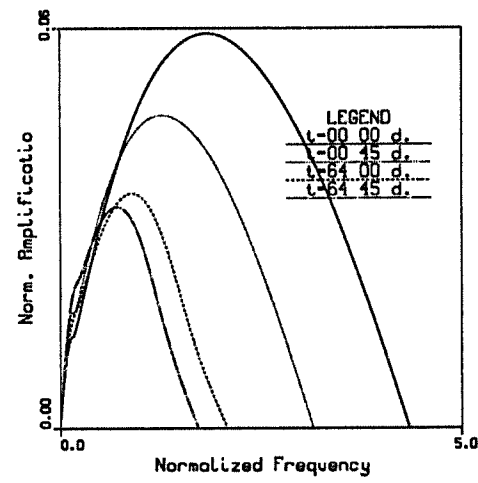
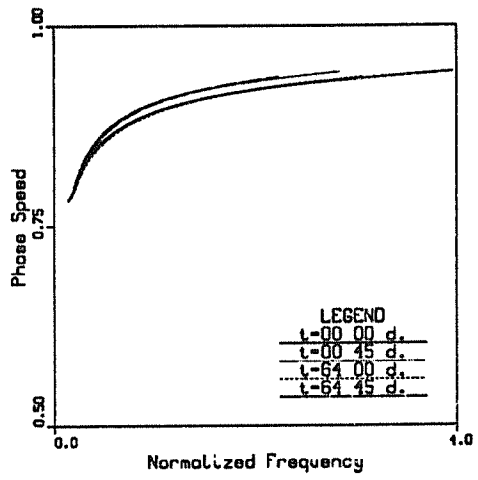
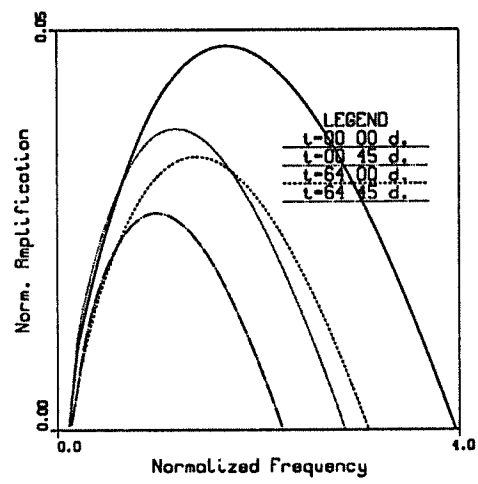


Figure 4.27: Same as figure 4.26 with the mean profile at $t = 64$ normalized to get $\delta_\omega = 1$.

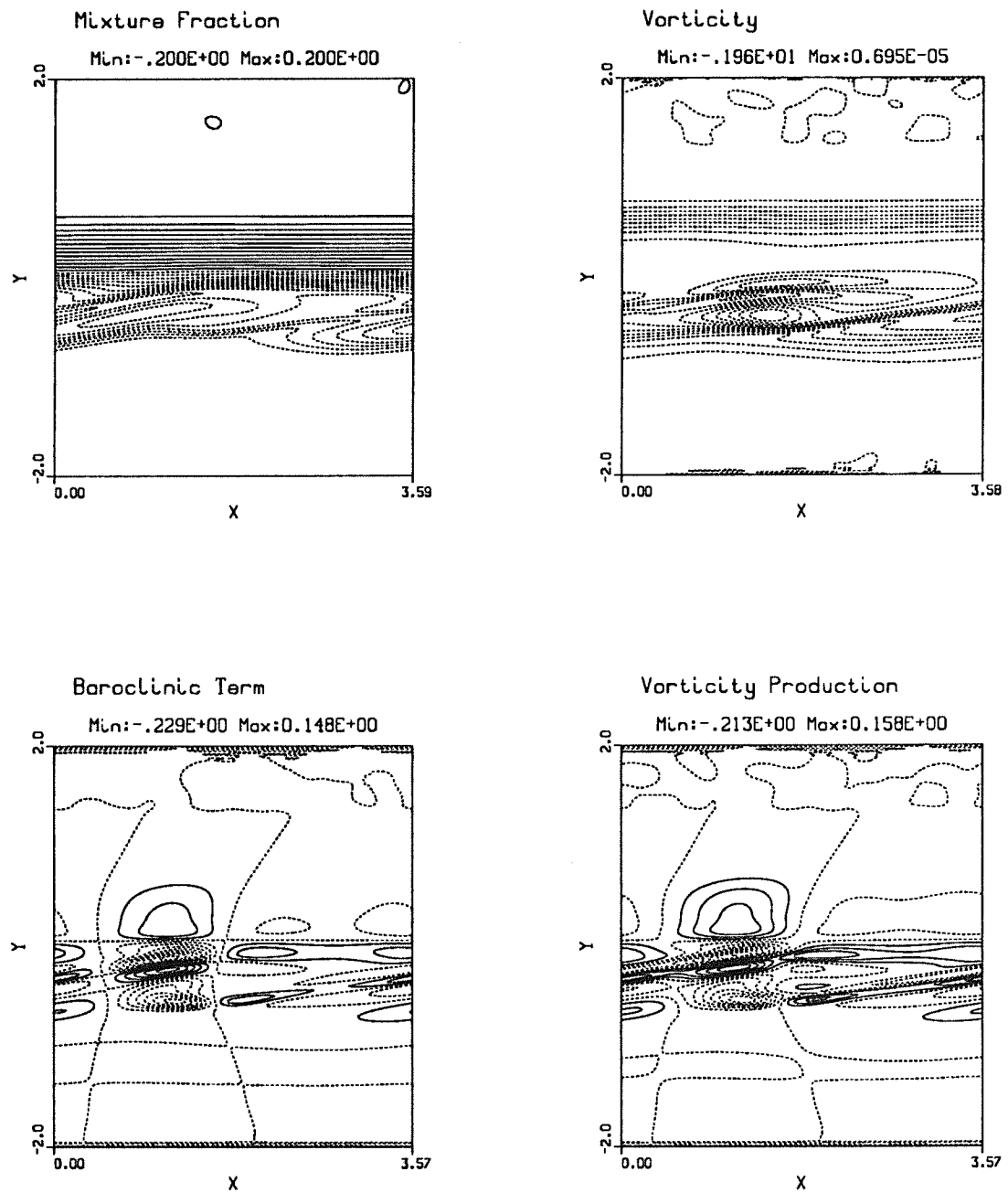


Figure 4.28: Behavior of the slow outer mode at high Reynolds number ($Re = 8000$) as its kinetic energy oscillates (see fig. 4.12). (time $t = 96$). (a) Mixture fraction; (b) vorticity; (c) baroclinic term; (d) vorticity production.

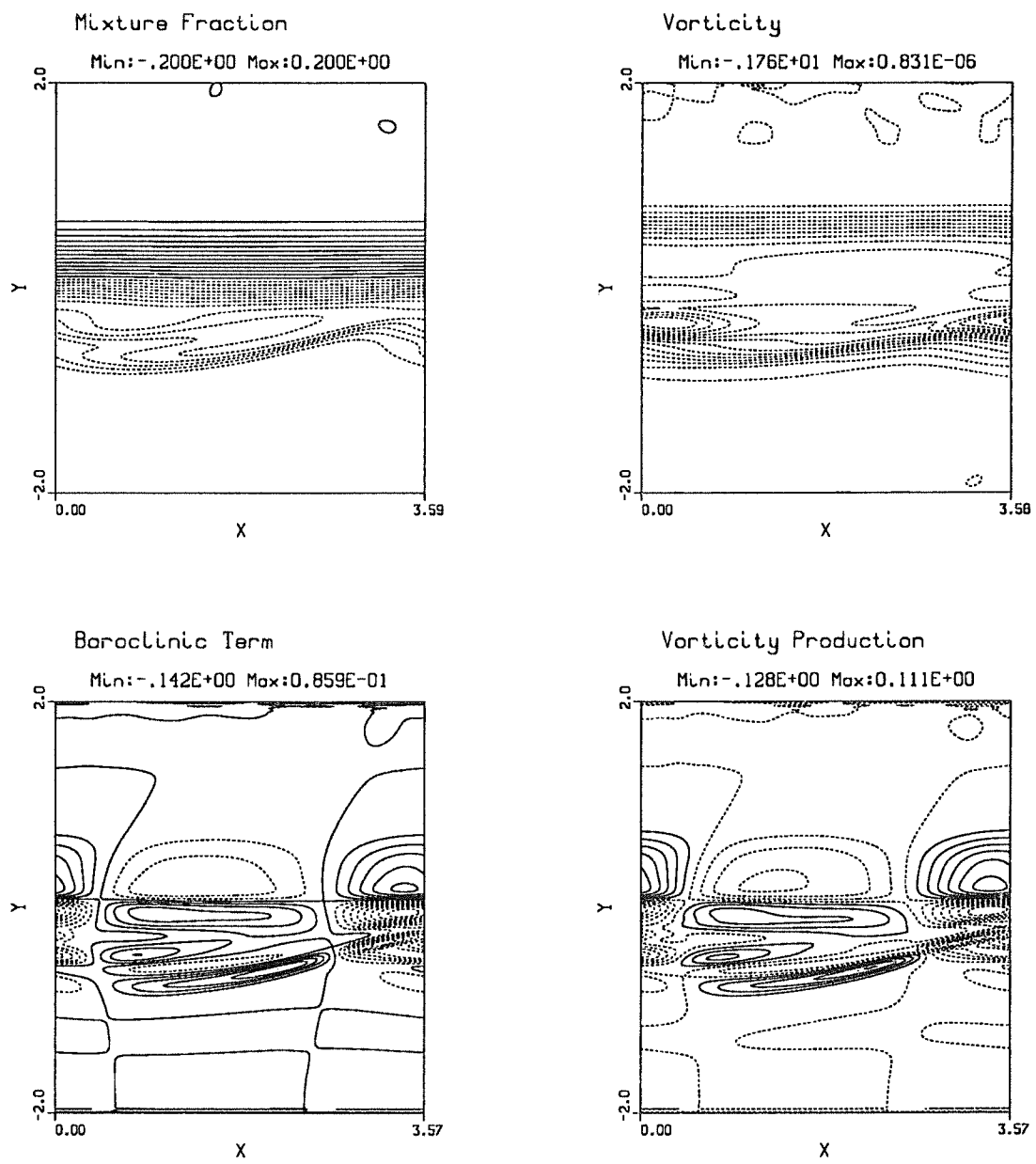


Figure 4.29: Behavior of the slow outer mode at high Reynolds number ($Re = 8000$) as its kinetic energy oscillates (see fig. 4.12). (time $t = 112$). (a) Mixture fraction; (b) vorticity; (c) baroclinic term; (d) vorticity production.

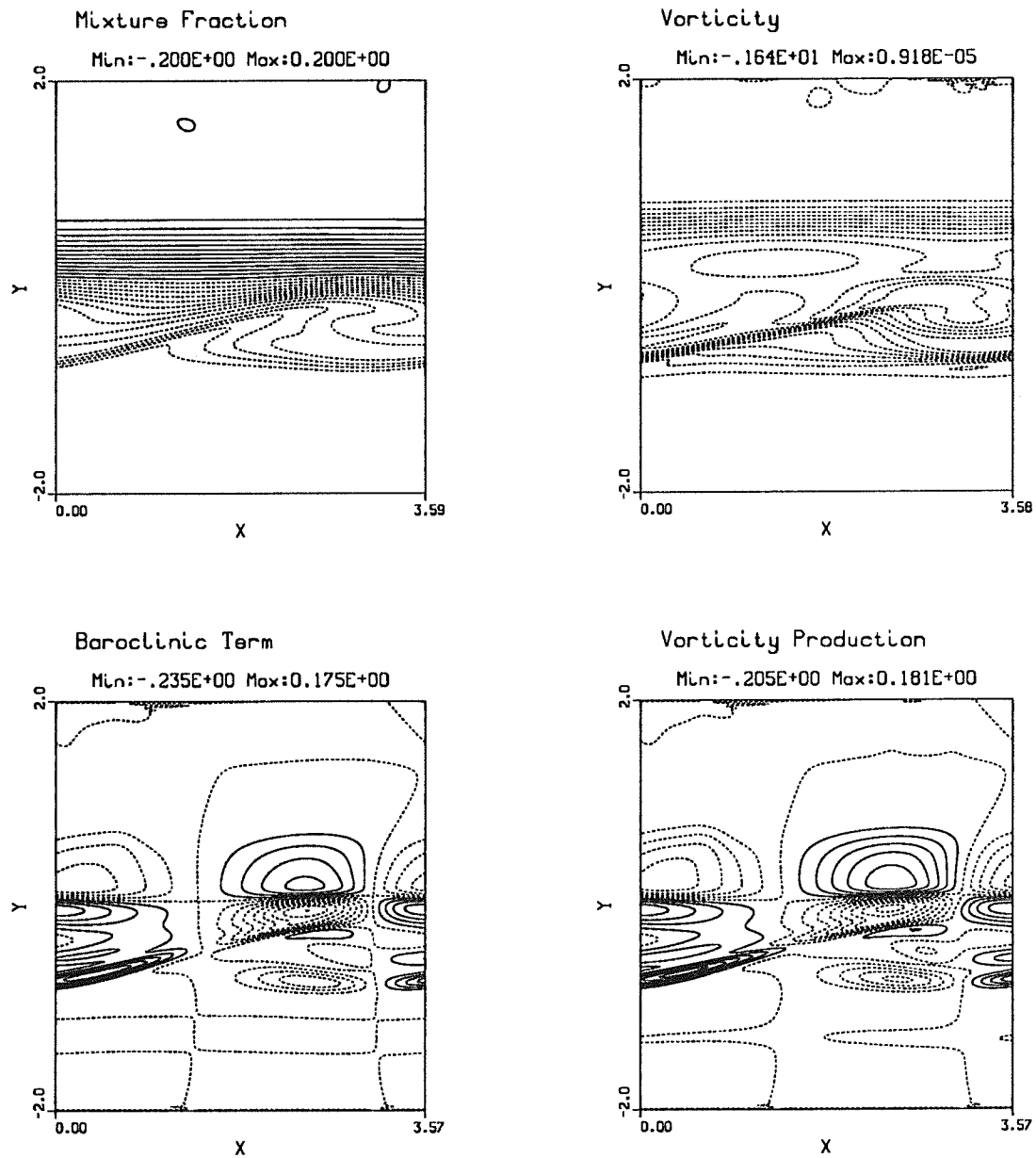


Figure 4.30: Behavior of the slow outer mode at high Reynolds number ($Re = 8000$) as its kinetic energy oscillates (see fig. 4.12). (time $t = 128$). (a) Mixture fraction; (b) vorticity; (c) baroclinic term; (d) vorticity production.

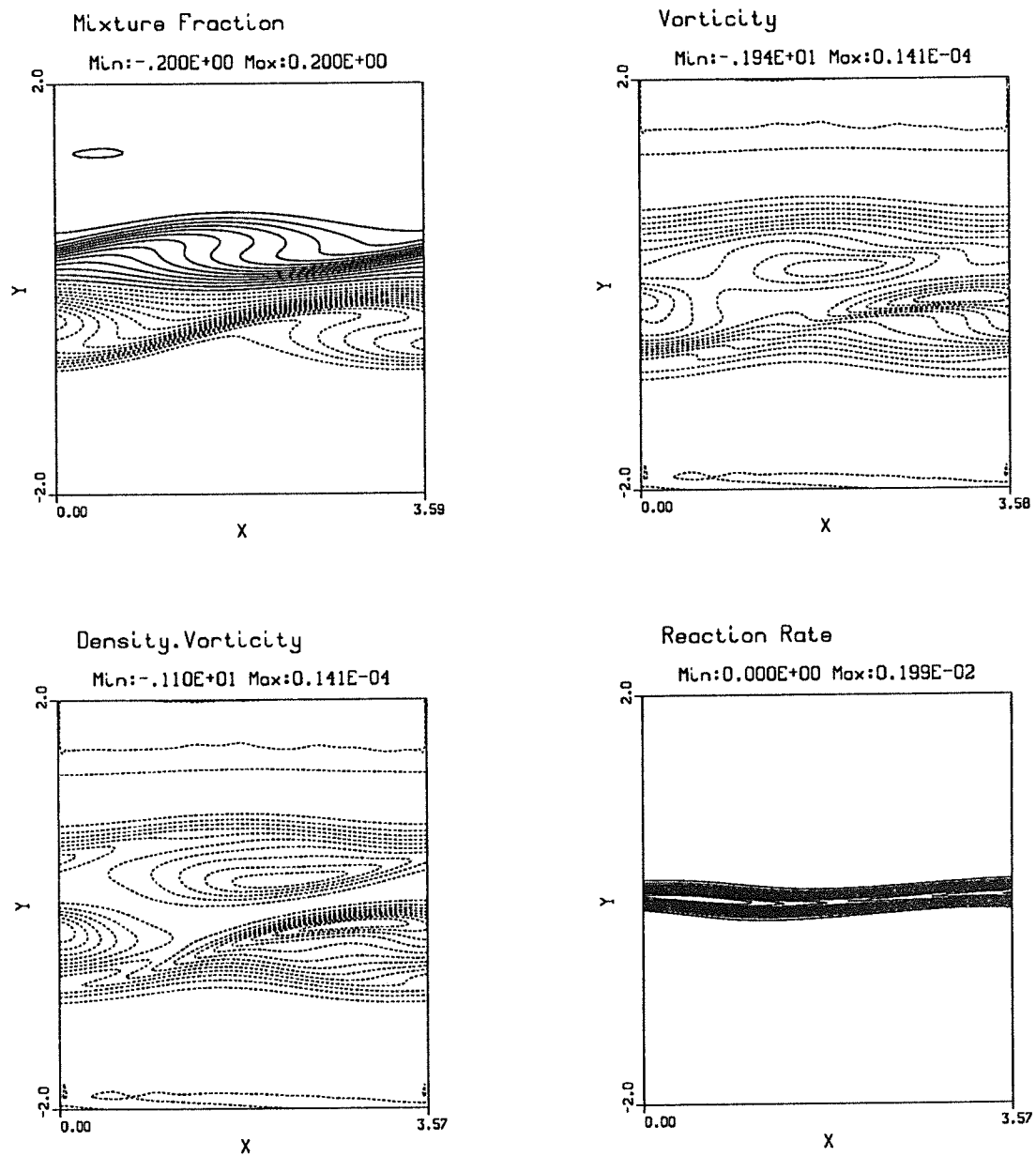


Figure 4.31: Simulation initialized with the fast and slow outer modes (Heat release $T_f = 3.0$, $M_c = 0.8$, $Da = 6$, $Ze = 2$, $U_2 = 0.5$, $Re = 4000$). Note the absence of interaction between the two colayers and compare the slow side of the layer with Figure 4.15. (a) Mixture fraction; (b) vorticity; (c) density-weighted vorticity; (d) reaction rate.

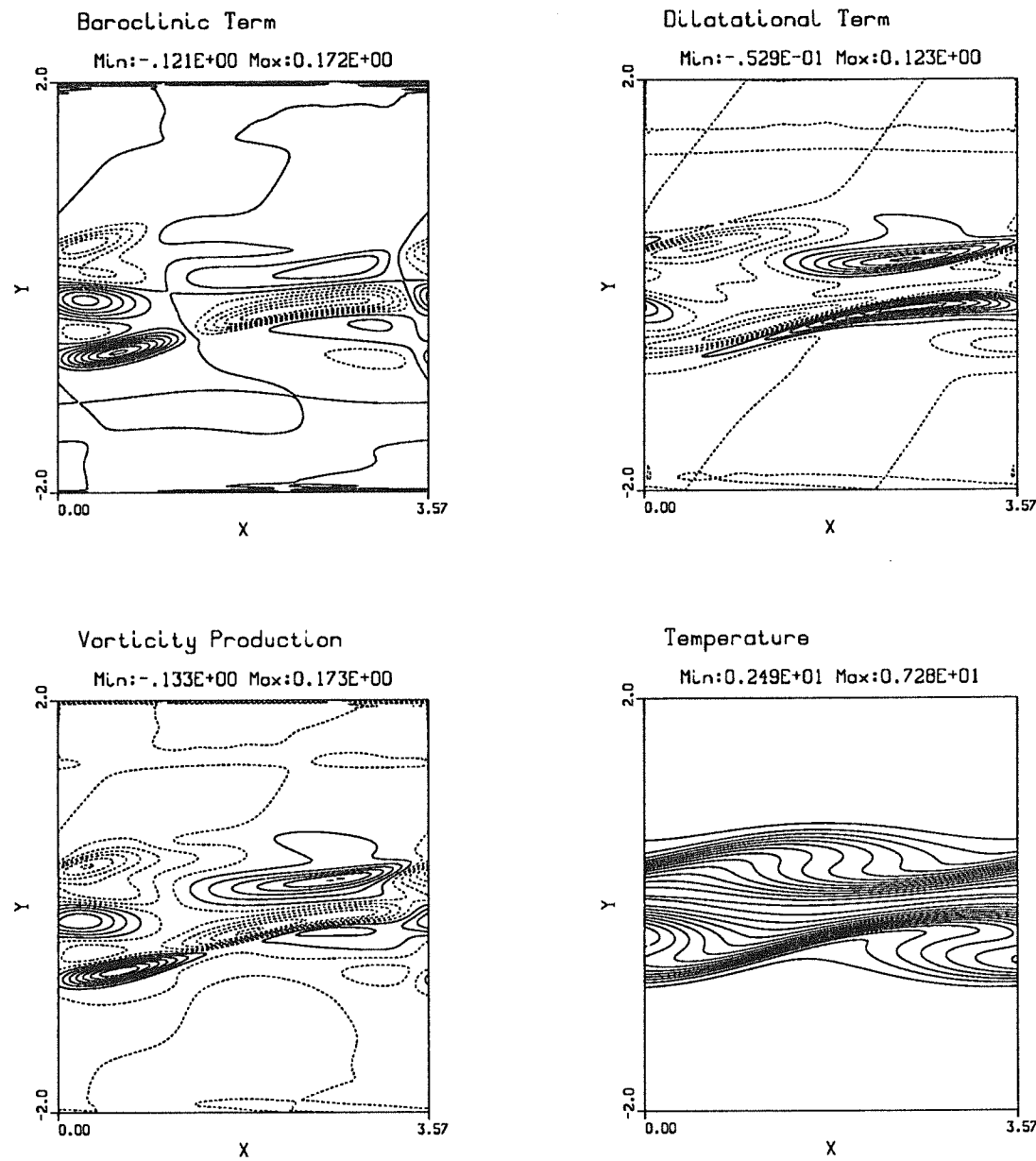


Figure 4.31 (continued): Simulation initialized with the fast and slow outer modes (Heat release $T_f = 3.0$, $M_c = 0.8$, $Da = 6$, $Ze = 2$, $U_2 = 0.5$, $Re = 4000$). Note the absence of interaction between the two colayers. (e) Baroclinic term; (f) dilatation term; (g) vorticity production; (h) temperature.

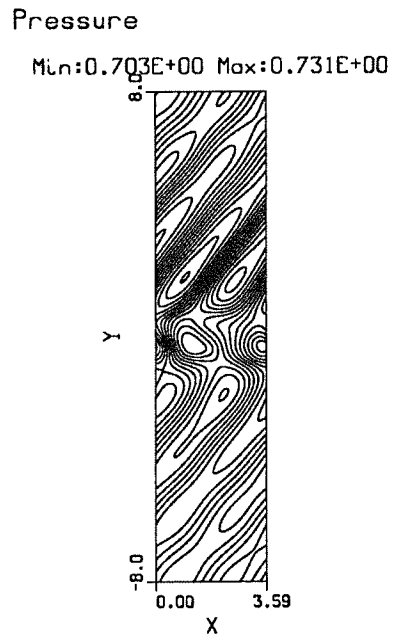


Figure 4.32: Pressure contours of the fast and slow outer modes of figure 4.31. Note the two systems of Mach waves.

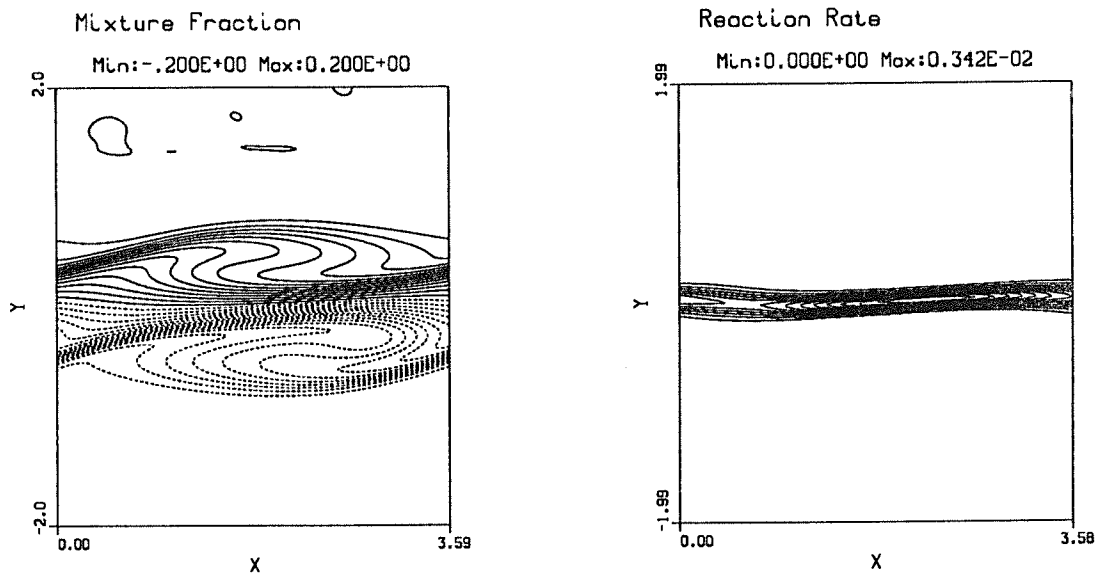


Figure 4.33: Simulation initialized with the fast and the slow outer mode. Same simulation than figure 4.32 at time $t = 80$. Note the quickly changing appearance of the layer and the increased reaction rate when the outer modes lie on top of each other. The fast outer mode, which has a smaller amplification rate, is still growing while the slow outer mode is decaying.

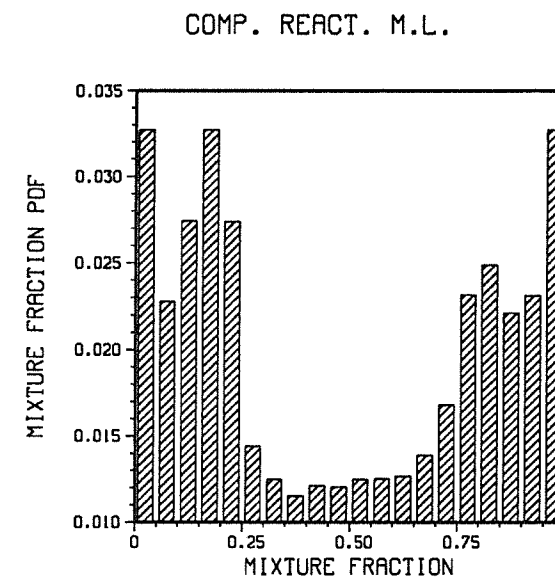


Figure 4.34: PDF of the mixture fraction for the simulation of figure 4.31 at time $t = 80$). Note the two bumps corresponding to two zones of mixing.

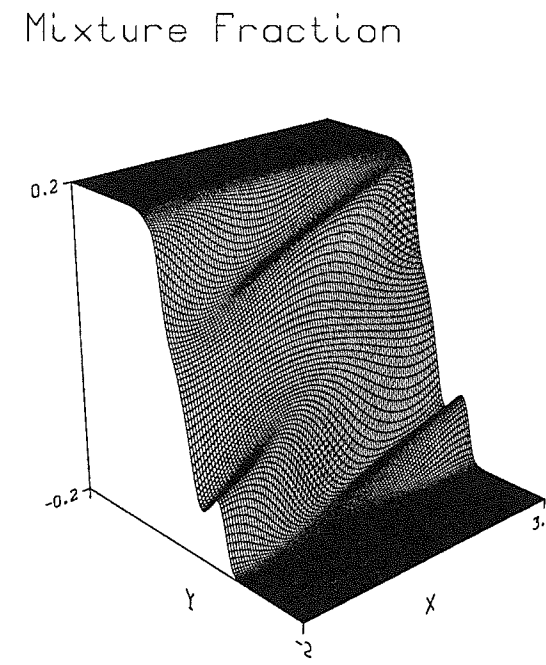


Figure 4.35: Surface-plot of the mixture fraction corresponding to figure 4.33. Note the existence of two ramps, one in each colayer.

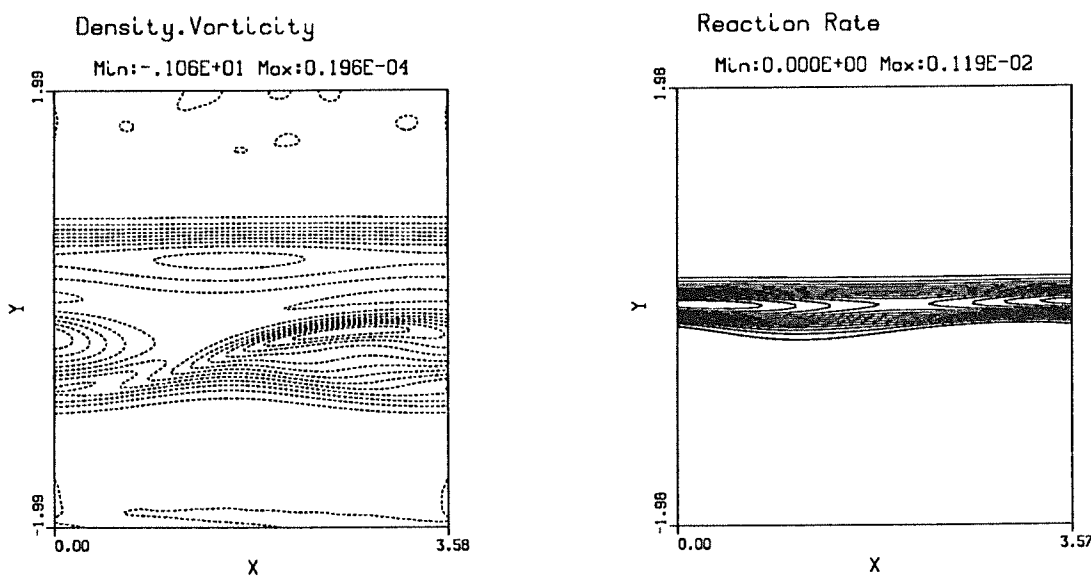
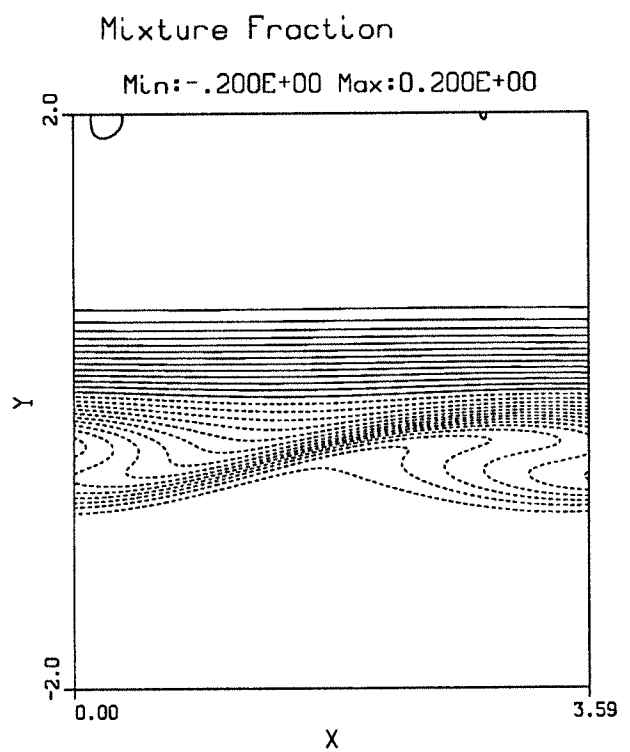


Figure 4.36: Influence of the Damköler number on the slow outer mode ($T_f = 3.00$, $Re = 4000$, $Da = 1.$, $M_c = 0.8$, $Ze = 2.$) to be compared with the slow outer mode of figure 4.15.

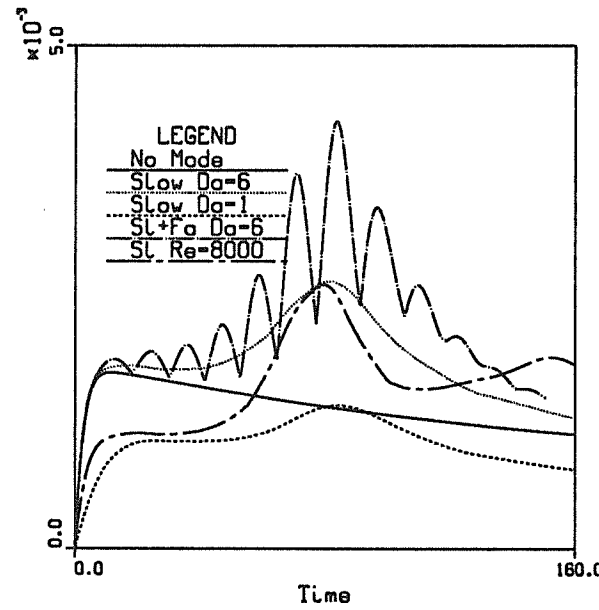
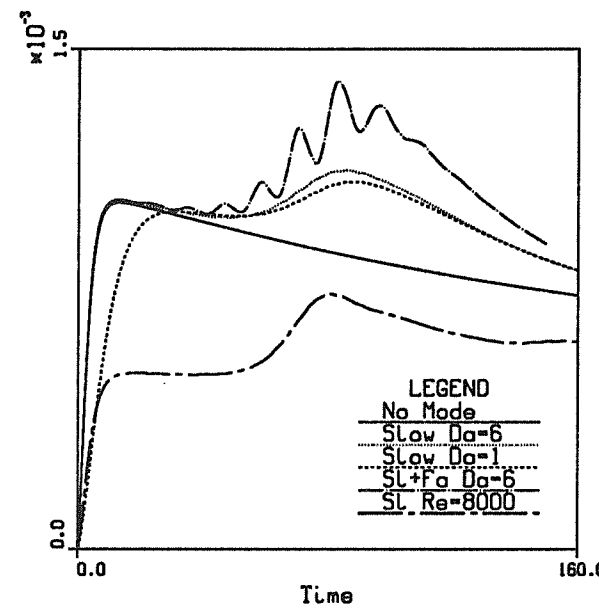


Figure 4.37: Influence of the Damkhöler number, of the interaction between fast and slow outer modes and of the Reynolds number on the (top) total reaction rate and (bottom) maximum reaction rate. Laminar (no outer mode, solid line) mixing layer with $Re = 4000$ shown for comparison. Note the oscillations of the total and maximum reaction rates when the fast and slow outer modes slide one on top of the other.

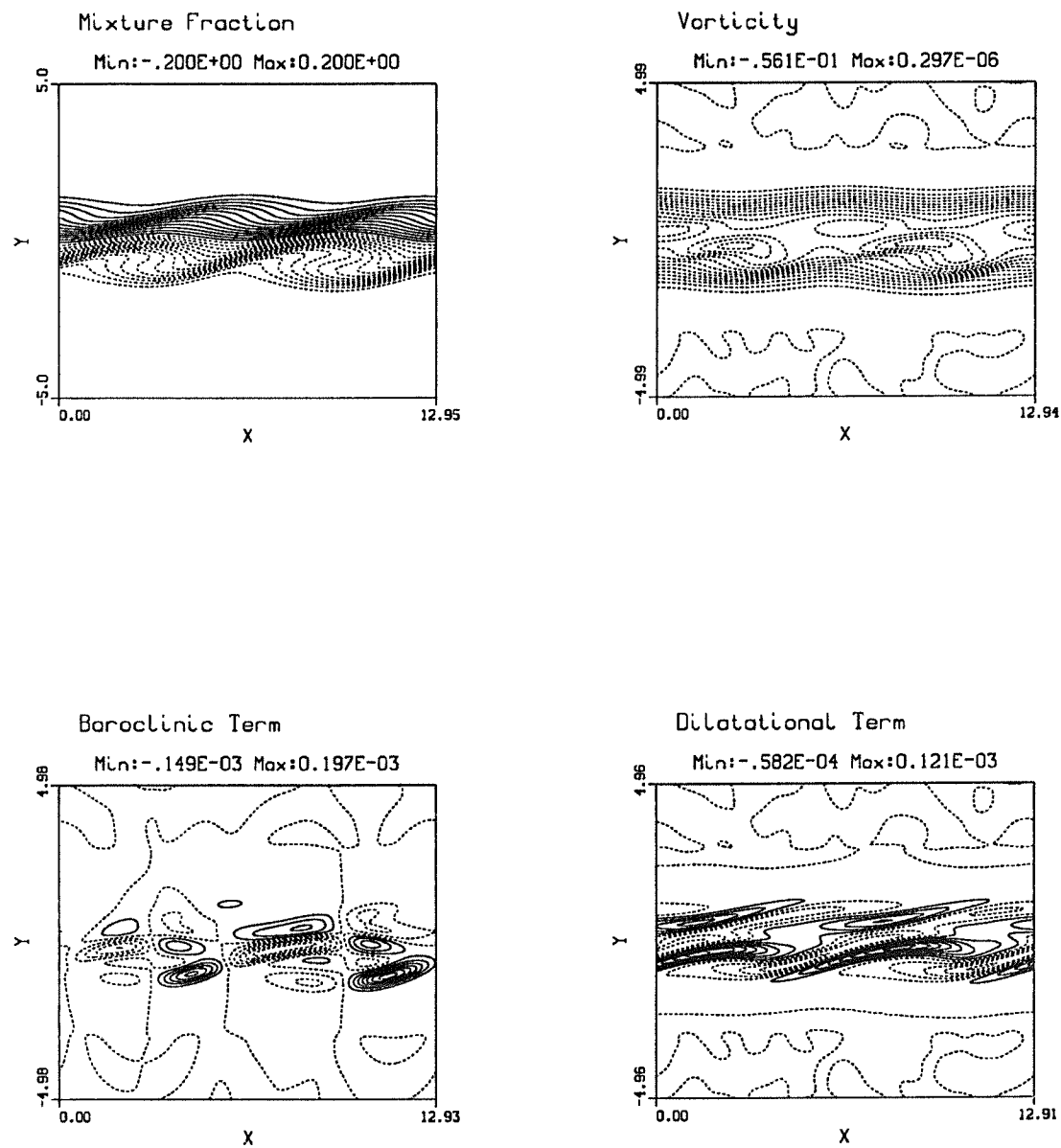


Figure 4.38: Typical slow incompressible outer mode and its subharmonics (Heat release $T_f = 3.0$, $M_c = 0.05$, $Da = 3$, $Ze = 2$, $U_2 = 0.5$, $Re = 1000$, $\phi = 0$., Amplitudes: 0.001 (fundamental) and 0.0005 (subharmonic), $t = 150$). (a) mixture fraction, (b) vorticity, (c) baroclinic term, (d) dilatation term.

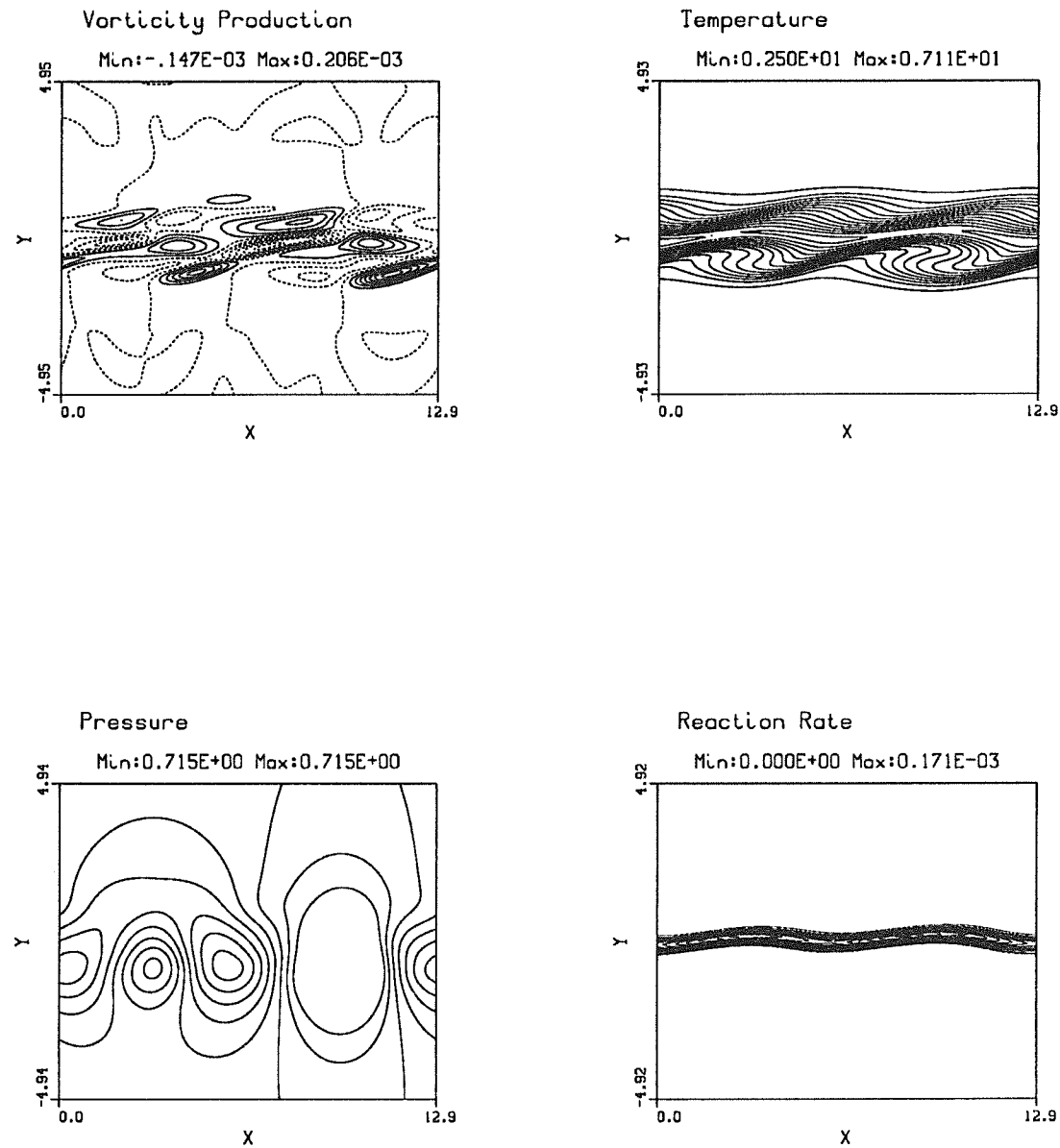


Figure 4.38: Typical slow incompressible outer mode and its subharmonics (Heat release $T_f = 3.0$, $M_c = 0.05$, $Da = 3$, $Ze = 2$, $U_2 = 0.5$, $Re = 1000$, $\phi = 0$., Amplitudes: 0.001 (fundamental) and 0.0005 (subharmonic), $t = 150$). (e) vorticity production, (f) temperature, (g) pressure, (h) reaction rate.

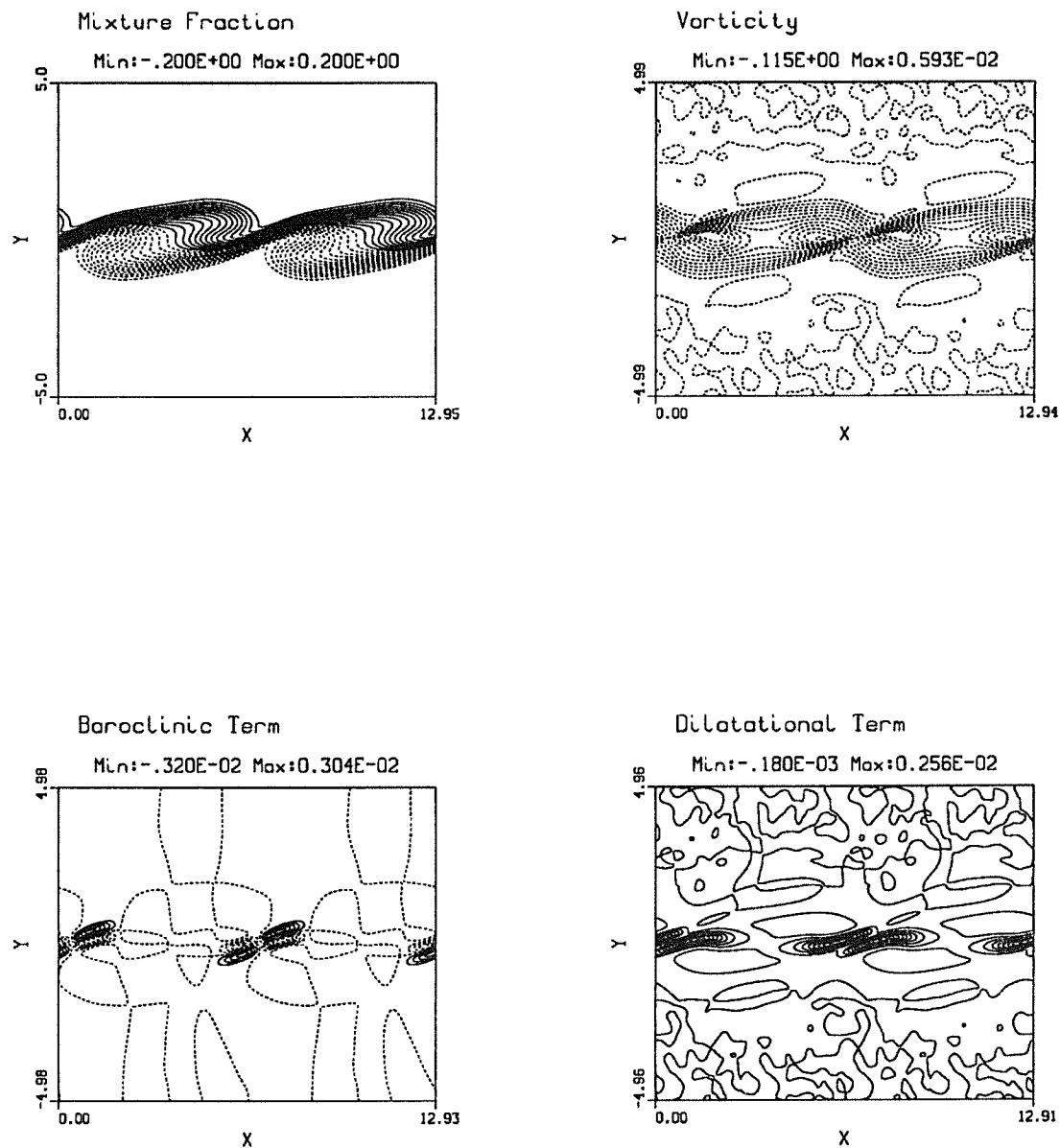


Figure 4.39: Transition from the central mode to the two outer modes. ($T_f = 4.0$, $M_c = 0.2$, $Re = 500$, $Da = 3.$, $Ze = 2..$ $U_2 = -1$, Time $t = 20$). (a) mixture fraction, (b) vorticity, (c) baroclinic term, (d) dilatation term.

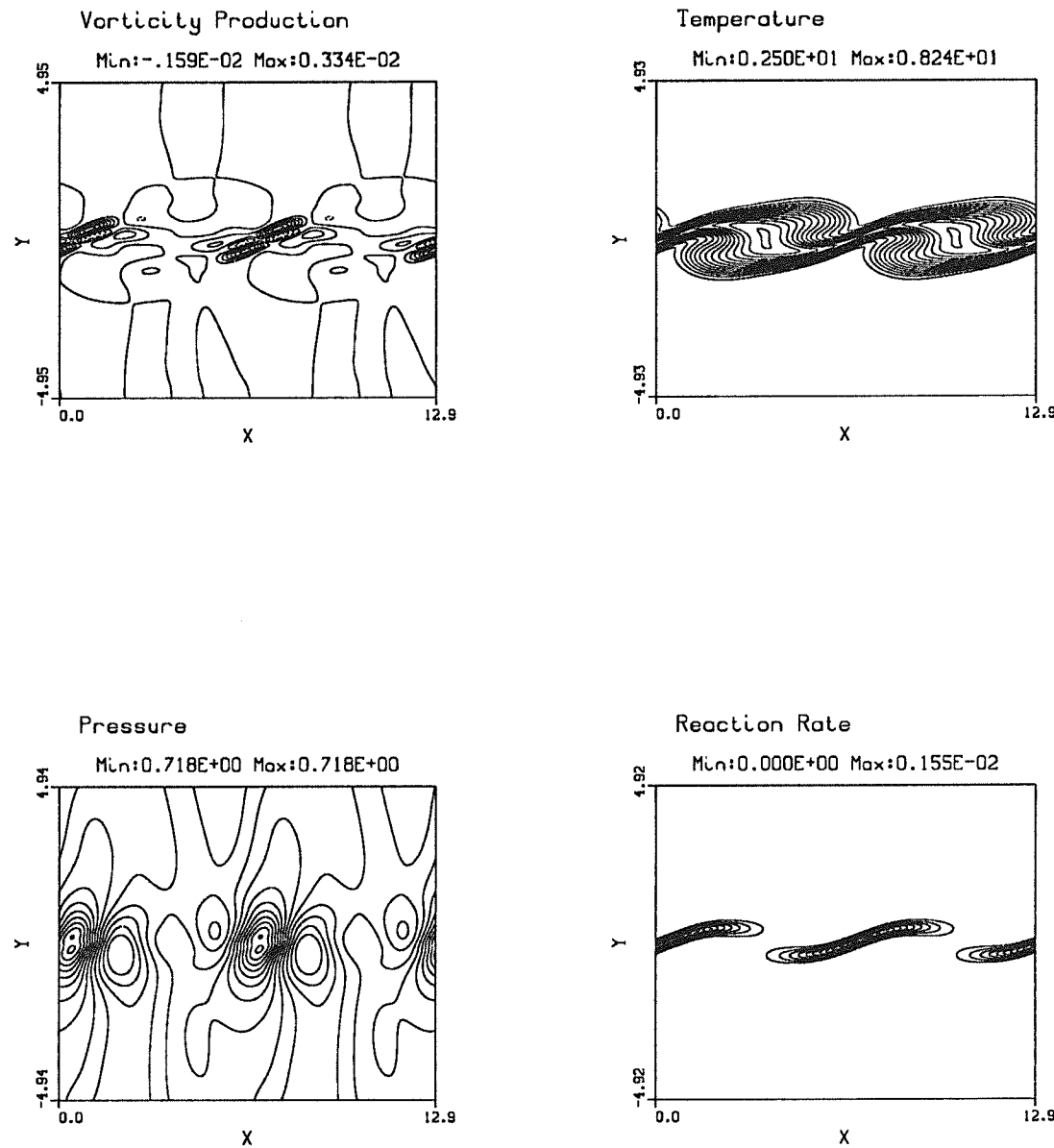


Figure 4.39: Transition from the central mode to the two outer modes. ($T_f = 4.0$, $M_c = 0.2$, $Re = 500$, $Da = 3.$, $Ze = 2..$ $U_2 = -1$, Time $t = 20$). (e) vorticity production, (f) temperature, (g) pressure, (i) reaction rate.

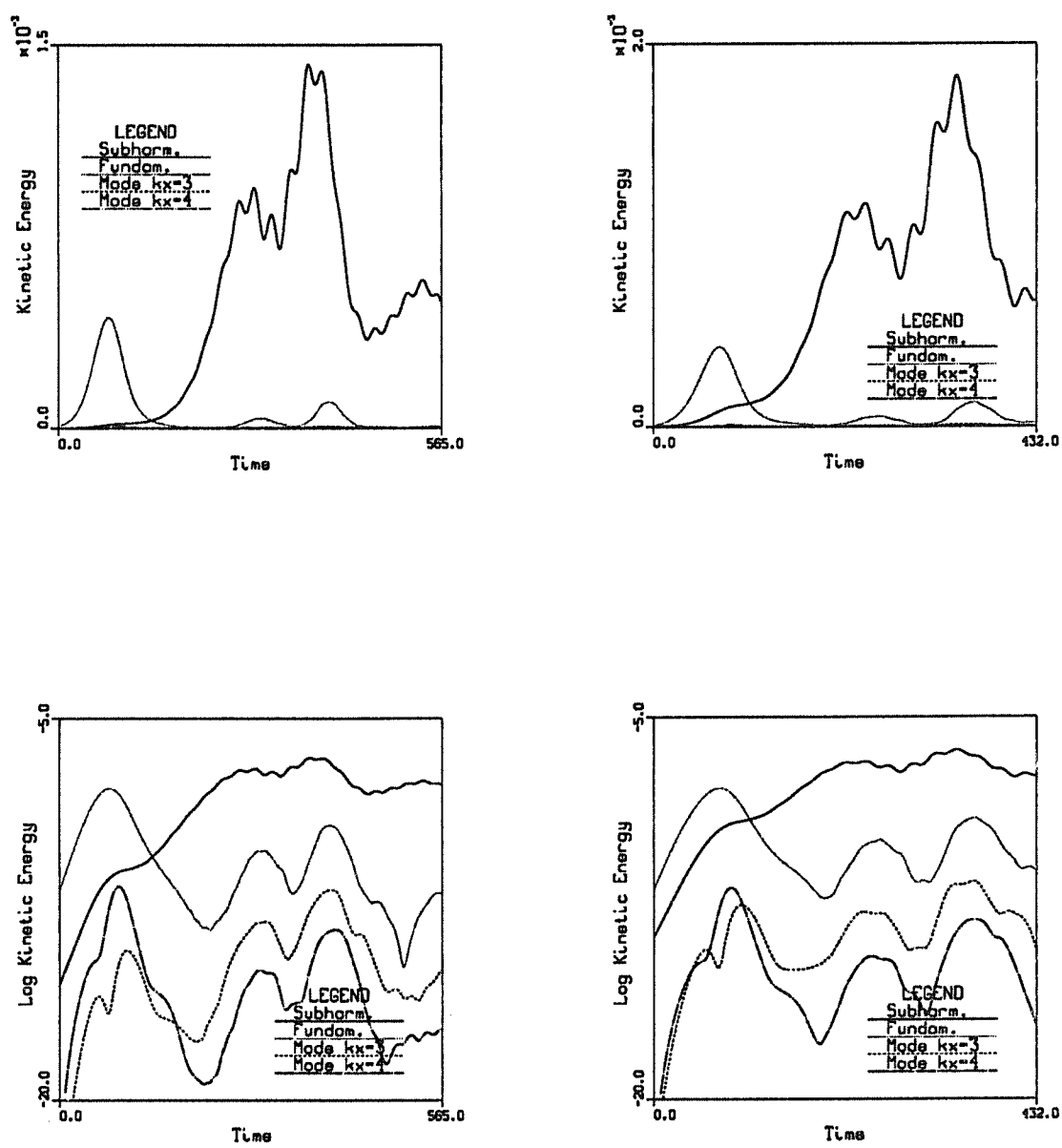


Figure 4.40: History of the kinetic energies of the fast outer mode and on its fast subharmonic for the simulation of figure 4.42. ($T_f = 3.0$, $M_c = 0.8$, $Re = 4000$, $Da = 6.$, $Ze = 2.$, $\phi = \pi$)

Left: Amplitudes: 0.002 (fundamental) and 0.0004 (subharmonic).

Right: Amplitudes: 0.002 (fundamental) and 0.001 (subharmonic).

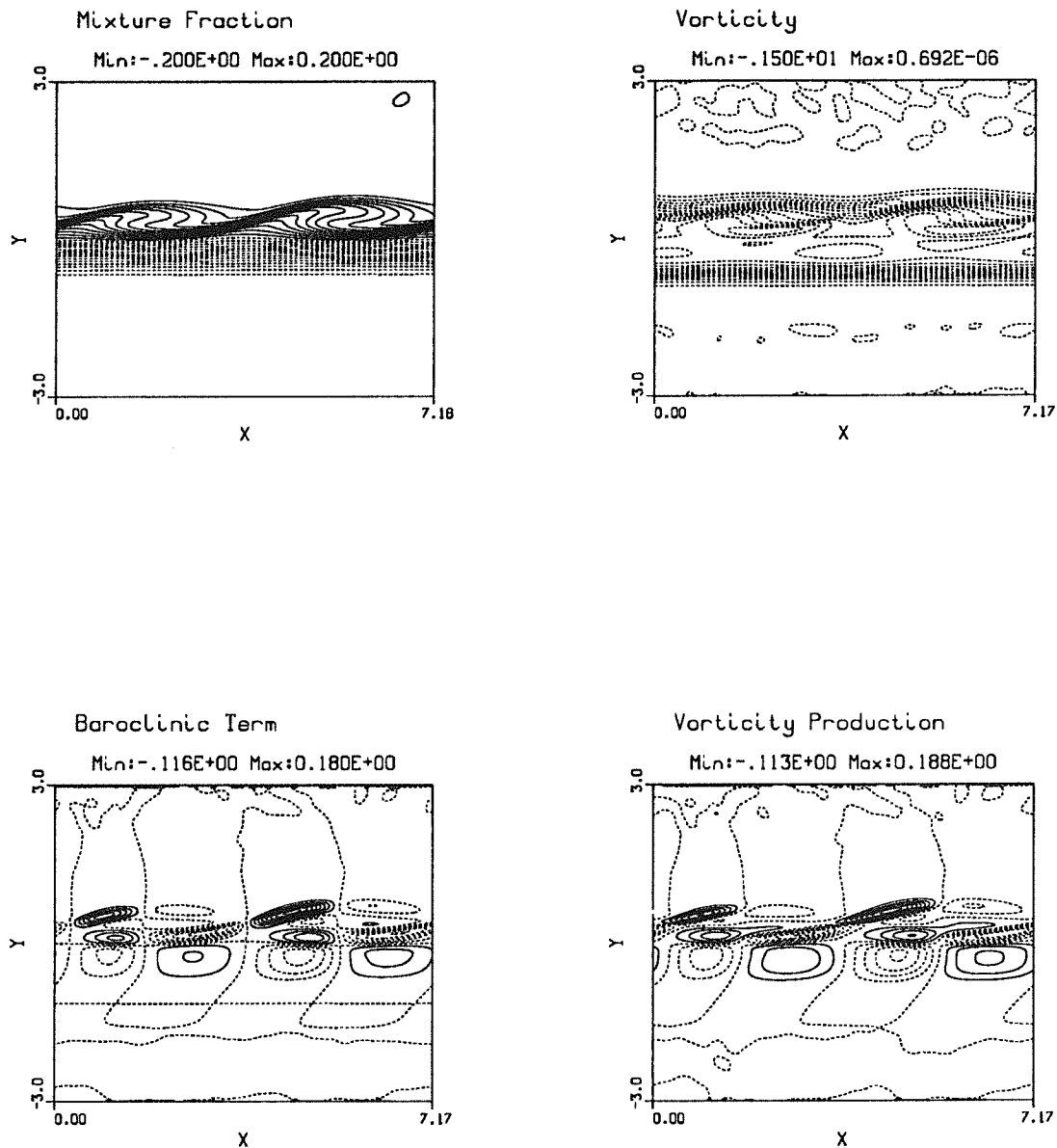


Figure 4.41: Interaction between a fast outer mode and its fast subharmonic. ($T_f = 3.0$, $M_c = 0.8$, $Re = 4000$, $Da = 6.$, $Ze = 2.$, $\phi = \pi$, Amplitudes: 0.002 (fundamental) and 0.001 (subharmonic)). Time $t = 80$. (a) mixture fraction, (b) vorticity, (c) baroclinic term, (d) vorticity production.

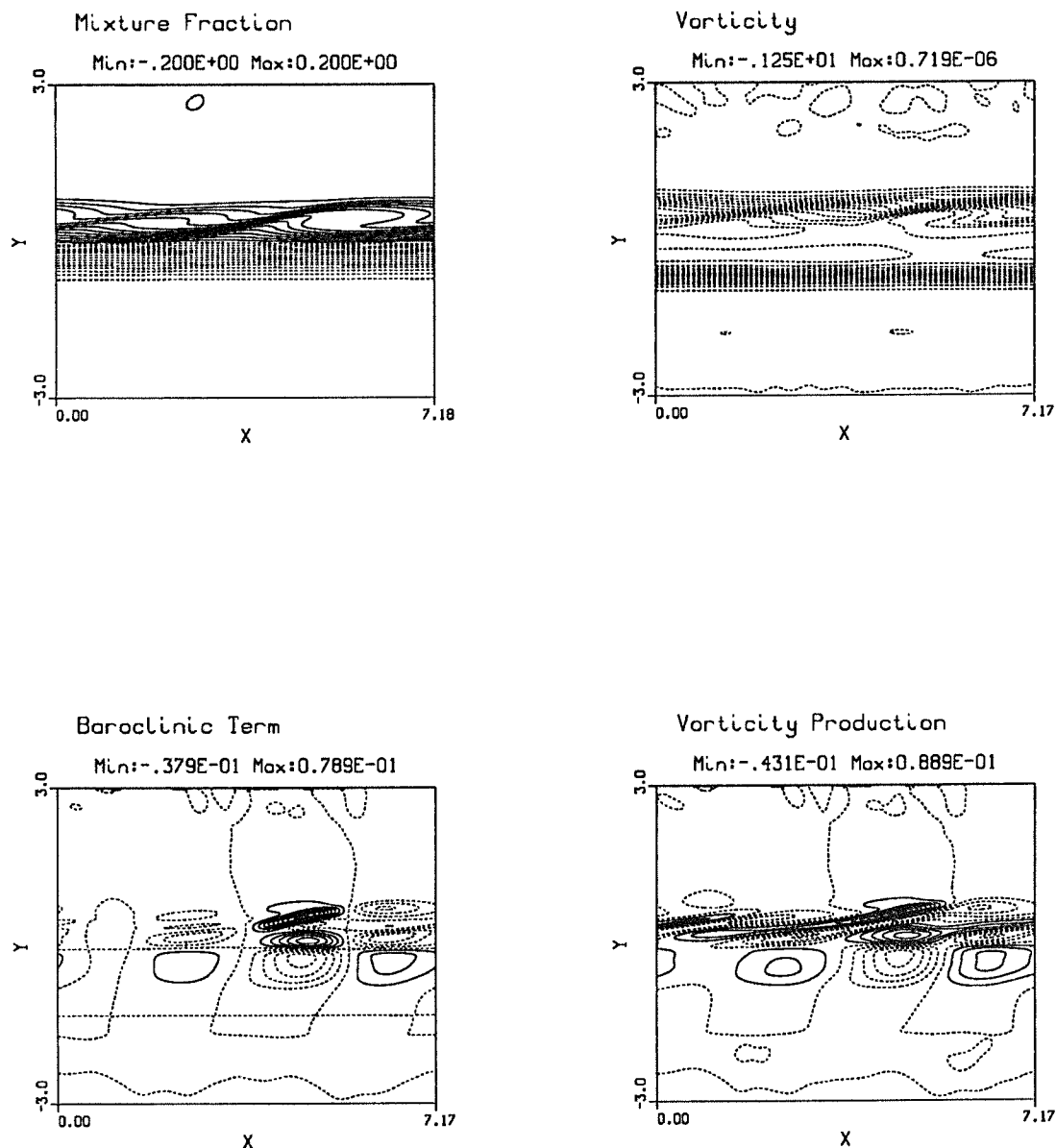


Figure 4.41 (cont'd): Interaction between a fast outer mode and its fast subharmonic. ($T_f = 3.0$, $M_c = 0.8$, $Re = 4000$, $Da = 6.$, $Ze = 2.$, $\phi = \pi$, Amplitudes: 0.002 (fundamental) and 0.001 (subharmonic)). Time $t = 112$. (a) mixture fraction, (b) vorticity, (c) baroclinic term, (d) vorticity production.

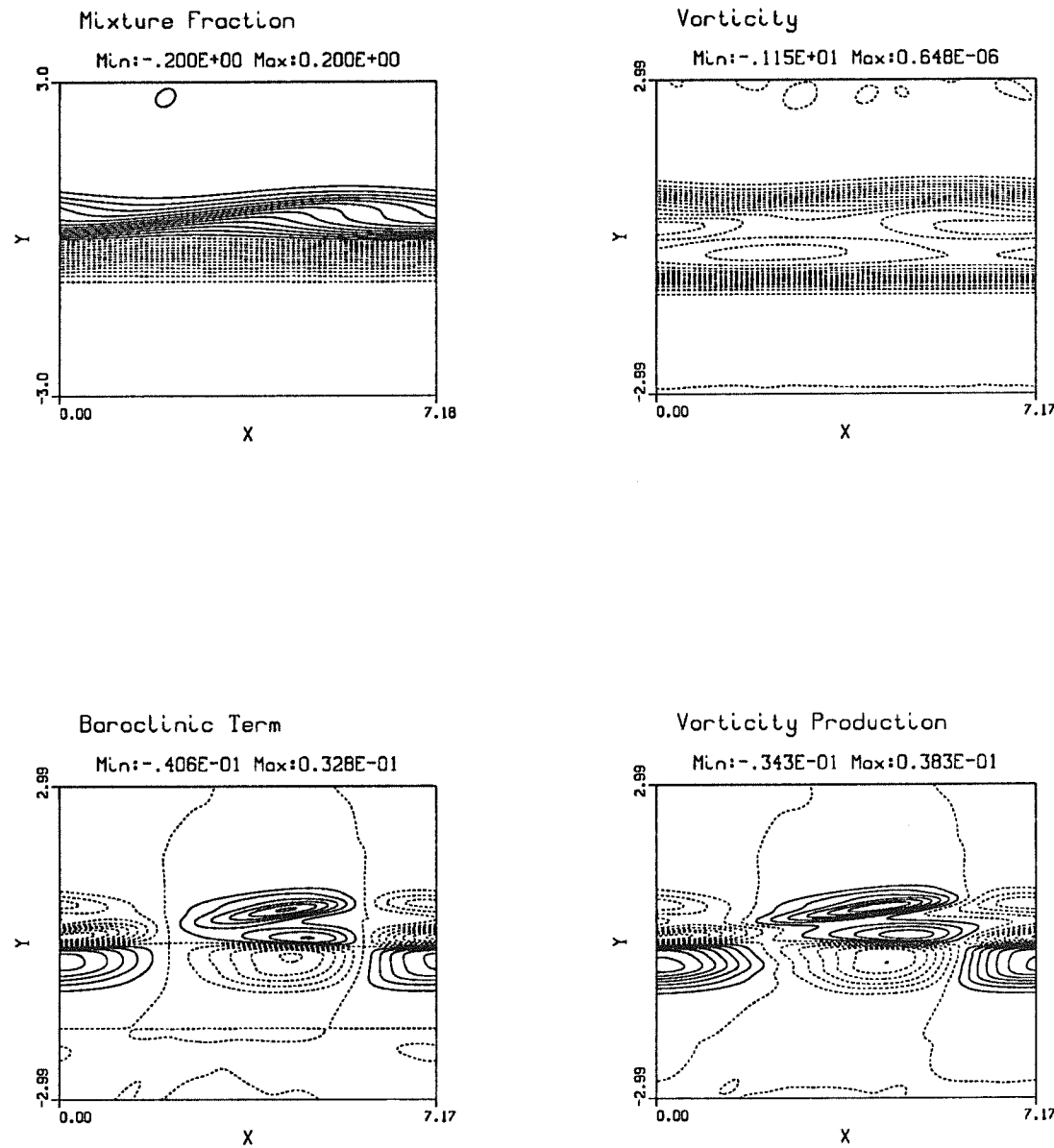


Figure 4.41 (cont'd): Interaction between a fast outer mode and its fast subharmonic. ($T_f = 3.0$, $M_c = 0.8$, $Re = 4000$, $Da = 6.$, $Ze = 2.$, $\phi = \pi$, Amplitudes: 0.002 (fundamental) and 0.001 (subharmonic)). Time $t = 176$. (a) mixture fraction, (b) vorticity, (c) baroclinic term, (d) vorticity production.

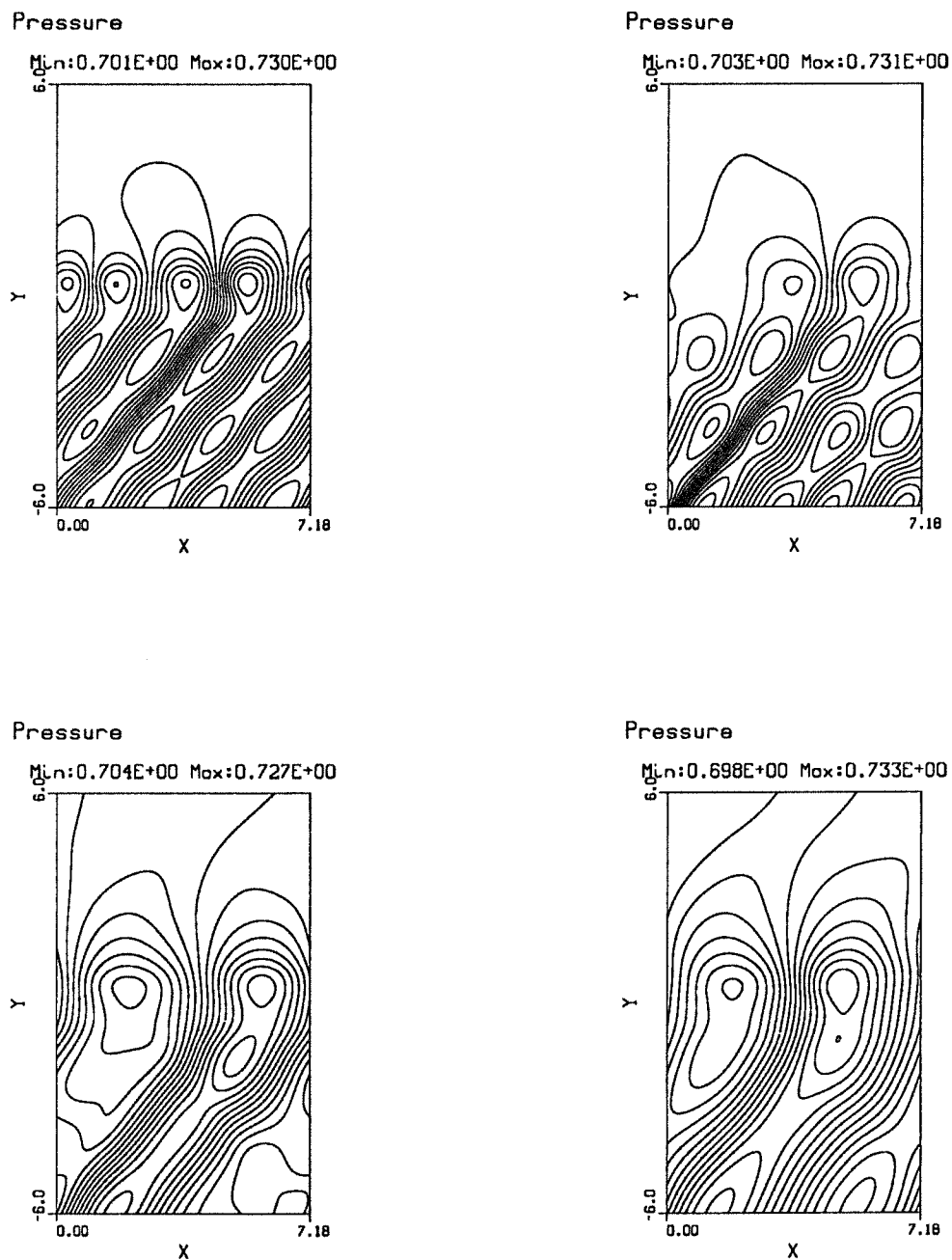


Figure 4.42: Pressure contours during the interaction of the fast outer mode and the fast subharmonic of figure 4.41. (Times (a) $t = 80$, (b) $t = 112$, (c) $t = 176$, (d) $t = 224$)

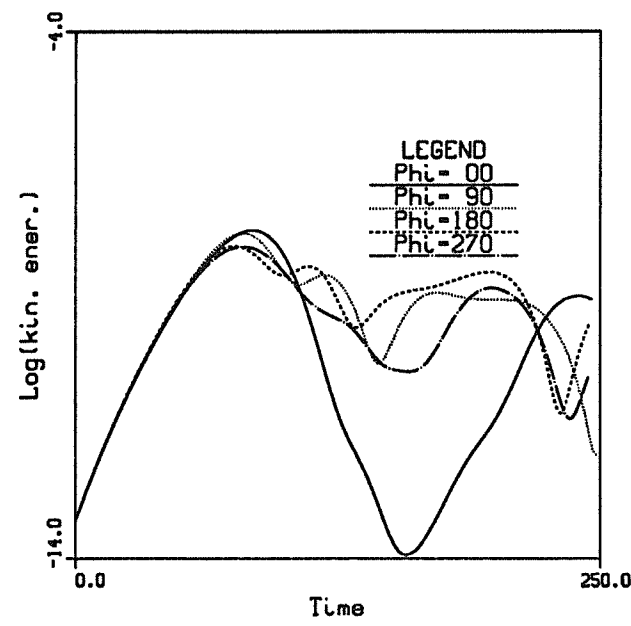
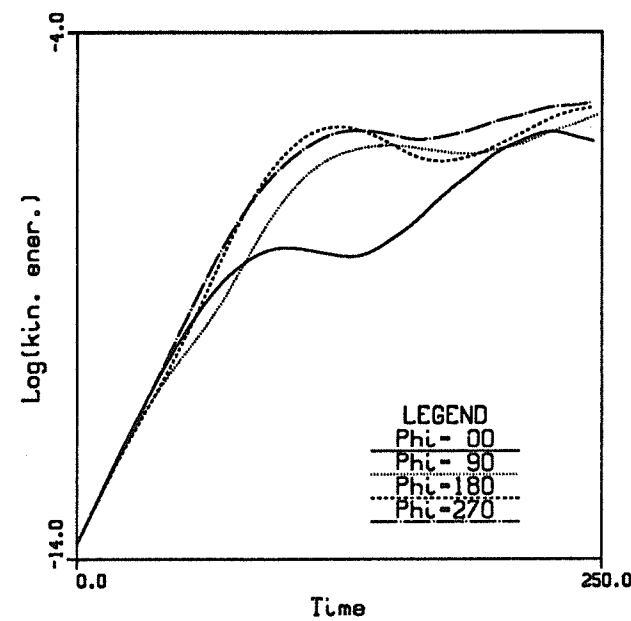


Figure 4.43: Influence of the initial phase delay on the kinetic energies of the subharmonic (top) and of the fundamental (bottom). ($T_f = 3.0$, $M_c = 0.8$, $U_2 = 0.5$, $Z_e = 2.0$, $Da = 0.85$, Amplitudes: 0.001 for fund. and subh.)

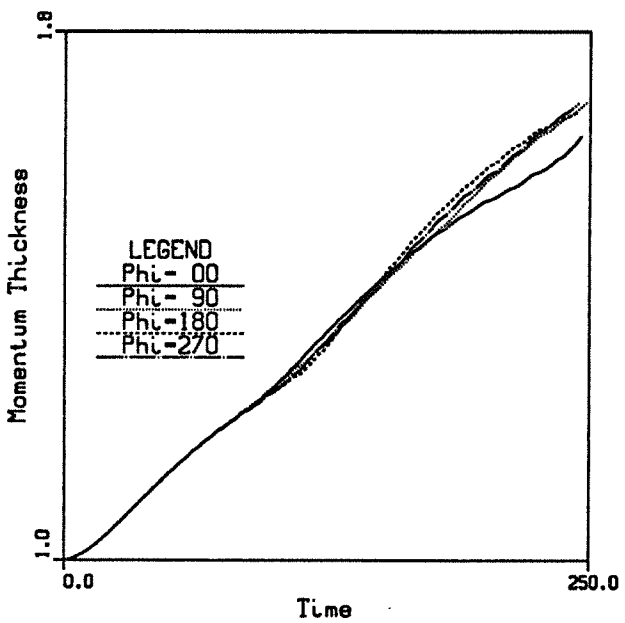
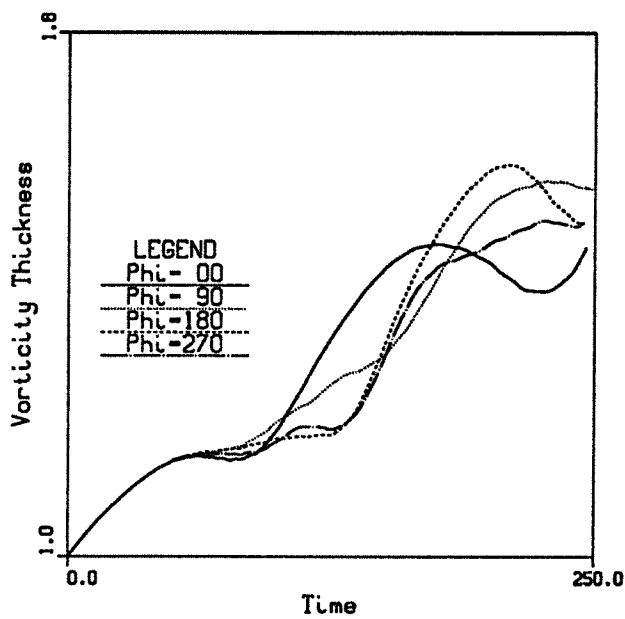


Figure 4.44: Influence of the initial phase delay on the growth rate of the layer:
 top: vorticity thickness; bottom: momentum thickness. ($T_f = 3.0$, $M_c = 0.8$, $U_2 = 0.5$,
 $Z_e = 2.0$, $Da = 0.85$, Amplitudes: 0.001 for fund. and subh.)

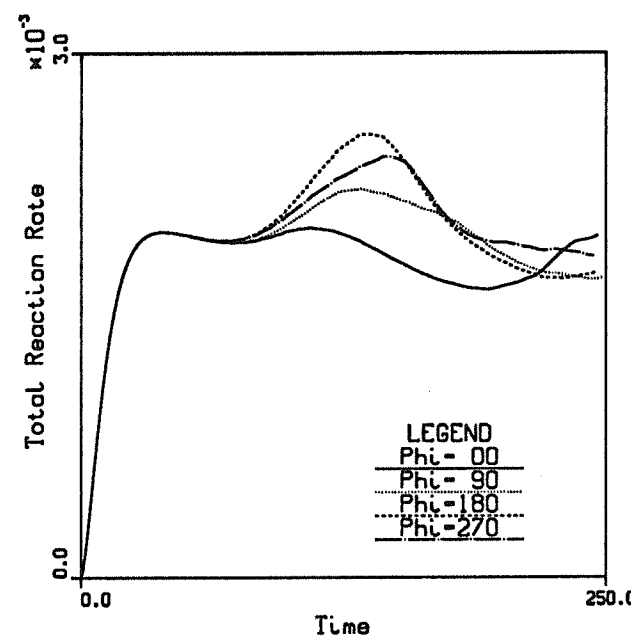


Figure 4.45: Influence of the initial phase delay on the total reaction rate. Gulping. ($T_f = 3.0$, $M_c = 0.8$, $U_2 = 0.5$, $Ze = 2.0$, $Da = 0.85$, Amplitudes: 0.001 for fund. and subh.)

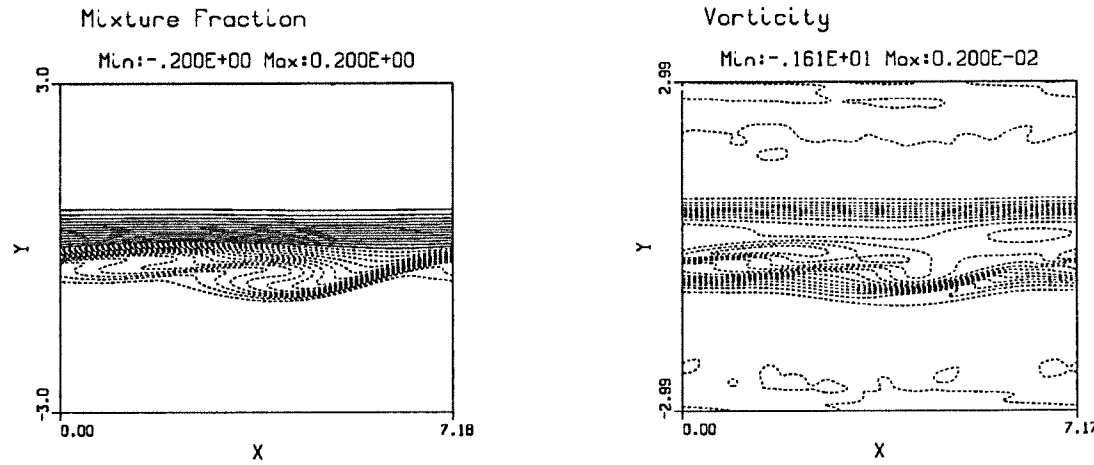


Figure 4.46: Interaction between a slow outer mode and its slow subharmonic. Gulping. ($T_f = 3.0$, $M_c = 0.8$, $U_2 = 0.5$, $Ze = 2.0$, $Da = 0.85$, $\phi = \pi$, Amplitudes: 0.001 for fund. and subh.) Time: $t = 96$

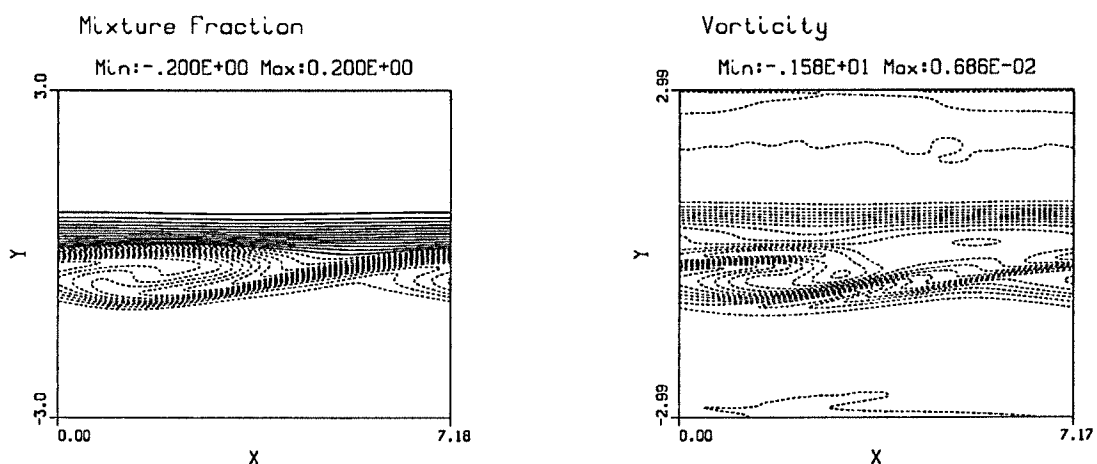
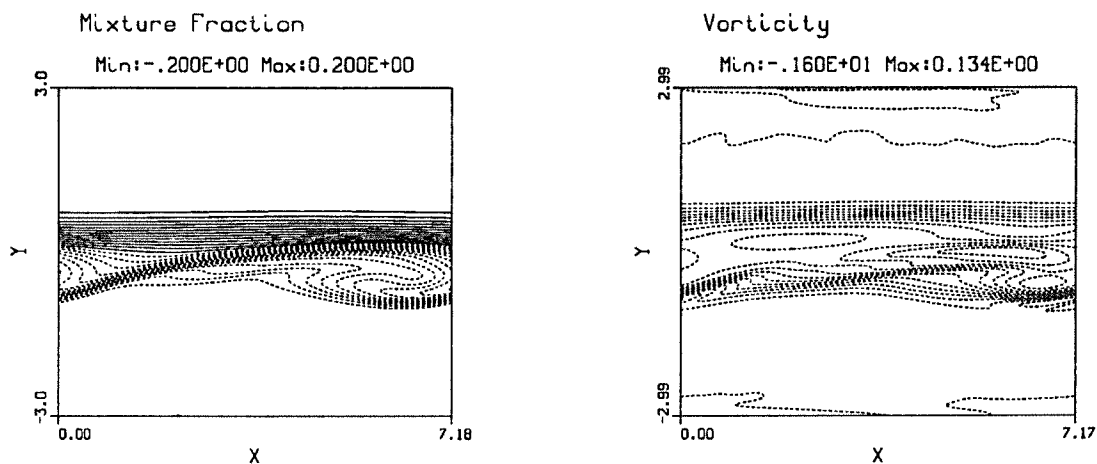


Figure 4.46: Interaction between a slow outer mode and its slow subharmonic. Gulp-ing. ($T_f = 3.0$, $M_c = 0.8$, $U_2 = 0.5$, $Z_e = 2.0$, $Da = 0.85$, $\phi = \pi$, Amplitudes: 0.001 for fund. and subh.) Time: $t = 112$ (top), $t = 128$. (bottom).

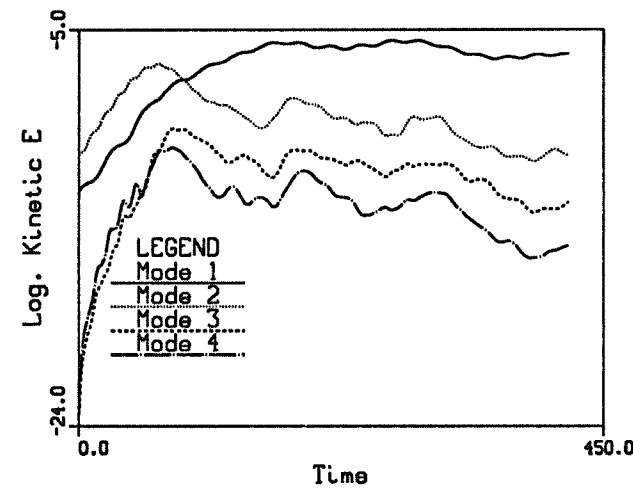
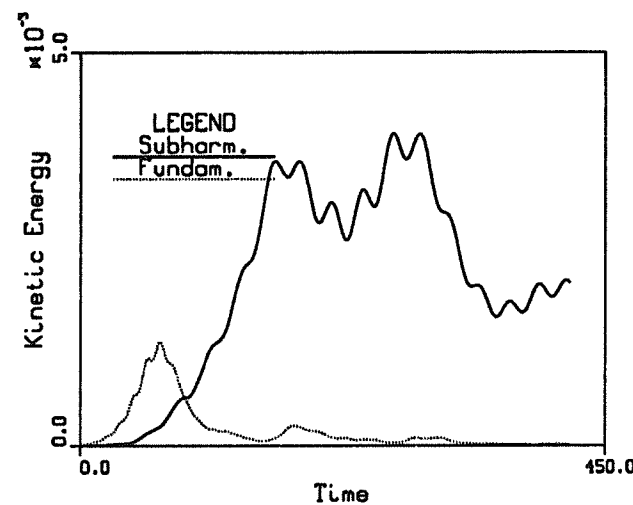


Figure 4.47: Time variations of the kinetic energies of the fast and slow fundamentals and subharmonics of figure 4.48. ($T_f = 3.0$, $M_c = 0.8$, $U_2 = 0.5$, $Ze = 2.0$, $Da = 0.85$, $\phi = \pi$, Amplitudes: 0.001 for fund. and 0.0005 subh.)

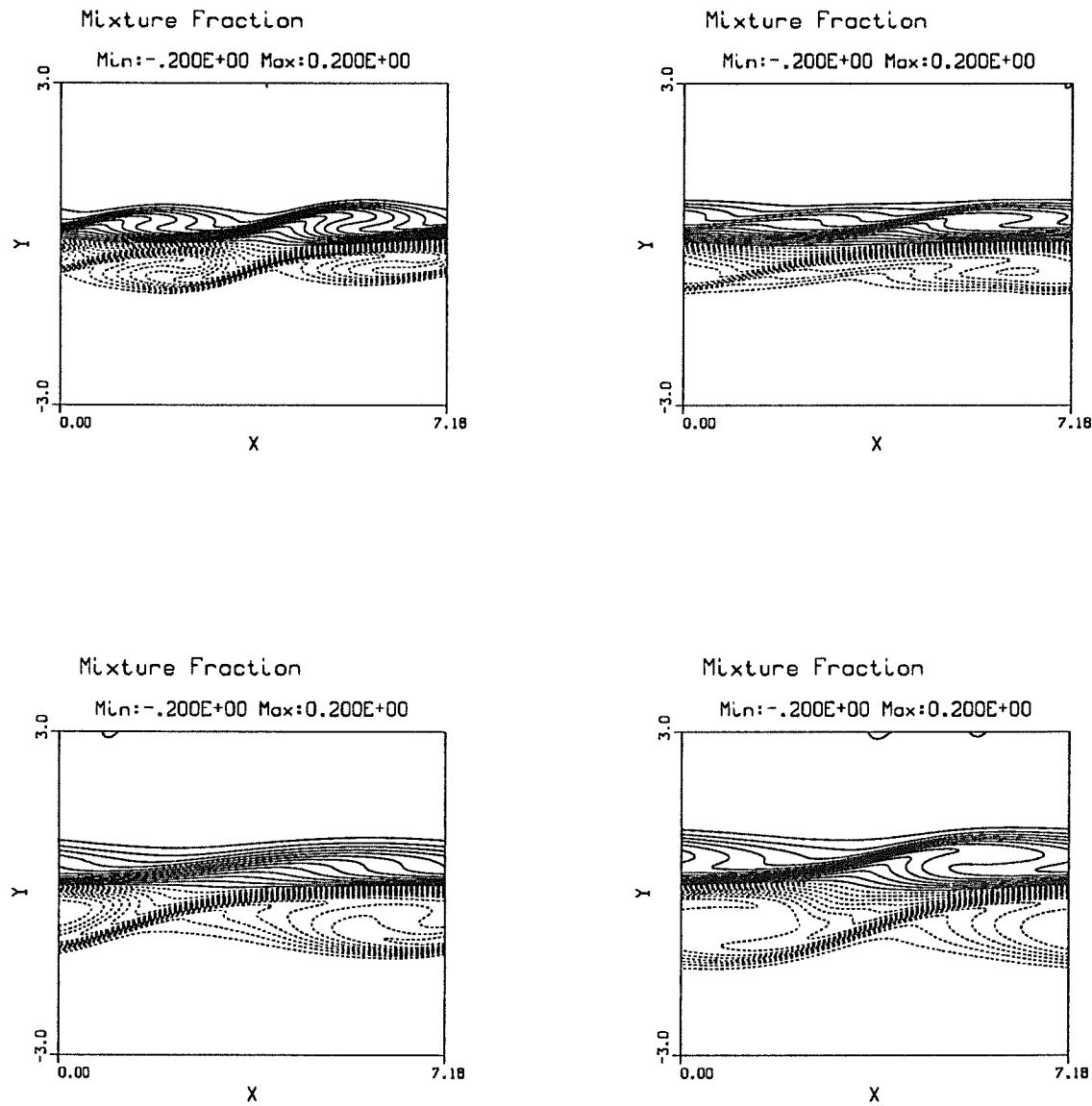


Figure 4.48: Mixture fraction contours for a simulation started with a fast and a slow outer mode and their fast and slow subharmonic. ($T_f = 3.0$, $M_c = 0.8$, $U_2 = 0.5$, $Z_e = 2.0$, $Da = 0.85$, $\phi = \pi$, Amplitudes: 0.001 for fund. and 0.0005 subh.) Time: $t = 80$, $t = 112$, $t = 192$, $t = 288$

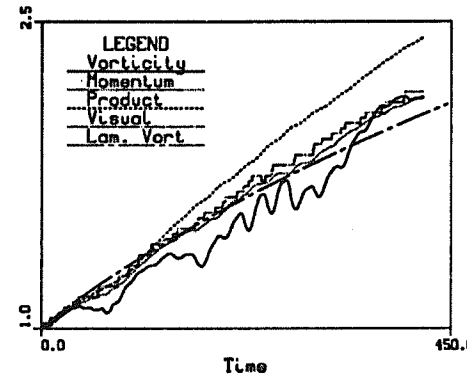


Figure 4.49: Variation of various thicknesses (momentum, product, visual, etc) for the simulation presented in figure 4.48. The vorticity thickness of the identical laminar mixing layer is shown for comparison.

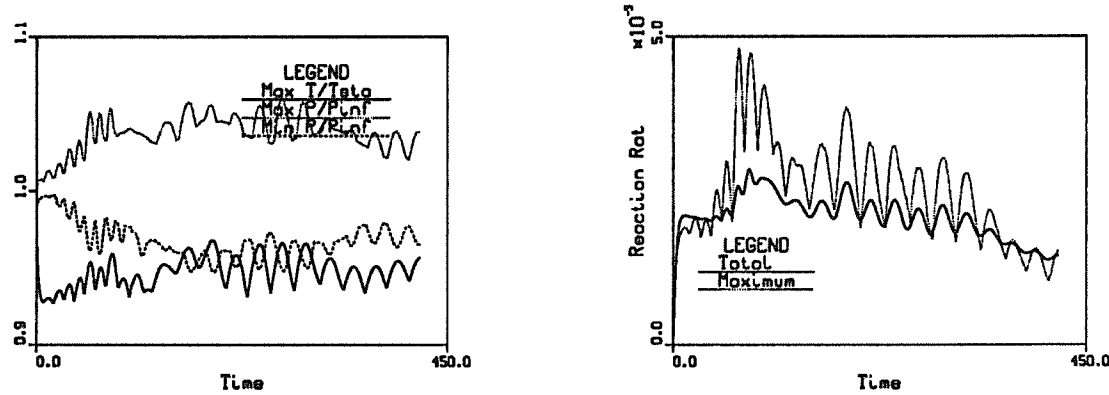


Figure 4.50: Left: Maximum temperature and maximum and minimum pressures for the simulation presented in figure 4.48. Right: Total and maximum reaction rates for the same simulation. Note the oscillations as the fast and the slow outer modes slide one on top of the other. The frequency of these oscillations is changed when the subharmonics become the dominant modes.

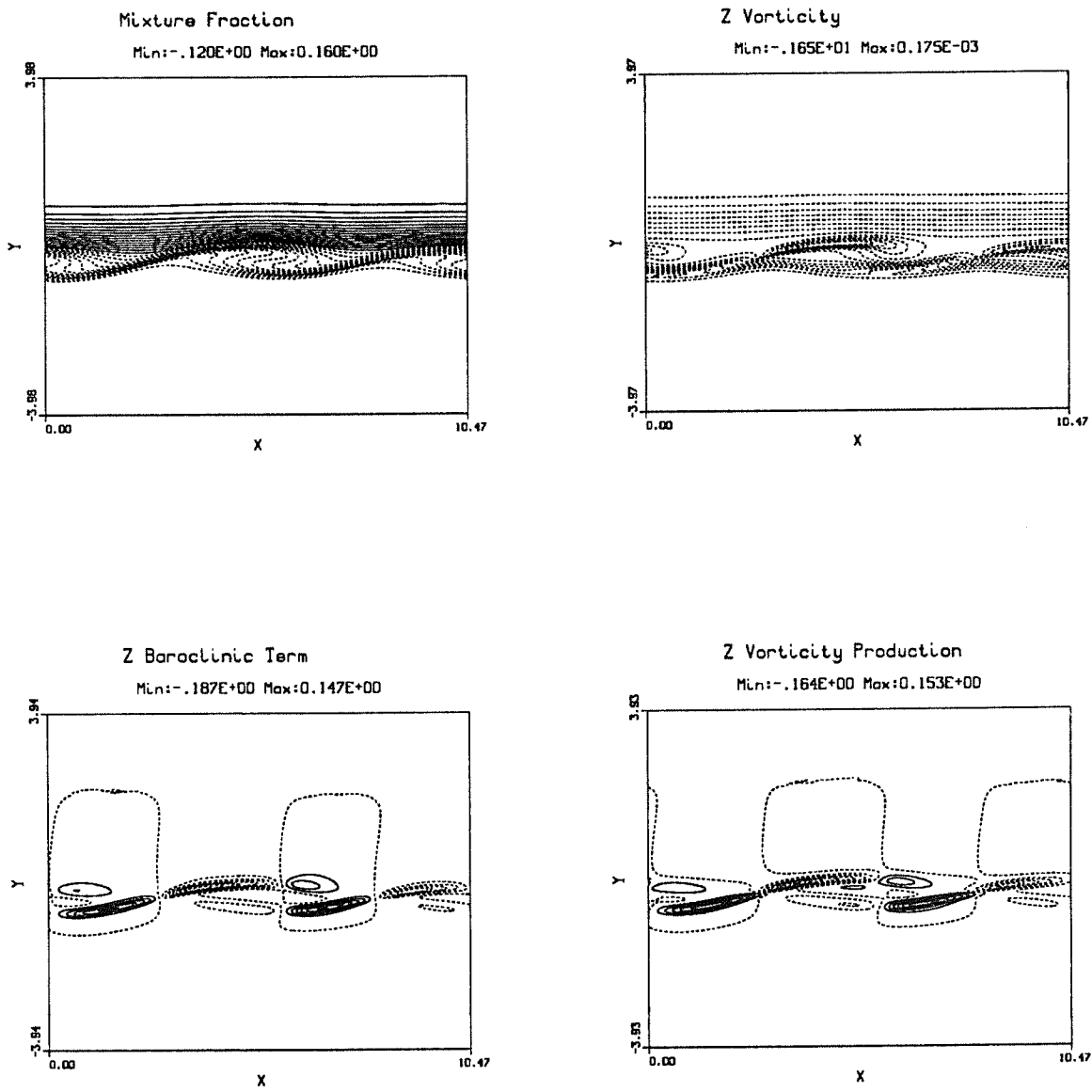


Figure 4.51: Simulation of the Stanford Experiment: ($\Theta = 0.142$, $M_c = 0.8$, $Re = 1200.$, $U_2 = 0.11$, $T_2 = 0.21$, $Ze = 0.0$, $\phi = \pi$, Amplitudes: 0.001 for fund. and 0.0005 subh.) Time: $t = 50.3$. (a) Mixture fraction; (b) vorticity; (c) baroclinic term; (d) vorticity production.

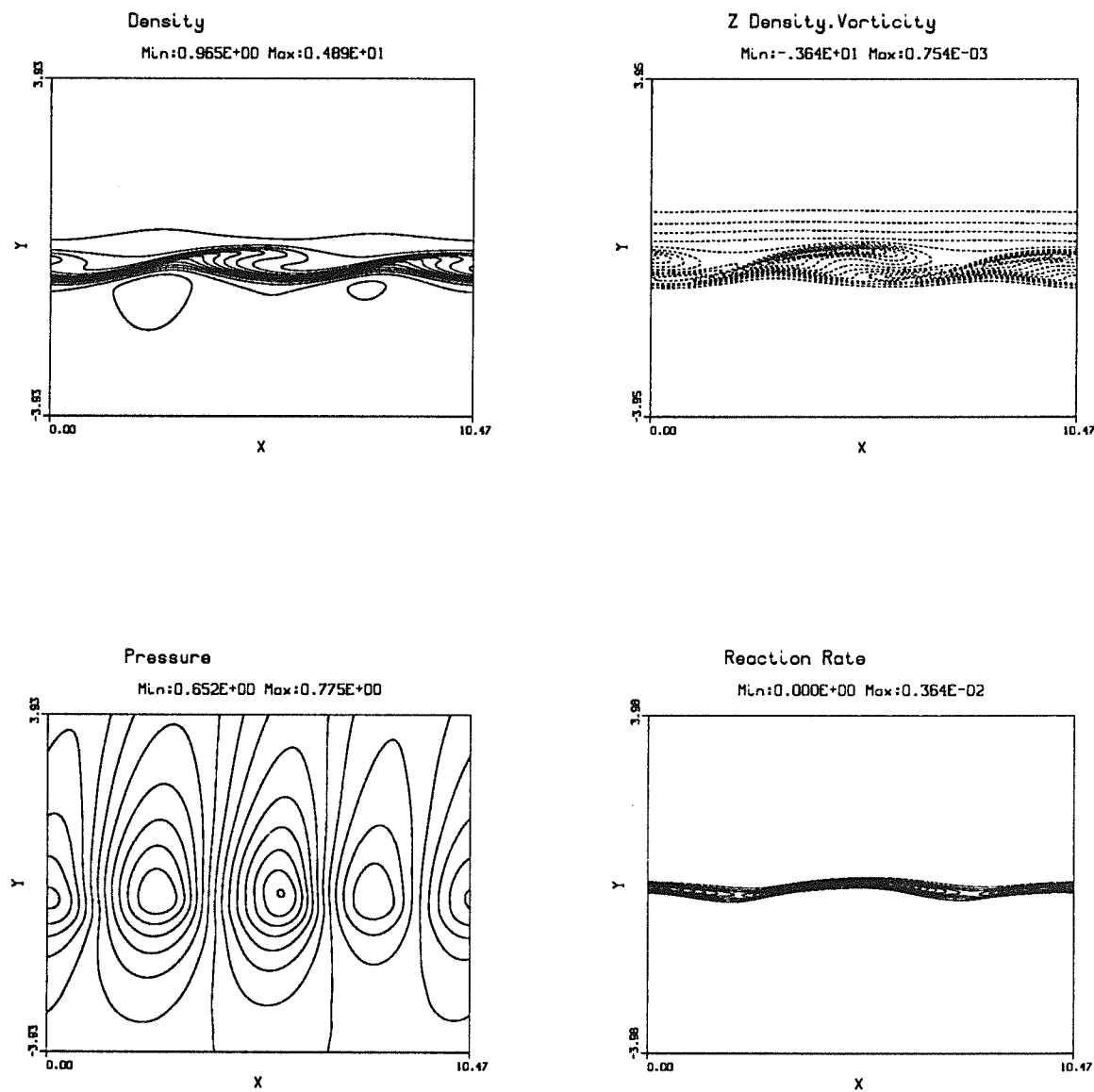


Figure 4.51 (continued): Simulation of the Stanford experiment: ($\Theta = 0.142$, $M_c = 0.8$, $Re = 1200.$, $U_2 = 0.11$, $T_2 = 0.21$, $Ze = 0.0$, $\phi = \pi$, Amplitudes: 0.001 for fund. and 0.0005 subh.) Time: $t = 50.3$. (e) Density; (f) density-weighted vorticity; (g) pressure; (h) reaction rate.

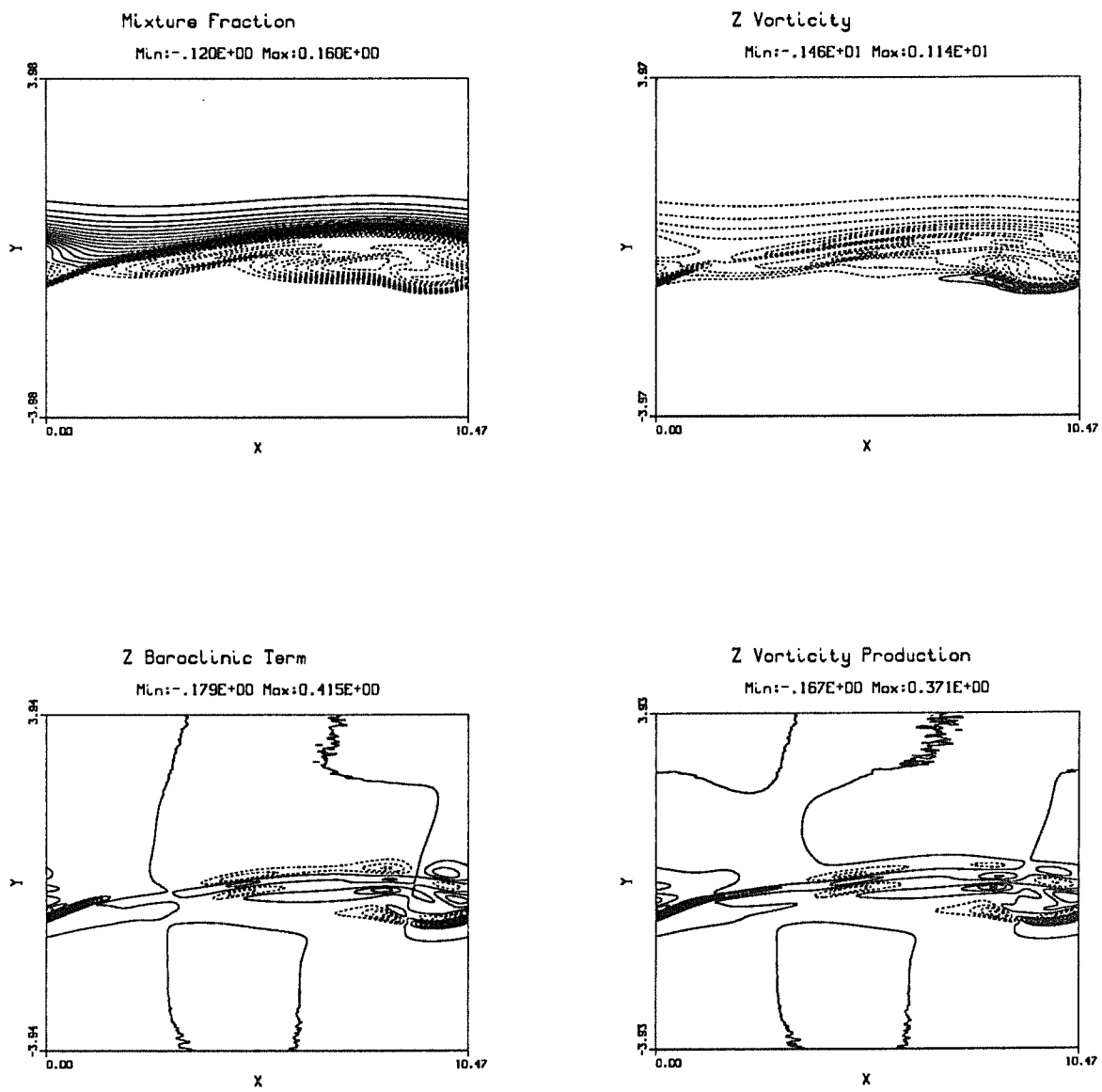


Figure 4.52: Simulation of the Stanford experiment: Same than figure 4.51 at time: $t = 82.0$. (a) Mixture fraction; (b) vorticity; (c) baroclinic term; (d) vorticity production.

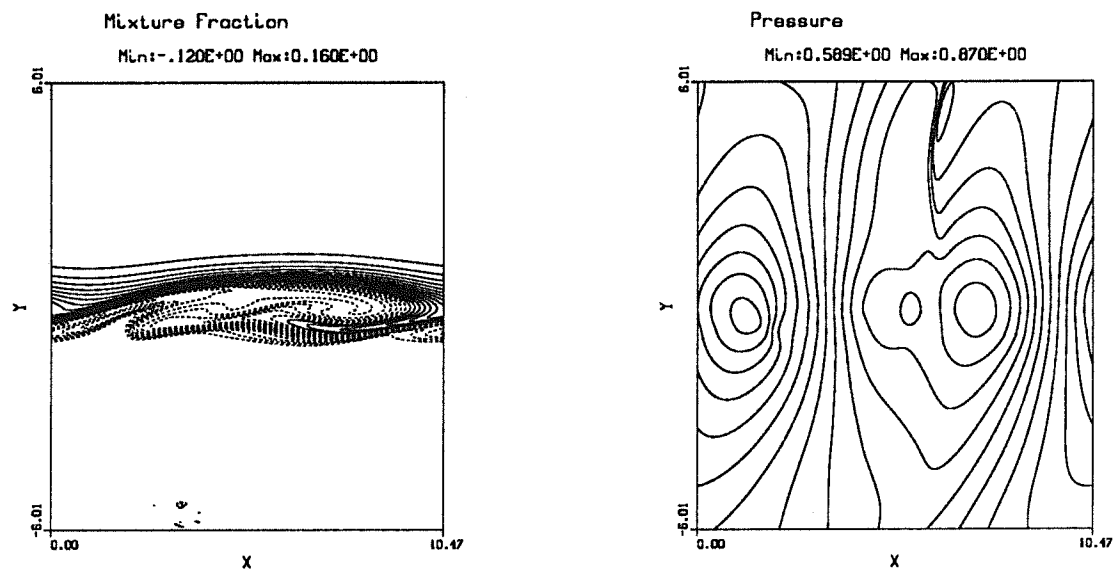


Figure 4.53: Mixture fraction and pressure contours for the same simulation as figure 4.51 at time $t = 102$. Note the presence of travelling shocks in the fast stream.

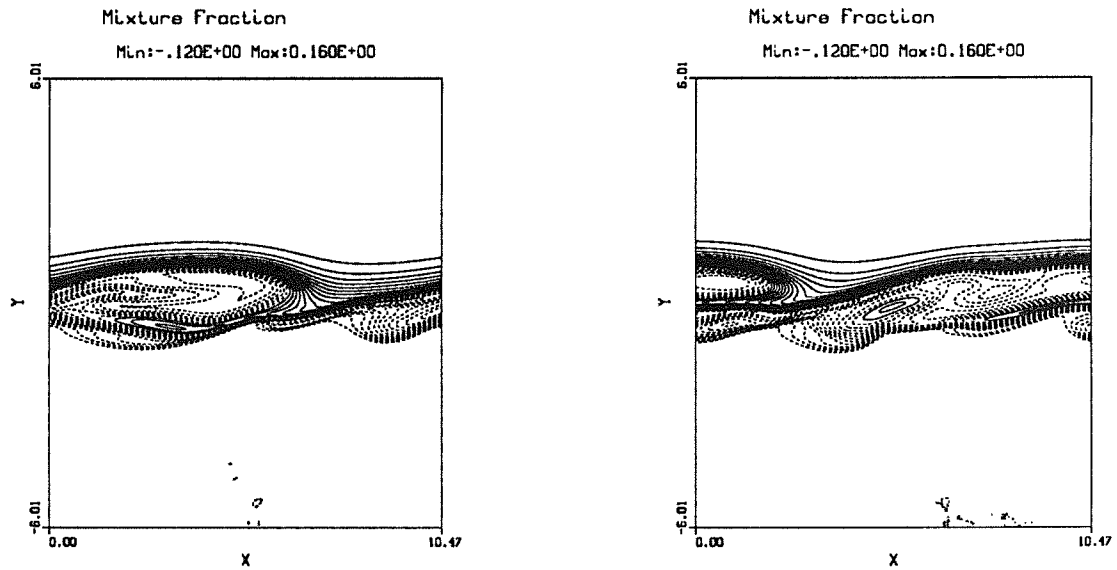


Figure 4.54: Mixture fraction contours for the same simulation as figure 4.51 at times $t = 119$, and $t = 130$.

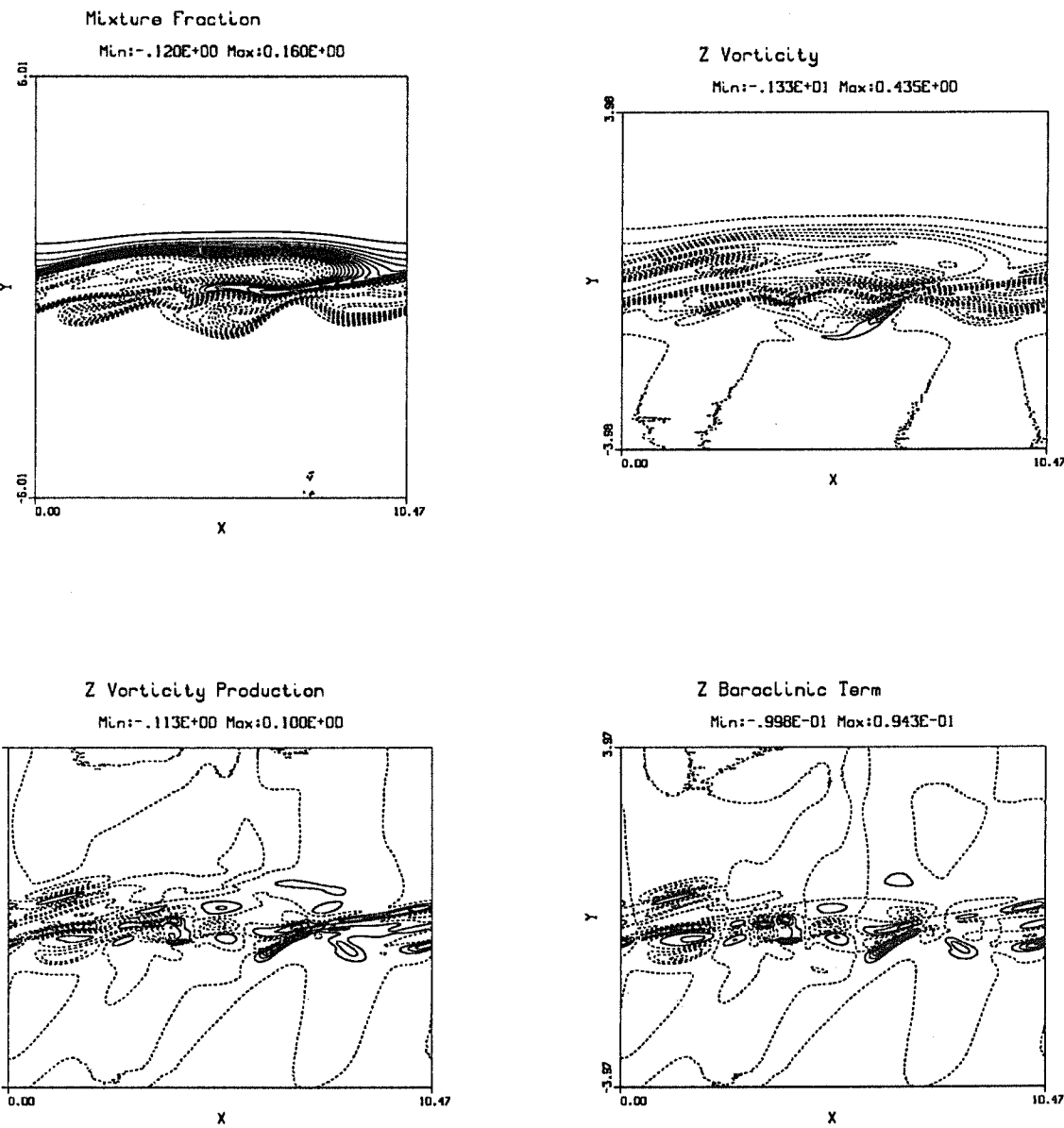


Figure 4.55: Comparison to experiment at time $t = 140$. Note the generation of small-scale vorticity by the baroclinic term. (a) Mixture fraction; (b) vorticity; (c) baroclinic term; (d) vorticity production.

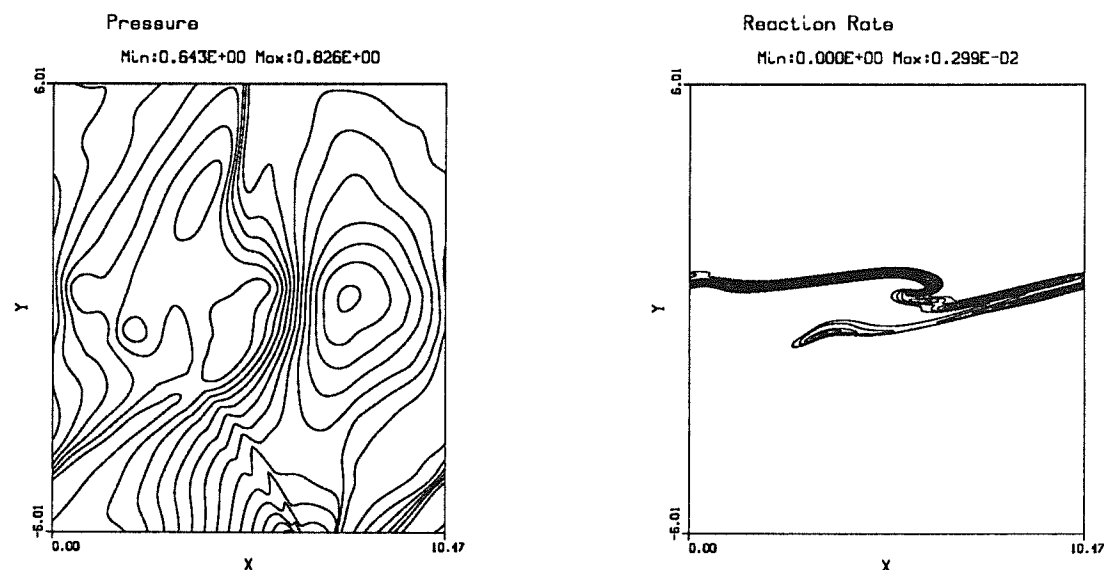
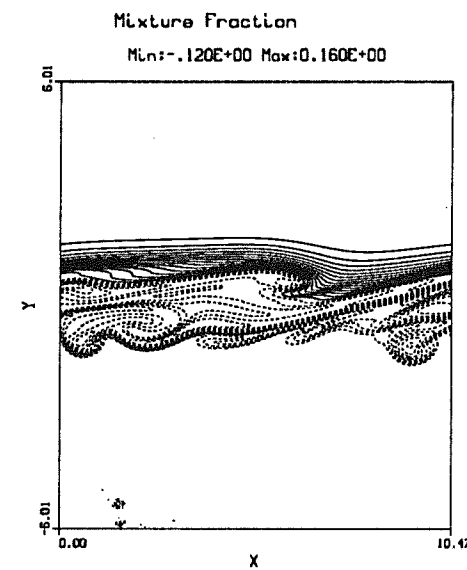


Figure 4.56: Simulation of the Stanford experiment (Same simulation as figure 4.51) at time: $t = 180.0$. Note the small-scale structures in the slow stream and the ejection of fast-stream fluid into the slow colayer.

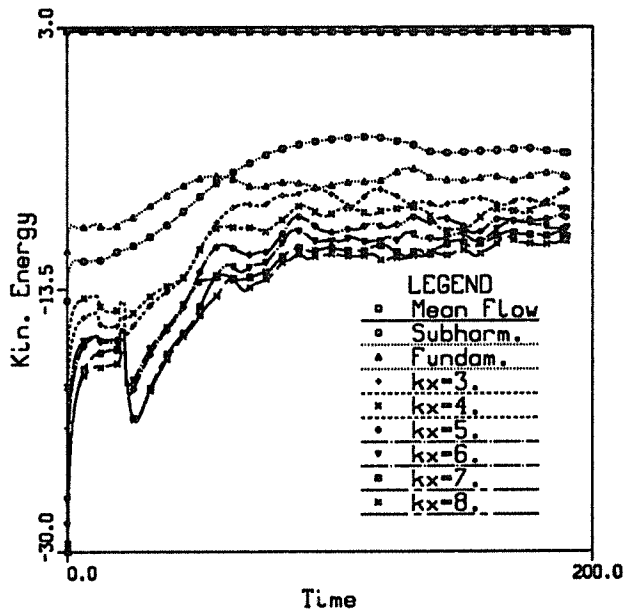


Figure 4.57: Variation of the logarithm of kinetic energies for the same simulation as figure 4.51. The discontinuity at the left corresponds to pressure waves generated at the initialization.

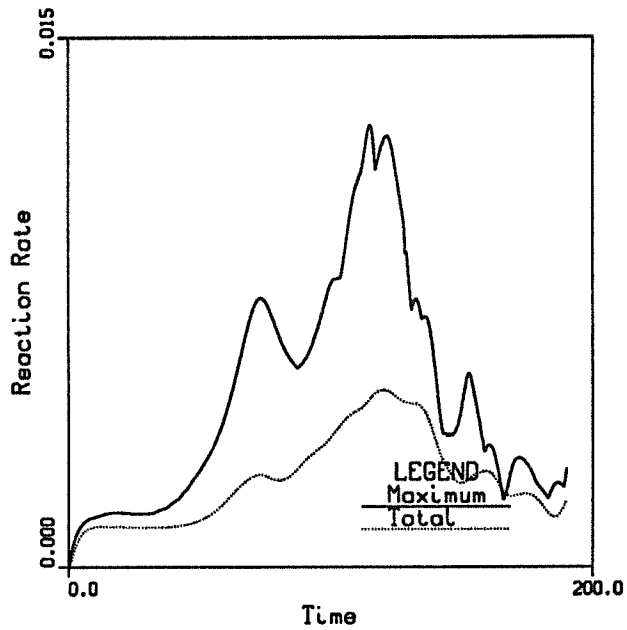


Figure 4.58: Variation of the total and maximum reaction rates versus time for the same simulation as figure 4.51.

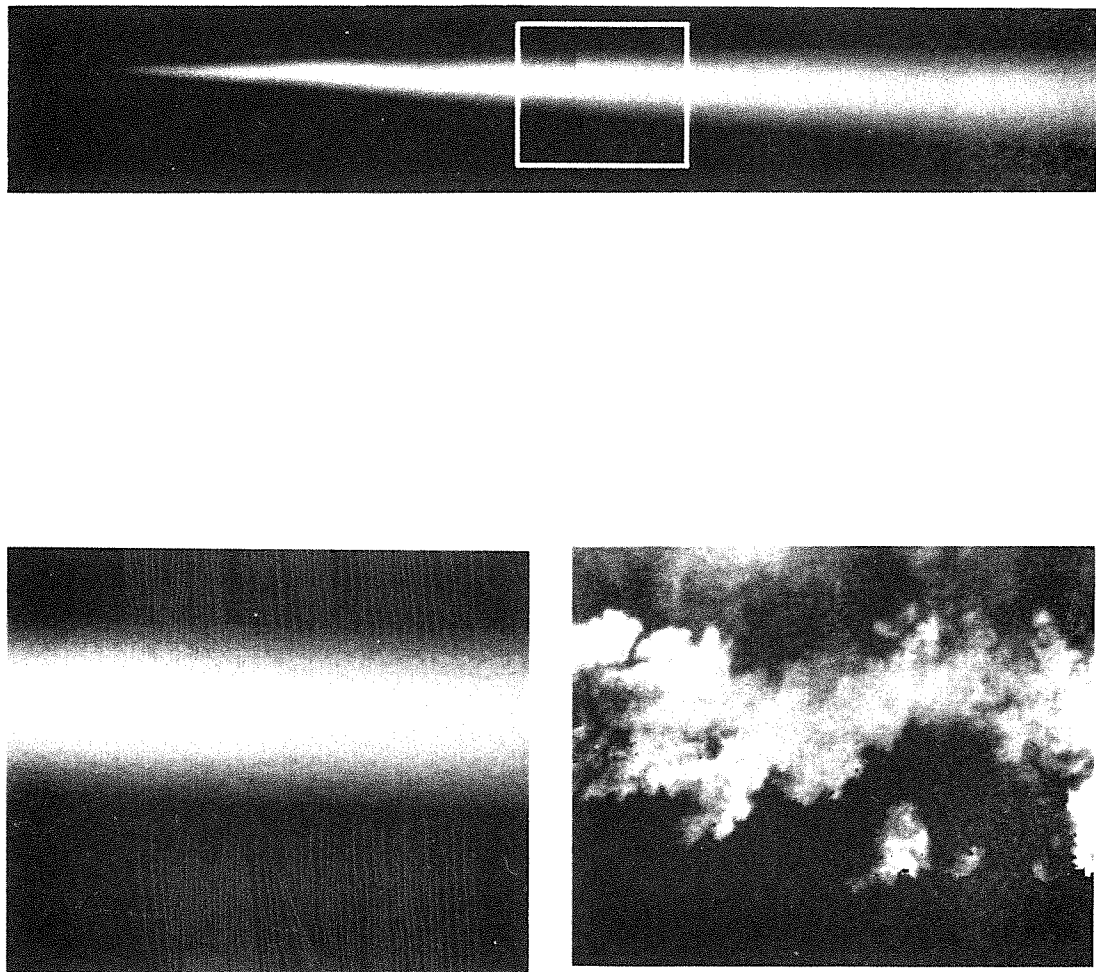


Figure 4.59: Results from the Stanford experiment.
Top: Time averaged OH emission indicating the reaction zone.
Lower left: Time averaged OH emission in the box area.
Lower right: Instantaneous PLIF image of OH indicating the primary reaction zone.

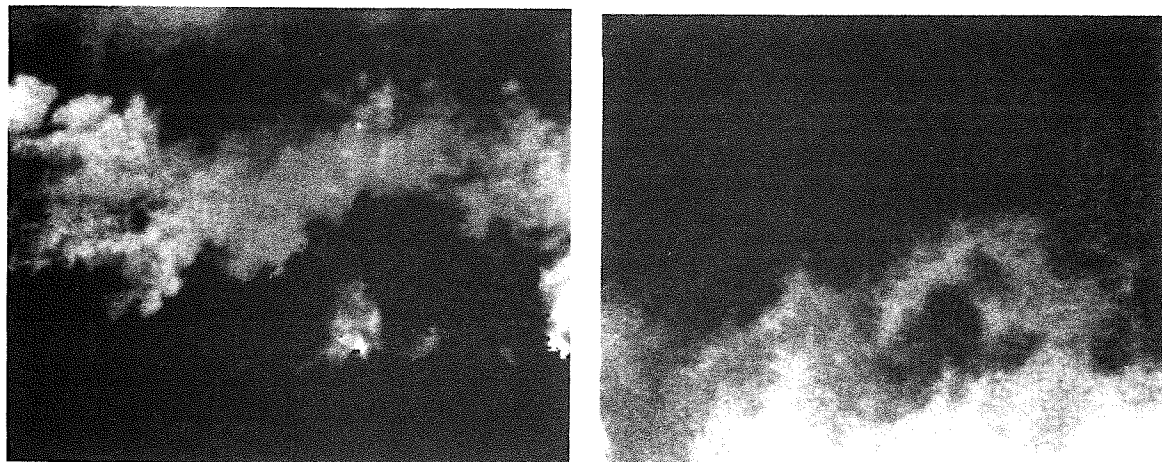


Figure 4.60: Results from the Stanford experiment: Image interpretation.
Top left: acetone PLIF indicating the slow cold flow.
Top right: OH PLIF indicating the reaction zone.
Top left: overlap of top pictures.

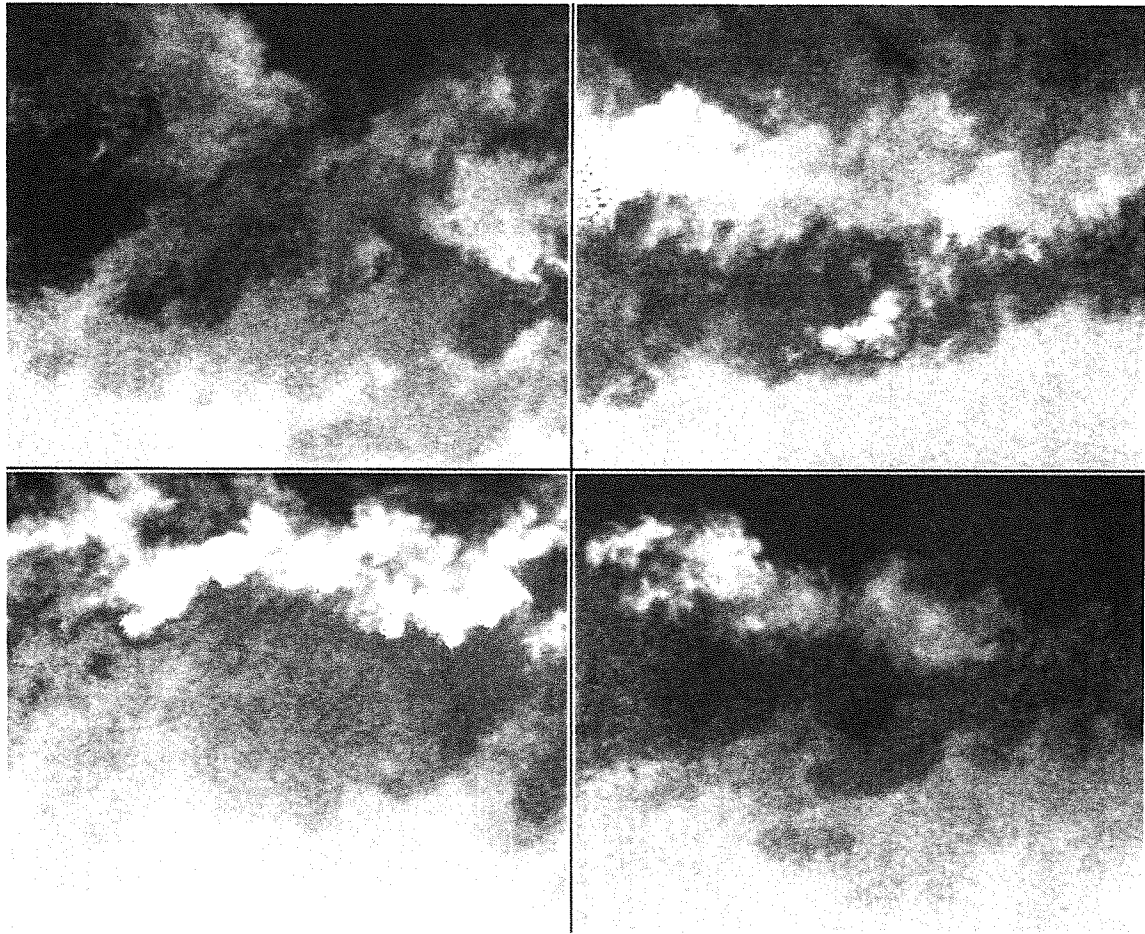


Figure 4.61: Results from the Stanford experiment: Mixing layer structure at four different unrelated instants. The bright upper zone is the PLIF of OH in the reaction zone. The darker lower zone is the PLIF from acetone in the layer. The lighter lower zone is the PLIF from acetone in the slow cold stream.

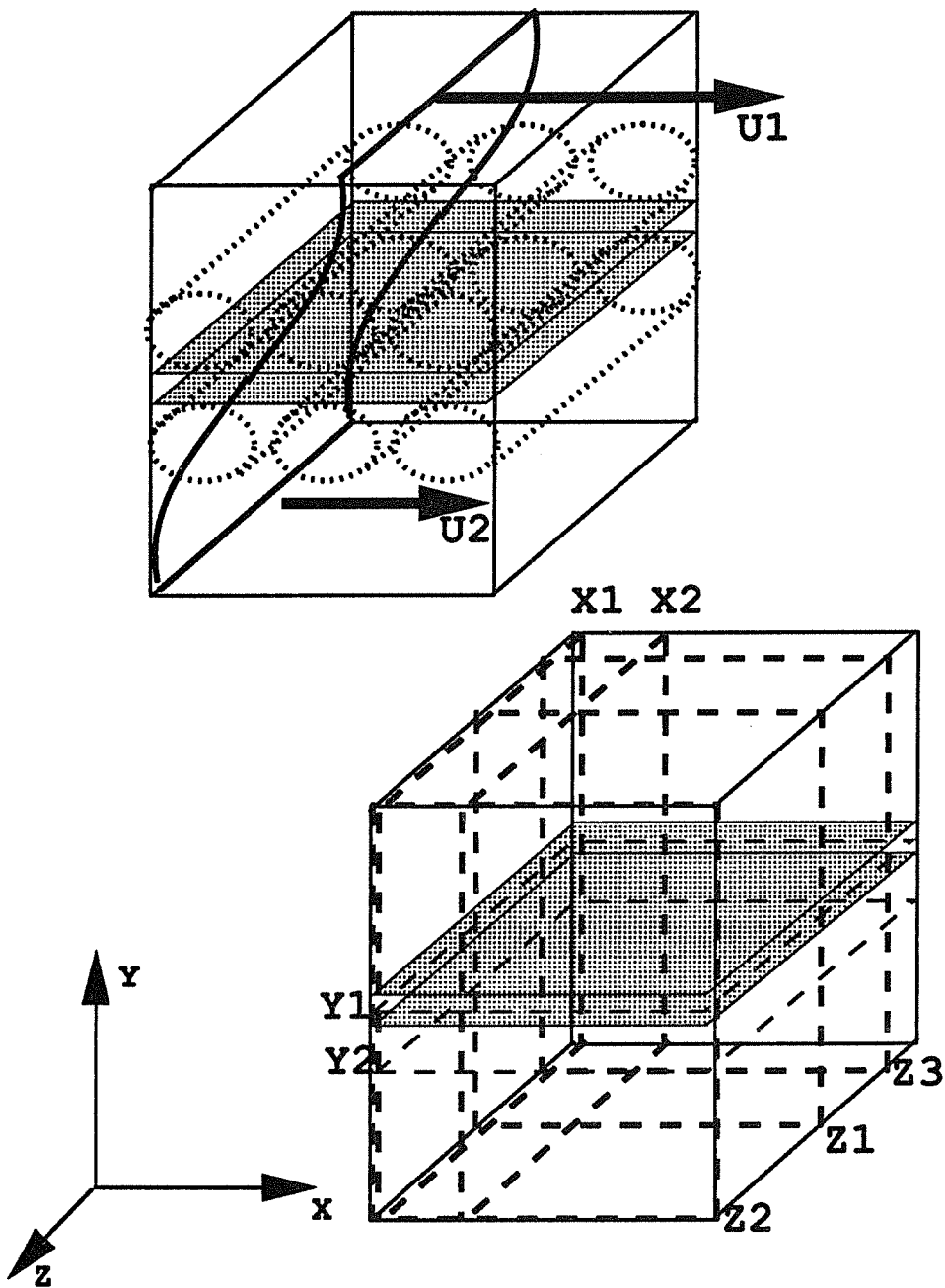


Figure 5.1: Computational domain showing the flow direction and the position of the reaction zone. The location of the plane-cuts used in this chapter is indicated. The plane Y_2 is located into the slow colayer and the plane Y_1 in the middle of the reaction zone.

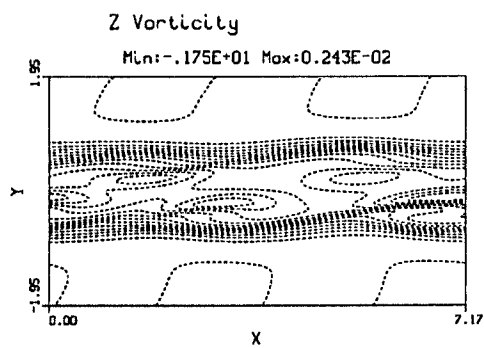
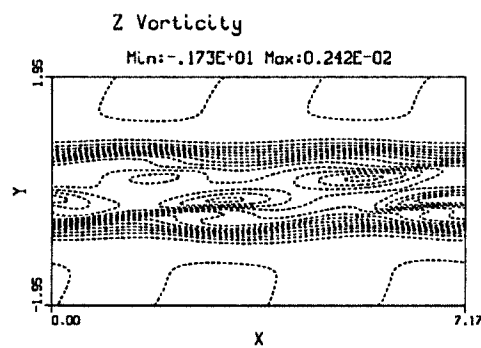
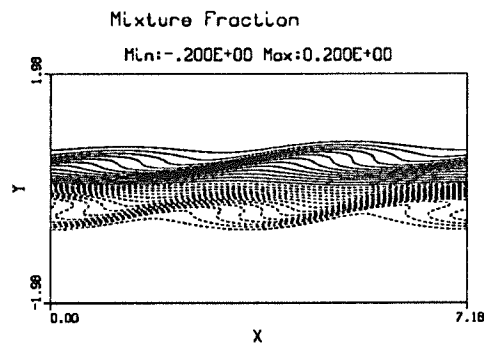
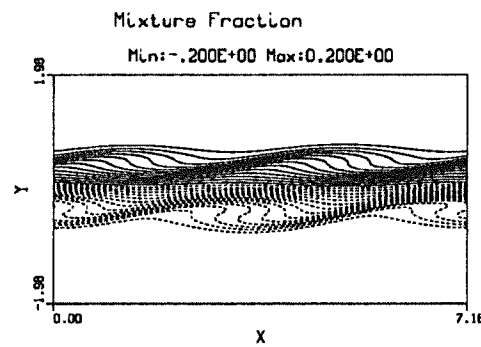


Figure 5.2: Plane-cuts of the mixture fraction and spanwise vorticity at $t = 70.9$ in the planes Z_1 (left) and Z_2 (right). Note the two-dimensionality of the layer and the similarity of the contours with those obtained in chapter 4 (fig 4.8)

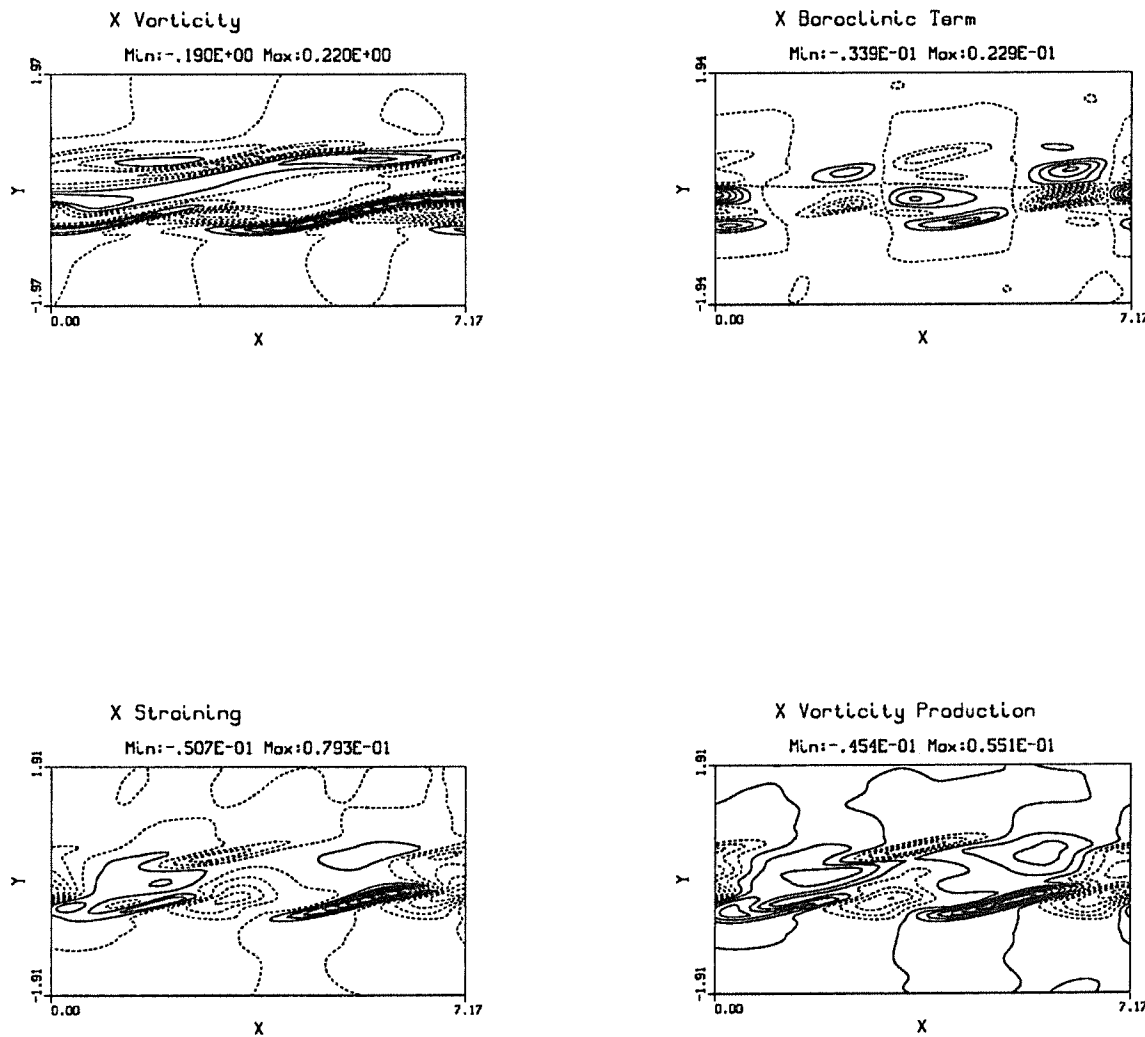


Figure 5.3: Streamwise vorticity production terms in plane Z_3 (braid region) ($t = 70.9$). Note the existence of two braid regions, one in each colayer. The straining term is large into the braids, where it dominates the vorticity production.

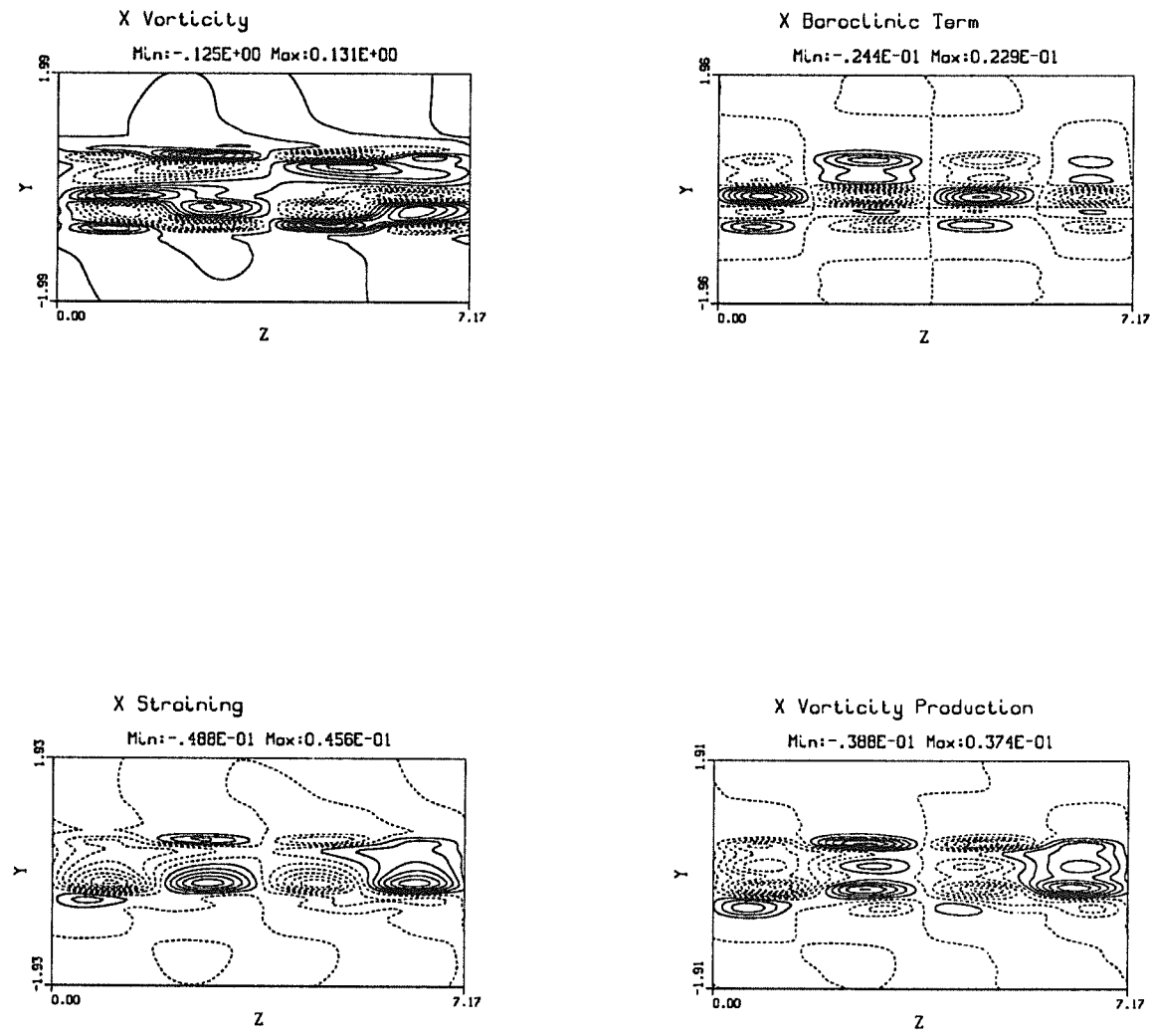


Figure 5.4: Plane-cut of the streamwise vorticity and vorticity production terms at $t = 70.9$ in the plane X_1 , through the slow outer mode large-scale structure. The baroclinic terms is large in the region where the streamwise vortices connect to the spanwise vortex.

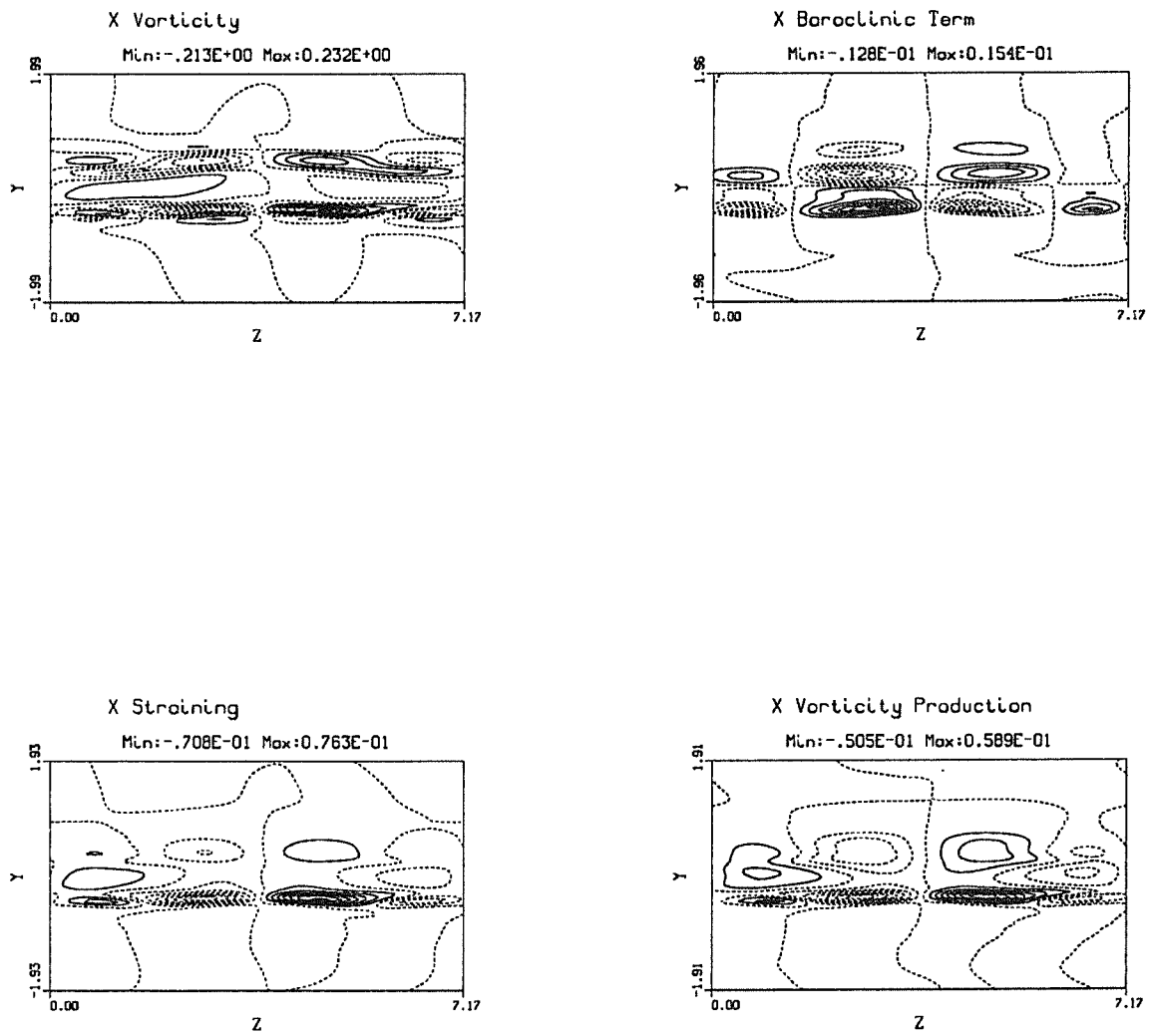


Figure 5.5: Plane-cut of the streamwise vorticity and vorticity production terms at $t = 70.9$ in the plane X_2 , through the slow outer mode braids. Here, the straining term is the dominant term of the vorticity production. The x-vorticity in the slow stream appears as four counter-rotating vortices.

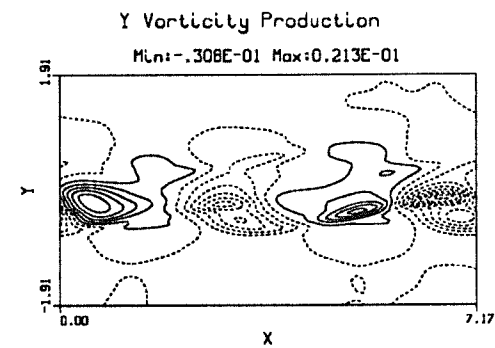
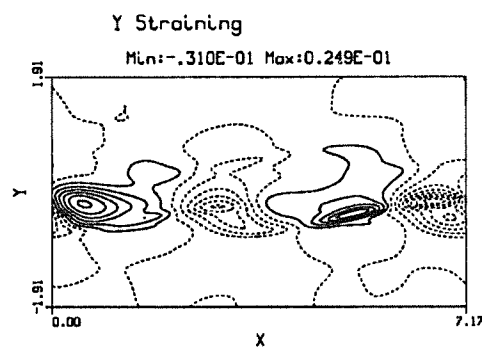
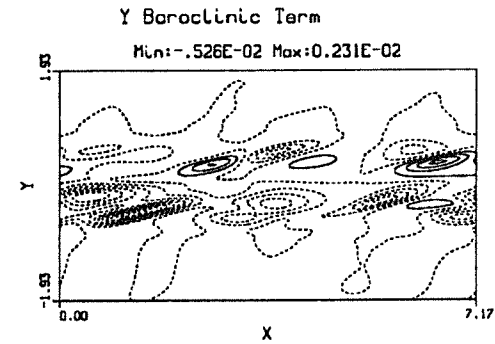
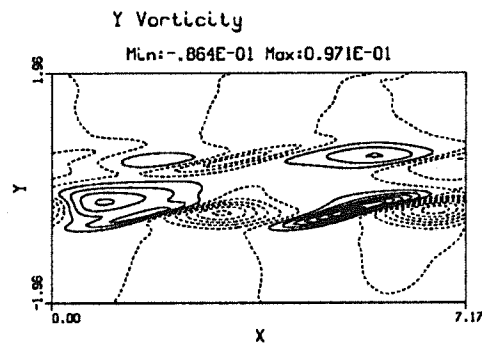


Figure 5.6: Cross-stream vorticity production terms in plane Z_3 (braid region) at $t = 70.9$.

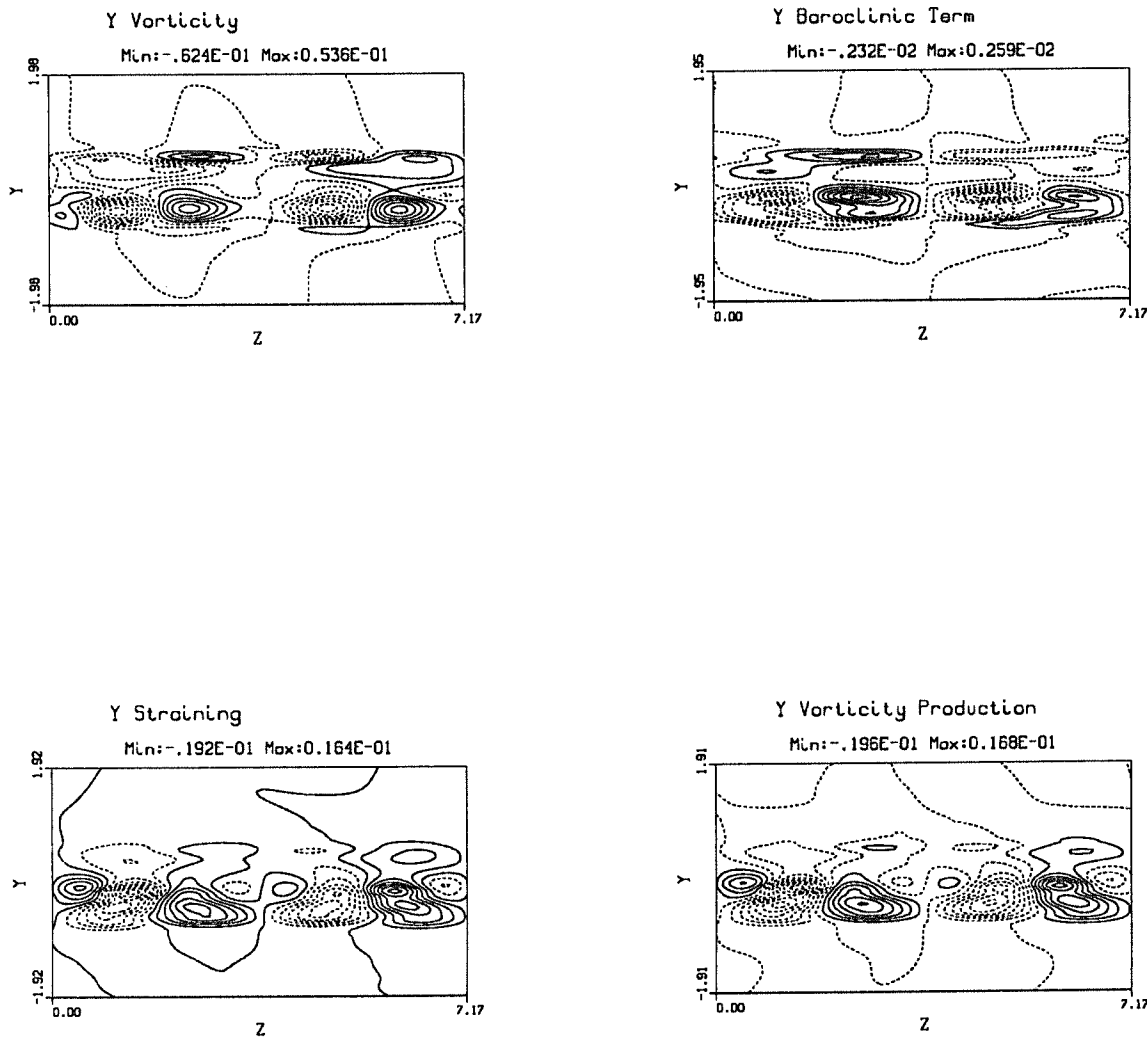


Figure 5.7: Plane-cuts of the cross-stream vorticity and vorticity production terms at $t = 70.9$ in the plane X_1 , through the slow outer mode large-scale structure. The baroclinic terms is very small and the straining term dominates the y -vorticity production. The magnitude of the cross-stream vorticity is approximately half that of the streamwise vorticity.

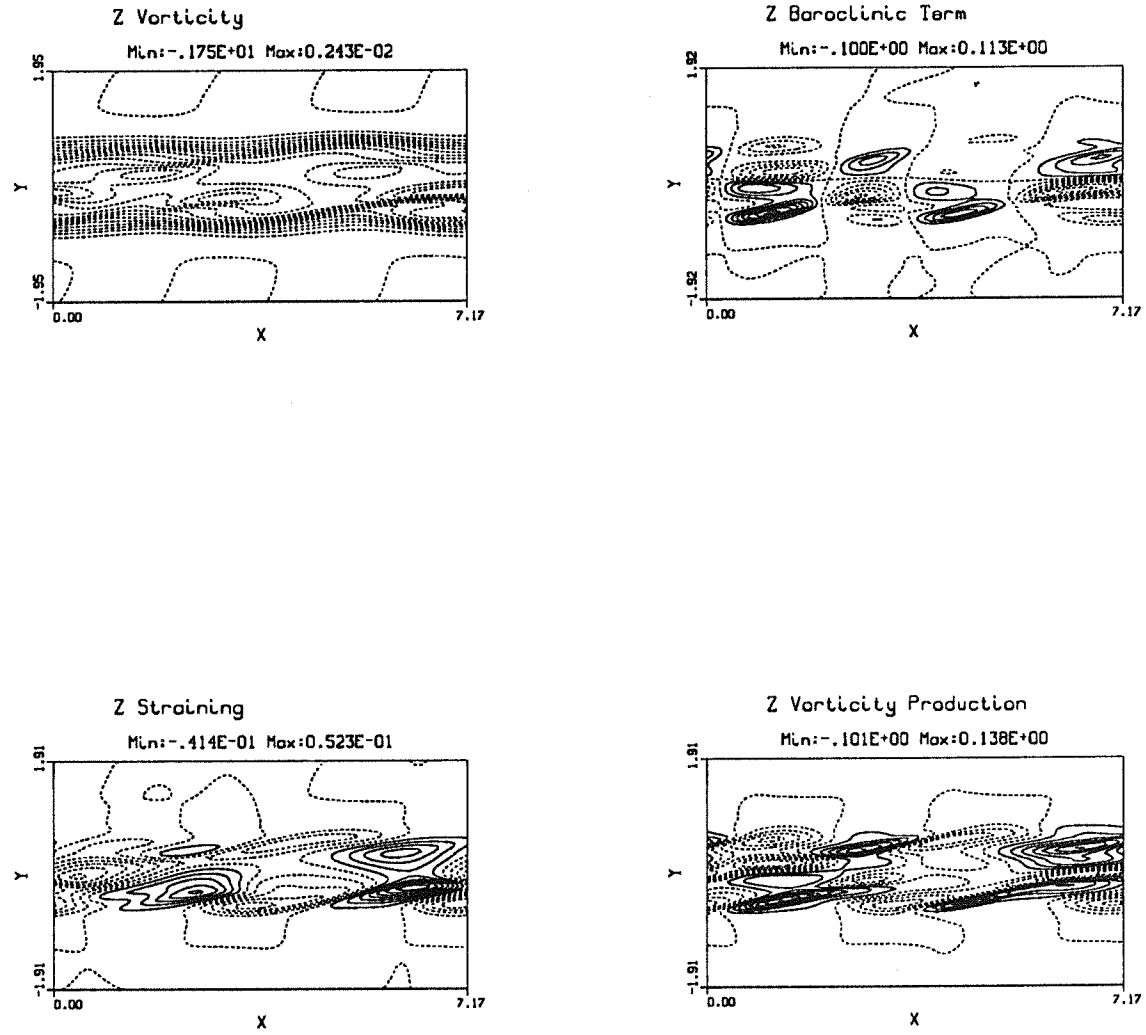


Figure 5.8: Spanwise vorticity in a plane of strong positive straining ($t = 70.9$). The baroclinic contours are very similar to the baroclinic contours in two-dimensional simulation. At this early time, where streamwise vortices are weak, the straining term is smaller than the baroclinic term. The straining term is largest in the region where the streamwise vortices connect to the large spanwise rollers.

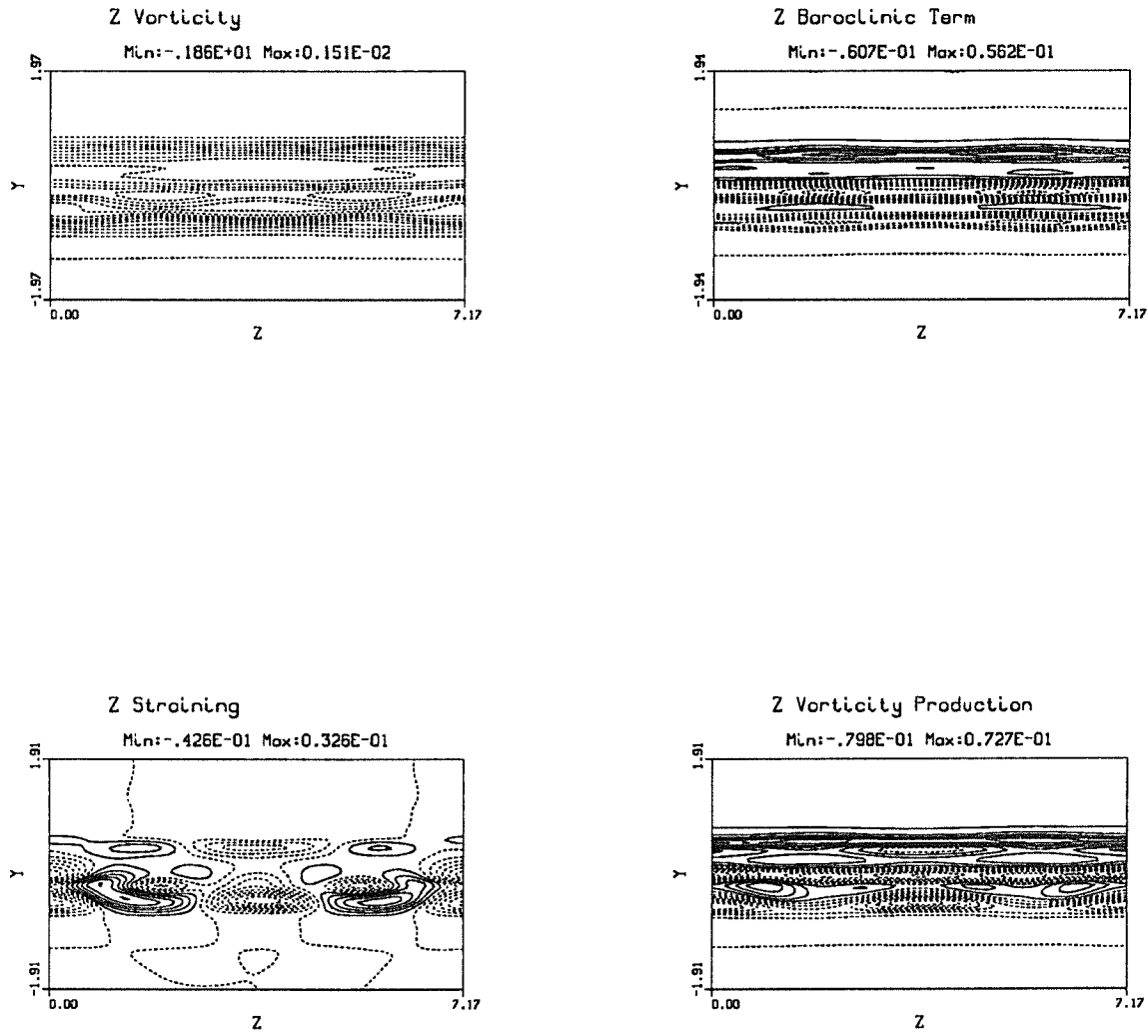


Figure 5.9: Plane-cut of the spanwise vorticity and vorticity production terms at $t = 70.9$ in the plane X_1 . The baroclinic term is uniform across the layer and negative in the core. The straining term caused by counter-rotating streamwise vortices yielding a non-uniform s-shaped spanwise vorticity production.

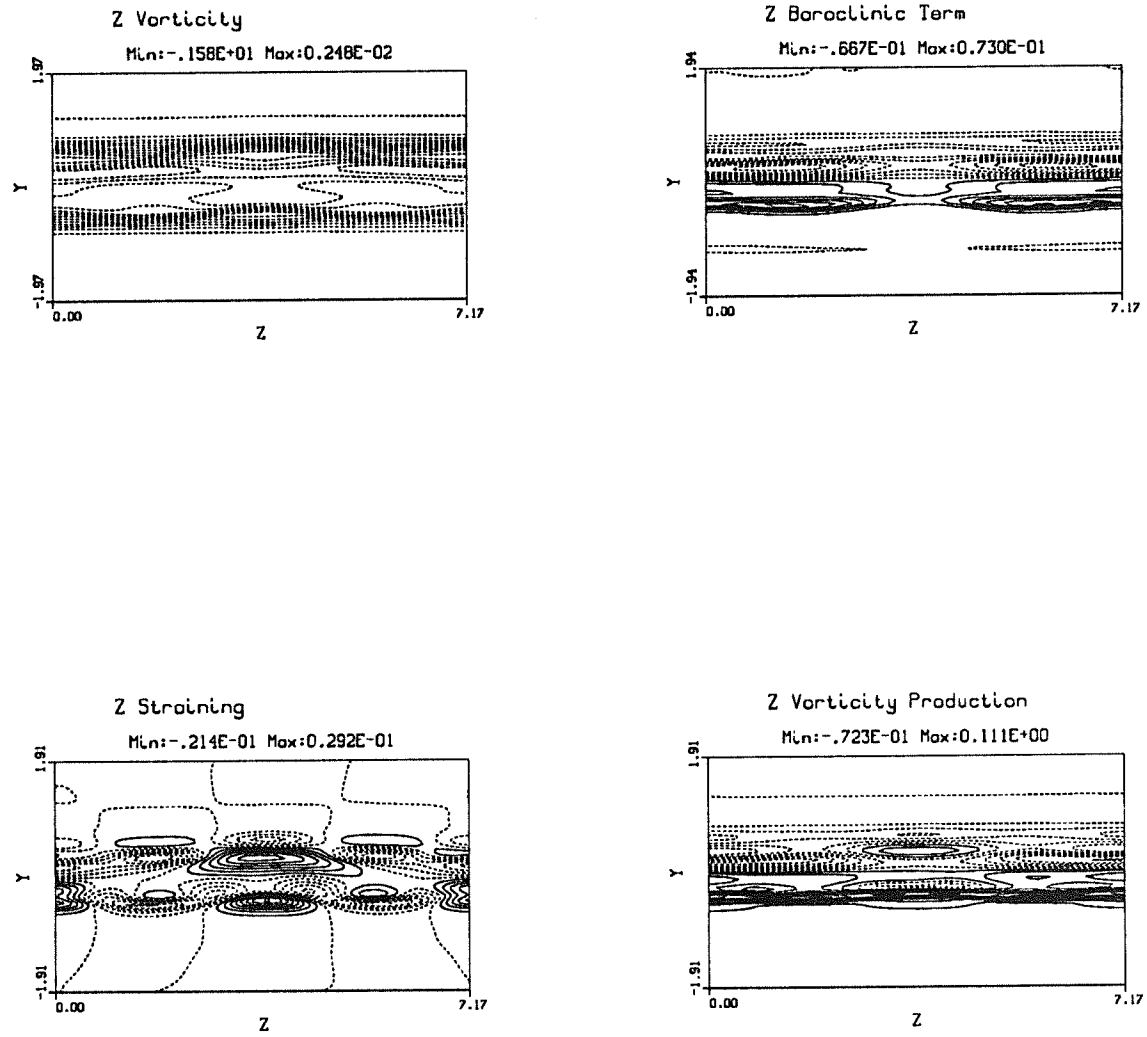


Figure 5.10: Plane-cut of the spanwise vorticity and vorticity production terms at $t = 70.9$ in the plane X_2 , through the slow outer mode braids. The baroclinic term dominates the vorticity production and destroys ω_z as in the 2-D case. Note that the straining term is non-zero in the braids.

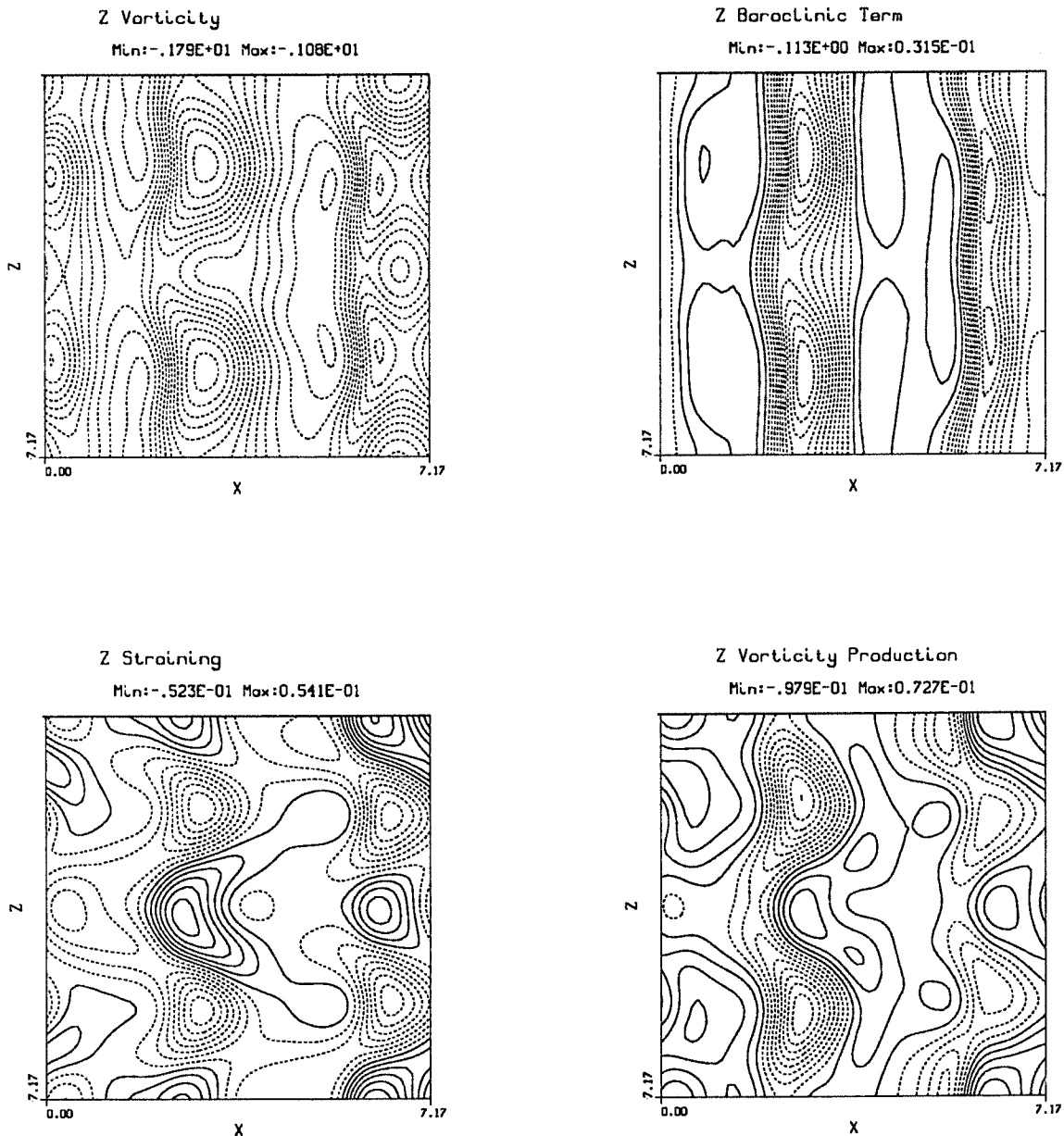


Figure 5.11: Top-view of the spanwise vorticity and vorticity production terms at $t = 70.9$ in the plane Y_2 (through the slow outer mode large-scale structure). The baroclinic term is two-dimensional but the straining term exhibits s-shaped contours and causes a strongly non uniform production of ω_z .

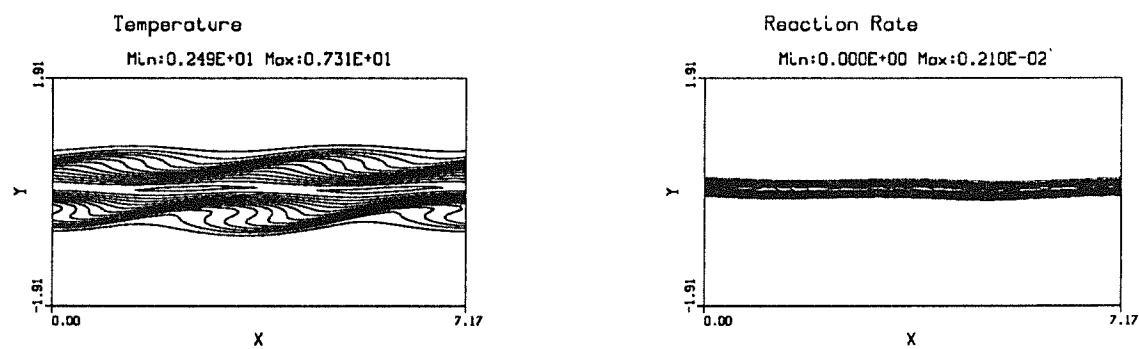
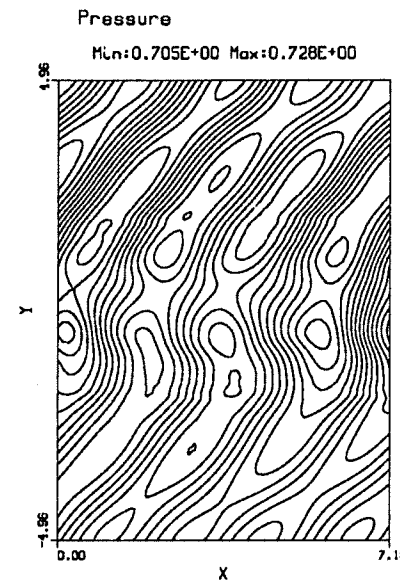
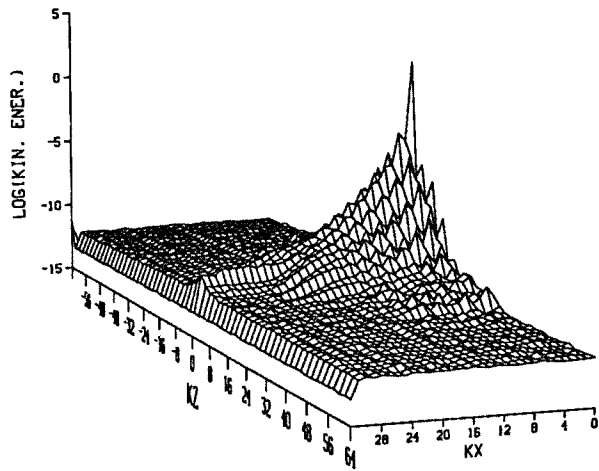
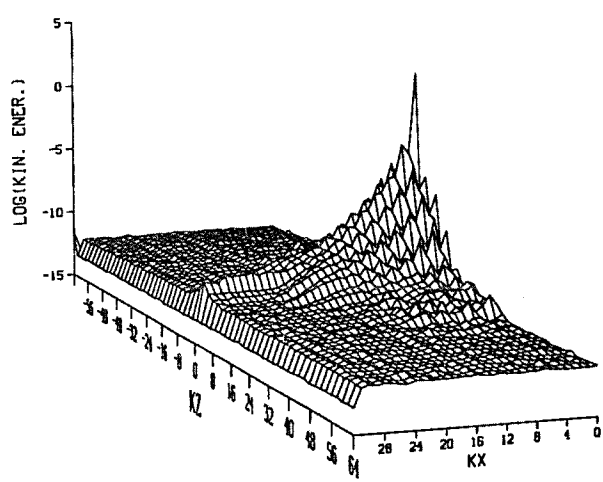


Figure 5.12: Contours of pressure, temperature and reaction rate in the plane Z_1 ($t = 70.9$). We retrieve at this early time the radiating Mach waves seen in the 2-D simulations. The temperature contours confirm the existence of a persistent hot temperature region between the two colayers. The reaction zone remains plane with no creation of flame surface.

MODAL ENERGY CONTENT



MODAL ENERGY CONTENT



MODAL KINETIC ENERGY

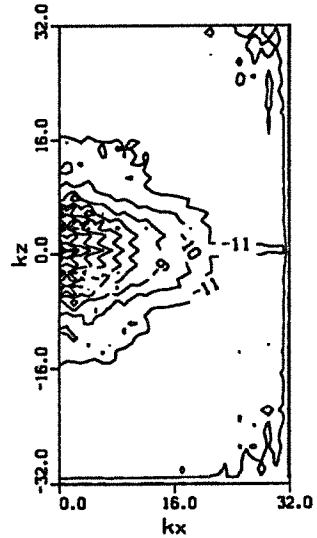


Figure 5.13: (Top) Modal energy content at time $t = 70.9$ (E_1). (bottom left) Same, taking into account the density variations (E_2). (bottom right) contour plot of the modal energy content shown on top. Note that iso-contours of kinetic energy are circular and that the kinetic energy is concentrated in a few wavenumbers.

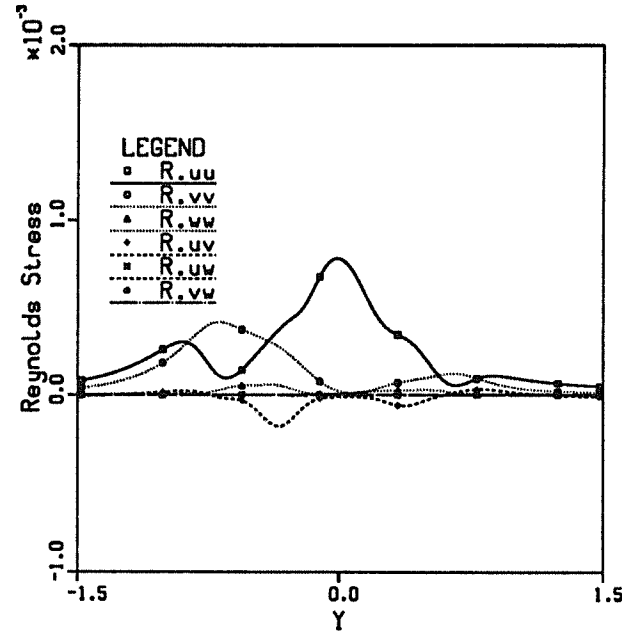
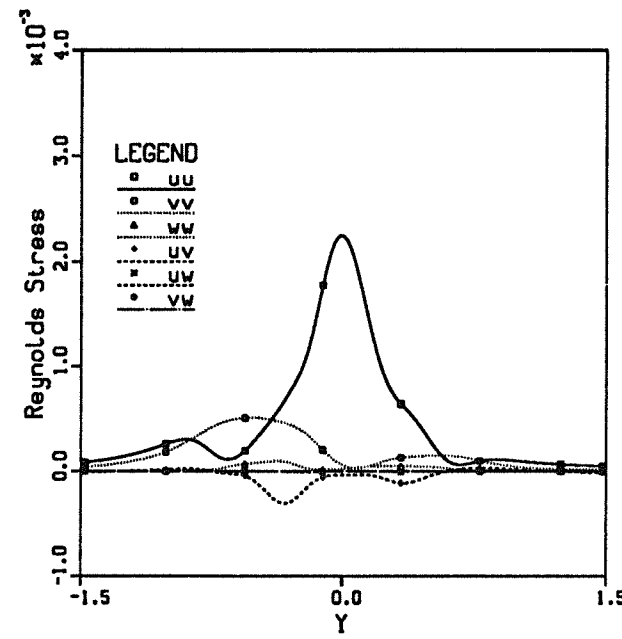


Figure 5.14: (Top) Mean Reynolds stresses at various y -location of the layer. The profiles are obtained by summation on the x - z planes. Note that \bar{uv} has two peaks as in the 2-D case associated with the two outer modes. (Bottom) Same as top multiplied by density.

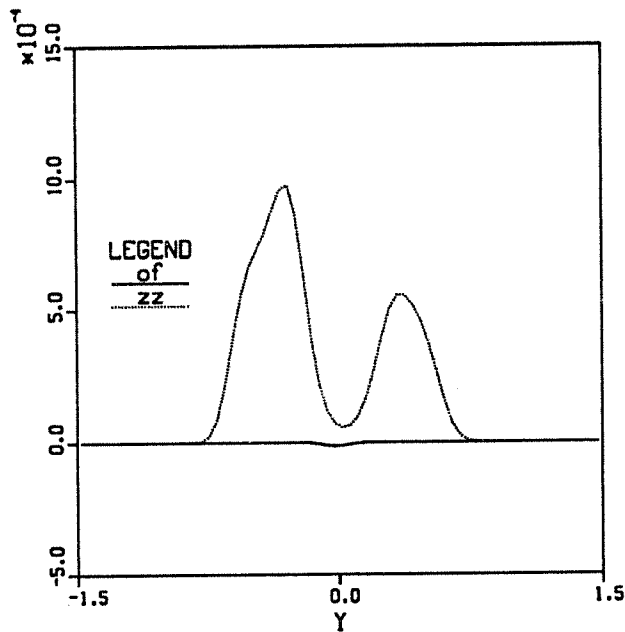
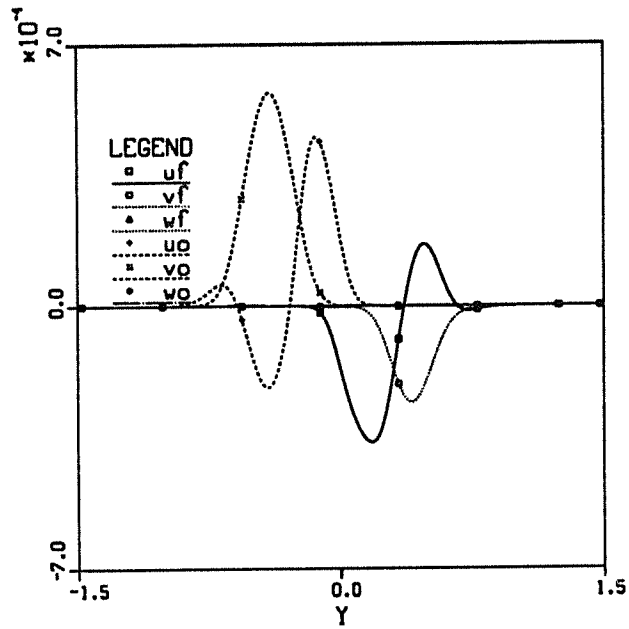


Figure 5.15: (Top) Turbulent transport of species. Note that \bar{v}_f and \bar{v}_o do not overlap suggesting little turbulent convection of fuel and oxidizer to the reaction zone. (Bottom) Mean profiles of $\bar{z}z$ and $\bar{o}f$ where z,o,f are the passive scalar, fuel mass fraction and oxidizer mass fraction, respectively. Note the two peaks of $\bar{z}z$ showing the two zones of mixing.

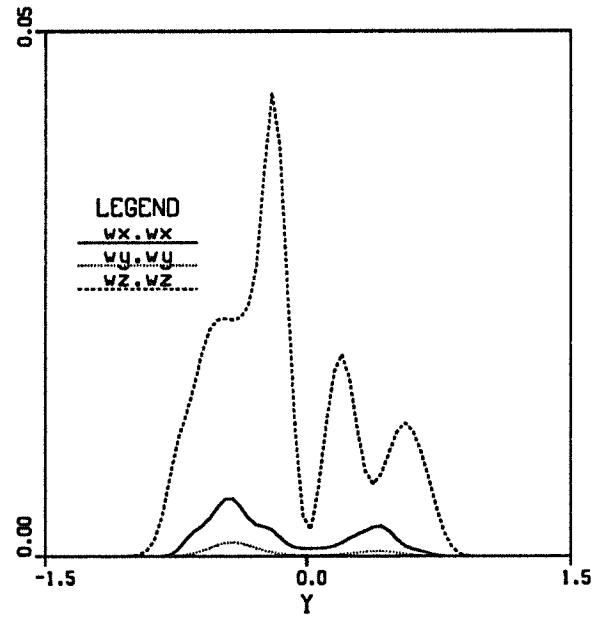
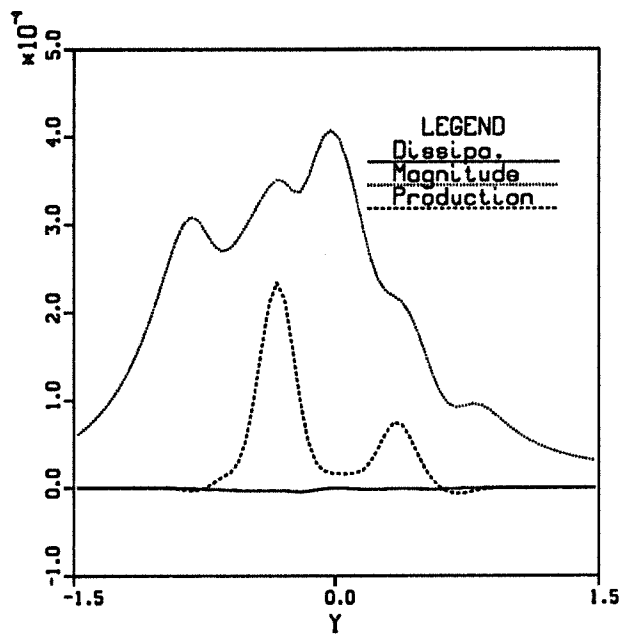


Figure 5.16: (Top) Production rate, dissipation rate and magnitude of the kinetic energy at $t = 70.9$. Note the two peaks of production in the two colayers and the very low dissipation at this early time. (bottom) Components of enstrophy. Note the distinct peaks of $\overline{\omega_z \omega_z}$ and the low magnitude of $\overline{\omega_x \omega_x}$ and $\overline{\omega_y \omega_y}$.

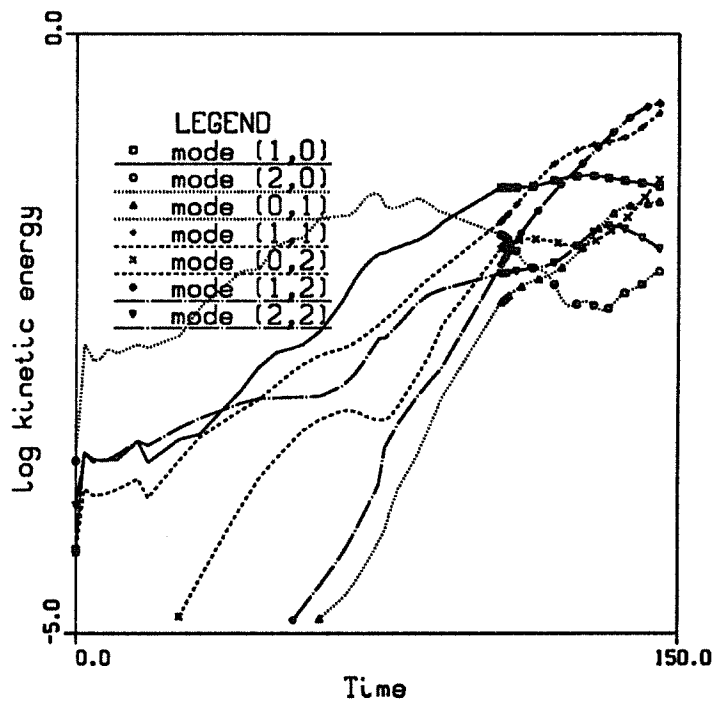
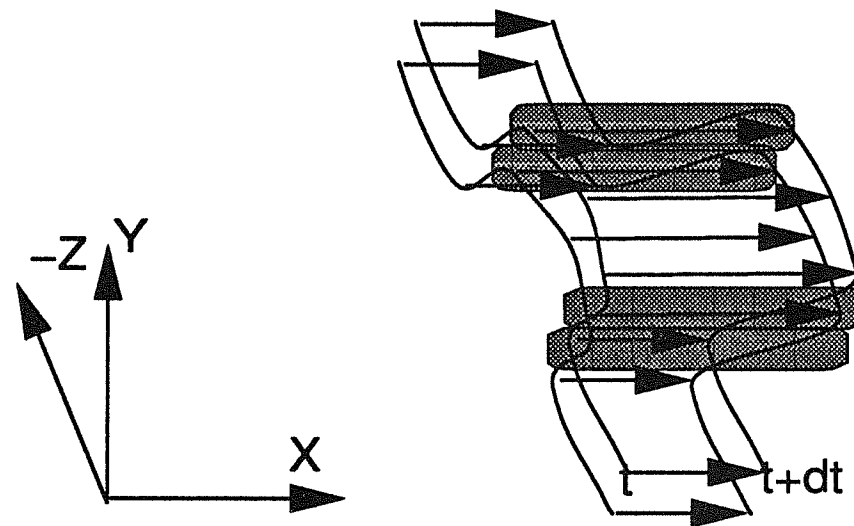
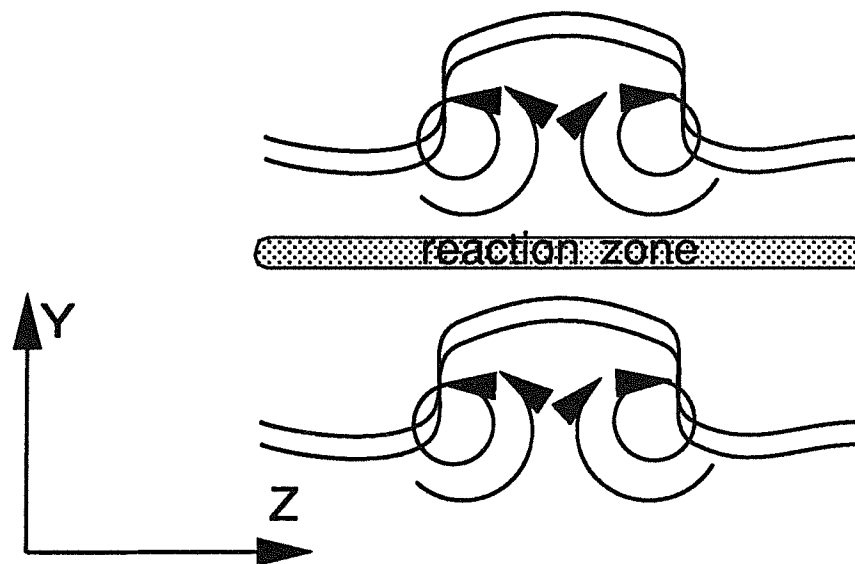


Figure 5.17: Time variation of the kinetic energies of various spectral modes. Note that initially the 2-D modes dominates and are growing faster than the 45° modes. Note also the rapid growth of the streamwise vortices and the saturation and decay of the 2-D modes at $t = 80$ and $t = 120$.



 creation of intense x and y vorticity

Figure 5.18: Transition to turbulence mechanism. Note that the transition occurs on both sides of the reaction zone and does not destroy the two colayers. The existence of 2-D and 45 degree modes generates streamwise vortices which appears a fundamental step in the transition to turbulence.

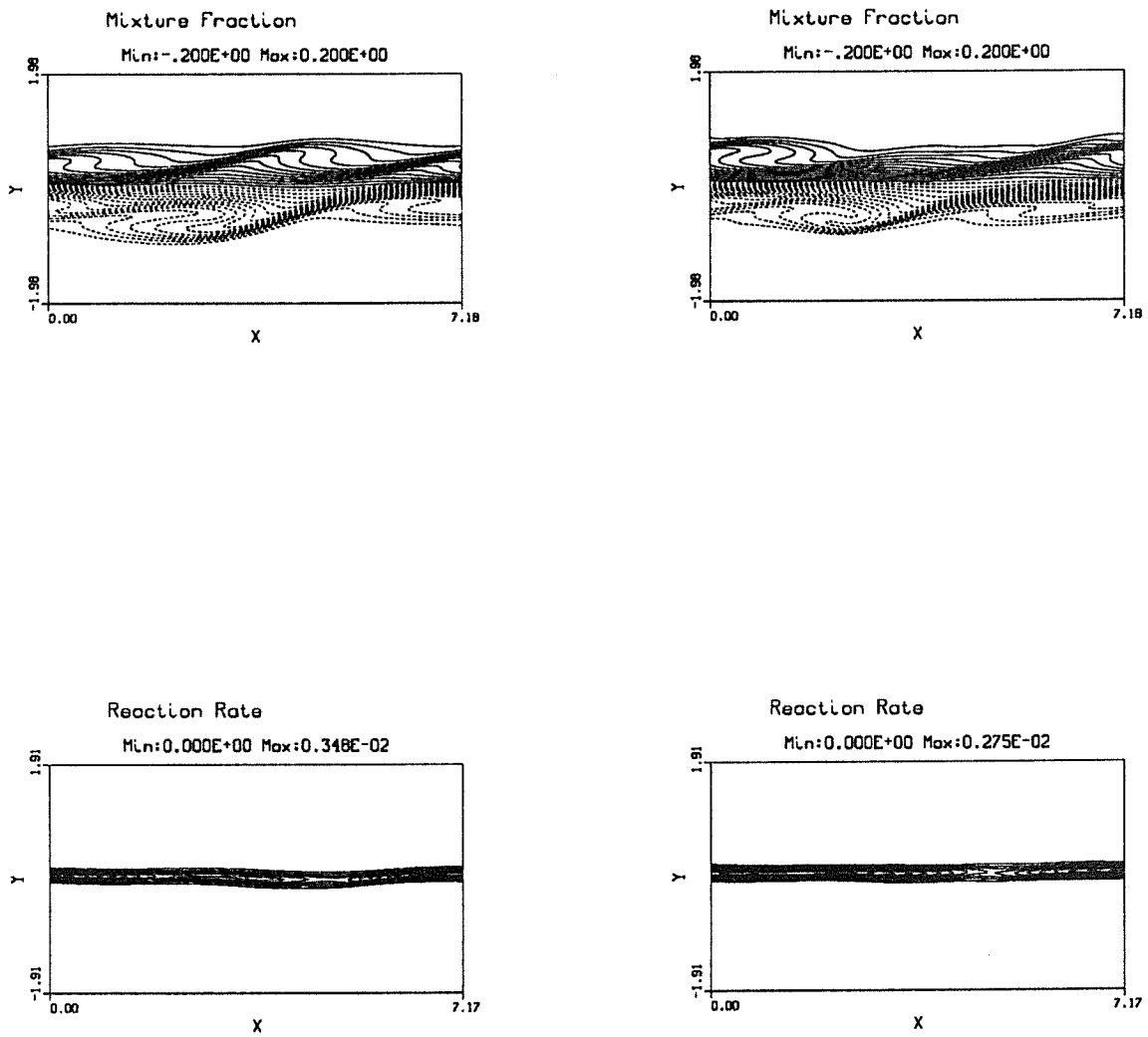


Figure 5.19: View of the layer at $t = 105.6$ in the planes Z_1 (left) and Z_2 (right). The two colayers still exist as indicated by the flat reaction zone but the two-dimensionality of the large-scale structures is partly destroyed during the transition, as seen on the mixture fraction contours.

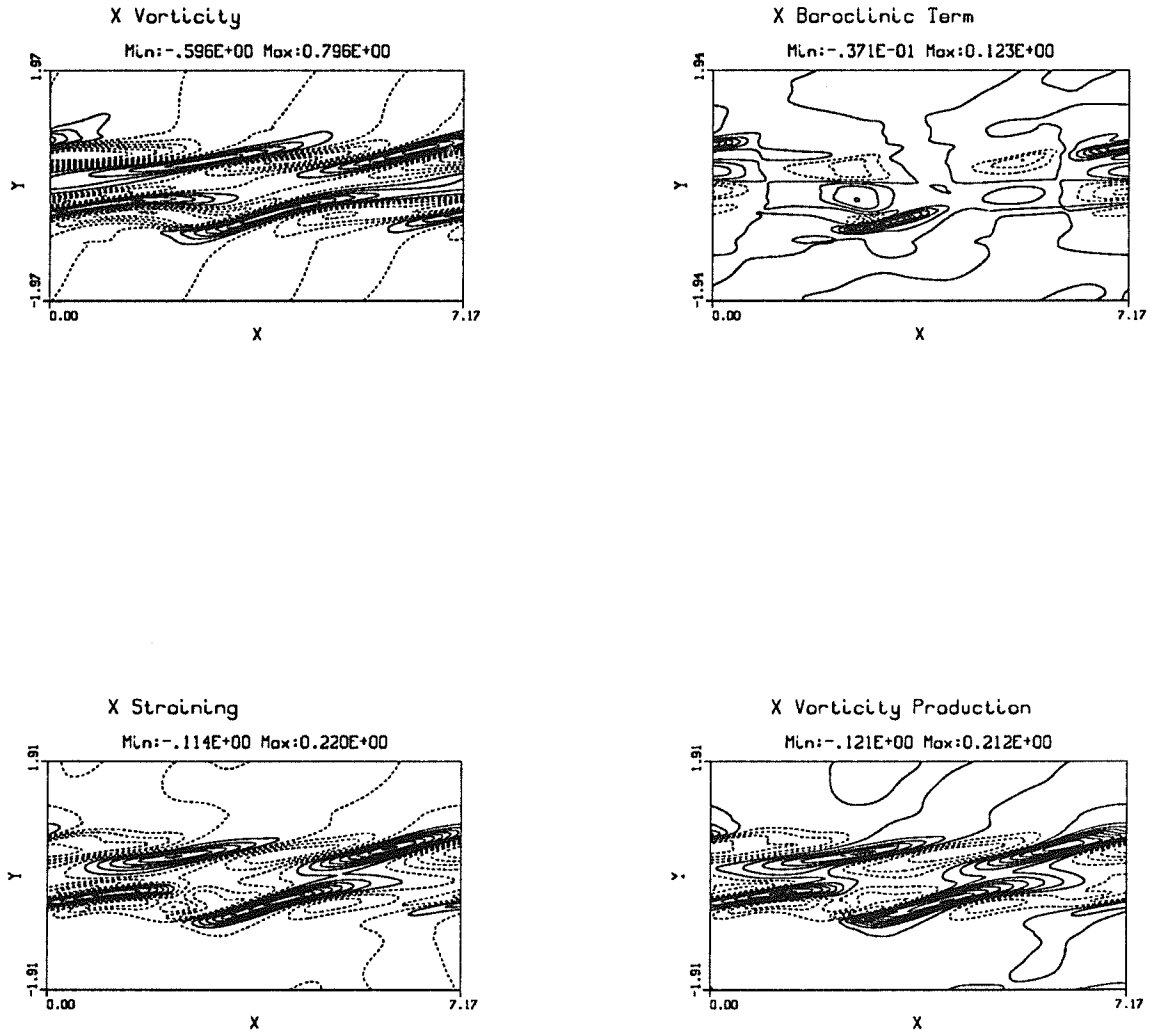


Figure 5.20: Streamwise vorticity and vorticity production terms in plane Z_2 ($t = 105.6$). Note the large increase in vorticity compared to earlier times. The vorticity is large in the high straining term region. We also note an increase of the baroclinic term which tends to create vorticity at the bottom (top) of the slow (fast) outer mode eddies.

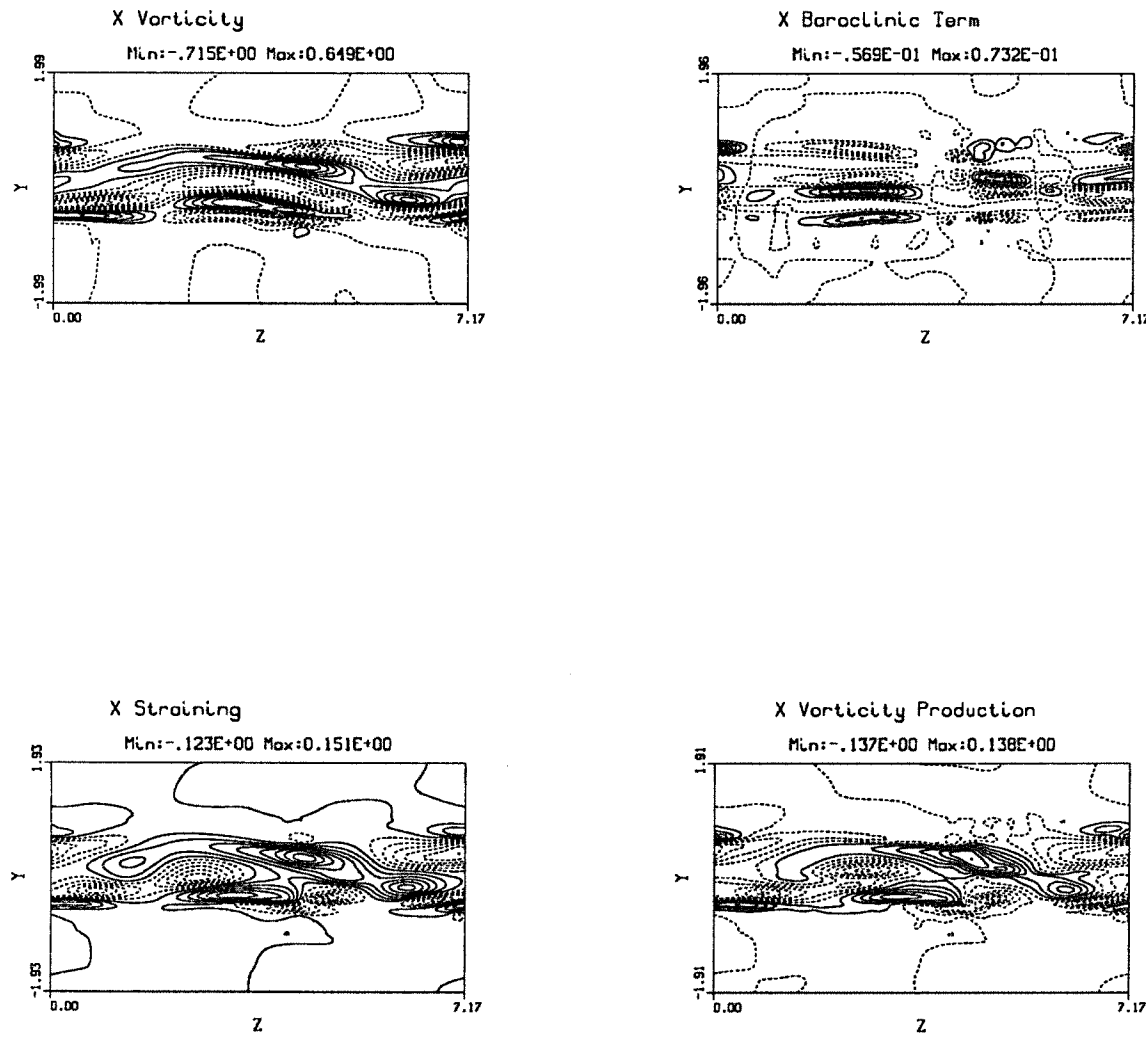


Figure 5.21: Plane-cut of the streamwise vorticity and vorticity production terms at $t = 105.6$ in the plane X_1 , through the fast outer mode large-scale structure and the braids of the slow outer mode. The baroclinic term and straining term contours show smaller scales than at earlier time. The braids do not appear anymore as the juxtaposition of thin counter-rotating vortices.

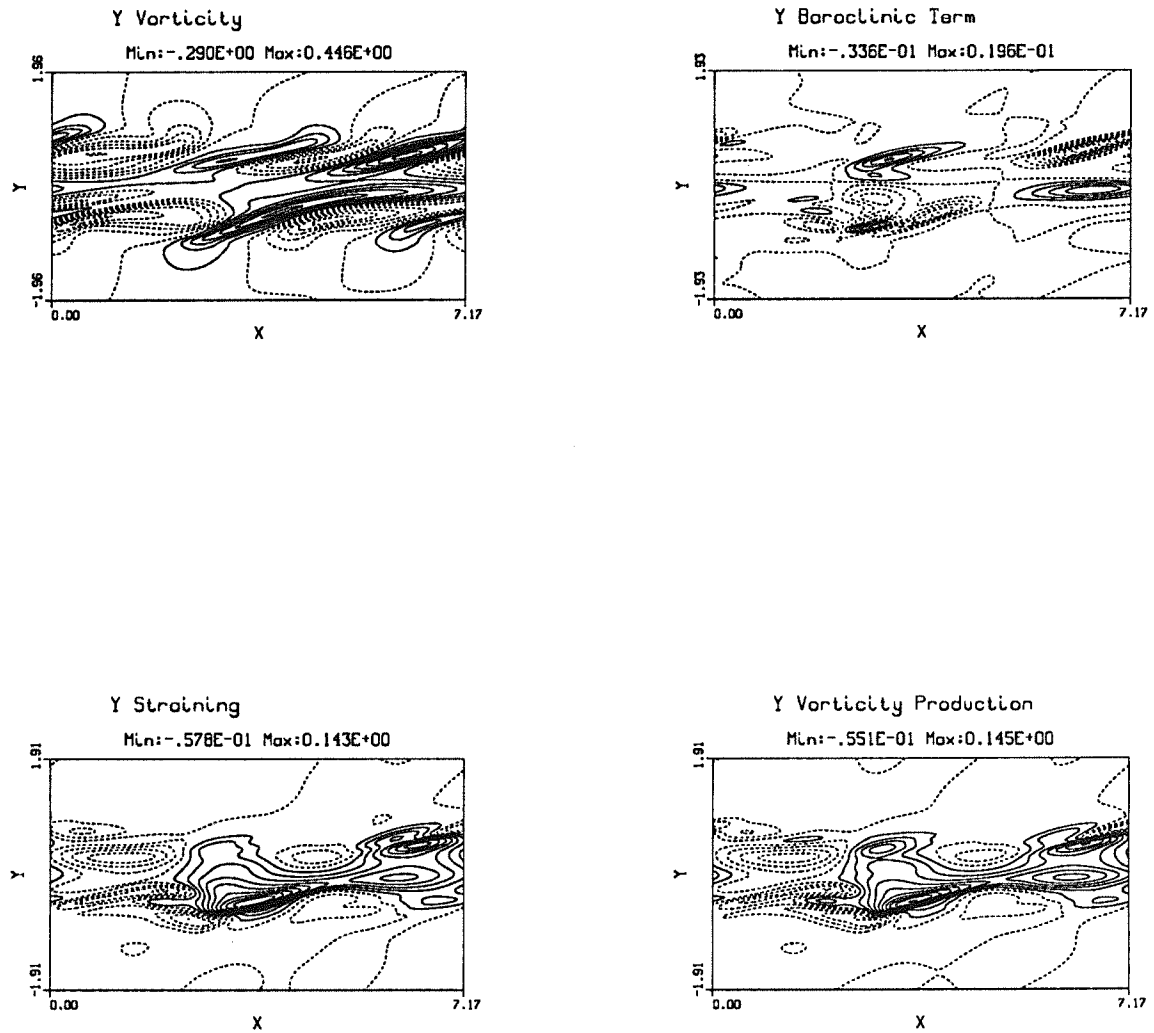


Figure 5.22: Cross-stream vorticity and vorticity production terms in plane Z_2 ($t = 105.6$). Note the large increase in vorticity compared to earlier times. The vorticity is large in the high straining term region and its magnitude is about half that of the x -vorticity. The baroclinic term remains small.

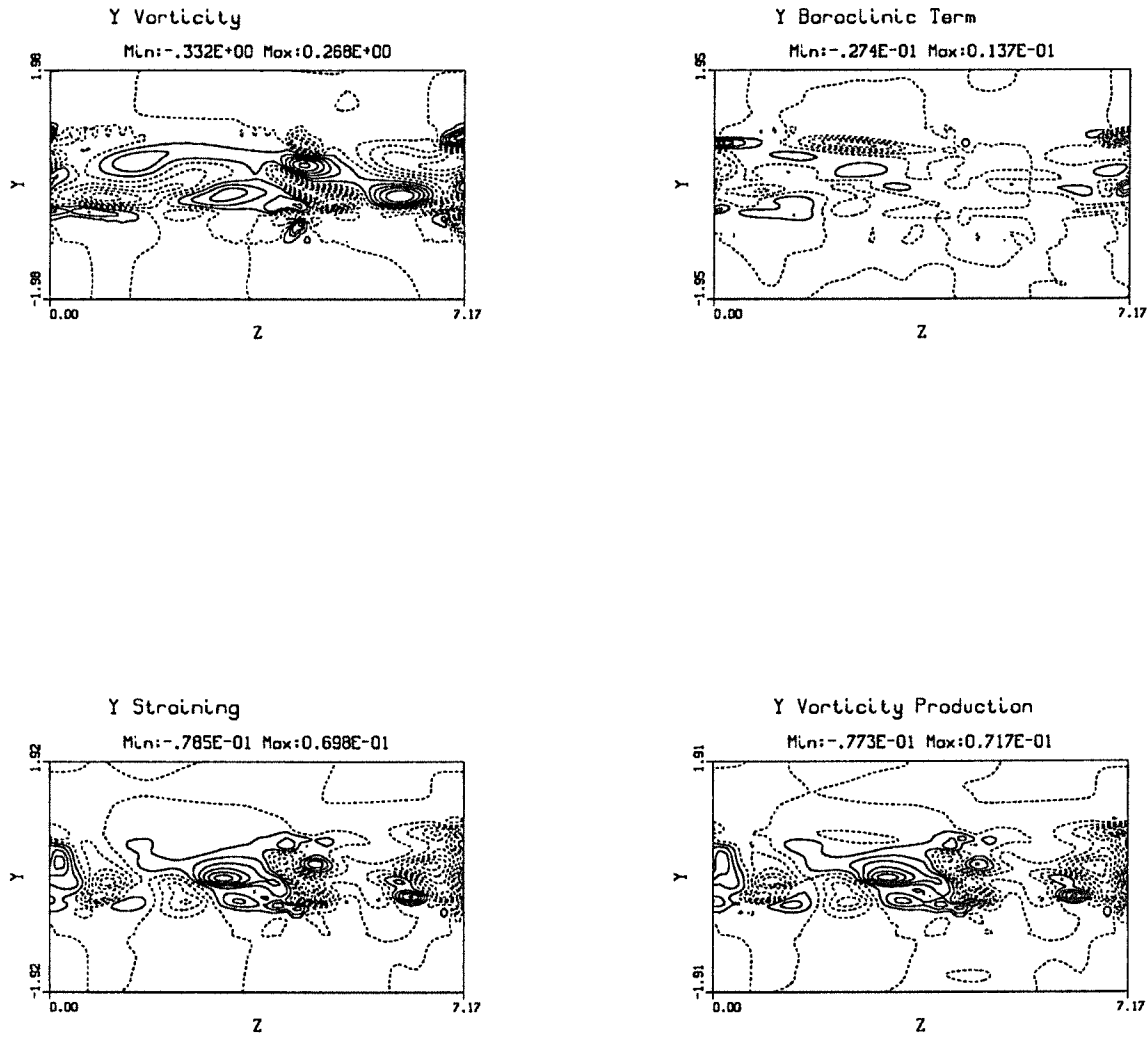


Figure 5.23: Plane-cut of the cross-stream vorticity and vorticity production terms at $t = 105.6$ in the plane X_1 , through the fast outer mode large-scale structure and the braids of the slow outer mode. The baroclinic term and straining term contours indicate smaller-scale counter-rotating vortices than at earlier time, especially in the plane Z_1 and Z_2 .

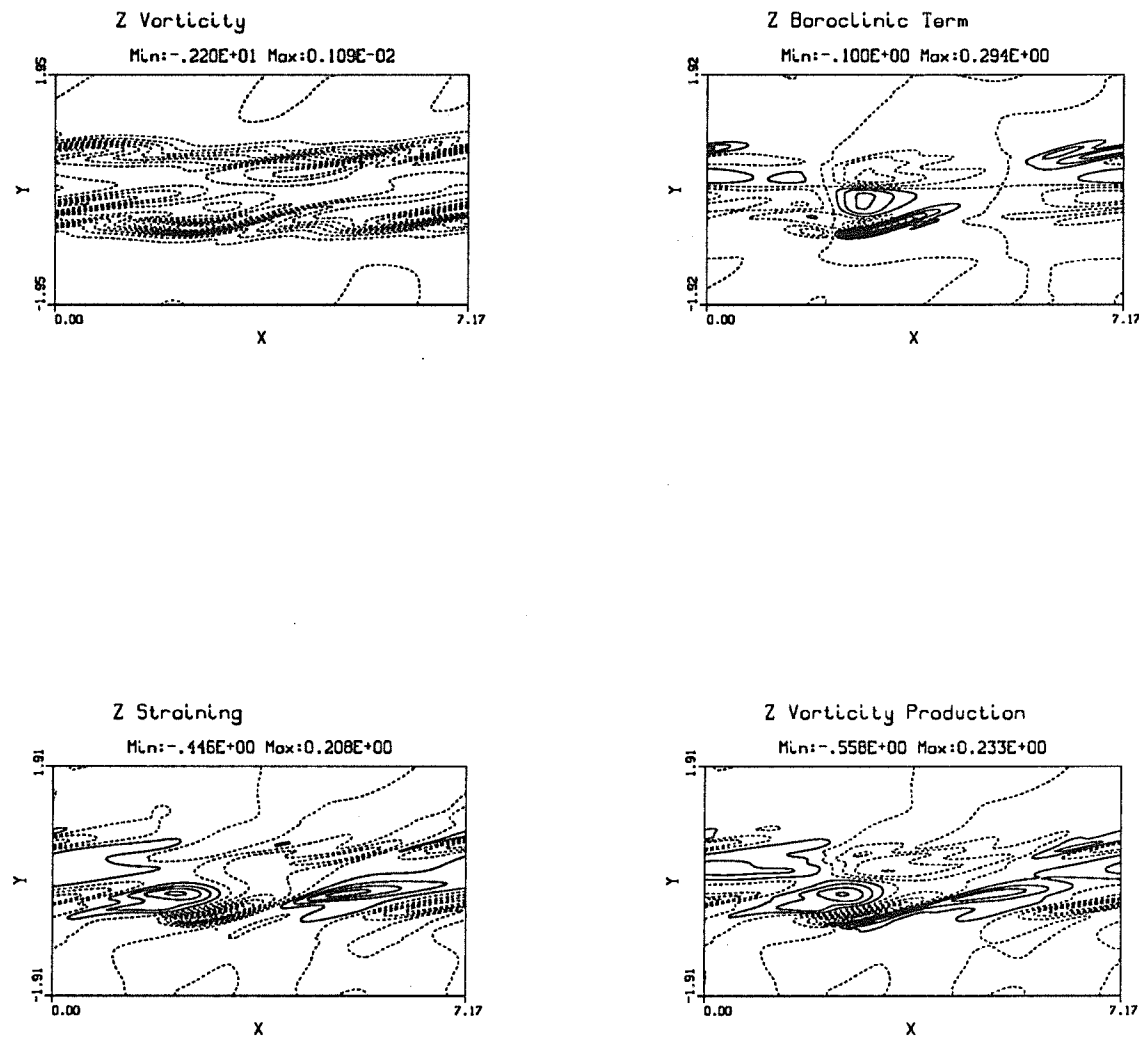


Figure 5.24: Spanwise vorticity and vorticity production terms in plane Z_2 at $t = 105.6$.

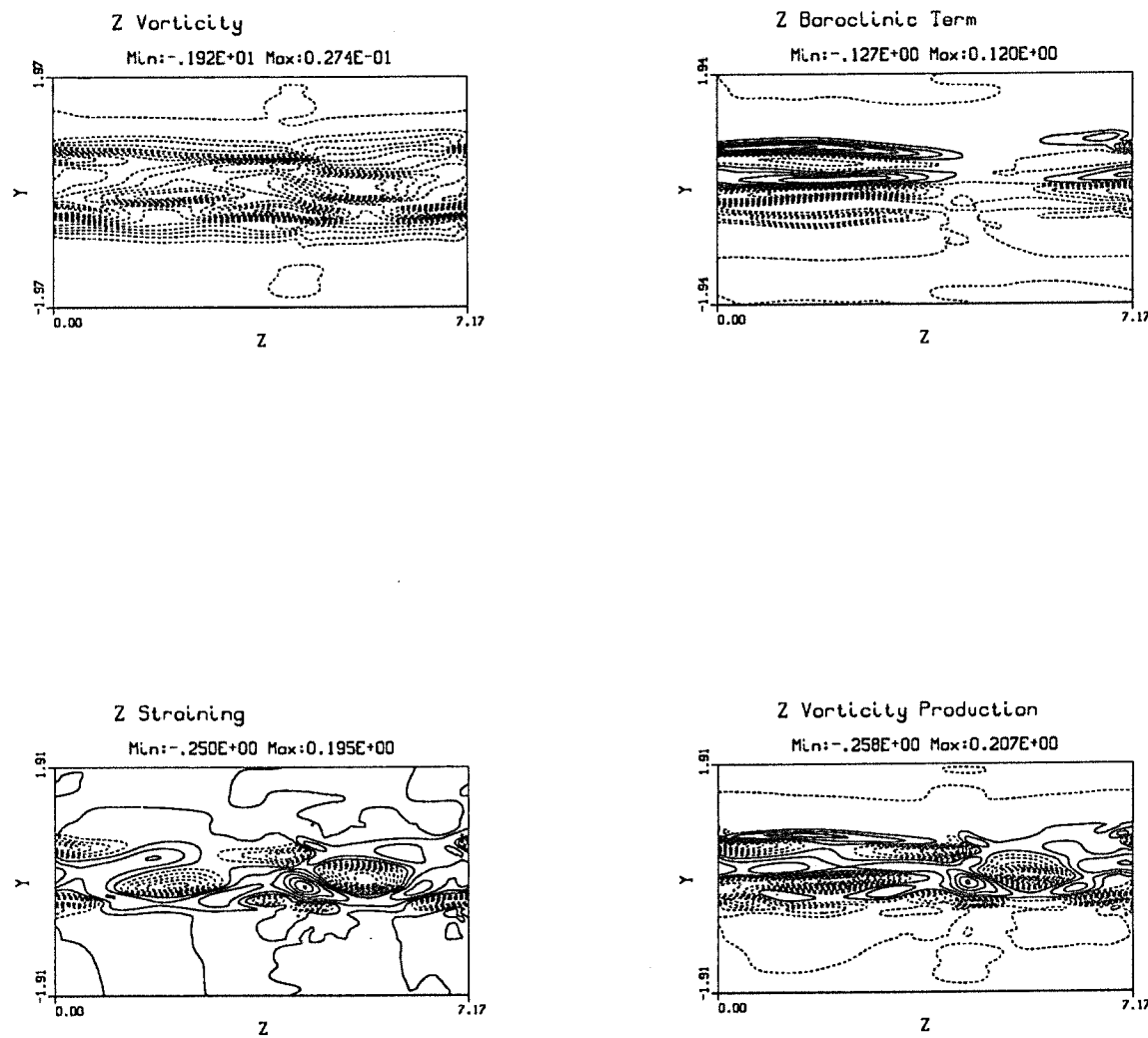
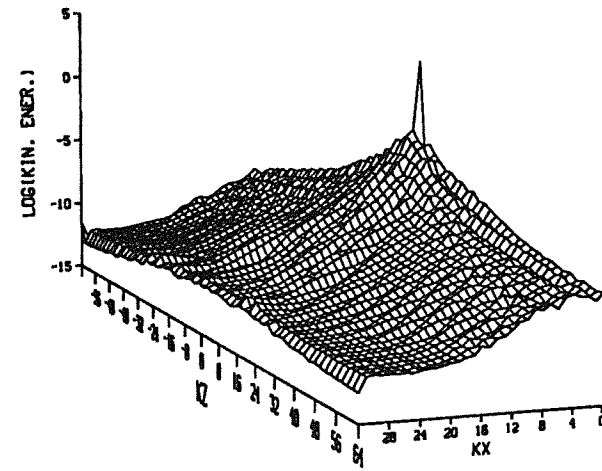


Figure 5.25: Plane-cut of the spanwise vorticity and vorticity production terms at $t = 105.6$ in the plane X_1 . The baroclinic term and straining term contours are more convoluted than at earlier times and the z-vorticity does not appear two-dimensional anymore.

MODAL ENERGY CONTENT



MODAL KINETIC ENERGY

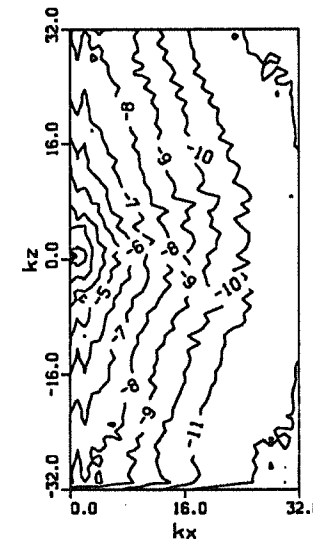


Figure 5.26: (Top) Logarithm of the modal kinetic energy content at time $t = 105.6$. (Bottom) Contour plot corresponding to the modal energy content shown on top. Note that the iso-contours of kinetic energy have become elliptic indicating a better transfer of energy to the small scale in the spanwise direction (streamwise vortices).

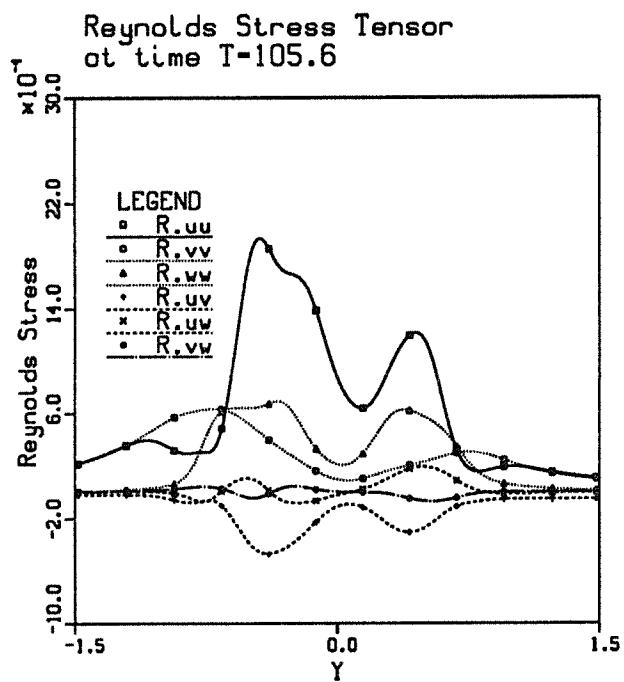
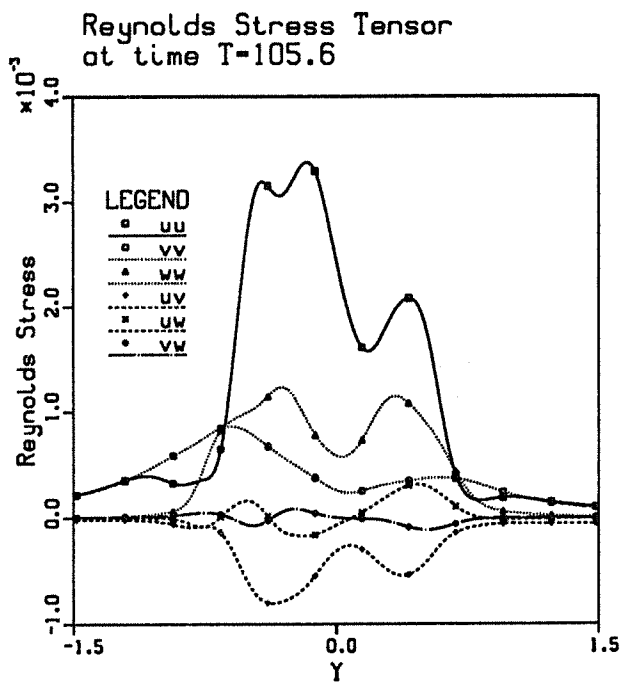


Figure 5.27: (Top) Mean Reynolds stresses profiles. Note that \bar{uv} has two peaks associated with the fast and the slow outer modes. The slow peak is more pronounced than the fast peak since the slow outer mode is more developed than the fast mode. (Bottom) Same as top multiplied by density.

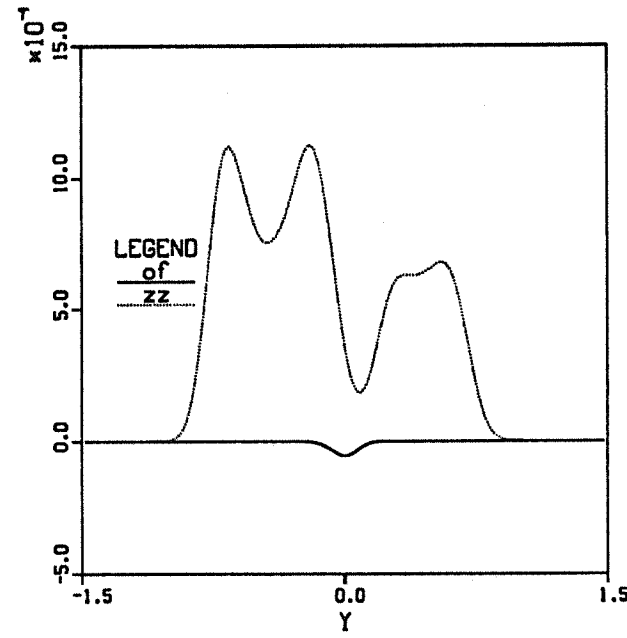
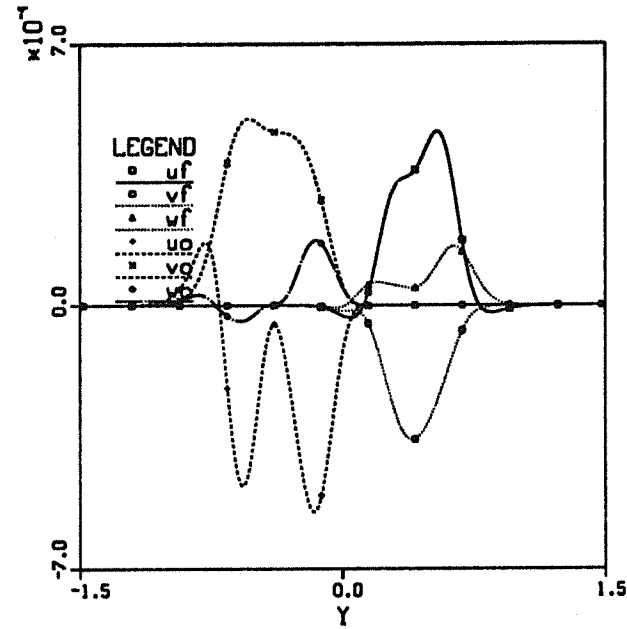


Figure 5.28: (Top) Turbulent transport of species. Note that \bar{v}_f and \bar{v}_o do not overlap as at $t = 70.9$. Both go to zero at $y = 0$ suggesting little turbulent transport of reacting species to the centerline. (Bottom) Profiles of \bar{zz} and \bar{o}_f . Note the two peaks of \bar{zz} showing the two zones of mixing, and the little but growing bump on \bar{o}_f indicating an increased turbulent mixing of fuel and oxidizer.

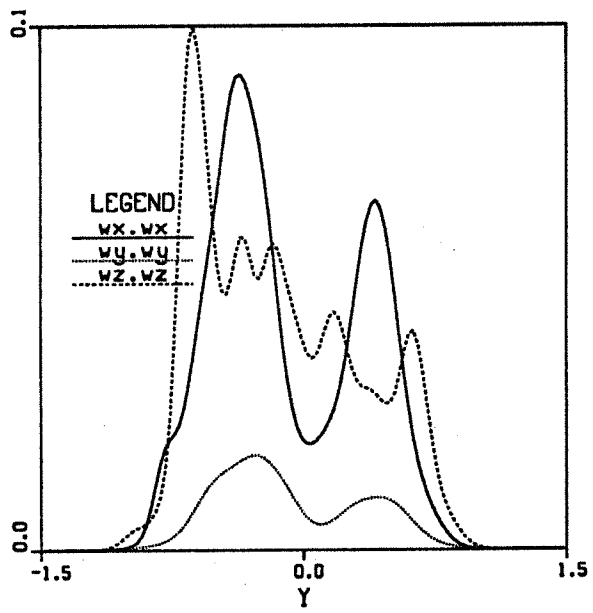
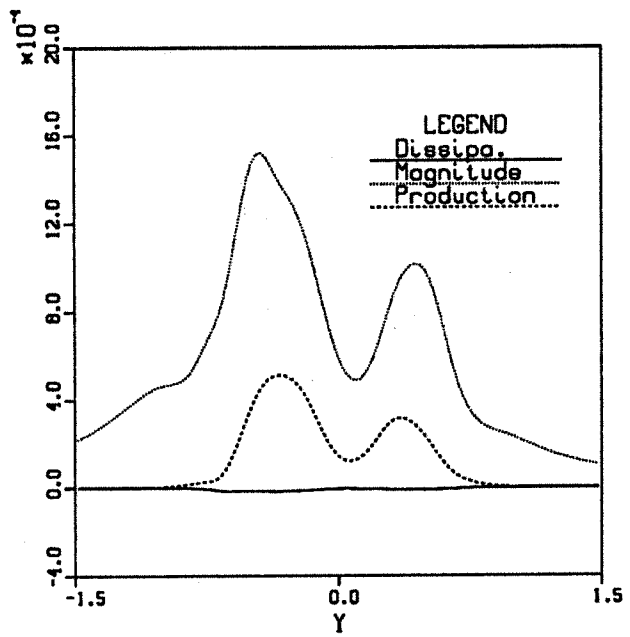


Figure 5.29: (Top) Production rate, dissipation rate and magnitude of the kinetic energy at $t = 105.6$. Note the two peaks of kinetic energy production, one in each. The dissipation rate remains low. (bottom) Components of enstrophy. Note the disparition of the two distinct peaks of $\omega_z \omega_z$. The magnitudes of $\omega_x \omega_x$ and $\omega_y \omega_y$ have strongly increased and $\omega_x \omega_x$ is now the largest component.

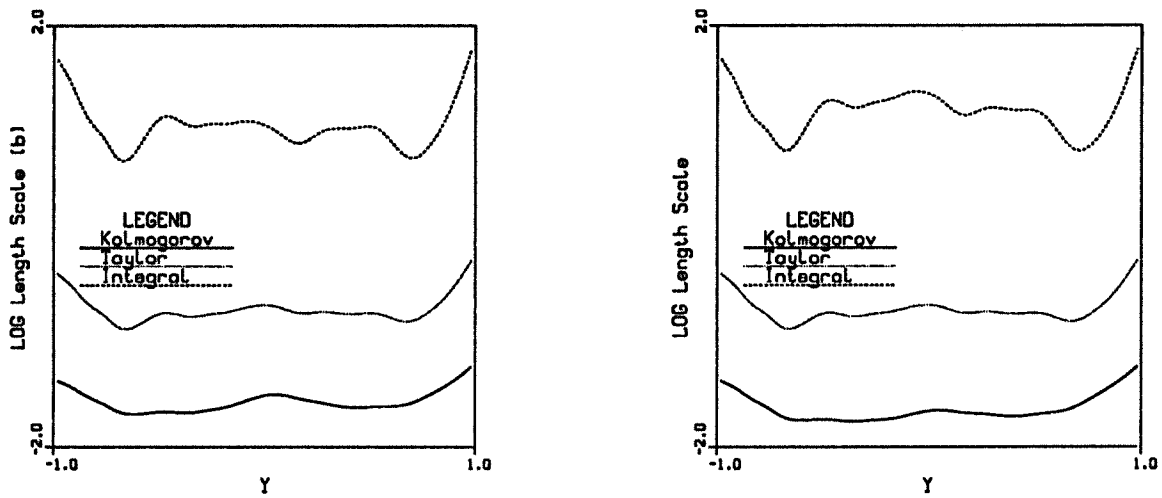


Figure 5.30: Averaged values of Kolmogorov, Taylor and integral scales in all the $y=\text{constant}$ planes, accounting for the fluctuation of viscosity with temperature (left) or using the cold stream viscosity (right).

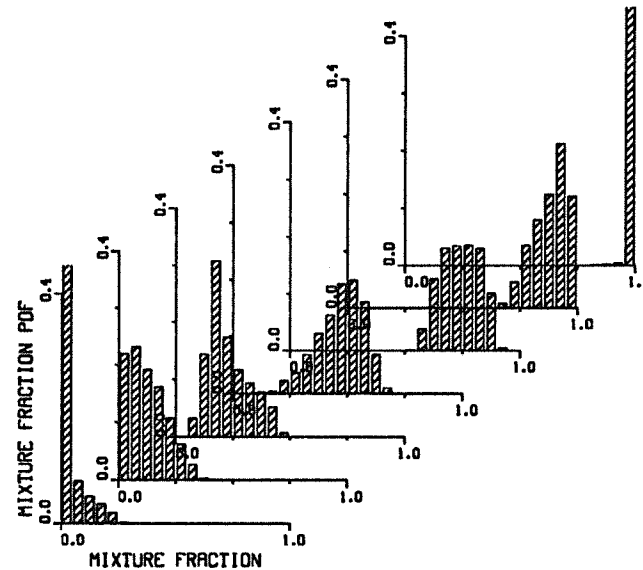


Figure 5.31: Marching PDF accross the layer. Note that the p.d.f. at every locations (7 equal slices from $y = -1$ to $y = +1$) is thin, indicating of poor mixing when the two colayers are present. At $y = 0$ (slice 4) the pdf is skewed towards the oxidizer; the slow outer mode entrains oxidizer from the slow stream better than the fast outer mode entrains fuel from the fast stream.

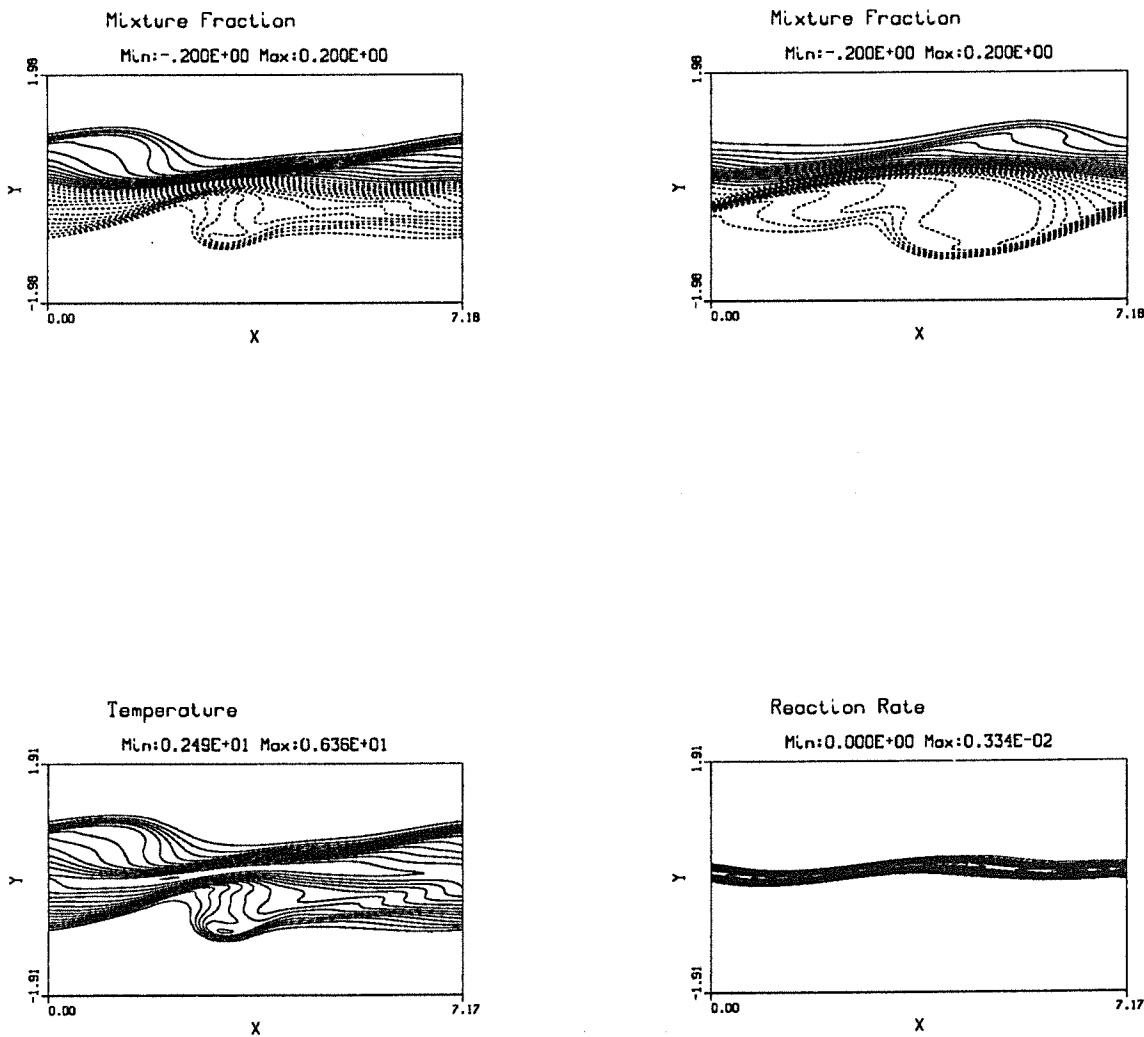


Figure 5.32: Top: Views of the mixture fraction contours at $t = 145.3$ in the plane Z_2 (left) and Z_1 (right). Bottom: Temperature and reaction rate contours in the plane Z_2 . We note that the two-dimensionality of the large-scale structures is lost. However, the reaction zone remains plane. The high temperature region in the middle of the layer is still present like the two colayers.

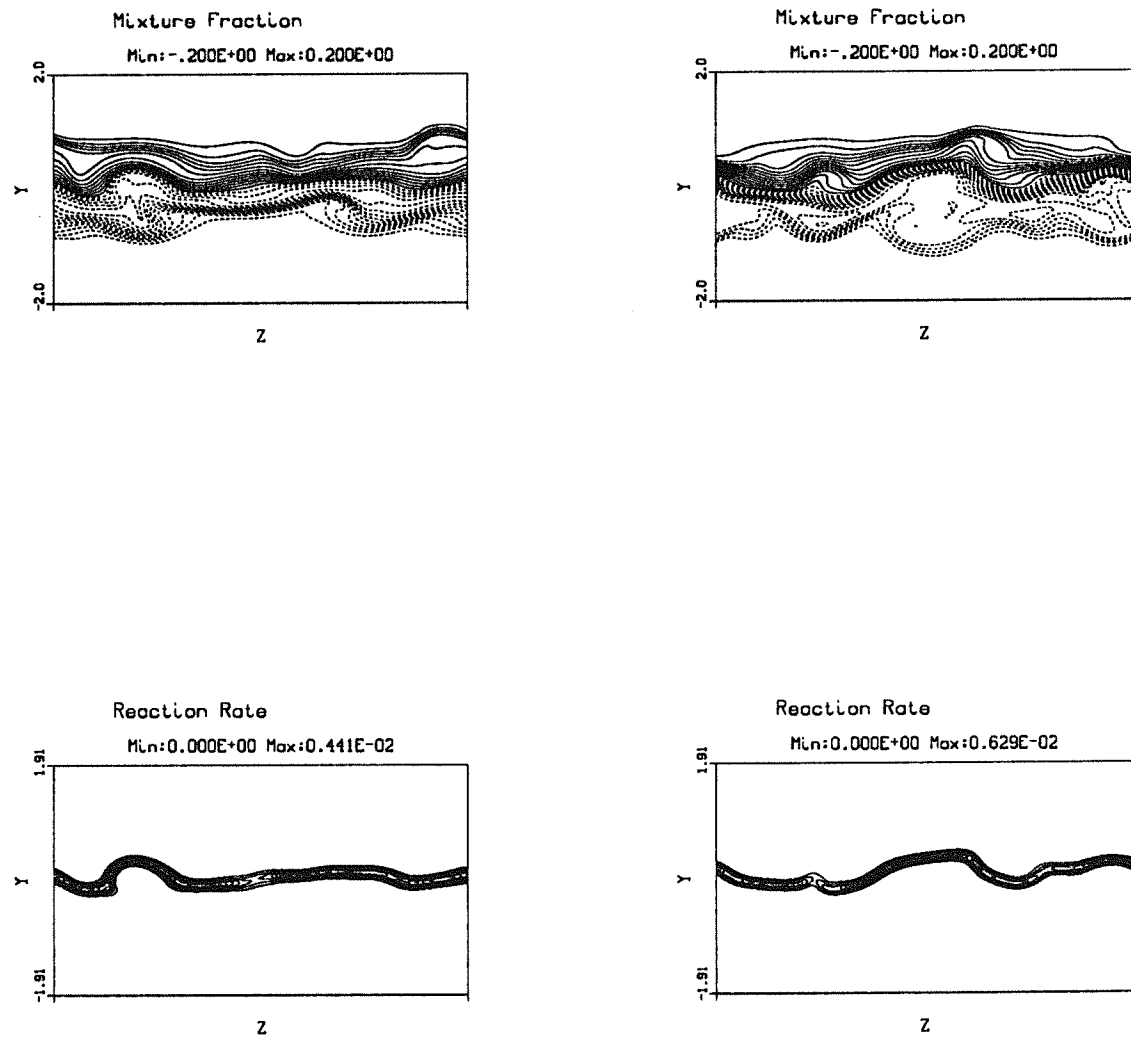


Figure 5.33: End views (flow is coming at you) of the mixture fraction in the plane $x = 0$ (plane X_1) and in the plane $x = 3.6$ ($t = 145.3$). Note the existence of lumps of fluid on both sides of the layer arising from strong streamwise vortices in the layer. The two colayers are preserved but the reaction zone becomes wrinkled by the streamwise vortices.

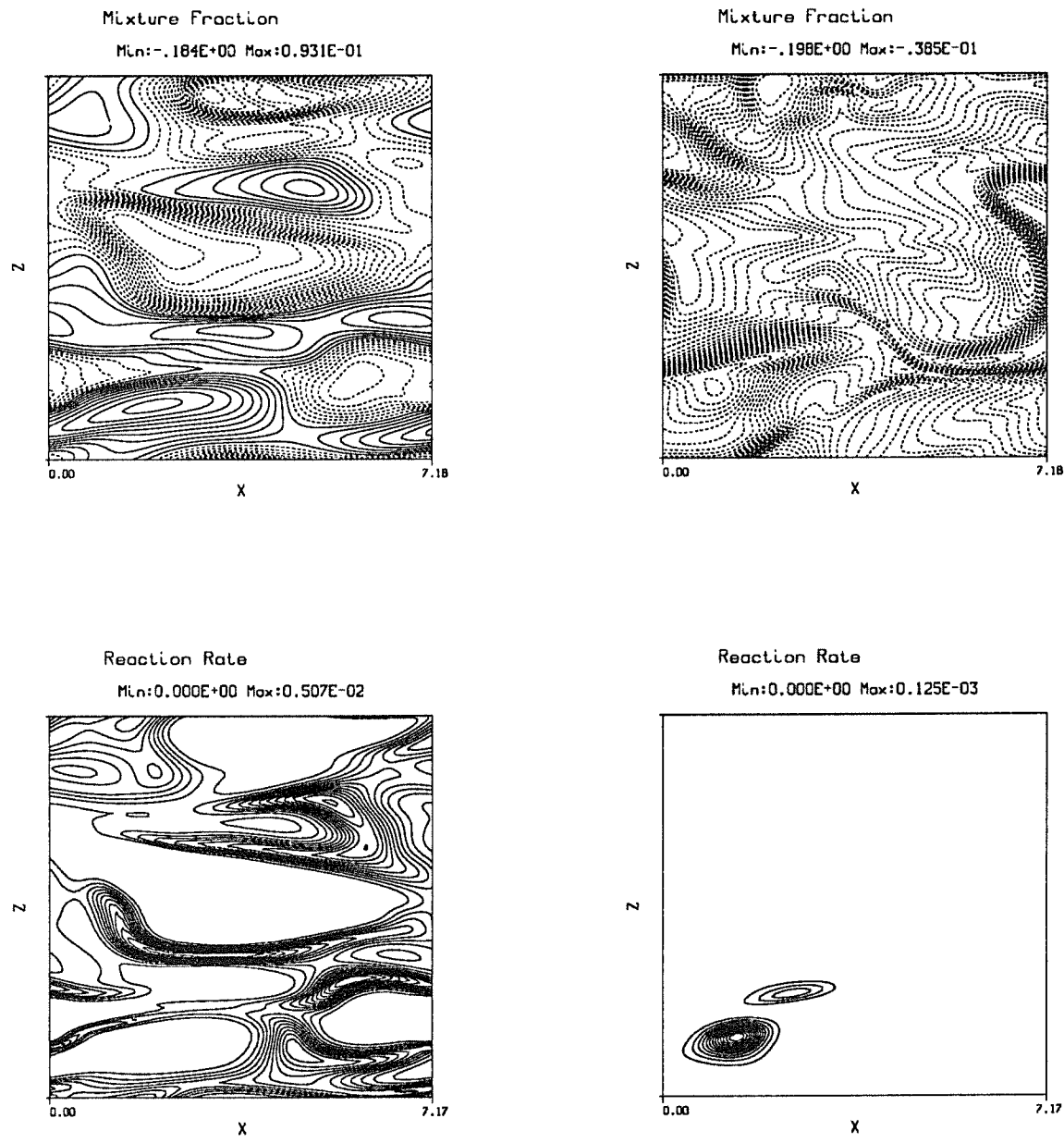


Figure 5.34: Plane cuts of the mixture fraction and reaction rate in the planes Y_1 (left) and Y_2 (right) ($t = 145.3$). Note that both the mixture fraction and reaction rate contours become elongated along x due to the action of streamwise vortices and that the range of mixture fraction present at any y location, is wider than at earlier times.

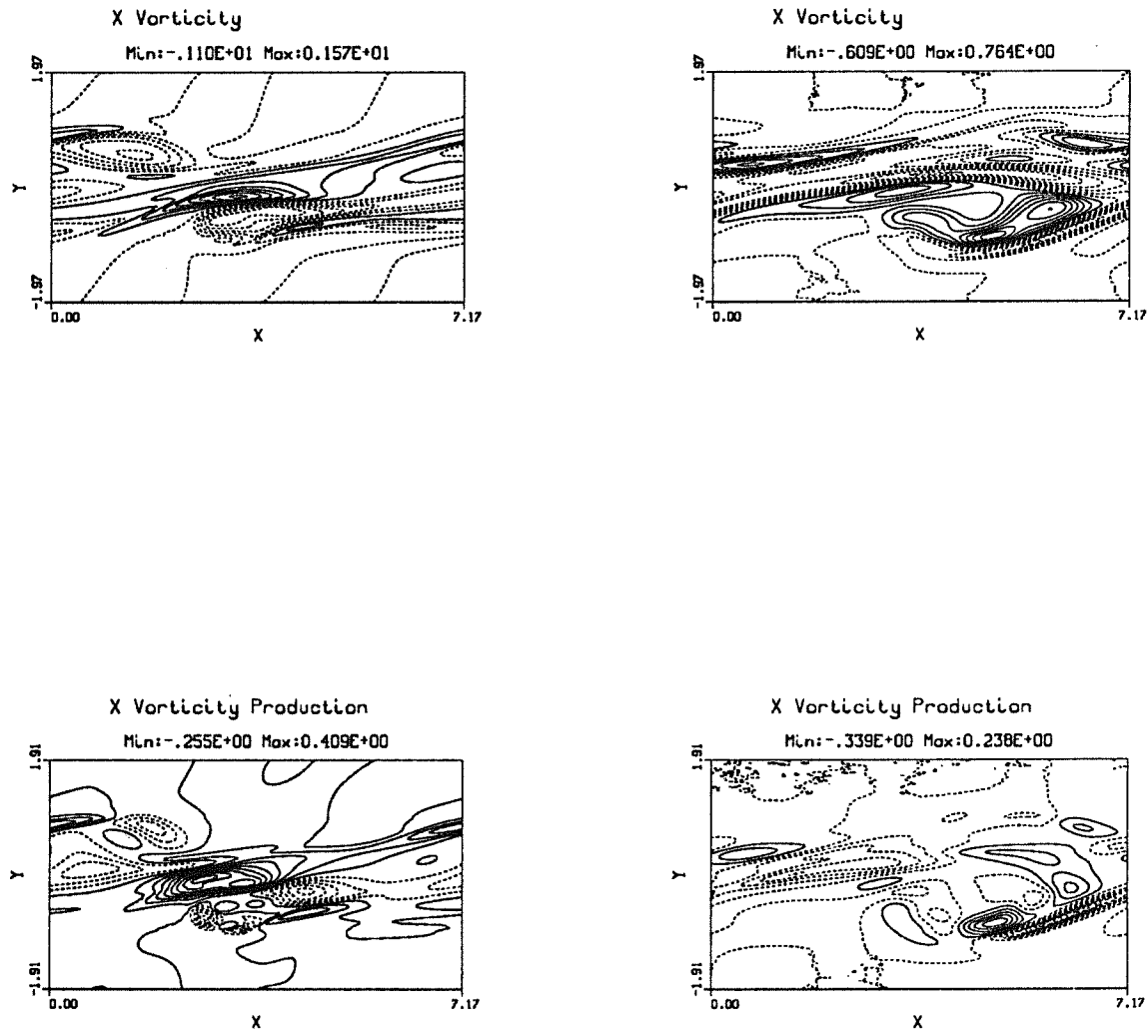


Figure 5.35: Streamwise vorticity and vorticity production terms in planes Z_2 (left) and Z_1 (right) ($t = 145.3$). Note that the vorticity and vorticity production contours are similar in both planes and that ω_x is still increasing with time.

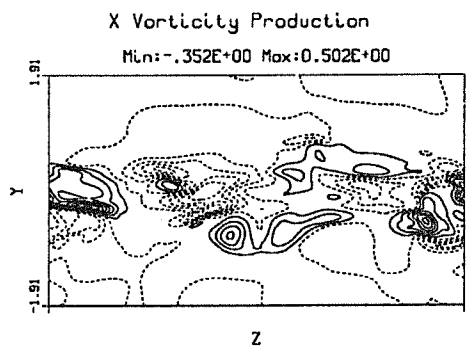
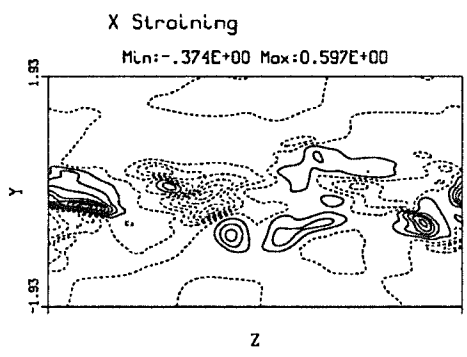
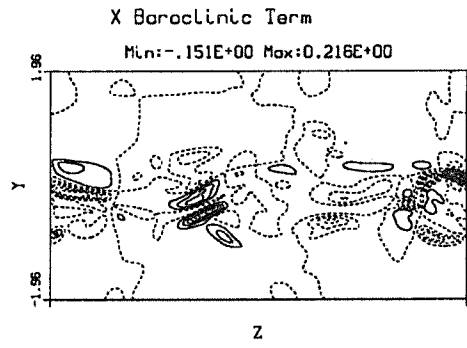
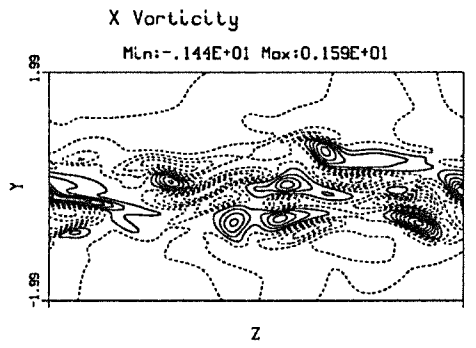


Figure 5.36: Plane cuts of the streamwise vorticity and vorticity production terms at $t = 145.3$ in the plane X_2 , through the slow outer mode large-scale structure. The ω_x field contains multiple structures. The baroclinic term and the straining terms have comparable magnitudes.

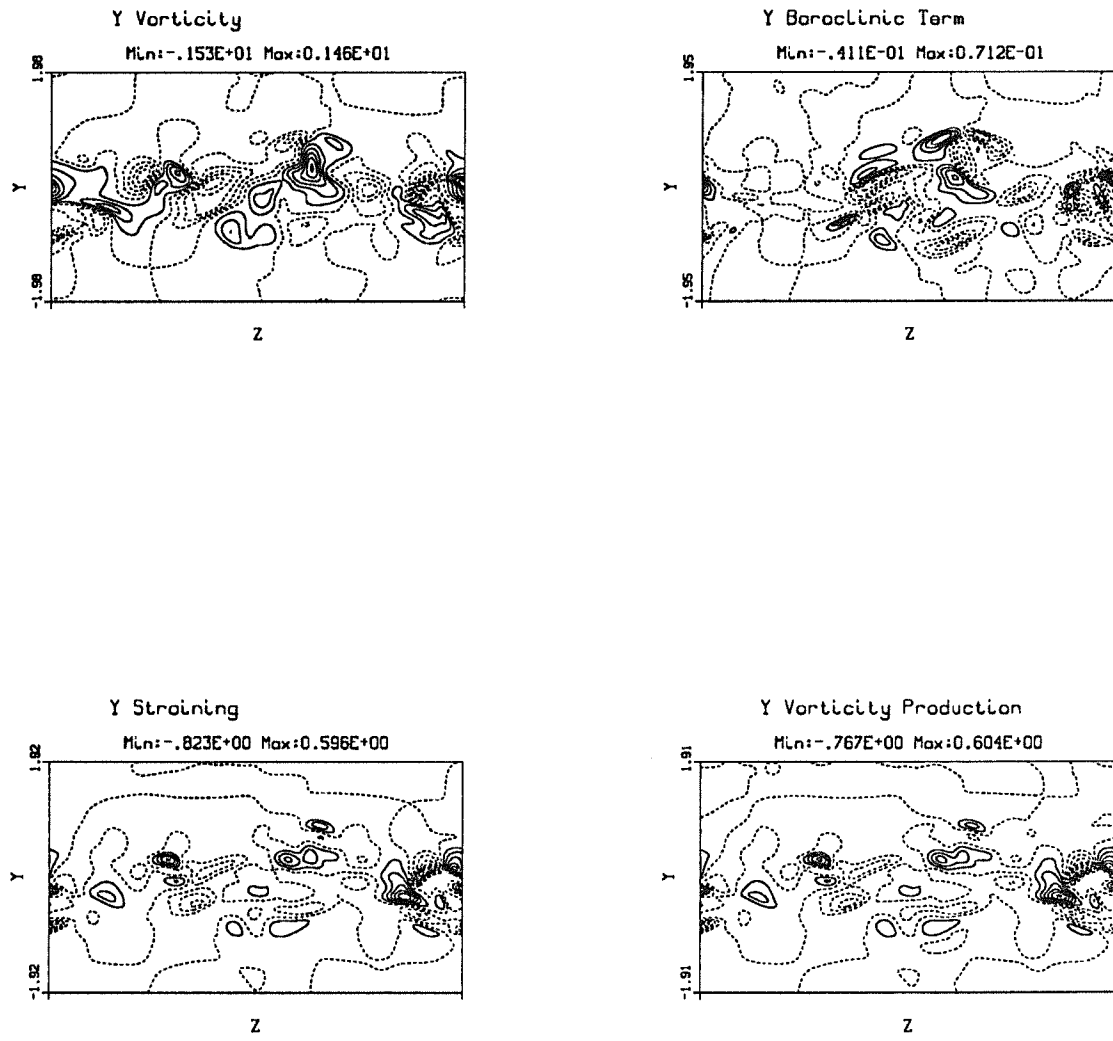


Figure 5.37: Plane cuts of the cross-stream vorticity and vorticity production terms at $t = 145.3$ in the plane X_2 . The ω_y field exhibits multiple small-scale structures. The magnitude of ω_y is comparable with ω_x . The baroclinic term is small compared to the straining term and the vorticity and vorticity production contours are less similar than in the X_1 plane.

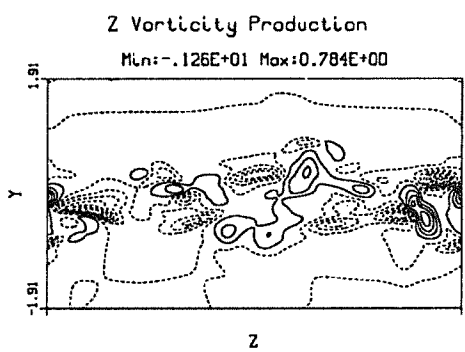
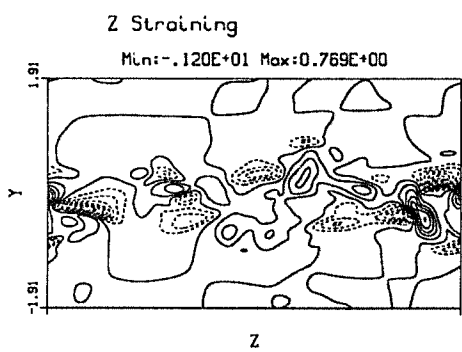
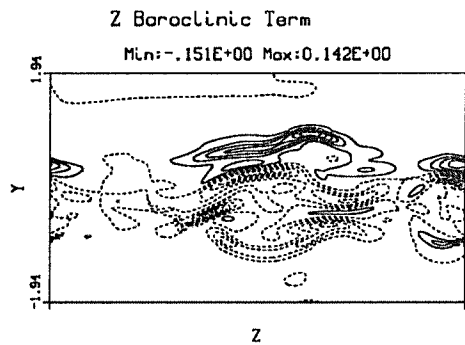
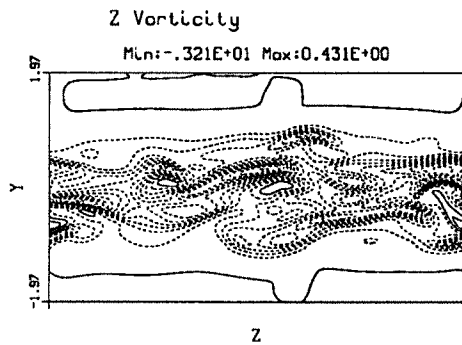
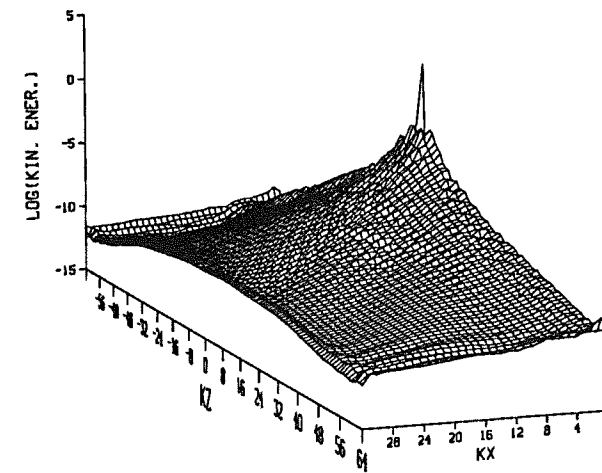


Figure 5.38: Plane cuts of the spanwise vorticity and vorticity production terms at $t = 145.3$ in the plane X_2 . The ω_z field contains multiple structures less energetic than in the plane X_1 and the baroclinic term is small compared to the straining term.

MODAL ENERGY CONTENT



MODAL KINETIC ENERGY

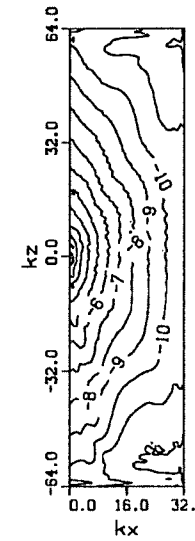


Figure 5.39: (Top) Modal energy content at time $t = 145.3$. (Bottom) Contour plot corresponding to the modal energy content shown on top. Note that iso energy content become elliptic indicating a better transfer of energy to the small-scale streamwise vortices.

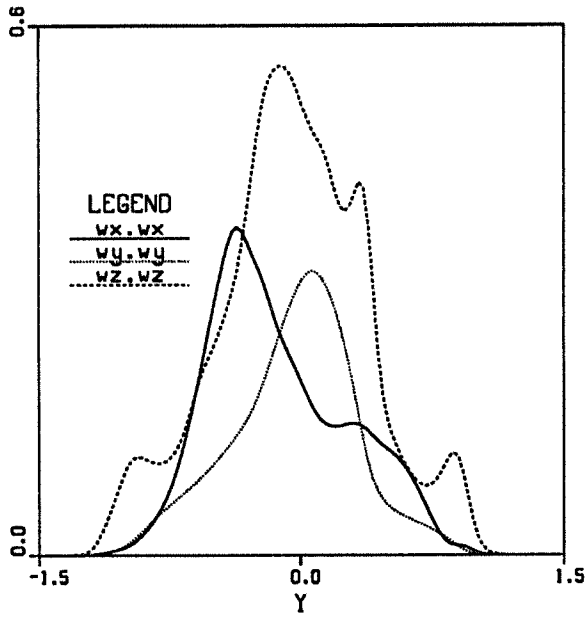
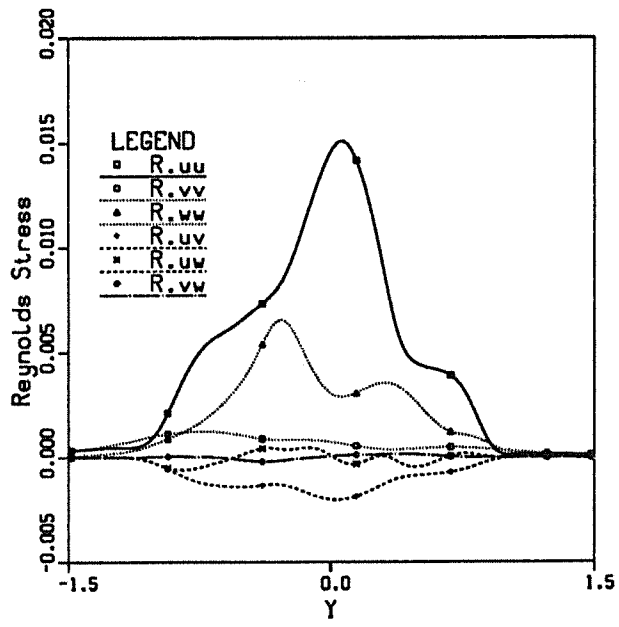


Figure 5.40: (Top) Mean Reynolds stresses at various y -locations of the layer ($t = 145.3$). Note that \overline{uv} now only has one peak in the slow stream as the slow outer mode fundamentals have decayed but before the complete development of the slow subharmonic. (Bottom) Components of enstrophy. Note the disparition of the two distinct peaks of $\overline{\omega_z \omega_z}$. The magnitudes of $\overline{\omega_x \omega_x}$ and $\overline{\omega_y \omega_y}$ strongly increased but $\overline{\omega_z \omega_z}$ is now the dominant term again.

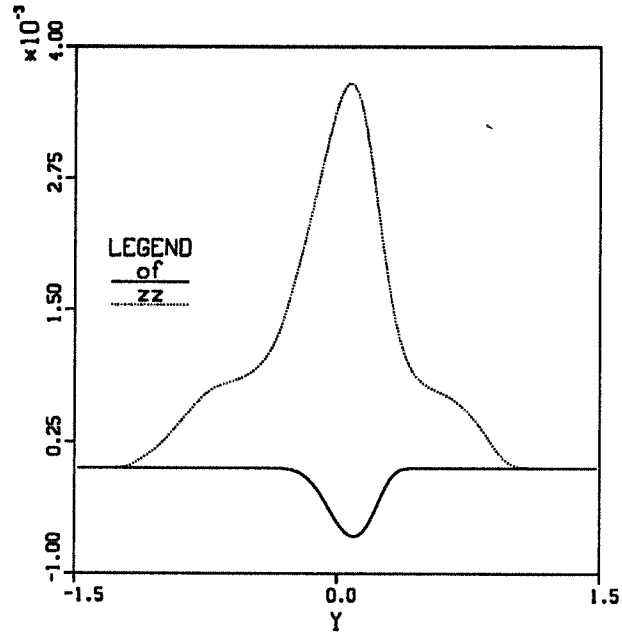
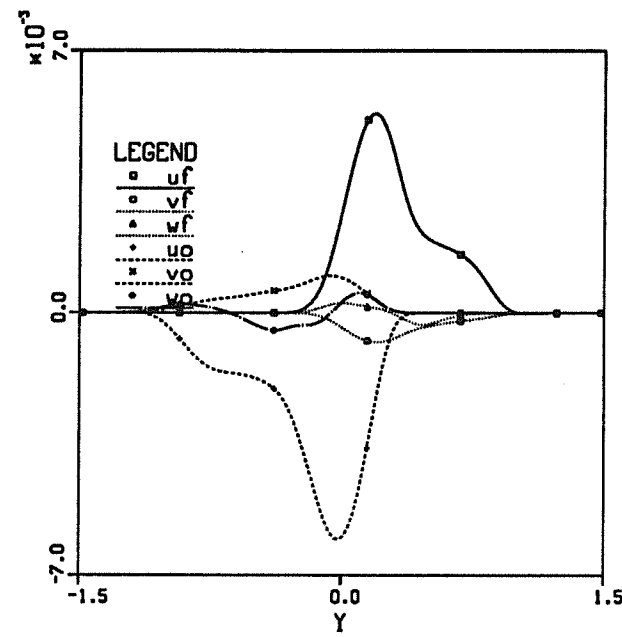


Figure 5.41: (Top) Turbulent transport of species ($t = 145.3$). Note that \bar{v}_f and \bar{v}_o now overlap as the turbulent transport of reacting species to the centerline develops. (Bottom) Variation along y of \bar{zz} and \bar{o}_f . Note the single peak of \bar{zz} showing that the two zones of mixing have disappeared. The growing bump on \bar{o}_f indicates an increase mixing of fuel and oxidizer.

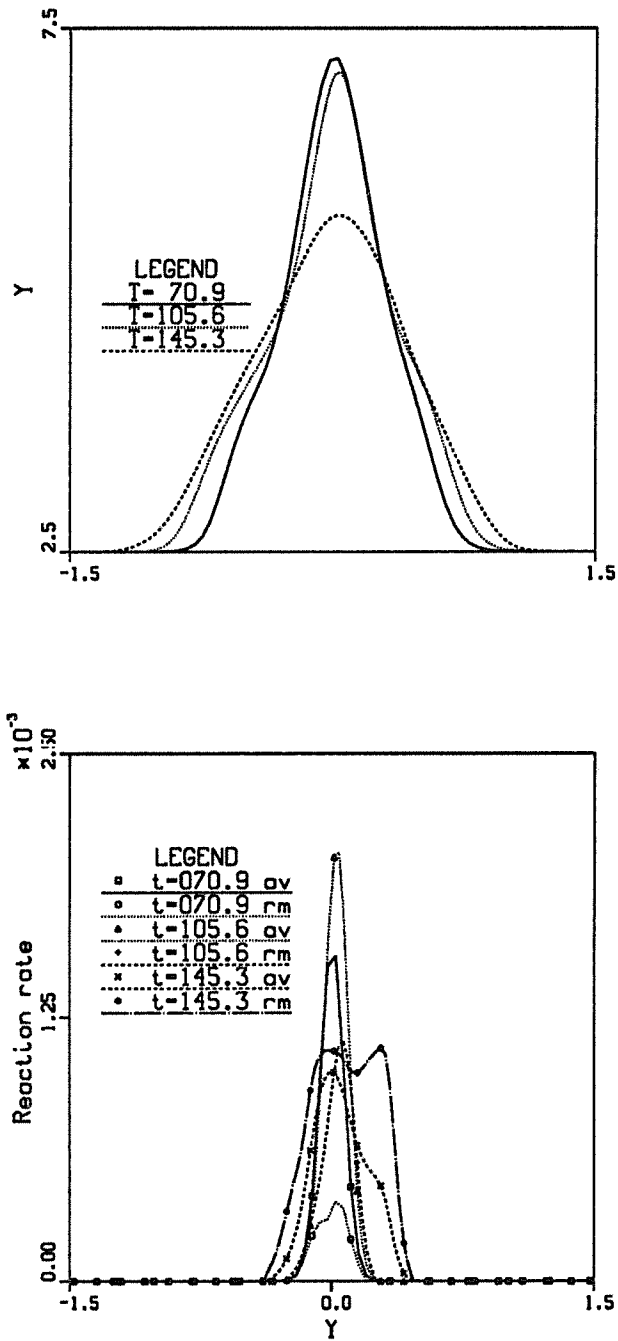


Figure 5.42: (Top) Mean temperature profile at three instants of time ($t = 70.9, t = 105.6, t = 145.3$). We note the temperature drops as the turbulent Damkhöler number gets lower. (Bottom) Mean reaction rate profile at the same times. The root mean square value of the reaction rate is also shown.

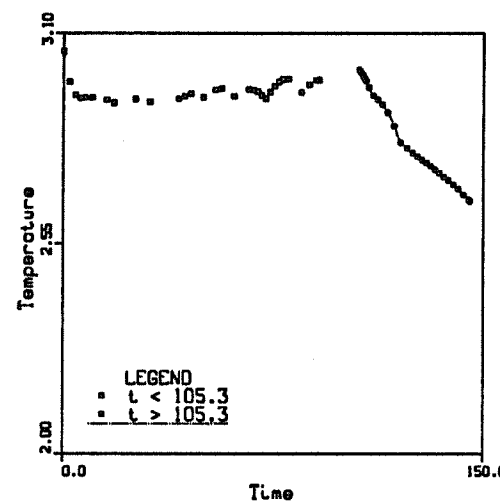


Figure 5.43: History of the maximum temperature in the layer. Note the temperature drop after the mixing transition (when the turbulent Damköler number becomes smaller).

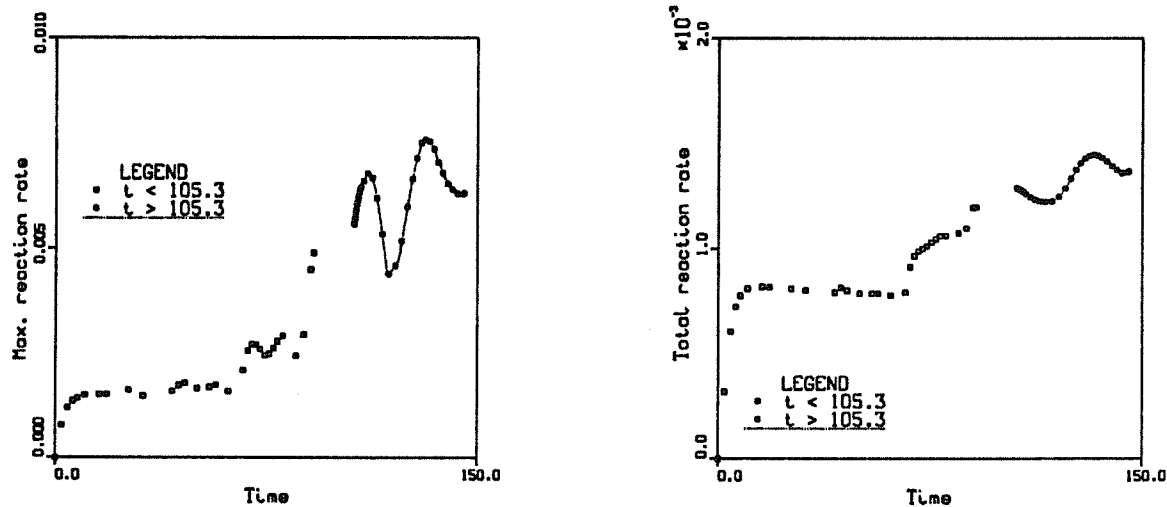


Figure 5.44: Maximum and total reaction rates. Note the strong increase of the total and maximum reaction rates after the mixing transition. The reaction rate shown here should be compared to figure 4.42.

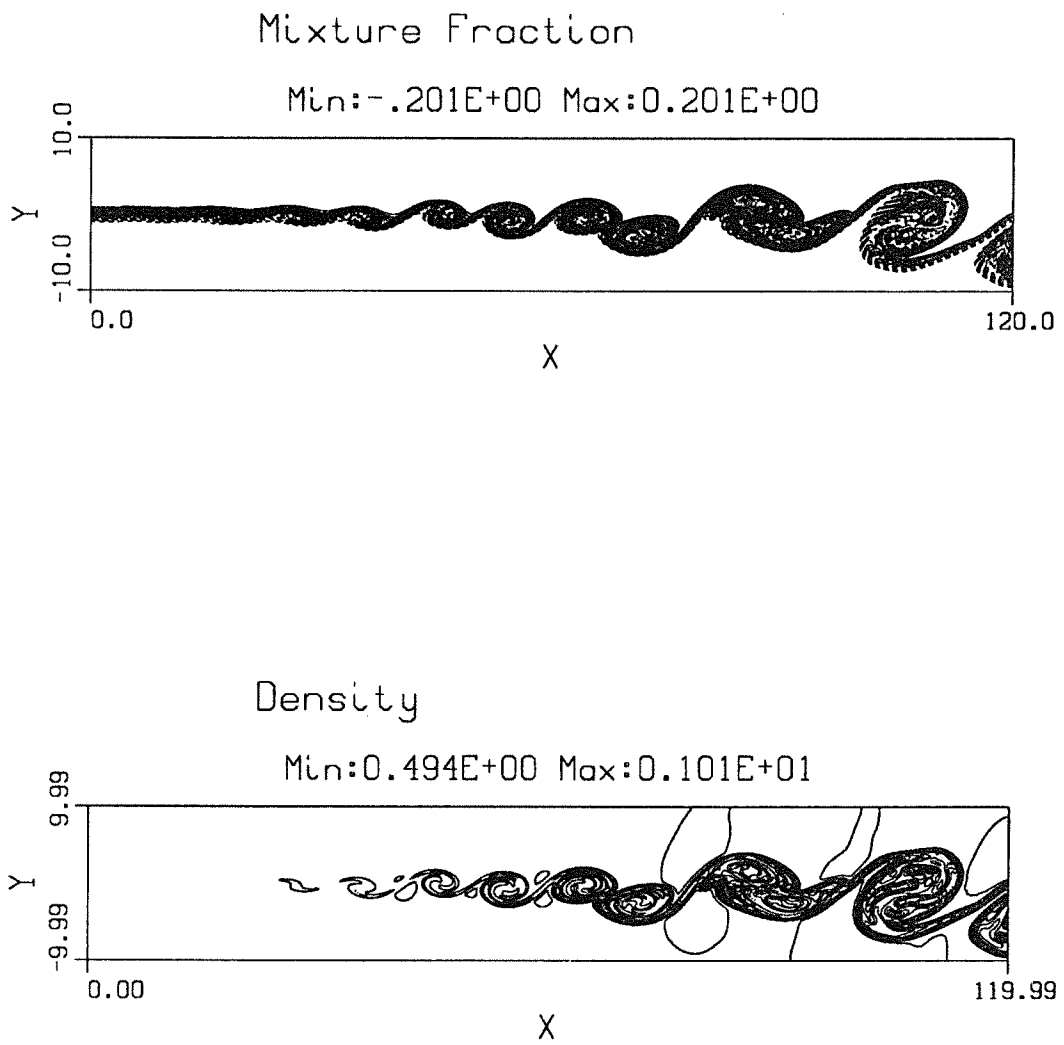


Figure B.1: Ignition of a low Mach number, slow chemistry reacting mixing layer. For this low heat-release mixing layer, the familiar large-scale structures of the central mode are observed, as in incompressible non-reacting mixing layers. ($M_c = 0.15$, $Re = 1000$, $U_2 = 0.5$, $T_2 = 1$, $\Theta = 3$, $Ze = 0$, $Da = 1$) (a) Mixture fraction, (b) density.

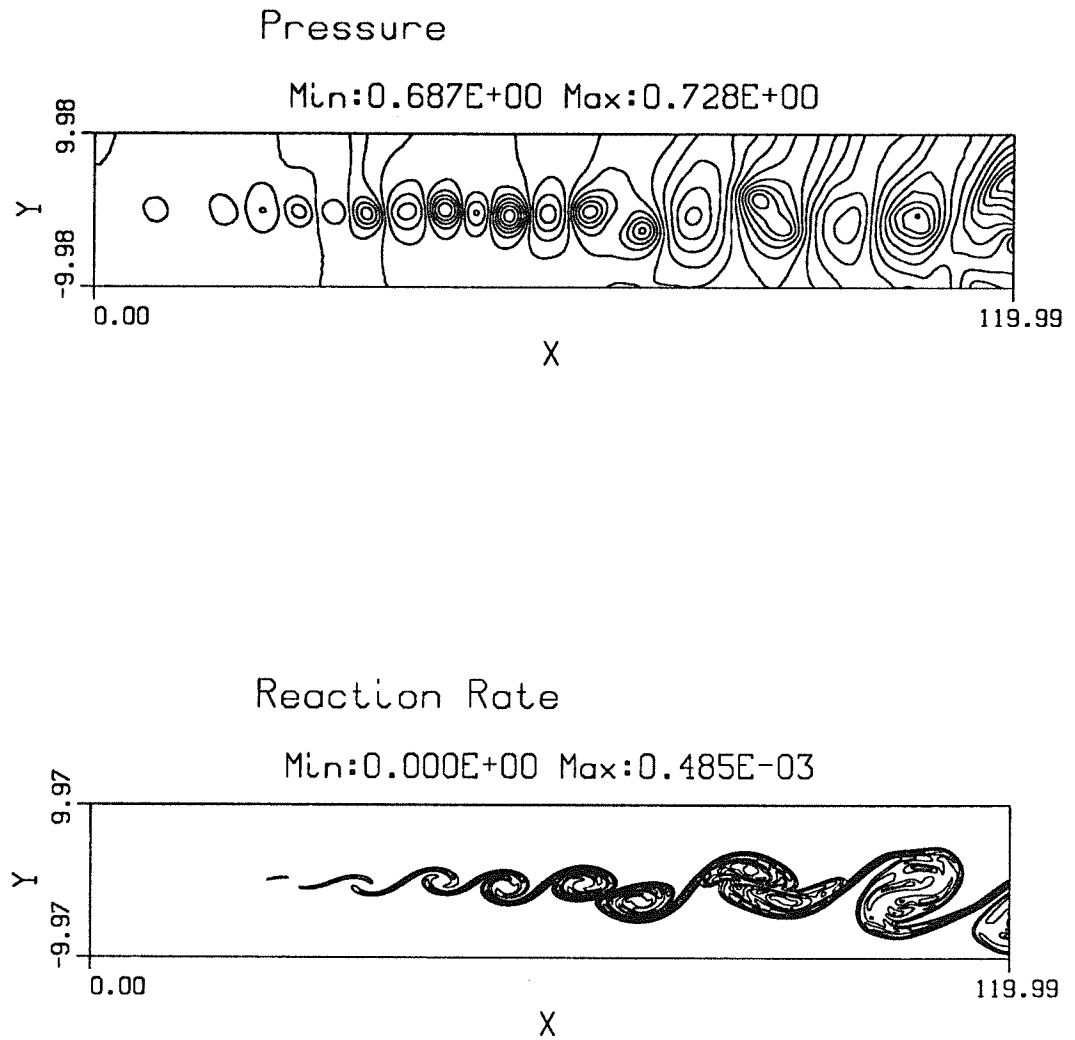


Figure B.1: Ignition of a low Mach number, slow chemistry reacting mixing layer. For this low heat-release mixing layer, the familiar large-scale structures of the central mode are observed, as in incompressible non-reacting mixing layers. ($M_c = 0.15$, $Re = 1000$, $U_2 = 0.5$, $T_2 = 1$, $\Theta = 3$, $Ze = 0$, $Da = 0.03$) (c) Pressure, (d) reaction rate.

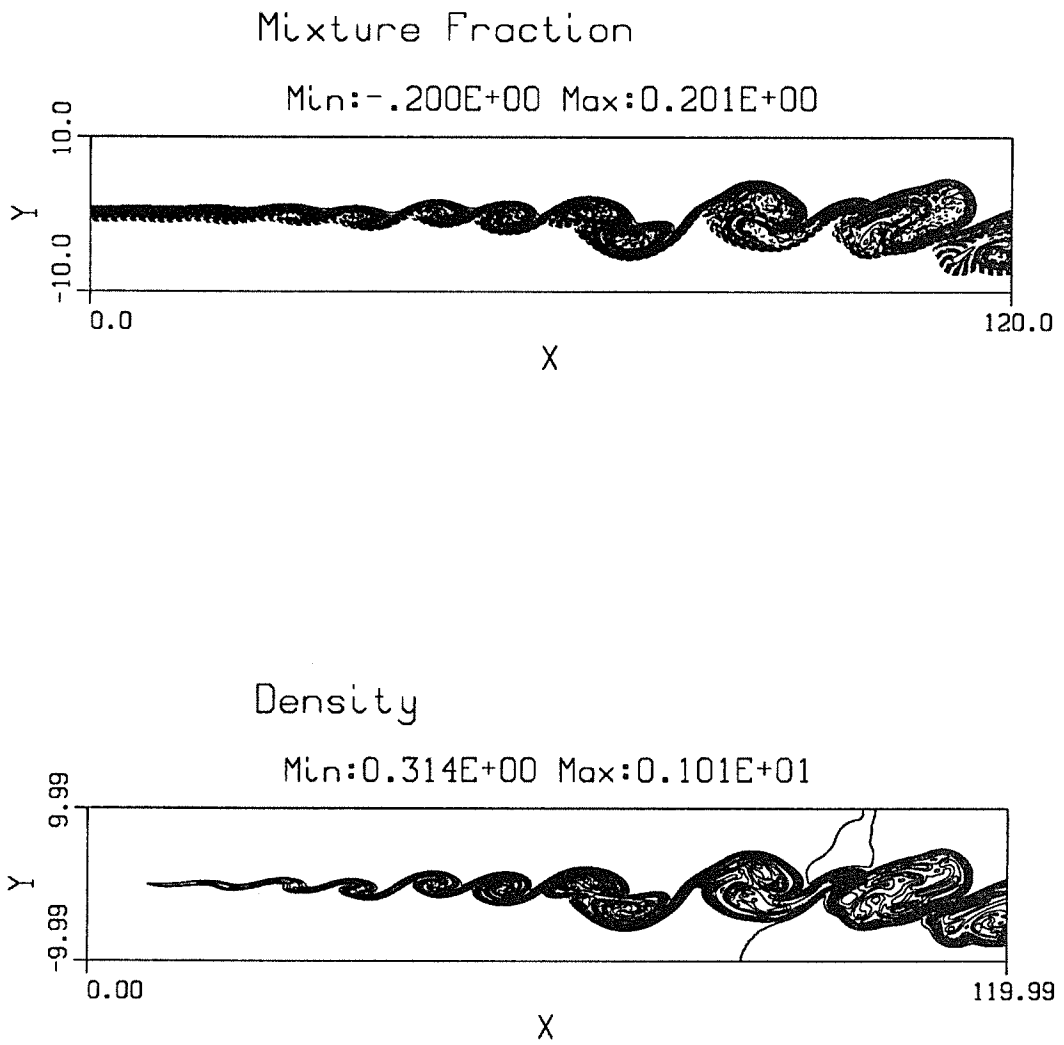


Figure B.2: Ignition of the same low Mach number mixing layer as in figure B.1, but with faster chemistry. For this higher heat-release case, the large-scale structures become inclined at the left of the computational domain. ($M_e = 0.15$, $Re = 1000$, $U_2 = 0.5$, $T_2 = 1$, $\Theta = 3$, $Z_e = 0$, $Da = 0.66$) (a) Mixture fraction, (b) density.

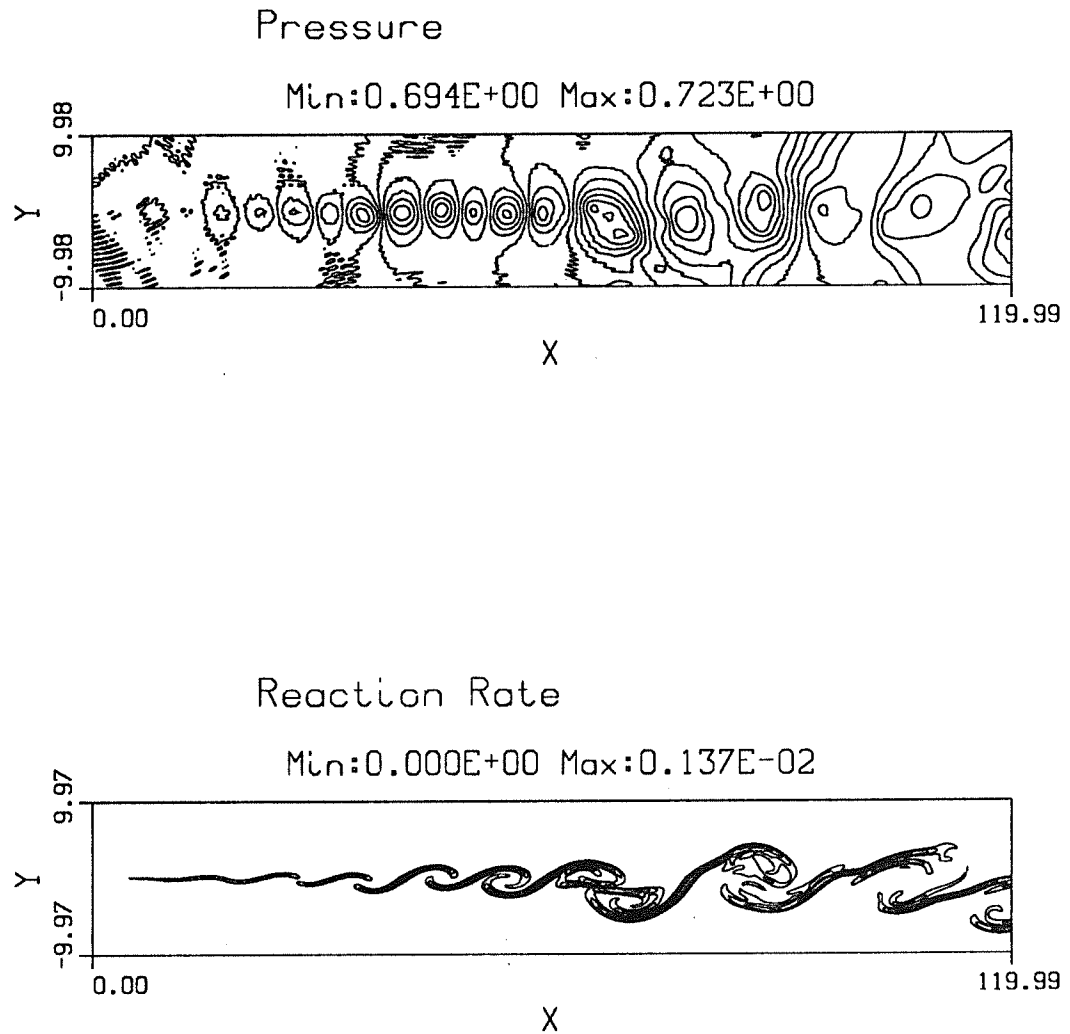


Figure B.2: Ignition of the same low Mach number mixing layer as in figure B.1, but with faster chemistry. Note the reduction of compressibility (smaller pressure fluctuations) and the alignment of the reaction zone with the mean flow. ($M_e = 0.15$, $Re = 1000$, $U_2 = 0.5$, $T_2 = 1$, $\Theta = 3$, $Z_e = 0$, $Da = 0.66$) (c) Pressure, (d) reaction rate.

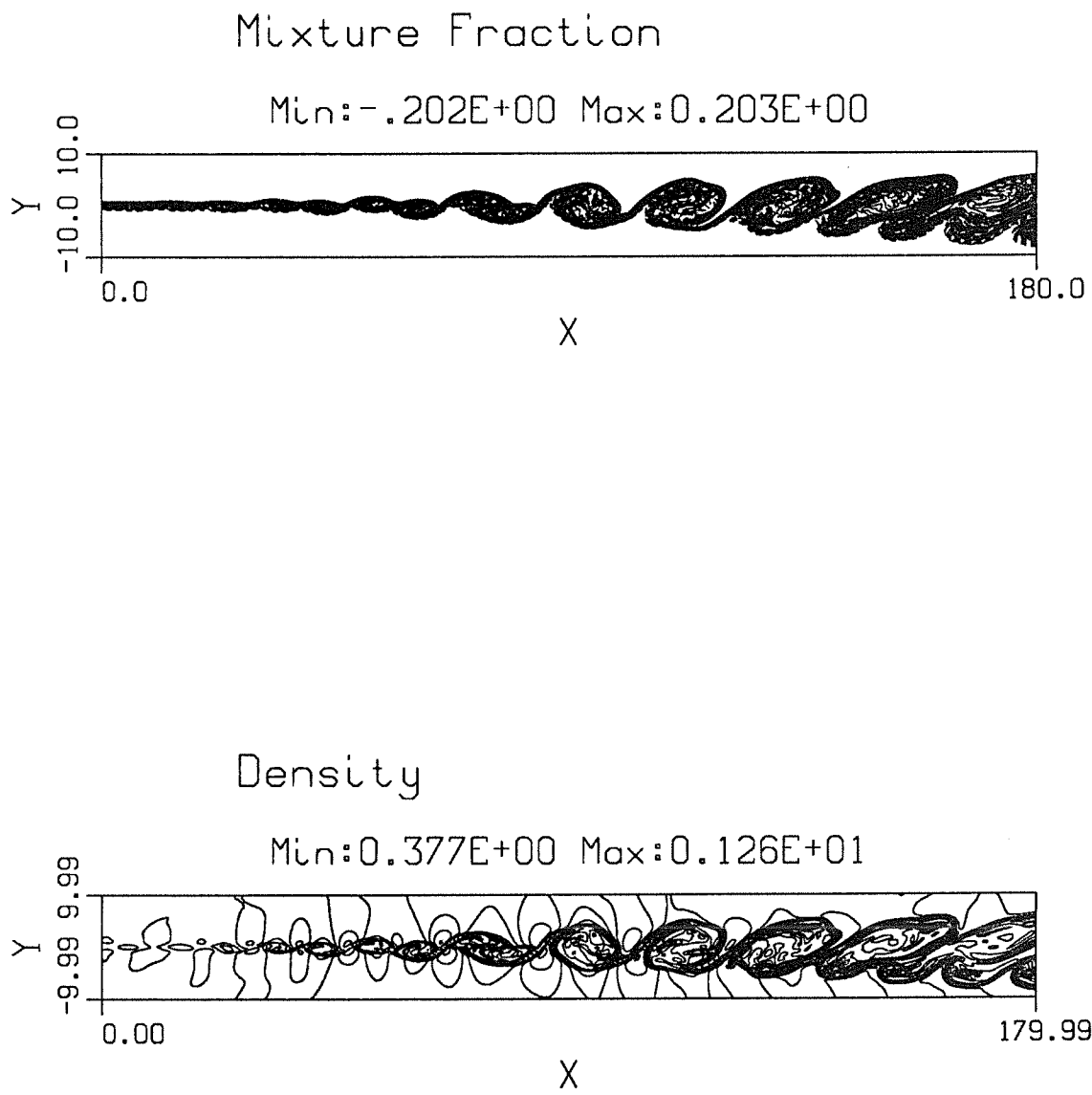


Figure B.3: Ignition of a compressible mixing layer with slow chemistry. For this compressible mixing layer, note the inclination of the large-scale structures during the ignition despite the moderate temperature rise. ($M_c = 0.60$, $Re = 1200$, $U_2 = 0.5$, $T_2 = 1$, $\Theta = 4$, $Ze = 0$, $Da = 0.04$) (a) Mixture fraction, (b) density.

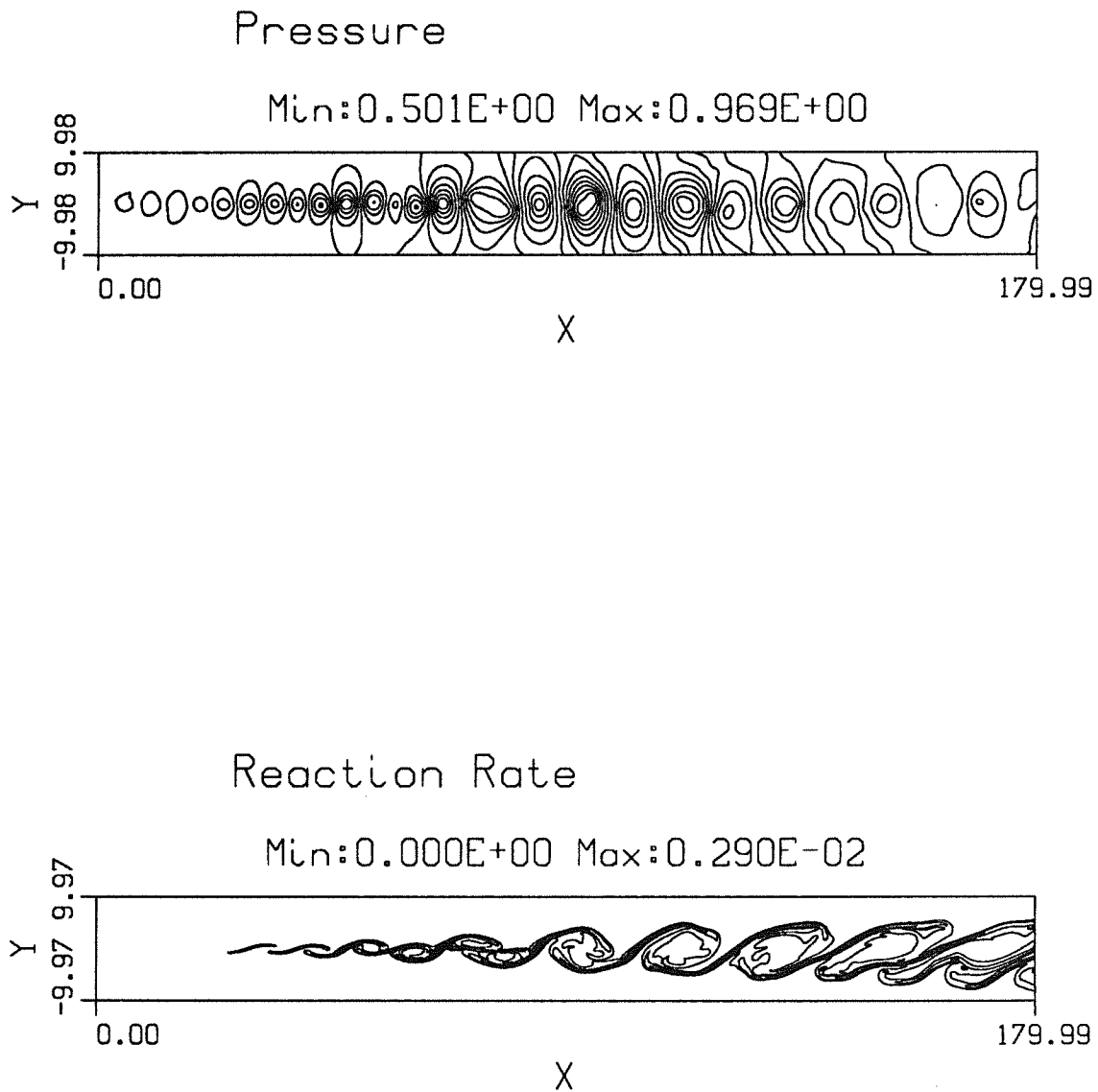


Figure B.3: Ignition of a compressible mixing layer with slow chemistry. For this compressible mixing layer, note the inclination of the large-scale structures during the ignition despite the moderate temperature rise. A reduction of the pressure fluctuations is also observed as on figure B.2. ($M_c = 0.60$, $Re = 1200$, $U_2 = 0.5$, $T_2 = 1$, $\Theta = 4$, $Ze = 0$, $Da = 0.04$) (c) Pressure, (d) reaction rate.

REGIME CHART

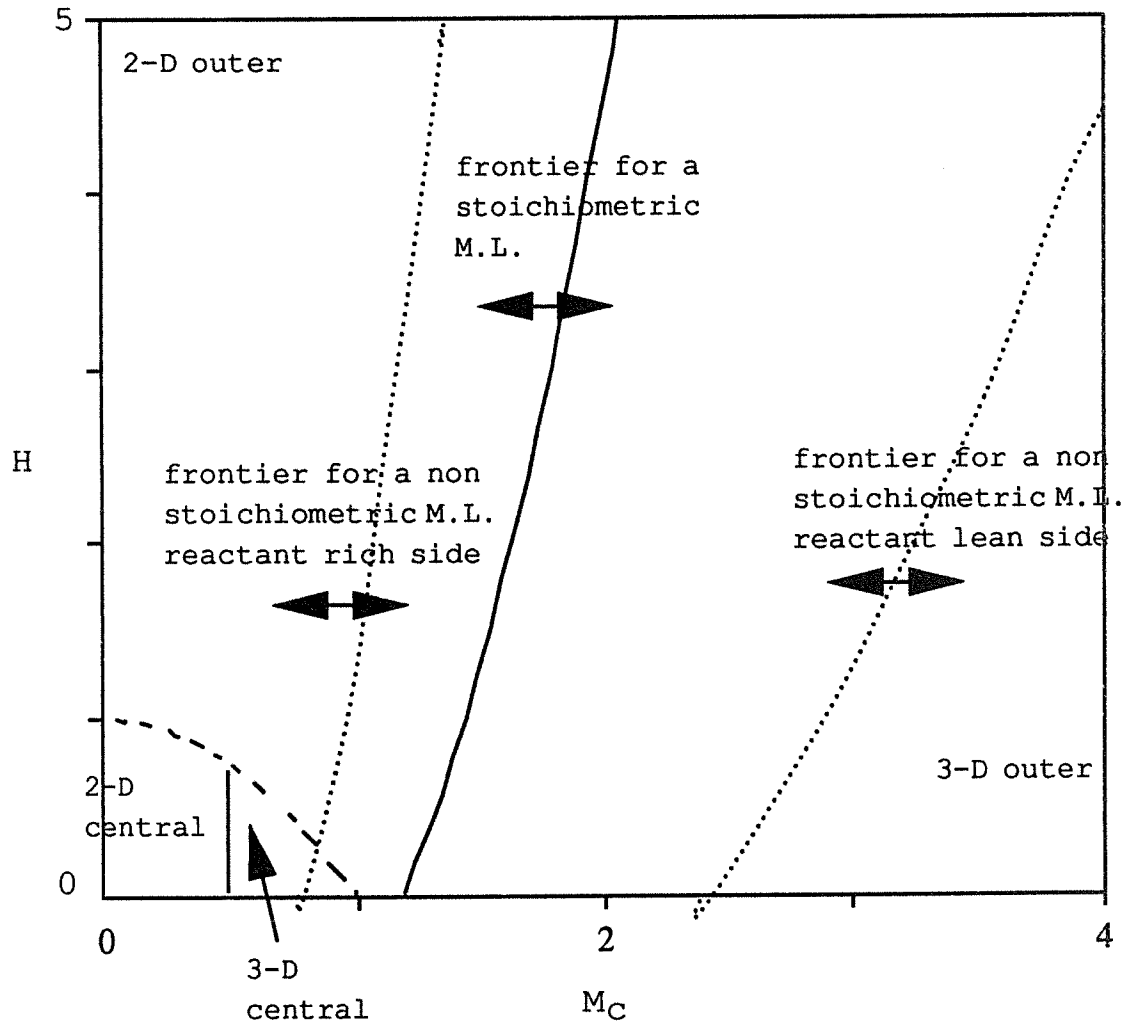


Figure C.1: Regime chart of a mixing layer with equal free-stream temperatures and $\bar{u}_2 = 0.5\bar{u}_1$. The dashed line corresponds to the frontier between central mode and outer modes. The plain line corresponds to the transition from 2-D to 3-D modes (central or outer). The dotted lines correspond to the transition from 2-D outer modes to 3-D outer modes for a non-stoichiometric mixing layer.

REPORT DOCUMENTATION PAGE

1a. REPORT SECURITY CLASSIFICATION Unclassified		1b. RESTRICTIVE MARKINGS													
1c. SECURITY CLASSIFICATION AUTHORITY		3. DISTRIBUTION / AVAILABILITY OF REPORT Approved for public release; distribution is unlimited.													
2b. DECLASSIFICATION / DOWNGRADING SCHEDULE															
4. PERFORMING ORGANIZATION REPORT NUMBER(S) TF-56		5. MONITORING ORGANIZATION REPORT NUMBER(S)													
6a. NAME OF PERFORMING ORGANIZATION Stanford University		6b. OFFICE SYMBOL (If applicable) AFOSR													
6c. ADDRESS (City, State, and ZIP Code) Stanford, CA 94305		7a. NAME OF MONITORING ORGANIZATION AFOSR													
7b. ADDRESS (City, State, and ZIP Code) Building 410 Bolling Air Force Base, DC 20332-6448															
8a. NAME OF FUNDING / SPONSORING ORGANIZATION AFOSR/NA		8b. OFFICE SYMBOL (If applicable) AFOSR-90-0151-C													
8c. ADDRESS (City, State, and ZIP Code) Building 410, Bolling AFB, DC 20332-6448		9. PROCUREMENT INSTRUMENT IDENTIFICATION NUMBER 10. SOURCE OF FUNDING NUMBERS													
		PROGRAM ELEMENT NO. 61103D	PROJECT NO. 3484												
		TASK NO. AS	WORK UNIT ACCESSION NO.												
11. TITLE (Include Security Classification) A Numerical Investigation of the Compressible Reacting Mixing Layer															
12. PERSONAL AUTHOR(S) O. H. Planche and W.C. Reynolds															
13a. TYPE OF REPORT Technical		13b. TIME COVERED FROM _____ TO _____													
		14. DATE OF REPORT (Year, Month, Day) 1992, October 10													
15. PAGE COUNT 376															
16. SUPPLEMENTARY NOTATION															
17. COSATI CODES			18. SUBJECT TERMS (Continue on reverse if necessary and identify by block number) Compressible flow, reacting mixing layer, linear stability, transition, turbulence.												
<table border="1"> <thead> <tr> <th>FIELD</th> <th>GROUP</th> <th>SUB-GROUP</th> </tr> </thead> <tbody> <tr> <td></td> <td></td> <td></td> </tr> <tr> <td></td> <td></td> <td></td> </tr> <tr> <td></td> <td></td> <td></td> </tr> </tbody> </table>			FIELD	GROUP	SUB-GROUP										
FIELD	GROUP	SUB-GROUP													
19. ABSTRACT (Continue on reverse if necessary and identify by block number) An important aspect of supersonic combustion is the proper mixing of fuel and oxidizer. Here, linear stability analysis and direct numerical simulations (DNS) are used to examine the effect of heat release and compressibility on mixing in high-speed mixing layers. The results suggest that mixing of fuel and oxidizer by large-scale engulfment of fluid from both sides does not occur at high Mach numbers.															
Linear stability analysis indicates that the existence of two maxima on the mean density weighted vorticity profile ($\rho d\bar{U}/dy$) leads to the existence of two distinct "outer modes", each associated with one of the free streams. Each mode mixes only fresh gas from this stream with product from the middle of the layer, and its phase velocity is comparable with the mean velocity on its side of the reaction zone. Increasing heat release is shown to reduce the obliquity of the outer modes and to increase the spreading angle of the layer.															
(continued)															
20. DISTRIBUTION / AVAILABILITY OF ABSTRACT <input checked="" type="checkbox"/> UNCLASSIFIED/UNLIMITED <input type="checkbox"/> SAME AS RPT. <input type="checkbox"/> DTIC USERS		21. ABSTRACT SECURITY CLASSIFICATION Unclassified													
22a. NAME OF RESPONSIBLE INDIVIDUAL Julian M. Tishkoff		22b. TELEPHONE (Include Area Code) (202) 767-4935													
		22c. OFFICE SYMBOL AFOSR/NA													

19. Abstract (continued)

The usual convective Mach number is inappropriate for the outer modes. Instead, the "flame convective Mach numbers" are introduced and shown to be preferable parameters for correlating compressibility effects on the outer modes. The possibility of controlling the mixing by judicious positioning of the flame sheet is also suggested by the analysis.

DNS of the temporally-developing mixing layer were run both on the Cray Y-MP and on the Intel iPSC860 Hypercube to confirm linear stability results and to study non-linear effects related to growth and pairing. It is shown that the reacting mixing layer behaves as two independent colayers arising from the outer modes, with mixing occurring between fuel and product on one side of the layer and between oxidizer and product on the other side. The reaction zone remains approximately plane, with little creation of new flame surface. The development of each outer mode is shown to be governed by the baroclinic torque. The familiar vortex roll-up and pairing seen in low-speed mixing layer are not observed. Instead, it is shown that the growth of each outer mode modifies of the mean density and baroclinic torque profiles, which in turn causes the decay of this outer mode and the emergence of new outer modes of larger scale.

The transition to turbulence was simulated and shown to preserve the two colayers. Transition arises from the rapid growth of streamwise vortices, and strongly increases the total reaction rate. The resulting turbulent mixing layer appears dominated by large fast and slow independent outer eddies and smaller-scale streamwise vortices.